Proceedings of the Fourth ASTM-EURATOM Symposium
on Reactor Dosimetry

RADIATION METROLOGY TECHNIQUES, DATA BASES, AND STANDARDIZATION

National Bureau of Standards
Gaithersburg, Maryland
March 22–26, 1982

Volume I

Proceedings of the Fourth ASTM-EURATOM Symposium on Reactor Dosimetry

RADIATION METROLOGY TECHNIQUES, DATA BASES, AND STANDARDIZATION

Volume I

National Bureau of Standards
Gaithersburg, Maryland
March 22–26, 1982

Edited by

F. B. K. Kam

SYMPOSIUM COMMITTEES

ASTM Symposium Committee

W. N. McElroy, Chairman, E10.15, Hanford Engineering Development Laboratory

F. B. K. Kam, Vice-Chairman, E10.05, Oak Ridge National Laboratory

G. P. Lamaze, Secretary, E10.05, National Bureau of Standards

ASTM Program Committee

Chairman, F. B. K. Kam, Oak Ridge National Laboratory

Co-chairman, E. B. Norris, Southwest Research Institute

Secretary, J. Schmotzer, Babcock and Wilcox

Local Arrangements Chairmen, C. M. Eisenhauer and J. A. Grundl, National Bureau of Standards

Members

S. L. Anderson, Westinghouse, USA

C. D. Bingham, U.S. DOE, New Brunswick Laboratory

A. M. Fabry, CEN/SCK, Belgium

J. R. Hawthorne, Naval Research Laboratory, USA

F. Hegedus, Swiss Federal Institute for Reactor
   Research, EIR, Switzerland

B. A. Magurno, Brookhaven National Laboratory, USA

E. D. McGarry, National Bureau of Standards, USA

A. Sekiguchi, University of Tokyo, Japan

C. Z. Serpan, Nuclear Regulatory Commission, USA

R. A. Shaw, Electric Power Research Institute, USA

F. W. Stallmann, University of Tennessee and
   Oak Ridge National Laboratory, USA

H. Tourwé, CEN/SCK, Belgium

Ex-officio Liaison Members

E10 Committee and Subcommittee Chairmen

European Symposium Committee

Chairman, J. P. Genthon, Centre d'Études Nucléaires de Saclay

Vice-Chairman, W. Schneider, Kernforschungsanlage, Jülich

Scientific Secretary, J. Röttger, Joint Research Center, Petten

Members

R. Dierckx, Joint Research Center, Ispra

A. Fabry, CEN/SCK, Belgium

A. Fudge, Atomic Energy Research Establishment,
   Harwell, U.K.

P. Mas, Centre d'Études Nucleaires de Grenoble

M. Petilli, CNEN, Casaccia

S. Wright, United Kingdom Atomic Energy Authority,
   Harwell

W. Zijp, ECN, Petten

PROGRAM SUMMARY

Monday, March 22, 1982

Welcoming Address: *J. D. Hoffman (NBS)*

SESSION A.1: Light Water Reactors-I

Chairmen: *R. A. Lewis* (B&W) and *W. Schneider (KFA)*

SESSION A.2: Fast Reactors

Chairmen: *P. B. Hemmig* (U.S. DOE) and *V. Sanguist* (CESNEF)

SESSION A.3: Data and Techniques

Chairmen: *J. A. Grundl* (NBS) and *A. J. Fudge* (AERE, Harwell)

WORKSHOP: Neutron and Gamma Transport Calculations

Chairmen: *R. E. Maerker* (ORNL) and *M. Austin* (RR&A)

ASTM Task Group Meetings—46th EWGRD Meeting

Tuesday, March 23, 1982

SESSION B.1: Light Water Reactors-II

Chairmen: *R. A. Shaw* (EPRI) and *J. Ahlf* (GKSS)

SESSION B.2: Benchmarks and Nuclear Data

Chairmen: *G. Hansen* (LASL) and *E. Alberts* (PTB)

SESSION B.3: Fusion-I

Chairmen: *C. E. Clifford* (PPPL) and *R. Dierckx* (JRC, Ispra)

Wednesday, March 24, 1982

SESSION C.1: Damage Correlation

Chairmen: *L. Steele* (NRL) and *A. Capgras* (CEN, Saclay)

SESSION C.2: Nuclear Data Needs and Problems

Chairmen: *J. W. Lewellen* (U.S. DOE) and *N. Kocherov* (IAEA)

SESSION C.3: Fusion-II

Chairmen: *L. Greenwood* (ANL) and *O. N. Jarvis* (AERE, Harwell)

WORKSHOP: Nuclear Data and Benchmarks

Chairmen: *B. Magurno* (BNL) and *A. Fabry* (CEN/SCK)

Joint Program Meeting for the 5th ASTM-EURATOM Symposium

Thursday, March 25, 1982

SESSION D.1: Light Water Reactors-III

Chairmen: *N. Randall* (NRC) and *P. Mas* (CEN, Grenoble)

SESSION D.2: Adjustment Codes and Uncertainties

WORKSHOP: LWR Surveillance & Dosimetry

Chairmen: *A. Lowe* (B&W) and *H. Tourwé* (CEN/SCK)

WORKSHOP: Adjustment Codes and Uncertainties

Chairmen: *F. W. Stallmann* (ORNL) and *W. L. Zijp* (Petten)

Planning Meeting for CAPRICE

Friday, March 26, 1982

Remarks: *C. Z. Serpan* (NRC) and *W. Schneider* (KFA)

Symposium Highlights: Chairmen of the Symposium

Closing Summary: *F. B. K. Kam* (ORNL) and *P. Von der Hardt* (JRC, Petten)

CONTENTS OF VOLUME I

SESSION A.3: DATA AND TECHNIQUES

SESSION B.1: LIGHT WATER REACTORS-II

PREFACE

These proceedings contain the papers that were submitted for the Fourth ASTM-EURATOM Symposium on Reactor Dosimetry. This series of biennial international symposia brings together specialists from many countries to provide a forum for the exchange of new and critical information concerning the techniques and applications of neutron and gamma dosimetry in materials irradiation studies.

These Symposia serve as the main reporting base for work associated with the improvement, standardization, and maintenance of dosimetry, damage correlation, and the associated reactor analysis procedures and data used for predicting the integrated effects of neutron exposure on fuels and materials for light water reactor (LWR), fast breeder reactor (FBR), and magnetic fusion reactor (MFR) nuclear power systems. The ultimate goal is to obtain international standardization of dosimetry methods with quantified uncertainty limits.

The first meeting, at the Joint Research Center (JRC), Petten (September 22-26, 1975), was directed toward defining the status of dosimetry and damage analysis programs and identifying the needs of the dosimetry community.

The second meeting, at the Electric Power Research Institute (EPRI), Palo Alto (October 3-7, 1977), emphasized the data, methods, and techniques used to characterize the neutron environment and the use of well-characterized neutron fields for irradiation programs on fuels, cladding, and structural materials.

The third meeting, at JRC, Ispra (October 1-5, 1979), focused on the interface between material experts and dosimetry metrologists.

The theme of the present symposium was radiation metrology techniques, data bases, and standardization. Application and requirements for radiation metrology of irradiated fuels and materials in fission and fusion technology were emphasized. The following topics involving light water reactors, fast breeder reactors, and fusion reactors were covered:
— Characterization of Environments
— Irradiation Monitoring of Experiments
— Adjustment Codes and Uncertainties
— Benchmark Fields and Calibration Procedures
— Nuclear Data Needs and Problems
— Metrology Techniques (new developments and improvements)
— Radiation Damage Correlations and Damage Analysis Techniques
— Nuclear Heating and Gamma Ray Dosimetry
— Neutron and Gamma Ray Transport Calculations
— LWR Surveillance Dosimetry.

The Symposium was attended by 119 participants from 15 countries. The Proceedings contain the full texts of approximately 100 papers plus highlights by the chairmen of the 11 sessions and 4 workshops. The following papers were presented at the Symposium but were not submitted for these proceedings:
- E. Opperman (HEDL), *Experimentation in the FMIT.*
- A. Lowe (B&W), *B&W Integrated Surveillance Program.*

- S. Anderson (Westinghouse Nuclear Tech. Div.), *Sensitivity of Vessel Exposure to Power Distribution Uncertainties.*
- S. E. Yanichko, T. R. Mager, and R. G. Lott, *Transition Temperature Behavior of Irradiated, Annealed, Reirradiated, and Reannealed Submerged Arc Welds.*
- E. P. Lippincott et al., *HEDL Reactor Dosimetry Center.*
- E. P. Lippincott et al., *FTR Dosimetry Measurement Laboratory.*
- G. L. Guthrie et al., *Monte Carlo Studies Indicating that Least Squares is a Biased Estimator for the Charpy Shift Fluence Exponent.*

One paper by W. Schneider, *Comparison and Limitation of Uncertainties in Surveillance and Lifetime Prediction of LWR Pressure Vessels*, was prepared for the CAPRICE planning meeting at the Symposium and is included with the papers of the Damage Correlation Session.

The following two papers have been replaced by A. Fabry:
1. *Progress Report on the Belgian Contribution to the Improvement of LWR Pressure Vessel Steel Embrittlement Surveillance*, and
2. *PCA and PSF Neutronic Characterization*, by one paper titled *Improvement of LWR Pressure Vessel Steel Embrittlement Surveillance: Progress Report on Belgian Activities in Cooperation with the USNRC and Other R&D Programs.*

In most instances the papers were submitted in camera-ready form and were printed as submitted.

A Certificate of Recognition was presented to C. Z. Serpan (former chairman of ASTM Subcommittee E10.05 on Dosimetry) and Ugo Farinelli (former chairman of the EURATOM Working Group on Reactor Dosimetry) for their foresight and joint efforts in establishing and strongly supporting this highly successful series of ASTM-EURATOM International Symposia on Reactor Dosimetry.

I wish to express my appreciation to all those whose efforts made this Symposium possible. The assistance of the National Bureau of Standards for hosting the meeting, the assistance and cooperation of the ASTM and EURATOM Program Committee, and the continuing support of the U.S. Nuclear Regulatory Commission, who provided the simultaneous translation services and will publish this proceedings, are all gratefully acknowledged.

Finally, special thanks to Vivian Jacobs, Carol Johnson, and the technical publication staff for their excellent job of editing, compiling, and publishing these proceedings in such a short time period.

F.B.K. Kam
Program Committee Chairman
Oak Ridge National Laboratory

WELCOMING REMARKS

J. D. Hoffman
Director of the National Measurement Laboratory
National Bureau of Standards
Washington, DC

Welcome to the Symposium on Reactor Dosimetry and to the National Bureau of Standards. This International Symposium, the fourth in a bienniel series, is sponsored jointly by EURATOM and the American Society for Testing and Materials and, more specifically, by the U.S. Nuclear Regulatory Commission, the Electric Power Research Institute, the U.S. Department of Energy, and the U.S. National Bureau of Standards.

You have come from more than 12 countries in Europe, Asia, and the Far East to share your knowledge on radiation metrology of irradiated fuels and materials in fission and fusion technology.

The first meeting in this series was held in Petten, The Netherlands. The emphasis there was on defining the state of the art of neutron metrology and damage analysis and identifying the requirements of the dosimetry community. The second meeting, held at Palo Alto, California in 1977, emphasized the data methods and techniques used to characterize the neutron environment and the utilization of well-characterized neutron fields for irradiation of nuclear fuels, cladding and structural materials. The third conference, in Ispra, Italy in 1979, was designed as an interface between materials experts and dosimetry metrologists. Benchmark fields and calibration procedures, nuclear data requirements, radiation damage analysis, neutron and gamma ray transport problems, and adjustment codes and uncertaintes are topics that will be discussed during this meeting.

Of the many people who had contributed to the success of these meetings over the past seven years, there are two who can genuinely be said to be the founders of the entire series. We are greatly indebted to Ugo Farinelli, of the National Center for Nuclear Energy in Casaccia, Italy, and to his counterpart in the United States, Charles Serpan of the U.S. Nuclear Regulatory Commission. Additional thanks go to Jean-Pierre Genthon, who has so capably chaired the European committee for this symposium. Also appreciated are the efforts of William McElroy, Chairman of the ASTM Symposium Committee, and Frank Kam, who is Vice-Chairman of the committee and Chairman of the Program Committee.

In addition to the programs that pertain directly to reactor dosimetry, the National Bureau of Standards is engaged in numerous projects in related fields. Our radiographic capability ranges from examining nuclear fuel and waste products to the study of rare paintings and artifacts from antiquity. Recently, a major new facility was developed for small-angle neutron scattering that can be used for nondestructive studies of microstructure in steel and other alloys, including those used for reactor pressure vessels. Because the primary responsibility of the National Bureau of Standards is measurement methods and standards and data, we are particularly pleased to be hosting this meeting on reactor dosimetry. On behalf of the National Bureau of Standards and, in particular, the National Measurement Laboratory, I wish you a productive conference.
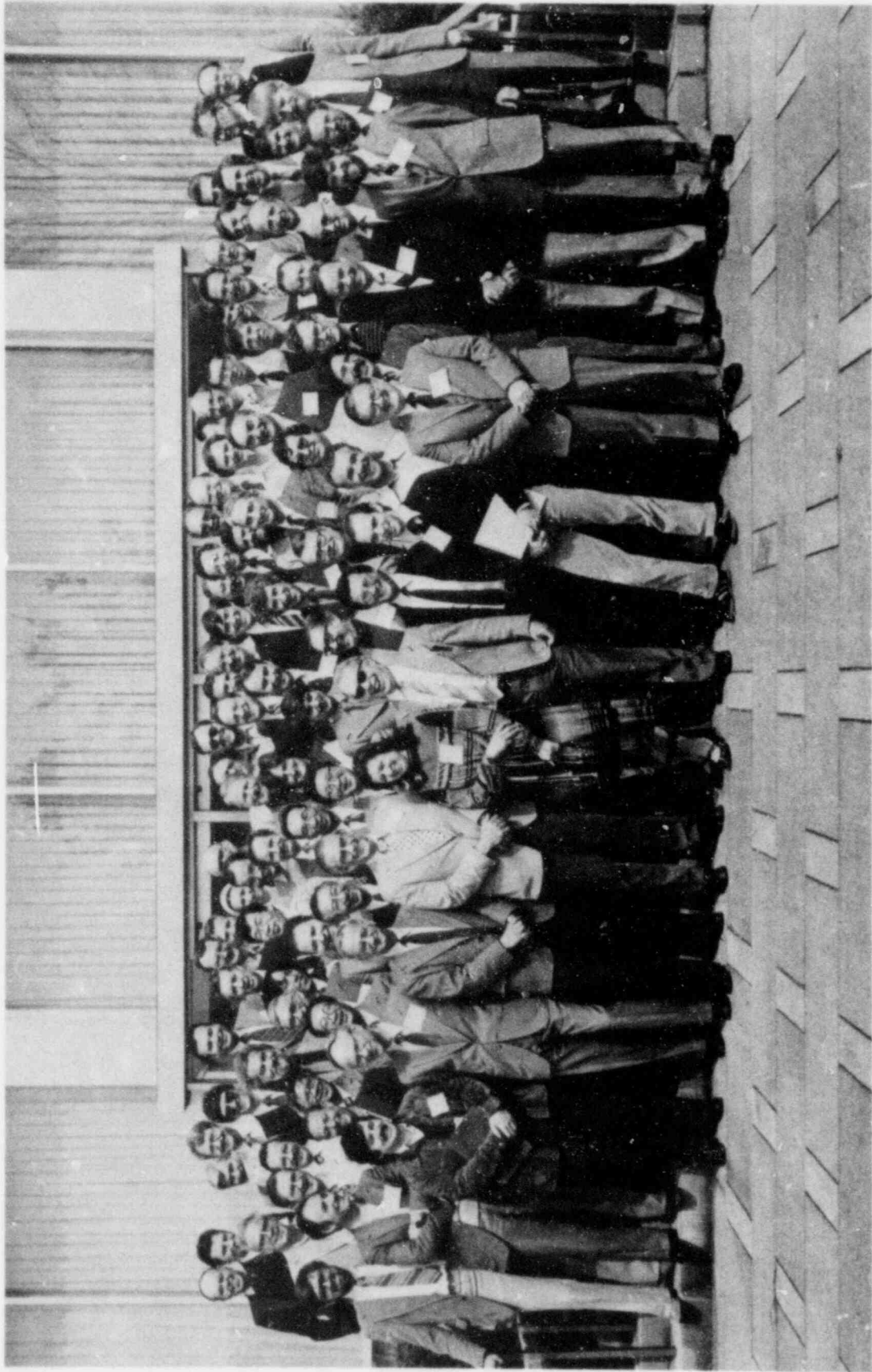
Session A.1
Light Water Reactors-I

SURVEILLANCE DOSIMETRY OF OPERATING POWER PLANTS*

W. N. McElroy, A. I. Davis, R. Gold, G. L. Guthrie, L. S. Kellogg,
A. C. Leaf, E. P. Lippincott, D. L. Oberg, F. A. Schmittroth,
and R. L. Simons (HEDL); F. B. K. Kam, R. E. Maerker and
F. W. Stallmann (ORNL); J. A. Grundl and E. D. McGarry (NBS);
A. Fabry and H. Tourwe (CEN/SCK); H. Farrar IV and B. M. Oliver (RI).

SUMMARY OVERVIEW

General Design Criterion 31 of Appendix A, "General Design Criteria for
Nuclear Power Plants," to 10 CFR Part 50,[1] "Domestic Licensing of Pro-
duction and Utilization Facilities," requires, in part, that the reactor
coolant pressure boundary be designed with sufficient margin to ensure
that, when stressed under operating, maintenance, testing, and postulated
accident conditions, 1) the boundary behaves in a nonbrittle manner and
2) the probability of rapidly propagating fracture is minimized. Appen-
dix G, "Fracture Toughness Requirements," and Appendix H, "Reactor Vessel
Material Surveillance Program Requirements," necessitate the prediction
of the amount of radiation damage to the reactor vessel of water-cooled
power reactors throughout their service life.

With reference to the United States Nuclear Regulatory Commission (NRC)
Regulatory Guide 1.99, Revision 1,[2]† the two main measures of radia-
tion damage are the adjusted reference nil-ductility temperature RT_{NDT}
(RT_{NDT} initial + ΔRT_{NDT}) and the decrease in upper-shelf energy level deter-
mined from Charpy V notch impact tests. The current measures of neutron
exposure most commonly used are fluence > 1 MeV and displaced atoms (dpa).

One category of postulated accidents, thermal shock, is the result of loss
of pressure vessel (PV) coolant with the subsequent introduction of colder
emergency cooling water, which comes in contact with the inner surface of
the initially hot (~550°F) vessel.[3] The resulting decrease in tempera-
ture and the development of high thermal stresses at the inner surface
introduces the possibility of propagation of pre-existing inner-surface
flaws. Figure 1 is a block diagram for a computer code, OCA-I, which was
recently developed for calculating the behavior of flaws on the inner
surface of a pressure vessel subjected to temperature and pressure
transients.[4]

---

*This paper serves also as the 1981 annual report for the LWR pressure
Vessel Surveillance Dosimetry Improvement Program.

†This is identified as Regulatory Guide 1.99.1 throughout the text.

Of immediate interest for this paper are the surveillance program require-
ments and what is being done to obtain and document needed information
related to: 1) the inner surface neutron fluence (F_O), 2) the 1/4 T neu-
tron fluence, 3) flux levels and fluence and dpa gradients in the PV, 4)
the PV steel initial reference nil-ductility temperature, RT_{NDTo}, and 5)
the steel property trend curves of ΔRT_{NDT} and the upper shelf energy
decrease versus the fluence (and dpa) derived from test reactor and power
reactor surveillance programs.

The NRC established the Light Water Reactor Pressure Vessel (LWR-PV) Sur-
veillance Dosimetry Improvement Program in 1977 to improve, standardize and
maintain dosimetry, damage correlation and the associated reactor analysis
procedures used for predicting the integrated effects of neutron exposure to
LWR-PVs. About the same time, the Electric Power Research Institute (EPRI)
established its own experimental and analytic Dosimetry Program.[7] The
objective of the program has been to carry out measurements in operating
power reactors for use in benchmarking new and improved methods of physics-
dosimetry analysis. Of particular interest for both the EPRI and NRC
programs has been the development of advanced physics-dosimetry methodolo-
gies based on least-squares adjustment procedures.[5,8] A brief overview
of these and related programs and an overall program status report are
provided in References 5 and 6, respectively. More complete information on
the EPRI program work is provided in References 7 and 8. Major benchmark
test facilities used or being established for this interlaboratory program
work are discussed in References 5 through 8. In Table 1, these as well as
other key benchmarks are identified along with the development time frame,
participants, and their intended purpose and use. In addition to those in
other countries, there are three main US programs to measure the fracture
toughness and Charpy properties of irradiated materials, principally high-
copper, submerged-arc weldments: 1) the NRC-funded Heavy-Section Steel
Technology (HSST) Program, 2) the program funded by the Babcock & Wilcox
(B&W) Owners' Group, and 3) the EPRI program.[9]

The main focus of the research efforts presently underway is the LWR power
reactor surveillance program in which metallurgical test specimens of the
reactor PV and dosimetry sensors are placed in three or more surveillance
capsules at or near the reactor PV inner wall. They are then irradiated in
a temperature and neutron flux-spectrum environment as similar as possible
to the PV itself for periods of about 1.5 to 15 effective full-power years
(EFPY)*, with removal of the last capsule at a fluence corresponding to the
30- to 40-year plant end-of-life (EOL) fluence. Because the neutron flux
level at the surveillance position is greater than at the vessel, the test
is accelerated with respect to the vessel exposure, allowing early assess-
ment of EOL conditions.

---

*For a surveillance capsule location with a lead factor of ~3, where the
 lead factor is the ratio of fluence (E > 1 MeV) at the surveillance
 location to that at the PV wall, see Table 5.

The surveillance capsule metallurgical and dosimetry results are used to verify and/or adjust the final safety analysis report's (FSAR) current and EOL projections of changes in the fracture toughness and embrittlement condition of the PV steel. As discussed in Regulatory Guide 1.99.1 and Reference 9, the derived plant-specific PV steel wall condition is used together with other information to determine the allowable pressure-temperature operating curve to be used for continued operation of the power plant. If however, the RT_{NDT} of the PV steel shifts from an initial beginning-of-life (BOL) value (usually in the range of -50° to 50°F) to a much higher value (in the range above 200°F) as a result of neutron radiation damage, it may be necessary to take corrective action; such as annealing the reactor PV, to obtain a lower operating RT_{NDT} value (i.e., to regain fracture toughness and ductility).* Consideration of other options, such as those involved in changes in the core power distribution to reduce the PV wall neutron exposure rate may also be necessary.

It is currently accepted that uncertainties in the reported values of the neutron exposure parameters of fluence > 0.1 and > 1.0 MeV and dpa should be in the range of ±10% to 30% ($l\sigma$).[10-15] To achieve such accuracy on a routine basis, however, it has now been well demonstrated that the reactor physics calculational and dosimetry measurement techniques must be benchmarked [i.e., verified at the ±5% to 15% ($l\sigma$) level.][5,6] This is shown graphically in Figure 2 where the estimated exposure parameter uncertainty range for FSAR and surveillance capsule reports is plotted versus time in years. The dramatic effect (in 1980 to 1981) of proper standardization and benchmarking is apparent, and it is expected that goal accuracies (±10% to 30%) will be routinely achievable after 1985. Thereafter, and depending on the need, some improvement in accuracy may be achieved; but no better than a ±10% to 20% ($l\sigma$) level of uncertainty is anticipated.

PROGRAM RESULTS

Figures 2 through 10 and Tables 1 through 14 provide summary highlight information related to surveillance dosimetry for operating power plants, most of which was developed as a result of multilaboratory work during 1981. As appropriate, comments are provided on individual Figures and Tables. In Table 15, an effort has been made to provide a summary of the procedures and requirements for LWR-PV embrittlement surveillance analysis. More detailed comments, information and justification for the present interlaboratory work will be found in two added reference sections on "Surveillance Dosimetry Accuracy Requirements" and "Program Direction and Status."

---

*Here and in Regulatory Guide 1.99.1, RT_{NDT} is used as a measure of PV steel ductility while upper shelf energy is used as a measure of toughness; clearly, it is the steel ductility and toughness that is of concern, not the actual values of RT_{NDT} and upper shelf energy. More information will be found on this subject in Reference 9, where it is concluded that embrittlement limits should be expressed in terms of fracture toughness, not in terms of Charpy impact energy.

SURVEILLANCE DOSIMETRY ACCURACY REQUIREMENTS

The use of RT_{NDT} data for base, heat-affected zone, and weld metal provides overall guidelines for the level of accuracy required of both metallurgy and physics-dosimetry. The uncertainties associated with the determination of RT_{NDT} continue to be studied.[9,14-16] Included in the physics-dosimetry work is not only surveillance capsule but ex-vessel dosimetry for derived values of exposure parameters. Two distinct uses or applications (cases) of RT_{NDT} data can be considered, namely:

1) **Plant Safety** -- What are the implications of current regulations for accuracy on RT_{NDT} and exposure parameter (fluence > 0.1 and > 1.0 MeV, and dpa) determinations?

2) **Standards Development** -- What current accuracy is required for the development of standards, procedures, and data needed to define spatial (lead factor) and exposure time (trend curve) extrapolations? These procedures and data are or will be given in Regulatory Guide 1.99.1 and a number of ASTM Standards[10] (Figures 3 and 4); particularly I-C through I-H, II-A through II-F, and III-A through III-E, which are under development.

For Case One, Figure 5, **Plant Safety** demands a high level of accuracy [generally at a 95% (2σ) or better confidence level] for the exposure parameter variables to avoid premature judgment that controlling property change limits have been reached or surpassed.* Improvement in the accuracy of reported values of the fluence (E > 0.1 and > 1.0 MeV) and dpa variables offer the principal opportunity for avoidance of premature action, since it is currently not possible to reduce the uncertainty on the RT_{NDT} variable (at a fixed position in the PV wall, such as at the surface or 1/4 T locations) below $\sim\pm30°F$ (2σ).[14-16] This latter value is typical for a power plant weld metal with a RT_{NDT} value of 100°F after $\sim$5 EFPY of plant operation with a PV inner surface fluence (E > 1.0 MeV) of $\sim6.0 \times 10^{18}$ n/cm^2. This example is based on a weld material with a high nickel and a 0.15% Cu and 0.012% P content and an initial RT_{NDTo} of 0°F. Based on Pool Critical Assembly/Pool Side Facility (PCA/PSF) and recent surveillance capsule studies, Table 5, the best upper and lower limits on measured-calculated values for the exposure variables (fluence > 0.1 and > 1.0 MeV, and dpa) at the surveillance position are ±20% (2σ), and only for benchmarked results.[5,6]

Considering these as best lower- and upper-bound limits, and for this example, a plant-specific controlling trend curve (at the 95% confidence level) can be defined and is shown as the dot-dashed curve in Figure 5.** The

---

*In Reference 9 it is stated: "The economic consequences of complying with federal regulations are demonstrably severe. Therefore, it is necessary to have the most accurate embrittlement predictive methodology possible."
**This is a simplified example that assumes a 95% confidence limit for both the fluence and temperature shift. The actual limits must be set using a statistical combination of these according to the confidence level that is deemed satisfactory.

determination of the intersection of this curve with an acceptable plant-specific upper-bound line that falls in a band of allowable EOL values of RT_{NDT} (for a nominal operating temperature of 550°F for LWR power plants) is required for plant safety. For the present example, a very conservative upper-bound line at RT_{NDT} equals 200°F will be used.* On this basis, the intersection point is at a fluence of $\sim 1.1 \times 10^{19}$ n/cm^2 (~ 9.2 EFPY, or 1/4 of the plant life) at the PV inner surface. If instead of a ±20% (2σ) [±10% (1σ)] uncertainty, a ±60% (2σ) [±30% (1σ)] fluence uncertainty had been used (which is more representative of current state-of-the-art values for reported surveillance capsule dosimetry, Table 5), the plant-specific controlling trend curve would shift to the left even further. The result would be that the intersection point would now be at a fluence value of $\sim 5.6 \times 10^{18}$ n/cm^2 (~ 4.7 EFPY). Consequently, if the reported fluence value uncertainty had been ±30% (1σ) and an RT_{NDT} value of 200°F were limiting, corrective action, such as annealing the reactor PV, changes in core power distribution to lower the PV neutron exposure rate, etc. would have to be considered immediately. If the reported uncertainty had been closer to ±10% (1σ), however, corrective action could be safely delayed until after another ~ 4 EFPY of operation. During this period, additional in- and ex-vessel physics-dosimetry measurements and calculations could be performed to verify, certify, and improve the accuracy of the original FSAR and second (and subsequent) surveillance capsule reported values of exposure parameters (fluence > 0.1 and > 1.0 MeV, and dpa). The use of dpa, to better account for spatial effects, might further increase or decrease the allowed current and EOL fluence values, see Figure 10.

The shape of the Charpy shift curve used in current regulations is based on trend curves with a power law dependence of N = 1/2 for the fluence variable.[2] Hence, for Case 2, _Standards Development_ efforts will produce improved and more reliable trend curves, such as those now being established for the ASTM Standard Guide E706(II-F), Figures 3 and 4. The importance of the trend curve in time exposure extrapolations can be seen in Figure 5. Extrapolation uncertainty, whether spatial (lead factor) or temporal (trend curve) depends upon how accurately the curve has been defined as well as how far the extrapolation extends. For example, using MPC, EPRI and NRC data bases, it now appears that the power law approximation of the trend curve possesses an exponent N $\sim$ 1/3 for most PV steels; see Figure 6.[14] This would represent a 33% change in the exponent relative to that used in Reg Guide 1.99.1. Clearly the error introduced through ill-definition of the trend curve cannot be neglected given representative ±10% to 30% (1σ) uncertainties for both dosimetry and Charpy data in power plant surveillance capsule work. Consequently, through proper _Standards Development_ efforts, one can fully

---

*For new plants, Regulatory Guide 1.99.1 states that the PV steel beltline materials should have the content of residual elements such as Cu, P, S and V controlled to low levels such that the EOL, 1/4 T position, RT_{NDT} is less than 200°F. In Reference 9, it is indicated that a ΔRT_{NDT} shift of, say, 252°F may cause real operational difficulty late in life (in startup and shutdown) for some PWR power plants. This, however, would be dependent on a number of factors, including the initial BOL RT_{NDT} value.

expect the generation of more accurate extrapolation procedures. For the more accurate definition of exposure time trend curves, well-controlled special research and power reactor metallurgical tests must generate higher quality data.[6,9,14-24] Here it is essential that ΔRT_{NDT} be determined at the ±10% (1σ) uncertainty level or better and that state-of-the-art reactor physics dosimetry be carried out to a comparable accuracy.

For plant safety, then, a knowledge of the uncertainty in the shape of the trend curve (N = 1/2, 1/3, or less) is essential for defining the point of intersection of a 2σ (plant-specific) trend curve with a plant-specific upper-bound line in the band of allowable EOL values of the adjusted RT_{NDT} (Figure 5). It is well to also note here that whether 10% (1σ), 30% (1σ) or higher values of uncertainty are accepted for derived values of exposure parameters, the routine acceptance of the validity of any exposure parameter value and its quoted uncertainty will be dependent on the periodic bench-marking of the applied experimental physics and dosimetry methodology. As discussed later in this paper, under Program Direction and Status, special benchmark facilities (Table 1) are being or have been established to provide the necessary validation and certification of both the accuracy and precision of the applied physics and dosimetry techniques. Proven and accepted techniques are and will be needed for the definition of values and uncertainties for spatial (lead factor) and exposure time (trend curve) extrapolations.

Although our presentation has focussed on trend curves, similar considerations obviously must arise for extrapolations based on spatial and metallurgical lead factors. Indeed the accuracy and limitations of these different extrapolation procedures have yet to be rigorously defined, let alone compared.

Consequently, comparable Standards Development efforts must go forward to accurately define spatial and metallurgical lead factors. With reference to Table 2, the present discussion has considered effects arising solely from reactor physics-dosimetry (Variables 3 - 10). Analogous considerations must be applied for Variable 1 (steel chemical composition and microstructure) and Variable 2 (steel irradiation temperature) for metallurgical lead factor extrapolations. Even though it is not the purpose of this paper to address metallurgical lead factor extrapolation methodology and uncertainties, some of the main elements involved in this methodology are summarized in Table 3.

In summary, the need for extrapolation in PV and support structure surveillance is an overriding concern. Within this framework, the selection of a "controlling variable", be it metallurgical or reactor physics-dosimetry related, is irrelevant. For example, in Figure 5 a horizontal extrapolation of the ±30°F error bars (to the left for the -30°F bar and to the right for the +30°F bar) results in a fluence band of ~3.0 x 10^{18} to ~1.0 x 10^{19} n/cm^2. Consequently, if the RT_{NDT} property change uncertainty of ±30°F were considered limiting (e.g., material variability in chemistry and microstructure) for a specific PV steel, then knowing the fluence value within a factor of ~3 might be considered adequate. This argument, however, has little relevance to setting safe (95% confidence level or better) current and EOL fluence operating limits for individual pressurized water reactor (PWR) power

plants. It is also clear that high accuracy exposure values are needed for establishing the value of "N" and its uncertainty for the slope (exposure time extrapolation variable) of a trend curve for a specific plant and PV steel. The "exposure time extrapolation" variable plays an extremely important part in extrapolating, in time, plant-specific surveillance capsule derived exposure and metallurgical results. In this context, the reason fluence (or dpa) is used as the extrapolating (independent) variable is that it obviously can be determined as or more accurately than the associated metallurgical (dependent) variable.

PROGRAM DIRECTION AND STATUS

The ASTM Standard E706-81,[10] "Master Matrix for LWR-PV Surveillance Standards," describes a series of 17 standard practices, guides and methods for the prediction of neutron-induced changes in LWR-PV and support structure steels throughout a PV's service life. Figures 3 and 4 provide updated information on the interrelationship of 19 standards (20 including the Master Matrix) and the schedule for their preparation, balloting, acceptance, validation and revision. Some of these are existing ASTM standards, some are ASTM standards that have been modified, and some are newly proposed ASTM standards. The scope of each standard and the general requirements for content and consistency are discussed in the Master matrix as well as writers' and users' information, justification, and specific requirements for the practices, guides and methods. Information is also provided on applicable documents and references.

Reactor physics and dosimetry analysis and interpretation are discussed in Section 4 of E706-81. Specific subsections deal with:

a) Required Accuracies and Benchmark Field Referencing

b) Power Plant Reactor Physics Analysis and Interpretation

c) PCA Blind Test

d) PWR and Boiling Water Reactor (BWR) Generic Power Reactor Tests

e) Operating Power Reactor Tests

Currently, the NRC is supporting a significant amount of multilaboratory work associated with all five items at HEDL, ORNL, BNL and NBS. Additional work is being supported at a number of laboratories in Europe and elsewhere, the most significant effort being at CEN/SCK, Mol, Belgium. EPRI and reactor vendors are also supporting significant multilaboratory work related to Items a), b), d) and e). Three of the U.S. vendors (Westinghouse, B&W and CE), two U.S. service laboratories (SWRI and BMI), as well as six other U.S. and foreign laboratories participated in the "PCA Experiments and Blind Test." This test was intended to provide a "necessary" but not "sufficient" test of the adequacy of reactor physics tools, procedures and data used for predicting FSAR flux-spectral values. These data are used, in turn, in the analysis of surveillance capsule dosimetry sensor reaction rates and in the

subsequent determination of values of neutron exposure parameters 1) in surveillance capsules, 2) at the inner surface and through vessel walls, and 3) in ex-vessel cavity locations. The initial results of the "PCA Experiments and Blind Test" are now available in a NUREG Report.[5] This PCA benchmark test established that the limiting accuracy of reactor-physics, dosimetry-derived values of group fluxes and exposure parameters are in the range of ±5% to 30% (1σ) and ±5% to 15% (1σ), respectively, if properly benchmarked; otherwise, errors can be a factor of two or more, see Figure 2.

Relative to Item (c) and by the end of 1982, HEDL, ORNL, NBS and CEN/SCK will complete the final work and documentation for the PCA for the 8/7, 12/13, 4/12 and 4/12 (SSC) configurations for this mockup physics-dosimetry test of a PWR power plant.* The 4/12 and 4/12 (SSC) results will be used primarily in support of the analysis of the physics and dosimetry for the PSF metallurgical test.[5,6] One important aspect of this combined metallurgical/physics/dosimetry test will be to provide benchmarked data to establish the uncertainties associated with the calculation and use of fluence (E > 1.0 MeV) and dpa to account for flux-spectral (spatial lead factor) effects, see Figures 9 and 10. Another important aspect of this effort will be the general use and application of the PCA experimental and analytical results to test and develop advanced physics-dosimetry methodologies based on least-squares adjustment procedures. Least-squares analyses of reactor dosimetry have been in vogue for some time now, and this approach has general world-wide acceptance.[11-13] Indeed least-squares analyses of PCA experiments and blind test results for NRC have already been conducted by HEDL and ORNL.[5] Initial results of the application of HEDL- PCA tested methodology to the analysis of surveillance capsule-derived exposure-parameter values and uncertainties are discussed herein. Work being supported at ORNL by EPRI is also discussed in this paper and in Reference 8.

Still required for this interlaboratory program effort is to complete the development and establishment of a set of ASTM-accepted generic BWR and PWR physics-dosimetry benchmarks, with required in- and ex-vessel dosimetry measurement verification (Table 4).[5-8,10-13] With Reference to ASTM E706-81,[10] these benchmarks are intended to provide a "necessary" and "partly sufficient" test of the adequacy of a vendor/utility group's power reactor physics computational tools.** The standards recommendation should be that the vendor/utility group's observed differences between their own calculated and the selected PWR or BWR measured integral and differential exposure and reaction rate parameters be used to validate and improve their computational tools and measurement resources (if differences fall outside the selected PWR or BWR experimental accuracy limits). (These C/E accuracy

---

*8/7, 12/13, etc. are the dimensions of the water gaps in cm between the reactor core edge and thermal shield/the thermal shield and pressure vessel inner wall for the PCA PV mockup facility.

**The successful analysis and interpretation of a number of surveillance capsule results for a specific PWR or BWR power plant, together with an appropriate generic plant, provides a "necessary" and "sufficient" test (see Section 4.4.5 of ASTM E706-81, Reference 10).

limits are identified and discussed in the ASTM E706(II-D) Transport Standard, Figure 3).*

As previously stated, the objective of the EPRI experimental program has been to carry out measurements in operating power reactors for use in bench-marking improved physics-dosimetry methods of analysis;[5,8] see Table 4. The reactors where measurements have been carried out included one BWR: TVA's Browns Ferry Unit 3 where ex-vessel measurements carried out by GE have recently been documented.[25] These measurements complement the in-vessel measurements funded by TVA and documented in Reference 26. Supporting transport calculations are being done by Science Applications Inc. The PWR measurements have been carried out at Arkansas Power and Light's Nuclear One-1 (ANO-1) by the University of Arkansas, NBS and HEDL.[6,27,28] Supporting transport calculations are being done at the University of Missouri, Rolla and at ORNL. The ANO-1 measurements have been carried out ex-vessel only. A set of in-vessel as well as ex-vessel measurements at Crystal River 3 and ANO-2 is presently under consideration, Table 4. An equivalent set of measurements on Duke Power Company's McGuire Unit 1 plant is awaiting startup of the reactor.

The objective of the EPRI analytic program has been the development of an advanced dosimetry methodology based on a least-squares adjustment procedure.[8,29] The methodology being developed by ORNL for EPRI utilizes direct neutron transport calculations together with dosimetry measurements and their uncertainties (or covariances) to determine the best (in a least-squares sense) estimates of the neutron fluxes and their reduced covariances. One of the most important features of the methodology is its ability to estimate the uncertainties in the adjusted flux spectrum. Other features include the capability of obtaining the fluxes at surveillance points as well as at any desired point within the pressure vessel, and the capability of simultaneous least-squares adjustment of fluxes in multiple fields. By simultaneously analyzing benchmark fields (prototypic fields as well as a particular LWR field of interest), it is possible to improve the accuracy of the prediction for the LWR field since the information "learned" from the former fields is used in the determination of the latter.

To date the EPRI-ORNL methodology has been applied to the analysis of a series of progressively more complex fields, including the NBS ^{252}Cf fission field, the Intermediate-Energy Standard Neutron Field (ISNF), the Federal German Republic-PTB ^{252}Cf fission field, and the PCA pressure vessel prototypic field.[8] (The method is presently being applied to the PCA/PSF. Future plans include the application of the methodology to the ANO-1 and, perhaps, ANO-2 measurements.) Results of both the ORNL and HEDL[5] studies have shown that uncertainties in the PCA flux determination can be considerably reduced by using simultaneous adjusting of all available data. Since the predictions have been found to be rather sensitive to the uncertainty estimates, a considerable amount of effort has been invested by

---

*A similar statement regarding differences applies to the "PCA Experiments and Blind Test" benchmark (see Section 4.4.3 of ASTM E706-81).

both ORNL and HEDL in the preparation of covariance information for measurements in the benchmark and prototypic fields as well as improvements to the ENDF/B-V covariance files for dosimetry cross sections.[5,8] These covariances together with the ENDF/B-V cross-section files constitute a general data base for any least-squares fitting program. As a matter of interest, Reference 30 describes the status of work related to the preparation of the ASTM E706 (II-B) Standard Guide for "Application of ENDF/A Cross Section and Uncertainty Files"; see also Reference 10.

For Item (e) and by the end of 1982, initial studies will have been completed for the NRC program; and more quantitative results will be available to certify the accuracy of surveillance dosimetry for operating LWR power plants. For individual and selected sets of surveillance capsules, results will be available from FERRET-SAND code-derived values of exposure parameters (see Table 5 and Sections 4.2 and 7.3 of Reference 5) for four vendors, two service laboratories, and EPRI surveillance capsule reports submitted for or by utilities to NRC. These results, together with those from physics computations, will be used to 1) define inner PV surface and wall gradient flux level and exposure parameter values, Figures 9 and 10, 2) verify the accuracy of FSAR predictions of current and EOL exposure parameter values (fluence > 0.1 and > 1.0 MeV, and dpa) for individual BWR and PWR power plants (see Table 5), and 3) provide higher accuracy [±10% to 30% (1σ)] values of exposure parameters for establishing improved trend curve shapes for MPC, EPRI, NRC and other metallurgical data bases. Least-squares adjustment procedures, as discussed in ASTM Standards E706(I-C), (I-E), and (II-A) (Figure 3) and developed for the NRC and EPRI programs, will be used to accomplish the above analysis.[5,8,14-16,17]

More specifically, the MPC, EPRI, and NRC data bases are being used together with test reactor data to develop trend curves to account for neutron radiation damage when plant-specific information is not available or is not completely adequate. That is, updated and new physics-dosimetry data are being used together with available metallurgical data to develop new ASTM ΔRT_{NDT} and upper shelf energy shift versus fluence (E > 0.1 MeV and > 1.0 MeV) and dpa curves to replace those in Regulatory Guide 1.99.1 (see Figure 3, ASTM Standard II-F, and Figure 6). In addition to a series of Westinghouse PWR plants (Table 5), the current emphasis and approximate order of priority of studying existing U.S. power plants under this effort is provided in Table 6. This priority listing is currently based on a need to have plant-specific input data to perform fracture analysis studies, including those using OCA-I, for those power plants with PV steels that are suspected of having high RT_{NDT} values (Table 6). As discussed in the section on Surveillance Dosimetry Accuracy Requirements, the correctness of these estimated RT_{NDT} values is critically dependent on the accurate definition and verification of surveillance capsule exposure parameter values, and capsule-to-PV-wall inner surface spatial (lead factor, see Table 5) and exposure time (trend curve, see Table 6) extrapolations. The determination of these spatial and time lead factors also depends on the proper definition and understanding of surveillance capsule perturbation and long-term core fuel subassembly

loading pattern effects. Figures 7, 9 and 10 and Tables 7 and 8 provide information and preliminary results of studies related to this aspect of surveillance capsule data analysis.

HEDL, ORNL, NBS, CEN/SCK, EPRI contractors, vendors and others are doing and will continue to do dosimetry measurement certification work in support of surveillance programs for operating power plants, Items (d) and (e) (see Figures 6 through 8 and Tables 4 through 14). Further, effort will be put forth in the area of validation/calibration of the Figure 3 ASTM Standard Methods:

III-A   Application and Analysis of Radiometric Monitors (RM) for Reactor Vessel Surveillance

III-B   Application and Analysis of Solid State Track Recorder (SSTR) Monitors for Reactor Vessel Surveillance

III-C   Application and Analysis of Helium Accumulation Fluence Monitors (HAFM) for Reactor Vessel Surveillance

III-D   Application and Analysis of Damage Monitors (DM) for Reactor Vessel Surveillance

III-E   Application and Analysis of Temperature Monitors (TM) for Reactor Vessel Surveillance

Related to Items (a), (b), (d) and (e), therefore, the participants of the LWR-PV Surveillance Dosimetry Improvement Program will jointly seek 1) to develop and establish a set of PWR and BWR Generic Power Reactor Benchmarks based upon conventional, benchmarked, neutron dosimetry, 2) to obtain ASTM acceptance of these and 3) to complete the necessary validation/calibration (round robin testing) of this set of five ASTM Standard Methods (III-A through III-E), consistent with the procedures given or to be given in I-A, Analysis and Interpretation of Nuclear Reactor Surveillance Results, and II-E, Benchmark Testing of Reactor Vessel Dosimetry.

In summary and with reference to Figure 2, the five measurement standard methods are essential to provide in and ex-vessel dosimetry and temperature measurement capabilities that vendors, service laboratories and utilities will need to certify to themselves and licensing and regulatory bodies the adequacy of their calculational and measurement tools. Of particular importance is the adequacy of individual power plant FSAR/surveillance-capsule-derived, BOL and EOL predictions of flux-spectra and exposure parameter values (fluence > 0.1 and > 1.0 MeV, and dpa for steel) needed for fracture analysis studies of PV and support structure steels. It is essential for the nuclear industry that errors be assigned to all values of calculated and measured flux-spectra, derived exposure-parameters, lead factors (radial, azimuthal, and axial), and trend curve slopes given in surveillance capsule reports; further, it is important that these values are based on a proper weighting of the results of individual dosimetry sensors, which includes uncertainties and neutron energy response weighting. One needs only to look

at recent as well as old surveillance program reports to determine the inadequacy of the present practice of stating that FSAR predictions and surveillance capsule measurements agreed or disagreed, but without stating the uncertainties associated with individual predictions and measurements.

ACKNOWLEDGMENTS

REFERENCES

1. Code of Federal Regulations, "Domestic Licensing of Production and Utilization Facilities," 10 CFR 50; "General Design Criteria for Nuclear Power Plants," Appendix A; "Fracture Toughness Requirements," Appendix G; "Reactor Vessel Material Surveillance Program Requirements," Appendix H; US Government Printing Office, Washington, DC, current edition.

2. Regulatory Guide 1.99, "Effects of Residual Elements on Predicted Radiation Damage to Reactor Vessel Materials," Rev. 1, US Nuclear Regulatory Commission, Washington, DC, April 1977.

3. R. D. Cheverton, "Pressure Vessel Integrity," Oak Ridge National Laboratory Review, Oak Ridge National Laboratory, Oak Ridge, TN, p. 34, W'81.

4. S. K. Iskander, R. D. Cheverton and D. G. Ball, OCA-I, A Code for Calculating the Behavior of Flaws on the Inner Surface of a Pressure Vessel Subjected to Temperature and Pressure Transients, NUREG/CR-2113, ORNL/NUREG-84, Oak Ridge National Laboratory, Oak Ridge, TN, Aug 1981.

5. W. N. McElroy et al., LWR Pressure Vessel Surveillance Dosimetry Improvement Program: PCA Experiments and Blind Test, NUREG/CR-1861, HEDL-TME 80-87, Hanford Engineering Development Laboratory, Richland, WA, July 1981.

6. W. N. McElroy et al., LWR Pressure Vessel Surveillance Dosimetry Improvement Program: 1980 Annual Report, NUREG/CR-1747, HEDL-TME 80-73, Hanford Engineering Development Laboratory, Richland, WA, April 1981.

7. H. A. Till, "Neutron Radiometric and Calculation Benchmarking for LWR Pressure Vessel Radiation Effects," Proceedings of the Third ASTM-EURATOM International Symposium on Reactor Dosimetry, EUR 6813, European Atomic Energy Community, Brussels, Belgium, p. 1275, 1980.

8. R. E. Maerker, J. J. Wagschal and B. L. Broadhead, Development and Demonstration of an Advanced Methodology for LWR Dosimetry Applications, EPRI NP-2188, Project 1399-1, Interim Report, Electric Power Research Institute, Palo Alto, CA, December 1981.

9. T. U. Marston and K. E. Stahlkopf, "Radiation Embrittlement: Significance of Its Effects on Integrity and Operation of LWR Pressure Vessels," Nuclear Safety 21 (6), p. 724, November - December 1980.

10. ASTM Standard E706-81, "Master Matrix for LWR Pressure Vessel Surveillance Standards," 1981 Annual Book of ASTM Standards, American Society for Testing and Materials, Philadelphia, PA, 1981.

11. J. M. Bâtiment, Compiler, Proceedings of the First ASTM-EURATOM International Symposium on Reactor Dosimetry, EUR 5667, Parts I & II, European Atomic Energy Community, Brussels, Belgium, 1977.

12. W. C. Morgan, Compiler, Proceedings of the Second ASTM-EURATOM International Symposium on Reactor Dosimetry, NUREG/CR-0004, Vol. 1 - 3, US Nuclear Regulatory Commission, Washington, DC, 1978.

13. H. Röttger, Compiler, Proceedings of the Third ASTM-EURATOM International Symposium on Reactor Dosimetry, EUR 6813, European Atomic Energy Community, Brussels, Belgium, 1980.

14. G. L. Guthrie, "A Determination of the Effect of Irradiation Temperature on the Irradiation Induced Charpy Shift," LWR-PV Irradiation Surveillance Improvement Program Progress Report for January - March 1981, HEDL-TME 81-33, NUREG/CR-2345, Vol. 1, Hanford Engineering Development Laboratory, Richland, WA, October 1981.

15. G. L. Guthrie, "An Investigation of the Dependence of Charpy Trend Curve Saturation on Nickel or Copper Concentration." LWR-PV Irradiation Surveillance Improvement Program Report for October - December 1980, HEDL-TME 80-6, NUREG/CR-1241, Vol. 3, Hanford Engineering Development Laboratory, Richland, WA, October 1981.

16. J. D. Varsik, Evaluation of Irradiation Response of Reactor Pressure Vessel Materials, TR-MCM-110, EPRI RP 1553-1, Semi-Annual Progress Report No. 3, July - December 1980, Combustion Engineering Inc, Winsor, CT, 1981.

17. T. J. Williams and R. L. Squires, Interim Analysis of the Results to Date from a Materials Test Reactor Irradiation Program, RRA/N/3467, Rolls-Royce & Associates Ltd, Derby, UK, November 1979.

18. J. S. Perrin et al., Point Beach Unit No. 2 Pressure Vessel Surveillance Program: Evaluation of Capsule V, Final Report, Battelle Memorial Institute, Columbus, OH, June 10, 1975.

19. J. A. Davidson, S. L. Anderson and R. P. Shogan, Analysis of Capsule T from the Wisconsin Electric Power Company Point Beach Nuclear Plant Unit No. 2 Reactor Vessel Radiation Surveillance Program, WCAP-9331, Westinghouse Nuclear Technology Division, Pittsburgh, PA, August 1978.

20. C. Z. Serpan, "Reliability of Fluence Embrittlement Projections for Pressure Vessel Surveillance Analysis," Nucl. Tech. 12, p. 108, September 1971.

21. S. E. Yanichko, S. L. Anderson, R. P. Shogan and R. G. Lott, Analysis of Capsule R from the Wisconsin Electric Power Company Point Beach Nuclear Plant Unit No. 2 Reactor Vessel Radiation Surveillance Program, WCAP-9635, Westinghouse Nuclear Technology Division, Pittsburgh, PA, December 1979.

22. S. E. Yanichko, S. L. Anderson, R. P. Shogan and R. G. Lott, Analysis of Capsule R from the Wisconsin Public Service Corporation Kewaunee Nuclear Plant Reactor Vessel Radiation Surveillance Program, WCAP-9878, Westinghouse Nuclear Technology Division, Pittsburgh, PA, March 1981.

23. D. Pachur, "Apparent Embrittlement Saturation and Radiation Mechanisms of Reactor Pressure Vessel Steels," Proceedings of the 10th International Symposium on Effects of Radiation on Materials, Savannah, GA, June 3-5, 1980.

24. T. R. Mager et al., Steady-State Radiation Embrittlement of Reactor Vessels, Semiannual Technical Progress Report No. 4, EPRI RP 1021-3, Electric Power Research Institute, Palo Alto, CA, April 1981.

25. G. C. Martin, Brown's Ferry Unit 3 Cavity Neutron Spectral Analysis, EPRI NP-1997, Electric Power Research Institute, Palo Alto, CA, August 1981.

26. G. C. Martin, Brown's Ferry Unit 3 In-Vessel Neutron Spectral Analysis, NED024793, General Electric Co., San Jose, CA, August 1980.

27. W. N. McElroy et al., LWR Pressure Vessel Surveillance Dosimetry Improvement Program: 1979 Annual Report, NUREG/CR-1291, HEDL-SA 1949, Hanford Engineering Development Laboratory, Richland, WA, February 1980.

28. J. Grundl et al., "NRC-EPRI Studies of Pressure-Vessel-Cavity Neutron Fields," Proceedings of the NRC Ninth Water Reactor Safety Information Meeting, NBS, Washington DC, October 26-30, 1981.

29. F. G. Perey, Least-Squares Dosimetry Unfolding: The Program STAY'SL, ORNL/TM-6062, Oak Ridge National Laboratory, Oak Ridge, TN, 1977.

30. E. P. Lippincott and W. N. McElroy, ASTM Standard Recommended Guide on Application of ENDF/A Cross Section and Uncertainty File: Establishment of the File, HEDL-SA 2540, paper presented at IAEA Advisory Group Meeting on Nuclear Data for Radiation Damage and Safety, Vienna, Austria, October 12-16, 1981.
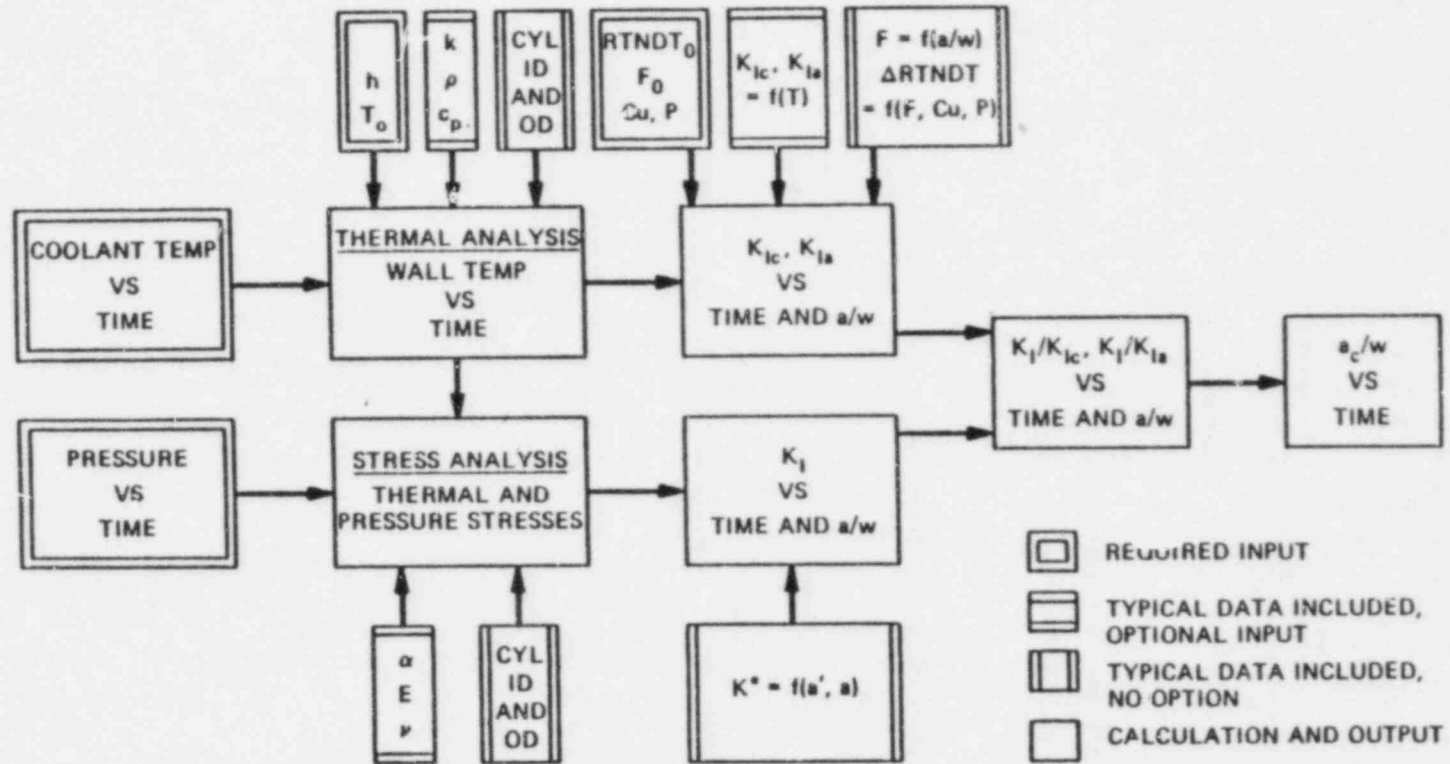
FIGURE 1. Block-Diagram Description of OCA-I, Indicating Basic Input, Calculations and Output.
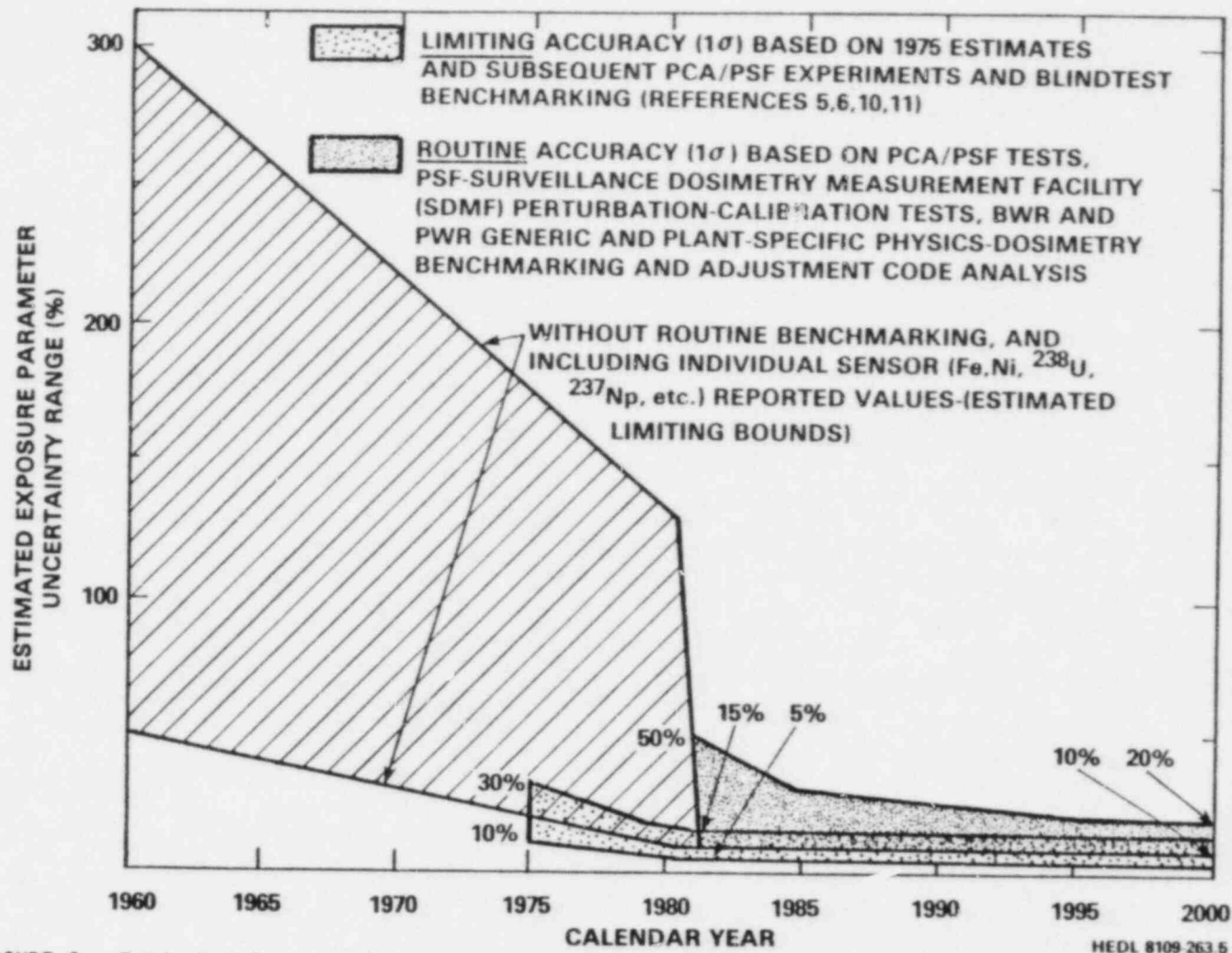
FIGURE 2. Estimated Exposure Parameter Uncertainties Obtained from FSAR and Surveillance Capsule Reports.
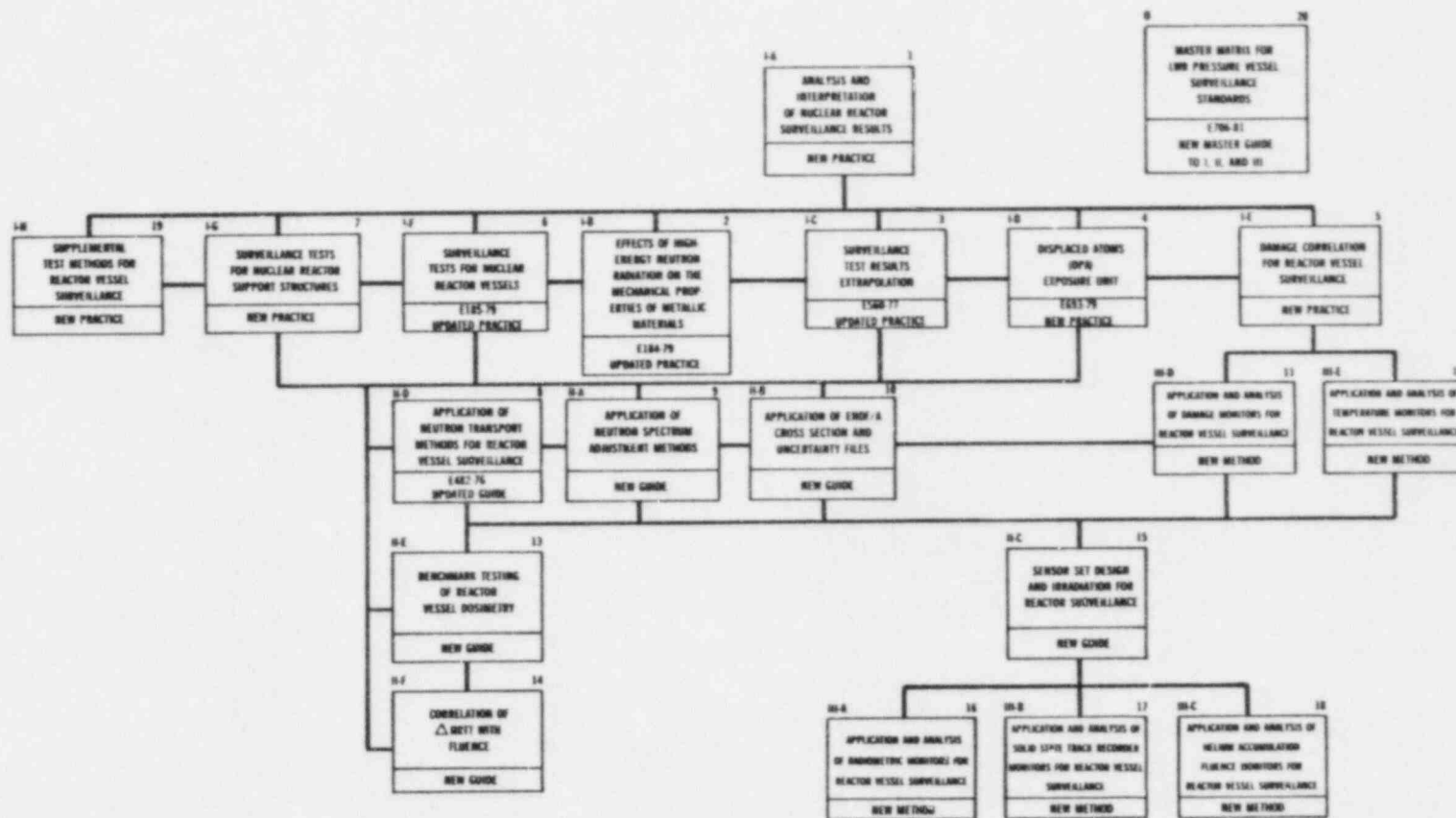
FIGURE 3. ASTM Standards for Surveillance of LWR Nuclear Reactor Pressure Vessels.
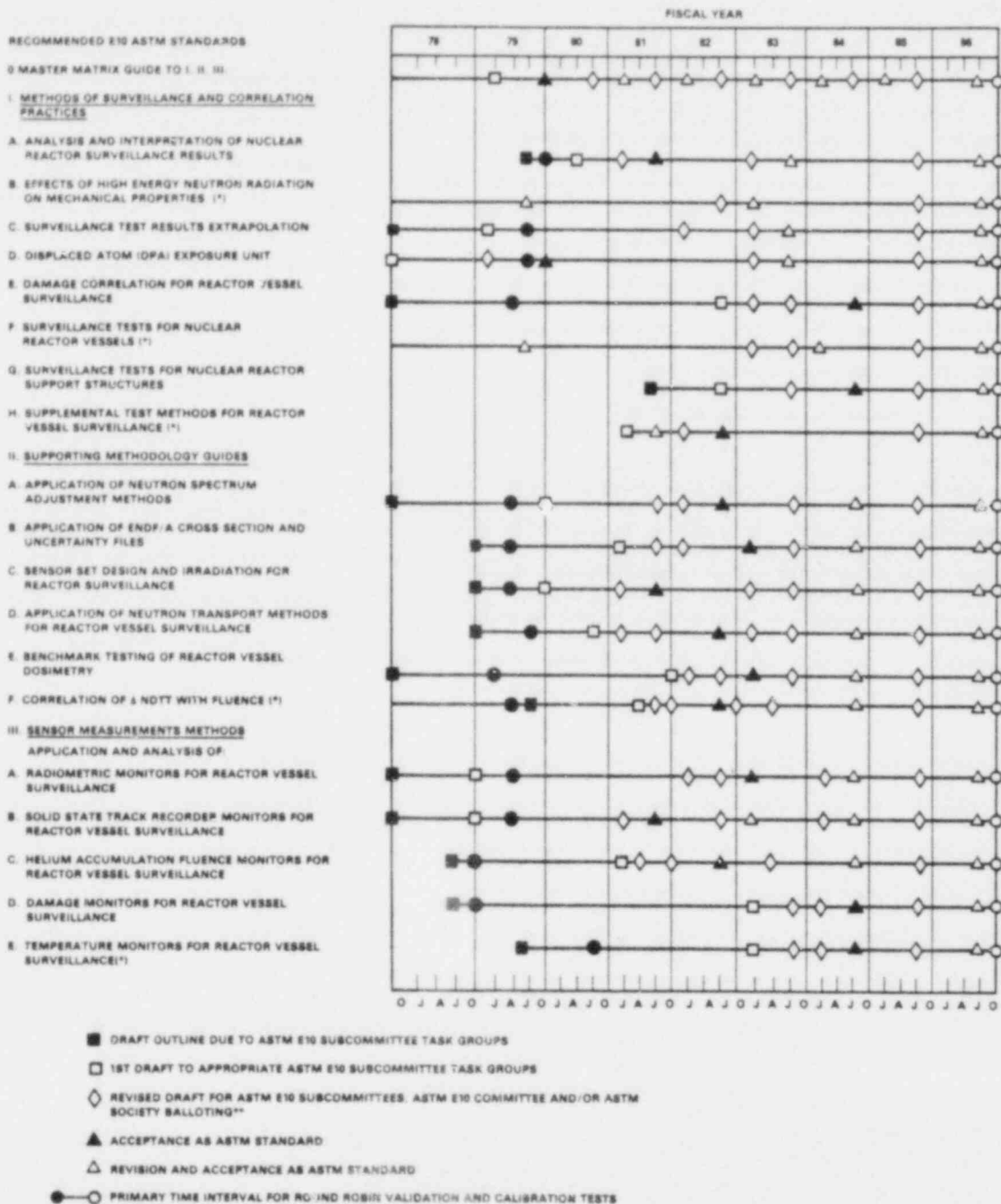
FIGURE 4. Preparation, Validation and Calibration Schedule for LWR
ASTM Pressure Vessel Surveillance Standards.
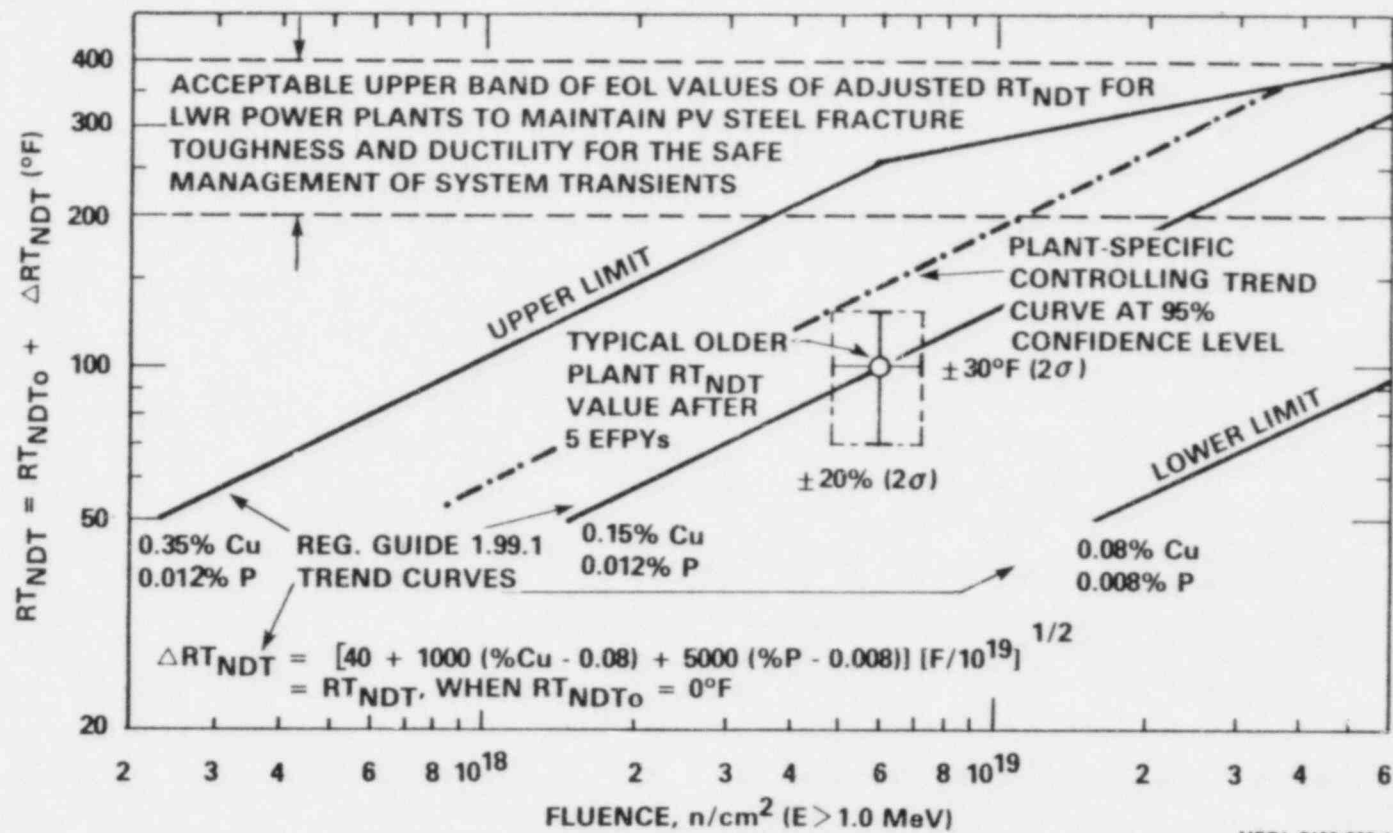
FIGURE 5. Limiting Accuracy of Second Sruveillance Capsule Derived Values of RT_{NDT} and Fluence (E > 1.0 MeV) at the PV Wall Inner Surface After ~5 EFPY of Plant Operation for a Typical PWR with an Older Radiation Sensitive Steel.

22
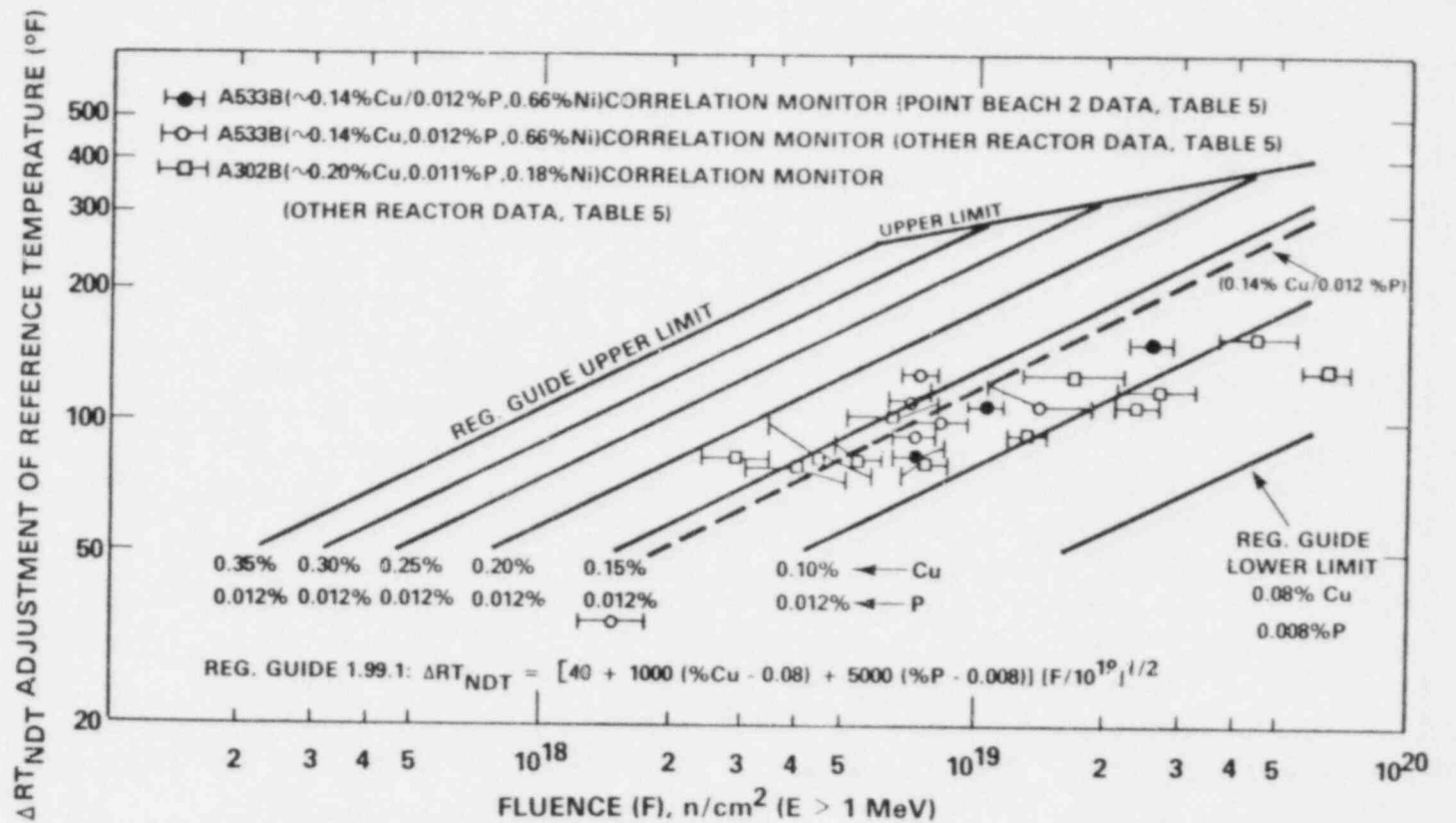
FIGURE 6. ΔRT_{NDT} Trend Curve Results for Correlation Monitor Material with New Exposure Values and Uncertainties.
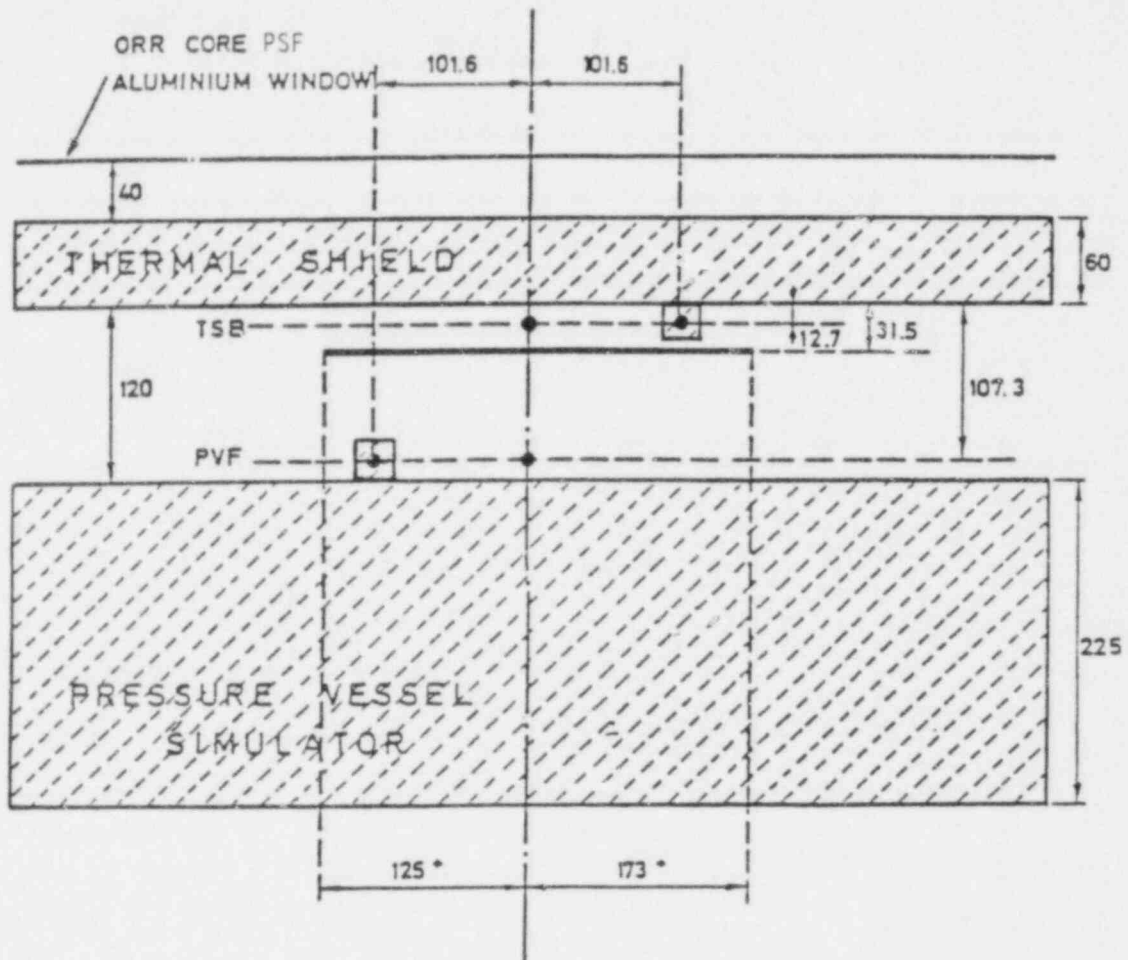
FIGURE 7. PSF-SDMF Perturbation Test Experimental Configuration. (Horizontal Cut at Maximum Axial Flux)

FIGURE 8. Point Beach Unit No. 1 and Connecticut Yankee Plant Specific Trend Curve Results.
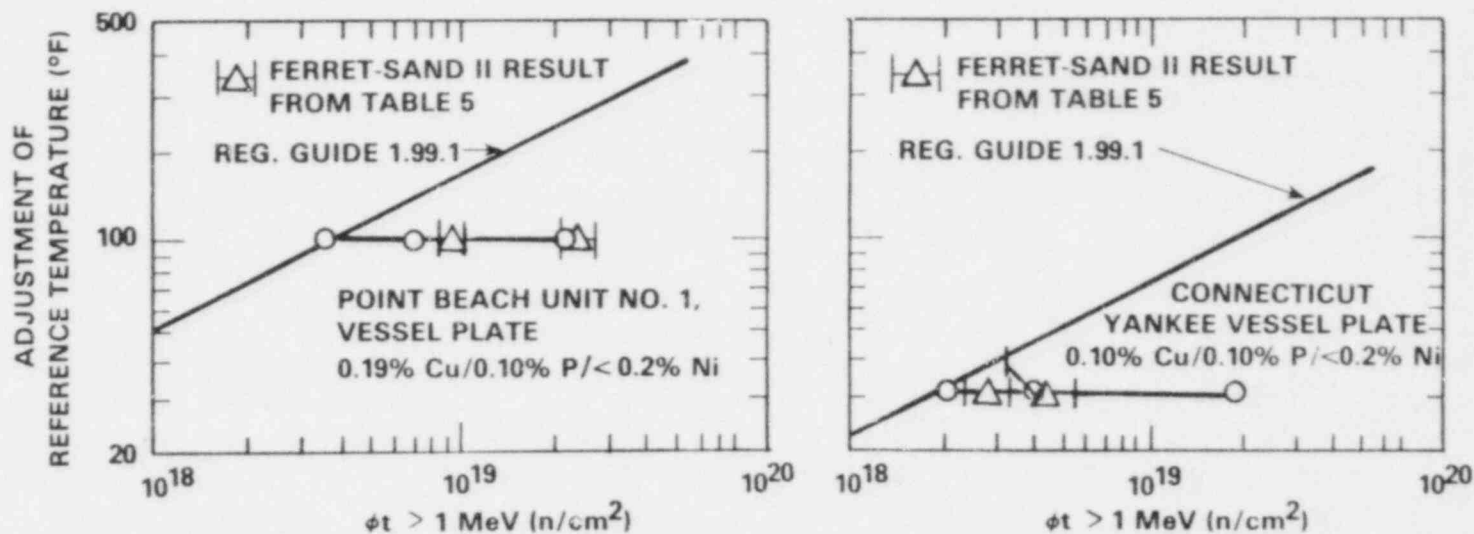
The vessel weldplate, not shown here, also shows apparent saturation. These results fit the hypothesis that materials containing significant amounts of nickel, i.e., greater than 0.5 wt%, do not show saturation in the range of fluence of interest. It appears that materials containing reduced amounts of nickel, i.e., about 0.2 wt%, do reach a saturation embrittlement level.[9] Studies are in progress by Guthrie,[14,15] Varsik,[16] Williams and Squires,[17] Yanichko et al.,[21,22] Pachur,[23] Mager et al.,[24] and others to verify such a hypothesis. It is concluded that there may be an effect of chemical composition on the shape of the trend curve, but data sets investigated to date have not shown any strong evidence of its existence.[14] Limited availability and the poor quality of some of the existing power reactor data are major reasons why this important question has not been answered, see Table 5 and Figure 6.

FIGURE 9. Calculated/Experimental Ratios for $\phi_{E>1.0}$ (PCA 12/13 Configuration) at the Thermal Shield Front (TSF), Thermal Shield Back (TSB), Pressure Vessel Front (PVF), Pressure Vessel 1/4 T, 1/2 T and 3/4 T (Thickness) Positions. (Note that the calculations, generally, underpredicted the magnitude of the flux in passing through the PV wall, by up to an average value of ~20%, at the 3/4 T position; see Reference 5.)

RATIO: dpa/Φ E > 1 MeV (arbitrary units)

DISTANCE FROM CORE (cm)
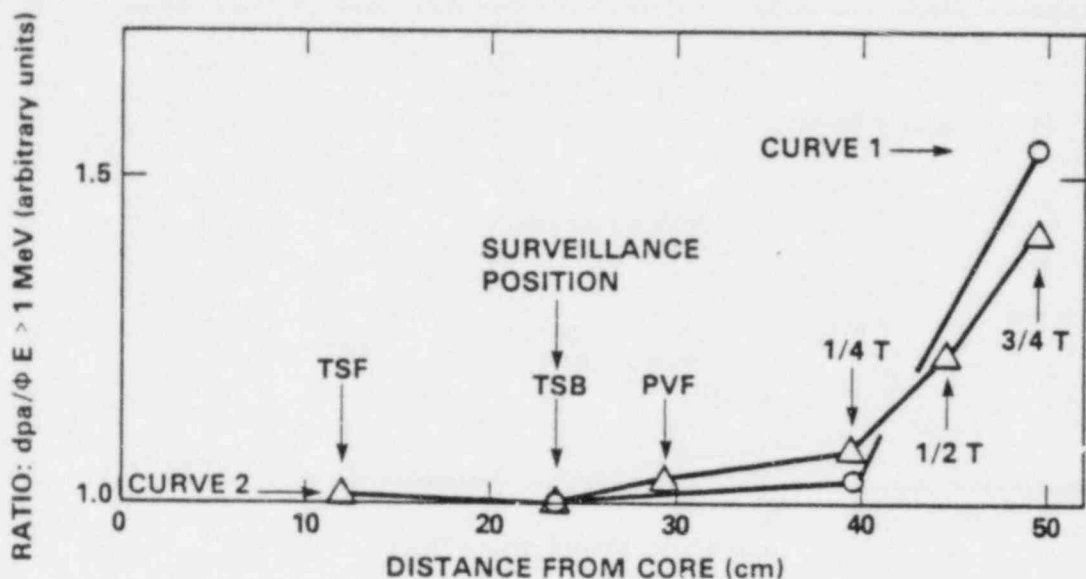
HEDL 8109-263.1

The use of $\phi_{E>1MeV}$ results in a nonconservative estimate of the neutron-produced embrittlement for deep penetration in the PV wall. A better exposure indicator is dpa for steel [using ASTM Standard E706 (I-D) (ASTM E693-79) of Figure 3]. The ratio of dpa to $\phi_{E>1MeV}$ is plotted in Curves 1 and 2. Verification of the applicability of dpa versus fluence (E > 1 MeV) will be accomplished via the PSF-PV Metallurgical Test, Table 1.[6,27]

Curve 1 is the result of calculations done for a PWR power plant. Curve 2 is derived from the PCA data used for Figure 9. The calculated neutron flux-spectra used to derive Curve 2 has been adjusted by passive dosimetry integral measurements and active spectrometry differential measurements as described in Reference 5.

Due to the similarity of conditions (i.e., water next to similar amounts of steel), the neutron spectral shapes are similar at higher energies for both the surveillance position and the 1/4 T position. However, deeper penetration in the PV steel causes substantial spectral changes.

The damage produced, as indicated by dpa, is about 50% higher at the 3/4 T position compared to what would be indicated by $\phi_{E>1MeV}$. Thus, the neutron embrittlement beyond one-fourth of the distance through the vessel may be significantly underestimated if $\phi_{E>1MeV}$ is used as a damage parameter.

FIGURE 10. Comparison of Definition and Implications of Spatial Lead Factors ($\phi_{E>1MeV}$ and dpa) at the Thermal Shield Front (TSF), Thermal Shield Back (TSB), Pressure Vessel Front (PVF), Pressure Vessel (PV) 1/4 T, 1/2 T, 3/4 T (Thickness) Positions.

TABLE 1

BENCHMARK FACILITIES[*] TIME FRAME, PARTICIPANTS, PURPOSE AND USE

METALLURGICAL CALCULATIONAL BENCHMARK (IRL-PV) 1969-1971	CALCULATIONAL DOSIMETRY CALIBRATION BENCHMARKS 1971-2000	CALCULATIONAL BENCHMARK (PCA-PV) 1978-1982	METALLURGICAL TESTING BENCHMARK (PSF-PV) 1980-1984	SURVEILLANCE CAPSULE BENCHMARK (PSF-SDMF) 1979-2000	CORE SOURCE BOUNDARY BENCHMARK (VENUS) 1982-1984	PWR CAVITY BENCHMARK (NESDIP) 1982-1984	GENERIC REACTOR BENCHMARKS (BWR-PWR) 1977-2000
NAT. LABS VENDOR	MULTILAB FOR FBR-LWR PROGRAMS	MULTILAB VENDORS, AE, SERVICE LABS	MULTILAB VENDORS, AE, SERVICE LABS	MULTILAB VENDORS, AE, SERVICE LABS	MULTILAB VENDORS, AE, SERVICE LABS	MULTILAB VENDORS, AE, SERVICE LABS	MULTILAB VENDORS, AE, SERVICE LABS
PHYSICS DOSIMETRY METALLURGY SENSOR TESTS	PHYSICS DOSIMETRY SENSOR CALIBRATIONS & QUALITY ASSURANCE	PHYSICS DOSIMETRY SENSOR TESTS & QUALITY ASSURANCE	METALLURGY DOSIMETRY SENSOR LEAD FACTOR TESTS & QUALITY ASSURANCE	SURVEILLANCE CAPSULE PHYSICS DOSIMETRY LEAD FACTOR TESTS & QUALITY ASSURANCE	NEUTRON SOURCE TO SURVEILLANCE & PV WALL POSITIONS LEAD FACTOR IN-VESSEL TESTS	PHYSICS DOSIMETRY SENSOR LEAD FACTOR EX-VESSEL TESTS	PHYSICS DOSIMETRY SENSOR LEAD FACTOR IN-VESSEL EX-VESSEL TESTS

*Acronyms:

```
AE        - Architect-Engineer
IRL-PV    - Industrial Research Laboratory Pressure Vessel (PV) Mockup Test (Reference 20).
PCA-PV    - Pool Critical Assembly Physics-Dosimetry PV Mockup at ORNL (Reference 5).
PSF-PV    - Oak Ridge Research Reactor Pool Side Facility Metallurgical-Dosimetry PV Mockup (Reference 6).
PSF-SDMF  - PSF Simulated Dosimetry Measurement Facility (Reference 6).
VENUS     - Critical Facility at Mol, Belgium.
NESDIP    - NESTOR Reactor Surveillance Dosimetry Improvement Program Ex-Vessel Cavity Mockup at Winfrith, UK.
BWR       - Boiling Water Reactor.
PWR       - Pressurized Water Reactor.
```

28

TABLE 2

PHYSICS, DOSIMETRY AND METALLURGICAL VARIABLES

To account for neutron radiation damage in setting pressure-temperature limits and making fracture analyses, neutron-induced changes in fracture toughness and embrittlement for power reactor PV and support structure steels must be predicted, then checked by extrapolation of surveillance program data during the vessel's service life. Uncertainties in the predicting methodology can be significant. The main variables of concern are associated with:

1) Steel chemical composition and microstructure

2) Steel irradiation temperature

3) Power plant configurations and dimensions - core edge to surveillance to vessel wall to support structure positions

4) Core power distribution

5) Reactor operating history

6) Reactor physics computations

7) Selection of neutron exposure units

8) Dosimetry measurements

9) Neutron spectral effects

10) Neutron dose rate effects

Variables associated with the physical measurement of PV and support structure steel property changes are not considered here.

TABLE 3

MAIN ELEMENTS OF METALLURGICAL LEAD FACTOR DEFINITION

I. Is the Charpy measurement itself in error?

    A. Do results (both pre- and post-irradiation) fall on an S-shaped curve with $\pm15°F$ or less uncertainty in both tests?

    B. Were the samples transferred promptly from cold bath to test rig in pre-irradiation case?

    C. Are the thermocouples calibrated in post-irradiated test?

    D. Has the Charpy machine been calibrated? Was it tested at or near the time of measurement?

    E. Are the pre-irradiated results believable for the particular chemistry and heat treatment?

    F. Were sufficient points taken?

    G. Were points outside the transition region used in a computer code to bias the result?

    H. Was the ASTM procedure followed?

II. Are the specimens nonrepresentative?

    A. What are the densities of both pre- and post-irradiated specimens?

    B. Do x-ray tests of pre-irradiated specimens show flaws?

    C. Do the fracture surfaces of the specimens show pre-existing voids (regions of surface texture different from surrounding areas on fracture surface)?

    D. Does a post-irradiation chemistry check indicate misidentified specimens?

    E. Were the specimens marked for identification?

III. Is the temperature correctly known?

    A. Were the specimens tightly packed?

    B. What is the gamma heating rate?

    C. What was the heat transfer gas? Was it actually there?

    D. Were there thermal monitors? What did they show? Did they transmute?

    E. Could the capsule have been running cold due to reduced plant power level?

IV. Can the observed Charpy shift be reconciled to the temperature and neutron exposure by any means?

    A. Can a formula be found to fit?

        1. Use weld formulas for weld metal and plate formulas for plate metal, if possible.

        2. If ex-vessel, take into account lower temperature (Odette formulas).

        3. Check nonconforming formulas to see if the data base used to develop the formulas extended to a composition range and heat treatment that includes that of the specimens. Watch Cu, Ni, V, Mo, Si and C concentrations.

        4. Possible formulas are:

            . Varsik (Plate and weld separate).   . Williams and Squires.

            . Guthrie (Plate and weld separate).   . Odette.

            . Guionnet.

            . ASTM recommended practice formulas involving copper, derived from MPC data base.

            . ASTM Practice I-E of Pressure Vessel Surveillance Dosimetry Program (see E706-81 standard).[10]

    B. Is there prior test reactor data on the same or a similar specimen at a similar temperature?

        1. Check data reported by Hawthorne, Williams and Squires, Metals Property Council, EPRI, NRC, and others.

        2. If test reactor data exists, remember rate effects should make surveillance capsule shifts smaller, if there is any significant difference.

V. If formulas don't match data but data appear to be error free, develop plant specific curves for reactor using data produced from surveillance capsules.

VI. Extrapolate to the surface and 1/4 T positions using fluence and dpa ratios developed by dosimetry and reactor calculations. Use ratio of surveillance capsule position to the surface and 1/4 T positions to determine lead factors. Use plant-specific curve of Charpy shift versus fluence or dpa to get allowed EOL fluence.

    A. Validate reactor calculations using PCA data base.

    B. Validate reactor calculations using BWR or PWR generic-plant data base.

    C. Validate reactor calculations using plant-specific data.

TABLE 4

BWR AND PWR GENERIC BENCHMARK FACILITIES

Generic Reactor Benchmark Field	Measurements				Calculations	
	Primary		Verification			
	Funding Organization	Laboratory	Funding Organization	Laboratory	Funding Organization	Laboratory
Browns Ferry 3 In-Vessel (General Electric)	TVA GE	GE(c)*	NRC	HEDL (RM - 1 capsule)*	EPRI	Science Applications Inc.
Browns Ferry 3 Cavity (General Electric)	EPRI	GE(c)*	CEN NRC/EPRI(p) NRC/EPRI(p)	CEN(c) (RM - 1 capsule)* HEDL (RM - 1 capsule)* HEDL (SSTR - 1 capsule)	EPRI	Science Applications Inc.
Arkansas 1** Cavity (Babcock & Wilcox)	EPRI	Univ of Arkansas(c)*	NRC NRC/EPRI(p)	HEDL (RM - ∿3 capsules)* HEDL (SSTR)	EPRI	Univ of Missouri(c) ORNL
Crystal River 3** In-Vessel and Cavity (Babcock & Wilcox)	B&W(p) EPRI?	B&W*	EPRI(p) NRC/EPRI(p)	? (RM)* HEDL (SSTR)	?	B&W(p)
Arkansas 2 (Combustion Engineering)	EPRI(p)	Univ of Arkansas*	EPRI(p) NRC/EPRI(p)	? (RM - 1 capsule)* HEDL (SSTR)	EPRI(p)	Univ of Missouri
McGuire 1 Cavity (Westinghouse)	EPRI(p)	?*	NRC/EPRI(p) NRC/EPRI(p)	HEDL (RM)* HEDL (SSTR)	EPRI(p)	?

(c) = completed; (p) = proposed; ? = unknown

*As appropriate, selected RM sensors (Fe, Ni, 0.1% Co-Al and Cu wires), Charpy specimens, and/or PV wall scrapings can be analyzed for generated helium by RI; see ASTM E706 (III-C) Method for Analysis of Helium Accumulation Fluence Monitors (HAFM) for Reactor Pressure Vessel Surveillance.

**Arkansas 1 and Crystal River 3 are both B&W 177-type plants; therefore, the test results from both are expected to be combined to establish a single set of data to be published for a 177 plant.

TABLE 5

RE-EVALUATED EXPOSURE VALUES FOR SURVEILLANCE CAPSULES

Reactor Unit	Capsule	Fluence ($\phi t > 1$ MeV) Old(a)	Fluence New(b)	To% Uncer	Ratio New/Old	dpa(b) Value	To% Uncer	Ratio dpa/ϕt New	dpa/s(b)	Time (s)	Cor. Mon. Charpy Shift (°F)	Charpy Shift (°F)	RT_{NDT} (°F) (c)	Weld Metal %Cu/%P/%Ni	Lead Factor(d)
WESTINGHOUSE															
Turkey Point 4	S	1.25 E+19	1.41 E+19	29	1.13	0.0215	26	1.52 E-21	1.98 E-10	1.084 E+8	110(e)	--	--	0.30/0.014/0.60	1.61
Turkey Point 4	T	6.05 E+18	8.22 E+18	15	1.36	0.0126	12	1.53 E-21	3.27 E-10	3.840 E+7	100(e)	225	225	0.30/0.014/0.60	2.48
Turkey Point 3	S	1.41 E+19	1.69 E+19	28	1.20	0.0244	25	1.44 E-21	2.33 E-10	1.047 E+8	130	--	--	0.31/0.011/0.57	1.61
Turkey Point 3	T	5.68 E+18	7.68 E+18	10	1.35	0.0112	12	1.46 E-21	3.23 E-10	3.473 E+7	80	162	165	0.31/0.011/0.57	2.48
H. B. Robinson 2	S	3.02 E+18	3.96 E+18	28	1.31	0.006040	25	1.61 E-21	1.46 E-10	4.385 E+7	80	185	110	0.34/0.021/--	1.61
H. B. Robinson 2	V	4.51 E+18	6.41 E+18	27	1.42	0.00976	24	1.52 E-21	9.20 E-11	1.061 E+8	102	27	-32	0.30/0.021/--	0.79
Prairie Island 1	V	5.21 E+18	7.00 E+18	11	1.34	0.0120	13	1.71 E-21	2.77 E-10	4.350 E+7	113(e)	63	-10	0.13/0.017/>0.2	2.5
Prairie Island 2	V	5.49 E+18	7.45 E+18	11	1.37	0.0128	11	1.71 E-21	2.87 E-10	4.454 E+7	130(e)	--	--	0.08/0.019/0.072	2.5
Point Beach 1	S	9.28 E+18	9.28 E+18	9	--	0.0155	10	1.67 E-21	1.34 E-10	1.163 E+8	110	165	120	0.24/0.019/0.52	1.4
Point Beach 1	R	2.22 E+19	2.41 E+19	11	1.11	0.0419	11	1.74 E-21	2.57 E-10	1.632 E+8	95	183	140	0.24/0.019/0.57	2.5
R. E. Ginna 1	R	7.60 E+18	1.32 E+19	9	1.73	0.0232	9	1.75 E-21	2.68 E-10	8.628 E+7	83	153	112	0.23/0.012/0.56	2.5
R. E. Ginna 1	W	5.32 E+18	5.55 E+18	12	1.04	0.00996	12	1.79 E-21	2.54 E-10	3.923 E+7	95(e)	175	115	0.23/0.012/0.56	3.3
Kewaunee	A	5.59 E+18	7.13 E+18	9	1.28	0.0124	11	1.72 E-21	2.97 E-10	4.167 E+7	120	60	60	0.20/0.016/0.77	2.5
San Onofre 1	A	1.20 E+18	2.65 E+19	19	2.21	0.0445	18	1.68 E-21	7.42 E-10	5.846 E+7	155	135	113	0.19/0.17/<0.2	4.8
San Onofre 1	D	2.36 E+19	4.40 E+19	20	1.87	0.0742	19	1.69 E-21	8.32 E-10	8.914 E+7	130	154	154	0.19/0.17/<0.2	5.1
San Onofre 1	F	5.14 E+19	6.45 E+19	12	1.25	0.110	15	1.71 E-21	4.49 E-10	2.451 E+8	110(e)	154	165	0.19/0.17/<0.2	1.8
Point Beach 2	T	9.45 E+18	1.04 E+19	9	1.10	0.0165	10	1.59 E-21	1.50 E-10	1.098 E+8	85(e)	236	230	0.25/0.014/0.59	1.6
Point Beach 2	V	4.74 E+18	7.24 E+18	12	1.53	0.0120	11	1.66 E-21	2.48 E-10	4.859 E+7	151(e)	95	45	0.25/0.014/0.59	2.5
Point Beach 2	R	2.01 E+19	2.56 E+19	11	1.27	0.0438	11	1.71 E-21	2.72 E-10	1.609 E+8	85	--	--	0.25/0.014/0.59	3.37
Conn. Yankee	A	2.08 E+18	2.92 E+18	17	1.40	0.00424	13	1.47 E-21	7.89 E-11	5.377 E+7	85	--	--	0.27/0.020/0.05	6.1
Conn. Yankee	F	4.04 E+18	4.38 E+18	30	1.08	0.00645	26	1.47 E-21	8.35 E-11	7.728 E+7	127	--	--	0.27/0.020/0.05	1.3
Conn. Yankee	H	1.79 E+19	2.19 E+19	32	1.22	0.0362	30	1.65 E-21	1.51 E-10	2.390 E+8		--	--	0.27/0.020/0.05	1.57
COMBUSTION ENGINEERING															
Maine Yankee	1	1.30 E+19	2.00 E+19	22	1.54	0.0640	25	1.72 E-21	1.24 E-9	2.776 E+7	145(e)	270	240	0.36/0.015/0.78	30.0
Maine Yankee	2	8.84 E+18	1.01 E+20	12	1.14	0.155	13	1.53 E-21	1.07 E-9	1.446 E+8	--	345	315	0.36/0.015/0.78	--
Maine Yankee	263	6.90 E+18	6.72 E+18	8	0.97	0.00988	9	1.47 E-21	6.84 E-11	1.446 E+8	--	252	192	0.36/0.015/0.78	1.76
BABCOCK & WILCOX															
Oconee	F	8.70 E+17	6.83 E+17	27	0.79	0.00095	21	1.38 E-21	3.60 E-11	2.625 E+7	14(e)	--	--	0.18/0.014/0.52	1.6
Oconee 1	E	1.50 E+18	1.65 E+18	13	1.10	0.00222	12	1.34 E-21	4.30 E-11	5.166 E+7	35(e)	65	75	0.32/0.016/0.58	1.65

Fluence Scale Adjustment Range (Maxima/Minima) = 2.80

(a) Surveillance capsule report values based on previous standards and recommended procedures and data.
(b) Preliminary FERRET-SAND II derived new values based on current standards and recommended procedures and data; an estimate of possible total bias uncertainties (physics-calculational, sensor QA, photofission, etc. corrections) is not included at present; see Table 10 and Figure 9.
(c) $RT_{NDT} = RT_{NDT0} + \Delta RT_{NDT}$ [41 J (30 ft-lb)].
(d) Calculated ratio of surveillance capsule to pressure vessel wall maximum fluence (E > 1.0 MeV) values.
(e) A533B steel (%Cu/%P/%Ni = 0.14/0.012/0.66, except for Oconee which is 0.17/0.013/0.64), otherwise A302B steel (0.20/0.011/0.18); 41 J (30 ft-lb) Charpy shift (ΔRT_{NDT}).

TABLE 6

OPERATING REACTORS WITH HIGH FLUENCE EXPOSURE

Plant	Manufacturer Plant	Manufacturer Vessel	Percent Copper Circ. Welds	Percent Copper Long. Welds	Time (EFPY)	Fluence(a) (E > 1.0 MeV) x 10^18 n/cm² Circ. Welds	Fluence(a) (E > 1.0 MeV) x 10^18 n/cm² Long. Welds	RT_NDT Calculated(b) Circ. Welds	RT_NDT Calculated(b) Long. Welds	RT_NDT Measured(c) Circ. Welds	RT_NDT Measured(c) Long. Welds	RT_NDT Measured(c) Surveillance Capsule Used
Fort Calhoun	CE	CE	0.35	0.35	4.8	8.2	8.2	280	280	--	--	--
H. B. Robinson	W	CE	0.34	0.34	6.8	11.7	10.8	290	290	175	165	V
Turkey Point 3	W	B&W	0.31	--	5.7	11.2	--	290	--	200	--	T
Turkey Point 4	W	B&W	0.30	--	5.2	10.2	--	280	--	250	--	T
San Onofre 1	W	CE	0.19	0.19	8.8	15.4	15.4	270	270	41	41	A
San Onofre 1	W	CE	0.19	0.19	8.8	15.4	15.4	270	270	44	44	F
Maine Yankee	CE	CE	0.36	0.36	5.5	4.7	4.7	240	240	160	160	2(d)
Maine Yankee	CE	CE	0.36	0.36	5.5	4.7	4.7	240	240	156	156	263
Calvert Cliffs 1	CE	CE	0.30	0.30	4.1	6.0	6.0	230	230	--	--	--
TMI 1	B&W	B&W	0.35	0.31	3.5	2.1	2.1	180	160	--	--	--
Oconee 1	B&W	B&W	0.26	0.31	4.9	2.6	2.3	150	170	76	71	E
Palisades	CE	CE	0.25	0.25	3.9	4.6	4.6	190	190	--	--	--
Yankee Rowe	W	B&W	(0.20 for plate)		14.1	(11.0 for plate)		(200 for plate)		--	--	--
Zion 1	W	B&W	0.35	0.31	4.3	2.7	0.9	!70	90	--	--	--
Arkansas 1	B&W	B&W	0.31	0.31	3.9	2.4	1.7	170	150	--	--	--
Indian Point 2	W	CE	(0.25 for plate)		4.0	(2.0 for plate)		(140 for plate)		--	--	--
Rancho Seco	B&W	B&W	0.31	0.31	3.3	2.1	1.9	160	150	--	--	--
Surry 1	W	B&W	0.25	0.18	4.5	7.0	1.5	190	60	--	--	--
Crystal River 3	B&W	B&W	0.35	0.31	2.2	1.3	1.2	150	130	--	--	--

(a) As of May 1, 1981.

(b) RT_NDT was calculated by P. N. Randall of NRC using known chemistry, presently believed fluence at PV front face and Regulatory Guide 1.99.1.

(c) RT_NDT was determined using measured Charpy shifts for surveillance-capsule weld material and new values of fluence (E > 1.0 MeV), Table 5. The Regulatory Guide 1.99.1[2] fluence dependency (N = 1/2) was used to scale the accelerated surveillance capsule results back to the column 7 and 8 values of fluence.

(d) The Reg. Guide 1.99.1 upper-limit fluence dependency, Figure 6, was used to scale back the Maine Yankee accelerated Capsule 2 results.

TABLE 7

PSF-SDMF PERTURBATION TEST RESULTS

	Unperturbed-to-Perturbed Reaction Rate Ratios					
Reaction	Thermal Shield Back (TSB)			Pressure Vessel Front (PVF)		
	Experiment	Calculation	C/E	Experiment	Calculation	C/E
$^{237}Np(n,f)$	0.756	0.749	0.991	--	0.798	--
$^{93}Nb(n,n')$	0.833	--	--	0.895	--	--
$^{238}U(n,f)$	0.852	0.840	0.986	--	0.871	--
$^{58}Ni(n,p)$	0.919	0.922	1.003	0.962	0.942	0.979
$^{54}Fe(n,p)$	0.887	0.937	1.056	0.936	0.953	0.974
$^{46}Ti(n,p)$	0.971*	0.990	1.020	0.978*	0.993	1.015
$^{63}Cu(n,\alpha)$	1.042	1.006	0.965	--	1.004	--

_____

*The reaction listed was Ti(n,x) by experimenter.

34

TABLE 8

TYPICAL SINGLE PLANT RATIOS (MAXIMA/MINIMA) FOR MEASURED
SURVEILLANCE CAPSULE REACTION RATES FOR INDIVIDUAL SENSORS
AS A RESULT OF DIFFERENCES IN CORE SOURCE DISTRIBUTIONS

Sensor Reaction	Approx Maxima/Minima* Reaction Rate Ratio
$^{58}Ni(n,p)^{58}Co$	1.6
$^{54}Fe(n,p)^{54}Mn$	1.4
$^{63}Cu(n,\alpha)^{60}Co$	1.3
$^{238}U(n,f)^{137}Cs$	1.5
$^{237}Np(n,f)^{137}Cs$	1.4

---

*Based on core fuel subassembly replacement calculational and measurement
studies. The fluence > 1 MeV at the inner PV surface will, generally,
follow these ratios. It is noted that a substantial part of the PCA pro-
gram has addressed the neutronic validation of LWR-PV lead factors in a
slab arrangement of thermal shield and pressure vessel simulator, driven
by a clean, well-characterized MTR-type core. It has focused upon the
deep-penetration projection uncertainties in this lead factor issue.
Actual LWR lead factors also involve significant azimuthal flux varia-
tions, whose calculational accuracy depends upon:

- Correct estimates of core source distributions, on a pin-to-pin
  basis for the last fuel row, in terms of the total absolute core
  power, and

- Correct modeling of core boundary heterogeneity effects and, in
  more recent plants, of the heterogeneity effect of neutron pads
  attached to the core barrel (thermal shield).

The LWR-PV VENUS, NESDIP, and the BWR and PWR generic benchmarks
(Table 1) are concerned with these issues.

TABLE 9

DOSIMETRY/PHYSICS RESULTS FOR POINT BEACH 2

	Capsule V	Capsule T	Capsule R
INITIAL ANALYSIS	4.74×10^{18} (n/cm^2 > 1.0 MeV)[a]	9.45×10^{18}[b]	20.1×10^{18}[c]
AFTER WESTINGHOUSE REANALYSIS	6.53×10^{18}	8.29×10^{18}	20.1×10^{18}
RATIO: AFTER/INITIAL	1.37	0.88	1.0
RELATIVE SWING	Capsule V/T = 1.37/0.88 = 1.56		Capsule R/T = 1.0/0.88 = 1.14
AFTER HEDL REANALYSIS[d]	$7.24 \times 10^{18} \pm 12\%$ (1σ)	$1.04 \times 10^{19} \pm 9\%$ (1σ)	$2.56 \times 10^{19} \pm 11\%$ (1σ)
RATIO: AFTER/INITIAL	1.53	1.10	1.27
RELATIVE SWING	Capsule V/T = 1.53/1.10 = 1.39		Capsule R/T = 1.27/1.10 = 1.15

CONCLUSION: All surveillance reports and test reactor reports must be reanalyzed to define new exposure values and uncertainties using current standards and recommended procedures and data.

(a) Surveillance Capsule Report V, June 10, 1975 (Reference 18).
(b) Surveillance Capsule Report T, August 1978 (Reference 19).
(c) Surveillance Capsule Report R, December 1979 (Reference 21).
(d) Preliminary FERRET-SAND II results (Table 5).

36

TABLE 10

COMPARISON OF HEDL AND WESTINGHOUSE ANALYSES OF POINT BEACH 2 CAPSULE R SURVEILLANCE DOSIMETERS[a]

Reaction and Axial Location[b]	R[b] (cm)	Saturated Activity (dps/g)		(West. - HEDL/HEDL) Comparison (%)
		HEDL	Westinghouse[b,c]	
$^{59}Co/Al(n,\gamma)$, Bare				
Top		11.67 E+10	11.8 E+10	+1.08
Mid Top		8.297 E+10	8.20 E+10	-1.17
Middle		8.639 E+10	8.67 E+10	+0.32
Mid Bottom		--	--	--
Bottom		11.53 E+10	11.47 E+10	-0.58
$^{59}Co/Al(n,\gamma)$, Cadmium-Covered				
Top		4.575 E+10	4.59 E+10	+0.26
Mid Top		4.426 E+10	4.43 E+10	+0.02
Middle		4.233 E+10	4.27 E+10	+0.80
Mid Bottom		5.055 E+10	5.09 E+10	+0.62
Bottom		4.794 E+10	4.82 E+10	+0.54
$^{63}Cu(n,a)$				
Top	158.33	4.382 E+5	4.28 E+5	-2.33
Mid Top	158.33	3.880 E+5	3.87 E+5	-0.25
Mid Bottom	158.33	4.318 E+5	4.28 E+5	-0.89
Bottom	158.33	4.593 E+5	4.54 E+5	-1.14
$^{54}Fe(n,p)$[d]				
V-13	157.33	6.16 E+6	6.18 E+6	+0.30
E-23	157.33	5.752 E+6	5.72 E+6	+0.56
E-13	157.33	5.183 E+6	4.96 E+6	-4.30
H-9	158.33	4.893 E+6	4.66 E+6	-4.76
R-14	158.33	4.904 E+6	4.77 E+6	-2.73
W-16	158.33	4.936 E+6	4.61 E+6	-6.60
$^{58}Ni(n,p)$				
Middle	158.33	7.390 E+7	7.45 E+7	+0.81
$^{237}Np(n,f)^{137}Cs$				
Middle	158.10	7.180 E+7	6.79 E+7	-5.43
$^{238}U(n,f)^{137}Cs$[e]				
Middle	158.10	9.534 E+6	9.03 E+6	-4.95

[a]Samples of Co/Al and Cu are being shipped to Rockwell International for He analysis. The remaining samples are to be shipped to CEN/SCK for additional radiometric analysis. Discussions have been held with NBS, and certified fission flux standard samples will be prepared by NBS and submitted to HEDL for analysis.

[b]Distance from core center, data from EPRI Progress Report, WCAP-9635, December 1979.[21]

[c]Westinghouse-reported values for Co/Al samples were reported per weight of alloy dosimeter material. Reported values were multiplied by 1/0.0025 to obtain activity per gram cobalt. QA confirmation of the Co alloy content is planned by neutron activation at NBS and calculation from both the certified thermal flux supplied by NBS and the relative ratio with SRM 953.

[d]Calculations for this reaction were made using the iron content as determined by HEDL for the specific solutions received from Westinghouse, see Table 10 continued.

[e]Calculations are based on the ^{238}U solution content determined by HEDL, see Table 10 continued. Corrections have not been made for ^{235}U impurity, $^{238}U(n,\gamma)^{239}Pu$ buildup or photofission contributions. Preliminary calculations at HEDL indicate corrections of as much as ~6% for ^{235}U and ~16% for ^{239}Pu may be required. Rough calculations at Westinghouse indicate <3% correction for photofission contribution.

TABLE 10 (Cont'd)

HEDL POINT BEACH 2 CAPSULE R SURVEILLANCE DOSIMETERS QA OVERCHECKS

Analyzing Laboratory	Analysis of	^{238}U Content (mg/200 ml)	Isotopic Analysis (at.%)				
			^{233}U	^{234}U	^{235}U	^{236}U	^{238}U
ORNL-Westinghouse	$^{238}U_3O_8$ Dosimeter Solution	11.91	<0.0001	0.0004	0.0322	0.0001	99.9673
HEDL (by IDMS*)	$^{238}U_3O_8$ Dosimeter Solution	12.10		<0.001	0.034	<0.001	99.963

HEDL (by Atomic Absorption)	Fe Charpy Solution	Fe Content (mg/ml)
	Sample No. 2450	2.436
	Sample No. 2451	4.053
	Sample No. 2452	7.665
	Sample No. 2453	4.433
	Sample No. 2454	6.459
	Sample No. 2455	4.858

		Co Content (wt%)
Vendor Certification	Co/Al Alloy	0.15
HEDL (by Neutron Activation)	Co/Al Alloy	

Irradiation will be made at NBS with subsequent analysis at HEDL. Comparative calculations will be made from both relative ratios to SRM 953, material irradiated simultaneously, and from the thermal cross section and certified flux-fluence.

*Isotope dilution mass spectrometry.

38

TABLE 11

REPORTED SURVEILLANCE CAPSULES SINGLE FOIL
FLUX/FLUENCE VALUES ($\phi_i > 1$ MeV) RELATIVE TO ^{54}Fe(n,p) RESULT

Reactor Name (Vendor-Type, Country, Operation Date)	Service Laboratory Report	Single Foil Flux/Fluence > 1 MeV			
		^{58}Ni(n,p)	^{63}Cu(n,a)	^{238}U(n,f)(f)	^{237}Np(n,f)(f)
Point Beach 1 (West. PWR, USA, 12/70)	BMI (1973)[a]	1.09	1.63	1.61	2.17
		[Reported[e] Surveillance Value: 1.0(Fe)]			
Same (Angle A)	West. (1979)[b]	0.80	1.51[c]	1.03	1.25
Same (Angle A + 180°)	West. (1979)[b]	1.01	1.41[c]	1.13	1.01
		[Reported[e] Surveillance Value: 1.0(Fe)]			
Average Values for Seven West. Power Plants	West. (1979)[b]	0.97	1.25[c]	1.08	1.15
Humboldt Bay 3 (GE BWR, USA, 8/63)	GE (1967)[a]	0.88	0.80	--	--
		[Reported[e] Surveillance Value: 1.0(Fe)]			
San Onofre 1 (West. PWR, USA, 1/68)	SWRI (1971)[a]	1.00	1.27	1.10	1.42 (BNW Spectrum 1)
(Wnst. PWR, USA, 1/68)	SWRI (1971)[a]	1.05	0.88	1.29	1.45 (BNW Spectrum 2)
		[Reported[e] Surveillance Value: 0.85 (SAND II, multiple foils)]			
Oconee 1 (B&W PWR, USA, 7/73)	B&W (1975)[a,b]	1.18	--	2.50	2.70
		[Reported[f] Surveillance Value: $\frac{1.0 + 2.5}{2} = 1.76$(Fe+U)]			
Doel 1 (Belgium-West. PWR, Belgium, 1/75)	CEN/SCK (1979)	1.09	1.51[c]	--	2.41
	CEN/SCK (1979)	1.09	1.06[d]	--	2.41
		[Reported[e] Surveillance Value: ~1.09(Ni)]			

(a)The results reported in Columns 3-6 are based on the application of old standards, procedures and data and are, therefore, not representative of current capabilities and technology (see Table 5).
(b)Surveillance capsule flux perturbation corrections were calculated by Westinghouse to provide necessary correlations between the U, Np, Cu, Ni and Fe results. No other results shown in the table were corrected for perturbation effects. The current Westinghouse and B&W analyses (Table 5) have made use of newer standards and recommended procedures and data and are, therefore, more representative of current capabilities and technology.
(c)ENDF/B-IV $\sigma(E)$ for ^{63}Cu(n,a).
(d)Mann-Schenter $\sigma(E)$ for ^{63}Cu(n,a).
(e)These reported surveillance capsule measured fluence values are used for correlating the surveillance capsule metallurgical data with other test and power reactor data. They are also used for making localized predictions of expected PV lifetime neutron exposures and/or can be used to simply confirm the correctness of one-, two- and three-dimensional reactor physics computations.
(f)Based on ^{137}Cs analysis; the Ni, Fe and Cu provide experimental fluence data for time periods up to about 1 year, 5 years and 25 years with a knowledge of the surveillance capsule flux level time history. This information is not needed, however, for a reliable interpretation of fission foil ^{137}Cs($t_{1/2} \sim 31$ yrs) results.

TABLE 12

RESULTS OF FAST NEUTRON DOSIMETRY FOR CAPSULES V AND R FOR KEWAUNEE
(Demonstration of the Value of Using Multiple Sensor and
Benchmarked Reactor Physics Results)

Capsule	Reaction	Adjusted Saturated Activity (dis/s)		ϕ (E > 1.0 MeV) (n/cm^2-s)		ϕ (E > 1.0 MeV) (n/cm^2)	
		Measured	Calculated	Measured	Calculated	Measured	Calculated
V	$Fe^{54}(n,p)Mn^{54}$	5.30×10^6	5.65×10^6	1.36×10^{11}	1.45×10^{11}	5.36×10^{18}	5.71×10^{18}
	$Cu^{63}(n,a)Co^{60}$	4.51×10^5	3.86×10^5	1.69×10^{11}		6.66×10^{18}	
	$Ni^{58}(n,p)Co^{58}$	7.27×10^7	8.37×10^7	1.26×10^{11}		4.96×10^{18}	
	$Np^{237}(n,f)Cs^{137}$	7.84×10^7	7.01×10^7	1.62×10^{11}		6.38×10^{18}	
	$U^{238}(n,f)Cs^{137}$	8.89×10^6	7.72×10^6	1.67×10^{11}		6.58×10^{18}	
R	$Fe^{54}(n,p)Mn^{54}$	3.77×10^6	5.65×10^6	9.68×10^{10}	1.45×10^{11}	1.37×10^{19} *	2.06×10^{19}
	$Cu^{63}(n,a)Co^{60}$	4.94×10^5	3.86×10^5	1.86×10^{11}		2.64×10^{19}	
	$Ni^{58}(n,p)Co^{58}$	8.50×10^7	8.37×10^7	1.47×10^{11}		2.09×10^{19}	
	$Np^{237}(n,f)Cs^{137}$	not determined	7.01×10^7	not determined		—	
	$U^{238}(n,f)Cs^{137}$	8.33×10^6	7.72×10^6	1.56×10^{11}		2.22×10^{19}	

*The $^{54}Fe(n,p)^{54}Mn$ results obtained from Capsule R are inconsistent with the remaining dosimetry from Capsule R as well as with the iron data from Capsule V. The iron data from Capsule V agree with the overall average (within 12%), while, for Capsule R, the iron data are low by 51%. The reason for this discrepancy is not known.[22] This demonstrates the value of having multiple sensor, more than one surveillance capsule, and benchmarked reactor physics results so that "bad" sensor data points may be easily identified and assigned higher uncertainty values.

40

TABLE 13

INTERLABORATORY COMPARISON OF RADIOMETRIC (RM) ANALYSIS PROCEDURES AND DATA[a]
[Range Evaluation (Maxima/Minima) of RM Results Based on First PSF-SDMF Test]

Sensor[b] Set No.	$^{58}Ni(n,p)$ Ratio 1	Ratio 2	Ratio 3	Labs	$^{46}Ti(n,p)$ Ratio 1	Ratio 2	Ratio 3	Labs	$^{63}Cu(n,\alpha)$ Ratio 1	Ratio 2	Ratio 3	Labs	$^{54}Fe(n,p)$ Ratio 1	Ratio 2	Ratio 3	Labs
HNF - 1	1.14 C/B	1.10 D/B	1.06 D/C	6	1.39 C/B	1.16 C/B	1.04 C/E	6	1.11 F/B	---	1.09 F/E	6	1.38 C/B	1.11 C/B	1.04 C/F	6
HNF - 3	1.28 C/B	1.09 A/B	1.05 A/C	6	1.48 C/B	1.21 C/B	1.04 C/A	6	1.05 C/E	1.06 C/F	---	6	1.27 C/B	1.10 A/B	1.04 A/F	6
HNF - 2	1.25 C/B	1.13 F/B	1.06 F/E	6	1.42 C/B	1.19 C/B	1.08 C/E	6	1.06 C/E	1.09 C/E	---	6	1.46 C/B	1.12 A/B	1.06 A/E	6
HNF - 4	1.28 C/B	1.14 F/B	1.06 F/E	6	1.41 C/B	1.09 C/B	1.08 C/E	6	1.08 C/E	1.09 F/E	---	6	1.43 C/B	1.13 C/B	1.04 C/F	6

	$^{58}Fe(n,\gamma)$ Ratio 1	Ratio 2	Ratio 3	Labs		Sensor Set No.	$^{59}Co/Al(n,\gamma)$ Ratio 1	Ratio 2	Ratio 3	Labs
HNF - 1	1.15 C/A	1.03 E/A	1.03 E/A	3[c]		HF - 3	1.15 C/B	1.09 C/B	1.06 C/F	6
HNF - 3	1.02 C/E	1.02 A/E	1.02 A/E	3		HF - 5	1.15 C/B	1.11 C/B	1.04 C/D	6
HNF - 2	1.23 C/A	1.04 E/A	1.04 E/A	3		HF - 4	1.06 F/B	1.09 C/B	1.05 C/F	6
HNF - 4	1.12 C/E	1.01 A/E	1.01 A/E	3		HF - 6	1.23 C/B	1.17 C/B	1.07 C/E	6

	$^{235}U(n,f)^{140}Ba$ Ratio 1	Ratio 2	Ratio 3	Labs	$^{235}U(n,f)^{103}Ru$ Ratio 1	Ratio 2	Ratio 3	Labs	$^{235}U(n,f)^{95}Zr$ Ratio 1	Ratio 2	Ratio 3	Labs	$^{235}U(n,f)^{137}Cs$ Ratio 1	Ratio 2	Ratio 3	Labs
HF - 3	1.06 A/E	---	---	3	1.19 C/D	1.22 A/C	1.08 A/D	4	1.09 D/C	1.22 D/C	1.08 D/E	5	---	1.11 E/C	---	3
HF - 5	1.19 A/D	---	---	3	1.73 C/D	1.19 C/D	1.07 C/E	4	1.51 C/B	1.29 C/B	1.12 C/E	5	---	1.31 C/D	---	3
HF - 4	1.05 A/D	--	---	3	1.30 C/D	1.09 A/C	---	4	1.13 D/C	1.14 D/C	1.07 A/C	5	---	1.05 F/C	---	3
HF - 6	1.13 A/D	---	---	3	1.43 C/D	1.14 A/D	---	4	1.15 C/E	1.11 A/C	1.07 A/B	5	---	1.07 E/D	---	3

	$^{237}Np(n,f)^{140}Ba$ Ratio 1	Ratio 2	Ratio 3	Labs	$^{237}Np(n,f)^{103}Ru$ Ratio 1	Ratio 2	Ratio 3	Labs	$^{237}Np(n,f)^{95}Zr$ Ratio 1	Ratio 2	Ratio 3	Labs	$^{237}U(n,f)^{137}Cs$ Ratio 1	Ratio 2	Ratio 3	Labs
HF - 1	1.10 A/F	---	1.04 A/D	4	1.37 C/F	1.11 A/C	---	5	1.16 A/E	1.21 B/C	1.16 A/E	6	---	1.09 D/C	---	4
HF - 2	1.13 A/E	---	---	4	1.27 C/F	1.12 A/F	---	5	1.14 D/F	---	---	6	---	1.12 F/D	---	4

	$^{238}U(n,f)^{140}Ba$ Ratio 1	Ratio 2	Ratio 3	Labs	$^{238}U(n,f)^{103}Ru$ Ratio 1	Ratio 2	Ratio 3	Labs	$^{238}U(n,f)^{95}Zr$ Ratio 1	Ratio 2	Ratio 3	Labs	$^{238}U(n,f)^{137}Cs$ Ratio 1	Ratio 2	Ratio 3	Labs
HF - 1	1.09 A/D	---	1.04 D/E	4	1.44 C/F	1.11 A/F	---	5	1.16 C/F	1.13 D/C	1.06 B/F	6	---	1.08 E/C	---	4
HF - 2	1.09 A/E	---	---	4	1.27 C/F	1.07 A/E	---	5	1.13 D/E	---	---	6	---	1.06 B/E	---	4

(a)Four vendors and two service laboratories participated in this test. All laboratories remain anonymous for these intercomparisons and are identified only as Laboratories A, B, C, D, E and F.[6] The table evaluation shows the present laboratory-to-laboratory comparative status but also shows the improvement in the data comparisons (Ratios 2 and 3) as a result of interim evaluations and discussions with participants. Ratio 2 was obtained after discussions with participants and subsequent reworking of data by participants. For Ratio 3, and for the case of nonfissile sensors, the results from Laboratory B appeared to be consistently biased low and were, therefore, not used. In the case of the fissile sensors, if a participant appeared to be definitely biased, those results were not used in Ratio 3.

(b)HNF-X and HF-X are sensor set identification numbers for specific perturbed locations in 1-in. x 1-in. stainless steel simulated surveillance capsules for this first PSF-SDMF test; see Table 7 for a preliminary comparison of C/E ratios.

(c)Results for the $^{58}Fe(n,\gamma)$ reaction were not reported by one laboratory after preliminary recalibration of their counting system.

TABLE 14

COMPARISON OF RESULTS OF INTERLABORATORY CONSISTENCY IN MEASURING NICKEL FLUENCE STANDARDS[a]

| Nickel Foil ID | 235U Fission Spectrum Fluence in 10^{15}m/cm² | | |
	Reported Value[b]	NBS Value[c]	Ratio of Reported to NBS Value
AP	1.48 ± 5.5 %	1.51 ± 2.5%	0.98
AR	1.479 ± 0.84%	1.47 ± 2.7%	1.01
AS	1.491 ± 1.2 %	1.49 ± 2.7%	1.00
AU	1.672 ± 2.9 %	1.58 ± 3.6%	1.06
BL	2.85 ± 4.0 %	2.66 ± 2.5%	1.07
BM	2.60 ± 2.26%	2.65 ± 2.7%	0.98
BN	2.388 ± 0.07%	2.74 ± 2.8%	0.87
BV	2.479 ± ---	2.36 ± 2.8%	1.05
BW	2.25 ± 2.0 %	2.23 ± 3.0%	1.01
BY	2.17 ± 4.0 %	2.23 ± 3.2%	0.97
BX(1)[b]	2.286 ± 3.1 %	2.20 ± 3.2%	1.04
BX(2)	2.232 ± 1.2 %	(2.20 ± 3.2%)	1.01
CA	1.964 ± ---	2.10 ± 3.2%	0.94
CD(1)[c]	2.08 ± (1.8 %)	2.12 ± 3.5%	0.98
CD(2)	2.10 ± (1.7 %)	(2.12 ± 3.5%)	0.99
CD(3)	2.13 ± (1.7 %)	(2.12 ± 3.5%)	1.00
CG	1.61 ± 3.0 %	1.66 ± 2.9%	0.97
CI	1.96 ± 1.6 %	1.73 ± 3.2%	1.13
CJ	2.14 ± ---	2.30 ± 2.7%	0.93
CL	2.26 ± 3.3 %	2.23 ± 2.9%	1.01

Fluence Scale Adjustment Range (1.13 ÷ 0.87) = 1.30

---

[a]Prepared by activation of the ^{58}Ni(n,p)^{58}Co reaction in the NBS Cavity ^{235}U Fission Spectrum.

[b]All laboratories remain anonymous for these intercomparisons, as also for the PSF-SDMF Test (Tables 7 and 13). Similar comparison of results for other sensors [^{54}Fe(n,p)^{54}Mn, ^{238}U(n,f)FP, ^{237}Np(n,f)FP, etc.] will be reported in the future by the LWR Surveillance Dosimetry Improvement Program participants.

[c]Accuracies differ within various sets because of positioning uncertainties in foil stacks and flux gradients. They also differ for various irradiations.

[d]One laboratory reported two values: One for Ga(Li) and one for NaI counting.

[e]Three different groups counted this foil but did not report fluence but specific activity on January 29, 1979. Group 1 reported 8164 ± 1.7% dps; Group 2 reported 8257 ± 1.8% dps; Group 3 reported 8373 ± 1.8% dps. Fluence values were derived using a 102-mb cross section.

TABLE 15

SUMMARY OF THE PROCEDURES AND REQUIREMENTS FOR
RPV EMBRITTLEMENT DOSIMETRY SURVEILLANCE ANALYSIS

1.0 Dosimetry - Physics

1.1 Flux, Fluence, MWt, EFPY from surveillance capsule measurements. (E_is).

1.2 Flux, Fluence, MWt, EFPY for EOL prediction (calculation) from FSAR. (C_is).

1.3 Make (C_i/E_i) comparisons, $i = 1, ...n$. If $1.30 < C_i/E_i < 0.70$ (30% discrepancies) start over and bring calculations into agreement with measurements using benchmarking methodology. [Note: The actual values (0.70 and 1.30) will depend on the variable "i" of interest; also see ASTM E706 (II-D).[10]]

2.0 Calculate ratios of $\phi > 1$ MeV, dpa [using ASTM E706 (I-D)]. (ϕ ≡ fluence, n/cm^2)

2.1 Accel. surveillance location; vessel wall surveillance location; vessel wall; 1/4 T; 3/4 T; ex-vessel locations (if necessary for support structures and physics verification).

2.2 Plot and tabulate results of azimuthal ϕ for accel. surveillance; vessel wall surveillance; vessel wall; 1/4 T; 3/4 T; ex-vessel locations.

3.0 Plot $\phi > 1$ MeV and dpa vs ΔRT_{NDT} for surveillance capsule. Plot also appropriate Regulatory Guide 1.99.1 and ASTM E706 (II-F) curves.[2,10]

3.1 Determine acceptable (conservative?) trend curve (for example, Figure 5).

3.2 If plant-specific curve is selected, the errors in ΔRT_{NDT}, ϕ and dpa, must be sufficiently small so that this curve can be accepted instead of Regulatory Guide 1.99.1 or ASTM E706 (II-F).

- ΔRT_{NDT} errors must be resolved using ASTM E706: I-A, I-C, I-E, I-F, I-G, I-H, II-F, III-D, and III-E (as required).

- ϕ errors must be resolved using ASTM E706: I-A, I-C, I-D, II-A, II-B, II-D, II-E, III-A-D (as required).
  Otherwise, use Regulatory Guide 1.99.1 or ASTM E706 (II-F) curve.

4.0 Revise/update PV wall and 1/4 T ΔRT_{NDT} vs ϕ and dpa curves.

5.0 Draw new MPT (minimum pressure-temperature) curve and determine remaining PV safe life. If it is less than FSAR predication (e.g., typically 30 to 40 years):

5.1 Consider replacing corner/edge fuel elements.

5.2 Consider annealing vessel.

5.3 Consider other options.

6.0 Additional data needed in Surveillance Reports in support of Steps 1.0 through 5.0.

6.1 Tabulated, with assigned uncertainties and correlations, spectrum (group fluxes) from core edge through surveillance capsule, vessel wall, 1/4 T, 1/2 T, 3/4 T and ex-vessel cavity locations.

6.2 Power-time history for surveillance capsule and cavity positions.

6.3 Fuel subassembly power distribution for physics computations.

6.4 Verification of FSAR values by BWR and PWR generic and PCA/PSF (SDMF)-PV mockup results and update of original FSAR values using surveillance capsule and cavity results (i.e., by application of appropriate ASTM E706 Standards, Figure 3).

6.5 Tabulated and verified dimensions and location of surveillance capsules and pertinent reactor internals, i.e., during normal PV inspections for flaws.

6.6 Tabulated physical dimensions, description and layout of surveillance capsule contents.

IMPROVEMENT OF LWR PRESSURE VESSEL STEEL EMBRITTLEMENT SURVEILLANCE:
PROGRESS REPORT ON BELGIAN ACTIVITIES IN COOPERATION WITH
THE USNRC AND OTHER R&D PROGRAMS

A. Fabry, J. Debrue, Ph. Van Asbroeck, G. and S. DeLeeuw,
G. Minsart, L. Leenders, H. Tourwe
CEN-SCK, Mol. BELGIUM

J. Widart, R. Salkin
S. A. Cockerill, Liege, BELGIUM

SUMMARY

The activities reviewed in this progress report encompass
three major areas: (1) application of fracture mechanics
structural integrity analysis to reactor pressure vessel
beltlines; (2) characterization of material properties; and
(3) neutron and gamma radiation field dosimetry and physics.

After placing these activities in current regulatory
context and indicating their scope, direction and goals,
engineering application of linear-elastic and elastic-plastic
fracture mechanics is illustrated using as example the BR3
Belgium reactor and assuming a projected saturation at the
threshold of which the 10 CFR 50 Appendix G Section IV.A.2
fracture toughness requirements would just be infringed. For
normal criticality operation and upset transient loads
under the hypothetized conditions, ductile tearing and ASME XI
crack initiation considerations indicate that safety margins
are still very substantial, due to an excessively conserva-
tive dimensional vessel design which results in low pressure-
induced stresses and negligibly small thermal stresses. For
severe postulated accidental loads, crack arrest and
warm-prestressing are not effective, but thermal stress effects
remain unimportant and initiation of hardly detectable shallow
flaws, an overwhelming concern in case of pressurized thermal
shock, appears precluded or very improbable; more work is
necessary to quantify this tentative assessment. The plant
specificity of safety analysis is again and most clearly
evidenced by this BR3 example.

Reviewed next are mechanical and metallurgical properties
for an advanced 508cl.3 steel forging from the integral vessel
of a modern plant, DOEL-IV. Irradiation-induced Charpy-V
transition temperature and upper shelf shifts observed at a
neutron fluence (>1 MeV) of $\sim 2.6 \times 10^{19}$ cm^{-2} in the Oak
Ridge PSF Simulated Surveillance Capsule (550°F) are
exceedingly small, and significantly below the USNRC
Regulatory Guide 1.99 rev. 1 predictions. General emphasis
of this steel irradiation program are outlined.

This is followed by a discussion of the PSF start-up environmental characterization program intended at indicating the work still useful to draw full advantage of this international applied dosimetry standardization opportunity and needed to link its interpretation with the extensive low level dosimetry and spectrometry experiments in the mock-up PCA 4/12 SSC and the PCA blind test configurations.

The status of physics and dosimetry activites in progress to benchmark transport theory calculations of surveillance capsule lead factors and exposures to ex-vessel support structures is finally summarized. Introduced here is a PWR engineering mock-up at the VENUS critical facility, being assembled for a forthcoming interlaboratory program to investigate the interface of core management and ex-core azimuthal fast neutron and gamma heating analytical predictions.

---

1. INTRODUCTION AND OVERVIEW

The objective of the present Light Water Reactor Pressure Vessel Surveillance (LWR-PVS) Research and Development work is to contribute developing a coordinated capability to assist the nuclear industry in assessing potential failure risks and eventual mitigation strategies related to the operation of the primary fluid containment and its support structures in PWR power plants. This capability is aimed at addressing in a timely and efficient manner any safety and licensing issue susceptible to arise relatively to the accepted and future regulatory practices which, for pressure vessel beltlines and their support structures, presently follow the U.S. Code of Federal Regulations 10 CFR 50 (App. G and H) and 10 CFR 21, respectively.

Extensive work in progress encompasses the activities and topics summarized by Table 1. A number of recent publications[1-6] as well as many related papers at this symposium[7-32] provide detailed insight into some of these efforts, the direction and current achievements of which are reviewed herein in the perspective of underlining activities that currently involve a significant Belgium contribution. This is done using outlines of a few illustrative example cases, with emphasis on material not covered in the quoted references.

The work strategy intensely relies upon a selective participation to dedicated international R&D activities in the considered field. Particularly successful thus far are direct cooperation exchanges between Belgium and: the USNRC research branch and its contractors at Hanford Engineering Development Laboratory, Oak Ridge National Laboratory, the National Bureau of Standards and the Naval Research Laboratory, the Electric Power Research Institute, the German program at KFA (Jülich) and the PTB. In the dosimetry and physics activities, these exchanges

Table 1. Scope and Interrelationship of Activities

Application of RPV
Structural Integrity Analysis

- Heat-Up and Cool-Down
  Pressure-Temperature Limits
    ASME III, 10 CFR 50 App. G

- Low Ductile-Shelf Tearing
    TAP-A11

- Accidents
    ASME XI, OCA-I

Material Properties:
Metallurgical and Mechanical

- Mechanical Testing

    Instrumented c_v and Tensile
    K_{Ic}
    J-R Curve Compliance

- RPV Steel Irradiations

    A508 cl. 3, A533 B cl. 2, Soudotenax

- Metallurgical Trend Curves Correlations

    Chemistry, Temperature, Heat Treatment
    Neutronic Exposure

- Assessment of Vessel Anneal

Standardization of Gamma-Ray Flux and Heating

    Measurements and Prediction

Neutron Dosimetry and Physics

- Lead Factor and Fuel Management
  Benchmarks

    PCA, VENUS, NESDIP (UKAEA)
    Mol Iron Shells

- Test Reactor Characterization

    PSF, HSST, FRJ-2, BR3

- Power Plant Characterization

    Calculations
    In- and Ex-Vessel Dosimetry
    BR3, DOEL I & II, TIHANGE I

Benchmark-Field Referencing

    Mol and NBS Cavity Fission Spectrum
    Standard Fields, Oak Ridge SDMF

47

have been extended to cover specialized links with the UK program at Harwell, Winfrith and Rolls Royce Associates, with the Dutch program at Petten and with the French program at Saclay and Grenoble. The development of new ASTM standards, practices and guides for LWR-PV surveillance[33] serves as a significant focus for these efforts. Further coordination and guidance is provided by regular contacts with the EURATOM Working Group on Reactor Dosimetry, the I.A.E.A. and the C.S.N.I.

The other important aspect to underline is the work "educational" value, more especially in helping to establish an improved ability to combine R&D findings with the recourse to and monitoring of commercially available expertise and consulting services. This is accomplished by trying to keep the R&D activities (Table 1) in "tune" with the logics and evolution of regulatory views and by trying to respond to identified or foreseeable needs of the nuclear utilities.

Two distinct licensing requirements form the backbone of the latest regulation relative to the fracture toughness of reactor pressure vessels:

1. Protection against failure by tearing instability (ductile regime, 100% shear fracture):

$$USE \geqslant 50 \text{ ft.lb (67.8 joules)} \tag{1}$$

USE: Upper shelf energy absorbed in the c_v-impact test (at the vessel operation temperature)

2. Protection against non-ductile failure:

$$\text{Applied Load} \times \text{Safety Margin} \leqslant \text{Material Strength} \tag{2}$$

$$2 K_{IP} + K_{IT} \leqslant K_{IR} (T-RT_{NDT})$$

↓ ↓	
Pressure Thermal	Reference Fracture Toughness =
	Lower Bound of Valid K_{Ic}, K_{Ia}, K_{Id}
Calculated Stress	Measurements
Intensity Factors	(indexed to reference temperature $T-RT_{NDT}$)

where RT_{NDT} = (unirradiated nil-ductility temperature) + ΔRT_{NDT} irradiation-induced shift. From this relationship are derived the pressure versus temperature heat-up and cool-down limit curves P(T); at core criticality, these limits must furthermore be shifted conservatively by an additional margin of 40°F.

Schematically, surveillance-capsule measurement results enter into the application of requirements of (1) and (2) at two stages:

*<u>Mechanical</u> <u>testing</u> and <u>dosimetry</u> data are used to consolidate
plant-specific "trend curves":

USE (neutronic exposure) $\qquad$ (3)

ΔRT_{NDT} (neutronic exposure) $\qquad$ (4)

the neutronic exposure is expressed as fluence of neutrons with
energy greater than 1 MeV or, more appropriately, as dpa.[34]

*<u>Dosimetry</u> data are used to consolidate <u>reactor physics</u> calculations
of <u>in-vessel</u> neutronic exposure projections (lead factors) at the
end of the considered plant service cycle: the derived exposures
are then input to (3) resp. (4) in order to apply (1) resp. (2);
to this respect, ex-vessel dosimetry measurements[27,52] are a
particularly relevant supplement to surveillance capsule dosimetry
and to the extensive low power benchmarking studies in PCA,[3] VENUS
(Sect. 4) and NESDIP.[20]

Whenever (1) or (2) or both are not satisfied, continued plant operation
can still be insured, pending (10 CFR 50 App. G Sect. V-C) complete
in-service inspection of the beltline Regulatory Guide 1.150, additional
fracture toughness assessment and the demonstration, by adequate <u>fracture
mechanics</u> analysis[35,36] (Sect. 2) that the safety margins remain <u>neverthe-
less</u> sufficient; if they are not, a vessel anneal* or the plant shut-down
are necessary.

Advances in steel-making and vessel fabrication technologies (Sect. 3)
have been so successful that for recent and future plants, (1) and (2)
are unlikely to become unsatisfied during the normally planned reactor
life. Some less recent vessels may however contain weldments that will
eventually become vulnerable for instance to a pressurized thermal shock
subsequent to an overcooling accident (OCA).[32,38] Timely reduction of
vessel wall exposure by fuel management methods (low leakage cores)[25]
provides a practical and relatively inexpensive approach to reduce or
eliminate the risk of such occurrence. On another hand, accelerated
test reactor irradiations of relevant base metal, heat-affected zone
and weld specimens allow early examination of the steel performances and
contribute to the elaboration of an adequate metallurgical data base:
trend curves and correlations. Such irradiations generally involve
excellent temperature stability and spatial uniformity. This is crucial,
given the sensitivity of RPV steel embrittlement to this parameter.
Conflicting views still exist regarding the actual difference of tempera-
ture between surveillance capsules and reactor vessel walls, while
heating within the reactor core internals remains ill-understood. A
systematic investigation of the gamma-ray components of the PWR radiation
field is in progress[28-30] and will be intensified in the frame of forth-
coming interlaboratory work in VENUS (Sect. 4) and in the Mol cavity
fission spectrum standard field.[22]

---

*
Licensing requirements as yet unspecified, but technology seems at hand.[37]

2. APPLICATION OF RPV BELTLINE STRUCTURAL INTEGRITY ANALYSIS

The example case used here for discussion is BR3, a 11 MWe one loop plant owned by CEN-SCK; vendor: Westinghouse; vessel manufacturer: Babcock-Wilcox. Test bed for advanced PWR fuel and plutonium recycling development and for steel irradiation (Table 1). Benchmark in terms of dosimetry, physics, metallurgy and fracture mechanics analysis activities (vessel and water shield tank support structure). Future decommissioning test bed also.

Beltline "weak links":

- Plate (Lukens): USE may be < 50 ft-lb

- Vertical weld seam (B&W): high cooper, high nickel, low USE;
  automatic submerged-arc;
  extensive stress relief (4.5 hours at 1150°F; 8 cycles);
  operation temperature: 500°F.

Highly conservative vessel design (Table 2):

- inner diameter: 58.2 in.

- thickness: 4.37 in.

- operation pressure: 2000 psi.

Defining arbitrarily end-of-life (EOL) as the time at which requirement(s) (1) or (2) in Sect. 1 become(s) unsatisfied (future economic and safety considerations may not favour such kind of definition for more modern vessels), it is relevant to question how much more time beyond "EOL" will a vessel operated under such conditions remain fracture-safe?

2.1 Requirement (1): Upper Shelf Fracture Toughness

- At a c_v-upper shelf energy as low as 35 ft.lb, the allowable BR3 primary coolant pressure according to a "J_{50} level" elastic-plastic fracture mechanics (EPFM) analysis[36],[39] is 6700 psi or more.[40] Safety margin relative to operation pressure: ⩾3.3; required: 2. The vessel is safe, Fig. 1.

  Under the same operation and metallurgical conditions, the "reference" vessel in Table 2 would be considered unsafe (margin: only 1.6 to 1.8).

- Furthermore, non-linear elastic effects are unimportant in this BR3 case and linear elastic fracture mechanics (LEFM) is applicable (negligible stable crack growth); conceivable conversion from slow ductile tearing to unstable cleavage crack propagation would pose no threat: because no crack initiation. Assumptions made for the
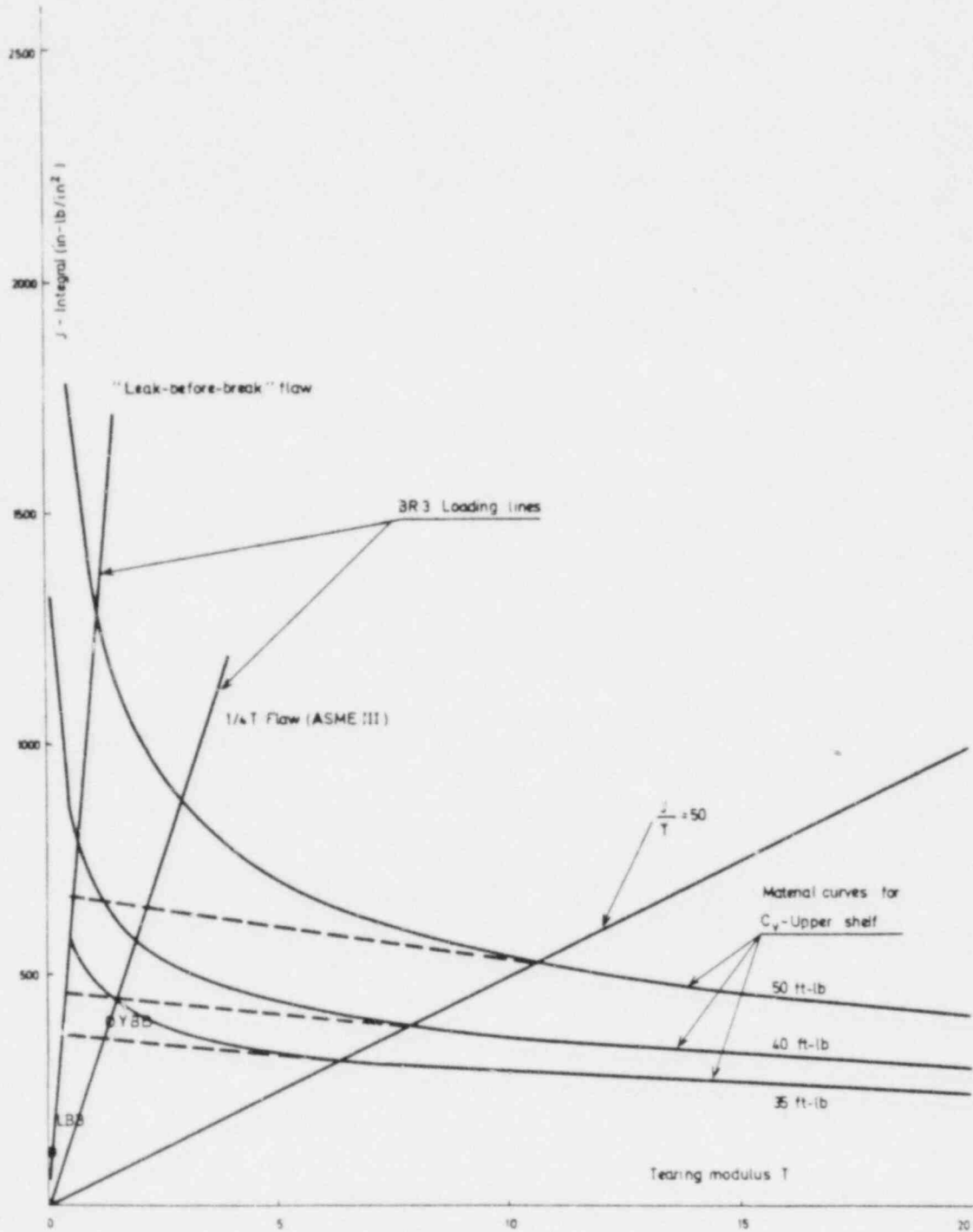
Fig. 1.   BR3 Tearing Instability Diagram.

Table 2. Geometrical Characteristics and Safety Performance
Ratio for Current Reactor Vessel Designs

Vessel type	Inner Radius (typ.)	Thickness (w) (typ.)	$\frac{\bar{r}}{w}$	Safety Performance[a] Ratio
ASME I	54.5"	8.25"	7.11	1.52
ASME VIII	77"	10.63"	7.74	1.23
ASME III	110"	10.88"	10.61	0.88
BR3	29.1"	4.37"	7.16	2.07
Reference	96"	8.5"	10.62	1[b]

[a]Limiting pressure relative to reference model, according to the relation

$$\frac{P_i^L}{P_{ref}^L} = \frac{\left(\frac{\bar{r}}{w}\sqrt{w}\right)_{ref}}{\left(\frac{\bar{r}}{w}\sqrt{w}\right)_i} \, .$$

[b]Normalization.

estimation of the upper shelf crack initiation static fracture toughness K_{Ic} are gathered in Table 3 (EOL yield strength estimate for BR3 plate: 85 ksi).

- Approximate illustration of the plant-specificity of requirement (1) severity is provided by Fig. 2. For ASME I or more conservative designs (BR3), the older regulatory requirement of USE $\leqslant$ 30 ft.1b does not seem unreasonable. On the other hand, for modern vessels meeting the ASME III design, it appears most warranted to develop improved ductile fracture instability criteria valid under extensive stable crack growth.[41]

2.2 Requirement (2): RT_{NDT}

- For the BR3 vessel design, the critical RT_{NDT} value is 400°F, Fig. 3. Thermal stress effects are very small and elementary hand calculations[42] agree well with a more exact computer analysis.[43] The unirradiated RT_{NDT} is 10°F[42] but ΔRT_{NDT} versus neutron exposure is currently very uncertain due to the lack of applicable irradiation data at a temperature of 500°F and at neutron fluences >1 MeV exceeding 2.5×10^{19} cm^{-2}: in particular, there is not a single observation under these exposure conditions for the considered "weak link" weld heat and the relevant heat treatment (the importance of stress relief[44] seems to deserve further scrutiny). Consequently an upper bound trend curve needs to be applied at present.

Table 3. Upper Shelf Fracture Toughness Estimates

Upper Shelf Energy USE (ft.lb)	K_{Ic} (Ksi$\sqrt{in}$) Estimated by Correlation				
	Rolfe-Novak[a] σ_{ys}=85 Ksi	Barsom[b] Rolfe	Merkel-Dougan[c]		Paris[d] J/T=50
			σ_o=85 Ksi	σ_o=100 Ksi	
35^e	114	113	106	99	104
40	12?	125	117	109	116
50^e	139	147	137	127	138

[a] $\left(\dfrac{K_{Ic}}{\sigma_{ys}}\right)^2 = 5\left[\dfrac{USE}{\sigma_{ys}} - 0.05\right]$ where σ_{ys} is the uniaxial tensile yield strength (Ksi).

[b] $\dfrac{K_{Ic}^2}{E'} = 2\,(USE)^{3/2}$ where E' is the effective modulus of elasticity (30700 Ksi for considered material at 500°F).

[c] See ref. 36.

[d] $\dfrac{K_{Ic}^2}{E'} = [5\,\sqrt{56.25 + 2\,USE} - 37.5]^2$.

[e] Lower bound of J_{50} experimental resistance curve data obtained by F. Loss (NRL):[56] at 35 ft.lb → K_{Ic} = 113 Ksi$\sqrt{in}$; at 50 ft.lb → K_{Ic} = 131 Ksi$\sqrt{in}$.

The definition of neutron exposure is probably rather conservative. It is based on transport theory calculations[18,19] which are signifi-cantly larger than measurements between the core boundary and the barrel.

• Figure 4 illustrates the considerable safety margin actually left at steady-state full power operation when point A on Fig. 3 has been reached. The LEFM crack-opening mode strain-plane stress-intensity factor K_I has been calculated for hypothetical surface flaws of variable relative depth a/w (w: vessel thickness) and for two flow aspect ratios: (a) the ASME III quarter thickness reference flaw shape[45] (a/ℓ = 1/6); (b) the long axial flaw (a/ℓ = 0) considered for overcooling accident analysis.[46]

This compared to K_{Ic} and K_{Ia} traverses for two assumed values of RT_{NDT}. Point A on Fig. 4 corresponds to point A on Fig. 3. Crack initiation occurs on the upper shelf for a/w = 0.6 to 0.7: i.e., in practice, it is ruled out. Because of the large RT_{NDT} values, crack arrest would not be effective, but is irrelevant in this case.
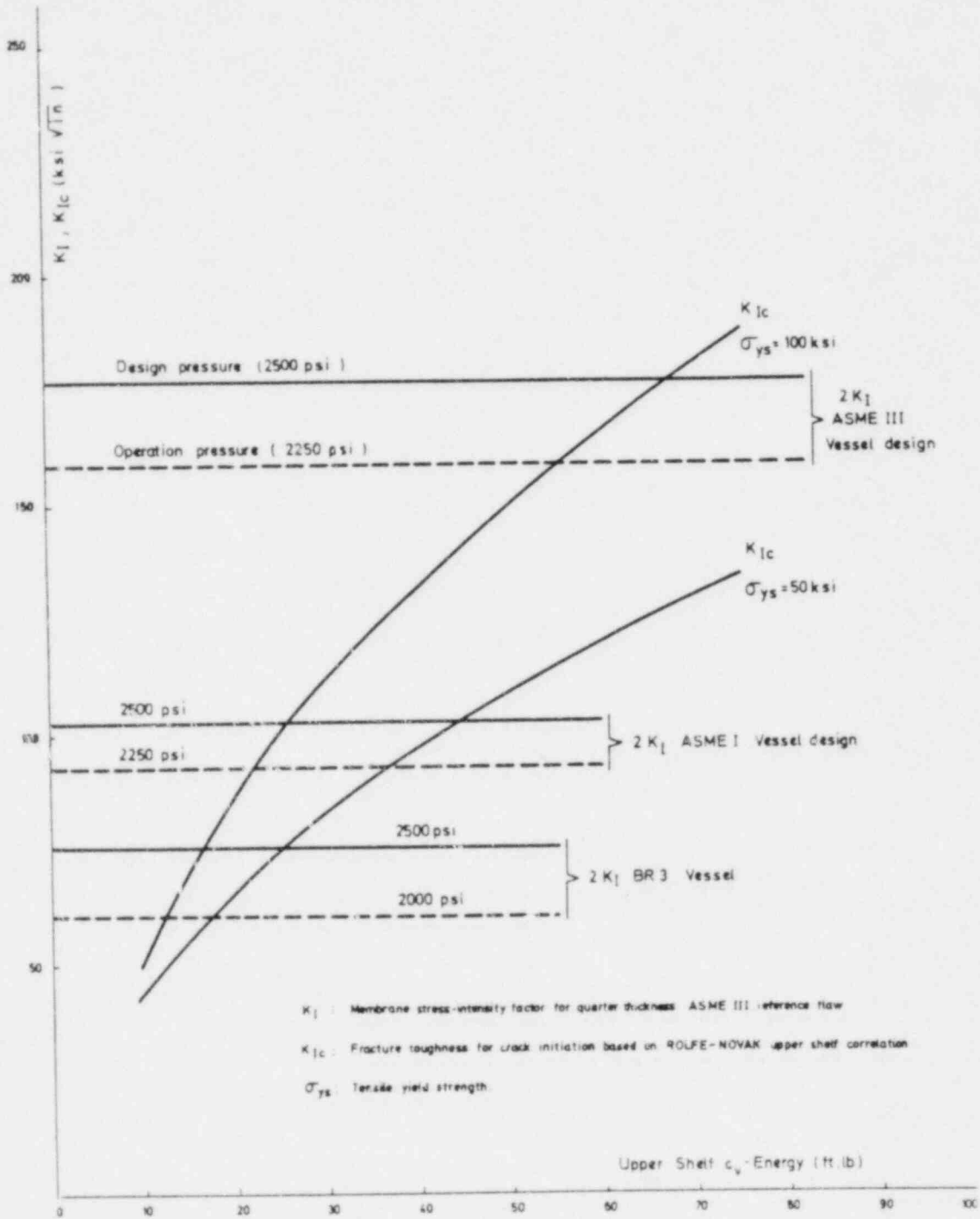
Fig. 2. Influence of Reactor Pressure Vessel Geometry on Beltline Safety Margins in Upper Shelf Operations Conditions.
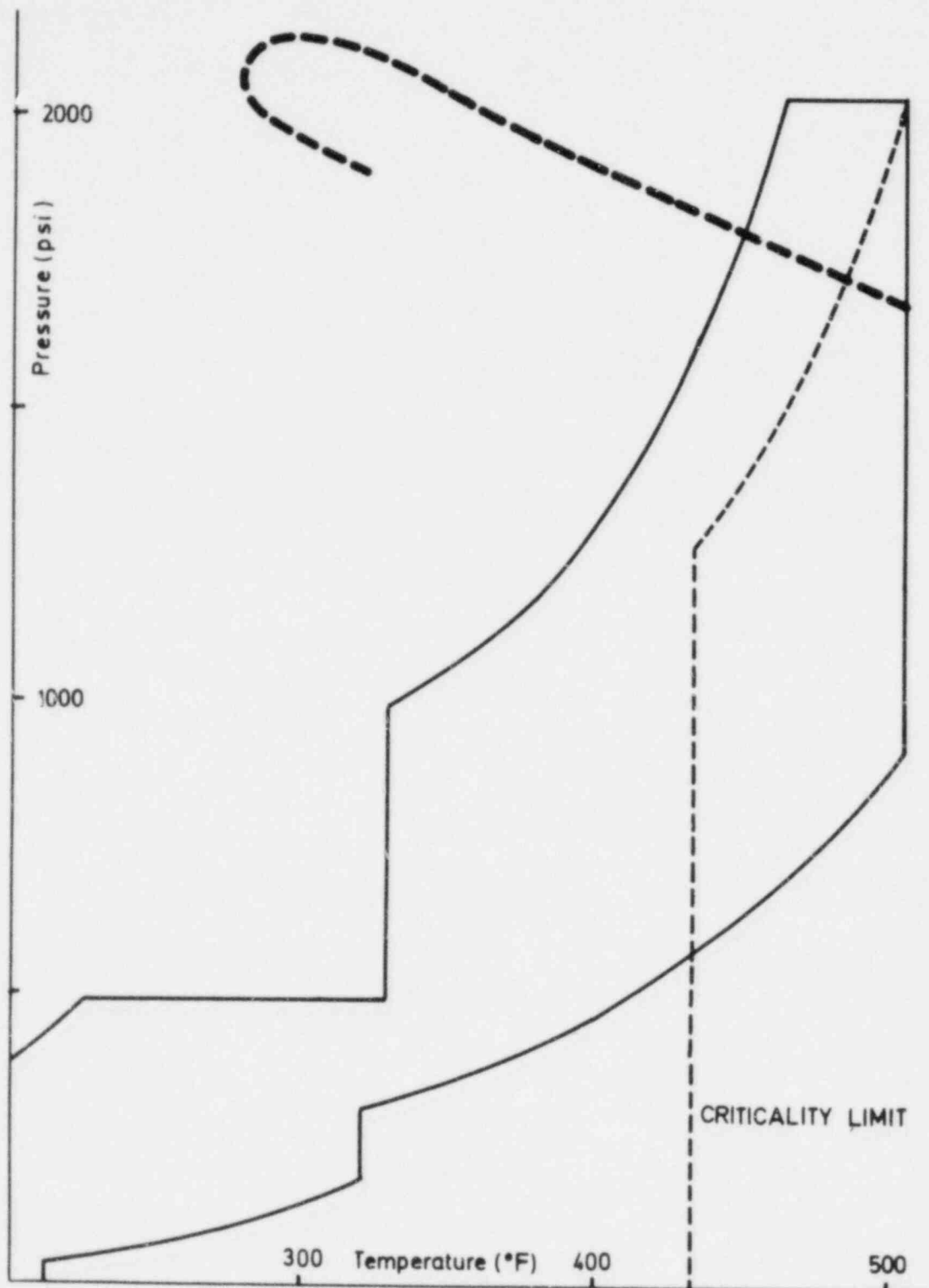
Fig. 3. Comparison of 10 CFR 50 Appendix G of End-of-Life Pressure-Temperature Limits and of a Postulated Rancho-Seco Over-Cooling Transient (- - -).
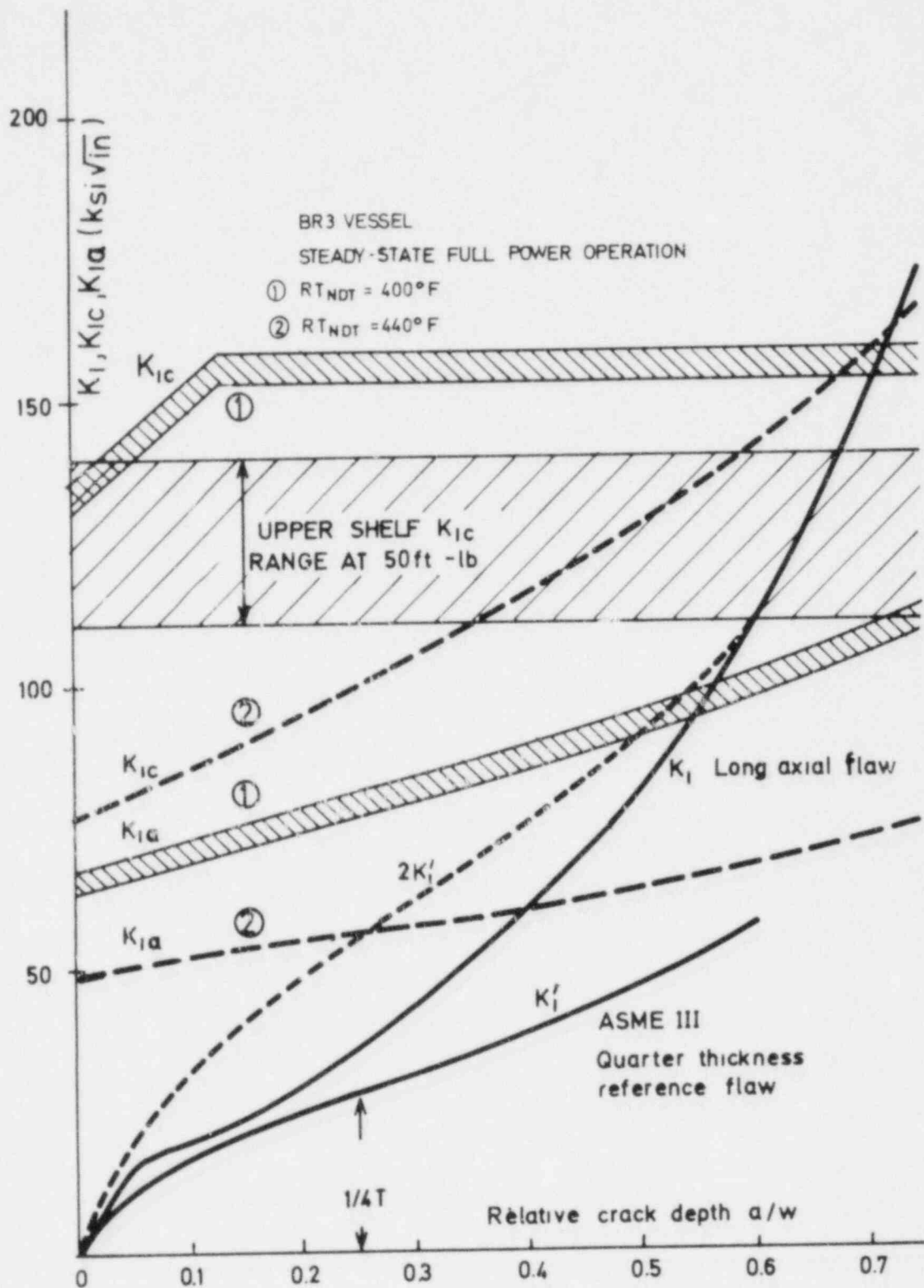
Fig. 4. Sensitivity of Fracture Toughness and Stress-Intensity Factor to Postulated Flaw Shape and EOL Quarter Thickness RT_{NDT}.

- For any normal or upset pressure-temperature transient contained between the limits in full lines on Fig. 3, and considering that ECCS repressurization in BR3 cannot exceed 1000 psi, it is similarly found that no crack initiation is realistically conceivable and that if it did nevertheless occur, it would be limited by warmprestressing (WPS) so that the remaining ligament would not burst.

2.3 Accidents

- Relatively poor regulatory guidance calls for enhanced R&D activities. The double-end large pipe break loss-of-coolant accident (LBLOCA) has long been a concern, largely extinct today, and obsolete for BR3 because the stresses during any transient are controlled by pressure. More realistic a threat is the pressurized thermal shock, given the significantly larger probability of an overcooling accident (OCA) such as the ones experienced at Rancho Seco (Fig. 3). These accidents are very plant-specific. Plant Final Safety Analysis Reports (FSAR) can be lacking crucial information relative to their probability.

- Should a "Rancho Seco" transient develop in BR3, the relative critical crack depth evolution with time for long axial flaws would be as displayed on Fig. 5: no crack arrest; warmprestressing effects unreliable as a safety barrier; but minimum critical flaw depth for initiation at $RT_{NDT} = 400°F$ comparatively substantial, i.e., $(a/w)_c = 0.15$ and $a_c = 16.6$ mm — as compared to 0.025 and 5.4 mm respectively for the reference vessel in Table 2, under the same material, irradiation temperature and neutron fluence conditions. Based on in-service inspection results of welds similar to the considered one, it is deemed unlikely that vertical axial surface flaws of depth exceeding 8-9 mm could be present in BR3; furthermore, they would not be infinitely long ($a/\ell = 0$) before initiation and would thus entail smaller K_I values than the ones adopted to generate Fig. 5 (see for ex. Fig. 4). Fatigue crack growth analysis based on non-destructive examination (NDE) results of the as-fabricated weld is planned as a means to conservatively assess this view.

- It must be noted that the most severe faulted transient observed in BR3 after approximately 20 years of operation does not entail EOL crack initiation. On another hand, at $RT_{NDT} = 360°F$ on Fig. 5, $a_c = 21.1$ mm, implicating that the OCA safety hazards long before "EOL" (time-wise, given the metallurgical trend curve considered) and at "EOL" are not significantly different.*

---

*Further work is necessary to improve upon the current evaluation of the evolution with neutronic exposure of the most credible overcooling accident probability compounded to the probability for flaws to exceed the corresponding critical initiation depth.
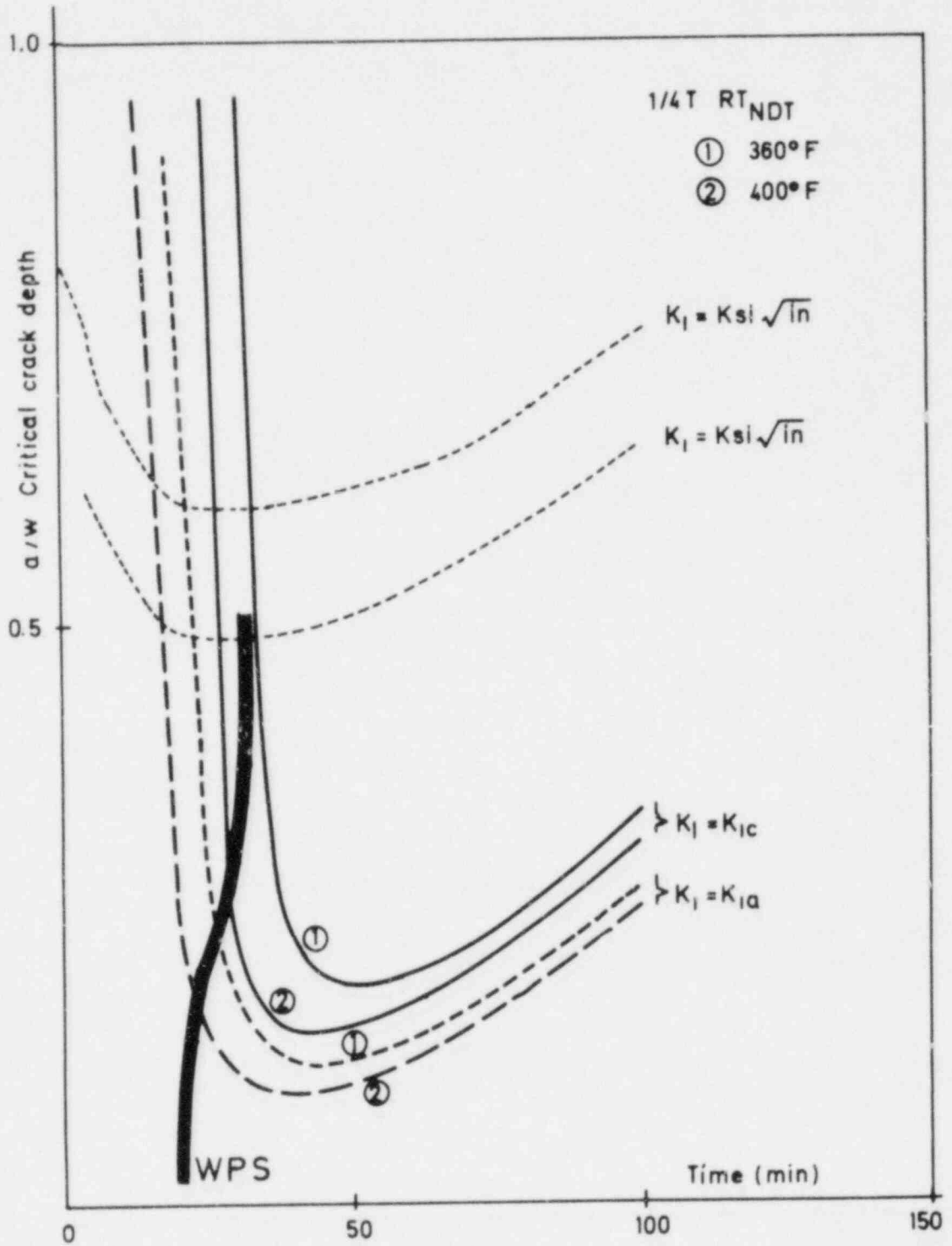
Fig. 5. Critical Crack Depth Curves for a Postulated "Rancho Seco" Transient at BR3 Reactor.

3. MATERIAL PROPERTIES: METALLURGICAL AND MECHANICAL

This work is aimed at contributing to unravel the effects of irradiation on steel embrittlement and is done in support of the current surveillance programs.

Table 4 summarizes the scope: extremely focused upon actual power reactor materials and Charpy-V indexation of fracture toughness variations — a safety conservative approach in the transition range but not on the upper shelf and operation temperatures of ~550°F. Careful irradiation monitoring is emphasized.

Table 4. General Emphasis of Steel Irradiation Program

- Base Metal, Haz and Weld: 508 cl. 3, 533B cl. 2, Soudotenax

- Specimens and Test Matrix:

  C_V (Full Transition Curve)   12-18 Samples

  Tensile (Room Temp.,
     Irradiation Temp.)   2-3 Samples

  Temp. Compression Cylinders   0-15 Samples

- Irradiation Conditions:

  Neutron Fluence Range[a] 1.10^{19}-6.10^{19} cm^{-2}[b]

  Flux Levels[a] 2.11^{11}-2.10^{13} cm^{-2} s^{-1}

  Temperature   550°F ($\pm$5-10°F)[c]

- Irradiation Monitoring:

  State-of-the-Art Dosimetry

  Correlation Steel: HSST Plate 03

  Thermocouples and/or melt wires

---

[a] >1 MeV.

[b] One series of exposures up to 1.3×10^{20} cm^{-2} (Br3).

[c] Except for test of support structure performance in the PSF void box (~150°F).

The example case here involves the characterization of an advanced steel from the forging shell of the Cockerill Integral Vessel for a plant still under construction: DOEL IV. The irradiation program for this SA508 cl-3 material is well advanced, with 10 complementary exposures of the base metal completed or nearing completion. Only one of these 10 capsules has, however, been tested so far.[47] For the weld and HAZ metals, two capsules have been unloaded (BR3) but not tested; a third irradiation under highly controlled temperature conditions is in preparation.

Table 5 presents a condensed documentation pertinent to the investigated material, as abstracted from the original certificate files of the voluminous forging (finished size: 4 meter I.D., 4.1 meter high, 20 cm thick; weight: 80 tons). Magnetic particle and ultrasonic (4MHz straight beam, 2 MHz at 45° and 60°) examination of the complete forging have given no recordable indication. The quality and homogeneity of this material matches the one of advanced laboratory melts. This has been recently confirmed by further extensive and detailed investigation of the chemistry, microstructure and mechanical properties, conducted by UKAEA Harwell, the UK Nuclear Installations Inspectorate and the John Harrison Weld Institute.

The current irradiation and testing results are synthetized by Table 5, the neutron dosimetry characterization results by Fig. 6. The corresponding capsule, SSC-1, was exposed at the "simulated surveillance capsule" location of the PSF metallurigal experiment[1] at the Oak Ridge Research Reactor (ORR). A second similar capsule, SSC-2, has been unloaded after a fluence of $\sim 4 \times 10^{19}$ cm^{-2}. Three capsules within the pressure vessel simulator will soon be unloaded after an ~ 2-year irradiation at fluences of ~ 1, 2, and 4.10^{19} cm^{-2}, and a HSST capsule, left hand-side on Fig. 6,[12] containing also the considered steel, is furthermore available for testing. The other 550°F irradiations which have been completed encompass the following fluences (>1 MeV) and environments:

BR3 LF: $\sim 1.6 \times 10^{19}$ cm^{-2} light water PWR
      HF: $\sim 1.3 \times 10^{20}$

FRJ-2 Core: $\sim 2.6 \times 10^{19}$
       Reflector: $\sim 4 \times 10^{19}$ heavy water (Jülich) test reactor

This set of experiments is expected to provide a complete "trend curve" for the material and, at least in an engineering perspective, some insight into the effect of different neutron flux levels and neutron spectra for a highly stable (Table 6), advanced steel, as compared to their effect on more radiation-sensitive heats.

Analysis of the c_v data as reported in Table 6 has been performed by a non-linear optimization technique[48] incorporating the hyperbolic tangent formulation developed for EPRI.[49] This is documented in detail elsewhere.[50]

Table 5. Characteristics of the Cockerill A508 cl.3 Advanced
Steel Base Metal (Japan Steel Works, Muroran)

1. Heat Treatment and Microstructure

• During Forging[a]

40 hr, 30 hr, 50 hr, 30 hr, 30 hr, 20 hr   1250°F   electric
                                                                furnace

After Forging

Normalizing:	12 h 50 min	900-955°C	air cooling
Tempering:	13 h 55 min	630-665°C	furnace cooling
Quenching	7 h 25 min	870-900°C	water quench
Tempering	6 h 20 min	650-668°C	air cooling

After Welding[b]

Stress Relief 24 h   600-620°C

• Microstructure: bainite, very homogeneous.

2. Chemical Composition

Test Coupon[c]	Composition (wt %) for elements										
	C	Si	Mn	P	S	Ni	Mo	V	Cu	Co	Al
A	0.20	0.28	1.43	0.008	0.008	0.75	0.53	≤0.01	0.05	0.013	0.031
B	0.20	0.27	1.37	0.006	0.007	0.73	0.49	≤0.01	0.04	0.013	0.033

3. Unirradiated Mechanical Properties

Test Parameter	Test Coupon A[c]		Test Coupon B[c]	
	RT	350°C	RT	350°C
Yield strength (0.2% offset), kg/mm^2	47.1	40.1	47.4	39.9
Tensile strength, kg/mm^2	62.7	56.1	62.9	55.9
Percent elongation, %	27.0	22.0	26.1	23.2
Reduction of area, %	71.7	71.9	72.1	71.4
Drop weight, RT_{NDT} (ASTM E208-69)	-20°F		-20°F	

[a]Following melting, degassing (∿0.2 torr) and deoxidation (Aℓ).

[b]Separate furnace simulation for the test coupons.

[c]These are two segments 1.9 m long each cut (at 800° from each other) out of
the top end (ingot bottom) of the DOEL-IV shell ring forging before
machining. A third adjacent segment 1 m long, 45 cm high and 23.8 cm thick
was used to extract the specimens for irradiation.

Table 6. Summary of Charpy-V Impact Test Results for Advanced
and Reference Base Metal RPV Steels Irradiated in the
PSF Simulated Surveillance Capsule SSC-1 at ORNL

Type of Data at irradiation temperature: 550°F at neutron fluence >1 MeV: 2.6, 10^{19} (cm^{-2})	ΔRT_{NDT} (°F)[a]	
	A508 cl.3 (Cockerill Forging)	A533B cl.2 (HSST Plate 03)
Fit[b] to Measurements:[c] Indexation at		
30 ft.lb	22.1 (±19)	110
50 ft.lb	21.8 (±12)	
0.89 mm lateral expansion	27.0 (±11)	124
Prediction: Reg. Guide 1.99 rev. 1	64.5	169

[a] Upper shelf drop: undetectable, including at 550°F.

[b] Ph. Van Asbroeck et al.[50]

[c] Performed at the Naval Research Laboratory, J. R. Hawthorne.[47] The
specimens were extracted from symetrical layers at the quarter thickness
of the experimental coupon [Table 5, footnote (c)] with the v-notches
directed along the tangential radial face of the forging; this is the
weak-link direction, as the main working direction during hydraulic
press forging was tangential to the shelf ring.

It is interesting to note that the nickel content of the investigated
508 cl.3 metal is relatively high (Table 5) while the transition temperature
shift is significantly less than predicted (Table 6); this supports the
views[6,47] that nickel alone does not seem to make steel sensitive to
neutron irradiation.

4. NEUTRON DOSIMETRY AND PHYSICS

4.1 Accuracy Goals and Status

(a) For definition of neutron exposures within surveillance or test
reactor irradiation capsules:

±10-15% (1σ) * needed for improvement of the metallurgical data
base[51]

* achievable with modest but necessary work

* attained in PSF and HSST[12] experiments.
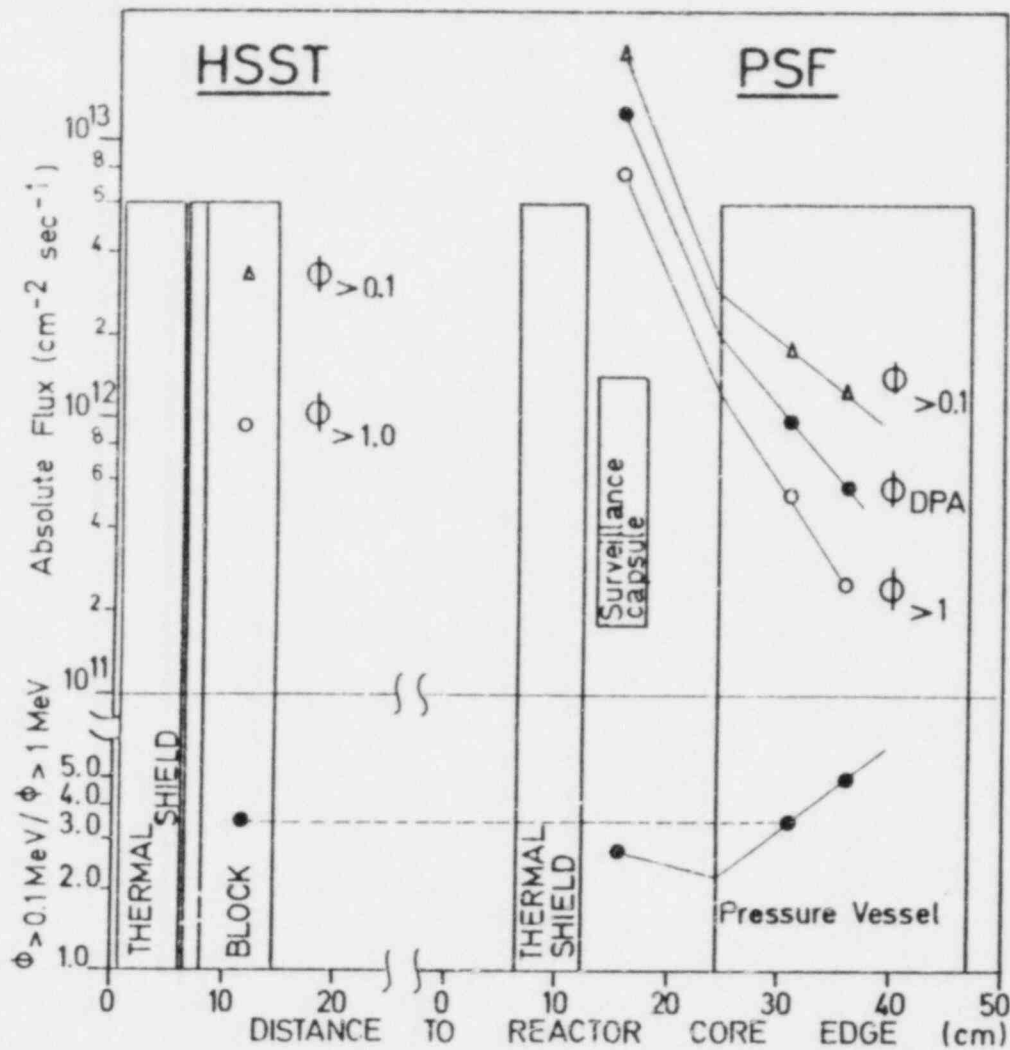
Fig. 6. PSF and HSST Neutronic Characterization.

(b) For definition of in-vessel neutron exposures and lead factors:

±15-20% (1σ) * needed for licensing[6] and structural integrity analysis (Sect. 2)

* relatively difficult to achieve; requires further physics and transport theory benchmark work (SDMF, VENUS, NESDIP[20]) as well as increased emphasis on ex-vessel versus in-vessel dosimetry and analytical comparisons in power plants (refs. 27 and 52; DOEL I, II, and THIHANGE I in progress)

* status: probably in the range ±40-50% (1σ) for critical weldments.

(c) For definition of ex-vessel exposures to support structures:

±25-30% (1σ) * same comments as under b.

Metallurgical, mechanical and temperature variables are also unsufficiently mastered; in particular, the metallurgical data base is probably biased, calling for emphasis on upper bound rather than on statistically-based interpretation. In practice, once a metallurgical trend curve has been justified for a plant, based on comparison of specific surveillance results with the regulatory guidances or on these guidances alone, in-vessel neutron exposure definition is the safety-controlling parameter whose eventual improvement by enhanced analysis and benchmarking is the most economic and immediate consideration.

4.2 Dosimetry

Example case: the PSF "start-up characterization program." It involves three steps:

1. A simplified mock-up at the PCA (PCA 4/12 SSC) in which have been systematically applied the large array of passive and active, integral and spectrally-resolved techniques used in support of the PCA "blind test;"[3] this includes the Belgium silicon damage monitors; absolute core power based on experimental fission rate maps.

2. A series of dedicated ORR irradiations at low and intermediate power in an "exact duplicate" of the PSF 4/12 SSC metallurgical configuation; the sensors exposed encompass (a) the radiometric ^{103}Rh(n,n'), ^{115}In(n,n'), ^{58}Ni(n,p), and ^{27}Al(n,a) reactions extensively used at PCA (under 1 above and in ref. 3) and BSR (HSST dosimetry mock-up);[12] and (b) the French graphite and tungsten damage monitors.[10] Power normalization relative to the next step.

3. An 18 d. high power run[14] in the above PSF 4/12 SSC duplicate; all high fluence U.S. and European neutron dosimeters have been exposed, including the UK sapphire damage monitors;[13] many laboratories participate; core power: ORR heat balance.

The primary objective was

- confirm the metallurgical irradiation configuration as defined by extensive mapping measurements at PCA ("trial and reject" of 8/7 SSC, 8/12 SSC, 9/12 SSC) and confirm the irradiation durations needed for the various capsules.

and the complementary objectives:

- link PSF and HSST fluence dosimetry to PCA physics benchmarking metrology

- provide an international neutron metrology and analysis opportunity including the validation of UK, French and Belgium damage monitors and of dosimetry cross section data for crucial but less well known long-half life radiometric monitors:

^{93}Nb(n,n') versus ^{237}Np(n,f) and ^{103}Rh(n,n')

^{63}Cu(n,α) versus ^{27}Al(n,α) .
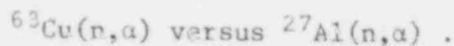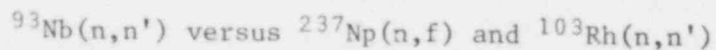
A number of papers deal with this experiment.[9-14] The complementary but important objectives have been met only partially; a good synthesis will require additional coordinated work. The "start-up characterization program" is actually an "applied standardization" undertaking whose difficulties can be roughly identified. This standardization hinges upon the eventual merging of:

- Predictive, physics-oriented flux spectrum characterization and actual, in-situ fluence spectrum dosimetry

  - Technical: the PCA 4/12 SSC mock-up is simplified, namely: the SSC is a solid steel piece, unperturbed by the gas cooling gaps of the PSF "exact duplicate;" an illustration of the influence of this structural difference is given by Fig. 7 (more details available):[53] vertical leakage effects in the PCA mock-up display the trends found in the blind test configurations[3] but are significantly perturbed in PSF 4/12 SSC.

  - Organizational (sponsorship and funding):

    PCA 4/12 SSC transport theory analysis by only one laboratory (Mol)[14]

    PSF 4/12 SSC transport theory analysis by only one laboratory (ORNL).[11]

    No direct comparison yet between the two.
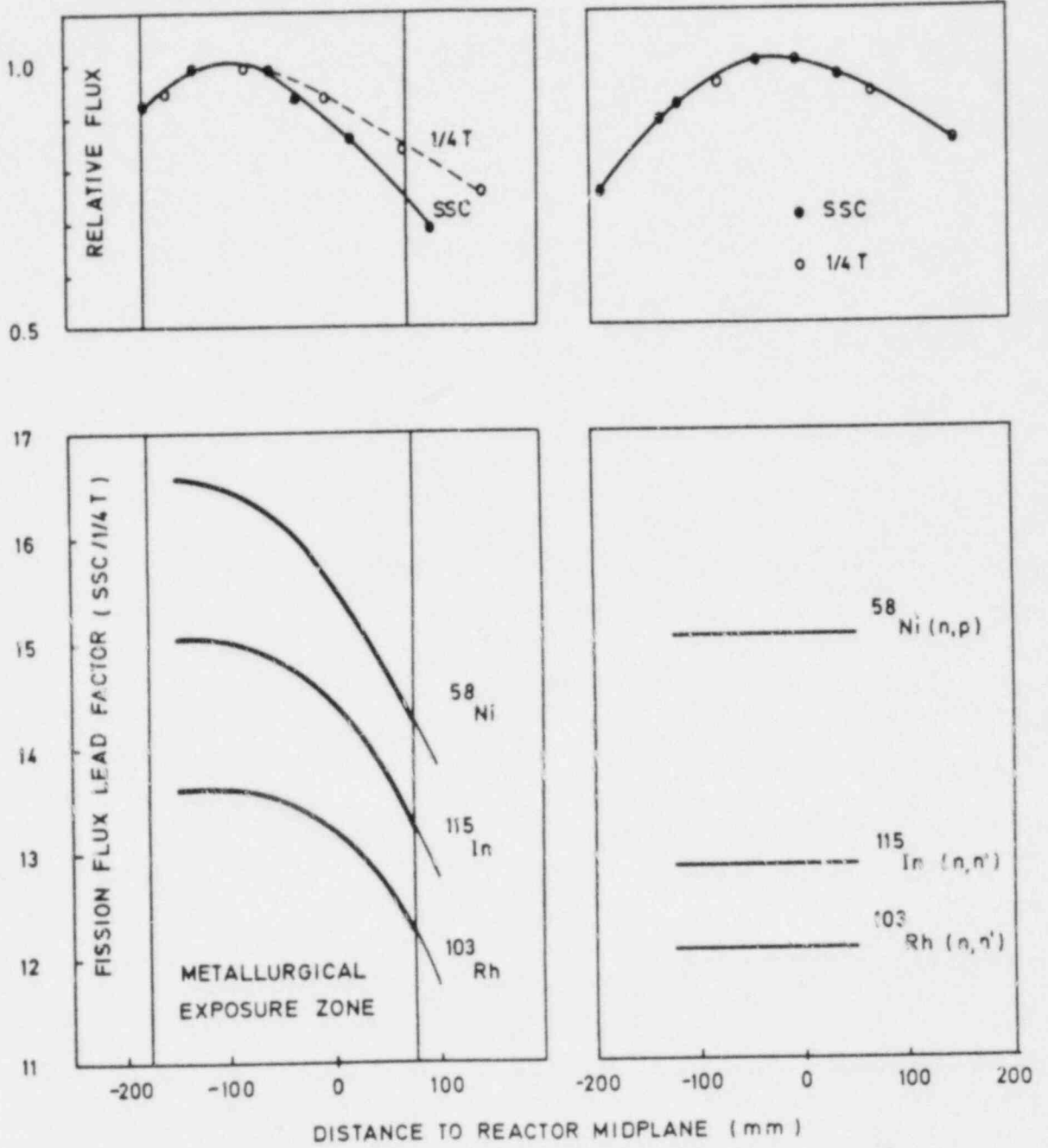
Fig. 7. PSF/PCA Fission Flux Lead Factors.

- Two dosimetry referencing "schools":

  1. Flux transfer from standard neutron fields[3,21,22]
  2. Reaction rate transfer[4] focused on radiometric techniques
     and relying upon - radioactivity standards
                       - cross section standards
                       - nuclear data (level schemes)

- European dosimetry which generally emphasizes damage monitors and
  niobium monitors.

  U.S. dosimetry which generally emphasizes fissionable monitors.

The merging is possible and beneficial.

4.3 Physics

Two considerations will be briefly discussed: core management
benchmarking plans and lead factor assessment.

The lead factor between surveillance capsule and vessel wall is a
complex parameter to determine at the stated accuracy goals (Sect. 4.1).
It can be conceptually decomposed into four parts:

radial × azimuthal × vertical × perturbation (by surveillance capsule)

$$(5)$$

as neutronic exposures are needed for all the "weak link" materials; the
"beltline region of reactor vessel" is defined as encompassing indeed
any material for which the predicted adjustment of reference temperature
at end of service life exceeds 50°F.[54]

Generally, the vertical correction can be easily derived from
dosimetry traverses within the surveillance capsule or from 2D(R,Z)
transport theory when the weak link material is significantly outside
of the experimental zone. This problem becomes difficult however for
support structures, and is particularly important in the case of water
shield tanks (Main Yankee, Connecticut Yankee, Surry, BR3) for which
the NDT temperature may be elevated by irradiation to equal or even
exceed the service temperature.[55] This will be addressed as part of
the NESDIP program.[20]

Benchmarking the neutron field perturbation by the surveillance
capsule is part of the SDMF program. Significant results have already
been obtained for Westinghouse-type capsules and are reported in
refs. 7 and 8.

Radial in-vessel projection has been addressed by the PCA blind
test[3] and is reasonably well understood. Three main areas of discrep-
ancies or inconsistencies remain:

1. integral C/E's at deep penetration and high neutron energy: this is traced to iron cross section inadequacies in current nuclear data files[3,4]

2. differences between fission chamber and SSTR[31] measurement results: further benchmark-field referencing work is expected to largely resolve them.

3. neutron spectrometry versus integral measurements and calculations: comparison of current transport theory with the envelope (Fig. 8) of all ^{6}Li(n,a) energy-dependent flux spectrum attenuations as function of steel penetration (PCA 8/7 and 12/13, 1/4T versus 1/2T and 1/2T versus 3/4T ratios) displays overall trends compatible with the ones under Fig. 9, but inconsistencies are claimed at the level of more detailed confrontations.[3]

Figure 9 has been prepared to illustrate the tranferability of neutronic benchmark observations to power reactor environments. From an applied RPV engineering viewpoint, the primary program goals have been reached; R&D improvement of the current PCA blind test results is not considered a priority, but may be useful for: (a) the analysis of pressurized thermal shock insofar as more accurate dpa steel traverses would ensue (the critical crack arrest depth after initiation of shallow flaws is relatively sensitive to these traverses, but a host of other uncertainties are more critical at present); and (b) the interpretation of ex-vessel physics and dosimetry, especially in the context of assessing support structure embrittlement.[55]

The benchmarking of azimuthal nuetron flux spectrum gradient predictions is addressed in the VENUS zero-power engineering mock-up of PWR core-baffle-barrel-thermal shield configuration (Fig. 10). These predictions depend on:

*   correct and detailed estimate of source distributions in the last core fuel rows relative to the plant power output

*   correct modeling of core boundary heterogeneity effects.

The first aspect is a particularly important focus for investigation because usual core management considerations do not call for an accuracy as large as needed for in-vessel RPV surveillance projections. Current lead factor uncertainties are therefore likely to be dominated by source uncertainties and are likely to be the most significant in plants displaying large azimuthal effects (Westinghouse, Combustion Engineering); these effects are little or not sensitive to fuel burn-up,[24] which enhances the value of a zero-power benchmark. On another hand, in-vessel azimuthal gradients are attenuated and distorted by scattering within the vessel and the ex-core components and their measurement is very relevant to the support structure issue but not so clearly to the RPV one, except in plants with very large cavities; nevertheless the VENUS and NESDIP programs are expected to jointly contribute to the development
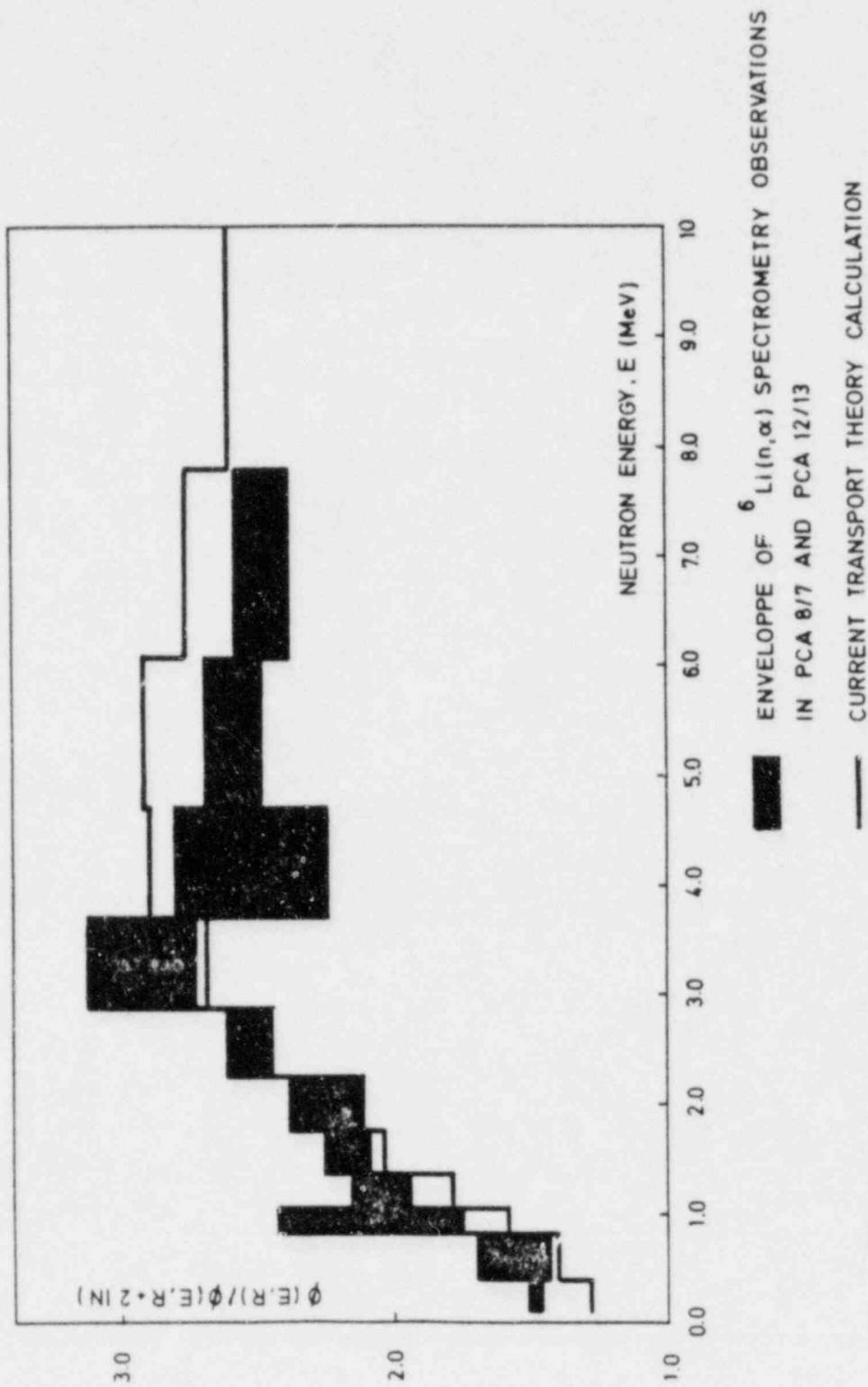
Fig. 8. Radial Neutron Flux Spectrum Attenuation by Steel in Simulated LWR Pressure Vessel Environments.
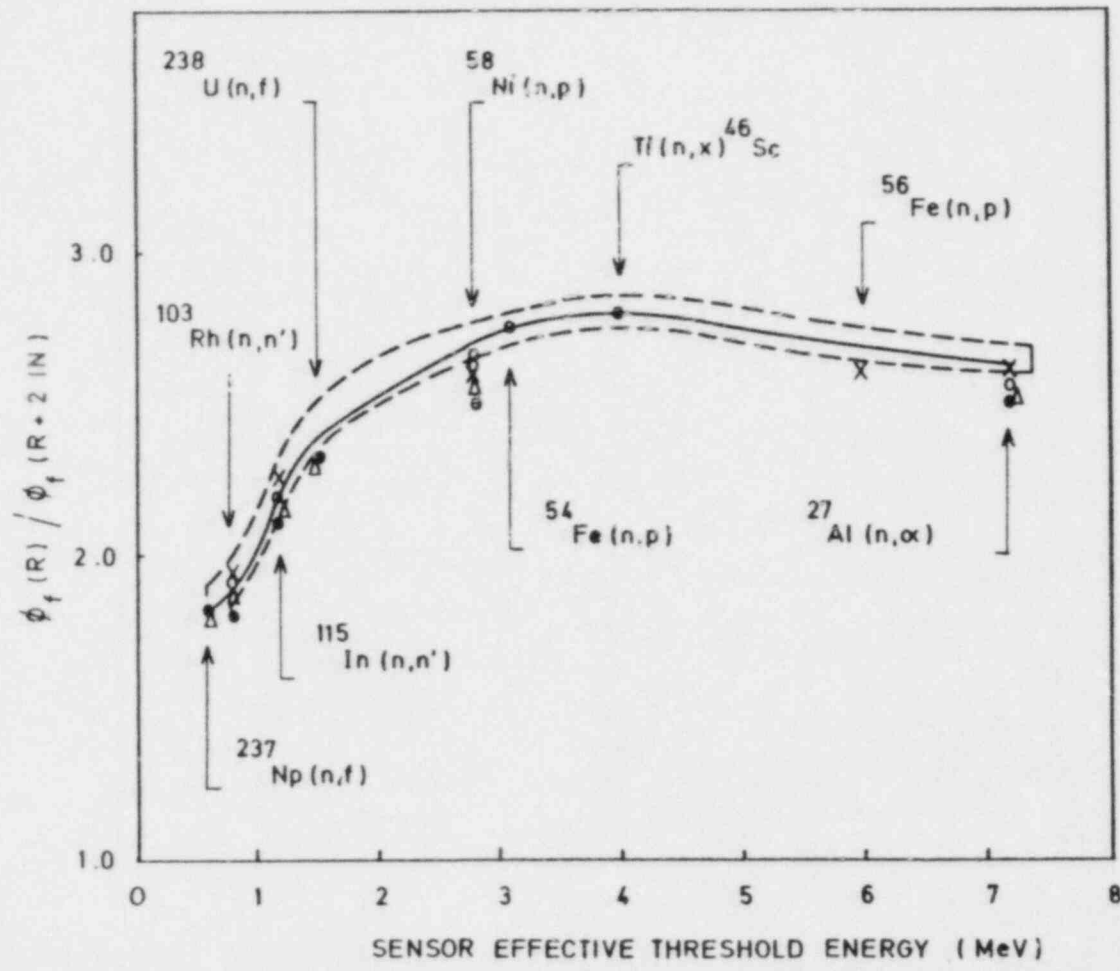
Fig. 9. Radial Fission Flux Attenuation by Steel in Typical LWR Pressure Vessel Environments.
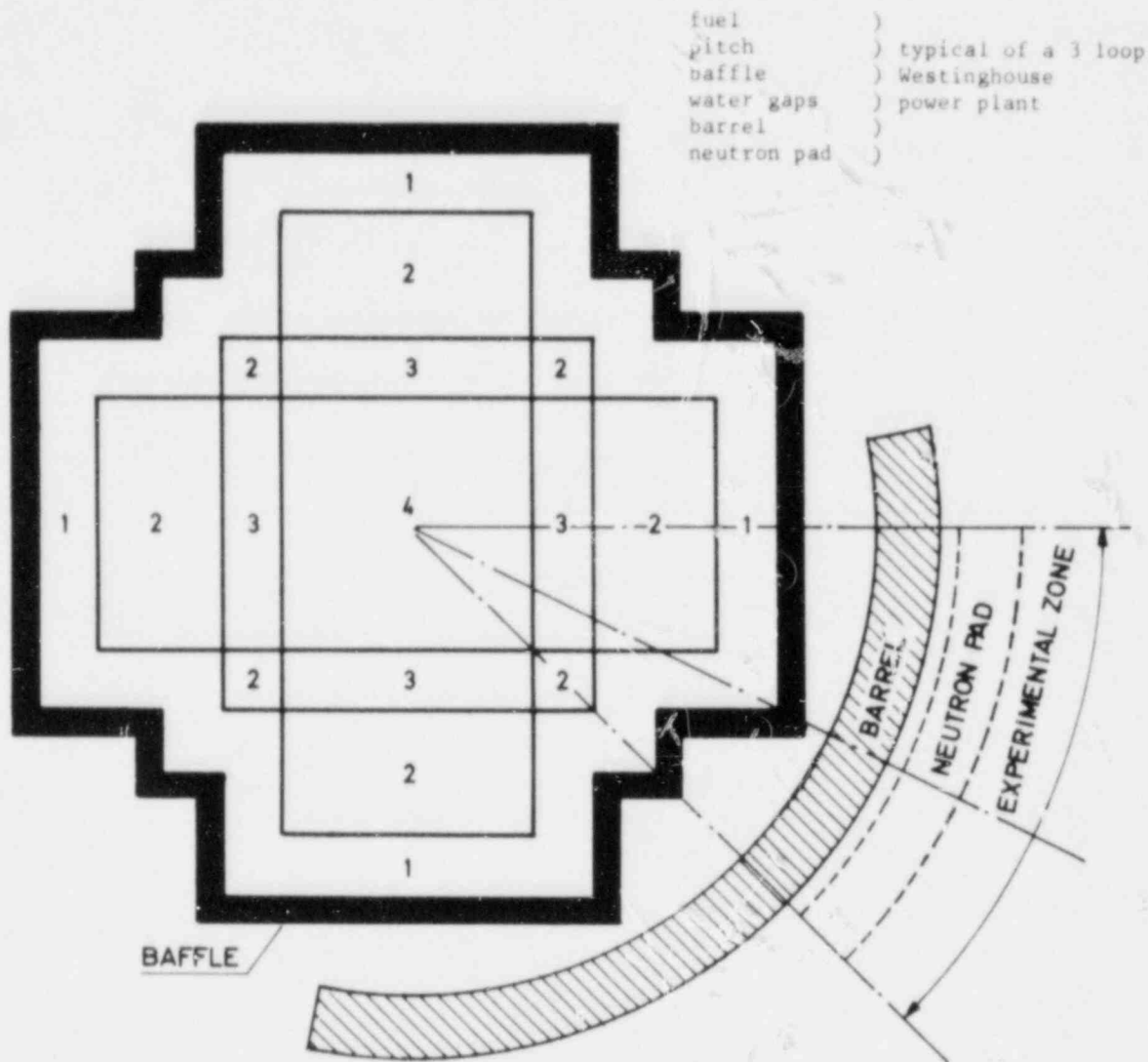
FUEL

1 : 3.3 w/o ^{235}U oxide, zircaloy clad (17 x 17)

2 : 4.0 w/o ^{235}U oxide, stainless steel clad

3 : 1·0 w/o PUO$_2$ + 3 w/o ^{235}U mixed oxide, stainless steel clad

4 : 2.7 w/o PUO$_2$ + 2 w/o ^{235}U mixed oxide, stainless steel clad

Total : 2800 fuel pins

Fig. 10. PWR Benchmark in Venus Critical Facility.

of a methodology for RPV application of ex-vessel dosimetry, which otherwise could never become comprehensive. Two other essential aspects of the VENUS effort, as already mentioned (Sect. 1), are the investigation of pressurized thermal shock mitigation by core management techniques and the investigation of PWR gamma heating.

Further discussion of VENUS is beyond the scope of this paper. It is useful to mention that the experimental and analytical program is interlaboratory and open to more participants than the ones already engaged in the U.S. and in Belgium. Core loading is scheduled for Fall 1982, measurement campaigns for Spring 1983 and the issuance of the initial interlaboratory report for September 1, 1983.

5. ACKNOWLEDGMENTS

REFERENCES

1. W. N. McElroy, et al., "Surveillance Dosimetry of Operating Power Plants," Proceedings 4th ASTM-EURATOM Symposium on Reactor Dosimetry (1982).

2. L. E. Steele, Editor, "Irradiation Embrittlement and Surveillance of Reactor Pressure Vessels," Working Group on Reliability of Reactor Pressure Components, IAEA, Vienna, Austria (October 19-21, 1981).

3. W. N. McElroy, Editor, LWR Pressure Vessel Surveillance Dosimetry Improvement Program: PCA Experiments and Blind Test, NUREG/CR-1861 (1981).

4. R. E. Maerker, J. J. Wagshal, and B. L. Broadhead, Development and Demonstration of an Advanced Methodology for LWR Dosimetry Applications, EPRI-NP 2188 Interim Report (1981).

5. W. Schneider, Editor, CAPRICE 79 "Correlation Accuracy in Pressure Vessel Steel as Reactor Component Investigation of Change of Material Properties with Exposure Data," IAEA Technical Committee Meeting, KFA Jülich (September 24-27, 1979).

6. P. N. Randall, "Status of Regulatory Demands in the U.S. on the Application of Pressure Vessel Dosimetry," Proceedings 4th ASTM-EURATOM Symposium on Reactor Dosimetry (1982).

7. H. Tourwe, and G. Minsart, "Surveillance Capsule Perturbation Studies in the PSF 4/12 Configuration," Proceedings 4th ASTM-EURATOM Symposium on Reactor Dosimetry (1982).

8. R. E. Maerker, and M. L. Williams, "Calculations of the Westinghouse Perturbation Experiment at the Poolside Facility," Proceedings 4th ASTM-EURATOM Symposium on Reactor Dosimetry (1982).

9. S. DeLeeuw, and R. Menil, "Silicon P.I.N. Diode Neutron Damage Monitors," Proceedings 4th ASTM-EURATOM Symposium on Reactor Dosimetry (1982).

10. A. Alberman, M. Benoist, and M. Thierry, "Mesure et Interprétation des Flux de Dommages dans le Simulateor de Cuve PWR d' Oak Ridge (ORR-PSF)," Proceedings 4th ASTM-EURATOM Symposium on Reactor Dosimetry (1982).

11. M. L. Williams, and R. E. Maerker, "Calculations of the Startup Experiments at the Poolside Facility," Proceedings 4th ASTM-EURATOM Symposium on Reactor Dosimetry (1982).

12. F.B.K. Kam, et al., "Neutron Exposure Parameters for the Fourth HSST Series of Metallurgical Irradiation Capsules," Proceedings 4th ASTM-EURATOM Symposium on Reactor Dosimetry (1982).

13. G. P. Pells, et al., "An Investigation into the Use of Sapphire as a Fast Neutron Damage Monitor," Proceedings 4th ASTM-EURATOM Symposium on Reactor Dosimetry (1982).

14. H. Tourwe, et al., "Interlaboratory Comparison of Fluence Neutron Dosimeters in the Frame of the PSF Startup Measurement Program," Proceedings 4th ASTM-EURATOM Symposium on Reactor Dosimetry (1982).

15. J. J. Wagschal, "Surveillance Dosimetry: Achievements and Disappointments," Proceedings 4th ASTM-EURATOM Symposium on Reactor Dosimetry (1982).

16. P. J. Maudlin, and R. E. Maerker, "Supplementary Neutron Flux Calculations for the ORNL Pool Critical Assembly Pressure Vessel Facility," Proceedings 4th ASTM-EURATOM Symposium on Reactor Dosimetry (1982).

17. K. Takeuchi, and N. Sasamoto, "Three-Dimensional Discrete Ordinates Calculation for Accurate Determination of Neutron Fluence in Reactor Pressure Vessel," Proceedings 4th ASTM-EURATOM Symposium on Reactor Dosimetry (1982).

18. G. Minsart, H. Tourwe, and J. Debrue, "Calculation of the Fast Neutron Flux and Damage in the Pressure Vessel of the BR3 Reactor," Proceedings 4th ASTM-EURATOM Symposium on Reactor Dosimetry (1982).

19. R. M. Rubin, "Neutron Flux Density Calculations for the BR3 Reactor," Proceedings 4th ASTM-EURATOM Symposium on Reactor Dosimetry (1982).

20. M. Austin, "Sense of Direction: An Observation of the Trends in Materials Dosimetry in the United Kingdom," Proceedings 4th ASTM-EURATOM Symposium on Reactor Dosimetry (1982).

21. E. D. McGarry, "NBS ISNF and Cavity Fission ^{235}U Standard Neutron Fields," Proceedings 4th ASTM-EURATOM Symposium on Reactor Dosimetry (1982).

22. A. Fabry, et al., "The Mol Cavity Uranium-235 Fission Spectrum Standard Neutron Field and its Applications," Proceedings 4th ASTM-EURATOM Symposium on Reactor Dosimetry (1982).

23. R. L. Simons, et al., "Re-evaluation of the Dosimetry for Reactor Pressure Vessel Surveillance Capsules," Proceedigns 4th ASTM-EURATOM Symposium on Reactor Dosimetry (1982).

24. S. L. Anderson, "Sensitivity of Vessel Exposure to Power Distribution Uncertainties," Proceedings 4th ASTM-EURATOM Symposium on Reactor Dosimetry (1982).

25. G. L. Guthrie, W. N. McElroy, and S. L. Anderson, "A Preliminary Study of the Use of Fuel Management Techniques for Slowing Pressure Vessel Embrittlement," Proceedings 4th ASTM-EURATOM Symposium on Reactor Dosimetry (1982).

26. A. Lowe, Jr., "B&W Integrated Surveillance Program," Proceedings 4th ASTM-EURATOM Symposium on Reactor Dosimetry (1982).

27. R. A. Shaw, "Browns Ferry and Arkansas Nuclear One Pressure Vessel Neutron Fluence Benchmarks," Proceedigns 4th ASTM-EURATOM Symposium on Reactor Dosimetry (1982).

28. N. Maene, R. Menil, and G. Minsart, "Gamma Dosimetry and Calculations," Proceedings 4th ASTM-EURATOM Symposium on Reactor Dosimetry (1982).

29. J. A. Mason, "Development of Sensitive Microcalorimeters for Absorbed Dose Measurements in Benchmark Radiation Fields," Proceedings 4th ASTM-EURATOM Symposium on Reactor Dosimetry (1982).

30. R. Gold, et al., "Gamma-Ray Spectrometry in LWR Environments," Proceedings 4th ASTM-EURATOM Symposium on Reactor Dosimetry (1982).

31. F. H. Ruddy, R. Gold, and J. H. Roberts, "Light Water Reactor Pressure Vessel Neutron Spectrometry with Solid State Track Recorders," Proceedings 4th ASTM-EURATOM Symposium on Reactor Dosimetry (1982).

32. R. D. Cheverton, "Integrity of Pressurized Water Reactor Pressure Vessels During Overcooling Accidents," Proceedings 4th ASTM-EURATOM Symposium on Reactor Dosimetry (1982).

33. ASTM Standard E706-81 "Master Matrix for LWR Pressure Vessel Surveillance Standards," 1981 Annual Book of ASTM Standards, American Society for Testing and Materials, Philadelphia, PA (1981).

34. ASTM Standard E693-79 "Practice for Characterizing Neutron Exposures in Ferritic Steels in terms of Displacements per Atom (DPA)," 1981 Annual Book of ASTM Standards, American Society for Testing and Materials, Philadelphia, PA (1981).

35. ASME Boiler and Pressure Vessel Code Section XI, Rules for Inservice Inspection of Nuclear Power Plant Components (July 1, 1974).

36. U.S. Nuclear Regulatory Commission, Task Action Plan A-11 Report NUREG-0744, Resolution of the Reactor Vessel Materials Toughness Safety Issue (September 1981).

37. T. U. Marston, and T. R. Mager, EPRI Thermal Anneal Program RP1021-1, Report to ASME Section XI Subcommittee on Repairs and Replacements, and to NRC (February 1982).

38. R. C. Kryter, et al., Evaluation of Pressurized Thermal Shock, Initial Phase of Study, NUREG/CR-2083, ORNL/TM-8072 (1982).

39. P. C. Paris, H. Tada, A. Zahoor, and H. Ernst, A Treatment on the Subject of Tearing Instability, USNRC Report NUREG-0311 (1977), and J. W. Hutchinson, and P. C. Paris, "Stability Analysis of J-Controlled Crack Growth," Elastic-Plastic Fracture, ASTM STP 668 (1979).

40. A Fabry, BR3 Pressure Vessel Safety Margins Against Upper Shelf Failure by Plastic Instability or Cleavage Fracture, CEN/SCK 380/81-50 (December 4, 1981).

41. M. F. Kanninen, C. H. Popelar, and D. Broeck, A Critical Survey of the Application of Plastic Fracture Mechanics to Nuclear Pressure Vessels and Piping, USNRC Report NUREG/CR-2110 (1981).

42. U.S. Nuclear Regulatory Commission Standard Review Plan, Office of Nuclear Regulation, Report NUREG-75/087 and Branch Technical Position MTEB 5.2 Fracture Toughness Requirements.

43. C.I.L. Evans, and T. R. Mager, Private Communication (1978).

44. T. J. Williams, Rolls Royce Associates, Private Communication, April 1982 and T. J. Williams, A. F. Thomas, R. L. Squires, The Influence of Neutron Exposure, Chemical Composition and Microstructure on the Irradiation Shift of Pressure Vessel Steels to be presented at Eleventh International Symposium on Effects of Radiation on Materials, ASTM Committee E-10, Scottsdale, Arizona (June 28-30, 1982).

45. ASME Boiler and Pressure Vessel Code Section III, Division I, "Rules for Construction of Nuclear Power Plant Components," and Appendix G Protection Against Nonductile Failure (July 1974).

46. S. K. Islander, R. D. Cheverton, and D. G. Ball, OCA-I, A Code for Calculating the Behavior of Flaws on the Inner Surface of a Pressure Vessel Subjected to Temperature and Pressure Transients, Report NUREG/CR-2113, ORNL/NUREG-84 (August 1981).

47. J. R. Hawthorne, Naval Research Laboratory, Private Communication (1982).

48. Ph. Van Asbroeck, et al., A Belgian Operating Experience in Pressure Vessel Surveillance Program, IAEA Specialists' Meeting on "Irradiation Embrittlement, Thermal Annealing and Surveillance of Reactor Pressure Vessel," Vienna (February-March 1979).

49. W. Oldfield, Curve Fitting Impact Test Data: A Statistical Procedure, ASTM Standardization News (November 1975), and Fitting Curves to Toughness Data, ASTM J. Testing and Evaluation 7, 6 (November 1979).

50. Ph. Van Asbroeck, et al., DOEL IV Reactor Cockerill Integral Pressure Vessel A508cl.3 Steel: Transition Temperature and Upper Shelf Energy Changes After Irradiation at 2.6×10^{19} n/cm^2 > 1 MeV, BLG-NUREG Report in print.

51. P. N. Randall, The Status of Trend Curves and Surveillance Results in USNRC Regulatory Activities, IAEA Specialists Meeting, Vienna, October 20, 1981.

52. N. Tsoulfanidis, et al., "Calculation of Neutron Spectra and the Pressure Vessel and Cavity of a PWR," Proceedings 4th ASTM-EURATOM Symposium on Reactor Dosimetry (1982).

53. A. Fabry, et al., Communication at Ninth Water Reactor Safety Research Information Meeting (October 29, 1981).

54. U.S. Code of Federal Regulations, Title 10, Energy, Part 50, Appendix G, Fracture Toughness Requirements, revised (January 1, 1981).

55. J. R. Hawthorne, and J. A. Sprague, Report by Task C of Interagency Agreement NRC-03-79-148, Radiation Effects to Reactor Vessel Support Structures (October 22, 1979).

56. F. J. Loss, J-R Curve Characterization of Irradiated Low-Upper Shelf Welds, Ninth Water Reactor Safety Research Information Meeting (October 29, 1981).

SURVEILLANCE DOSIMETRY: ACHIEVEMENTS AND DISAPPOINTMENTS

J. J. Wagschal
Racah Institute of Physics, Hebrew University, Jerusalem, Israel
R. E. Maerker and B. L. Broadhead
Oak Ridge National Laboratory, Oak Ridge, Tennessee, USA

ABSTRACT

A methodology has been developed for reducing the uncertainties in estimates of neutron fluence spectra within the pressure vessel of a PWR from dosimetry measurements performed at a surveillance location. This new procedure, named the LEPRICON methodology, has three desirable features not presently available in other spectral unfolding codes: 1) the derivation of flux covariances at each of the two locations; 2) the correlations of these two matrices to one another (i.e., the translation problem); and 3) the development of a flexible data base which can be expanded as more dosimetry measurements become available and are analyzed. The technique is applied to the PCA, where reductions in the uncertainties of the estimated fluxes in the pressure vessel of the order of a factor of two are demonstrated.

INTRODUCTION

The lifetime of a PWR is usually determined by the embrittlement of the pressure vessel caused by neutron-induced displacements of the atoms constituting the steel. Updated estimates of the lifetime are based on analysis of sequential extraction of metallurgical specimens and passive dosimeter foils from an easily accessible position in the water gap between thermal shield and the pressure vessel or in the reactor cavity behind the pressure vessel. The information concerning the fluence and spectrum at these surveillance locations must then be extrapolated or interpolated to the pressure vessel, both in space and in time, in order for a judgment to be made as to when to shut down the reactor. The reactor is then either to be decommissioned or subjected to some form of annealing process. Recent concerns of pressure vessel integrity to thermal shock transients would also involve the interpretation of similar data.

This paper describes and analyzes recent results obtained by employing a methodology that can be eventually packaged into a computer code which can be used to reduce significantly the uncertainties linking the surveillance reaction rate measurements with the estimation of the

fluence and spectrum at points within the pressure vessel. The success-
ful implementation of this methodology would then leave as the only
remaining major uncertainty the one involved in the prediction of
pressure vessel damage from a given fluence and spectrum. The use of
metallurgical specimens from the same melt as the pressure vessel can
significantly reduce this latter uncertainty because it can establish a
meaningful trend curve for the pressure vessel steel under similar tem-
perature conditions when exposed in an accelerated position such as the
water gap between the thermal shield and pressure vessel.

Specific calculational uncertainties addressed in this paper involve
those pertaining to the nuclear data base used in the transport calcula-
tions, to method approximations such as geometric modeling, and to the
choice of transport method parameters such as group structures and angu-
lar quadratures. For the nuclear data base, uncertainties in the fission
spectra, the cross sections involved in the neutron transport, and the
dosimeter cross sections themselves need to be estimated.

The first step in this methodology for variance reduction is the ana-
lysis of integral measurements in benchmark fields (i.e., neutron
environments in which the spectrum is well characterized and perhaps the
absolute flux as well). The most important outcome of this analysis is a
reduced uncertainty in the driving fission spectrum and the dosimeter
cross sections. These better established parameters are then used in the
analysis of more complex fields which allows for the adjustment and
reduced uncertainty of other parameters which affect the calculations,
such as the cross sections involved in the neutron transport and bias
factors introduced by transport method approximations. The methodology
is convergent in the sense that the more integral measurements that are
used (provided the uncertainties in both the measurements and calcula-
tions are well understood) the more universal are the adjustments made
and the smaller the uncertainties become.

The methodology is being applied in this paper to the Oak Ridge
Poolside Critical Assembly (PCA) Pressure Vessel simulator experiment.
This unique experiment plays a two-fold role. The flux at the T/4 loca-
tion of the pressure vessel is estimated using the above mentioned method-
ology utilizing dosimetry measurements at the surveillance position.
These fluxes can then be used to calculate the reaction rates of dosim-
eters placed at the T/4 position. For the PCA such dosimetry measurements
have actually been performed and these calculations can not only be
directly compared to their experimental counterparts, but they can also
enter directly into the data combination process.

Numerical results describing these procedures will be discussed
paying special attention to the reduction of all uncertainties concerned.

THEORY OF THE LEAST-SQUARES ADJUSTMENT PROCEDURE

Introduction

We define a data combination as one in which various types of data used to define a data base are altered in such a fashion as to produce a more consistent data base. The general types of data involved in our present application may be integral measurements, $r \equiv (r_i)$, $i = 1, 2, \ldots I$, (e.g., reaction rates, spectrum averaged cross sections or their ratios) or differential data, $\alpha \equiv (\alpha_i)$, $i = 1, 2, \ldots, N$, (e.g., cross sections, fission spectra, and calculational method bias factors). Any or all of these data types may be used to define the data base. The combination procedure must make use of calculations of the integral experiments using the differential data including any method corrections, $\bar{r} \equiv (r_i(\alpha))$, must have some criterion which defines "consistency" in a mathematical sense, and must operate within the framework of estimated uncertainties of the data. Depending on the particular direction of emphasis, the data combination used in our present application can also be described as a few-channel spectral unfolding process, or an adjustment procedure.

The consistency criterion is expressed mathematically as minimizing the quadratic loss function of the data base subject to the relationships between the differential and the integral data. The problem to be solved is: given a series of dosimetry measurements performed at an accessible (i.e., the "surveillance") location of a power reactor, together with a calculation of these measurements and of the absolute spectrum at another location (for example in the pressure vessel), what are the "best" estimates of this absolute spectrum and what are the "best" estimates of the uncertainties in this spectrum?

The well established generalized least squares adjustment procedure[2,3,4,5] will not be rederived here. Only a few key expressions that will be used in our discussion will be written explicitly in this section. The uncertainty in calculated responses $\bar{r}$ due to propagated uncertainties in the parameters α is given by

$$C_{\bar{r}\bar{r}} = S_r \, C_{\alpha\alpha} S_r^\dagger , \tag{1}$$

where the covariance matrices of the parameters $C_{\alpha\alpha}$, and of the calculated responses $C_{\bar{r}\bar{r}}$, are linked by the sensitivity matrix $S_r \equiv (\partial r_i / \partial \alpha_n)$.

In particular, the *a priori* uncertainty in the calculated flux (or fluence) ϕ at a given location in the pressure vessel is given by

$$C_{\phi\phi} = S_\phi C_{\alpha\alpha} S_\phi^\dagger , \tag{2}$$

where $S_\phi \equiv (\partial \phi_i / \partial \alpha_n)$.

Using the modified parameter data base, α', based on the data combination process utilizing the dosimetry measurements, the "best" estimate of the same flux, considered as a deactivated response, is given by

$$\phi' = \phi + S_\phi(C_{\alpha r} - C_{\alpha\alpha}S_r^\dagger)C_{dd}^{-1} d \ . \tag{3}$$

The rectangular matrix $C_{\alpha r}$ represents possible cross covariances between "active" (i.e., participating in the adjustment) responses, r, and the parameters, α. The covariance of $d \equiv (d_i) = \bar{r} - r$, the discrepancies between measured and calculated active responses, is denoted by C_{dd}:

$$C_{dd} = S_r C_{\alpha\alpha}S_r^\dagger + C_{rr} - S_r C_{\alpha r} - C_{r\alpha}S_r^\dagger \ , \tag{4}$$

where C_{rr} is the covariance matrix of the measured responses.
The uncertainty of the flux calculated with α' is reduced to

$$C_{\phi'\phi'} = C_{\phi\phi} - S_\phi[(C_{\alpha r}-C_{\alpha\alpha}S_r^\dagger)C_{dd}^{-1}(C_{r\alpha}-S_r C_{\alpha\alpha})]S_\phi^\dagger. \tag{5}$$

A measure of the quality of the modified data base (N parameters and I responses) is given by

$$\chi^2 = d^\dagger C_{dd}^{-1} d \ , \tag{6}$$

and $\chi^2/I \lesssim 1$ indicates that the data base is a consistent one.

The consistency of a particular response measurement with the parameter data base ("individual χ^2") is given by

$$\chi^2 = (\bar{r}_i - r_i)^2/(C_{rr}+S_r C_{\alpha\alpha}S_r^\dagger - S_r C_{\alpha r} - C_{r\alpha}S_r^\dagger), \tag{7}$$

which is just the square of the discrepancy between the calculated and corresponding measured quantity expressed in units of their combined variance.

Data Necessary for the Normal Unfolding Procedure

The following is a general description of the information that is needed to serve as input to the differential parameter adjustment and spectral unfolding procedure as applied to the PCA dosimetry problem based on surveillance measurements only. The specifics of the calculations necessary to obtain most of this information are presented in detail elsewhere.[6]

1. Calculated and measured values of all the dosimeter responses at the surveillance location in the PCA 12/13 configuration[1] and in all other fields to be simultaneously analyzed. In the present case, these other benchmark fields are the Intermediate Energy Standard Neutron Field

(ISNF)[7,8] at the National Bureau of Standards (NBS), and the standard ^{252}Cf fields at NBS[9,10] and the Physikalisch-Technische Bundesamstalt (PTB) facility in Braunschweig, FRG.[11,12]

2. Covariances of all the integral experiments used in the analysis, including possible correlations between the measurements made at one facility to those made at another. In addition to these explicit correlations, a further correlation exists between most of the PCA measurements and measurements made in the ^{235}U facility at MOL, Belgium.[13]

3. Covariances of all the differential parameters, i.e., the more important partial cross sections used in the transport calculations in both the ISNF and PCA facilities, the fission spectrum from thermal fission of ^{235}U and from spontaneous fission of ^{252}Cf, and the dosimeter cross sections all as functions of energy, as well as of estimated bias factors arising from methods approximations used in the calculation of the responses in both the PCA and ISNF. These covariances are assumed *à priori* to be uncorrelated with those of the integral experiments.

4. Sensitivities of each integral measurement to all of the parameters. The sensitivities to both the bias factors from method approximations and to dosimeter cross sections are simply expressed; sensitivities to the transport cross sections and the fission spectrum must be obtained with the aid of adjoint calculations for the PCA surveillance location and the ISNF.

5. Sensitivities of the group fluxes at the PCA pressure vessel location to the differential parameters. These are calculated using similar methods to those employed for the reaction rates at the PCA surveillance location.

6. Finally, calculations of the group fluxes at the pressure vessel position using the same differential data that were used in the calculation of the responses at the surveillance position (i.e., the same cross sections and methods; usually the fluxes at both locations are obtained from a single calculation). These group fluxes are necessary for the spectral unfolding only, since they explicitly appear in Eq. (3) as the reference points of the adjustments.

Simultaneous Unfolding at Both Locations

In the case where measurements are made at both the surveillance and pressure vessel positions, integral experiments at both locations are included as part of the data base, not just the one, and the covariance description of the measured (and also the calculated) values must include any correlations that exist among the data at the two positions. There is now no extrapolation necessary, only a simultaneous unfolding of the measurements at both locations.

CALCULATION OF THE INTEGRAL EXPERIMENTS

The calculation of the integral measurements analyzed in this work is described in detail in Ref. 6. A more recent ISNF one dimensional model[8] was used to calculate the fission reaction rate ratios in the ISNF. In this section only the PCA calculations will be mentioned, and then only briefly, in order to clarify the use of calculational bias factors.

Calculation of the PCA Experiments

A complete description of the PCA facility together with the "12/13 configuration" that was built beside it may be found elsewhere.[1] Our discrete ordinates calculations of the fluxes throughout the configuration have also been documented,[1,6] and can be summarized by Eq. (8) below for the group fluxes in the vicinity of the axial midplane ($z \approx 0$) and radial centerline ($x \approx 0$):

$$\phi_g(171,XYZ) = \left[\phi_{g'}(51,XY)\right] \cdot \left[\frac{\phi_g(171,Y)}{\phi_{g'}(51,Y)}\right]_{1-D} \cdot \left[\frac{\phi_{g'}(51,YZ)}{\phi_{g'}(51,Y)}\right]_{2-D}, \quad g\varepsilon g', \qquad (8)$$

where the first bracket represents a midplane two dimensional calculation using a 51 group cross section library, the second bracket represents an energy dependent correction factor that injects a finer 171 group flux structure into the calculation, and the third bracket represents a spatial correction factor for the effects of a finite source height and cosine distribution. The latter factor involves the ratio of the results of two two-dimensional calculations, even though one is one-dimensional. Typical values of this ratio are 0.75 at the surveillance position and 0.65 at the T/4 position inside the pressure vessel.

Estimated Method Approximation Bias Factors and Their Uncertainties for the PCA Calculations

The "base calculation" as given by Eq. (8) demonstrates the concept of method bias factors. The first term itself must be corrected for several method approximations used in the transport calculation. The second and third terms each introduce a unique method uncertainty of their own. Several method approximations come to mind, such as the coarse spatial mesh, the finite angular quadrature, the finite (though high) number of energy groups and the truncation of the scattering moments. The bias factor for the finite core height was obtained by comparing the results using this flux scaling procedure with those using a Monte Carlo 3-D calculation. The fluxes agreed to within the statistics of the Monte Carlo fluxes ($\sim 5\%$).[14]

Although uncertainties in the non-nuclear data such as dimensions and densities do not change the most probable result of the calculations,

they do contribute to the uncertainty of the calculations, and as such can
be considered as further method approximations which given rise to bias
factors of unity but to perhaps non negligible bias factor uncertainties.
These effects are calculated as the ratio of two ANISN calculations for
example, but they assume the roles of uncertainties in the unit bias
factors, not the bias factors themselves.

In Table 1 are listed the nonnuclear data in which uncertainties were
assumed, together with the two most important method approximations. The
bias factors along with their uncertainties to be applied to the base
calculation, Eq. (8), appear in Table 1 for the ^{58}Ni(n,p) reaction rate
at each of the two locations for the 12/13 configuration. The base
calculations of the ^{58}Ni(n,p) reaction rate should thus be multiplied by
1.024, and the uncertainty of these calculations arising from methods and
non-nuclear data uncertainties is about 7%. The uncertainty of the
calculations arising from nuclear data uncertainties such as fission
spectra, material cross sections, and dosimeter cross sections must also
be considered, of course. It should be reiterated that the bias factors
and their uncertainties discussed here are functions of energy and this
dependence has been retained in the subsequent analysis, but they have
been averaged over the ^{58}Ni(n,p) reaction rate to simplify the presen-
tation of the results in Table 1.

Table 1. Method Approximations and Nonnuclear Data Uncertainties
Used in Analysis of the 12/13 Configuration, and Bias Factors with
Uncertainties for the ^{58}Ni(n,p) Reaction Rate

Method Approximation or Non-Nuclear Data Uncertainty	Bias Factor ±Uncertainty	
	Surveillance	Pressure Vessel
1. Homogeneous mixture of fuel plates and water in core	1.024 ±0.012	1.024 ±0.012
2. 2-D to 1-D scaling to estimate effects of finite Z in core	1.00 ±0.050	1.00 ±0.050
3. Relative 15% uncertainty in peripheral core power distribution	1.000 ±0.033	1.000 ±0.031
4. Detector location uncertainty (1mm)	1.000 ±0.016	1.000 ±0.015
5. First water gap thickness uncer- tainty (1mm)	1.000 ±0.018	1.000 ±0.017
6. Thermal shield thickness uncer- tainty (1mm)	1.000 ±0.019	1.000 ±0.020
7. Second water gap thickness uncer- tainty (1mm)	1.000 ±0.002	1.000 ±0.018
8. Thermal shield density uncertainty (1%)	1.000 ±0.010	1.000 ±0.010
9. Deviations of thermal shield thick- ness due to surface imperfections (1.5mm)	1.000 ±0.003	1.000 ±0.004
10. Pressure vessel density uncertainty (1%)		1.000 ±0.008
Combined net bias factor	1.024 ±0.069	1.024 ±0.071

SOME RESULTS OF THE UNFOLDING PROCEDURE

Introduction

The integral data used in our analysis are given in Table 2. Ten responses were measured in ^{252}Cf fields, four in the ISNF field and four at the surveillance position of the PCA 12/13 configurations. Five additional measurements were made within the PCA pressure vessel itself at the T/4 position. The measured and calculated responses, their respective standard deviations, and values of "individual χ^2" (see an earlier section) are all presented in Table 2. Details on most of the information needed and used in our analysis can be found in Ref. (6).

The reason for applying a least squares procedure to the dosimetry problem is generally twofold. First, to obtain a more consistent flux estimate at the T/4 position of the pressure vessel and second, to reduce the uncertainty of the flux estimate at the T/4 position. Although we do not have measured fluxes at the T/4 position in the pressure vessel, we do have, for the PCA, reaction rate measurements there. Thus, the calculated reaction rates using adjusted flux estimates, adjusted flux bias factors and adjusted dosimetry cross sections can be compared with their experimental counterparts.

Uncertainty Sources

Before we analyze the success of the adjustment, it is worthwhile to identify the various sources of uncertainty in the flux calculation. In Table 3 are presented the total relative standard deviations of the calculated flux at the T/4 position of the PCA for those energies responsible for the pressure vessel radiation damage (above 0.1 MeV). This uncertainty varies from about 18% for energies above 11 MeV to about 10% for energies below 1 MeV. Three sources contribute to these uncertainties: first, the uncertainty in the ^{235}U thermal fission spectrum;[15] second, the uncertainties in the bias factors applied to the calculated flux in order to account for modeling and method approximations; and third, the uncertainties in the cross sections of the structural materials used in the PCA transport process (H, O, Fe, etc.).

As can be seen from Table 3, the dominant contributor to the flux uncertainty above 8 MeV is the fission spectrum; between 1.5 and 8 MeV the cross sections of the structural materials (in particular ^{56}Fe) tend to be more important; and below 1.5 MeV the bias factors (relatively flat as a function of energy) are the most important.

Table 3. Relative à Priori Standard Deviations (%) of the Calculated Extrapolated Fluxes Due to Various Sources of Uncertainty

g	E_L MeV	Total	χ_{25}	Bias Factors	PCA-σ	Fe-σ *
1	11.05	18.2	14.1	6.5	9.5	6.0
2	8.19	15.9	10.5	6.7	9.9	8.9
3	6.06	14.4	7.9	6.9	9.8	8.7
4	4.07	14.1	5.8	7.2	10.6	9.5
5	3.01	13.3	5.3	7.2	9.8	8.6
6	2.59	11.7	4.7	7.2	8.0	6.4
7	2.12	11.6	4.3	7.2	8.1	6.6
8	1.83	11.3	4.4	7.1	7.6	6.0
9	1.50	11.0	4.3	7.1	7.3	5.6
10	1.22	10.8	4.3	7.0	6.9	5.1
11	0.91	10.7	4.4	7.0	6.9	5.2
12	0.61	9.5	4.3	7.0	4.9	2.2
13	0.37	9.5	4.3	7.0	4.8	1.8
14	0.21	9.5	4.2	7.0	4.8	1.9
15	0.11	9.4	4.1	7.0	4.7	1.7

*Included in PCA-σ

Table 2. The Integral Measurements. Experimental (E) and
Calculated (C) Values, Standard Deviations, Relative
Deviations and "Individual χ^2"

Field	Response	E	Standard Deviation E(%)	C	Standard Deviation C(%)	$\frac{E-C}{C}$ %	χ^2 ind.
252Cf-NBS							
	$\bar{\sigma}(^{63}Cu(n,\alpha))$	0.000709b	2.37	0.000807	9.55	-12.1	1.51
	$\bar{\sigma}_f(^{235}U)$	1.205b	2.10	1.239	1.96	-2.74	0.94
	$\bar{\sigma}_f(28)/\bar{\sigma}_f(25)$	0.2644	1.06	0.2532	1.85	4.42	4.21
	$\bar{\sigma}_f(37)/\bar{\sigma}_f(25)$	1.105	2.08	1.093	9.38	1.10	0.01
	$\bar{\sigma}_f(49)/\bar{\sigma}_f(25)$	1.500	1.33	1.447	1.99	3.66	2.29
252Cf-PTB							
	$\bar{\sigma}(^{27}A\ell(n,\alpha))$	0.001006b	2.14	0.001157	10.15	-13.05	1.60
	$\bar{\sigma}(^{46}Ti(n,p))$	0.0138b	2.37	0.01381	13.80	- 0.07	0.00
	$\bar{\sigma}(^{54}Fe(n,p))$	0.0846b	2.36	0.0889	4.91	- 4.82	0.78
	$\bar{\sigma}(^{58}Ni(n,p))$	0.118b	2.35	0.1146	7.34	2.97	0.15
	$\bar{\sigma}(^{115}In(n,n'))$	0.1964b	2.28	0.1820	12.01	7.91	0.42
ISNF-NBS							
	$\bar{\sigma}_f(28)/\bar{\sigma}_f(25)$	0.0919	0.68	0.0910	4.28	0.99	0.05
	$\bar{\sigma}_f(28)/\bar{\sigma}_f(25)$	0.0926	1.39	0.0910	4.28	1.76	0.15
	$\bar{\sigma}_f(37)/\bar{\sigma}_f(25)$	0.510	2.03	0.513	10.30	-0.58	0.00
	$\bar{\sigma}_f(49)/\bar{\sigma}_f(25)$	1.155	1.28	1.143	2.64	1.05	0.13
PCA-SP*							
	$^{27}A\ell(n,\alpha)$	3.16E-34	7.14	3.12-34	13.96	1.44	0.01
	$^{58}Ni(n,p)$	2.48-32	7.14	2.37-32	11.93	4.64	0.11
	$^{115}In(n,n')$	3.77-32	7.14	3.49-32	14.89	8.02	0.23
	$^{237}Np(n,f)$	2.98-31	7.14	2.75-31	12.75	8.36	0.31
PCA-T/4*							
	$^{27}A\ell(n,\alpha)$	7.20E-35	6.48	6.56-35	15.32	9.83	0.33
	$^{58}Ni(n,p)$	5.64-33	6.48	4.90-33	13.54	15.1	0.95
	$^{115}In(n,n')$	1.10E-32	6.48	1.01-32	15.84	9.41	0.29
	$^{237}Np(n,f)$	1.20-31	6.48	1.14-31	13.84	5.26	0.12
	$^{238}U(n,f)$	1.86-32	8.83	1.63-32	10.49	14.11	0.94

*Reaction rates are reactions per nucleus per core neutron

88

Table 4. Relative à Priori Standard Deviations (%) of the Calculated Dosimetry Reaction Rates at the Two PCA Locations Due to Various Sources of Uncertainty

	Reaction	Total	X_{25}	Bias Factors	PCA-σ	Dosimetry-σ
S.P	$^{27}Al(n,\alpha)$	14.0	9.4	6.4	4.8	5.6
	$^{58}Ni(n,p)$	11.9	5.8	6.8	5.1	6.1
	$^{115}In(n,n')$	14.9	4.2	6.9	4.4	11.7
	$^{237}Np(n,f)$	12.8	4.2	6.9	4.5	8.8
T/4	$^{27}Al(n,\alpha)$	15.5	10.0	6.7	8.0	5.5
	$^{58}Ni(n,p)$	13.5	5.7	7.1	8.0	6.1
	$^{115}In(n,n')$	15.8	4.2	7.1	6.2	12.0
	$^{237}Np(n,f)$	13.8	4.2	7.0	6.1	9.4
	$^{238}U(n,f)$	10.5	4.4	7.1	6.2	1.3

It is thus easy to comprehend the contributions to the uncertainty of the calculated reaction rates at the PCA-SP and PCA-T/4 positions as shown in Table 4. Here we also have to take into account the uncertainties in the dosimetry cross sections, which are based on ENDF/B-V values. The large uncertainties in the ENDF/B-V $^{115}In(n,n')$ and $^{237}Np(n,f)$ dosimetry cross sections are reflected in the corresponding reaction rate uncertainties where the dosimetry cross section uncertainty is dominant. The $^{27}Al(n,\alpha)$ reaction is the highest threshold reaction investigated. Its high sensitivity to the high energy tail of the fission spectrum is therefore not surprising. The $^{58}Ni(n,p)$ reaction has a somewhat lower threshold and the corresponding reaction rates are therefore relatively more sensitive to the PCA structural cross sections.

Uncertainty Reduction

As more and more integral measurements actively participate in the adjustment process, the added information reduces the uncertainty in the adjusted fluxes. This is demonstrated in Table 5.

Table 5. Relative à Posteriori Standard Deviations (%) of the Calculated Extrapolated Fluxes as a Function of the Integral Measurements Considered in the Adjustment Process

g	E_L MeV	None	^{252}Cf	$^{252}Cf + ISNF$	$^{252}Cf + ISNF + PCA-SP$	PCA-SP	$^{252}Cf + ISNF + PCA-SP + PCA-T/4$
1	11.05	18.3		14.9	11.1	12.5	9.0
2	8.19	15.9		13.3	10.2	11.0	7.1
3	6.06	14.4		13.1	9.8	10.3	7.1
4	4.07	14.1		13.3	10.3	10.6	7.3
5	3.01	13.3	No	12.7	9.6	9.9	6.9
6	2.59	11.7		11.2	8.4	8.7	5.9
7	2.12	11.6		11.2	8.6	8.9	6.0
8	1.83	11.3	Change	10.8	8.1	8.4	5.7
9	1.50	11.0		10.5	7.8	8.1	5.5
10	1.22	10.8		10.3	7.5	7.8	5.4
11	0.91	10.7		10.2	7.4	7.7	5.4
12	0.61	9.5		9.0	6.1	6.4	5.2
13	0.37	9.5		8.9	6.2	6.4	5.5
14	0.21	9.5		8.9	6.3	6.6	5.8
15	0.11	9.4		8.8	6.3	6.5	5.8

The à priori uncertainty (column "none") is not reduced by the adjustment involving only the measurements performed in the PTB and NBS ^{252}Cf fields. These measurements can serve only to adjust the ^{252}Cf fission spectrum and the dosimetry cross sections involved, and the corresponding adjustments do not involve any parameter used in the PCA flux calculation. Since

both the PCA and the ISNF are driven by ^{235}U fission neutrons, the inclusion of the four ISNF measurements results in some reduction of the adjusted flux uncertainty expecially at the high energies. The inclusion of the information measured at the surveillance position reduces the adjusted flux uncertainty at T/4 to about two-thirds of its original value (column "^{252}Cf + ISNF + PCA-SP" in Table 5). This latter information is more effective in reducing the uncertainty because it involves data not only sensitive to the ^{235}U fission spectrum but also to both the cross sections of the structural materials and the bias factors. As a matter of fact, the data obtained at the surveillance point is so effective in the uncertainty reduction that excluding the earlier data (^{252}Cf and ISNF measurements) results in only a slight loss of information as far as the uncertainty of the T/4 flux is concerned (column "PCA-SP" Table 5). It is, of course, not at all surprising that incorporating dosimetry measurements performed at the same T/4 location reduces the flux uncertainty even further ("^{252}Cf + ISNF + PCA-SP + PCA-T/4" in Table 5). However, although these data can be used as part of the dosimetry data from benchmark fields, there will of course be no similar data in a real working power reactor.

Some Additional Observations

Using surveillance adjusted cross sections and fluxes at the T/4 position not only reduces the calculational uncertainties, but it leads to significant reductions in the discrepancies between calculated and measured reaction rates at the T/4 position. Including the additional information from the T/4 position leads to further improvement.

Employing all the twenty-three integral measurements in Table 2 leads to a χ^2/I value of 2.1, indicating an inconsistency in our data base. Deactivating response number three, having the highest individual χ^2 value, already reduces χ^2/I to 1.2. Deactivating in addition response number five, again because it has a high individual χ^2 value, further reduces χ^2/I to 1.1, which is acceptable.

The main adjustments effected using all data, including the PCA T/4 measurements but excluding the two ^{252}Cf $\bar{c}$ ratios mentioned above are:

1. A drastic reduction in the ENDF/B-V uncertainties of the ^{237}Np fission cross section, the ^{46}Ti (n,p) cross section and the ^{115}In (n,n') cross section. The uncertainties have dropped by a factor of 3 to 5.

2. A softening of the ^{252}Cf spontaneous fission spectrum by about one standard deviation (2%) of its Maxwellian temperature, and a reduction in the uncertainty of this parameter by a factor of about three.

3. A lowering of the inelastic scattering cross section of ^{56}Fe by up to 1.8 standard deviations (i.e., up to 10%).

CONCLUSIONS AND NEED FOR FUTURE WORK

Conclusions

From the results of the analysis presented, it is readily apparent that the flux uncertainties at the extrapolated position are significantly reduced, indicating the real possibility of increasing LWR pressure vessel lifetimes. This new methodology has been demonstrated using in some cases rather crude estimates for some of the covariances involved. However, the combination of refining these covariances together with applying the methodology to more and more well characterized dosimetry measurements performed in PWR's could lead to dramatic decreases in the flux uncertainties in the pressure vessel, and which should improve upon the analysis presented in this paper that was based on several rather disparate fields.

Looking at the results when the PCA-T/4 measurements are actively participating in the adjustment, it seems that using information only up to the PCA-SP is not sufficient for the adjustment of the fluxes in the pressure vessel itself, because new bias factors are brought into play as are also higher sensitivities to the iron cross sections (in particular, the total inelastic). Consequently, measurements at some point beyond the PCA-T/4 location would contain more sensitive information relevant to the unfolding at T/4. Thus, when measurements in power reactors come to be used, surveillance dosimeters placed in the reactor cavity immediately behind the pressure vessel would contain more meaningful information relative to obtaining unfolded fluences in the pressure vessel itself; the combination of dosimetry and metallurgical specimens at an accelerated location along with dosimetry in the reactor cavity would ideally satisfy the requirements for surveillance.

Directions of Future Work

It seems to be clear that the information derived from the ^{252}Cf field measurements useful to the solution of the pressure vessel damage problem is limited only to improvement of the dosimetry cross sections. This improvement can be quite sensitive to the high energy "tail" and covariance of χ_{82}. Additional effort should be made to improve χ_{82} and its covariance in this energy region beyond the simple Maxwellian expressions assumed so far and to reanalyze the measurements involving high threshold reactions such as ^{27}Aℓ(n,α), ^{46}Ti(n,p) and the more recent ^{63}Cu(n,α).

On the other hand, more measurements in ^{235}U-driven fields will be analyzed, such as in the Poolside Facility (PSF) at Oak Ridge and in the cavity of the ANO-1 reactor, leading to further adjustments in both χ_{25} and the iron inelastic cross sections. These results will have a more direct bearing on reactor flux adjustments in general.

The analysis has been based so far on dosimetry cross sections and covariances taken from ENDF/B-V, which does not contain adequate information on estimated cross-material correlations. More recent evaluations of these data, including these correlations, are now available[16] and will be used in future adjustments.

REFERENCES

1. W. N. McElroy et al., LWR Pressure Vessel Surveillance Dosimetry Improvement Program: PCA Experiments and Blind Test, NUREG/CR-1861, HEDL-TME 80-87,R5, (1981).

2. F. G. Perey, "Least-Squares Dosimetry Unfolding: The Program STAY'SL," ORNL/TM-6062, ENDF-254, (1977).

3. J. J. Wagschal and Y. Yeivin, "The Significance of Lagrange Multipliers in Cross-Section Adjustment," Trans. Am. Nucl. Soc. 34, 776 (1980).

4. J. Barhen, J. J. Wagschal, and Y. Yeivin, "Response-Parameter Correlations in Uncertainty Analysis," Trans. Am. Nucl. Soc. 35, (1980).

5. J. J. Wagschal, R. E. Maerker, and Y. Yeivin, "Extrapolation of Surveillance Dosimetry Information to Predict Pressure Vessel Fluences," Trans. Am. Nucl. Soc. 34, 631 (1980).

6. R. E. Maerker, J. J. Wagschal and B. L. Broadhead, "Development and Demonstration of an Advanced Methodology for LWR Dosimetry Applications," EPRI NP-2188 (1981).

7. C. M. Eisenhauer, J. A. Grundl, and A. Fabry, National Bureau of Standard Special Publication 493 (1977).

8. J. J. Wagschal and B. L. Broadhead, "Evaluation of the New ISNF One-Dimensional Model," Trans. Am. Nucl. Soc. 39, 887 (1981).

9. D. M. Gilliam, C. Eisenhauer, H. T. Heaton, II, and J. A. Grundl in "Nuclear Cross Sections and Technology," NBS-SP-425, 1, 270 (1975).

10. G. Winkler, V. Spiegel, C. M. Eisenhauer, and D. L. Smith, "Measurement of the Average Activation Cross Section for the Reaction $^{63}Cu(n,\alpha)$ ^{60}Co in the Spontaneous Fission Neutron Fields of ^{252}Cf," Nucl. Sci. Eng. 78, 415 (1981).

11. W. G. Alberts, E. Gunther, M. Matzke, and G. Rassl, "Measurement of Integral Cross Sections in the Californium-252 Fission Neutron Spectrum," Proc. First ASTM-EURATOM Symp. Reactor Dosimetry, Petten, September, 1975, EUR 5067 e/f, 131 (1977).

12. W. Mannhart and F. G. Perey, "Covariance Matrices of ^{252}Cf Spectrum-Averaged Cross Sections," Proc. of the Third ASTM-EURATOM Symposium on Reactor Dosimetry, Ispra, EUR6813 EN-FR 2, 1016 (1980).

13. A. Fabry, H. Ceulemans, P. Vandeplas, W. N. McElroy, and E. P. Lippincott, "Reactor Dosimetry Integral Reaction Rate Data in LMFBR Benchmark and Standard Neutron Fields: Status, Accuracy and Implications," Proc. First ASTM-EURATOM Symp. Reactor Dosimetry, Supplement, Petten, September, 1975, ERU 5667 e/f, 23 (1977).

14. P. J. Maudlin and R. E. Maerker, "Supplementary Neutron Flux Calculations for the ORNL Pool Critical Assembly Pressure Vessel Facility," Proc. this Conference.

15. R. E. Maerker, J. H. Marable, and J. J. Wagschal, "Estimation of the Uncertainties in the ENDF/B-V ^{235}U Fission Spectrum," Trans. Am. Nucl. Soc. 35, 555 (1980).

16. C. Y. Fu and D. M. Hetrick, "Experience in Using the Covariances of Some ENDF/B-V Dosimetry Cross Sections," Proc. this Conference.

THREE-DIMENSIONAL DISCRETE-ORDINATES CALCULATION FOR
ACCURATE DETERMINATION OF NEUTRON FLUENCE IN REACTOR
PRESSURE VESSEL

K. Takeuchi and N. Sasamoto
Ship Research Institute and Japan Atomic Energy Research Institute
Tokai-mura, Ibaraki-ken, Japan

ABSTRACT

Three-dimensional (X,Y,Z) transport calculation
is made for a typical 1000 MWe-class PWR core, and two-
dimensional (R,θ) transport calculation is made for its
core barrel and pressure vessel on the basis of the
angular flux predicted by the three-dimensional (X,Y,Z)
transport calculation at the boundary defined outside
the core. In addition, two transport calculations are
made for comparison in two-dimensional (R,θ) and (R,Z)
geometries for the PWR core, barrel and pressure vessel.
The calculational accuracy is confirmed by analyzing
the PCA experiment. Discussion focuses on modelling
of the core and pressure vessel of the practical power
reactor.

INTRODUCTION

The determination of detailed neutron fluences in reactor pressure
vessel is of importance in analyzing the extent of radiation embrittlement.
The objective of this study is, therefore, to provide a reasonably
detailed estimate of neutron fields at critical locations in the reactor
pressure vessel and the internals. The estimate of the detailed neutron
fields is in general made by neutron transport calculation. At present,
however, the neutron transport analysis involves some errors mainly
due to the modelling of the practical geometry and choice of parameters
and group constants used in transport calculation.

The Pool Critical Assembly Pressure Vessel Facility (PCA) was
instituted to serve as a benchmark for validating calculational
procedures in predicting neutron fluences in reactor pressure vessels
for estimation of damage[1]. The result of comparisons of various cal-
culations with the experiment in terms of reaction rates has revealed
that the modelling of the three-dimensional PCA geometry is of primary

importance for the accurate prediction of neutron fluences[2]. Most
of the calculations approximated the PCA configuration by one- and
two-dimensional geometries[1]. Even if knowing some factors to correct
the discrepancies between the calculations and the experiment, we can
not apply them to practical power reactors. Because of a rectangular
core and cylindrical shell configuration of a core-barrel and pressure
vessel in most power reactors, we should represent their configurations
by a combination of (X,Y,Z) and (R,θ,Z) geometries.

This study focuses on the examination of the effect of modelling
of a practical PWR on prediction of neutron field at the beltline of
the pressure vessel. Both axial and azimuthal variations in the neutron
fields around the core are of importance, in particular, for determination
of maximum radiation damage. For this purpose a three-dimensional
(X,Y,Z) transport calculation was made using a PALLAS-XYZ code[3]. While
for prediction of neutron fluences in the core barrel and pressure
vessel, however, a two-dimensional (R,θ) calculation was unavoidably
made using a PALLAS-2DRT code[4], since a transport code in (R,θ,Z) has
not been completed yet. Two additional transport calculations were
made to examine the modelling effect : the one was in two-dimensional
(R,Z) geometry and the other in (R,θ) geometry. The reactor chosen
for consideration is a typical 1000 MWe class PWR plant adopted from
Ref.5.

Prior to application to the power reactor, we examine the accuracy
of the neutron transport calculation in the combination of (X,Y,Z)
and (R,Z) geometries through analyzing the PCA experiment.

REACTOR MODELS

Typical 1000 MWe Class PWR

Figure 1 shows the plan configuration of a typical 1000 MWe class
PWR[5] with a vessel inner radius of 220.28 cm. For simplicity the core
region is assumed to be homogeneous in our calculations. The material
compositions are given in Table 1, in which only main nuclides included
in each material region are chosen from Tab.2.3 in Ref.5. The power
distributions used for our calculations are shown in Fig.2 for the
(X,Y)- or (R,θ)-plane (taken from Fig.2.5 in Ref.5) and in Fig.3 for
the axitial distribution together with the radial distribution used
for a two-dimensional (R,Z) calculation (also taken from Figs.2.1 and
2.8 in Ref.5). The source normalization is
$3425 (MW_t) \times 7.84 \times 10^{10} (n/W.sec) \times 10^6 (W/MW_t)$[5].

Three-Dimensional Model For PWR Core

Figure 4 shows the three-dimensional (X,Y,Z) model for the core
and its barrel, in which the upper (A) and lower (B) illustrate the
elevation and plan configurations, respectively. As shown in Fig.4(A),
the model is assumed to be symmetrical about the core midplane (the

reflection boundary condition is set at this plane)because of reduction of computer core storage. Furthermore, it exhibits 1/4 core symmetry as seen in Fig.4(B). The modelling of the barrel is inadequate, however the present PALLAS-XYZ code can not choose fine material regions because of restriction of the number of regions. The power distribution in (X,Y)-plane is the same as that shown in Fig.2, while the axial one is taken from that provided in Fig.3.

Two-Dimensional Models For PWR

Figure 5 illustrates the two-dimensional (R,θ) model at the core midplane, in which the solid line denoted as "Boundary" means that the two-dimensional transport calculation starts at this boundary with the angular flux already predicted by the three-dimensional calculation in the geometry shown in Fig.4. Another (R,θ) model is presented in Fig.6, in which the core is also represented by (R,θ)geometry. The power distribution in this (R,θ) core geometry is taken from that shown in Fig.2. The source is set also at the mesh points drawn by the black points in the figure to simulate the rectangular core geometry. Besides, the two-dimensional (R,Z) model is also used for comparison, in which the core radius is defined so as to make the equal source area to the real one on the horizontal plane and radial power distribution is the same as given in Fig.3.

NEUTRON TRANSPORT CALCULATION

The calculations were made using the PALLAS-XYZ, -RT and -RZ codes for (X,Y,Z), (R,θ) and (R,Z) geometries, respectively. The nuclear data were taken from PALLAS library[6] (based on the data from ENDF/B-IV). A vacuum boundary condition was applied at the top and right boundaries, while a reflected boundary condition was set at the left and bottom boundaries.

Analysis For The PCA Experiment

The PCA 8/7 configuration has already been analyzed with the PALLAS-XYZ code in (X,Y,Z) geometry[1], in which no geomerical modelling was necessary. To examine the error produced by the combination calculation of the PALLAS-XYZ and PALLAS-2DCY codes, the transport calculation was made in (R,Z) geometry for the configuration shown on the right side of the A_1-plane in Fig.7, with use of the boundary angular flux predicted by the (X,Y,Z) calculation at the A_1-plane. A result of comparison of the calculation with the experiment and with the other calculation is given in Table 2, in which the calculation labeled as "A" is a reference one in the many calculations presented to compare with the experiment[1]. It is found from Table 2 that the accuracy of the combination calculation is of the order of 20%.

Analyses for the PWR

The neutron transport calculations were made for the PWR modelled in (R,θ) and (R,Z) geometries using the PALLAS-2DRT and also -2DCY codes, respectively. Twenty-five energy meshes were used in the energy region above 0.1 MeV. The power normalization was made for the calculation in (R,θ) geometries by dividing the total source neutrons by the core height of 360 cm: $3425 \times 7.84 \times 10^{16}/360 = 7.46 \times 10^{17}$ n/cm·sec.

The PALLAS-XYZ code was applied to predict neutron fluxes in the model shown in Fig.4, using 17 energy meshes in the energy region above 0.1 MeV. Successively, the transport calculation was made with the PALLAS-2DRT code for the model presented in Fig.5, in which the calculation started at the boundary drawn in the figure with the boundary angular flux predicted by the XYZ code.

RESULTS AND DISCUSSION

The calculated results are given in Figs.8~11 on the neutron-flux distribution as a function of distance measured from the core center on the core midplane and on the azimuthal peaking of neutrons as well as dpa at the pressure vessel inner surface and 1/2 depth. In the figures three cases of the transport calculations are plotted: The solid lines represent the results calculated in (R,Z) geometry and both dotted and dot-solid lines represent those in (R,θ) geometry. In addition, the black points denote those in the combination of (X,Y,Z) and (R,θ) geometries. The evaluation of dpa in the pressure vessel is made using the displacement cross section for ferritic steel[7].

It is found from Figs.8 and 9 that the neutron-flux attenuation trend is quite similar in both calculations made in combining (X,Y,Z) and (R,θ) geometries and in only (R,θ) geometry. For the neutron flux distribution at 40-deg direction, in which the corner of the core is located very close to the core barrel, the absolute values are slightly larger in the combination calculation than in the (R,θ) calculation because of more detailed source distribution in the rectangular corner of the core adopted in (X,Y,Z) geometry. The attenuation trend in the (R,Z) calculation is different from that in the other cases at 0-deg direction in the region around the core because of the difference in the core radius and its geometry. Whereas the other difference seen within the pressure vessel is ascribed to that of geometrical attenuation: No neutron leakage is assumed into the axial direction in (R,θ) geometry, while the axial leakage is taken into account in (R,Z) geometry. It is found from the figures that the results calculated in both $(X,Y,Z)+(R,\theta)$ and (R,θ) geometries are 1.1~1.4 times as large as those in (R,Z) geometry with penetrating distance in the pressure vessel. The azimuthal peaking in neutron flux is obvious from the attenuation curves at 40 deg shown in the figures. The more detailed azimuthal variations are shown in Figs.10 and 11 of neutron fluxes and also of dpa. In the figures again three cases of the calculations

are plotted. The maximum difference in the azimuthal variation is
a factor of approximately three for almost all cases. The cause of
the asymmetrical azimuthal distribution about 45 deg in the (R,θ)
calculation is ascribed to the calculational error. Futhermore, the
vertical variation in neutron flux at the PV inner surface is found
to be negligibly small (about 5%) from the (R,Z) calculation.

CONCLUSION

From a result of the transport calculations for three different
models for a 1000 MWe class PWR, we may conclude that: (1) The common
power normalization is successfully made for three different models,
which means that neither the axial power distribution nor the axial
neutron leakage in the core has influence on the neutron flux outside
the core barrel because of the very large core size. (2) The (R,θ)
calculation can provide fairly accurate results on neutron flux and
dpa as well as on their azimuthal variations at the beltline of the
pressure vessel, although it produces 10~40% overestimations due to
disregard of the axial neutron leakage. (3) The accuracy of the
combination calculation in different geometries is confirmed through
the analysis of the PCA 8/7 configuration, which results in 5~27%
errors in the calculated reaction rates due to the comparatively small
core size. (4) It is found th the azimuthal peaking is a factor
of approximately three compared with the results at 0 deg for this
type of PWR. (5) The transport calculation in (X,Y,Z) geometry is
useful as a standard for other calculations.

REFERENCES

1. W.N. McElroy(Ed.), LWR Pressure Vessel Surveillance Dosimetry
   Improvement Program : PCA Experiments and Blind Test, NUREG/CR-1861
   (1981)
2. R.E. Maerker and P.J. Maudlin, Supplementary Neutron Flux Calculations
   for the ORNL Pool Critical Assembly Pressure Vessel Facility, ORNL/TM-
   7602 (1981)
3. N. Sasamoto and K. Takeuchi, Direct Integration Method for Sloving
   the Neutron Transport Equation in Three-Dimensional (X,Y,Z) Geometry,
   Nucl. Sci. Eng. (in printing)
4. K. Takeuchi and N. Sasamoto, PALLAS-2DRT, Revision of PALLAS-2DCY,
   A Code for Direct Integration of Transport Equation in Two-Dimensional
   (R,Z) Geometry, JAERI-M 9014 (1980)
5. M.L. Grïtner, et al., PWR and BWR Radiation Environments for Radiation
   Damage Studies, EPRI NP-152 (1977)
6. N. Sasamoto, et al., Multi-group Neutron Cross Section Library for
   Code PALLAS, JAERI-M 7445 (1977)
7. ASTME-10, Standard Practice for Characterizing Neutron Exposures in
   Ferritic Steels in Terms of Displacements per Atom (DPA), E693-79 (1979)

Table 1   Material composition

Zone	Nuclide	Nuc. Density($\times 10^{24}$)
Core	H O Zr U-238	0.04014 0.03390 0.00562 0.00681
Barrel (SS-304)	Cr Fe	0.02005 0.06685
Coolant (Water)	H O	0.0669 0.0334
Pressure Vessel (A533B)	Cr Fe	0.00330 0.08273

Table 2   Comparison of the Combination Calculation with Experiment and A Reference Calculation

	A_3^*	A_4^*	A_5^*	A_6^*
		^{115}In(n,n')		
CAL		5.84-32**	2.20-32	9.81-33
EXP		6.37-32	3.01-32	1.34-32
C/E		0.92	0.73	0.73
		^{103}Rh(n,n')		
CAL		3.24-31	1.46-31	7.50-32
EXP		3.43-31	1.86-31	9.46-32
C/E		0.95	0.79	0.79
		$\phi(\geq 1.0$ MeV)		
CAL	9.17-7	2.65-7	1.05-7	4.76-8
A***	7.82-7	2.69-7	1.24-7	5.33-8
C/A	1.17	0.99	0.85	0.89
		$\phi(\geq 0.1$ MeV)		
CAL	1.91-6	8.97-7	5.23-7	3.18-7
A	1.65-6	9.44-7	6.20-7	3.69-7
C/A	1.16	0.95	0.84	0.86

$A_3^* \sim A_6^*$ are the measuring positions.
5.84-32** : 5.84×10^{-32} (reaction rate).
A*** is a reference calculation.

Fig.1
Plan Configuration of PWR Core and Pressure Vessel
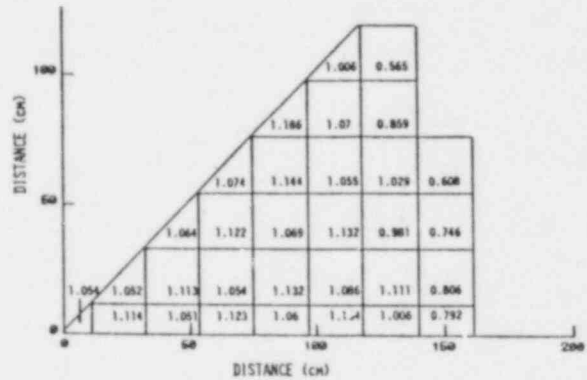
Figure 2

PWR Fuel Assembly Relative Power Distribution.

Percent of Core Height from Bottom or Radius from Core Center
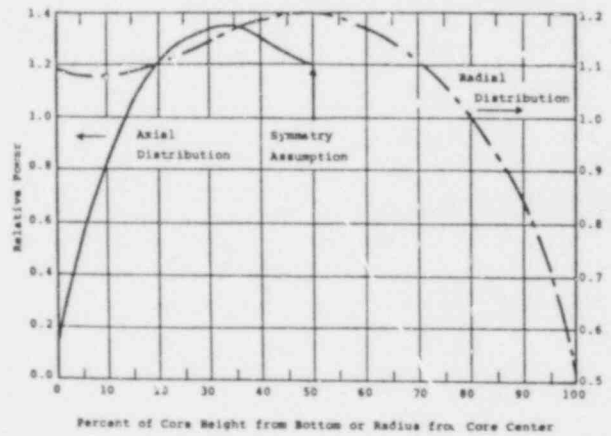
Fig.3   PWR Axial and Radial Power Distribution
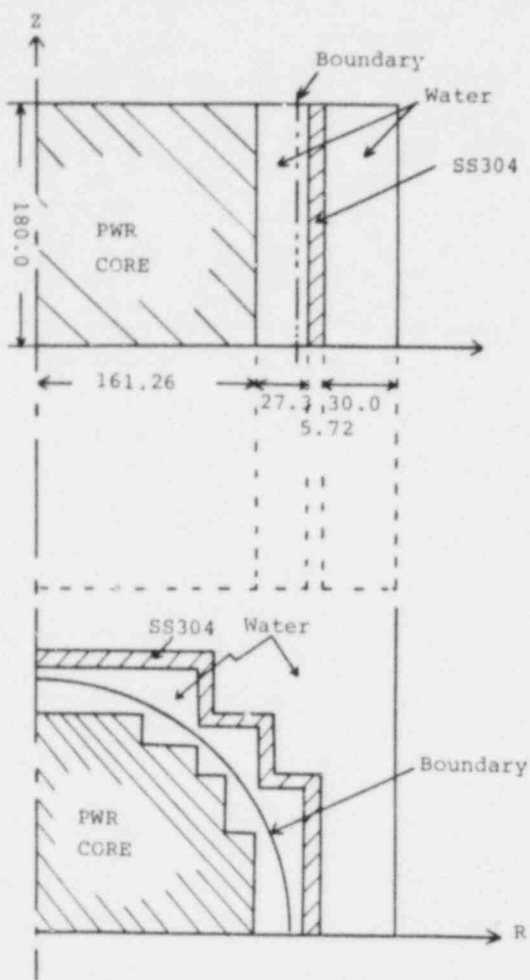
Fig.4   3D-(X,Y,Z) calculational model
         for within-pressure vessel of PWR

Fig.5   Plan conf. of 3D-(X,Y,Z)+2D-(R,θ)
         for PWR
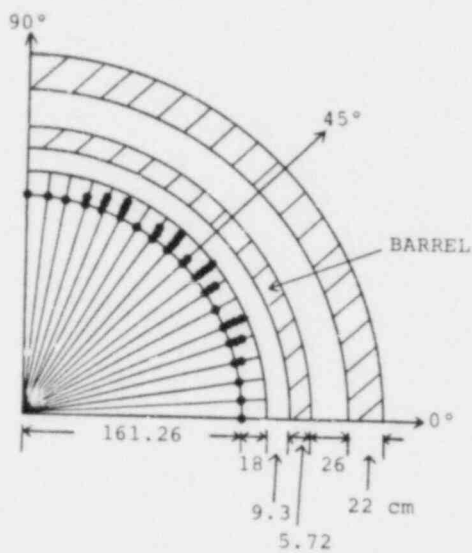
Fig.6   Plan conf. 2D-(R,θ) model for PWR

Fig.7   PCA Experiment 8/7 Conf
         and Its (R,Z) Model
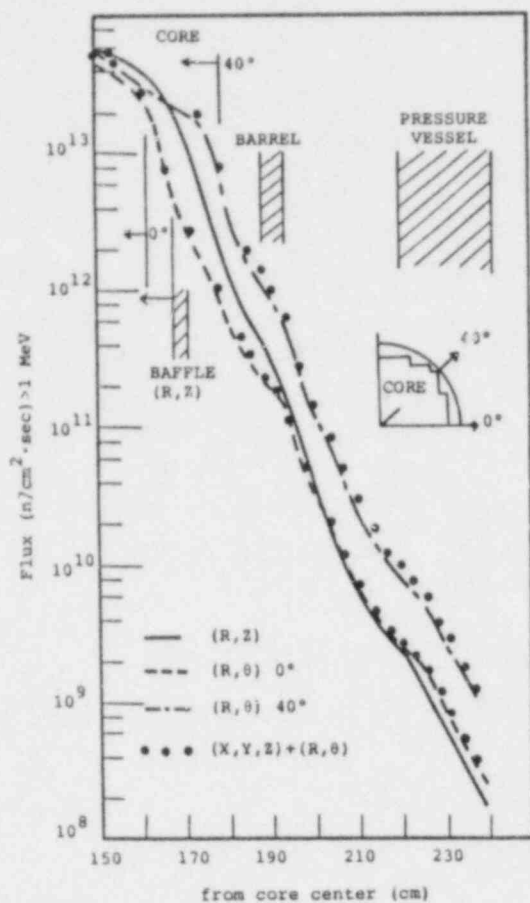
Fig.8   Neutron Flux Distribution (>1 MeV) at
        Distances from Core Center on the Core
        Midplane
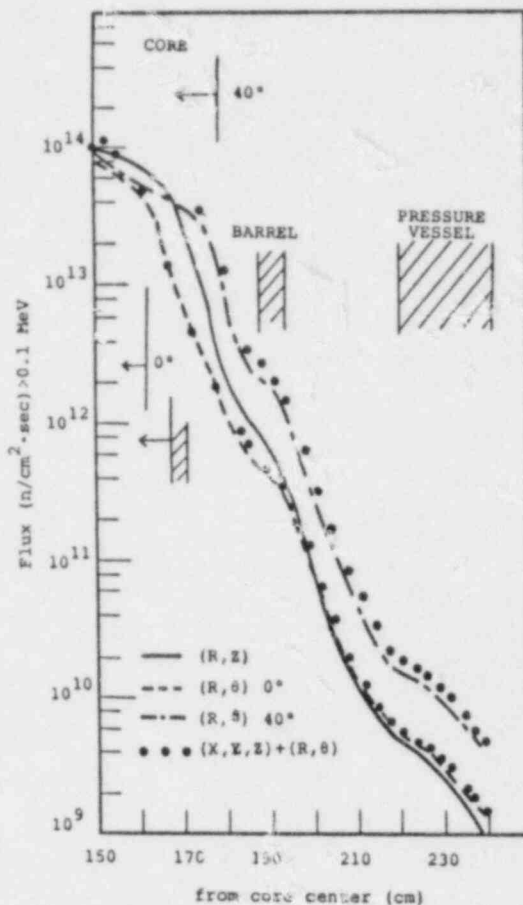
Fig.9   Neutron Flux Distribution (>0.1 MeV)
        at Distances from Core Center on the
        Core Midplane
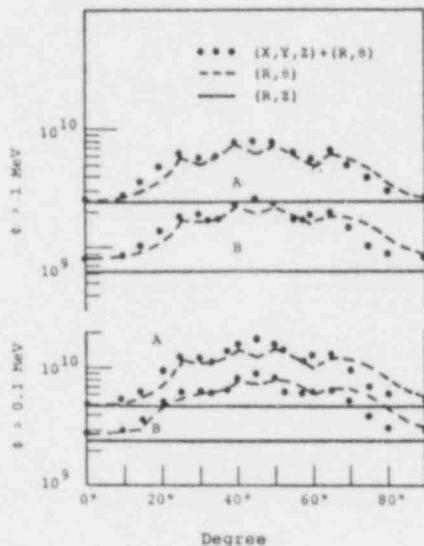
Fig.10 Azimuthal Peaking of Neutrons
        with Energies >1 MeV and >0.1
        MeV at Pressure Vessel Inner
        Surface (A) and 1/2 Depth (B)
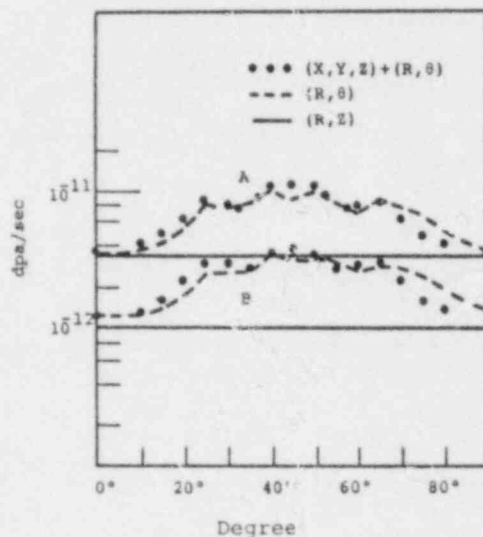
Fig.11 Azimuthal Peaking of DPA/sec at
        Pressure Vessel Inner Surface (A)
        and 1/2 Depth (B)

DOSIMETRIE LIEE AU PROGRAMME DE SURVEILLANCE DES CUVES DES REACTEURS
DE L'ELECTRICITE DE FRANCE

A.BEVILACQUA[1] - P.BOURNAY[2] - R.LLORET[1] - M.POITOU[4] - J-B.SERVAJEAN[3]

(1) C.E.N. GRENOBLE - Service des Piles - 85 X - F.38041 GRENOBLE Cedex
(2) E.D.F. S.P.T. - 71 rue de Miromesnil - F 75384 PARIS Cedex 08
(3) E.D.F. Boîte Postale 23 - F 37420 AVOINE.
(4) FRAMATOME - Tour Fiat - 1 pl. de la Coupole F 92084 LA DEFENSE

ABSTRACT

DOSIMETRY ASSOCIA.ED WITH THE SURVEILLANCE PROGRAM OF EDF REACTORS PRESSURE VESSEL.

The surveillance dosimetry program of ELECTRICITE de FRANCE's reactors pressure vessel built by FRAMATOME consists of neutronic computation by means of ANISN-DOT procedure on the one hand and of two experimental parts on the other hand.

For the first one, a light instrumentation with activation wires was put outside the PV of one power plant, during the first 18 months cycle at nominal power. This instrumention is described : it gave the possibility to do measurements along two vertical lines and an horizontal diameter under the vessel. Experimental and computed results are compared respectively for thermal, epithermal and fast neutrons.

For the second experimental part the first surveillance capsules have been extracted from six power plants and the dosimeters have been measured. The difficulties encountered during some steps of the process are described.

The reproducibility of the different results is excellent. Their consistency and agreement with the calculations are discussed.

---

1. MESURE DE FLUX A L'EXTERIEUR DE LA CUVE D'UN REACTEUR PWR.

1.1. Objet.

Une instrumentation légère de mesure de flux a été installée à l'extérieur de la cuve d'une des premières tranches PWR de 900 MWe du programme français. Cette instrumention était indépendante du programme réglementaire de surveillance des cuves de réacteur décrit dans la seconde partie. Elle avait pour objectif d'une part, d'améliorer notre confiance dans les calculs prévisionnels ayant permis d'établir ce programme de surveillance et, d'autre part de nous fournir des informations sur les flux dans des régions peu accessibles par le calcul.

1.2. Procédé de la mesure, instrumentation et résultats des comptages.

Le principe retenu a consisté à placer des fils verticaux et/
ou horizontaux au voisinage de la cuve (Fig.1-1) et à les laisser pen-
dant toute la durée du premier cycle de fonctionnement du réacteur.

1.2.1 Conditionnement.

Afin d'assurer une bonne réalisation de la me-
sure, les fils dosimètres ont été conditionnés de la manière suivante :

- des chaînes ont été constituées à partir de tubes d'aluminium (lon-
  gueur 1 m, Ø 1 cm, épaisseur 1 mm) reliés par des anneaux.
- des fils dosimètres ont été positionnés dans ces tubes au moyen de
  pastilles d'alumine.

Ce conditionnement sous aluminium présente l'avantage de ne pas pertur- ber le flux à mesurer et de ne pas donner de rayonnements gênants pour la récupération.

1.2.2. Fils dosimètres.

Flux de neutrons rapides: fil de fer Ø 1 mm, pureté 99,995%. Flux de neutrons thermiques et épithermiques: fil d'alliage Al-Co à 0.504% ±0.014% de cobalt. Ø : 0.381 mm, pureté : 99.804%. Le fil de cobalt est lo- calement recouvert d'un manchon de cadmium.

① ANNEAU D'ETANCHÉITÉ DE CUVE

② ANNEAU SUPPORT DE CUVE

③ PASSERELLE D'INSPEC- TION DU FOND DE CUVE

IMPLANTATION DES TUBES PORTE DETECTEURS

Fig 1-1

1.3 Résultats des comptages.

Retirés de leur position d'irradiation lors du premier arrêt du réacteur pour rechargement, les tubes porte-dosimètres ont été confiés au C.E.A (Service des Piles - C.E.N. GRENOBLE) pour comptages et interprétation.

Les comptages ont été effectués en prélevant sur chaque fil des échantillons d'environ 5 cm à raison de 3 par mètre. Les activités mesurées, ramenées à la date de la fin d'irradiation sont résumées dans le tableau 1.1.

TABLEAU 1.1

	ACTIVITES MESUREES EN $Bq.mg^{-1}$		
	COBALT NU	COBALT SOUS Cd	FER
Fils entre 1 et 2	10^3 à 10^4	8.10^2 à $3~10^3$	$3~10^{-2}$ à $3~10^{-1}$
Fils entre 2 et 3	$4.5~10^3$ à $2~10^5$	$1.5~10^3$ à $7~10^4$	$4~10^{-2}$ à 25
Fils au niveau 3	$2~10^3$ à $3~10^3$	$4.5~10^2$ à $7.5~10^2$	$3~10^{-3}$ à 10^{-2}

La précision absolue des comptages est pour la plupart de l'ordre de ±3%. Cependant pour les activités les plus faibles des dosimètres de fer, elle peut atteindre 15%.

1.4 Mesures de flux.

Le calcul des flux s'effectue au moyen du programme ACTIGE qui prend en compte :
- le diagramme réel de fonctionnement du réacteur pendant l'irradiation.
- la section efficace moyenne obtenue à l'aide du spectre de neutrons calculés et la bibliothèque ENDFB-IV.

1.4.1 Spectre neutronique. Le spectre des neutrons a été calculé dans le plan médian du coeur à l'aide du code DOT en géométrie(R, θ) avec une bibliothèque de sections efficaces à 21 groupes dont 9 au-dessus de 1 MeV (Fig.1.2). En toute rigueur, ce spectre n'est pas applicable à tout le domaine instrumenté. Il a toutefois été utilisé partout sachant que les flux calculés ne sont que des ordres de grandeur quand on s'éloigne trop du plan médian du coeur.

1.4.2 Section efficace. Calculée sur ce spectre, et rapportée au flux de neutrons d'énergie supérieure à 1 MeV, la section moyenne de la réaction $^{54}Fe(n, p)$ ^{54}Mn est :

$$\sigma_{>1~Mev} = 35.4~mb$$
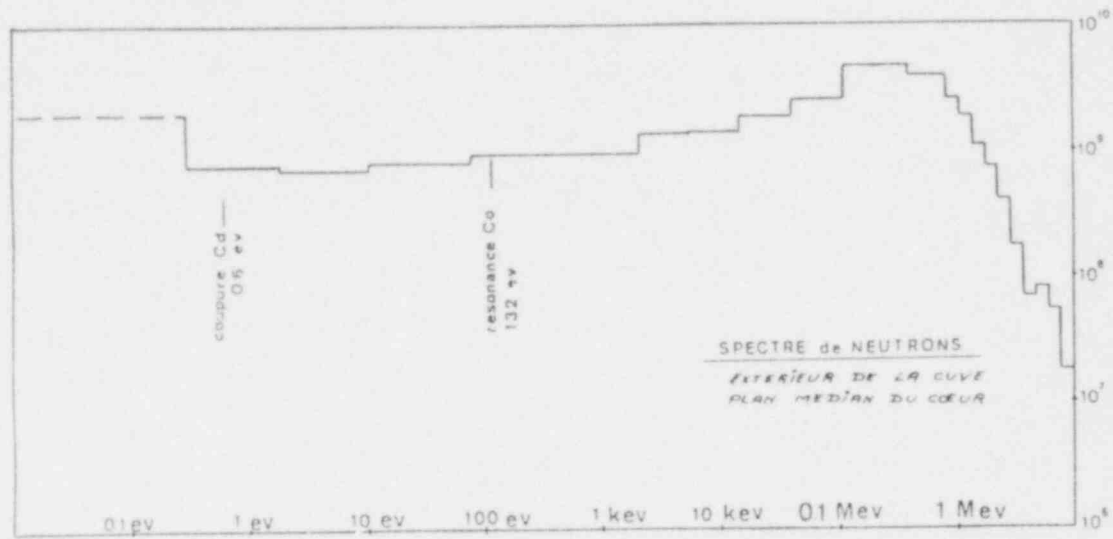
Fig 1.2   Flux par unité de léthargie calculé par le code DOT au
          plan médian du coeur à l'extérieur de la cuve.
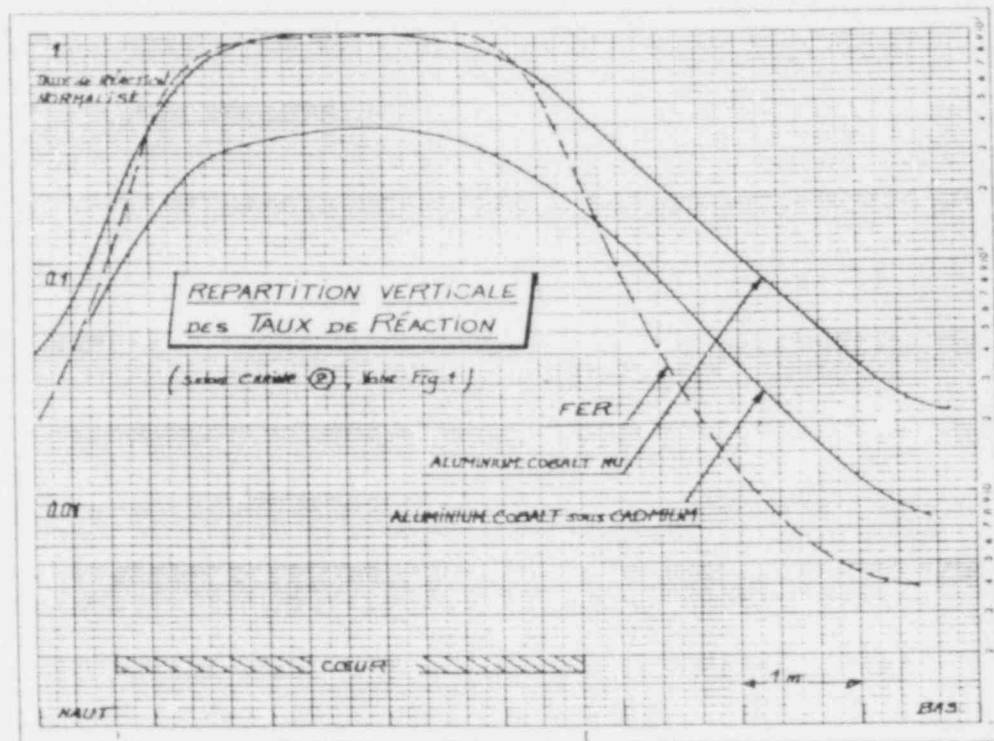
Fig 1.3 Répartition verticale des taux de réaction mesurés le
        long de la chaîne 2 (Voir Fig. 1.1).

1.5 Résultats.

La figure 1.3 donne la répartition axiale le long de la position 2 de la Fig 1.1, des taux de réactions relatifs donnés par les dosimètres de cobalt, cobalt sous /Cd et de fer. Des comparaisons ont été effectuées au voisinage du plan médian du coeur du réacteur entre les flux calculés et les flux mesurés.

- Flux thermique conventionnel.

La comparaison est très bonne et l'écart entre mesure et calcul est inférieur à 10%.
- Flux de neutrons d'énergie supérieure à 1 MeV.

La comparaison est moins satisfaisante : la valeur calculée est inférieure de 30 à 40% par rapport à la valeur mesurée.
Pour commenter cet écart, on peut remarquer que :
- le point de calcul est situé à l'extérieur de la cuve.
- le découpage n'accorde que quelques groupes au domaine de sensibilité du fer, qui ne contient que 10% des neutrons rapides.

2. DOSIMETRIE DES CAPSULES DE SURVEILLANCE.

2.1 Rappel sur les programmes de surveillance.

La mise en place d'un programme de surveillance des effets de l'irradiation sur le matériau des cuves PWR françaises répond aux exigences de l'arrêté ministériel du 20 février 1974. La dosimétrie qui est associée à ce programme est la reconduction de la pratique Westinghouse, licencieur de FRAMATOME. Son but est de déterminer le flux intégré de neutrons d'énergie supérieure à 1 MeV reçu par les éprouvettes d'essais mécaniques et d'accéder à l'aide des facteurs de flux calculés, au flux intégré reçu par la cuve. Ce dernier est le paramètre par rapport auquel sont exprimés les $\Delta_{RT_{NDT}}$ sur les courbes de référence.
Cette communication porte sur l'expérience d'exploitation des premières capsules des tranches FESSENHEIM 1 et 2 et BUGEY 2,3,4 et 5.

2.2 Procédure de dosimétrie.

2.2.1 Exploitation. L'exploitation du programme de surveillance est assurée par le Service Contrôle des Matériaux Irradiés(EDF) pour le compte des centrales. Le S.C.M.I. assure le démantèlement des capsules, la récupération des blocs dosimètres et des détecteurs. La partie mesures d'activités et calculs des fluences a été confiée au C.E.A (Service des Piles , CEN-GRENOBLE).

2.2.2 Dosimètres et leur implantation dans le réacteur.   Les dosi-
mètres à activation sont de trois types : cuivre, nickel, cobalt. Ils
se présentent sous forme de fils placés à l'intérieur de blocs dosi-
mètres. Les dosimètres fissiles sont de deux types : uranium 238 et
neptunium 237. Ils se présentent sous forme d'une pastille frittée
(^{237}Np), et de poudre (^{238}U), respectivement placées dans un double
boîtier en nickel entouré de poudre d'oxyde de cadmium et logé dans
un bloc dosimètre. Des blocs dosimètres se situent à l'intérieur de
la capsule de surveillance(Figure 2.1).

2.2.3 Mesures d'activité.   Les mesures d'activité des nickel, cuivre
et Al-Co ne posent aucune difficulté, ce qui n'est pas le cas des dosi-
mètres fissiles. En effet, les boîtiers en nickel les contenant sont
très actifs en ^{58}Co et ^{60}Co. Pour améliorer les mesures, il a fallu
retirer le boîtier extérieur. Les délais de refroidissement obliga-
toires dus au démantèlement des capsules ont conduit à orienter les
mesures d'activité sur les radioisotopes ^{95}Zr, ^{103}Ru, ^{137}Cs. Cepen-
dant, seul ce dernier, du fait de sa période, pourra convenir sur toute
la durée du programme. Pour cette première période de fonctionnement
de l'ordre de 18 mois, l'activité en ^{137}Cs est obtenue avec une pré-
cision de 5% dans le ^{237}Np et 10% dans le ^{238}U.

2.2.4 Spectres et sections efficaces. On a calculé au moyen du code
DOT en géométrie (R, θ), les spectres des neutrons :
      . sur la paroi interne de la cuve et au quart de son épaisseur.
      . pour les quatre positions d'éprouvette (Fig 2.1) : la posi-
tion 15° (capsule S) étant celle traitée ici. Le spectre est donné en
15 groupes au-dessus de 5,53 KeV jusqu'à 10 MeV (Fig 2.2). Les sections
efficaces moyennes d'activation et de fission et la section de dommage
utilisée (Cf tableau ci-dessous) sont obtenus à partir de ces spectres
calculés et de la bande ENDFB IV.

TABLEAU 2-1

Réaction	$\sigma_{>1}$ MeV (mbarn)
^{58}Ni(n,p)	96.8
^{63}Cu(n,α)	0.76
^{237}Np(n,f)	2523
^{238}U(n,f)	345

SPECTRE	σ_{dpa_1} (barn)	Indice : $\emptyset_{0.1} / \emptyset_1$
Capsule	1 525	3.02
Paroi	1 450	2.49
1/4épaisseur	1 664	2.52

$\sigma_{>1MeV}$, σ_{dpa_1} , $\emptyset_1$: grandeur relative à E > 1 MeV.

$\emptyset_{0.1}$: grandeur relative à E > 0.1 MeV.

POSITION DES CAPSULES DANS LE REACTEUR
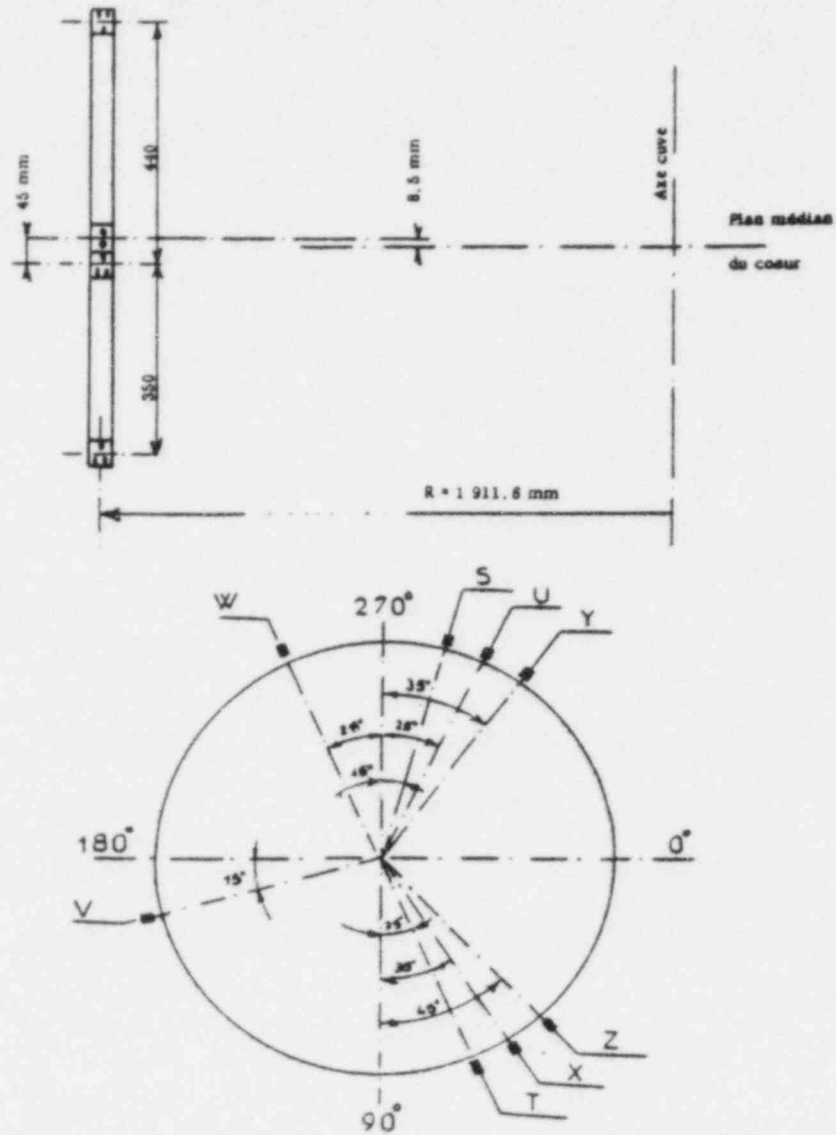
Position angulaire	Facteur multiplicatif de flux
15	1,57
25	0,90
35	0,61
45°	0,50

Fig 2.1   Implantation axiale et radiale des capsules du programme de surveillance.
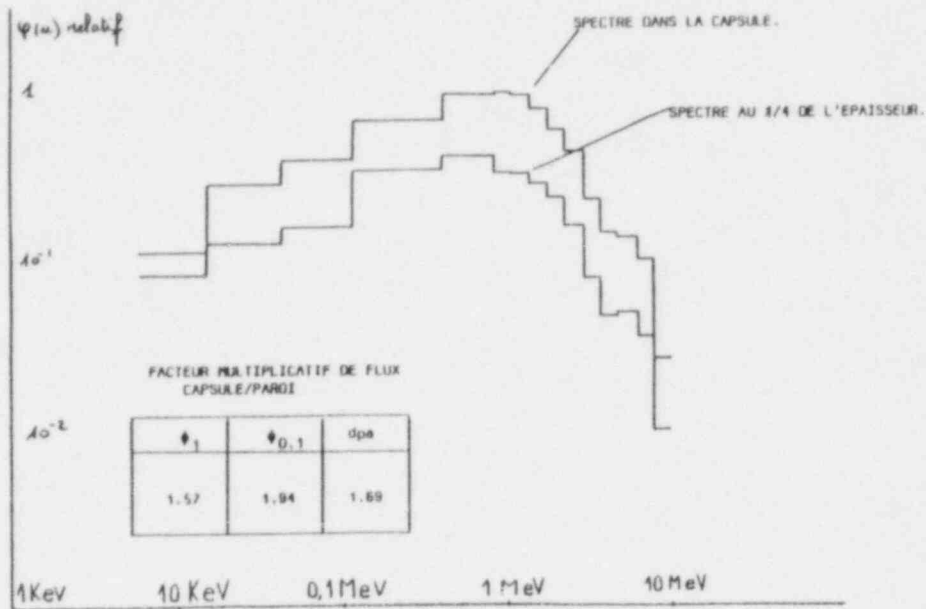
Fig. 2.2 Spectre des neutrons (DOT) par unité de léthargie.

2.2.5 Calcul des flux. Le calcul des flux s'effectue comme au chapitre précédent, au moyen du programme ACTIGE. Le principe est de comparer les activités calculées à partir des schémas d'activation (Fig 2.3) et du diagramme de fonctionnement du réacteur considéré, et les activités mesurées, et de déduire le flux par un procédé itératif.
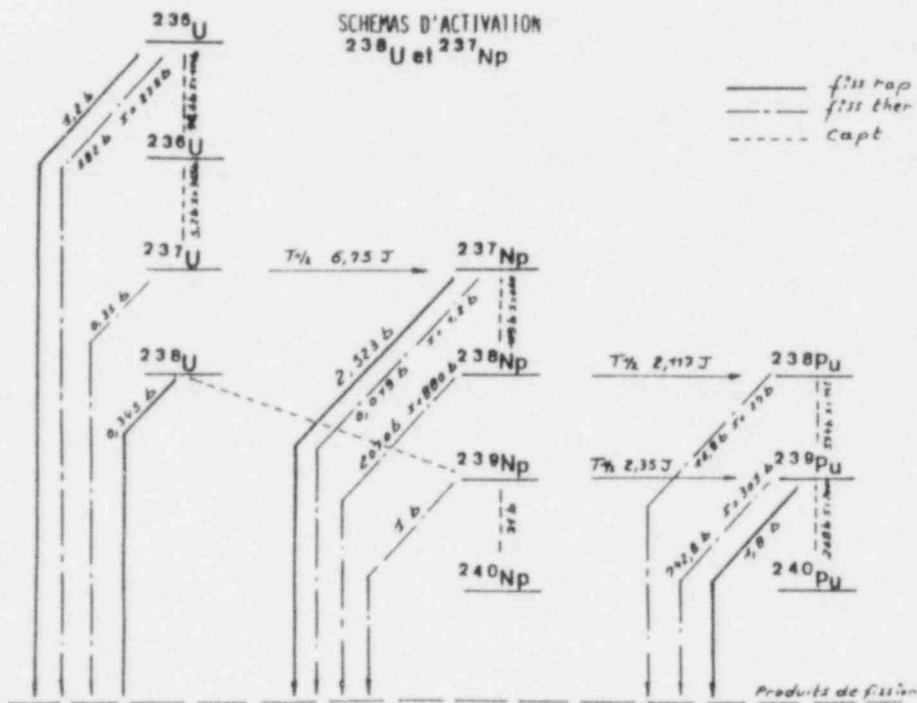
Fig. 2.3 Schéma d'activation du ^{237}Np et de ^{238}U utilisé dans le calcul du flux de neutrons rapides.

2.2.6 Résultats. Le tableau 2.4 contient les flux thermiques mesurés ainsi que les flux rapides obtenus au moyen des dosimètres de nickel, ramenés à la puissance nominale.

TABLEAU 2.4

CENTRALES	FSH 1	FSH 2	BUGEY 2	BUGEY 3	BUGEY 4	BUGEY 5
CYCLES	MAR 77 MAR 79	SEP 77 JUIL 79	AVR 78 AVR 80	AVR 78 MAR 81	FEV 79 AOU 80	JUIL 79 FEV 81
FLUX THERMIQUES	$4.07 \ 10^{11}$	$4.11 \ 10^{11}$	$3.86 \ 10^{11}$	$3.70 \ 10^{11}$	$3.85 \ 10^{11}$	$3.97 \ 10^{11}$
FLUX RAPIDE $\emptyset_1$ (Ni)	$8.04 \ 10^{10}$	$8.24 \ 10^{10}$	$8.14 \ 10^{10}$	$9.24 \ 10^{10}$ (a)	$8.16 \ 10^{10}$	$7.95 \ 10^{10}$
FLUX RAPIDE $\emptyset_1$ CALCULE	$7.84 \ 10^{10}$					

Le tableau 2.5 permet une comparaison des flux obtenus au moyen des différents dosimètres.

TABLEAU 2.5.

CENTRALES	FSH 1	FSH 2	BUGEY 2	BUGEY 3	BUGEY 4	BUGEY 5
Flux Ni	1	1	1	1	1	1
Flux Cu	1.01	0.99	1.03	1.05	1.02	1.01
Flux U	1.34	1.35	1.35	-	1.48	-
Flux Np	2.4	2.38	2.17	-	2.39	-
Flux rapide $\emptyset_1$ calculé	0.98	0.95	0.97	0.85 (a)	0.96	0.99

A la vue des résultats, il faut souligner :
- la régularité des flux ramenés à la puissance nominale.
- le bon accord entre les flux déduits du nickel, du cuivre et ceux obtenus par le calcul.
- la divergence reproductible des flux déduits du neptunium avec le flux du nickel. Elle pourrait être imputable à la présence d'impuretés fissiles non quantifiées dans les dosimètres. Une analyse est en cours.

(a) Eprouvette voisine d'un assemblage rechargé au 3/4 de la durée d'irradiation.

A PRELIMINARY STUDY OF THE USE OF FUEL MANAGEMENT TECHNIQUES

FOR SLOWING PRESSURE VESSEL EMBRITTLEMENT*

G. L. Guthrie and W. N. McElroy, Hanford Engineering Development
Laboratory, (HEDL), Richland, WA.
S. L. Anderson, Westinghouse Nuclear Technology Division,
Monroeville, PA.

ABSTRACT

A technique involving shifting of core fuel loadings
was investigated as a method for reducing the neutron flux
at points of high damage accumulation in the pressure ves-
sel wall of a light water reactor. DOT calculations were
performed for six types of commercial generic PWR's. Par-
ticular core fuel assemblies were identified as contribu-
ting heavily to the flux at the vessel wall azimuthal
location having the highest damage accumulation rate.
Calculations were made with normal fuel loadings and also
with the high damage contributing assemblies replaced by
stainless steel dummies. The fuel modification reduced
the PV wall exposure rate by factors of 5.8 to 17.9 at the
position of the existing maximum. The azimuthal position
of the maximum exposure rate point is shifted by the modi-
fication. The ratio of the old maximum to the new maximum
ranges between 1.58/1.0 and 3.44/1.0.

INTRODUCTION

A technique involving shifting of core fuel loadings has been inves-
tigated as a method for reducing the neutron flux at points of high damage
accumulation in the pressure vessel wall of a light water reactor.

Particular core fuel assemblies can be identified as contributing
most heavily to the flux at the point on the vessel wall which has the
highest damage accumulation rate. These assemblies can be replaced by
spent fuel, zircaloy, stainless steel, or water to reduce the damage rate
at the point of greatest accumulated exposure in the vessel wall. Pre-
sumably, the rest of the core would then have to be refueled w th a higher
enrichment of fissionable fuel. Another scheme for damage reduction

involves loading fresh fuel into the center of the core and moving it outward in later cycles. The present report does not specifically investigate this latter method of pressure vessel damage rate reduction.

As a preliminary guide in deciding whether any proposals of the types suggested above are practical, HEDL and Westinghouse Nuclear Technology Division cooperated in a study of the benefits to be derived from a very simple change in core power distribution. A 2-D transport calculation was used to determine the benefit to be gained by replacing a few fuel assemblies by stainless steel dummies, with appropriate water fractions to account for the coolant. The core power distribution in the remaining fuel assemblies was assumed to be unchanged except for a re-normalization factor which maintained the same total power output. The calculations were run for six types of commercial generic PWR's. The choice of reactor types was made primarily on the basis of the immediate availability of required information. The purpose of the calculations is merely to indicate whether NRC could reasonably suggest to the utilities that further investigations of such solutions in greater depth might be worthwhile. Some of the details of the calculations follow.

In general the fuel modification appears capable of reducing the existing exposure rate at the posit'on of the existing maximum by factors of 5.8 to 17.9. The position of the maximum exposure point is shifted, however, and the ratio of the old maximum to the new maximum ranges between 1.58/1.0 and 3.44/1.0.

It appears that fuel management techniques for reducing the neutron exposure at points of high accumulated exposure show considerable promise. It is recognized that there are other potential solutions to the over-all embrittlement problem, and in-depth studies of all solutions, and the associated economic implications, are required before firm decisions are made.

TRANSPORT CODE FEATURES AND REACTOR TYPES

The calculations were done with the Westinghouse version of the DOT-3 neutron transport code,[1] using a $P_1 S_8$ angular description* and a 21 group energy structure as shown in Table 1.** An (R,θ) two dimensional calculation was used in one octant of the reactor, with P_1 cross section

---

*An S_8 angular ordinate system and $P_1 (+P_0)$ scattering laws.
**The calculations were done with a neutron energy group boundary at 1.05 MeV. Fluence and flux (E > 1.05 MeV) were therefore readily available from the calculations, and were used to infer conclusions regarding use of fluence and/or flux (E > 1.0 MeV) as independent variables in damage studies. For convenience in the discussions, terminologies of (E > 1.05 MeV) and (E > 1.0 MeV) are used interchangeably in drawing qualitative conclusions from results of the current studies.

Table 1 Energy Group Structure and Fission Spectrum
for DOT Calculations

GROUP NO.	LOWER ENERGY (MeV)	F(E)
1	7.79	5.9642×10^{-3}
2	6.07	1.7059×10^{-2}
3	4.72	3.9468×10^{-2}
4	3.68	6.8770×10^{-2}
5	2.87	9.6324×10^{-2}
6	2.23	1.1411×10^{-1}
7	1.74	1.1895×10^{-1}
8	1.35	1.1244×10^{-1}
9	1.05	9.8671×10^{-2}
10	0.821	8.1806×10^{-2}
11	0.388	1.5219×10^{-1}
12	0.111	7.8617×10^{-2}
13	0.0409	1.2486×10^{-2}
14	0.0150	2.8786×10^{-3}
15	5.53×10^{-3}	2.6119×10^{-4}
16	5.83×10^{-4}	
17	7.89×10^{-5}	
18	1.07×10^{-5}	
19	1.86×10^{-6}	
20	3.00×10^{-7}	
21	0.00	

HEDL 8203-112.5

descriptions derived from the GAMB-1T cross section library.[2] This combination was benchmarked in the Pool Critical Assembly (PCA) at Oak Ridge National Laboratory. The benchmark results compared well (±10%) to results from PCA Monte Carlo calculations and PCA dosimetry measurements. The DOT iteration scheme used a fixed source in the core, emitting a Cranberg fission spectrum. For the six different reactor types the core power distribution was based on core power calculations, verified by experimental data. For five of the reactor types having 17 x 17 pin arrays in the fuel subassemblies, each subassembly was divided into a 17 x 17 (x,y) mesh detail for power distribution purposes and this was remapped into the (R,θ) mesh. The transport calculations for all six generic types were run with sufficient surveillance capsules rotated into the octant under examination to allow interpretation of all surveillance results. DOT runs were made (1) with the capsules in place and a normal fuel distribution, (2) with capsules in place and high-damage- contributing-fuel subassemblies replaced by dummies, and (3) with normal fuel but with surveillance capsules removed. The third case above (capsules out) was run for only two of the six generic reactors. For all six reactor types, the power level was renormalized for the modified fuel cases in order to maintain the same total power level. However, in the modified fuel cases, the shape of the power distribution was assumed unchanged in those fuel assemblies which were retained, while the power in the dummy assemblies was of course set to zero. The reactor types are listed below.

1. PWR type A, having both accelerated and wall capsules, (2600 MWT)

2. PWR type B, two Loop Shield Reactor (1960 MWT), accelerated capsules only

3. PWR type C, three Loop Shield Reactor (2900 MWT), accelerated capsules only

4. PWR type D, four Loop Shield Reactor (3565 MWT), accelerated capsules only

5. PWR type E, three Loop "Pad" Reactor (2900 MWT), accelerated capsules only

6. PWR type F, four Loop "Pad" Reactor (3565 MWT), accelerated capsules only

Reactor type A is distinguished by the fact that it has both accelerated and wall capsules, while types B, C, D, E and F have only accelerated capsules. Reactor types B, C, and D, (shield reactors) are representative of older generic models of three different power ratings. The thermal shield is 360° in extent, in contrast to the reduced angular sweep of the neutron "pad" used in later reactor designs. The "pad" reactors are represented by reactor generic types "E" and "F".

The calculations were similar for the six reactor types. A few differences were, (1) the DOT modeling mesh varied slightly due to differences

in geometry, (2) the modeling of the surveillance capsules varied, again due to differences in geometry and (3) capsule perturbation effects were studied only for reactor types A and B.

CALCULATIONS AND RESULTS

The exact details of the DOT coordinate mesh system and surveillance capsule modeling depended on the reactor under study. The number of θ mesh lines was in the mid fifty range for reactors A and B, and in the 90 to 100 range for reactors B, C, D, E and F. The number of R mesh lines used for reactors B, C, D, E and F was in the 100 to 115 range while approximately 140 radial mesh lines were used in modeling reactor A. The surveillance capsules were modeled using mesh cells numbering in the range of 15 to 30 cells per capsule, depending on the complexity of the geometry and mounting arrangement. The DOT mesh-system extended into the concrete containment vessel for reactors B, C, D, E and F, and extended into the shield tank for reactor A. The locations of the surveillance capsules used in the modeling is given in Table 2.

Table 2. Capsule Modeling

Reactor	Accelerated Capsule Locations	Wall Capsule Locations
A	35°, 45° Before thermal shield	3° Attached to PV wall
B	13°, 23°, 33° Behind thermal shield	
C	15°, 25°, 35°, 45° Behind thermal shield	
D	4°, 40° Behind thermal shield	
E	17°, 19.67° Behind neutron pad	
F	29°, 31.5° Behind neutron pad	

The effect of the fuel modification for the various reactors can be seen in Tables 3 and 4.

Table 3. Maximum PV Wall Exposure dpa Improvement Ratios

REACTOR TYPE	MAX POSITION REG FUEL	MAX POSITION MOD FUEL	REDUCTION OF ORIGINAL MAX dpa	RATIO OF OLD MAX TO NEW MAX
TYPE A ACCEL + WALL CAPSULE	0°	28.5°	13.6	1.58
TYPE B TWO LOOP SHIELD	0°	32.1°	11.64	2.33
TYPE C THREE LOOP SHIELD	0°	23°	17.9	3.44
TYPE D FOUR LOOP SHIELD	45°	8°	5.81	2.74
TYPE E THREE LOOP PAD	0°	28.75°	16.43	2.19
TYPE F FOUR LOOP PAD	45°	9.25°	5.82	1.6

HEDL 8203-112.4

Table 4. Fuel Replacement Per Octant

REACTOR TYPE	REPLACED ELEMENTS	TOTAL ELEMENTS
TYPE A ACCEL + WALL CAPSULE	TWO ASSEMBLIES ON FLAT NEAR 0°	27.125
TYPE B TWO LOOP SHIELD	1.5 ASSEMBLIES ON FLAT NEAR 0°	15.125
TYPE C THREE LOOP SHIELD	1.5 ON FLAT NEAR 0°	19.625
TYPE D FOUR LOOP SHIELD	2 AT CORNERS NEAR 25° AND 40°	24.125
TYPE E THREE LOOP PAD	1.5 ON FLAT NEAR 0°	19.625
TYPE F FOUR LOOP PAD	2 AT CORNERS NEAR 25° AND 40°	24.125

HEDL 8203-112.3

Table 3 deals with the reduction of the maximum dpa exposure on the PV wall for a 32 effective full power year (EFPY) operation. The comparison is between a 32 EFPY operation with regular fuel and a 32 EFPY operation with modified fuel. With the regular fuel loading, the angular position having the highest dpa exposure rate on the PV inner radius is given in column one. At this angular location, the change in fuel loading reduces the rate of dpa accumulation by the factor given in column three. The position of the maximum rate of dpa accumulation on the PV inner radius with the modified fuel loading is given in column two. The ratio of the maximum dpa accumulation rate (PV inner radius) with normal fuel, to the maximum dpa accumulation rate (PV inner radius) with modified fuel is given in column four.

The fuel replacement adopted in the study is shown in Table 4. The table shows for example, that 1.5 fuel elements per octant were replaced by stainless steel dummies (with appropriate water fractions) in the study of the Type C reactor. This constituted a replacement of less than 10% of the fuel (1.5/19.625) and produced the benefit shown in Table 3.

The material in Tables 3 and 4 can be better appreciated by reference to Figures 1 and 2 which deal with the Type F reactor. Figure 1 shows the midplane geometry for a Type F, 4-loop pad reactor. Table 3 shows that the maximum exposure rate on the PV wall occurs at 45° with a normal fuel loading. Table 4 shows that one fuel element was replaced at each of the corner positions (25° and 40°). Reference to Figure 2 shows that the fuel modification depressed the original exposure peak at the 45° position, but the maximum with the modified loading occurs at 9.25°. The increase at the 0° position is due to the renormalization required to maintain equal power levels.

Capsule perturbation studies were performed for reactor types A and B. This was accomplished by repeating the DOT calculation with normal fuel loading but with the surveillance capsules removed. The results were similar to those found earlier by S. L. Anderson.[3]

The presence of the capsule causes an increase in neutron exposure, measured either in dpa or in fluence (E > 1.05 MeV) units.

The exact amount of the increase at the capsule center depended slightly on the particular reactor and also on the capsule. For the 3° capsule of the Type A reactor the presence of the capsule causes an increase of 24.1% in the dpa exposure value or an increase of 22.9% for the fluence (E > 1.05 MeV). For the Type A reactor accelerated capsule, the similar increases were 26.9% (dpa) and 24.0% (fluence (E > 1.05 MeV)).

For the Type B reactor the increases were 34.9% (dpa) and 26.5% (fluence (E > 1.05 MeV)) for the capsule located at the 13° azimuthal position.

These results have important implications. When a transport calculation is performed without explicit modeling of the capsule, a correction
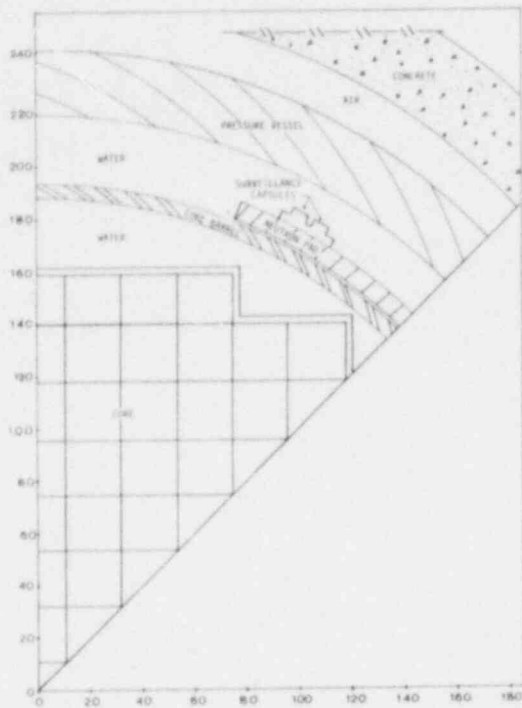
Figure 1. Midplane Geometry for a
           Type F, 4-Loop Pad Reactor
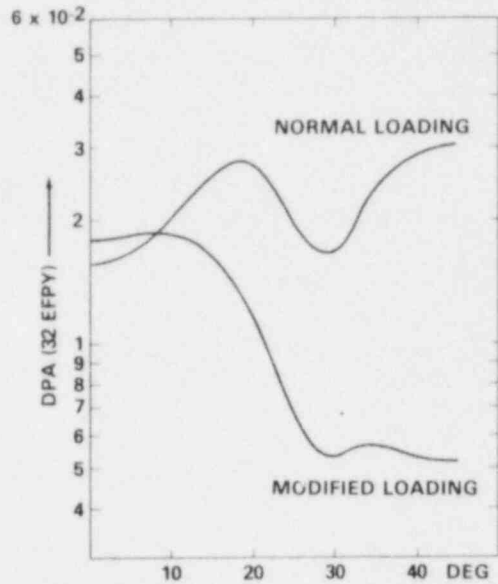
Fig. 2. Four Loop Pad
Reactor (Type F) dpa on
Vessel Inner face for 32EFPY.

of the order of 25 to 30% is needed in the calculation of the "lead fac-
tor," based on fluence (E > 1.05 MeV). The difference between the dpa
and fluence (E > 1.05 MeV) correction factors for the Type B capsule
illustrates the importance of using an exposure index that correlates
well with property degradation.

For each of the six reactor types, the ratio of dpa/fluence (E >
1.05 MeV) was calculated as a function of radial position for a traverse
at a particular azimuthal angle. The traverse extended out through the
PV wall. In each case the azimuthal angle of the traverse was chosen to
take the traverse through the center region of a surveillance capsule.

It was found that the ratio of dpa/fluence (E > 1.05 MeV) generally
increased by a factor of the order of 2.0 in traversing from the inner to
the outer radius of the PV wall. The radial traverse angle chosen and
the ratio-increase factors are shown in Table 5 for each of the six reac-
tor types studied. The change in the ratio of dpa/fluence (E > 1.05 MeV)
was less dramatic when comparing the ratio at the surveillance capsule to
that found at the 1/4 T position of the PV wall. For this comparison the
ratio changed by factors of 1.2 or less.

Table 5. Factor by which dpa/φt (E< 1.05 MeV) Increases
in Outward Traverse Through PV Wall.

REACTOR TYPE	INCREASE FACTOR	RADIAL TRAVERSE ANGLE
TYPE A ACCEL + WALL CAPSULE	2.23	35°
TYPE B TWO LOOP SHIELD	1.62	13°
TYPE C THREE LOOP SHIELD	1.96	14.72°
TYPE D FOUR LOOP SHIELD	2.12	39.7°
TYPE E THREE LOOP PAD	2.0	19.875°
TYPE F FOUR LOOP PAD	2.18	31.7°

HEDL 8203-112.2

There are two important implications of the calculated results found
in this part of the study. (1) If we assume that dpa is a suitable inde-
pendent variable for use in developing trend curves, then fluence (E >
1.05 MeV) is of doubtful value if the information developed is intended
for use at depths beyond 1/2 T in the vessel wall. (2) If information on
mechanical properties is developed at the surveillance position and
applied at the 1/4 T position, using fluence (E > 1.05 MeV) as an inde-
pendent variable, the mechanical property degradation error caused by the
shift in the dpa/fluence ratio will be of the order of 7% or less. This
last conclusion is based on the assumptions that mechanical property
degradation is proportional to dpa to the 0.3 power and the results for
other reactors will be similar to the results found in this study.

SUMMARY AND CONCLUSIONS

In general the fuel modification appears capable of reducing the
existing exposure rate at the position of the existing maximum by factors
of 5.8 to 17.9. The position of the maximum exposure point is shifted
however, and the ratio of the old maximum to the new maximum ranges
between 1.58/1.0 and 3.44/1.0. In the pressure vessel wall, the ratio of
dpa/φt (E > 1.05 MeV) is a function of radial position and this ratio

(dpa/φt) changes by roughly a factor of two in going from the inner
surface of the pressure vessel to the outer surface. The actual factors
varied between 1.62 and 2.23. Capsule perturbation studies undertaken
for the Type A and Type B reactors show that the presence of the surveil-
lance capsule increases the neutron exposure at the center of the capsule
by 25% to 35%.

It appears that fuel management techniques for reducing the neutron
exposure at points of high accumulated exposure show considerable promise.
It is recognized that there are other potential solutions to the over-all
embrittlement problem, and in-depth studies of all solutions, and the
associated economic implications, are required before firm decisions are
made.

A more complete report of this study is available in the Light Water
Reactor Pressure Vessel Surveillance Dosimetry Improvement Program
Quarterly Progress Report for October - December 1981.[4]

REFERENCES

1. G. Collier et al., Second Version of the GAMBIT Code, WANL-TME-1969,
    Westinghouse Astronuclear Laboratory, Pittsburgh, PA, November 1969.

2. R. G. Soltesz, R. K. Disney, J. Jediuch and S. L. Zingler, "Two-
    Dimensional Discrete Ordinates Transport Technique," Nuclear Rocket
    Shielding Methods, Modification, Updating and Input Data Preparation,
    WANL-PR-(LL)034, Vol. 5, Westinghouse Astronuclear Laboratory,
    Pittsburgh, PA, August 1970.

3. S. L. Anderson, "Characterization of the Neutron Environment for
    Commercial LWR Pressure Vessel Surveillance Programs," Proceedings
    of the Second ASTM-EURATOM Symposium on Reactor Dosimetry,
    NUREG/CP-0004, Palo Alto, CA, October 3-7, 1977.

4. G. L. Guthrie, W. N. McElroy and S. L. Anderson, "Investigations
    of Effects of Reactor Core Loadings on PV Neutron Exposure,"
    LWR Pressure Vessel Surveillance Dosimetry Quarterly Progress Report,
    Oct.-Dec., 1981. HEDL TME 81-36, NUREG/CR 2345, Vol. 4. (1982)

SURVEILLANCE DE LA CUVE DE LA CAP
Programme, Mesures et calculs neutroniques

J-M.FARRUGIA - TECHNICATOME
J-C.NIMAL et B.TOTTH - CEA/SERMA

CENTRE D'ETUDES NUCLEAIRES DE SACLAY
BP.18-91190 GIF/YVETTE - FRANCE

R.LLORET et R.PERDREAU - SERVICE DES PILES

CENTRE D'ETUDES NUCLEAIRES DE GRENOBLE
85X - 38041 GRENOBLE CEDEX-FRANCE

ABSTRACT

Starting with the design of the CAP (Prototype Advanced NSSS), a programme for pressure vessel surveillance has been prepared, including dosimetry.

The dosimetry programme encompasses activation dosimeters (Cu, Nb, Co) and fission dosimeters (^{237}Np, ^{238}U) located either inside the pressure vessel with the monitoring test-samples, or in a tube outside the pressure vessel.

In the first part, a description of the method for neutronic calculations is given ; such calculations use the codes ANISN and MERCURE 4 allowing assessment of the neutron spectrum seen by the detectors and the related reaction rates. This is followed by a description of the instrumentation.

The initial dosimetry results available after the first operating cycles are in good agreement with calculations.

1 - DESCRIPTION SOMMAIRE DU PROGRAMME DE SURVEILLANCE

La Chaufferie Avancée Prototype (CAP) est un réacteur de type PWR implanté sur le Centre d'Etudes Nucléaires de Cadarache. Conçu, construit et exploité par Technicatome, pour le compte du C.E.A., ce réacteur constitue un moyen d'essais largement utilisable dans la filière à eau légère pressurisée et, plus spécialement, un moyen d'essais des éléments combustibles.

La chaufferie nucléaire est de type intégrée, c'est-à-dire que le couvercle de la cuve est réalisé par le générateur de vapeur et les pompes primaires sont portées par deux cornes qui font partie intégrante de la cuve. Cette cuve a été réalisée en acier de nuance 80 HLES et, dès la conception, un programme de surveillance a été

établi et réalisé de la façon suivante :

Quatre tubes porte-conteneurs, fixés sur les structures internes et situés à quelques centimètres de la cuve (voir fig. 1 et 2), ont été chargés de conteneurs de dimensions 20x50x140 mm. Les conteneurs contiennent soit des éprouvettes Charpy V, soit des éprouvettes Pellini, soit encore des éprouvettes de traction. Les éprouvettes prélevées dans le métal de base ont été placées au niveau du plan médian combustible. Les éprouvettes prélevées dans le joint soudé et dans la zone affectée thermiquement (ZAT) ont été placées dans les zones de plus faible flux (voir Fig. 1). Les conteneurs seront prélevés au fur et à mesure des besoins tout au long de la vie du réacteur.

Chaque conteneur a été muni de boîtiers de détecteurs placés dans les faces supérieure et inférieure des conteneurs (voir Fig. 3).

Un deuxième programme de dosimétrie a été également entrepris en installant derrière la cuve un tube sur toute la hauteur. Ce tube est destiné à recevoir des détecteurs par activation, dont le chargement et le déchargement s'effectuent au moyen d'un câble semi-rigide lors des arrêts normaux du réacteur.

L'intégration du flux neutronique est assurée par les détecteurs suivants :

. niveau plan médian combustible :

- détecteur fer en disque diamètre 7 mm, épaisseur 0.1 mm,
- détecteur Cu-Co à 1.12 % de cobalt, fil de longueur 5 mm, diamètre 0.7 mm.

. niveau soudure basse :
- détecteur fer en disque diamètre 7 mm, épaisseur 0.1 mm,
- détecteur cobalt pur en disque diamètre 7 mm, épaisseur 0.1 mm.

Ce programme permet de suivre la fluence neutronique reçue par la cuve et de vérifier les calculs neutroniques réalisés pour chacun des coeurs.

2 - SCHEMA DE CALCUL DE L'ACTIVATION DES DETECTEURS ET DES TAUX DE FORMATION DE DOMMAGES

Nous avons utilisé dans ce cas les codes ANISN et MERCURE 4.

Le schéma de calcul permet une représentation à trois dimensions de la géométrie et de la distribution des sources de neutrons. Ceci est essentiel pour la représentation du coeur. Nous décrivons ci-après les deux codes MERCURE 4 et ANISN ainsi que le schéma de calcul.

2.1 - Mercure 4 [1] [2]

Ce code intègre le noyau d'atténuation en ligne droite dans

deux cas :

- rayonnement gamma avec une structure multigroupe pour les sections efficaces et avec une bibliothèque de facteurs d'accumulation,

- neutrons rapides dont l'atténuation est calculée au moyen de sections efficaces de déplacement données par l'utilisateur.

Nous ne décrivons ici que le cas des calculs neutroniques. Pour calculer un taux de réaction donné τ_d, pour un détecteur d, MERCURE 4 utilise la formule donnée par la relation(1), où le noyau $G(r_o, r, d)$ caractérise l'atténuation des particules nées en r_o, arrivant en r et contribuant au taux de réaction d.

$$\tau_d = \iiint_{Vs} dr_o \, S(r_o) \, G \, (r_o, \, r, \, d) \qquad (1)$$

VS est le volume contenant les sources. Le noyau G est calculé en utilisant la section de déplacement $\Sigma_{i,d}$ pour le détecteur d et la région i :

$$G(r_o, \, r, \, d) = (Ad \, / \, 4\pi(r - r_o)^2) \, \exp \, (- \sum_i \Sigma_{i,d} \, ti) \quad (2)$$

où t_i est la distance traversée en ligne droite dans la ième région

Ad est un coefficient dépendant seulement du détecteur d.

La description géométrique dans MERCURE 4 pour les régions sources et les régions de protection est à trois dimensions : des surfaces, soit planes soit du second degré, sont définies par l'utilisateur. Ces surfaces limitent des volumes homogènes qui ont une distribution quelconque dans l'espace.

Finalement, l'intégration de la formule (1), donnant le résultat τ_d est effectuée par une méthode de Monte Carlo avec un calcul exact des fonctions d'importance qui donne une très bonne précision statistique sur le résultat pour des temps de calcul brefs. L'utilisation de la méthode de Monte Carlo évite des erreurs systématiques dues au calcul par discrétisation de l'intégrale (1).

2.2. ANISN [3]

ANISN est le code américain bien connu résolvant la forme intégro-différentielle de l'équation du transport par la méthode des ordonnées discrètes (discrétisation du flux angulaire sur un maillage spatial et angulaire). Les sections efficaces ont une structure multigroupe et sont représentées par un développement en série de polynômes de Legendre. La géométrie est à une dimension.

2.3. SCHEMA DE CALCUL

2.3.1. Nous définissons une géométrie à une dimension en respectant les épaisseurs de matériaux traversés dans la direction où les résultats sont souhaités. Nous effectuons alors les calculs suivants :

- un calcul ANISN en configuration cylindrique donnant le spectre de neutrons s (E, r) dans la protection et tous les taux de réactions τ_d donnés par la formule (3) :

$$\tau_d(r) = \int_0^\infty S(E, r) \, r_d(E) \, d E \qquad (3)$$

r_d : fonction de réponse du détecteur d.

En particulier, nous obtenons les taux de réaction à chaque frontière des régions de protection.

- dans la même géométrie, nous effectuons plusieurs ensembles de calculs MERCURE 4, un ensemble par détecteur. Dans ces calculs nous ajustons les sections efficaces de déplacement $\Sigma_{i,d}$ pour obtenir par MERCURE 4 et ANISN le même taux de réaction à chaque frontière. L'ajustement donne aussi le coefficient A_d.

2.3.2. A l'aide des sections efficaces de déplacement $\Sigma_{i,d}$ nous effectuons le calcul exact à trois dimensions d'espace par MERCURE 4 en tenant compte de la distribution la plus précise des sources de neutrons.

2.4. Application à la CAP

Les calculs ont été effectués pour le cycle 1 de la CAP, les densités spatiales des sources de neutrons sont déduites des calculs de suivi de coeur effectués au CEA-SERMA.

Les sections efficaces nécessaires au calcul de transport par ANISN sont obtenues par condensation à 100 groupes de VITAMIN C[4] avec comme bibliothèque de données ENDF/B4. Elles sont traitées dans l'approximation P3. Le calcul de référence ANISN est effectué en géométrie cylindrique avec l'ordre de quadrature S4. La figure 4 représente les spectres de neutrons :

- à l'emplacement des éprouvettes,
- à l'entrée de la cuve,
- à l'emplacement du tube de mesure.

Pour le calcul à trois dimensions par MERCURE 4 nous avons considéré les fonctions réponses suivantes :

- fluence de neutrons d'énergie supérieure à 1 MeV,
- fluence de fission équivalente pour la formation de zones,
- énergie cédée au réseau (eV/g),
- taux de fission sur ^{238}U et ^{237}Np,
- taux de réaction sur ^{93}Nb et ^{63}Cu,

Les taux de fission et de réaction peuvent être comparés aux valeurs expérimentales ce qui confirme le modèle de calcul. Les autres réponses permettent de corréler les dommages formés dans les éprouvettes et ceux créés dans la cuve.

Pour la comparaison avec les expériences, les sections efficaces expérimentales des détecteurs sont données dans la partie 4.

3. DOSIMETRIE NEUTRONIQUE DANS LE TUBE EXTERIEUR

Cette dosimétrie assure l'intégration des flux pour chaque cycle de fonctionnement. Une courte campagne, menée lors d'un démarrage, a fourni des valeurs de l'indice de spectre épithermique, ainsi qu'une section efficace expérimentale moyenne de la réaction ^{54}Fe(n p) ^{54}Mn par comparaison avec ^{115}In(n, n') ^{115m}In.

On trouvera dans le tableau suivant un aperçu des résultats obtenus sur un cycle :

	ϕ epi/ϕth	Fluence thermique (n/cm^2)	σ_1(Fe) mb	Fluence rapide > 1 MeV	
				mesurée	calculée
Niveau médian	0.044	$1.55 \ 10^{17}$	121.	$2.3 \ 10^{16}$	$2.5 \ 10^{16}$
Niveau soudure	0.040	$0.90 \ 10^{16}$	127.	$6.5 \ 10^{14}$	$6.2 \ 10^{14}$

4. DOSIMETRIE NEUTRONIQUE AUX EMPLACEMENTS DE SURVEILLANCE

4.1. Description des dosimètres

Chaque conteneur d'éprouvettes contient 4 boîtiers de dosimètres (Figure 3) :

2 boîtiers pour détecteur par activation (Co, Cu, Nb),
1 boîtier pour détecteur fissile ^{237}Np,
1 boîtier pour détecteur fissile ^{238}U.

Le boîtier des détecteurs par activation est une coupelle en aluminium à couvercle soudé par ultra-sons en atmosphère d'Hélium. Il contient :

a/ pour la dosimétrie des neutrons rapides, un disque de cuivre de diamètre 4 mm et d'épaisseur 1 mm et un disque de Niobium de diamètre 4 mm et épaisseur 20 μm,

b/ pour la dosimétrie des neutrons thermiques un disque d'alliage Aluminium-Cobalt à 2 %, diamètre 4 mm, épaisseur 0.2 mm.

Le boîtier des dosimètres fissiles est en titane (diamètre 9,8 mm, épaisseur 1 mm), il contient le support du dépôt de matière fissile. La masse nominale de dépôt est 10.5 mg. Ce boîtier est fermé par soudage électronique. Le boîtier ^{238}U est irradié à l'intérieur d'un filtre en Gadolinium.

4.2. Mesure et traitement des activités

Les rayonnements émis par chaque source sont mesurés, dans une géométrie étalonnée, à l'aide de diodes :
-Si-Li pour les X du ^{93m}Nb,
-Ge intrinsèque de 50 cm^3 pour les autres.

Pour le traitement des activités, les hypothèses suivantes sont admises :

a/ les rapports entre les composantes, thermique, rapide et épithermique du flux se maintiennent dans le temps. L'initialisation du traitement itératif des activités est établie à partir des valeurs déduites du spectre théorique (figure 4),

b/ le flux neutronique dans l'emplacement de mesure est proportionnel à la puissance du réacteur. Le diagramme de fonctionnement du réacteur, fourni par l'exploitant de la CAP, donne donc la fonction inconnue : le flux en fonction du temps, à une constante près. Cette constante est déterminée par le programme ACTIGE.

c/ les sections efficaces au-dessus de 1 MeV sont déterminées dans le spectre à l'emplacement des éprouvettes avec des valeurs de bibliothèque ENDF/B et recalées aux valeurs $\bar{\sigma}_{exp}$ publiées. Le jeu obtenu est le suivant :

Réaction	Seuil Es MeV	Période	$\bar{\sigma}$ Biblio.	$\bar{\sigma}$ exp /Référence/	$\sigma > 1$MeV
^{63}Cu(n,α) ^{60}Co	6.8	5.27 ans	0.505 mb ENDF/BV	0.5 mb	2.43 mb
^{93}Nb(n,n')^{93m}Nb	1	16.11 ans	Rh(n,n') CCDN normé à 153 mb	153 mb *	236.8 mb
^{237}Np(n,f) PF	0.6		1 336 mb ENDF/BIV	1 312 mb [6]	1 959 mb
^{238}U(n,f) PF	1.5		300 mb ENDF/BIV	305 mb [6]	499 mb

*Actualisation avec T=16.11 ans et KX=0.116 de [7].
$\bar{\sigma}$: valeur moyennée sur un spectre de fission de ^{235}U.

Pour l'exploitation des dosimètres fissiles une grandeur importante est le rendement de fission Y, dans le domaine des neutrons rapides. Les valeurs utilisées sont données ci-après.

P.F	Y % Np	U	Raie traitée E KeV	Taux branch. I%	Période
^{137}Cs	6.08	6.01	661.6	85.	30 ans
^{95}Zr	5.78	5.13	756.7 et 724.2	55 et 44.5	64.05 j
^{95}Nb			765.8	100	34.97 j
^{106}Ru	2.24	2.51	621.8	9.81	369 j

5. RESULTATS

5.1 Fluences mesurées

Les fluences au-dessus de 1 MeV obtenues à partir des dosimètres associés au conteneur n° 6 sont les suivantes :

Détecteur	Cuivre	Niobium	Neptunium	Uranium
Fluence en 10^{18} n/cm²	0.67	0.78	0.95 (^{137}Cs) 0.85 0.82 (^{106}Ru) 0.68 0.72 (^{95}Zr) 0.53 0.67 (^{95}Nb) 0.61	

La précision des mesures d'activité de certains produits de fission est trop faible pour être prise en compte. Compte tenu de la durée d'irradiation, seul le ^{137}Cs est valide, la fluence qu'il donne est en accord avec celle des dosimètres par activation.

Dans le spectre des neutrons incidents sur le conteneur n° 6, la section efficace de déplacement des atomes de fer pour les neutrons d'énergie > 1 MeV est trouvée $\sigma > 1$ (dpa) = 1353 b. A partir de la fluence déduite du cuivre on déduit que les éprouvettes ont subi $9.1\ 10^{-4}$ déplacement par atome.

5.2 Comparaison des calculs et des mesures

Les calculs de taux de réaction décrits dans la section 2 se rapportent à 45 % de l'irradiation totale. On les ramène à l'irradiation totale en admettant que la distribution des sources dans le coeur n'a pas été très différente de celle du cycle objet du calcul théorique. Les taux de réaction attendus sur les dosimètres se déduisent alors des valeurs calculées en ramenant celles-ci aux sections efficaces expérimentales selon : $\tau'_m = \dfrac{\tau_d\ \text{calculé}}{\overline{\tau}_d} \times \overline{\sigma}_{exp}$

Ces valeurs et celles effectivement mesurées sont comparées dans le tableau ci-dessous :

Taux de réaction par noyau	CUIVRE	NIOBIUM	NEPTUNIUM	URANIUM
τ mesuré	$1.62 \ 10^{-9}$	$1.84 \ 10^{-7}$	$1.86 \ 10^{-6}$ (^{137}Cs)	$4.25 \ 10^{-7}$
$\tau'm$	$1.94 \ 10^{-9}$	$2.35 \ 10^{-7}$	$2.12 \ 10^{-6}$	$4.24 \ 10^{-7}$

On peut noter l'excellent accord entre la mesure issue du dosimètre Uranium et le calcul théorique. Pour les autres dosimètres l'écart calcul/mesure est de l'ordre de 20 %, écarts qui ne mettent pas en cause la corrélation entre les deux modes de détermination.

CONCLUSION

A la vue des premiers résultats et de leur cohérence on peut dire que les moyens mis en oeuvre dans le programme de dosimètrie associé à la surveillance de la cuve de la CAP sont adaptés. Soulignons en certaines particularités :

- Présence du tube de mesure à l'extérieur de la cuve.
- Choix du titane dans l'élaboration des dosimètres fissiles et leur boîtier.
- Choix du niobium comme détecteur.
- Schéma de calcul permettant une représentation tridimensionnelle.

REFERENCES

/1/ C.DEVILLERS- C.DUPONT. MERCURE 4 - Un programme de Monte Carlo à trois dimensions pour l'intégration de noyaux ponctuels d'atténuation en ligne droite. Note CEA.N 1726 (Juillet 1974).

/2/ C.DUPONT - J-C.NIMAL. MERCURE 4 - Un programme de Monte Carlo à trois dimensions pour l'intégration de noyaux pontuels d'atténuation en ligne droite. Rapport interne (juillet 1980).

/3/ C.DEVILLERS. Système ANISN - Description et mode d'utilisation du programme aux ordonnées discrètes ANISN et des programmes auxiliaires. Note CEA.N.1358 (octobre 1970).

/4/ DLC.41 RSIC - Oak-Ridge National Laboratory.

/5/ E.JUNOD (ACTIGE). Communication privée.

/6/ W.L.ZIJP and H.H.BAARD. Nuclear Data Guide for reactor neutron metrology : EUR 7164.(Edition 1979).

/7/ R.LLORET. Utilisation du niobium comme intégrateur de fluences élevées de neutrons. Présenté au Groupe de Dosimétrie EURATOM (PETTEN 1973).

Conteneur pour
éprouvettes de surveillance

Logements pour parailla
de collecteur

Figure 3

Coupe dans le plan
median

8 tubes pour éprouvettes de surveillance

Figure 2

Cuve
Coupe A-A
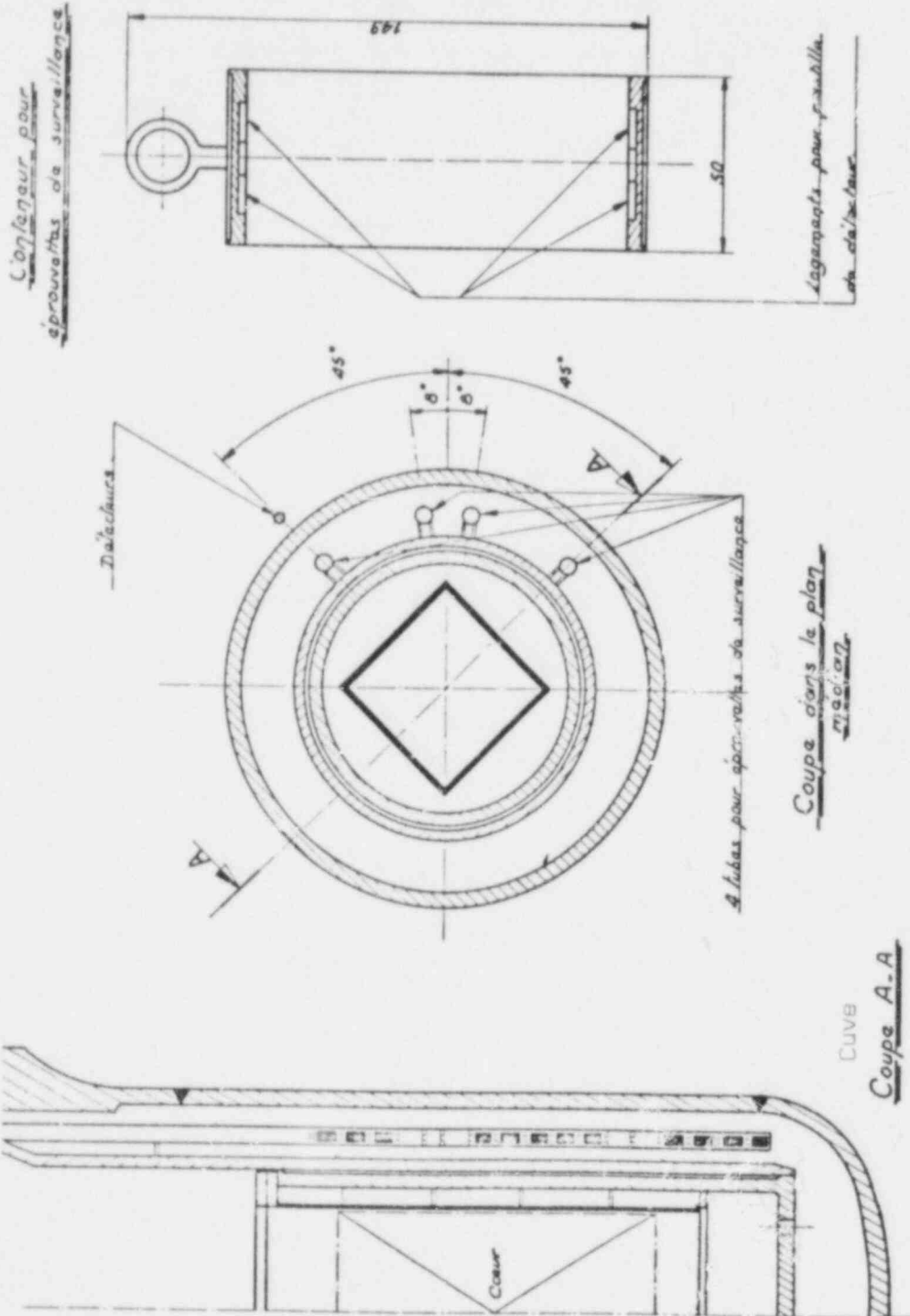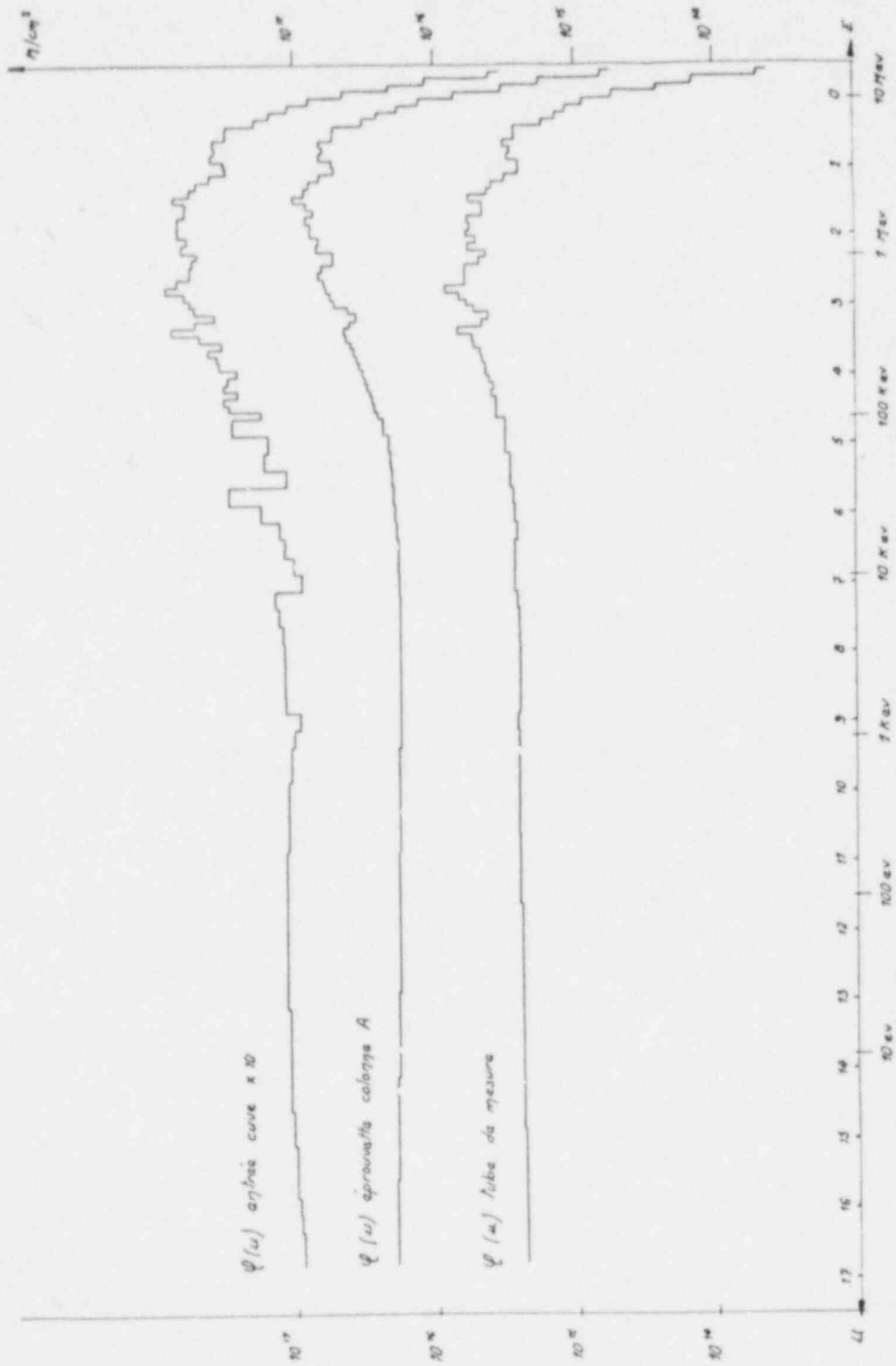
Figure 1

Figure 4 : Spectre par unité de léthargie

CALCULATIONS OF THE WESTINGHOUSE PERTURBATION EXPERIMENT AT THE POOLSIDE FACILITY

R. E. Maerker and M. L. Williams
Oak Ridge National Laboratory
Oak Ridge, Tennessee, USA

ABSTRACT

Discrete ordinate calculations are made and the results compared with measurements performed in the Poolside Facility for the purpose of validating various procedures adopted for the analysis of this facility. In addition, these calculations can be specifically used to verify the interpretation of measurements made to infer the perturbation effect of a Westinghouse surveillance capsule in a typical radiation environment. Comparisons indicate agreement on an absolute scale between measured and calculated reaction rates to within about 10% and agreement of the perturbation effect to within about 2%.

INTRODUCTION

The Oak Ridge Poolside Facility (PSF),[1] like the Pool Critical Assembly Pressure Vessel Facility (PCA-PVF), is currently being used to benchmark dosimetry measurements that can serve to validate various aspects of the transport methods used in calculating energy dependent neutron fluences in light water reactor pressure vessels. These fluences are required to estimate the neutron damage to the pressure vessels in the form of embrittlement. The PSF is driven by the 30MW Oak Ridge Reactor (ORR), whereas the geometrically similar core of the PCA-PVF has a maximum power of only 10KW. Earlier analyses of measurements performed in the PCA-PVF started with a fission source distribution that was determined from both core calculations and some in-core measurements. For the PSF, no in-core source measurements are available and hence the analysis must rely completely on a calculated fission source distribution. The first objective of this study, therefore, is to evaluate the validity of a calculational procedure that predicts fluxes and reaction rates exterior to the ORR core that does not depend on any core measurements (other than total power). The particular set of measurements chosen to test this procedure may be collectively called the Westinghouse perturbation experiment, in which various reaction rate measurements were made in a Westinghouse simulated surveillance capsule simultaneously with

measurements made essentially in the absence of the capsule, but at somewhat different locations.[2,3,4] The second objective of this study is to calculate the perturbation effect itself by repeating the surveillance capsule calculations but replacing the capsule with water, and to compare the magnitude of this effect with that deduced experimentally from the measurements.[3,4]

PHYSICAL DESCRIPTION OF THE EXPERIMENT

A view looking down from the top of the facility is shown in Fig. 1. The configuration of the core with masses of 92% enriched fuel present at the beginning of the 17 day cycle in which all the measurements were made is also indicated, along with the location of non fissionable materials and on-going in-core experiments present. The fresher outside fuel is almost symmetrically placed with respect to the horizontal centerline; the only significant fuel asymmetry in affecting fluxes leaking the aluminum window occurs in the second row, where sources south of the centerline are a little higher. There is also a vertical asymmetry caused by the control rods, producing a peaking about six centimeters below the centerline. Both source asymmetries were retained in all the calculations of the PSF. The aluminum window is followed by 4 cm of water, a 6 cm. stainless steel thermal shield, a 12 cm water gap and finally a carbon steel simulated pressure vessel wall 22.5 cm thick. All series of measurements were performed in the 12 cm water gap. Two vertical traverses on either side of the horizontal centerline inside a simulated Westinghouse surveillance capsule were made, and two more were made on the centerline inside small microtubes (ie., essentially satisfying the requirement of being unperturbed, in-water measurements). A fifth series of measurements was made in a horizontal microtube behind the thermal shield at a vertical position corresponding to the peak flux location.

CALCULATIONAL DETAILS

All calculations of the reaction rates follow the sequence outlined in Fig. 2. Burnup calculations for the atom densities of the fission products and fuel were first performed using VIPORR, which also prepares input necessary for VENTURE,[5] a three-dimensional diffusion-theory code. The irradiation commenced some six days into cycle 152-A, and lasted for nine complete days (216 hrs) before the experiment was pulled. Middle of cycle conditions for burnup and control rod position were thus used in this core analysis, which should adequately calculate the time averaged source distribution during irradiation. The seven group cross section set used in the core calculation was collapsed from a 218 group standard library[6] in use at ORNL.

ORNL-DWG 81-19678
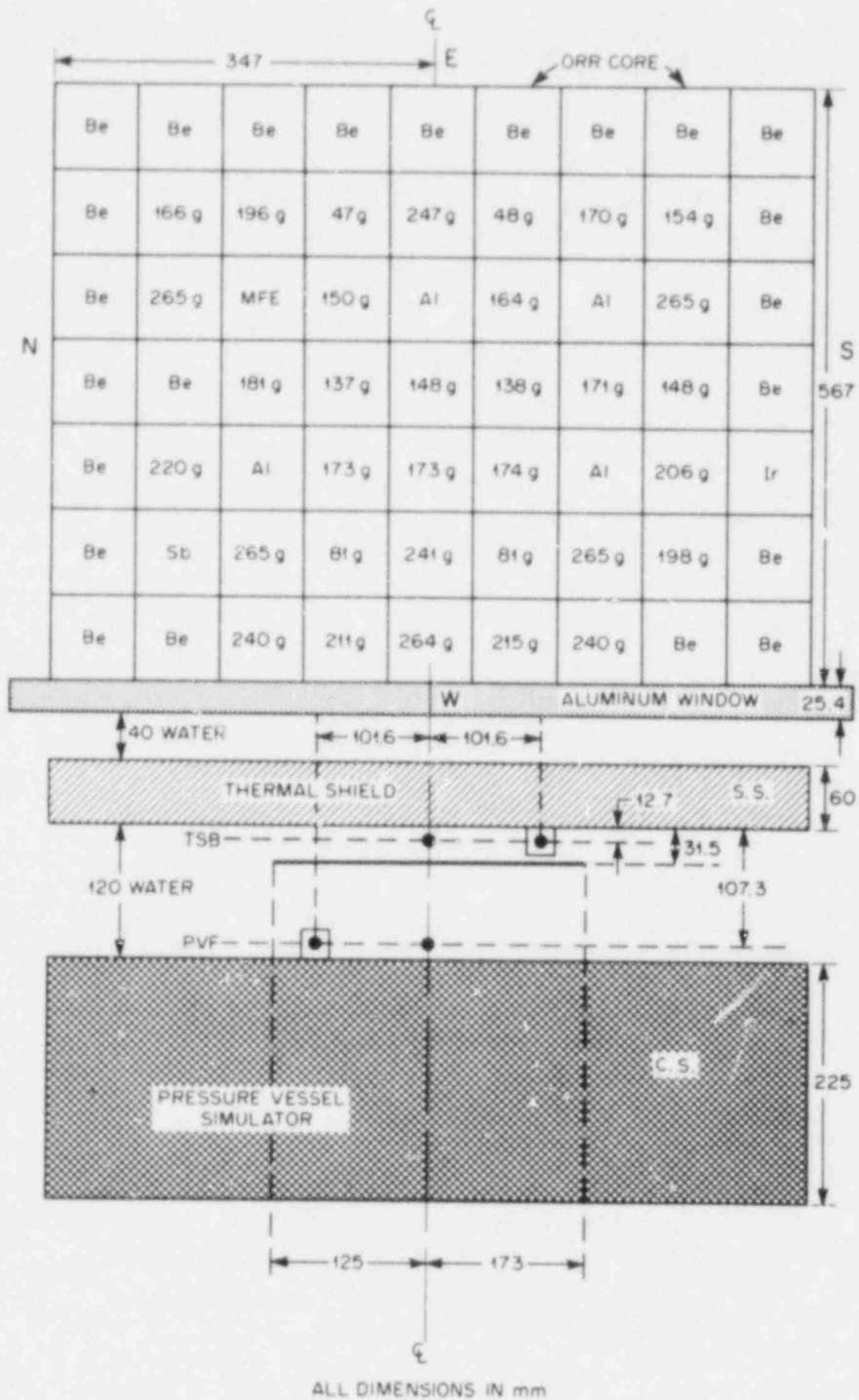
Fig. 1. Horizontal Cut at Location of Maximum Axial Flux of ORR-PSF
Westinghouse Perturbation Experiment
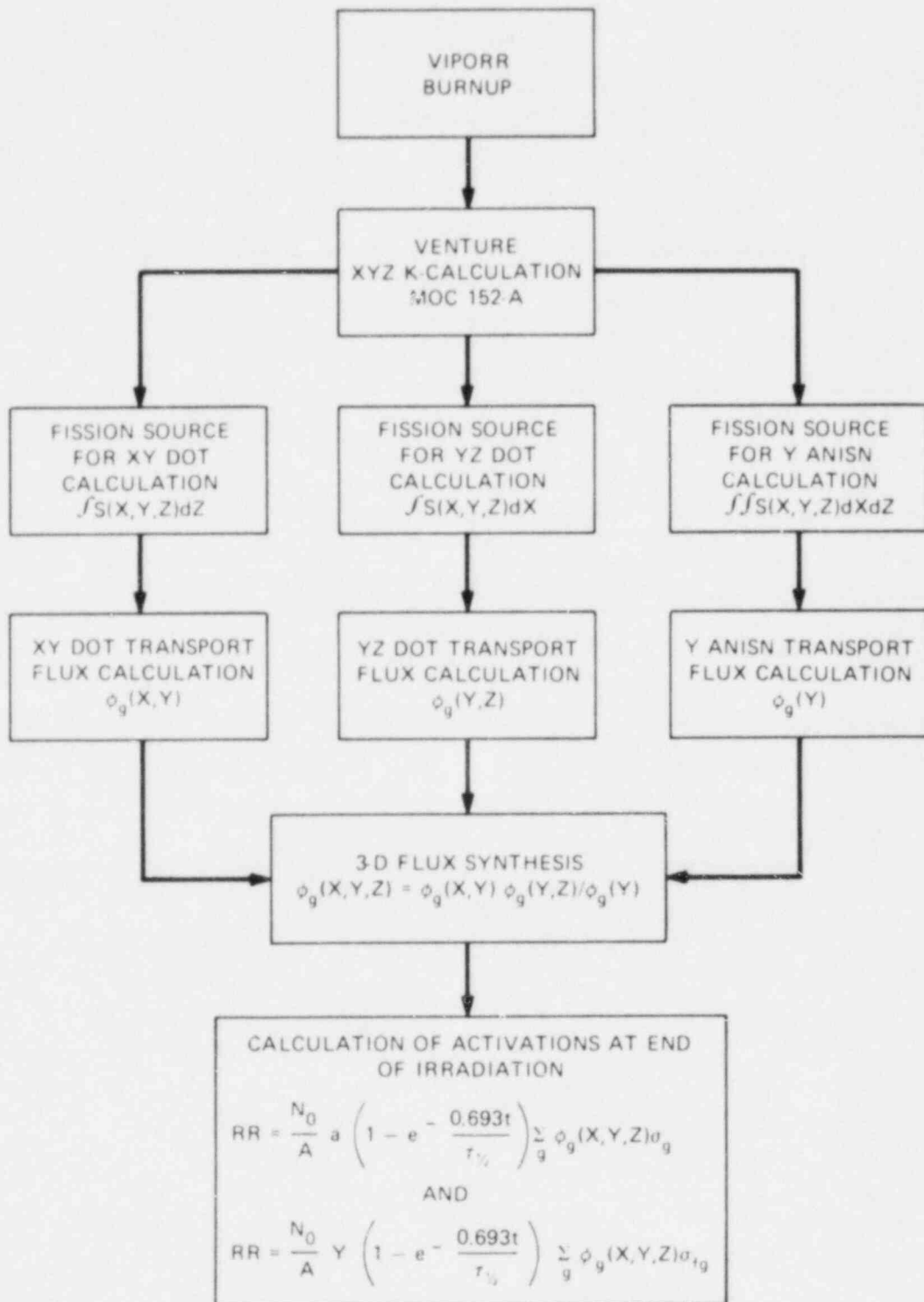
Fig. 2. Calculational Procedures for Analysis of ORR-PSF Westinghouse Perturbation Experiment

The three-dimensional fission neutron source distribution calculated by VENTURE was first integrated over the vertical direction (z) to provide a fixed source for a two-dimensional (xy) transport calculation throughout the core, water gaps, thermal shield, and pressure vessel wall. These fluxes were calculated for the first 102 groups of the 171 group VITAMIN-C structure (0.098-17.3 MeV) using the infinitely dilute VITAMIN-C cross section library[7] for beryllium, aluminum, and water, and two specially generated sets of stainless steel and carbon steel cross sections weighted $(E\Sigma_t)^{-1}$. The lower limit of 0.098 MeV in the 102 group structure is below the thresholds of all the threshold activities measured. This study thus does not calculate non-threshold (n,γ) activities that were also measured. All cross sections involved in the transport process were based on ENDF/B-IV. These fluxes represent z-integrated values, and were calculated using the DOT-IV discrete ordinates code.[8]

Next, the three-dimensional VENTURE source distribution was integrated over the core width (x) and used as the fixed source in another two-dimensional discrete ordinates transport calculation: this time (yz) with the fluxes interpreted as integrals over x.

Finally, a third fixed source was obtained from the VENTURE calculation by integrating the source distribution over both x and z. A one-dimensional (y) calculation using ANISN[9] was then performed to obtain fluxes integrated over both x and z.

The fluxes from these three discrete ordinates calculations were combined to form a three-dimensional flux according to the following prescription:

$$\phi_g(x,y,z) \simeq \phi_g(x,y)\,\phi_g(y,z)/\int\phi_g(y,z)dz , \tag{1}$$

or more simply,

$$\phi_{XYZ} \simeq \phi_{XY}\left[\frac{\phi_{YZ}}{\phi_Y}\right] . \tag{2}$$

To the extent that the three-dimensional flux is separable in x and y, Eq. (1) or (2) is identical to the flux synthesis procedure adopted previously in the analysis of the PCA-PVF.[10] It is easy to see that integrating both sides of Eq. (1) over all z, for example, yields the correct integrated fluxes:

$$\int\phi_g(x,y,z)dz = \phi_g(x,y) = \phi_g(x,y)\int\phi_g(y,z)dz/\phi_g(y) = \phi_g(x,y), \tag{3}$$

where $\quad \phi_g(y) \equiv \int\phi_g(y,z)dz \equiv \int\phi_g(x,y)dx. \tag{4}$

By defining the discrete ordinate calculated fluxes to be integrals over one or two dimensions, we have replaced the somewhat arbitrary interpretation of the component fluxes in Eq. (2) from the PCA-PSF formulation with more physically meaningful quantities. It should also be

pointed out that in regions where vertical (z) or horizontal (x) variations in materials occur, such as in the control rods and over the midplane area of the core, flux weighting of the various material cross sections over the third dimension is necessary.[11] These weightings were neglected in the earlier PCA-PSF analysis but were considered in the present analysis. Also, since the integral in Eq. (1) is over all z, it is best calculated with ANISN rather than integrating a DOT calculation, in contrast to the PCA-PSF procedure,[10] because it is easier to integrate over the finite source than over an infinite flux range.

Finally, after the synthesized fluxes have been obtained, saturated activities are calculated and where necessary to compare with measurements, corrected to activations at the end of irradiation.

RESULTS AND COMPARISON WITH MEASUREMENTS

End of Irradiation Activities in the Surveillance Capsules

Calculated saturated activities using ENDF/B-V dosimetry cross sections in each of the two surveillance capsules (see Fig. 1) were corrected to end of irradiation activities (see Fig. 2) with the help of ENDF/B-V fission yields and half-lives and universally accepted natural abundances, and compared with measurements[2] in Table I. For purposes of clarity, only the vertically averaged values are presented. The vertical profiles were compared at all measured locations within 120 mm of the peak flux location, and no vertical trend of any kind was observed between the calculated and measured activities.

TABLE I. COMPARISON* OF CALCULATED AND MEASURED ACTIVITIES[†]
IN THE SURVEILLANCE CAPSULES

REACTION	CAPSULE BEHIND THERMAL SHIELD			CAPSULE AHEAD OF PRESSURE VESSEL		
	CALC.	MEAS.	C/E	CALC.	MEAS.	C/E
$^{54}Fe(n,p)^{54}Mn$	6.17(3)[#]	6.59(3)	0.94	1.12(3)	1.22(3)	0.92
$^{63}Cu(n,\alpha)^{60}Co$	7.56(1)	7.81(1)	0.97	1.80(1)	1.85(1)	0.97
$^{46}Ti(n,p)^{46}Sc$	4.75(3)	5.45(3)	0.87	1.03(3)	1.16(3)	0.89
$^{58}Ni(n,p)^{58}Co$	3.90(5)	4.31(5)	0.90	6.89(4)	7.72(4)	0.89
$^{237}Np(n,f)^{140}Ba$	9.43(5)	1.10(6)	0.86	1.11(5)	1.32(5)	0.84
$^{237}Np(n,f)^{103}Ru$	3.70(5)	4.20(5)	0.88	4.36(4)	5.00(4)	0.87
$^{237}Np(n,f)^{95}Zr$	2.32(5)	2.71(5)	0.86	2.74(4)	3.27(4)	0.84
$^{238}U(n,f)^{140}Ba$	1.51(5)	1.67(5)	0.90	2.26(4)	2.68(4)	0.84
$^{238}U(n,f)^{103}Ru$	6.11(4)	6.67(4)	0.92	9.14(3)	1.05(4)	0.87
$^{238}U(n,f)^{95}Zr$	3.12(4)	3.49(4)	0.89	4.68(3)	5.70(3)	0.82

AVERAGE OF SIX REACTIONS: 0.91   0.89

*AVERAGED OVER ALL VERTICAL LOCATIONS EXCEPT THE +6.1 mm LOCATION IN THE THERMAL SHIELD CAPSULE AND THE +11.8 mm LOCATION IN THE PRESSURE VESSEL CAPSULE FOR THE ^{238}U FISSION MEASUREMENTS ONLY.

[†]UNITS ARE bq/mg OF THE NATURAL ELEMENT AT THE END OF IRRADIATION FOR THE NONFISSION REACTIONS AND bq OF FISSION PRODUCT PER mg OF FISSIONING ISOTOPE, ALSO AT THE END OF IRRADIATION, FOR THE FISSION REACTIONS.

[#]READ 6.17 X 10³, etc. THE REACTOR POWER WAS ASSUMED TO BE 29.7 MW$_{th}$.

From Table I it is clear that no alarming discrepancies are evident, and that with the possible exception of the ^{238}U(n,f) comparisons at the pressure vessel location (no photofission corrections to the measured data were made) and of the ^{63}Cu(n,α) reaction rate calculations (ENDF/B-V is suspected to overestimate this cross section in several energy intervals), a generally satisfactory agreement exists. Since the absolute fission neutron source integrated over the core is known only to about 5% from uncertainties in both the absolute power determination measurements and in the conversion to neutron source, and from Monte Carlo analysis[10] the flux synthesis procedure has only been verified to within about another 5%, any disagreement less than about the existing 10% between calculation and measurement is probably fortuitous.

End of Irradiation Activities in the Microtubes

The same flux calculations used in the analysis of the surveillance capsule results were also used in the analysis of the two vertical and one horizontal microtube results (see Fig. 1). In contrast to the surveillance capsule calculations presented above in which the square 2.54 cm x 2.54 cm x 35.56 cm capsules actually appeared in the geometry, the microtubes were so thin that their presence was neglected.

Vertical Microtubes

A comparison of the calculated activities with measurements made in the vertical microtubes by SCK/CEN[3-4] is shown in Table II. As indicated

TABLE II. COMPARISON* OF CALCULATED AND MEASURED ACTIVITIES[†] IN THE VERTICAL MICROTUBES

REACTION	BEHIND THERMAL SHIELD			AHEAD OF PRESSURE VESSEL		
	CALC.	MEAS.	C/E	CALC.	MEAS.	C/E
^{54}Fe(n,p)^{54}mn	6.41(3)[#]	6.78(3)	0.95	1.22(3)	1.42(3)	0.86
^{63}Cu(n,α)^{60}Co	8.66(1)	9.28(1)	0.93			
^{46}Ti(n,p)^{46}Sc	5.11(3)	5.77(3)	0.89	1.15(3)	1.40(3)	0.82
^{58}Ni(n,p)^{58}Co	3.99(5)	4.39(5)	0.91	7.55(4)	8.95(4)	0.85
^{237}Np(n,f)^{137}Cs	1.30(3)	1.54(3)	0.85			
^{237}Np(n,f)^{103}Ru	3.04(5)	3.44(5)	0.88			
^{237}Np(n,f)^{95}Zr	1.91(5)	2.18(5)	0.87			
^{238}U(n,f)^{137}Cs	2.07(2)	2.34(2)	0.88			
^{238}U(n,f)^{103}Ru	5.65(4)	5.96(4)	0.95			
^{238}U(n,f)^{95}Zr	2.89(4)	3.16(4)	0.91			

AVERAGE OF SIX REACTIONS: 0.91   AVERAGE: 0.84

*AVERAGED OVER ALL VERTICAL LOCATIONS FOR THE ^{54}Fe, ^{46}Ti, AND ^{58}Ni ACTIVITIES. THE REMAINING ACTIVITIES WERE MEASURED AT ONLY ONE LOCATION.

[†]UNITS ARE bq/mg OF THE NATURAL ELEMENT AT THE END OF IRRADIATION FOR THE NONFISSION REACTIONS AND bq OF FISSION PRODUCT PER mg OF FISSIONING ISOTOPE, ALSO AT THE END OF IRRADIATION, FOR THE FISSION REACTIONS.

[#]READ 6.41 X 10^3, etc. THE REACTOR POWER WAS ASSUMED TO BE 29.7 MW$_{th}$.

in the table, all comparisons involving $^{54}Fe(n,p)$, $^{46}Ti(n,p)$ and $^{58}Ni(n,p)$ were spatially averaged in a fashion similar to all the surveillance capsule data; the remaining comparisons were made at only one vertical location. The agreement behind the thermal shield is considered satisfactory, and is consistent with the capsule comparisons at the same location. There is a more significant disagreement at the pressure vessel location, however, which is somewhat less consistent with the capsule comparisons here, but this could be explained by a small inaccuracy in the horizontal location of the microtube as given in Fig. 1.

Horizontal Microtube

A comparison of the calculated activities with measurements made in the horizontal microtube, also by SCK/CEN$^{3-4}$, is shown in Table III.

TABLE III. COMPARISON OF CALCULATED AND MEASURED ACTIVATION PROFILES IN THE HORIZONTAL MICROTUBE BEHIND THE THERMAL SHIELD IN Bq/mg

DISTANCE FROM HORIZONTAL CENTERLINE (mm)	$^{54}Fe(n,p)^{54}Mn$			$^{58}Ni(n,p)^{58}Co$		
	CALC.	MEAS.	C/E	CALC.	MEAS.	C/E
120 LEFT*	3.94(3)†	4.19(3)	0.94	2.44(5)	2.71(5)	0.90
100	4.25(3)	4.29(3)	0.99	2.63(5)	2.78(5)	0.95
75	4.53(3)	4.68(3)	0.97	2.81(5)	3.03(5)	0.93
50	4.74(3)	4.86(3)	0.97	2.93(5)	3.17(5)	0.92
25	4.86(3)	5.01(3)	0.97	3.00(5)	3.22(5)	0.93
0	4.93(3)	5.10(3)	0.97	3.05(5)	3.30(5)	0.93
25 RIGHT	4.96(3)	5.11(3)	0.97	3.08(5)	3.30(5)	0.93
50	4.94(3)	5.13(3)	0.96	3.06(5)	3.22(5)	0.95
75	4.87(3)	4.88(3)	1.00	3.02(5)	3.29(5)	0.92
100	4.58(3)	4.81(3)	0.95	2.87(5)	3.12(5)	0.92
125	4.36(3)	4.56(3)	0.96	2.71(5)	3.00(5)	0.90
150	3.88(3)	4.12(3)	0.94	2.41(5)	2.65(5)	0.91
169	3.40(3)	3.74(3)	0.91	2.11(5)	2.34(5)	0.90
AVERAGE	4.48(3)	4.65(3)	0.96	2.78(5)	3.01(5)	0.92

*ORIENTATION RELATIVE TO AN OBSERVER STANDING AT THE PRESSURE VESSEL AND FACING THE REACTOR.
†READ 3.94 X 10^3, etc. THE REACTOR POWER WAS ASSUMED TO BE 29.7 MW$_{th}$.

Although not specifically stated in this table, the activities presented are referenced to the end of irradiation. The horizontal profile is observed both experimentally and calculationally to be asymmetric with respect to the horizontal (y) centerline due to a combination of two effects: first, the fuel loading is asymmetrica, as has been previously discussed, leading to a higher core leakage on the right (Table III) or south (Fig. 1) side, and second, the presence of the surveillance capsule on the south side. It is to be observed from Table III that the absolute measured profile is well reproduced by the calculations for the two reactions investigated.

Perturbation Effect Introduced by the Westinghouse Surveillance Capsule

Starting with the same fixed source as before, a second (xy) calcula-
tion was performed of the vertically integrated fluxes with the sur-
veillance capsule absent. Assuming that the effects of finite z are not
affected by the presence of the capsule, the unperturbed three-
dimensional fluxes may be synthesized using the same ϕ_{yz} and ϕ_y in Eq.
(2) as before. The unperturbed activities were then compared with the
original perturbed activities at the same x,y,z locations. A comparison
of the calculated perturbations with those inferred from the measurements
by SCK/CEN[3-4] is shown in Table IV, where the perturbation factor is
defined as the ratio of the activity in the capsule to the activity at
the same location in water. It is to be observed that the general trends
of the perturbation as functions of energy (the reactions in Table IV are
listed in order of decreasing threshold) and location are consistent,
ie., the perturbation effect is stronger the less the energy and the
closer to the thermal shield. The magnitudes of the factor also compare
favorably, being at most 6% apart for the $^{54}Fe(n,p)$ reaction at the ther-
mal shield location. This latter disagreement may be due to an inability
of the measurements to distinguish fully between the effects of fuel
asymmetry and capsule perturbation.

TABLE IV. COMPARISON OF CALCULATED AND MEASURED REACTION RATE
PERTURBATIONS* INTRODUCED BY THE CAPSULE

REACTION	BEHIND THERMAL SHIELD		AHEAD OF PRESSURE VESSEL	
	CALC.	MEAS.	CALC.	MEAS.
$^{63}Cu(n,\alpha)^{60}Co$	0.994	0.960	0.996	
$^{46}Ti(n,p)^{46}Sc$	1.010	1.030	1.007	1.022
$^{54}Fe(n,p)^{54}Mn$	1.067	1.127	1.049	1.068
$^{58}Ni(n,p)^{58}Co$	1.085	1.088	1.062	1.040
$^{238}U(n,f)\ X$	1.190	1.174	1.148	
$^{237}Np(n,f)\ X$	1.335	1.323	1.253	

*DEFINED AS REACTION RATE AT THE HOLLOW CENTER OF THE
SURVEILLANCE CAPSULE DIVIDED BY THE REACTION RATE AT THE SAME
LOCATION IN WATER.

A plot of the calculated perturbation factor as a function of energy
is shown in Fig. 3 for the case of the thermal shield capsule. It is
seen to be strongly energy dependent with many fluctuations, but the
general trend is a larger effect with decreasing energy.

ORNL-DWG 84-19679
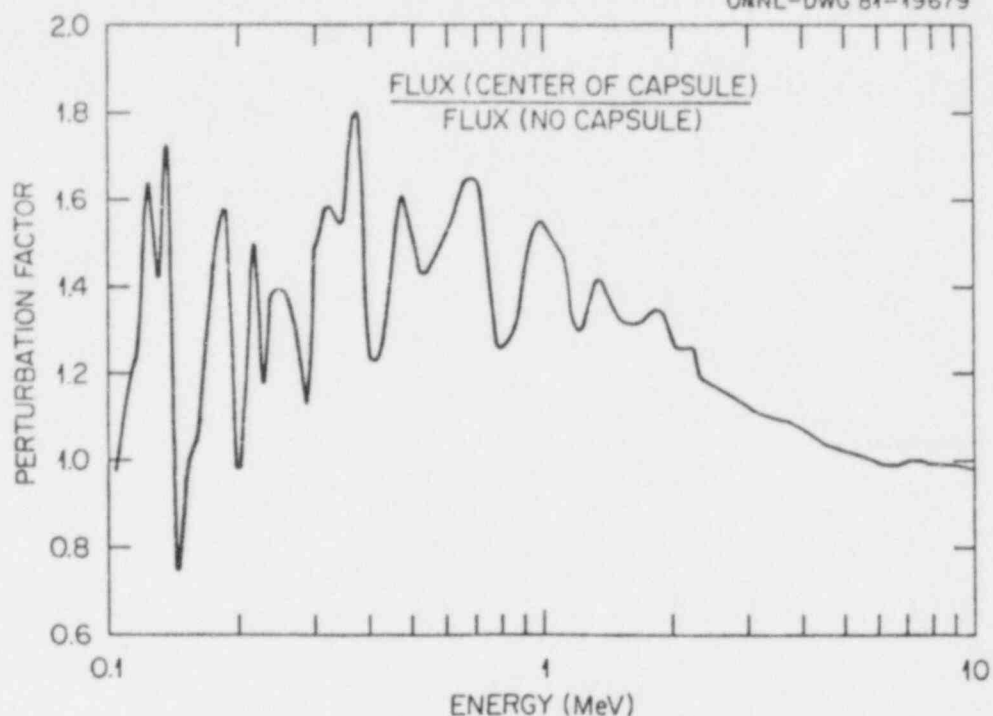
Fig. 3. Calculated Flux Perturbation Factor at the Thermal Shield Position as a Function of Energy.

CONCLUSIONS

For the first time, definitive calculations of the PSF have been made starting with an ORR core diffusion calculation to obtain a source distribution which is then used as a fixed source in a discrete ordinates transport calculation to provide energy dependent fluxes throughout a configuration following the core. Using a flux construction technique that synthesizes three-dimensional fluxes from the results of one-and two-dimensional transport calculations, comparison of predicted reaction rates with extensive measurements made in a configuration following the core validate the general accuracy of the calculational technique, and indicate that the PSF, like the PCA-PVF, also can be used as a benchmark facility.

Interpretations of measurements in the PSF for the purpose of inferring the perturbation effect of a Westinghouse surveillance capsule on surveillance dosimetry measurements have been verified by these same calculations, thus lending additional credance to both the interpretation of the measurements, the measurements themselves, and the calculational analysis.

REFERENCES

1. W. N. McElroy, et al., "Light Water Reactor Pressure Vessel Surveillance Dosimetry Improvement Program: 1979 and 1980 Annual Reports" NUREG/CR-1291 (1980) and NUREG/CR-1741(1981).

2. L. S. Kellogg, et al., Sixth Light Water Reactor Pressure Vessel Surveillance Dosimetry Program Meeting Results, "Perturbation Studies: PSF/PCA," pp. 6-1 thru 6-8, Oct. 27-31 (1980).

3. H. Tourwe, et al., "Surveillance Capsule Perturbation Studies in the PSF 4/12 Configuration" C.E.N. Reactor Physics HT/eu 380/81-27, Mol, Belgium (1981).

4. H. Tourwe, et al., "Surveillance Capsule Perturbation Studies in the PSF 4/12 Configuration," Proc. this Conference.

5. D. R. Vondy, T. B. Fowler, and G. W. Cunningham III, "The Bold Venture Computation System for Nuclear Reactor Core Analysis, Version III," ORNL-5711, Oak Ridge National Laboratory (1981).

6. W. E. Ford III, C. C. Webster, and R. M. Westfall, "A 218-Group Neutron Cross-Section Library in AMPX Master Interface Format for Criticality Safety Studies," ORNL/CSD/TM-4 (1976).

7. R. W. Roussin, et al., "Experience in Developing and Using the VITAMIN-C 171-Neutron, 36-Gamma-Ray Group Cross Section Library," ORNL/RSIC-41, Oak Ridge National Laboratory (1978).

8. W. A. Rhoades, D. B. Simpson, R. L. Childs, and W. W. Engle, Jr., "The DOT-IV Two-Dimensional Discrete Ordinates Transport Code with Space-Dependent Mesh and Quadrature," ORNL/TM-6529, Oak Ridge National Laboratory (1979).

9. W. W. Engle, Jr., "ANISN, a One Dimensional Discrete Ordinates Transport Code with Amsotropic Scattering," K-1693 (1967).

10. P. J. Maudlin and R. E. Maerker, "Supplementary Neutron Flux Calculations for the ORNL Pool Critical Assembly Pressure Vessel Facility," Proc. this Conference.

11. R. E. Maerker and M. L. Williams, "Calculations of the Startup Experiment at the Poolside Facility," Proc. this Conference.

ANS SHIELDING STANDARDS FOR LIGHT WATER REACTORS

D. K. Trubey
Engineering Physics Information Centers
Oak Ridge National Laboratory
Oak Ridge, Tennessee, USA

ABSTRACT

The purpose of the American Nuclear Society Standards Subcommittee, ANS-6, Radiation Protection and Shielding, is to develop standards for radiation protection and shield design, to provide shielding information to other standards-writing groups, and to develop standard reference shielding data and test problems. A total of seven published ANS-6 standards are now current. Additional projects of the subcommittee, now composed of nine working groups, include: standard reference data for multigroup cross sections, gamma-ray absorption coefficients and buildup factors, additional benchwork problems for shielding problems and energy spectrum unfolding, power plant zoning design for normal and accident conditions, process radiation monitors, and design for postaccident radiological conditions.

INTRODUCTION

The American Nuclear Society (ANS) is a standards-writing organization member of the American National Standards Institute (ANSI). The ANS Standards Committee has a subcommittee denoted ANS-6, Radiation Protection and Shielding, whose charge is to develop standards for radiation protection and shield design, to provide shielding information to other standards-writing groups, and to develop standard reference shielding data and test problems. This paper is a progress report of this subcommittee. Significant progress has been made since the last comprehensive report.[1]

The purpose of a standard is to set forth acceptable practices, procedures, dimensions, material properties, specifications, etc. that have been agreed on by representatives of a broad segment of the subject activity. Ideally, because of the standardization process, a standard is a high-quality, highly reliable, comprehensive summary of the state of the art.

The organization responsible for promulgating voluntary standards in the USA is ANSI. The Institute, a nonprofit corporation, is a federation of leading trade, technical and professional organizations, government agencies, and consumer groups. The principal functions of the ANSI are to coordinate standards development, minimize duplication and overlap, and provide a neutral forum to consider and identify standards needs.

The standards-writing organization of interest here is the ANS. Among its committees is one on standards composed of a steering committee and several subcommittees. The subcommittees, in turn, have established ad hoc working groups for preparation of individual standards.

The subcommittee on radiation protection and shielding standards, ANS-6, now composed of nine working groups, was established in 1964. The goals and accomplishments of the working groups are briefly described below.

ANS-6.1: Shielding Cross Section Standards

The first standard developed by the cross-section working group provides a reference set of neutron and gamma-ray flux-to-dose-rate factors for use by shielding design engineers.[2] This standard will be revised in the near future. Issues to be resolved are: the usefulness of the dose equivalent index, low-energy interpolation in the neutron dose equivalent table, and the relationship to other standards.

Current efforts of the working group are directed toward developing a standard to establish criteria for standard sets of multigroup cross sections to be used for radiation protection calculations. The group is also testing candidate data sets which appear to meet the criteria and therefore can be considered to be standard reference data. A draft standard has been approved by ANS-6 and is being submitted to ANSI Committee N17, Research Reactors, Reactor Physics, and Radiation Shielding.

ANS-6.2: Benchmark Problems

The primary objective of the benchmark problems effort is to compile in convenient form a limited number of well-documented problems in radiation transport which will be useful in testing computational methods used in shielding.

Four problem solutions were published in 1969 in loose-leaf form by the Radiation Shielding Information Center. Revisions were issued in 1970 and 1974. The work slowed for a period, but now additional problems are being developed, including several for typical reactor configurations. The group now is collecting and evaluating solutions to two problems specifying PWR shielding configurations and a problem which defines a radwaste configuration.

A second working group, ANS-6.2.2, is developing test procedures for neutron energy spectrum unfolding codes which treat the "many-channel" problem. This group is interested in both gamma-ray and neutron spectrum unfolding, but initial efforts have concentrated on tests of neutron unfolding codes using idealized, calculated response functions.[3]

ANS-6.3: Shield Performance Evaluation

The initial goal of this group was attained in 1972 with the publication of ANSI N18.9-1972. The group has developed a replacement standard which has now been published and is titled "Program for Testing Radiation Shields in Light Water Reactors.[4]

ANS-6.4: Shield Materials

The first major effort of this group resulted in a guide for the design of concrete shields for nuclear power plants and similar applications.[5] Plans are being made to update this standard in the near future.

The group is now developing a standard on compensatory shielding materials, i.e., special materials to be used in shield penetrations to compensate for the reduction in effectiveness of the bulk shield.

A more recent project, designated ANS-6.4.3, has been undertaken to develop standard reference absorption coefficient and buildup factor data for selected materials. A need for reliable low-energy data is especially recognized. These data are frequently used by design engineers in point kernel calculations, but no modern generally-recognized compilation of data exists.

ANS-6.5: Shielding Nomenclature

The group developed a glossary for use in radiation protection and shielding which was published in 1979.[6] The document also includes definitions of reactor physics terms, compiled by ANS-19.2, and a power reactor systems glossary compiled by ANS-50. The glossary was issued for trial use, and comments are desired by the group to use in developing succeeding drafts. Further work will be required to ensure that the most useful terms will be incorporated into the "Glossary of Terms in Nuclear Science and Technology," which continues development under ANS-9.

ANS-6.6: Calculation and Measurement of Direct and Scattered Radiation from Nuclear Power Plants

The group has developed a standard which defines calculational requirements and measurement techniques to estimate exposures near nuclear power plants due to direct and scattered radiation from contained sources on site.[7] Nitrogen-16 gamma-rays are a prime consideration.

ANS-6.7: Radiation Zoning for Design for Nuclear Power Plants

The proposed standard, "Radiation Zoning for Design of Nuclear Power Plants," has been sent to the Nuclear Power Plant Standards Committee (NUPPSCO) for approval as an ANSI standard. At the request of NUPPSCO,

the scope of the standard is being extended to cover the entire area of the plant in addition to the areas inside the main plant building.

A second group under 6.7 is organizing to begin the process of determining the scope of a project to establish zoning standards for design of shielding which takes account of possible reactor accident conditions.

ANS-6.8: Location and Range of Detection of Area and Process Fluid Radiation Monitoring Systems for Nuclear Steam Generating Plants

Organized in early 1975 as a joint project with the Health Physics Society Standards Committee, the group has developed a standard titled "Locations and Design Criteria for Radiation Monitoring Systems for Light Water Nuclear Reactors."[8] The standard was published in 1981.

The group is now working on a companion standard on continuous process and effluent radiation monitoring systems.

ANS-6.9: Designing for Postaccident Radiological Conditions

A new working group was organized in late 1981 to develop one or more standards to provide guidance in designing for postaccident radiological conditions which can arise at LWR power plants. This group will function in cooperation with groups under NUPPSCO sharing similar interests.

REFERENCES

1. D. K. Trubey, "The Development of Radiation Shielding Standards in the American Nuclear Society," Trans. Am. Nucl. Soc. 22, 828 (1975) and ORNL/RSIC-39 (November 1975).
2. American National Standards Institute, "Neutron and Gamma-Ray Flux-to-Dose-Rate Factors," ANSI/ANS-6.1.1-1977, American Nuclear Society, $12.
3. W. Meyer, W. H. Miller, and C. B. Wallace, "Standardization of Neutron Spectrum Unfolding Codes: The Benchmarking Problem," Trans. Am. Nucl. Soc. 34, 660-661 (June 1980).
4. American National Standards Institute, "Program for Testing Radiation Shields in Light Water Reactors," ANSI/ANS-6.3.1-1980, American Nuclear Society, $20.
5. American National Standards Institute, "Guidelines on the Nuclear Analysis and Design of Concrete Radiation Shielding for Nuclear Power Plants," ANSI/ANS-6.4-1977, American Nuclear Society, $38.
6. American Nuclear Society, "Trial Use Nuclear Glossary," ANS (1979), Amerian Nuclear Society, $25.

7.   American National Standards Institute, "Calculations and Measurement of Direct and Scattered Gamma Radiation for LWR Nuclear Power Plants," ANSI/ANS-6.6.1-1979, American Nuclear Society, $32.

8.   American National Standards Institute, "Location and Design Criteria for Radiation Monitoring Systems for Light Water Nuclear Reactors," ANSI/ANS-HPSSC-6.8.1-1981, American Nuclear Society, $20.

CALCULATIONS OF THE STARTUP EXPERIMENTS
AT THE POOLSIDE FACILITY

M. L. Williams and R. E. Maerker
Oak Ridge National Laboratory
Oak Ridge, Tennessee, USA

ABSTRACT

Discrete ordinate calculations are made and the results compared with measurements performed in the startup experiment at the Poolside Facility. Because of the physical size of the simulated surveillance capsule used in this experiment, the analytic procedure is more complicated than one adopted in earlier calculations of the PCA-PVF and PSF. The comparisons indicate the pressure vessel fluences in the long-term irradiation experiments still presently going on at the PSF, and which are geometrically identical to the startup experiment, can only be predicted to within about 20%.

INTRODUCTION

Previously described ORNL analyses of measurements performed in the Pool Critical Assembly Pressure Vessel Facility (PCA-PVF)[1,2,3] and the Poolside Facility (PSF)[4,5] have been relatively successful in predicting activities. The PCA-PVF comparisons indicate agreement to within about 10% in the water gap preceding the pressure vessel mock-up, and to within about 20% for all three locations in the pressure vessel itself. The PSF comparisons for the Westinghouse perturbation experiment again indicate agreement to within about 10% in the water gap, which is the only location where measurements were made. Different sets of dosimeters were used in these two experiments, with some duplication, so that it can be generally concluded that the calculated neutron spectral shape is consistent with the measurements made in water, but that there is strong evidence from the PCA-PVF comparisons in the pressure vessel that this agreement deteriorates somewhat with increasing penetration in the iron.

The present series of PSF calculations are intended to fulfill a dual purpose. First, they fill in the gap left by the earlier PSF comparisons where no measurements were performed in the pressure vessel, and second, they can serve as accurate estimates of flux intensities throughout the identical 4/12 configuration with simulated surveillance capsule and simulated pressure vessel capsule that is being used for the long-term irradiation experiment currently under way at the PSF.

PHYSICAL DESCRIPTION OF THE EXPERIMENT

Unfortunately from the analytical point of view, the geometry of the startup (and long-term irradiation) configuration is complicated by the presence of the simulated surveillance capsule (SSC). This is essentially a solid slab of stainless steel (except for a 1-inch void located near the top) whose dimensions are such that it covers about one-half of the area of the core (see Figs. 1 and 2). Since the macroscopic cross section of water is less than that of stainless steel for energies above 2 MeV, neutrons in this energy range leaking the core tend to "short circuit" the steel in their transport to the detectors in the pressure vessel. The combination of a decrease in leakage toward the edges of the core relative to the centerline and an increase in transmission over and around the SSC relative to the centerline tends to flatten both the vertical and horizontal flux profiles incident on the pressure vessel. Thus, the transport of high energy neutrons into the pressure vessel detector locations is determined to a significant degree by the three-dimensional geometry in the region of the SSC.

The remaining details in Figs. 1 and 2 show the core fuel loading at the beginning of cycle 151-A, the last 18 days of which were used at full power to irradiate the dosimeters in the startup measurements, the approximate locations of the detectors whose responses are analyzed in the present study, and the as-built dimensions of the configuration. Notice that the detectors as indicated in Fig. 2 were placed two inches below the reactor midplane, near the location of the peak flux. In reality, a vertical profile was calculated for each of the four detector locations so that the activities can eventually be compared with the measurements of all the laboratories participating in the experiment, which in general were made at different vertical positions.

METHOD OF CALCULATION

The method of discrete ordinates was employed in the solution of the transport equation, using DOT-IV[6] with a fixed source determined from middle of cycle (MOC) burn-up and control rod conditions. The fixed source was calculated using the three-dimensional diffusion code VENTURE[7], the input to which was supplied by the auxilliary code VIPORR. The general method of solving for the three-dimensional fluxes throughout PSF configurations has been outlined elsewhere[5], but the complications introduced by the relatively small dimensions of the SSC in both the vertical and horizontal directions necessitates the use of an iterative procedure in the flux synthesis method.

Adopting the cartesian coordinate system shown in Figs. 1 and 2, with μ, η, and ξ the corresponding direction cosines of the vector $\hat{\Omega}$ along the x,y,z axes respectively, the three-dimensional Boltzmann equation may be written

Fig. 1 (left diagram):

E
¢

347 — X — ORR CORE

Be	Be	Be	Be	Be	Be	Be	Be	Be
Be	158 g	199 g	49 g	246 g	53 g	165 g	157 g	Be
Be	265 g	MFE	157 g	Al	157 g	Al	265 g	Be
Be	HT	178 g	137 g	157 g	138 g	174 g	157 g	Be
Be	214 g	Al	176 g	176 g	176 g	Al	208 g	Be
Be	Xe	265 g	77 g	239 g	77 g	265 g	196 g	Be
Be	Be	241 g	209 g	265 g	214 g	241 g	Be	Be

N 567   S

25.4

W   Al WINDOW

39.3 WATER

60.0 THERMAL SHIELD   SS

8.7 WATER   180.9   203.2   SSC (DUMMY) SS
50.0   SSC

61.7 WATER   6.3 VOID   1.6 VOID   1.0 VOID   6.3 VOID
3.0 SS

SPVC (DUMMY) SS   X T/4   59.5
224.8   X T/2   51.4   SS
X 3T/4   54.6
38.0
7.2 VOID
9.5 SS

298.4   VOID BOX   3.2 Al

WATER

Y

Fig. 1. Horizontal (XY) Cut at Location of Maximum Axial Flux of ORR-PSF Startup Experiment.

Fig. 2 (right diagram):

E
¢

304.8 — Z — ORR CORE

WATER   BERYLLIUM
FUEL FOLLOWER
WATER   FUEL
CONTROL ROD (CADMIUM)   FUEL FOLLOWER
WATER   372 BOC
CONTROL ROD (CADMIUM)   FUEL FOLLOWER
FUEL

TOP 567   BOTTOM

25.4

W   Al WINDOW

39.3 WATER

60.0 THERMAL SHIELD   SS

8.7 WATER   155.6   187.3   SSC (DUMMY) SS
50.0   SSC

61.7 WATER   25.4 VOID   177.8   6.3 VOID
50.8

6.3 VOID   59.5   T/4   SPVC (DUMMY) SS
224.8   51.4   T/2   SS
54.6   3T/4
216.0   38.0   7.2 VOID   114.4

9.5 SS

298.4   VOID BOX   3.2 Al

WATER

Y

ALL DIMENSIONS IN MILLIMETERS
X DETECTORS ANALYZED
(NOT TO SCALE)

Fig. 2. Vertical (YZ) Cut at Location of Radial Centerline of ORR-PSF Startup Experiment.

$$\mu \frac{\partial \phi}{\partial x} + n \frac{\partial \phi}{\partial y} + \xi \frac{\partial \phi}{\partial z} + B(x,y,z)\phi = S, \tag{1}$$

where $\quad B \equiv \Sigma_t - \iint \Sigma_s(E',\hat{\Omega}' \to E,\hat{\Omega})dE'd\hat{\Omega}',$ (2)

ϕ is the angular flux and S an external source. Integrating Eq. (1) from $z=z_B$ to z_T yields

$$\mu \frac{\partial \phi_{XY}}{\partial x} + n \frac{\partial \phi_{XY}}{\partial y} + B_{XY}\phi_{XY} + L_Z = S_{XY}, \tag{3}$$

where

$$\phi_{XY} = \int_{z_B}^{z_T} \phi(x,y,z)dz, \tag{4}$$

$$B_{XY} = \int_{z_B}^{z_T} B(x,y,z)\phi(x,y,z)dz \Big/ \int_{z_B}^{z_T} \phi(x,y,z)dz, \tag{5}$$

$$S_{XY} = \int_{z_B}^{z_T} S(x,y,z)dz, \tag{6}$$

and $\quad L_Z = L_Z(x,y,\mu,n) = \xi[\phi(x,y,z_T) - \phi(x,y,z_B)].$ (7)

Similarly, integrating Eq. (1) from $x=x_L$ to x_R yields

$$n \frac{\partial \phi_{YZ}}{\partial y} + \xi \frac{\partial \phi_{YZ}}{\partial z} + B_{YZ}\phi_{YZ} + L_X = S_{YZ}, \tag{8}$$

where $\quad L_X = L_X(y,z,n,\xi) = \mu[\phi(x_R,y,z) - \phi(x_L,y,z)],$ (9)

and ϕ_{YZ}, B_{YZ}, and S_{YZ} are defined in a fashion analogous to Eqs. (4)-(6). As written, Eqs. (3) and (8) are exact. They are coupled together in two ways: first, through the cross-section weighting in B_{XY} and B_{YZ}, and second, through the leakage terms. If (z_T, z_B) and (x_L, x_R) are chosen such that $B(x,y,z)$ is constant over the x or z interval, then no cross section weighting needs to be done and only the leakage-coupling terms need to be estimated:

$$L_Z(x,y,\mu,n) \approx \left\{ \frac{\int_{y_1}^{y_2} dy \int_{\hat{\Omega}} \xi(\hat{\Omega})[\phi_{YZ}(y,z_T,\hat{\Omega}) - \phi_{YZ}(y,z_B,\hat{\Omega})]d\hat{\Omega}}{\int_{y_1}^{y_2} dy \int_{z_B}^{z_T} dz \int_{\hat{\Omega}} \phi_{YZ}(y,z,\hat{\Omega})d\hat{\Omega}} \right\} \phi_{XY}(x,y,\mu,n), \tag{10}$$

and

$$L_X(y,z,\eta,\xi) \approx \left\{ \frac{\int_{y1}^{y2} dy \int_{\hat{\Omega}} \mu(\hat{\Omega})[\phi_{XY}(x_R,y,\hat{\Omega}) - \phi_{XY}(x_L,y,\hat{\Omega})]d\hat{\Omega}}{\int_{y1}^{y2} dy \int_{x_L}^{x_R} dx \int_{\hat{\Omega}} \phi_{XY}(x,y,\hat{\Omega})d\hat{\Omega}} \right\} \phi_{YZ}(y,z,\eta,\xi) \quad (11)$$

Our calculations of the fluxes ϕ_{XY} and ϕ_{YZ} used the following iterative procedure. Estimates of the bracketed quantity in Eq. (10) are first made using a YZ calculation in which L_X is assumed to be zero, the source is integrated completely over all x, and there is no spatial cross-section weighting.* The values of z_T and z_B are chosen to be the vertical extent of the SSC. The fluxes ϕ_{XY} are then calculated using these estimates of L_Z/ϕ_{XY} with x_R and x_L consistently chosen to be the width of the SSC, and in the same calculation estimates of the bracketed quantity in Eq. (11) are also made. The estimates of leakage in the x direction are then used in a revised YZ calculation, the source and revised z leakages this time being derived from consistent values of z_T and z_B. A revised XY calculation was finally made in which the bracketed terms from the revised YZ calculation were used, and the fluxes differed from those in the first iteration by less than 2%, thus effectively establishing the rapid convergence of the procedure.

Since the x and z limits over which the fluxes are integrated represent the cross-sectional area of the SSC, no spatial weighting of the water and stainless steel cross sections in this region is necessary, and the region is also sufficiently small that the approximation may be made that the flux is separable in x and z. Thus, the flux synthesis prescription described in Ref. 5 is applicable:

$$\phi_g(x,y,z) \approx \phi_g(x,y)\phi_g(y,z)/\phi_g(y), \quad (12)$$

but where now $\phi_g(x,y)$ is the solution for $S(x,y) = \int_{z_B}^{z_T} S(x,y,z)dz,$ \quad (13)

$\phi_g(y,z)$ is the solution for $S(y,z) = \int_{x_L}^{x_R} S(x,y,z)dx,$ \quad (14)

and $\phi_g(y)$ is the solution for $S(y) = \int_{x_L}^{x_R} S(x,y)dx = \int_{z_B}^{z_T} S(y,z)dz,$ \quad (15)

and where, in addition, leakages out the finite x and z faces must be considered.

___

*The programmed output using DOT-IV must be changed from the existing DB^2 in the y-direction to DB^2 in the z-or x-direction. Using a variable mesh, the number of x or z intervals varies with y interval; this establishes y as the basic dimension, but it is not the direction in which the leakages are desired.

BIAS FACTORS FOR THE CALCULATIONAL METHOD

For the case where all the steel slabs extend at least as high and as wide as the core, it has been verified that near-centerline fluxes based on the use of Eq. (12) agree within statistical uncertainties of about 5% with results of three-dimensional Monte Carlo calculations.[8] For the case of smaller slabs such as the SSC, however, the approximations introduced by the coupling of the XY and YZ calculations necessitate a further evaluation.

Consequently, fluxes were calculated and synthesized using two different procedures for the case of a simplified geometry. This geometry preserved the dimensions of the core but replaced all ex-core materials by a water medium of infinite extent in x and z, but into which a 10-cm thick steel slab also of infinite extent in x and z was placed 20 cm from the core face. (The introduction of this slab should not be necessary, but was done to incorporate steel as well as water cross sections into the procedure). Synthesized centerline fluxes using Eq. (12) were obtained from a pair of XY and YZ DOT-IV calculations and a Y ANISN calculation in which the limits of the integrations in Eqs. (13)-(15) were unbounded. These fluxes represent essentially values that have been verified by Monte Carlo methods and hence can be regarded as correct. Synthesized centerline fluxes again using Eq. (12), but with finite values for the limits in Eqs. (13)-(15) corresponding approximately to those used in the startup calculations and including leakages, were obtained in a manner identical to that used for the startup calculations. Values of the two flux integrals occurring in Eq. (15), each calculated by integrating the two-dimensional fluxes, agreed to within 1.5% for all groups and locations. Comparison of the two sets of synthesized fluxes indicate that the bias factors (ie., factors that multiply the finite + leakage results to correct for methods approximations) are somewhat different from unity for centerline detector locations at distances from the core corresponding to the pressure vessel, and they increase with increasing energy. The trends are indicated in Table 1.

Table 1. Synthesized Flux Bias Factors for the Startup Calculations

Energy Range(MeV)	SSC	T/4	T/2	3T/4
11.05-19.64	1.016	1.075	1.085	1.095
8.19-11.05	1.012	1.077	1.084	1.094
6.07-8.19	1.009	1.068	1.073	1.080
4.07-6.07	1.004	1.045	1.050	1.055
3.01-4.07	1.003	1.029	1.035	1.039
2.59-3.01	1.001	1.019	1.023	1.028
2.12-2.59	0.996	1.009	1.014	1.018
1.83-2.12	0.993	1.004	1.009	1.013

It is clear that the additional approximations used in the present
analysis do not seriously compromise the accuracy of the calculations,
and that biases of at most 10% can account for these relatively minor
effects.

COMPARISON OF CALCULATED AND MEASURED RESULTS

Fluxes were calculated and corrected by the method outlined in the
previous sections, using the highest 102 energy groups (0.1-17 MeV) of
the same library used in a previous calculation.[4,5] Cross sections for
those truncated transverse regions in which several materials were still
present, such as the core and the steel and vacuum capsules, were pre-
pared from Eq. (5) and its YZ counterpart. These fluxes were folded
with ENDF/B-V dosimetry cross sections and the activities compared with
some measured saturated activities[9,10,11] in Table 2.

As was first suggested in Ref. 5, the ENDF/B-V dosimetry cross sec-
tions for the $^{63}Cu(n,\alpha)$ reaction are apparently somewhat too high, and
the comparisons in Table 2 further substantiate this. A revised set of
dosimetry cross sections evaluated by C.Y.Fu,[12] which are proposed for
ENDF/B-VI, produce about 9% lower values for this activity while leaving
the remaining activities relatively unchanged. Thus, the overall com-
parisons suggest an agreement of the calculated activities to within
about 20% for the first three locations and about 25% for the fourth one,
the latter consistent with earlier PCA comparisons that indicated a
somewhat too high value for the ENDF/B-IV inelastic cross section of
iron.[13,14,15]

CONCLUSIONS

The comparisons in Table 2 clearly indicate a somewhat greater discre-
pancy, even at the SSC location, than either of the former series of
experiments analyzed,[1-5] and one is somewhat at a loss to explain why.
The complexities introduced by the SSC seem to be well handled by the
method described, since the discrepancy does not appear to appreciably
worsen with increasing depth into the configuration, with the exception
of the 3T/4 location which can be explained as being due to iron cross-
section deficiencies. A source normalization error of about 10% would
bring the two PSF experiments analyzed into agreement, but the maximum
uncertainty in the power measurements has been estimated as 4%.[16]
Effects on ex-core fluxes of cycle-to-cycle and within cycle time depen-
dent source distributions have been investigated and found to be of the
order of 2%; more accurate calculations using transport theory and multi-
thermal group cross sections with upscattering for the core analysis have
also indicated very small (~1%) perturbations in the ex-core fluxes. It
is undoubtedly significant that all three PCA-PVF and PSF experiments are

somewhat undercalculated, but unless reasons for this soon become apparent and the calculations corrected, the calculated fluences in the long term irradiation experiment currently under way at the PSF will be low by about 20%.

Table 2. Comparison of Some Calculated and Measured[†] Saturated Activities in the Startup Experiment in Bq per Nucleus at 30 Mw

	SSC	T/4	T/2	3T/4
Calculated ^{63}Cu(n,α)	2.69-15*	2.00-16	7.30-17	2.51-17
Measured ^{63}Cu(n,α)	3.07-15	2.10-16	7.97-17	2.81-17
C/E	0.88	0.95	0.92	0.89
Calculated ^{46}Ti(n,p)	4.97-14	3.30-15	1.17-15	3.85-16
Measured ^{46}Ti(n,p)	6.12-14	4.04-15	1.47-15	5.30-16
C/E	0.81	0.82	0.80	0.73
Calculated ^{54}Fe(n,p)	3.91-13	2.32-14	8.30-15	2.76-15
Measured ^{54}Fe(n,p)	4.67-13	2.75-14	1.02-14	3.74-15
C/E	0.84	0.84	0.81	0.74
Calculated ^{58}Ni(n,p)	5.28-13	3.15-14	1.15-14	3.91-15
Measured ^{58}Ni(n,p)	6.45-13[†]	3.90-14	1.49-14	5.56-15
C/E	0.82	0.81	0.77	0.70
Calculated ^{238}U(n,f)		1.31-13		
Measured ^{238}U(n,f)		1.56-13[††]		
C/E		0.84		
Calculated ^{237}Np(n,f)		1.21-12		
Measured ^{237}Np(n,f)		1.40-12[††]		
C/E		0.86		

† All measurements except the ^{58}Ni(n,p) measurement in the SSC are taken from Refs. 9 and 10. The exception is taken from Ref. 11. The vertical locations vary between 50.8 and 76.2 mm below the reactor midplane.
* Read 2.69x10⁻¹⁵ etc.
††Average of the ^{137}Cs and ^{95}Zr fission product results only; the ^{144}Ce fission product results were ignored because they seemed less consistent with the others.

REFERENCES

1. F. W. Smallman, F.B.K. Kam, J. F. Eastham, and C. A. Baldwin, "Reactor Calculation 'Benchmark' PCA Blind Test Results," ORNL/NUREG/TM-428, Oak Ridge National Laboratory(1981).

2. W. N. McElroy, editor, "LWR Pressure Vessel Surveillance Dosimetry Improvement Program: PCA Experiments and Blind Test," 'UREG/CR-1861, HEDL-TME 80-87,R5, Hanford Engineering Development Laboratory(1981).

3. R. E. Maerker, 'S$_n$ Transport Calculations of the PCA Experiments with Some Estimated Uncertainties," Trans. Am. Nucl. Soc. 34, 628(1980).

4. R. E. Maerker and M. L. Williams, "Comparison of Calculations with Neutron Dosimetry Measurements Performed at the Oak Ridge Poolside Facility," Trans. Am. Nucl. Soc. 39, 812(1981).

5. R. E. Maerker and M. L. Williams, "Calculations of the Westinghouse Perturbation Experiment at the Poolside Facility," Proc. this Conference.

6. W. A. Rhoades, D. B. Simpson, R. L. Childs, and W. W. Engle, Jr., "The DOT-IV Two-Dimensional Discrete Ordinates Transport Code with Space-Dependent Mesh and Quadrature," ORNL/TM-5529, Oak Ridge National Laboratory(1979).

7. D. R. Vondy, T. B. Fowler, and G. W. Cunningham III, "The Bold Venture Computation System for Nuclear Reactor Core Analysis, Version III," ORNL-5711, Oak Ridge National Laboratory(1981).

8. P. J. Maudlin and R. E. Maerker, "Supplementary Neutron Flux Calculations for the ORNL Pool Critical Assembly Pressure Vessel Facility," Proc. this Conference.

9. D. J. Ketema, H. J. Nolthenius, and W. L. Zijp, "Neutron Metrology in the ORR: ECN Activity and Fluence Measurements for the LWR Pressure Vessel Surveillance Dosimetry Program," ECN-80-164, Petten, the Netherlands(1980).

10. D. J. Ketema, H. J. Nolthenius and W. L. Zijp, "Neutron Metrology in the ORR: Second Contribution of ECN Activity and Fluence Measurements for the LWR Pressure Vessel Surveillance Dosimetry Program," ECN-81-097, Petten, the Netherlands(1981).

11. Informal communication from A. Fabry.

12. C. Y. Fu and D. M. Hetrick, "Experience in Using the Covariances of Some ENDF/B-V Dosimetry Cross Sections," Proc. this Conference.

13. J. J. Wagschal, R. E. Maerker, and B. L. Broadhead, "LWR-PV Damage Estimate Methodology," Proc. of 1980 Advances in Reactor Physics and Shielding Conference, Sept. 14-17, Sun Valley, Idaho, pp. 612-624(1980).

14. R. E. Maerker, J. J. Wagschal, and B. L. Broadhead, "Development and Demonstration of an Advanced Methodology for LWR Dosimetry Applications," EPRI NP-2188 Project 1399-1 Interim Report(1981).

15. J. J. Wagschal and R. E. Maerker, "Surveillance Dosimetry: Achievements and Disappointments," Proc. this Conference.

16. F.B.K. Kam, private communication.

INTERLABORATORY COMPARISON OF FLUENCE NEUTRON DOSIMETERS
IN THE FRAME OF THE PSF START-UP MEASUREMENT PROGRAMME

H. Tourwé, A. Fabry, SCK/CEN, Mol, Belgium
F. Kam, ORNL, Oak Ridge, U.S.A.
A. Fudge, AEE, Harwell, United Kingdom
W.L. Zijp, H.J. Nolthenius, ECN, Petten, Netherlands
W. Mannhart, PTB, Braunschweig, Germany
A. Thomas, RR & A, Derby, United Kingdom

INTRODUCTION

Much effort has gone during the last years towards programmes for the surveillance of the safety of LWR vessels. The U.S. NRC supported the dosimetry-steel irradiation programme in the poolside facility (PSF) of the ORR reactor at Oak Ridge, undertaken in this frame. It aims to establish the interrelationship between dosimetry, metallurgy and fracture mechanics. This two year irradiation programme started in 1980. Different neutronic characterization runs were organized at low and high reactor power in an engineering mock-up 4/12 configuration (x/y : x is the core to thermal shield distance in cm and y is the thermal shield to pressure vessel distance in cm) before the start of the main programme. One of these runs at high power included a 18 days irradiation, in which extensive neutron dosimetry measurements were performed by different European and U.S. laboratories. The main results of the European laboratories are presented in this paper.

DOSIMETRY CAPSULES

AERE Harwell and RR & A Derby supplied ORNL with stainless steel capsules containing Fe, Cu, Ti, Ni, Nb and Co/Al detectors together with some prototype sapphire damage dosimeters.

SCK/CEN Mol supplied ORNL with interlaboratory steel and gadolinium capsules and with different sets of foils. The final mounting of the SCK/CEN capsules was done at ORNL. Each capsule contained 6 Ag, 6 Al, 6 Nb, 6 Fe, 6 Ti, 6 Ni and 2 Cu foils. The gadolinium capsules were filled by ORNL with fission detectors supplied by HEDL.

The AERE/RR & A and SCK/CEN capsules and the fission detectors were located in the LWR simulator according to the specifications given in table 1 (only these samples, that were afterwards measured

by the European laboratories, are considered in table 1).

TABLE 1. DETAILS OF SAMPLE LOCATION

IRRADIATION LOCATION	SAMPLE	AXIAL HEIGHT ABOVE MIDPLANE (mm)
SSC	INTERLABORATORY CAPSULE	- 51
	AERE/RR & A CAPSULE	- 3.5
1/4 T	INTERLABORATORY CAPSULE	- 75
	AERE/RR & A CAPSULE	-122
	FISSION DETECTORS	0
1/2 T	INTERLABORATORY CAPSULE	- 75
	AERE/RR & A CAPSULE	-122
3/4 T	INTERLABORATORY CAPSULE	- 75
	AERE/RR & A CAPSULE	-122

IRRADIATION HISTORY

The activation detectors were irradiated in the PSF facility of the ORR reactor during about 18 days. Details of the irradiation histories are given in table 2. For each position the irradiation interval was somewhat different due to loading and unloading procedures.

The interlaboratory capsules were after irradiation dismantled at ORNL. Part of the interlaboratory capsule content was sent to

TABLE 2. IRRADIATION HISTORIES FOR THE 18 d. PSF CHARACTERIZATION RUN

LOCATION	BEGIN EXPOSURE (LOCAL TIME)	END EXPOSURE (LOCAL TIME)	TOTAL IRRADIATION TIME (s)	EFFECTIVE IRRADIATION TIME AT 30 MW (s)
SSC	OCT.27,1979 14h26	NOV.14,1979 8h55	$1.5377 \ 10^6$	$1.5105 \ 10^6$
1/4 T	OCT.27,1979 14h26	NOV.14,1979 8h43	$1.5370 \ 10^6$	$1.5097 \ 10^6$
1/2 T	OCT.27,1979 21h11	NOV.14,1979 8h55	$1.5134 \ 10^6$	$1.4902 \ 10^6$
3/4 T	OCT.27,1979 21h18	NOV.14,1979 8h55	$1.5130 \ 10^6$	$1.4898 \ 10^6$

SCK/CEN-Mol, the remaining part being sent to HEDL. SCK/CEN provided afterwards ECN-Petten and PTB-Braunschweig each with a detect set of each irradiation location. All detectors were counted by SCK/CEN before shipment to ECN and PTB.

The AERE/RR & A capsules were dismantled by AERE-Harwell. The dosimeters of these capsules were counted at AERE-Harwell and AEE-Winfrith.

The Cu foils of the interlaboratory capsules were sent by SCK/CEN in a round robin to all European participants.

AXIAL FAST NEUTRON FLUX DISTRIBUTIONS

The axial fast neutron flux distributions in the different irradiation locations were measured by means of Ni detectors. Cosine functions $\cos [B(y-C)]$, wherein y is the axial distance in mm to the reactor midplane, were fitted through the measuring points. The fitted B and C parameters are summarized in table 3. The axial distribution becomes flatter when penetrating into the vessel wall, while the axial maximum is shifting from negative to positive values.

TABLE 3. FITTED PARAMETERS OF THE AXIAL FAST NEUTRON FLUX DISTRIBUTIONS COS $[B(y-C)]$

IRRADIATION LOCATION	B (m^{-1})	C (mm)
SSC	$4.42 \ 10^{-3}$	$- 45.4$
1/4 T	$3.34 \ 10^{-3}$	$- 20.6$
1/2 T	$2.82 \ 10^{-3}$	$- 4.9$
3/4 T	$2.80 \ 10^{-3}$	3.2

COUNTING RESULTS

The counting results (specific activities at the end of irradiation) of the different laboratories, normalized to the SCK/CEN results, are shown in table 4. All results were considered at the reactor midplane level, taking into account the measured axial fast neutron flux distributions discussed in the previous section.

TABLE 4. SPECIFIC ACTIVITIES MEASURED BY THE DIFFERENT LABORATORIES

	REACTION	SPECIFIC ACTIVITIES RELATIVE TO SCK/CEN				RECOMMENDED SPECIFIC ACTIVITIES $(Bq\ g^{-1})$	σ (%)
		INTERLABORATORY CAPSULE		AERE/RR & A CAPSULE			
		ECN	PTB	$(AERE)_1$ (1)	$(AERE)_2$ (1)		
SSC	$^{93}Nb(n,n')$	1.17			1.02	$2.062\ 10^7$	9.0
	$^{58}Ni(n,p)$		1.01	1.09	1.05	$7.242\ 10^8$	3.9
	$^{54}Fe(n,p)$	1.01	1.00	1.07	1.10	$1.103\ 10^7$	4.3
	$^{46}Ti(n,p)$	0.99	1.02	1.12	1.07	$8.508\ 10^6$	5.3
	$^{63}Cu(n,\alpha)$	1.02	1.01	0.99(2) (1.29)	(1.05)	$1.201\ 10^5$	1.4
1/4 t	$^{237}Np(n,f)\{\ ^{95}Zr$	0.97	0.98			$3.437\ 10^7$	1.6
	^{137}Cs	0.96	0.98			$2.522\ 10^5$	2.0
	$^{238}U(n,f)\{\ ^{95}Zr$	0.95	0.98			$3.508\ 10^6$	2.6
	^{137}Cs	0.99	0.97			$2.738\ 10^4$	1.4
	$^{93}Nb(n,n')$				1.00	$1.330\ 10^6$	0.3
	$^{58}Ni(n,p)$	1.00	1.00	1.07	1.03	$4.472\ 10^7$	3.1
	$^{54}Fe(n,p)$	1.00	0.98	1.11	1.09	$6.956\ 10^5$	6.0
	$^{46}Ti(n,p)$	1.00	1.01	1.12	1.04	$5.851\ 10^5$	4.9
	$^{63}Cu(n,\alpha)$	1.01	1.01	1.01(2) (1.15)	(1.08)	$9.206\ 10^3$	0.5
1/2 t	$^{93}Nb(n,n')$				0.85	$6.643\ 10^5$	11.8
	$^{58}Ni(n,p)$	0.99		1.09	1.02	$1.721\ 10^7$	4.4
	$^{54}Fe(n,p)$	0.97	1.00	1.10	1.10	$2.606\ 10^5$	6.0
	$^{46}Ti(n,p)$	0.98	1.02	1.13	1.07	$2.161\ 10^5$	5.8
	$^{63}Cu(n,\alpha)$	1.03	1.02	1.02(2) (1.37)	(1.30)	$3.465\ 10^3$	1.0
3/4 t	$^{93}Nb(n,n')$				0.84	$3.338\ 10^5$	11.9
	$^{58}Ni(n,p)$	1.00	0.99	1.07	1.00	$6.310\ 10^6$	3.3
	$^{54}Fe(n,p)$	1.00	1.00	1.10	1.07	$9.306\ 10^4$	4.7
	$^{46}Ti(n,p)$	0.96	0.98	(0.76)	1.01	$7.566\ 10^4$	2.2
	$^{63}Cu(n,\alpha)$	1.00	1.01	1.02(2) (1.46)	(1.27)	$1.245\ 10^3$	0.9

(1) $(AERE)_1$: MEASUREMENTS PERFORMED AT HARWELL; $(AERE)_2$: MEASUREMENTS PERFORMED AT WINFRITH

(2) Cu FOIL FROM INTERLABORATORY CAPSULE

Small radial flux corrections were applied to the detectors from the interlaboratory capsules since the detectors in these capsules were not all positioned on the same vertical axis. Somewhat different decay scheme parameters were used by the participants. In order to intercompare the countings, all reported results were rescaled using the same decay scheme parameters, taken from reference [1].

The agreement between SCK/CEN, ECN and PTB is excellent : in general better than 2 % for all non-fission detectors and better than 5 % for the fission detectors. The agreement between the $(AERE)_1$ and $(AERE)_2$ results is reasonable : the $(AERE)_1$ results are, on an average, 4 % to 5 % higher than the $(AERE)_2$ results, while the average difference for the Cu detectors is about 10 %. The observed differences for $^{93}Nb(n,n')$ are somewhat larger than could be expected taking into account the results from a recent niobium intercomparison [2]. The specific activities deduced from the detectors in the AERE/RR & A capsules are systematically higher (except for Nb) than the specific activities deduced from the detectors in the interlaboratory capsules : 5 % to 10 %, on average, for the $^{58}Ni(n,p)$, the $^{54}Fe(n,p)$ and the $^{46}Ti(n,p)$ reactions, while a difference of $\sim$ 25 % is noted for $^{63}Cu(n,\alpha)$ reaction. These differences are apparently not due to a bias in the calibration of the counting equipment of the participants, since a round robin of Cu detectors of the interlaboratory capsules resulted in an excellent agreement (better than 3 % : see table 4). Preliminary investigations indicate also that local fast neutron flux perturbations, created by the dosimetry capsules, can be excluded, so that a major reason for the observed 5 % to 10 % differences could not be identified. The high specific activities from the $^{63}Cu(n,\alpha)^{60}Co$ reaction in the AERE/RR & A capsules are probably due to Co impurities in the Cu material.

The overall uncertainties on the measured specific activities, as quoted by the different laboratories, are given in table 5. The uncertainties are of the order of 1.5 % to 3 % for most reactions, except $^{93}Nb(n,n')$.

The recommended specific activities (table 4) at the end of the irradiation were calculated by averaging the available results. The Cu results of the AERE/RR & A dosimeter capsules were not considered in the calculation of the recommended specific activities (values given between brackets in table 4).

The results of the thermal dosimeters are not discussed in this paper since they are of less importance to the PCA/PSF programme. These results were only used to apply minor corrections as e.g. the ^{58}Co and $^{58}Co^m$ burn-up of the Ni detectors.

TABLE 5. OVERALL UNCERTAINTIES ON THE MEASURED SPECIFIC ACTIVITIES

REACTION	UNCERTAINTY (1 σ) IN %			
	ECN	PTB	AERE	SCK/CEN
$^{237}Np(n,f)\{\ ^{95}Zr$	2.9	1.7		2.1
^{137}Cs	2.9	1.4		2.0
$^{238}U(n,f)\{\ ^{95}Zr$	2.9	2.5		2.1
^{137}Cs	2.9	1.4		2.0
$^{93}Nb(n,n')$	5.6		4.6	4.5
$^{58}Ni(n,p)$	2.6	1.5	3.4	1.9
$^{54}Fe(n,p)$	2.2	1.5	2.4	1.9
$^{46}Ti(n,p)$	2.3	1.5	3.2	1.9
$^{63}Cu(n,\alpha)$	2.7	1.5	3.2	1.9

NEUTRON FLUXES

One-dimensional ANISN transport calculations in a 171 energy group structure were performed by ORNL, while two-dimensional discrete ordinate transport DOT calculations in a 17 group structure were performed by SCK/CEN [3]. In both cases, the PSF core configuration was replaced by the PCA core configuration, described in reference [4]. These calculations could not take into account in a proper way the neutron leakage problems created by the SSC capsule :
1) the axial dimensions of this capsule are shorter than the axial dimensions of the thermal shield and pressure vessel wall.
2) a gas gap on top of the capsule creates neutron field perturbations illustrated in a companion paper [5].
Three-dimensional calculations are required to deal with these leakage problems. Nevertheless the main features of presently computed spectral shapes are expected to be realistic enough for the considerations that follow.

Spectrum averaged cross-sections were calculated with the ENDF/B-V data, except for the $^{93}Nb(n,n')$ reaction where the Hegedüs data multiplied by a bias factor 1.37 have been used [6]. Neutron flux ratios $\emptyset(> 1\ MeV)_i/\emptyset(> 1\ MeV)_{Ni}$, wherein $\emptyset(> 1\ MeV)_i$ is the measured reaction rate divided by the corresponding calculated spectrum averaged cross section above 1 MeV, at the dif-
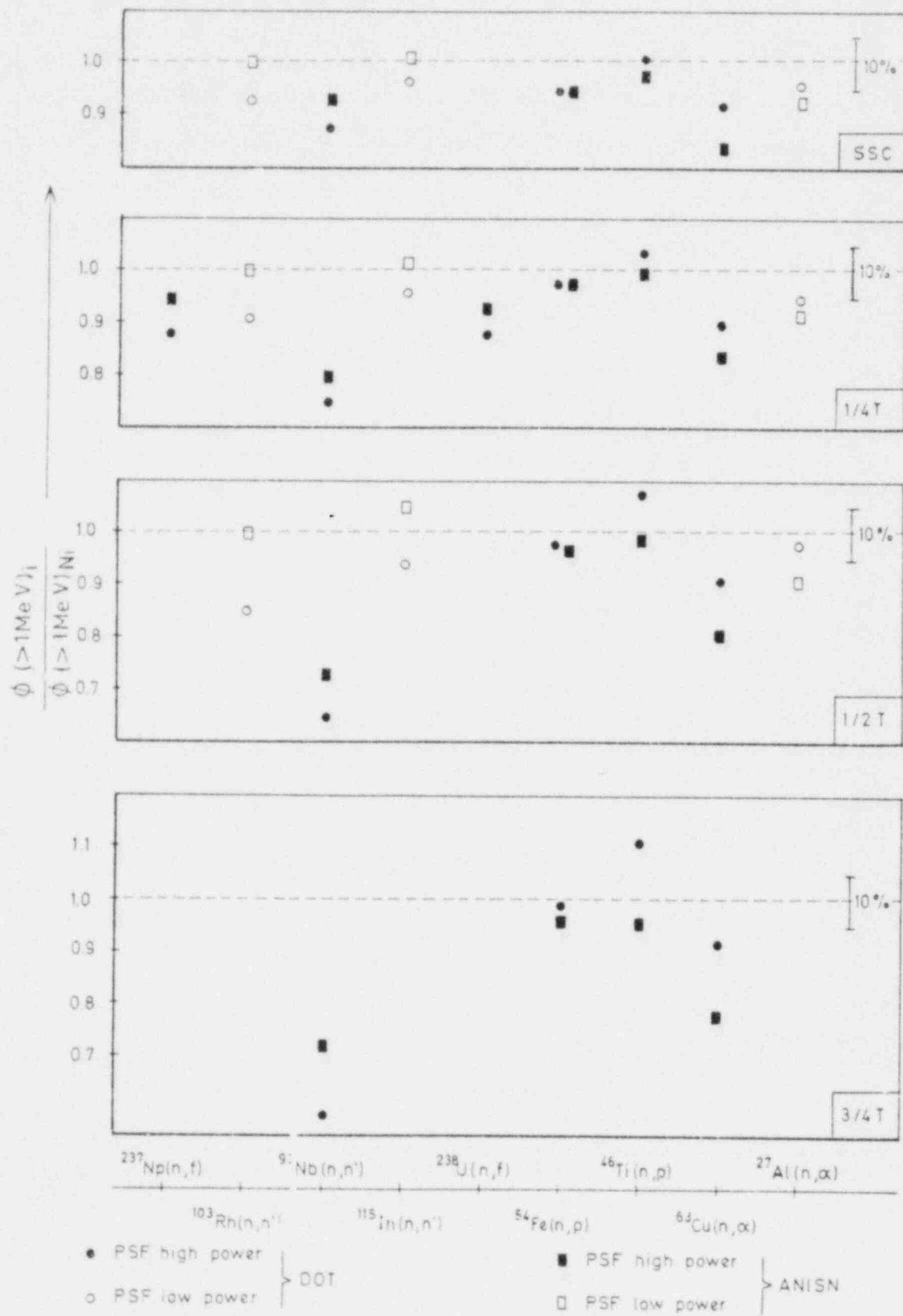
Fig. 1. Neutron flux ratios in the PSF 4/12 configuration.

TABLE 6.   MEASURED REACTION RATES IN PSF 4/12 AT A NOMINAL POWER OF 30 MW

REACTION	REACTION RATES (s^{-1})			
	SSC	1/4 T	1/2 T	3/4 T
^{237}Np(n,f)		$1.413 \cdot 10^{-12}$		
^{238}U(n,f)		$1.548 \cdot 10^{-13}$		
^{93}Nb(n,n')	$1.575 \cdot 10^{-12}$	$1.016 \cdot 10^{-13}$	$5.141 \cdot 10^{-14}$	$2.584 \cdot 10^{-14}$
^{58}Ni(n,p)	$6.580 \cdot 10^{-13}$	$4.061 \cdot 10^{-14}$	$1.583 \cdot 10^{-14}$	$5.806 \cdot 10^{-15}$
^{54}Fe(n,p)	$4.635 \cdot 10^{-13}$	$2.925 \cdot 10^{-14}$	$1.110 \cdot 10^{-14}$	$3.965 \cdot 10^{-15}$
^{46}Ti(n,p)	$6.212 \cdot 10^{-14}$	$1.74 \cdot 10^{-15}$	$1.598 \cdot 10^{-15}$	$5.595 \cdot 10^{-16}$
^{63}Cu(n,α)	$2.920 \cdot 10^{-15}$	$1.239 \cdot 10^{-16}$	$8.539 \cdot 10^{-17}$	$3.068 \cdot 10^{-17}$

ferent irradiation locations are shown in fig. 1. The reaction
rates at midplane level from which they were deduced are given in
table 6. The following fission yields were considered : 5.78 %
(95Zr) and 6.08 % (137Cs) for 237Np(n,f), 5.20 % (95Zr) and 6.03
(137Cs) for 238U(n,f). Photofission corrections for 237Np(n,f)
and 238U(n,f) were taken from reference [7]. PSF low power
(20.7 KW) radiometric data [5,8] obtained in begin-of-life con-
ditions are also given in fig. 1. The average cross sections
involved in these low power flux ratios were also obtained using
the ENDF/B-V data, except for 103Rh(n,n') where the Butler and
Santry data were used.

    From fig. 1 one can conclude that :
- the low power PSF data are in good agreement with the high power
  PSF data
- the considered 93Nb(n,n') and 63Cu(n,α) cross section data are
  overestimating the detector responses. The overestimation for
  63Cu(n,α) is of the same order of magnitude in the different
  neutron spectra. This phenomenon was already mentioned in re-
  ference [9]. The overestimation for 93Nb(n,n') becomes more
  important in softer neutron spectra. The cause of this pheno-
  menon is apparently the non adequate shape of the used 93Nb(n,n')
  cross section data
- the consistency of the neutron flux ratios decreases when going
  deeper inside of the pressure vessel simulator. The tendency
  is the same for both types of calculations : ~ 15 % spread in
  the SSC position against ~ 25 % in the 1/2 T position, when
  excluding 93Nb(n,n').

    The absolute $\emptyset$(> 1 MeV) values at a nominal power of 30 MW are
given in table 7. These $\emptyset$(> 1 MeV) values were obtained by

TABLE 7. NEUTRON FLUX VALUES IN THE PSF 4/12 CONFIGURATION

		SSC	1/4 T	1/2 T	3/4 T
$\emptyset(> 1$ MeV)* $(n\ s^{-1}\ cm^{-2})$	DOT σ (%)	$7.44\ 10^{12}$ 4.3	$4.89\ 10^{11}$ 7.2	$2.56\ 10^{11}$ 6.8	$1.20\ 10^{11}$ 7.8
	ANISN σ (%)	$6.84\ 10^{12}$ 7.6	$4.65\ 10^{11}$ 6.4	$2.18\ 10^{11}$ 9.3	$9.24\ 10^{10}$ 10.9
	$\dfrac{DOT}{ANISN}$	1.09	1.05	1.17	1.30
$\left[\dfrac{\emptyset(> 98\ keV)}{\emptyset(> 1\ MeV)}\right]_C$	DOT	3.21	4.37	6.21	8.62
	ANISN	3.09	4.10	5.78	7.81
	$\dfrac{DOT}{ANISN}$	1.04	1.07	1.07	1.10
$\dfrac{\overline{\sigma}_d}{\displaystyle\int_{1\ MeV}^{\infty} \emptyset(E)\ dE}$ (b)	DOT	1648	1969	2470	3134
	ANISN	1556	1783	2158	2637
	$\dfrac{DOT}{ANISN}$	1.06	1.10	1.14	1.19

$^*\ \emptyset\ (> 1\ MeV) = \dfrac{(\sigma\ \emptyset)_{MEASURED}}{\left(\overline{\sigma}_{E\ >\ 1\ MeV}\right)_{CALCULATED}}$

averaging the $\emptyset(> 1$ MeV) values from the different detector types, irradiated in the PSF high power run. $^{93}Nb(n,n')$ was not considered in this calculation. The spectrum averaged damage cross sections in table 7 are based on the ASTM E 693-79 data.

Appreciable differences are observed in the $\emptyset(> 1$ MeV) data according to the interpretation based on the DOT spectra or on the ANISN spectra : the differences become more important when penetrating into the pressure vessel wall. The neutron flux > 1 MeV in the SSC position and the 1/4 T position could be determined with an accuracy better than 10 %.

CONCLUSIONS

Neutron flux values, based on countings performed at different European laboratories, were presented. The fast neutron flux > 1 MeV in the SSC and 1/4 T position was determined with an accuracy better than 10 %.

The considered ENDF/B-V cross sections are consistent. However the ENDF/B-V data of $^{63}Cu(n,\alpha)$ tend to overestimate detector

responses. It was also pointed out that more accurate data for the ^{93}Nb(n,n') cross section data are required.

REFERENCES

[1] W.L. Zijp, J.H. Baard, "Nuclear data guide for reactor neutron metrology," EUR 7164, 1979.

[2] H. Tourwé et al., "Niobium dosimetry intercomparison in EBR II and BR2," this symposium.

[3] G. Minsart : private communication.

[4] W.N. McElroy, "LWR pressure vessel surveillance dosimetry improvement program : PCA experiments and blind test," NUREG/CR-1861 (July 1981).

[5] A. Fabry et al., "PCA and PSF neutronic characterization," this symposium.

[6] H. Tourwé, N. Maene, "Fast neutron fluence measurements with the ^{93}Nb(n,n') reaction and the application to long-term irradiations," Proc. of the 3th ASTM-EURATOM symposium on Reactor Dosimetry, Ispra (October 1-5, 1979).

[7] Minutes of the 8th LWR-pressure vessel surveillance dosimetry program meeting, NBS (October 26-30, 1981).

[8] Minutes of the 6th LWR-pressure vessel surveillance dosimetry program meeting, NBS (October 27-31, 1980).

[9] W. Mannhart, "Results of neutron fluence monitors at the PSF simulated pressure vessel irradiation facility," IAEA advisory group meeting on nuclear data for radiation damage assessment and reactor safety aspects, Vienna (October 12-16, 1981).

Session A.2
Fast Reactors

PNC/DOE COLLABORATIVE DOSIMETRY TEST IN JOYO

S. Suzuki, M. Sasaki, Y. Yamashita
Power Reactor and Nuclear Fuel Development Corporation
Ibaraki-ken, Japan

T. Taniguchi, M. Nakazawa, A. Sekiguchi
University of Tokyo
Tokyo, Japan

E. P. Lippincott
Hanford Engineering Development Laboratory
Richland, Washington U.S.A.

ABSTRACT

The first PNC/DOE(HEDL) Collaborative Dosimetry Test was conducted in the Experimental Fast Reactor "JOYO" in Japan. Both PNC and DOE(HEDL) activation dosimeters were irradiated in the JOYO reflector region, material surveillance test position (9A1) at the core midplane, during the 75 MWt second duty cycle.

In this test, resonance reactions including $^{58}Fe(n,\gamma)^{59}Fe$, $^{59}Co(n,\gamma)^{60}Co$, $^{45}Sc(n,\gamma)^{46}Sc$, and $^{181}Ta(n,\gamma)^{182}Ta$, and threshold reactions such as $^{93}Nb(n,n')^{93m}Nb$, $^{237}Np(n,f)^{95}Zr$ or ^{103}Ru, $^{58}Ni(n,p)^{58}Co$, $^{46}Ti(n,p)^{46}Sc$, $^{54}Fe(n,p)^{54}Mn$, and $^{63}Cu(n,\alpha)^{60}Co$ were independently measured by both laboratories. The results of the PNC-DOE(HEDL) reaction rates measurements showed good agreement, generally within 3%.

Utilizing these measured reaction rates,[1] the neutron spectrum at the test position was unfolded with the J1-Unfolding code "NEUPAC" at PNC, and also unfolded with the SAND-FERRET code at DOE(HEDL). Group constants for the neutron spectrum unfolding code were based on ENDF/B-IV and V, and the initial guess spectrum for NEUPAC and/or SAND-FERRET was calculated using the two dimensional transport code DOT3.5. The reaction rates calculated from the guess spectrum showed a difference of 72%(1σ) with the measured values. But the reaction rates calculated from the unfolded spectrum agreed with measurement within ±11%(1σ). The total neutron flux and flux above 0.1 MeV at 75 MWt determined from the PNC unfolded spectrum were 1.28×10^{14} n/cm$^2 \cdot$sec and 3.19×10^{13} n/cm$^2 \cdot$sec, respectively. In comparison, the values determined by HEDL were 1.08×10^{14} and 2.94×10^{13}, respectively.

1. INTRODUCTION

Summary of JOYO

JOYO is an experimental sodium cooled fast breeder reactor and is the first of its kind in Japan. Through the JOYO experience in design, construction, fabrication and operation, it is expected to establish new techniques for the fast breeder reactor. In addition, JOYO is planned to be utilized as an irradiation facility for research and development of reactor fuels and materials.

The rated output of the reactor is 50 MWt at the first stage, 75 MWt at the second stage (present) and will be raised up to 100 MWt in early 1983. The reactor is of a loop type and has two identical cooling circuits, each having heat removal capacity of 50 MWt. Each circuit consists of a primary loop, intermediate heat exchanger and secondary loop. In the secondary loop there are air blast coolers. The heat generated in the core is finally dissipated in the air through the air blast cooler. The first and second stage of JOYO is called the MK-I core, and uses plutonium uranium mixed oxide fuel in the core region (60 cm height) and depleted uranium oxide in the blanket region. The MK-I core provides fundamental LMFBR nuclear physics data and plant experience. The third stage of JOYO is called MK-II core and will have plutonium uranium mixed oxide fuel (55 cm height) surrounded by SUS reflector. The purpose of the MK-II core is an irradiation bed for reactor fuels and materials. The duty cycle of JOYO is 45 days operation and 15 days refueling.

Surveillance Test

In the MK-I core, the surveillance rigs are irradiated in the reflector region and the irradiation pots. These surveillance rigs have flux monitors made from Fe, Ni, and Cu. For the dosimetry test program, dosimeter sets consist of Nb, Ni, Ti, Cu, Fe, Ta-V, Co-Al, Sc, and fissionable materials (^{232}Th, ^{237}Np, ^{235}U, and ^{238}U), inserted in the surveillance rigs. The surveillance test position [reflector (9A1) position] is shown in Fig. 1.

PNC/DOE Collaborative Dosimetry Test

At the PNC/DOE Fuel and Materials Joint Working Group meeting at DOE/HQ in Germantown, in December 1977, it was agreed to exchange dosimetry techniques and calculational methods. This agreement resulted in the holding of the First PNC/DOE Specialists' Meeting on Collaborative Dosimetry in December 1978 at the Hanford Engineering Development Laboratory (HEDL) in Richland, Washington. At that meeting, the necessary planning was accomplished for the exchange of dosimeter sets for irradiation in JOYO and EBR-II. Subsequently, the dosimeter sets were
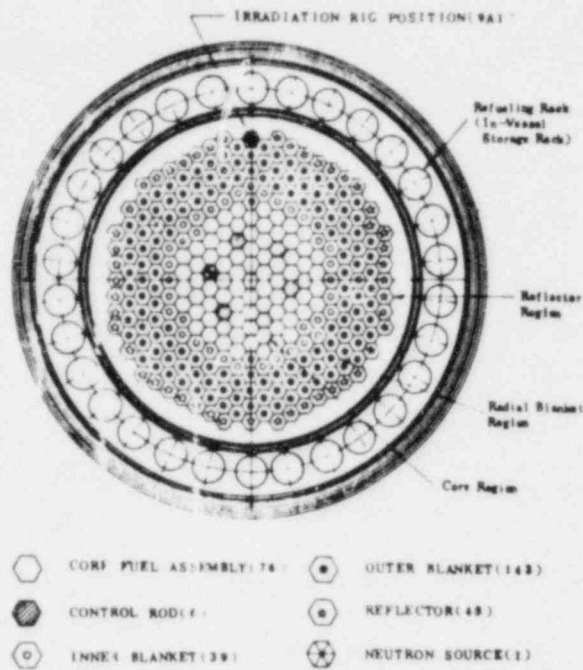
FIG. 1 Core Location of Dosimetry Test(75MWt 2nd Duty Cycle)

exchanged and irradiated in RUN 106 in EBR-II and during the second 75 MWt duty cycle of JOYO.

The second PNC/DOE Specialists' Meeting on Collaborative Dosimetry Testing was held at the PNC Experimental Fast Reactor Division in Oarai, Japan on January 26-29, 1981. The objectives of meeting were to exchange information on the dosimetry test results, and the analyses of the test results. In addition, the future joint PNC and DOE dosimetry test programs were reviewed, and recommendations to the PNC/DOE Fuel and Materials Joint Working Group regarding additional dosimetry exchange activities were made.

2. REACTION RATE MEASUREMENT AND ANALYSIS

Dosimetry Capsule, Irradiation Rig and Dosimeter Design

The PNC and DOE dosimeters were encapsulated into a JOYO dosimeter capsule DE-1, and were loaded in the dosimetry test rig (surveillance test rig). The dosimeter capsule is 100 mm (3.94 in.) in length, 12 mm (0.472 in.) outer diameter, and 10 mm (0.394 in.) inner diameter. Since the capsule had been exposed directly to high-temperature primary sodium coolant (approximately 824°F) during irradiation, all of the capsule elements were fabricated of 316-SS. One spacer and three dosimeter holders are contained in the capsule, and each holder has a hole of

2.6 mm (0.102 in.) inner diameter used to cradle the dosimeters. To prevent oxidation of dosimeter materials, Helium gas at one atmosphere pressure was sealed in the capsule. Figure 2 shows an X-ray radiograph of dosimeter capsule DE-1.
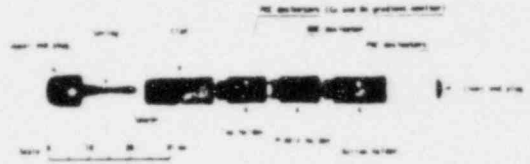
FIG. 2 X-ray Radiograph of Dosimeter Capsule DE-1

The dosimetry test rig is a special reflector sub-assembly used for reactor material surveillance testing in the reflector region, and is shown in Fig. 3. The dimensions of the assembly are 2970 mm (116.93 in.) in height, and 76.3 mm (3 in.) in diameter. For the material surveillance and dosimetry tests, the surveillance test specimens, temperature monitors, neutron flux monitors, and dosimeters were loaded at various core height levels in this rig. The DE-1 capsule containing the PNC and HEDL dosimeters was loaded at the core midplane, and another capsule DJ-1 was loaded at 240 mm (9.45 in.) above the core midplane.

The PNC and HEDL dosimeters used in this collaborative dosimetry test are listed in Tables 1 and 2. All of the PNC dosimeter weights were measured with a chemical balance at JOYO, and HEDL dosimeter weights were measured at HEDL. All dosimeters were fabricated in wire form except Nb.

FIG. 3   Illustration of Surveillance Test Rig
(Dosimetry Test Rig)

There are difficulties in the activity measurement of ^{93m}Nb since it is a low energy X-ray emitter and contains impurity Ta activity. The Nb dosimeter was not evaluated in this test, and Nb dosimetry techniques are currently being developed in the JOYO Dosimetry Program.

The purities of the dosimeter materials were 99.9 to 99.999%. Almost all dosimeter materials had no impurities which obstructed the measurements of reaction rates. On reaction rate analysis of dosimeters, the Co impurity in Cu and the Sc impurity in Ti were matters of utmost concern. The Co in Cu was found to be less than 0.1 ppm with mass spectrographic analysis, and the Sc in Ti was not detected with optical emission arc spectrography.

Table 1. Material Weight of PNC Dosimeter Set(DE-1)
Irradiated at JOYO 75 MWt 2nd Duty Cycle
DE-1 (PNC-1) Set

Dosimeter	Description (mm)	Weight (mg)	Remarks
N1	2.5L × 0.76D	9.87 ± 0.02[b]	
T1	3.3L × 1.3D	17.80 ± 0.02	
Cu UP-A	8.0L × 0.76D	33.07 ± 0.02	
UP-B	8.0L × 0.76D	32.79 ± 0.02	
LOW	8.0L × 0.76D	31.96 ± 0.02	
Fe	2.9L × 0.76D	10.39 ± 0.02	
TaV (a)	1.0L × 0.5D	1.80 ± 0.02	0.1% Ta in V
COAf	7.9L × 1.0D	17.07 ± 0.02	0.61% Co in Al
Nb	1.5L × 1.0D	9.83 ± 0.03	
Rh UP-A	7.0L × 0.50D	17.83 ± 0.02	
UP-B	7.0L × 0.50D	17.78 ± 0.01	
LOW	7.0L × 0.50D	17.83 ± 0.01	

[a] DOE dosimeter.

[b] Absolute error (1σ uncertainty).

Gamma-Spectrometric Techniques and Reaction Rate Analysis

In the JOYO neutron dosimetry measurements, to evaluate reaction rates with activation dosimeters,[2] the activities of the dosimeters were measured by means of gamma-ray or X-ray spectroscopy using a Ge(pure) detector system (Gamma-X SSD System). The detector used was an ORTEC 63 CC high-purity Germanium coaxial solid state detector. In using this system, the source-detector distance can be changed from about 3 cm to a maximum 6 m for the varying intensity of gamma-rays emitted from the dosimeters. The measurable activity ranges from a minimum 0.01 μCi to a maximum 5 mCi with reasonable counting time and counting rates. As the Gamma-X SSD System also has sensitivity for very low energy photons, few Kev X-ray can be measured with this system.

Energy calibration and efficiency calibration of the Gamma-X SSD System were made with ^{137}Cs, ^{54}Mn, ^{65}Zn, ^{22}Na, ^{60}Co, and ^{152}Eu, which were supplied from "Laboratorie de Metrologie des Rayonnements Ionistants (LMRI, France)." Gamma-ray emission rates for these sources are 10^4 to 10^5 gamma/(sec.4π) based on LMRI calibrations, and their accuracies are 2 to 3% (3σ uncertainty).

Table 2. Material Weight of HEDL Dosimeter (Set No. 1)
Irradiated at JOYO 75 MWt 2nd Duty Cycle

No.	Dosimeter	Batch	Form	Material Weight (mg)	Vanadium capsule description
1	Np-237	24HP	NpO_2 wire	6.992	0.089 cm O.D. 0.787 cm L. 28590 mgs wt
2	SC	SCW-001	0.05 cm O.D. (wire)	2.030	0.127 cm O.D. 0.305 cm L. 4.0940 mgs wt
3	Co	Mol-1	12Co in V wire 0.038 cm D.0.32 cm L	2.593	
4	Fe	Sc53	Wire 0.05 cm D, 0.32 cm L	4.623	
5	Ni		Wire 0.05 cm D, 0.24 cm L	3.910	
6	Ti	139-w	Wire 0.05 cm D, 0.32 cm L	2.718	
7	Cu	CPO3054	Wire 0.05 cm D, 0.32 cm L	5.212	
8	Ta		0.12 Ta in V wire 0.05 cm D	1.80 ± 0.02	
9	Nb		Wire 0.05 cm D, 0.5 cm L	8.33 ± 0.02	
10	Nb		Foil	0.476 ± 0.014	divided some pieces at capsule cutting

176

The measured gamma spectrum data was analyzed with the BOB75 code,[3] which was developed by H.BABA and his co-workers in JAERI.

The reaction rates were calculated using the following expression for corrected activities at the end of irradiation.

$$RR = A_c \cdot \frac{1}{P \, a \, N_a \, f_i \, f_b} \frac{1}{s}$$

$$S = \frac{\lambda}{P_0} \int_0^{t_i} P(t) \, e^{-\lambda(t_i - t)} dt$$

where

RR = reaction rates (1/atom·sec)
S = saturation factor
A_c = corrected activity of dosimeter at the end of irradiation
P = purity of dosimeter material
a = isotope abundance
N_a = Avogadro's number (6.0020×10^{23})
f_i = correction factor for impurity
f_b = burn-up of dosimeter material
P_0 = nominal reactor power (75 MWt for JOYO and 2nd duty cycle)
λ = decay constant
t_i = irradiation time
$P(t)$ = time dependent reactor power

In this expression, A_c is corrected for decay, weight, gamma-ray self-absorption,[4] random summing and dead time.

The results of PNC and HEDL reaction rate measurement at the JOYO surveillance position (reflector region) [9A1] are listed in Table 3.

3. NEUTRON SPECTRA DETERMINATION AND RESULTS

Initial Guess Flux

The initial guess flux value used for input data to the neutron unfolding code was calculated with the following considerations.

1. Code used   : DOT-3.5
2. Condition for calculation   : 20 energy groups for neutron flux
                                       $S_{30} - P_3$
3. Cross section   : ENDF/B-IV library
                                       Collapsed by AMPX-I code
4. Configuration for calculation : MK-I 75 MWt 1st duty cycle
                                       equivalent
5. Flux normalization   : Power normalization to 75 MWt

Table 3. Results of Reaction Rates at JOYO (9A1)
JOYO 75 MWt 2nd Cycle Dosimetry Results

Reaction	HEDL results Reaction Rate (DOE set) 1 $Z = -1.7$ cm	JOYO results Reaction Rate (DOE set) 2 $Z = -1.7$ cm	Reaction Rate (PNC set) 3 $Z = -3.0$ cm	Ratios Ratio 1/2	Ratio 1/3	Ratio 2/3
^{93}Nb(n,n')^{93m}Nb		5.047^{-12} $(5.26)^a$	5.106^{-12} $(5.05)^a$			0.9884 (7.3)
^{58}Ni(n,p)^{58}Co	1.905^{-13} $(2.6)^a$	2.045^{-13} (2.07)	1.963^{-13} (2.24)	0.9315	0.9705	1.042 (3.1)
^{46}Ti(n,p)^{46}Sc	1.606^{-14} (2.4)	1.725^{-14} (2.37)	1.708^{-14} (2.37)	0.9310	0.9403	1.010 (3.3)
^{63}Cu(n,α)^{60}Co	8.02^{-16} (2.1)	8.418^{-16} (2.91)	7.968^{-16} (2.85)	0.9527	1.007	1.056 (4.1)
^{54}Fe(n,p)^{54}Mn	1.365^{-13} (3.5)	1.419^{-13} (2.62)	1.399^{-13} (2.88)	0.9619	0.9757	1.014 (3.9)
^{58}Fe(n,γ)^{59}Fe	3.89^{-12} $(3.0)^b$	4.264^{-12} (4.63)	4.362^{-12} (4.76)	0.9122	0.8918	0.9775 (6.6)
		$(3.876^{-12})^b$	$(3.965^{-12})^b$	(1.004)	(0.9811)	
^{181}Ta(n,γ)^{182}Ta	9.54^{-10} (4.8)		9.990^{-10} (3.42)		0.9550	
^{59}Co(n,γ)^{60}Co	1.647^{-10} (4.7)	1.739^{-10} (2.57)	1.733^{-10} (2.66)	0.9520	0.9504	0.9983 (3.7)
^{45}Sc(n,γ)^{46}Sc	1.609^{-11} (3.1)	1.609^{-11} (2.33)		1.000		
^{237}Np(n,f)^{103}Ru	1.284^{-11} (3.9)	1.165^{-11} (8.52)		1.102		
^{237}Np(n,f)^{95}Zr	1.259^{-11} (3.6)	1.165^{-11} (5.22)		1.081		

[a] 1σ uncertainty as a percentage error.

[b] Same Fe-58 isotope abundance (0.33%) were used.

Note. The reaction rate of ^{93}Nb(n,n')^{93m}Nb is a preliminary value, and is being rechecked.

Z: Distance from core center level (mm).

Reaction Rate: Reaction/sec/atom/75.0 MWt.

Unfolding Code

The NEUPAC (Neutron Unfolidng Code Package)[5] estimates neutron flux spectra and other integral quantities from integral data of activation foils, etc.

A basic equation is $R_i = \int \sigma_i(u)\phi(u)du$ (i = 1, number of reactions). The input quantities are measured reaction rates R_i, reaction cross sections $\sigma_i(u)$ and the estimated $\phi_o(u)$ of spectrum $\phi(u)$. It is required to attach an error to every input quantity.

From the above, the spectrum $\phi(u)$ is obtained as a solution together with its uncertainty. Alternatively, the estimate and error of the integral quantity $I = \int W(u)\phi(u)du$ [in this case, $W(u)$ is entered] is obtained based on the J_1 type unfolding method.[6,7] Thus, in problems of this type, the method can be applied also to other than activation foil problems.

The NEUPAC code calculates the output spectrum and integral quantities, chisquare test of output data, plotter output, and error analysis (including sensitivity analysis) of integral quantities.

The neutron cross section used for neutron unfolding has 103 energy group structure and was collapsed from ENDF/B-IV and V.

PNC/HEDL Results of Neutron Spectrum Analysis

Table 4 and Fig. 4 show the results of the neutron spectrum analysis with the neutron unfolding code package NEUPAC at the JOYO (9A1) position.

The estimated total neutron flux agrees to within about 16% between PNC and that of HEDL. HEDL used both the FERRET and SAND-II codes for the neutron unfolding calculation. The estimated spectrum by the SAND-II code is distributed among the error width of the NEUPAC in the case of JOYO (Fig. 4), but FERRET result (Table 4) for the total flux is not. This is due to difference in treatment of the flux below the range of response of the threshold detectors.

The comparison of neutron flux with E > 0.1 MeV shows better agreement due to its better definition by the threshold detectors. In this case the PNC results is $3.19 \times 10^{13} \pm 10\%$ whereas the HEDL results is $2.94 \times 10^{13} \pm 20\%$. The agreement is thus well within quoted uncertainties.

The average ratio of the calculated reaction rates to the measured reaction rates is improved from 1.45 ± 0.72 to 1.06 ± 0.11 using the unfolded neutron spectrum with NEUPAC. This means an improvement of the neutron spectrum and flux using NEUPAC.

Table 4. Comparison of Unfolded Total Neutron Flux
in unit of $1/cm^2 \cdot sec$

Position	Initial value	Estimated	
		NEUPAC (PNC)	FERRET[a]
JOYO (9A1)[b]	$1.37^{+14} > 30\%$	$1.28^{+14} \pm 10\%$	$1.08^{+14} \pm 14\%$
EBR-II (2B1)			
(F4)[c]	2.33^{+15}	$2.54^{+15} \pm 10\%$	2.30^{+15}
(F2)[d]	8.97^{+14}	$9.17^{+14} \pm 10\%$	7.90^{+14}

[a]Reference 8.

[b]Midplane position of the reflector.

[c]Midplane position of the (2B1) core region.

[d]36.6 cm under the midplane, the (2B1) reflector position.

FIG. 4 Comparison of Unfolded Neutron Spectra.

on JOYO (9A1) Reflector Position

4. CONCLUSION AND DISCUSSION

The purpose of the PNC/DOE(HEDL) Collaborative Dosimetry Test is the improvement of dosimetry techniques and analysis through the intercomparison of the dosimetry results. The intercomparisons consist of two parts. One part is intercomparison of reaction rates of dosimeters, and the other is the unfolding of the neutron spectrum.

From intercomparison of the reaction rates measured at JOYO and HEDL, the following results were obtained.

1. The reaction rates agreed to within ±3.5% except for the $^{237}Np(n,f)$ reaction.

2. $^{237}Np(n,f)$ reaction rates shows a discrepancy of 10%. The reason for this discrepancy has not yet been clearly explained, so we have been rechecking the ^{237}Np results.

The uncertainties (1σ) of the reaction rates for all reactions are evaluated to 2-5% by PNC and HEDL. From this, it is found that almost all reaction rate results agree within uncertainty, except for $^{237}Np(n,f)$ reaction.

From intercomparison of the neutron spectrum analysis at PNC and HEDL, the following results were obtained:

1. The estimated total neutron flux agrees to within 15% for the PNC result and the HEDL result for all cases.

2. The average ratio of the calculated reaction rates to the measured reaction rates is improved from 1.45 ± 0.72 to 1.06 ± 0.11 using the unfolded neutron spectrum.

The error (2-4%) of estimated neutron total flux by the NEUPAC is smaller than the discrepancy between PNC and HEDL. The reason for this is the fact that the error estimation by NEUPAC does not include the uncertainties from the neutron cross section, its energy collapsing effect and the estimation of the covariance matrices of the neutron spectrum and the neutron cross sections.

REFERENCES

1. Willem L. Zijp and Jan H. Baard, Nuclear Data Guide for Reactor Neutron Methodology. Part 1: Activation Reactions (1979 edition), Part 2: Fission Reactions (1979 edition), Netherlands Energy Research Foundation ECN.

2. C. Michael Ledere and Virginia S. Shirley, Table of Isotopes (7th edition): Lawrence Berkeley Laboratory, University of California, Berkeley.

3. Hiroshi Baba, Usage of the BOB7-series Programs for the Analysis of Ge(Li) Gamma-Ray Spectra JAERI-M 7017 (March 1977).

4. Ellery Storm and Harvey I. Israel, Photon Cross Section from 0.001 to 100 MeV for Elements 1 through 100: Los Alamos Scientific Laboratory of the University of California (June 1967).

5. Makoto Sasaki and Masaharu Nakazawa, Production of Analysis Code for JOYO Dosimetry Experiment — User's Manual of Neutron Unfolding Code Package NEUPAC, PNV N941 80-192Tr (January 1981).

6. Masaharu Nakazawa and Akira Sekiguchi, "New Data Processing Technique for Reactor Neutron Dosimetry," NUREG-CP-004 (Vol. 3), 1423-1433 (1977) "Proceedings of the 2nd ASTM-EURATOM Symposium on Reactor Dosimetry" (Palo Alto, 1977).

7. Masaharu Nakazawa and Akira Sekiguchi, "Several Applications of J_1 -unfolding Method of Multi-foil Data to Reactor Neutron Dosimetry," "Proceedings of the 3rd ASTM-EURATOM Symposium on Reactor Dosimetry" (Ispra, 1979).

8. F. Schmittroth, FERRET Data Analysis Code, HEDL TME 79-40, 1979.

FFTF GAMMA RAY MEASUREMENTS

W. L. Bunch
Hanford Engineering Development Laboratory
Richland, Washington, USA

ABSTRACT

A series of gamma ray measurements was made in the
reactor of the Fast Flux Test Facility (FFTF) to determine
the absolute magnitude and the spatial distribution of the
gamma ray field and its associated energy deposition.
Detectors used in the measurements included five different
types of ionization chambers, three different types of
calorimeters, thermoluminescent dosimeters, and self-
powered gamma ray detectors. Preliminary evaluation of the
data indicates agreement among the methods to within about
10%; analyses are continuing to refine and establish
absolute values and associated uncertainties.

INTRODUCTION

Historically, the study of gamma rays within a fission reactor has
played a very minor role, with almost the entire emphasis being on neu-
trons. Neutrons are the basis for the chain reaction and are the major
source of damage or change to structural materials. As knowledge of
radiation damage has increased, the need for information regarding the
gamma ray field has surfaced. Approximately fourteen percent of the
energy deposited in a fast reactor is associated with the gamma ray
field, and most of the energy deposited in structural materials is from
gamma rays. Since radiation damage is temperature dependent, the gamma
ray intensity is important in characterizing the radiation environment
for materials tests. The Fast Flux Test Facility (FFTF) was designed and
built for the purpose of testing and developing fuels and materials for
use in commercial fast breeder reactors. In order to support that devel-
opment program, a comprehensive gamma ray measurement program was designed
with the objective of acquiring data with sufficient accuracy and detail
to support the mission of the facility. In addition, the experimental
program is intended to provide a basis for validating and improving
analytical methods and nuclear data.

183

MEASUREMENTS PROGRAM

One of the major problems associated with making a measurement within a reactor is that of potential bias. The goal of any measurement method is to eliminate all biases and to minimize uncertainties; however, in any single method it cannot be assured that all biases have been eliminated. For this reason, a diverse array of gamma ray detectors was selected for use in this program. Detection diversity minimizes the potential that a common bias will compromise the validity of the results and increases the likelihood of achieving the desired accuracy goals.

The FFTF reactor is contained in a vessel approximately twenty feet in diameter and forty feet tall that is filled with molten sodium. The sodium must be kept above its freezing point at all times and must have an inert cover gas. The high temperature and sealed environment limit experimental flexibility. Three different types of test vehicles were designed and fabricated to permit access for the nuclear characterization measurements. These were the In-Reactor Thimble (IRT),[1] the Vibration Open Test Assembly (VOTA), and Characterizers. The IRT was installed near the core centerline and provided a void region that went from below the core up through the sodium pool and reactor cover to the operating deck. A forty-foot long vacuum bottle inside the thimble provided insulation from the sodium and a nitrogen cooling system cooled the central void region of the thimble. This thimble permitted the use of both active and passive measuring devices within the core, and also made it possible to obtain axial traverses.

The VOTA is an instrumented assembly that is located in the outer row of fuel adjacent to the inconel reflector surrounding the core. This assembly contains a number of sensors to measure vibration; however, it also contains a number of neutron and gamma ray sensors as well as temperature and pressure monitors. The VOTA sensors are immersed directly in the liquid sodium and instrument leads are brought out through seals in the shield plug through the reactor cover. All detectors are at fixed elevations and radial positions. Whereas the IRT experiments were all made at power levels of one megawatt or less, the VOTA measurements are being made at full power and through several operating cycles or until the detectors fail.

Characterizers are special core assemblies that neutronically and physically resemble the core component that they replace: fuel, shim or reflector. The assemblies were modified to permit removal and replacement of sensor pins. The sensor pins were made of fuel cladding and contained an array of radioactivants for neutron measurements and Thermal Expansion Difference (TED) temperature monitors. These passive devices provide a method of measuring the temperature distribution throughout the reactor in both the axial and radial directions; however, they do not provide a direct measure of the gamma ray field and must be interpreted through the use of thermal hydraulics calculations.

The gamma ray measurements program in the FFTF reactor[2] included the following parameters: the spectrum, through use of a Compton recoil gamma ray spectrometer developed for this application; the dose or dose rate, through the use of ionization chambers, self-powered gamma ray detectors, and thermoluminescent dosimeters (TLD); and heating, through the use of calorimeters and TED monitors. Three different type of calorimeters and five different types of ionization chambers were used together with the self-powered gamma ray detector, the TLDs, TEDs and the gamma ray spectrometer in the effort to define the gamma ray field accurately. The program is summarized in Table 1.

Table 1. Gamma Ray Measurements Program in FFTF Reactor

Device	Test Vehicle		
	IRT	VOTA	CH
Spectrometer	X		
Graphite Ion Chamber	X		
Steel Ion Chamber	X	X,X	
Tungsten Ion Chamber	X		
Calorimeter (Steel)	X	X,X	
Thermoluminescent Dosimeter	X		
Thermal Expansion Difference			X
Self-Powered Detector		X	

Preliminary results of the Compton recoil gamma ray spectrometer measurements were presented at an earlier meeting.[3] More detailed information will become available when a basis is established for unfolding the higher energy information that was obtained as a result of the spectacularly successful operation of the unique system. Therefore, these results are not included in this report. Measurements in the VOTA will continue for some time in the future during operation of the reactor. Although all of the Characterizers have been irradiated, not all of the TEDs have been processed at this time. Because of the ongoing work of obtaining information, all of the data that have been obtained have not been fully evaluated. This presents a status report together with some preliminary results.

IRT Gamma Ray Measurements

Ionization Chambers

In addition to establishing the axial profile of the gamma ray intensity through the core, the IRT ionization chamber measurements also established experimentally the dependence of the dose rate on the atomic number of the wall material. The ionization chambers were designed and fabricated specifically for this application. As illustrated in Figure 1, alumina insulators were used to support the center electrode and an argon
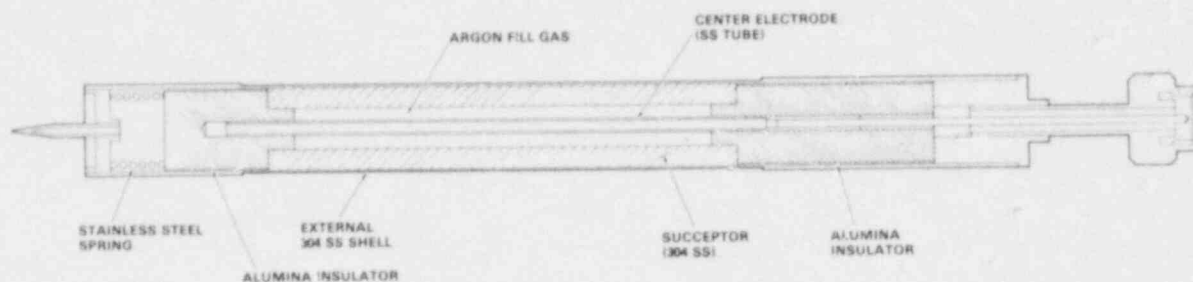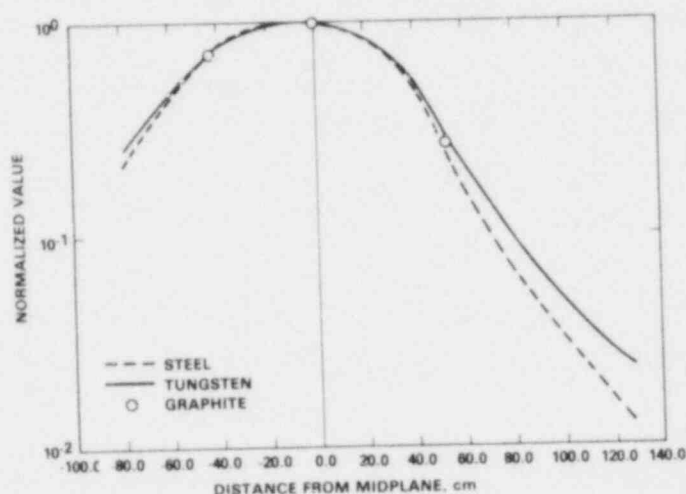
Figure 1. Steel Bragg Gray Chamber

Figure 2. Ion Chamber

gas fill was employed. Sensor walls were sized to obtain electron equilibrium. Unfortunately, graphite wall thickness requirements made those chambers too large to traverse and fixed chambers were used instead to obtain axial data. The chambers were calibrated through the use of a cobalt source known to an accuracy of ±5% in a free-air calibration facility. Results of the measurements in the IRT are summarized in Figure 2. The maximum intensity is located below the axial midplane of the core because of the presence of poison control rods partially inserted from above.

Calorimeter

Energy deposition in stainless steel is of primary interest because it is a commonly used structural material for cladding and fuel hardware. For this reason all of the calorimeters employed steel as the heating element. The IRT calorimeter was of the adiabatic type and is illustrated in Figure 3. The stainless steel sensor is supported by nylon thread at the center of a gold plated copper shield. Heater controls are provided for the copper sleeve to maintain the shield at the same temperature as the sensor to minimize heat losses. For the measurement, the reactor was brought up on a fast period to a power level of about 0.5 MW and then maintained constant. For a constant heat generation rate, the time-dependent temperature of the sensor is given by the relation:

$$\dot{q} = C \frac{dT}{dt} + k\left(T-T_s\right) \qquad (1)$$

where $\dot{q}$ = energy deposition rate, C = specific heat of sensor, k = heat loss coefficient, T = sensor temperature, and T_S = shield temperature. One of the two runs with the calorimeter is illustrated in Figure 4. Relatively good agreement was achieved in the two runs.
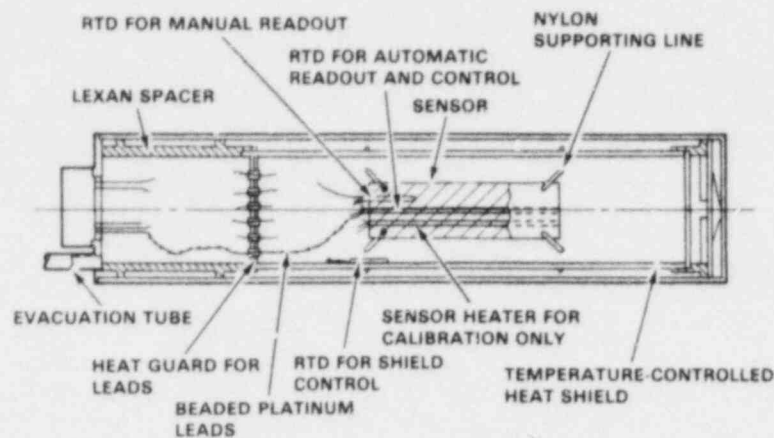
Figure 3. IRT Calorimeter
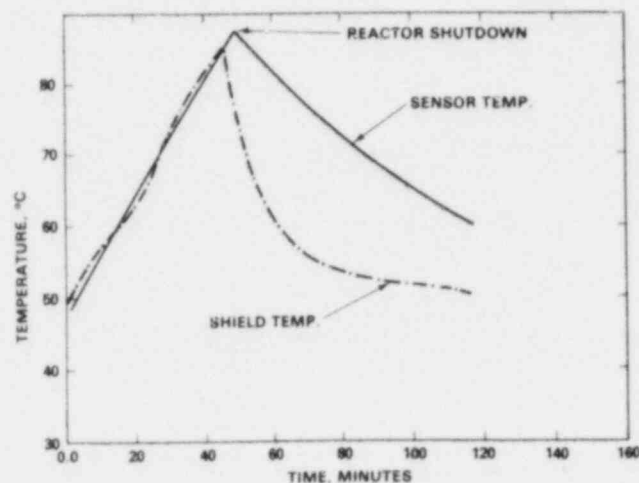
Figure 4. IRT Calorimeter, Run #2

Thermoluminescent Dosimeters

The calcium fluoride TLDs that were employed consisted of bars that are about 6 millimeters long and 1x1 millimeter square. The small size of the detectors made it possible to obtain spatial information in both the axial and radial direction. The TLDs were irradiated within a pure iron bar that was 6.0 cm in diameter and 450 cm long. Five TLDs were placed in iron plugs as illustrated in Figure 5, and these in turn screwed into holes drilled through the iron bar. Radial traverses such as this were made at 55 different axial positions, giving a total of

275 measurements within the iron bar. The TLDs irradiated in the IRT were selected on the basis of response, all being within ±3% of the average at the one-sigma confidence level.

Results of the axial traverse from the TLDs are shown in Figure 6, where the shape is in good agreement with the chamber traverses. By encasing some of the TLDs in tungsten rather than iron sleeves, it was also possible to establish the relative energy deposition rate in iron and tungsten, for comparison to the ionization chamber data.
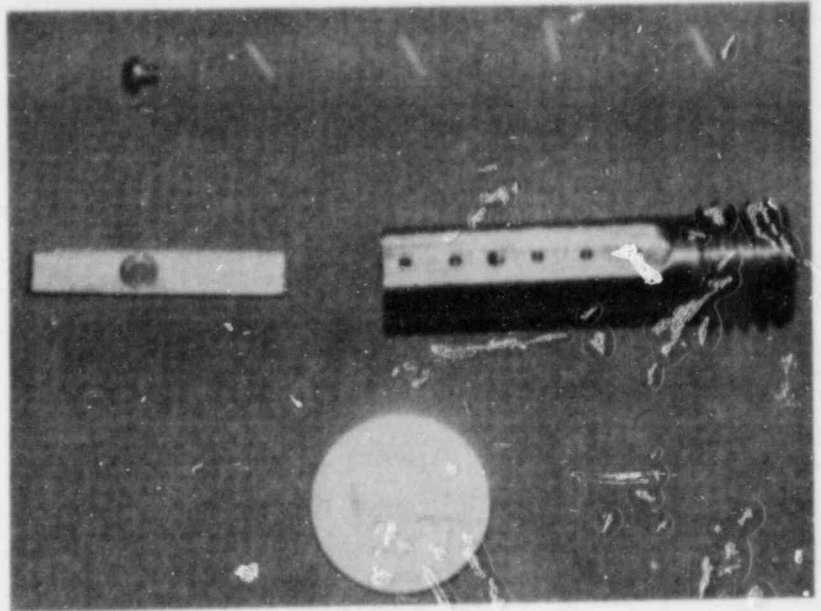
Figure 5. TLD Sample Holder
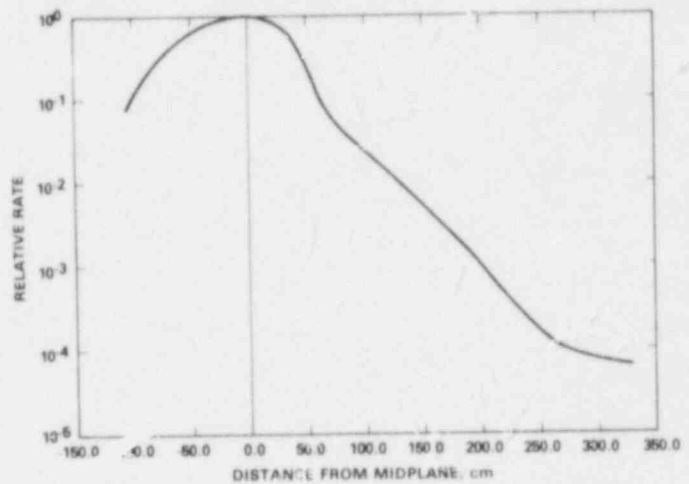
Figure 6. TLD Measurements

VOTA Gamma Ray Measurements

Ionization Chambers

Ionization chambers from two commercial sources were procured and installed at various elevations within the VOTA. These chambers were all encased in stainless steel and had steel cables for service within the hot flowing sodium at temperatures up to about 1000°F. Although the chambers were all calibrated prior to installation, the VOTA resided in the

sodium pool for over a year prior to the time fuel was placed in the reactor. During this time operating characteristics of some of the chambers changed, making the absolute sensitivity suspect. Nevertheless, the chambers have provided data during startup of the reactor, power level changes, and scrams. Chamber response during a startup is illustrated in Figure 7. The response is found to be directly proportional to reactor power level.
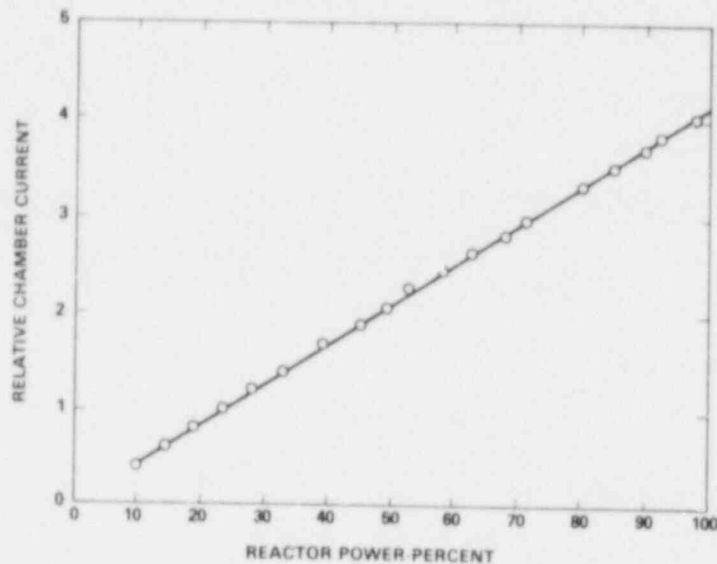
Figure 7. VOTA Gamma Ray Ionization Chamber #2

Calorimeters

Two different types of calorimeters were placed in the VOTA in order to eliminate the potential that the same bias could compromise the results. The first of these was procured from the Whiteshell Nuclear Research Establishment operated by Atomic Energy of Canada, Limited at Pinawa, Manitoba. The design, illustrated in Figure 8, had been used successfully in light water reactor applications and needed only slight modifications for use in a sodium-cooled reactor. The second type of VOTA calorimeter was designed at the Hanford Engineering Development Laboratory (HEDL) as an extrapolation of a previous design used successfully.[4] It is illustrated in Figure 9. Whereas the Canadian calorimeter depends on the conductivity of argon, the HEDL calorimeter depends on the conductivity of steel. Both types of calorimeters do rely on the use of thermocouples to measure temperatures. Preliminary evaluation of the data indicates consistent results, both in the energy deposition rate and in the spatial distribution.
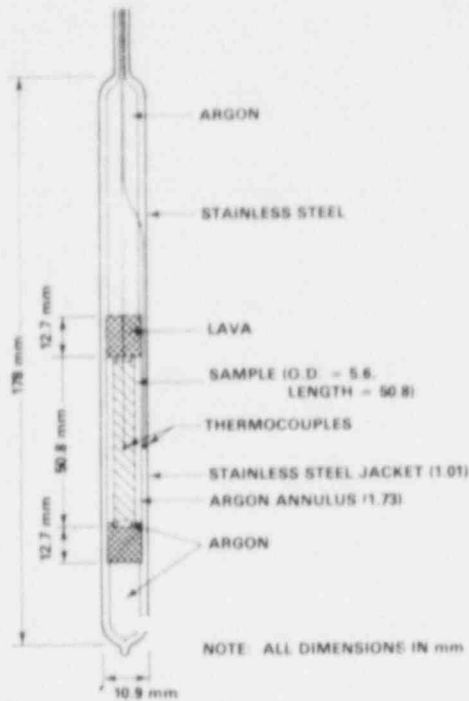
Figure 8. Whiteshell High
Temperature Calorimeter
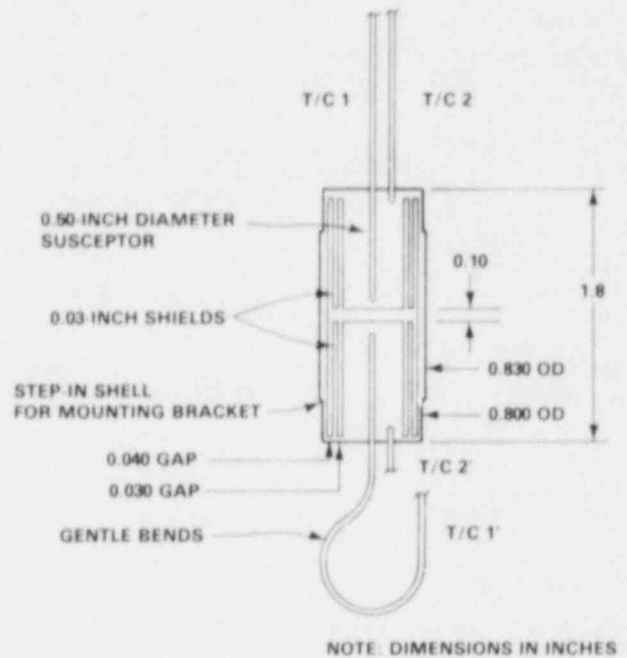
Figure 9. HEDL VOTA Calorimeter

Self-Powered Gamma Ray Detectors

Commercial self-powered gamma ray detectors were procured for use in the VOTA to compare both response times and absolute measurements with those obtained from ionization chambers. The self-powered detector relies on an imbalance in the flow of electrons from the receptor to the collector to generate a current in the absence of superimposed potential difference. In self-powered neutron detectors, the electrons are generated primarily by neutron capture in the receptor with subsequent beta decay. In self-powered gamma ray detectors the materials are selected to have small capture cross sections so that beta rays are produced primarily as a result of photon reactions. The self-powered gamma ray detectors have operated successfully in the VOTA and are also providing input for noise measurements. The dose rate from the self-powered detectors is also in relatively good agreement with ionization chamber values.

Characterizer Temperature Measurements

Thermal Expansion Difference Temperature Monitors

Thermal Expansion Difference (TED) temperature monitors consist of steel capsules filled with sodium, as illustrated in Figure 10. Sodium has a greater temperature-dependent coefficient of expansion than does stainless steel. When the sealed capsules are heated, the expansion of the sodium permanently deforms the steel capsule with an increase in
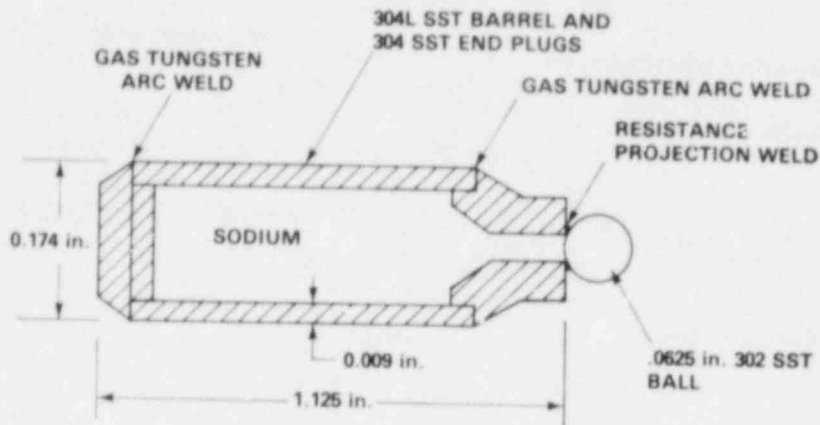
Figure 10. Thermal Expansion Difference Temperature Monitor

volume that is related to the maximum temperature achieved. Because of their small size and passive nature, it is possible to distribute a large number of these throughout the core and reflector of the reactor in Characterizer assemblies. These were employed since no other device, such as TLDs, could be used to measure gamma rays directly at the elevated temperatures encountered at full power (400 MW). The axial temperature profile measured in the in-core shim Characterizer is illustrated in Figure 11. The in-core shim consists of 217 steel pins each 0.23 inches in diameter and eight feet long encased in a standard hexagonal fuel duct. In the Characterizer, several of the steel pins were replaced by sensor pins containing TEDs and radioactivants for neutron measurements. Interpretation of the TED results in terms of energy deposition requires a thermal hydraulics analysis. The TEDs were irradiated during November 1981 and we are still in the process of recovering these from the Characterizers and reading them out.
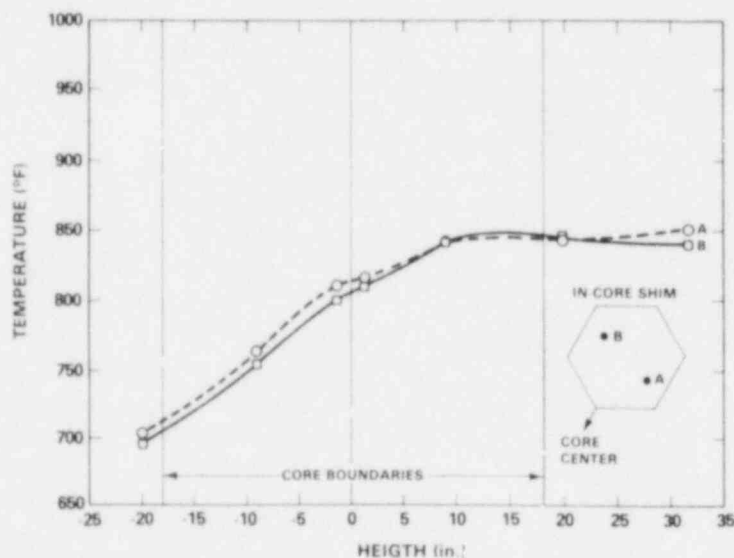
Figure 11. TED Temperatures in Shim

SUMMARY

Table 2 presents a summary of the IRT gamma ray intensity measurements in the FFTF reactor normalized to the core midplane elevation readings in the steel ionization chamber. It can be seen that relatively consistent agreement was achieved by the different methods that were employed. The energy deposition rates in steel at the center of the core range from a low of 0.98 as measured by the TLDs to a high of 1.07 as measured by the calorimeter. The relative energy deposition rates in graphite, steel, and tungsten are in qualitative agreement with predictions. Consistent values are obtained at the position of the VOTA for the various detectors that were employed. These preliminary results indicate that we will be able to meet our goal of providing gamma ray information with the required accuracy to support testing programs to be carried out in the FFTF.

Table 2. Energy Deposition in IRT at Core Midplane

Measurement	Result
Graphite Ion Chamber	0.81
Steel Ion Chamber	1.00
Tungsten Ion Chamber	1.28
TLD (Steel)	0.98
TLD (Tungsten)	1.16
Steel Calorimeter	1.07

ACKNOWLEDGMENTS

Reactor Characterization Program was under the direction of R. A. Bennett, with the core neutronics measurements being developed by J. W. Daughtry and J. A. Rawlins.

REFERENCES

1. A. T. Luksic, W. L. Bunch and G. Felgate, "In-Reactor Thimble System for FTR Characterization," Trans. Am. Nucl. Soc., 39, 893-895 (1981).

2. F. S. Moore, W. L. Bunch, B. J. Kaiser and M. R. Wood, "Gamma-Ray Measurements in the FTR," Trans. Am. Nucl. Soc., 39, 895-896 (1981).

3. Raymond Gold, et. al., "Continuous Gamma-Ray Spectrometry in the Fast Flux Test Facility (FFTF)," Proceedings of the Conference 1980 Advances in Reactor Physics and Shielding, September 14-17, 1980, Sun Valley, Idaho, Pg. 803-815 (1980).

4. Charles C. Price, Paul N. English and John C. Courtney, "An Improved Design for an Active Calorimeter," Trans. Am. Nucl. Soc., 844-845, (1977).

THRESHOLD RESPONSE HELIUM ACCUMULATION
FLUENCE MONITORS FOR FAST BREEDER REACTOR DOSIMETRY

James G. Bradley, B. M. Oliver, Harry Farrar IV
Rockwell International Corporation
Canoga Park, California 91304, USA

and

E. P. Lippincott
Hanford Engineering Development Laboratory
Westinghouse Hanford Company
Richland, Washington 99352, USA

ABSTRACT

Helium accumulation fluence monitors (HAFMs) fabricated using nine new sensor materials with differing energy sensitivities have provided reliable and reproducible neutron dosimetry data in several EBR-II irradiation environments. The (n,total helium) reactions for the nine materials (^{7}Li, Be, N, O, F, S, Cl, K, and Ca) each have different threshold responses, and effectively supplement the dosimetry information now being routinely obtained from the previously well-characterized ^{6}Li and ^{10}B HAFMs.

All the HAFM materials, encapsulated in various chemical forms, were irradiated in a number of different core and blanket neutron environments in EBR-II. The subsequent helium analysis results have been correlated in detail with radiometric multiple foil reaction rate data and with derived neutron flux-spectral information, both obtained during the same test irradiations.

INTRODUCTION

A primary goal of the breeder reactor program in the United States is the development of reactor systems and components that will endure high-energy neutron fluxes for long periods of time. The testing of reactor components to establish practical lifetimes can require irradiations lasting several years in high-flux locations. In reactor surveillance work at low-flux locations, irradiations may last decades. In all cases, it is essential that accurate measurements be made of neutron fluences and energy spectral shapes to provide effective correlations with materials characteristics, and thus to predict component lifetimes.

The transfer of these predictions to other reactor environments and other materials can also be most accurately made when neutron data have been well determined. The most commonly used present dosimetry techniques depend on nuclear reactions that produce radionuclides whose radioactivity can be readily measured. However, many reactions are available that produce stable end-products conveniently measurable for dosimetry. Examples include reactions that alter the ratios of stable isotopes such as $^{10}B/^{11}B$, heavy-element fission that produces specific stable neodymium isotopes, and the formation of helium by a variety of (n,α) reactions with many elements.

Neutron-induced helium generation is the foundation of the helium accumulation fluence monitor (HAFM) technique, which uses a variety of elements and isotopes to achieve a wide range of neutron energy responses. The fact that the measured end-product, helium, is stable and is not itself burned up by neutron interactions, makes the HAFM technique particularly applicable to long-term irradiations. The stability of the helium also means that the analyses can be performed later at a central facility, with no concern that time delay will compromise accuracy. The helium can be measured with $\sim 1\%$ (1σ) absolute accuracy over a very broad range of concentrations using mass spectrometric techniques.[1,2]

Many elements have significant helium production cross sections in fast breeder reactor (FBR) neutron spectra, providing a wide variety of energy response ranges which supplement the response ranges of radiometric neutron dosimeters. For some time, HAFMs using ^{10}B and ^{6}Li as sensors have been included as an integral part of most multiple-foil dosimetry sets used in the U.S. breeder reactor program. In addition to this, the ^{10}B and ^{6}Li helium production cross sections have been integrally tested in four benchmark facilities.[3,4]

This paper reports the initial results of tests in EBR-II of an extended set of elements with different threshold helium generation cross sections. The results of these tests demonstrate the differing energy responses of the different sensors, and provide valuable spectrum integrated checks on the ENDF/B-V helium production cross sections through correlations with cross sections calculated using the SAND-II code.[5-7] The spectral information that can be obtained from each HAFM sensor is unique because each has a different energy-dependent cross section. The selection of a set of HAFM sensors for neutron dosimetry in a given neutron environment must then be based on careful study of the expected spectral sensitivities of each sensor in the neutron spectrum to be measured.

HAFM Description

In simplest terms, a helium accumulation fluence monitor consists of a sensor material which is irradiated and subsequently analyzed for the helium produced by neutron reactions. The helium-generating materials are chosen for the differing energy responses of their helium production

cross sections. For breeder reactor and other high-temperature environments, it has been advantageous to encapsulate the sensor materials to prevent adverse chemical or physical interaction with the surroundings, and to prevent loss of helium generated by the irradiation. A number of materials have been successfully used to make miniature capsules, including vanadium, niobium, gold, platinum, and stainless steel. Direct tests have shown no helium leakage significant for dosimetry from any of these materials in EBR-II. The most commonly used material has been vanadium, because of its strength, low induced radioactivity, and relatively low helium production cross section, although an Au-Pt alloy has advantages in the last category. Typical capsules are 6.4 mm long and either 0.9 or 1.3 mm in diameter. The helium analysis of an encapsulated HAFM is performed by vaporizing the entire capsule and its contents in the mass spectrometer vacuum system to release the helium. Adjustments are made for the helium generated in the capsule material, based on calculations or on measurements of the helium generated in pieces of the encapsulation material irradiated at the same location.

THRESHOLD RESPONSE HAFMS

Helium accumulation fluence monitors fabricated using sensor elements with different energy response ranges, including ^{7}Li, Be, N, O, F, S, Cl, K, and Ca, have been irradiated as part of dosimetry tests conducted during EBR-II Runs 75D, 97, and 106. For convenience in handling, and to enable precise mass assay, most sensor elements were used in chemical combination with another low (n,α) cross section element. Table 1 lists the sensor elements, the chemical forms in which they were irradiated, and their typical 90% response limits in the EBR-II core as calculated using a SAND-II spectral unfolding code, in combination with ENDF/B cross sections. The 90% response limits are the energies above and below which 5% of the reactions occur. These distinct but overlapping energy response ranges for the sensors are illustrated in Figure 1. Most of the HAFM materials were irradiated in more than one chemical form (e.g., Al_2O_3, SiO_2, GeO_2, Nb_2O_5, and PbO for oxygen) to determine which chemical forms and material lots would provide the most reliable data. These demonstration HAFMs were irradiated at several core and blanket locations during three special EBR-II dosimetry test irradiations, to provide test dosimetry data in a range of neutron environments. In each case, the HAFM materials were located adjacent to multiple-foil dosimetry sets to permit accurate correlation with neutron spectral data obtained by radiometric dosimetry spectral unfolding. Table 2 contains a summary of the nominal locations of the HAFM sets, and adjacent multiple foil sets to which all HAFM data are referred, along with neutron fluences and mean neutron energies determined from spectral unfolding using ENDF/B-V cross sections and the SAND-II code.

Table 1. Partial List of Threshold Response HAFM Materials Irradiated in EBR-II Runs 75D, 97, and 106

Sensor Element or Isotope	Typical 90% Response Limits (MeV)[a]	Physical Form	EBR-II Run		
			75D	97	106
^7Li	4.0-8.8	^7LiF	X	X	X
^9Be	2.2-6.7	Be	X	X	X
^{14}N	1.6-5.2	Si_3N_4	–	–	X
		TiN	X	X	X
		ZrN	X	X	X
		NbN	–	–	X
^{16}O	4.0-9.0	Al_2O_3	X	–	X
		SiO_2	X	X	–
		GeO_2	X	–	X
		Nb_2O_5	–	–	X
		PbO	–	–	X
^{19}F	3.6-9.3	^7LiF	X	X	X
		NaF	X	X	X
		FeF_2	X	X	–
		CaF_2	X	X	X
		NdF_3	X	–	–
		PbF_2	–	–	X
S	0.2-5.0	Cu_2S	X	–	X
		PbS	X	X	X
Cl	2.3-7.8	NaCl	X	X	X
		KCl	X	X	X
		$PbCl_2$	–	–	X
K	2.4-7.6	KCl	X	X	–
		KI	X	X	X
Ca	0.1-7.4	CaF_2	X	X	X

[a]Approximate energy limits above and below which 5% of the reactions occur in the EBR-II core center.

NEUTRON ENERGY (MeV)
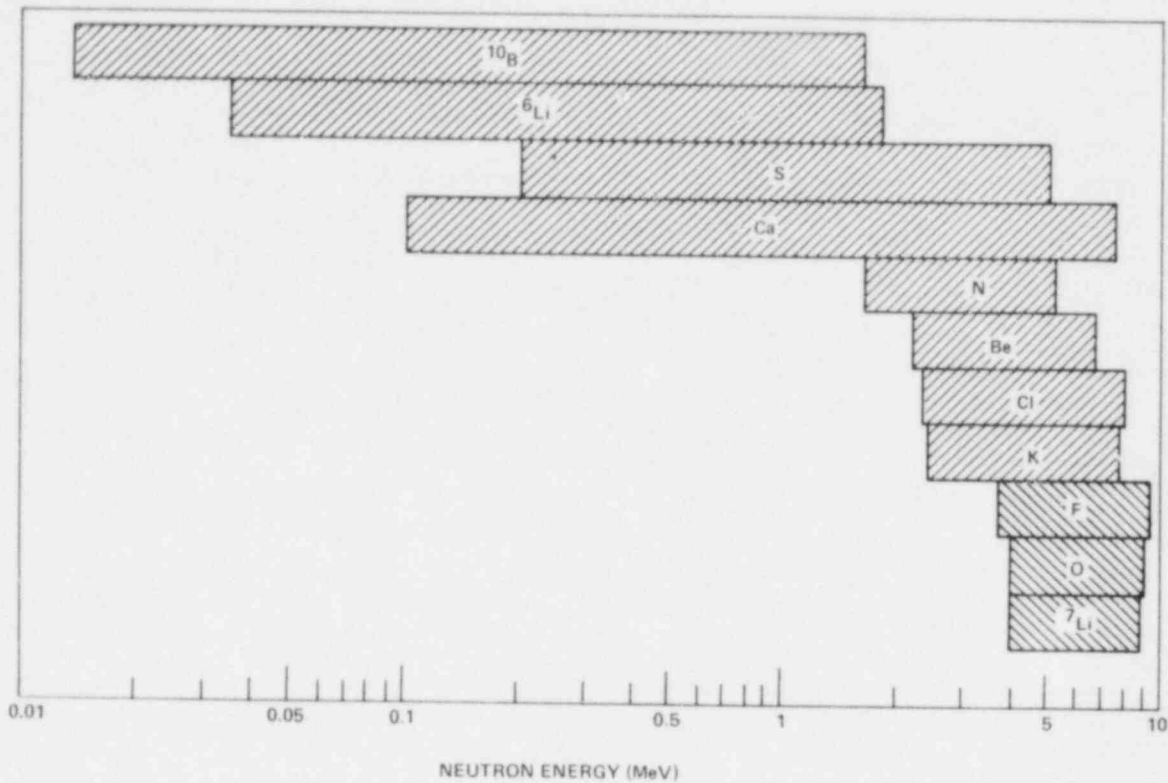
Fig. 1. Typical 90% Energy Response Ranges at EBR-II Core MIdplane for Eleven HAFM Sensors.

The parameter measured in the analysis of a HAFM for neutron dosimetry, helium concentration per atom of sensor material, is the time-integrated reaction rate of the sensor element. The full-power equivalent reaction rate is the helium concentration divided by the full-power equivalent irradiation time. The spectrum-integrated cross section can be calculated by dividing by the equivalent full-power flux. This cross section then can be compared to the equivalent integral cross sections calculated from unfolding data, and energy-dependent cross sections, to determine the accuracy of the energy-dependent cross section and unfolding process.

EXPERIMENTAL RESULTS

A total of more than 300 HAFMs irradiated in EBR-II containing the nine sensors listed in Table 1 have been analyzed for neutron dosimetry applications using standard mass spectrometric techniques. To obtain the helium concentrations and reaction rates in the sensor elements alone, the helium content measured in each HAFM capsule was adjusted for the composition of the compound, for helium from the chemically combined carrier element (e.g., Al in Al_2O_3), if any, and for the helium generated

Table 2.   Summary of EBR-II Dosimetry Test
Irradiation Conditions and Locations

EBR-II Run Number	Irradiation Time (10^6 s)	Power (MW)	Set Name[a]	Nominal Set Location (cm) r	z	Total Neutron Fluence (10^{21}/cm^2)	Mean Neutron Energy $\bar{E}$ (MeV)
75D	0.806	62.5	R-1	17.3	3.9	-	0.79
			H-9	17.3	-1.6	1.79	0.80
			R-2	17.3	-9.5	-	0.80
			H-7	17.3	-23.5	1.09	0.50
			R-4	17.3	-26.5	-	0.44
			H-6	17.3	-36.6	0.654	0.29
			R-5	17.3	-39.0	-	0.26
			H-43	38.3	-1.4	0.857	0.41
			R-3	38.3	-4.6	-	0.40
97	3.15	62.5	R-2	5.9	1.9	-	0.73
			H-F4	5.9	0	7.53	0.74
106	3.86	57.25	R-1	5.9	2.1	-	0.69
			H-F6	5.9	0	8.80	0.70
			R-2	5.9	-35.2	-	0.27
			H-F4	5.9	-36.6	3.09	0.26

[a]"R" indicates a HAFM set; "H" indicates a multiple foil dosimetry set.

in the capsule material. Most often, the carrier contributions were deter-
mined by analysis of the pure carrier element irradiated with the HAFMs
at the same locations. In most other cases, however, the contributions
were determined from other HAFM data. For example, the helium generation
data from HAFMs containing FeF$_2$, along with data from pure iron wires, were
used to determine the fluorine contribution to the helium in the ^{7}LiF HAFMs.
In the remaining cases, the carrier contributions were calculated from
ENDF/B-V cross sections and radiometric unfolding data. For the elements
Ge, I, Nd and Pb, accurate cross section data were not available, but since
the (n,α) cross sections of these carrier elements are expected to be very
small, the uncertainties in the estimates make little impact on the final

results. The contributions to the helium from the capsules themselves were determined by analyses of encapsulation material irradiated with the HAFMs. Uncertainties in the final results due to these adjustments for the helium from the carrier elements and capsule materials generally ranged from ~1 to 2% for core locations, and from 1 to 5% in the blanket, depending on the sensor compound and encapsulation material.

Using the measured reaction rates for each HAFM type at each irradiation location, two comparisons can be made that demonstrate the consistency and accuracy of the HAFM technique. First, the good self-consistency and differing energy sensitivities of the different HAFM types can be seen by comparing the measured HAFM sensor reaction rates with radiometrically-measured $^{54}Fe(n,p)^{54}Mn$ reaction rates. This could be done because there were iron wire segments throughout all the irradiation capsules. These wires were subsequently radiometrically counted, and provided a suitable means for interpolating other dosimetry data obtained at slightly different reactor locations, as discussed later. For convenience, all the measured HAFM data have been plotted in Figures 2 and 3 as a ratio to the $^{54}Fe(n,p)$ reaction results at the same location. These reaction rate ratios, for each sensor element, are plotted versus mean neutron energy. For simplicity, the ratios for those separate compounds with common sensor elements have been combined, and the average result has been used.

DISCUSSION

A generally smooth systematic increase can be seen in the reaction rate ratios for ^7Li, N, S, and Ca with decreasing mean neutron energy (Figs. 2a, 2c, 3a, 3d). This trend indicates that the (n,He) reactions in these four elements are sensitive to neutrons of lower energy than the reference $^{54}Fe(n,p)$ reaction. Similarly, the flat-to-decreasing curves for the Be, O, F, Cl and K sensors (Figs. 2b, 2d, 2e, 3b and 3c) at lower mean energies indicate that these elements respond primarily to neutrons with energies the same as or higher than those that produce the $^{54}Fe(n,p)$ reaction.

The pattern of energy sensitivities relative to $^{54}Fe(n,p)$ for each of the sensors is consistent with their energy sensitivity ranges, as given in Table 1 and shown in Figure 1. Nitrogen, sulfur and calcium have 90% response limits that extend down to 1.6, 0.2 and 0.1 MeV, respectively, compared with the equivalent 90% response of the $^{54}Fe(n,p)$ reaction which extends from 7.5 MeV down to 2.3 MeV. On this basis alone, it can be expected that these three elements should have enhanced sensitivity for low energy neutrons. In the cases of Be, Cl and K, on the other hand, which have energy response ranges quite similar to the $^{54}Fe(n,p)$ reaction, the corresponding ratios in Figures 2 and 3 demonstrate a sensitivity close to that of ^{54}Fe. Finally, the O and F sensor reactions, which have 90% response limits that extend only down to 4.0 and 3.6 MeV (compared with 2.3 MeV for ^{54}Fe), clearly demonstrate an enhanced high

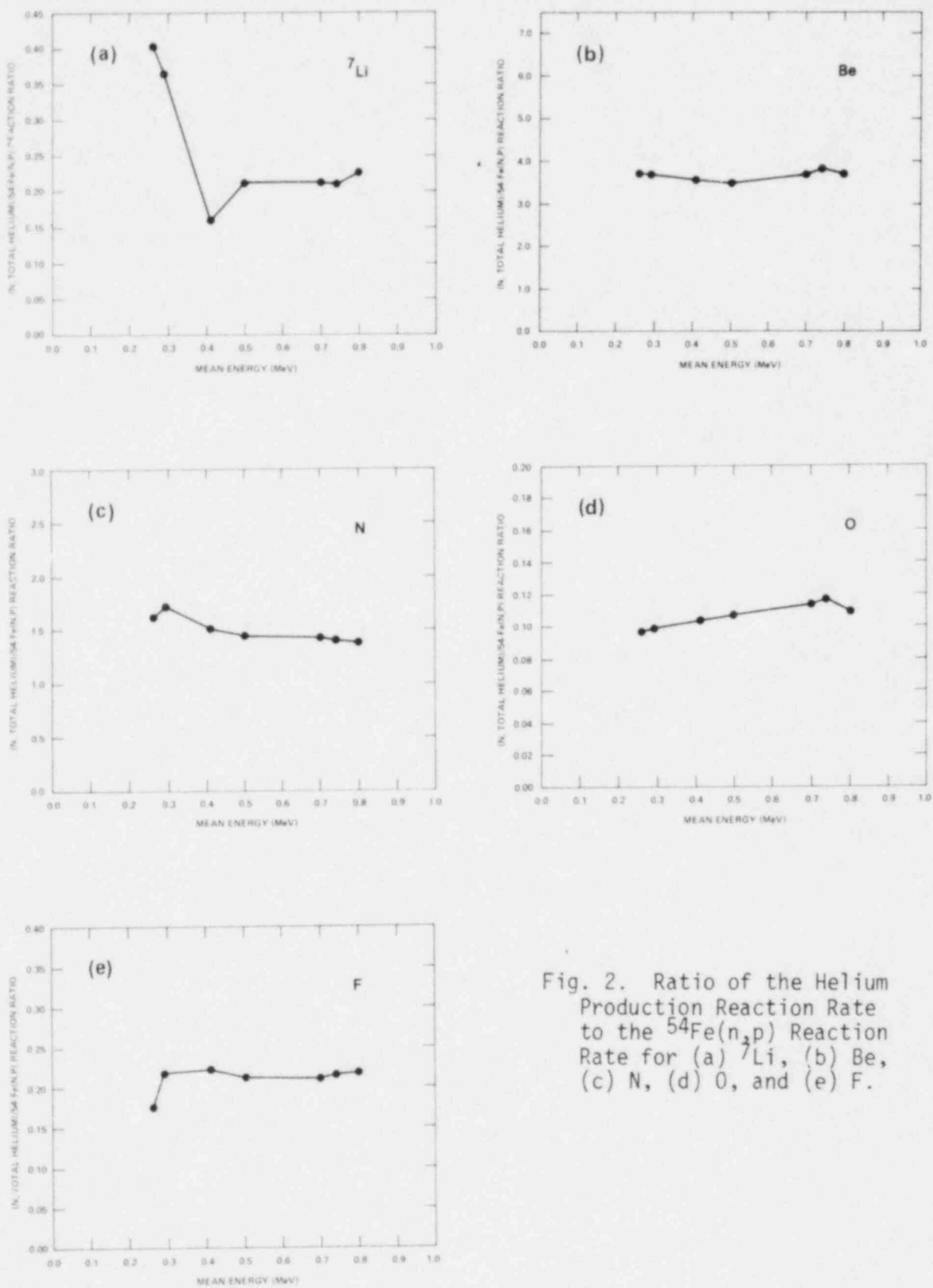Fig. 2. Ratio of the Helium Production Reaction Rate to the ^{54}Fe(n,p) Reaction Rate for (a) ^{7}Li, (b) Be, (c) N, (d) O, and (e) F.
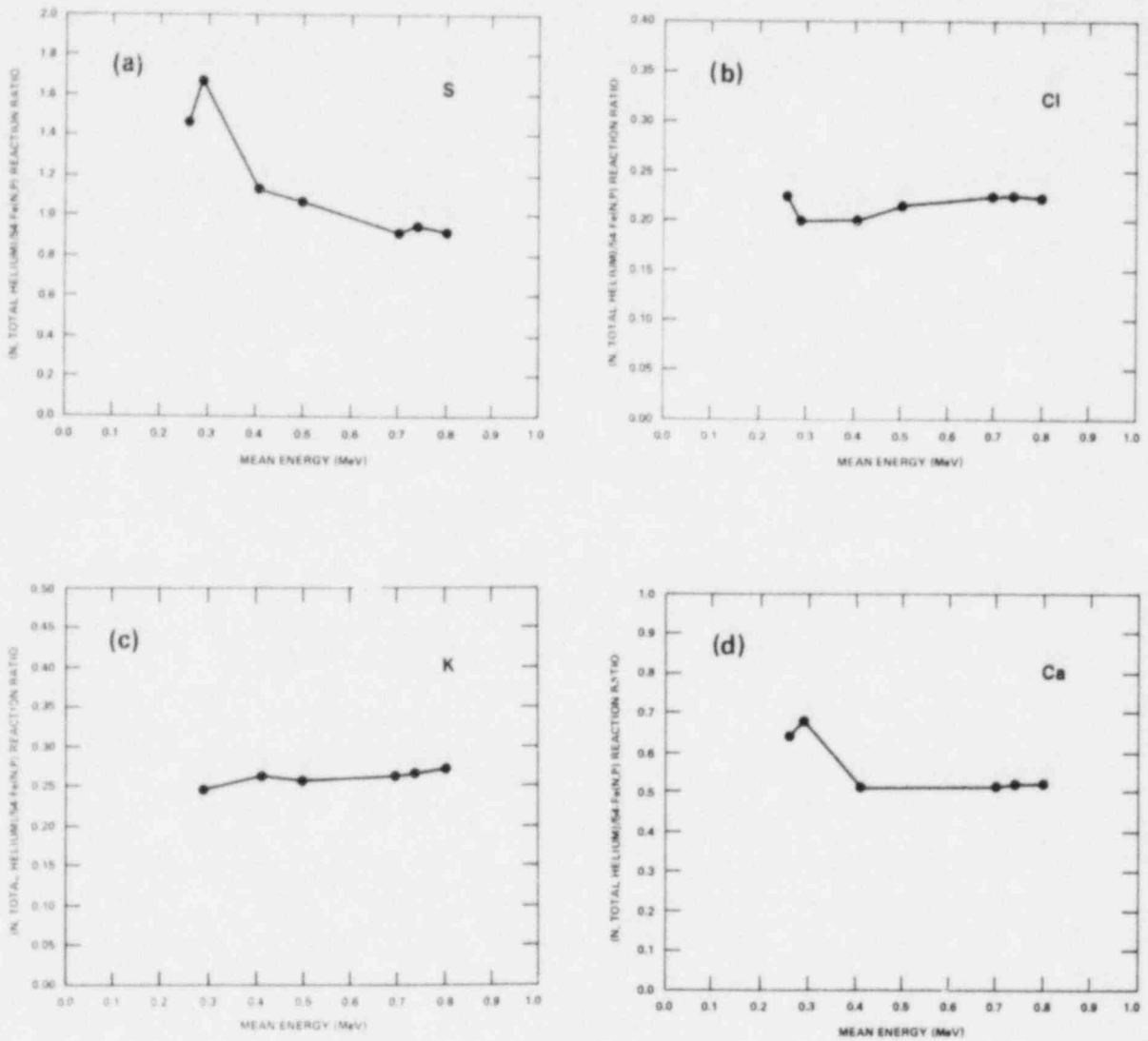
Fig. 3. Ratio of the Helium Production Reaction Rate to the ^{54}Fe(n,p) Reaction Rate for (a) S, (b) Cl, (c) K, and (d) Ca.

energy sensitivity. The remaining sensor, ^7Li, follows an expected trend at the higher energies, but, as discussed later, there appears to be an anomalous lower energy contribution, presumably from a greater-than-expected presence of ^6Li.

The accuracy of the ENDF/B-V energy-dependent cross sections can be estimated by comparing the spectrum-integrated helium production cross sections determined from the analyses of the HAFMs containing the nine sensor elements, with calculated values. The spectrum-integrated helium production cross sections for each of the nine HAFM sensors were calculated at the locations of the radiometric dosimetry sets, listed in Table 2. The neutron energy spectrum at each location was determined using the multiple-foil radiometric dosimetry data in combination with the SAND-II unfolding code. The spectrum-integrated helium production cross sections of the nine sensor elements were then calculated using the SAND-II spectra in combination with energy-dependent cross sections derived from the ENDF/B-V gas production file. Because spectral unfolding with good accuracy was possible only at the location of the multiple-foil spectral sets, this location was chosen for the comparison of calculated and measured cross sections. Thus, each of the measured HAFM sensor cross sections (reaction rates) was adjusted, for comparison purposes, to account for the fast flux gradients between the actual HAFM irradiation locations, and the spectral set locations. The adjustment was performed using a combination of $^{54}Fe(n,p)$ reaction rates measured at the various irradiation locations, along with published EBR-II $^{54}Fe(n,p)$ reaction rate matrices.[8] This method of renormalization of the HAFM results is valid because the (n,α) cross sections of the HAFMs, as well as the $^{54}Fe(n,p)$ cross section, are sensitive predominantly to fast neutrons, and therefore they can be expected to follow similar trends over the small distances between adjacent irradiation locations. The interpolation adjustments were small, and had uncertainties of from 1 to 4%, depending on the flux gradient. It should be noted here that the additional uncertainties of these interpolations are introduced only to make comparisons of the HAFM technique with radiometric foils located nearby. In routine applications, however, the HAFMs and the foils would be located in much closer proximity, so this source of uncertainty would all but vanish.

The ratios of calculated-to-measured helium production cross sections for the nine HAFM sensor elements are plotted in Figures 4 and 5. The absolute ratios, together with the trends in the ratios with mean neutron energy, provide indications of the accuracy of the unfolded spectra and the ENDF/B-V cross sections, as well as an indication of possible uncertainties in the measured integral values. Figures 4b, 4c, and 5c show that the calculated and measured spectrum-integrated helium production cross sections of Be, N, and K are in very good agreement (within ±10%) at all neutron energies. Figures 4d, 4e, and 5b show that the calculated cross sections for O, F, and Cl have a nearly constant ratio to the measured cross sections, although the calculations are high by 10 to 30%. Thus some renormalization of the ENDF/B-V cross sections for these elements
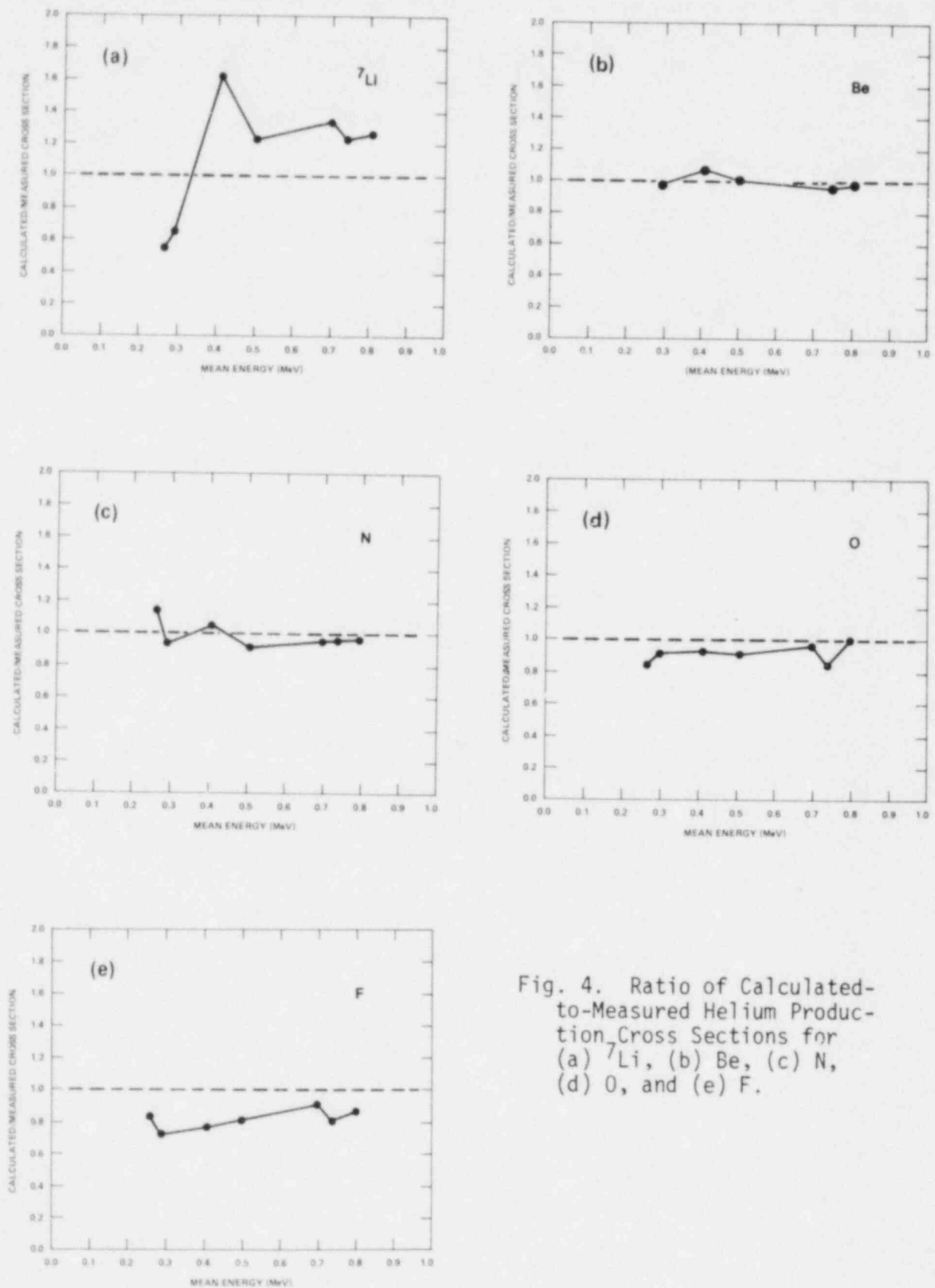
Fig. 4. Ratio of Calculated-to-Measured Helium Production Cross Sections for (a) ^{7}Li, (b) Be, (c) N, (d) O, and (e) F.
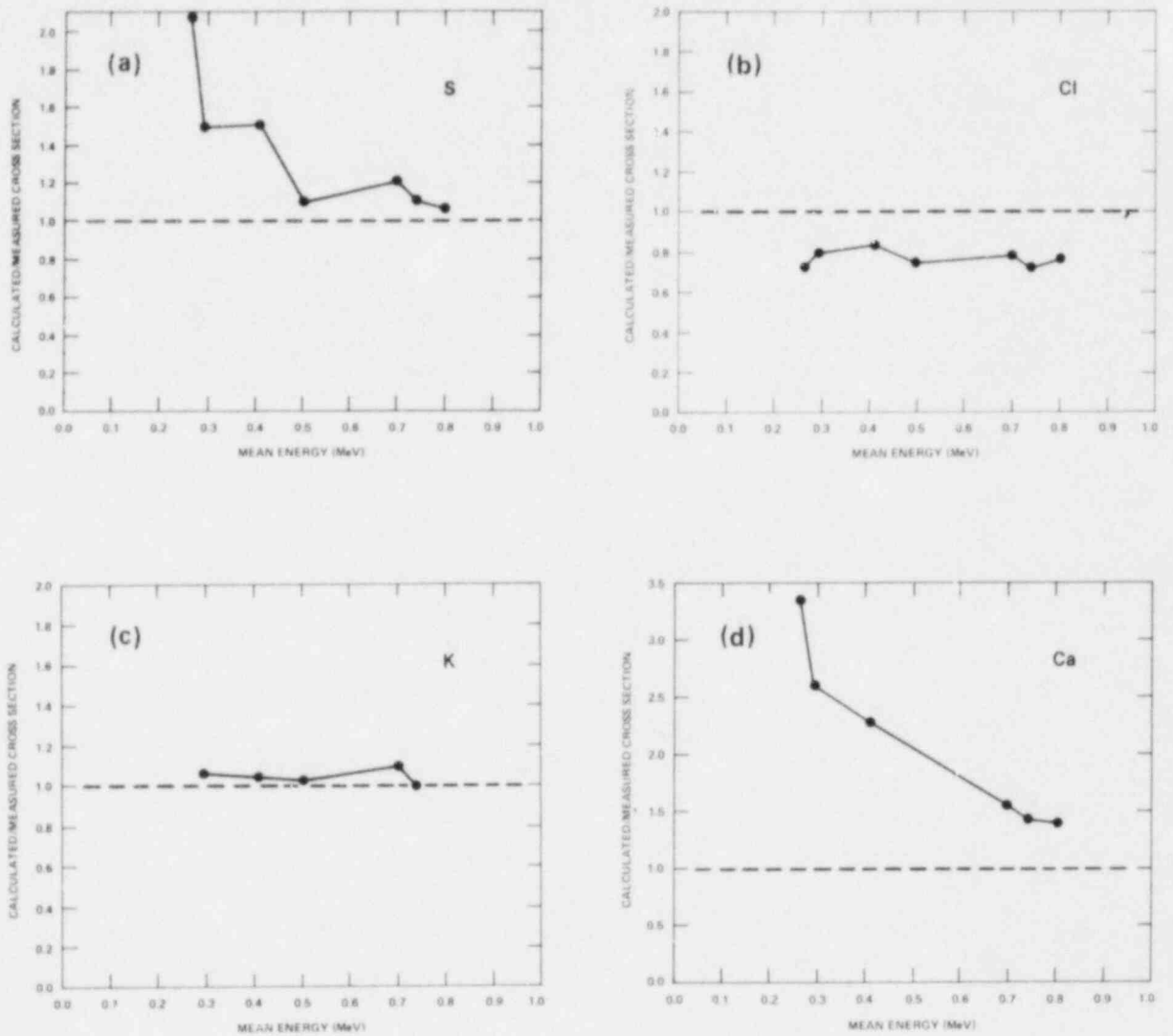
Fig. 5. Ratio of Calculated-to-Measured Helium Production Cross Sections
for (a) S, (b) Cl, (c) K, and (d) Ca.

may be appropriate. The calculated spectral averaged cross sections for
S and Ca, on the other hand, show significant discrepancies, which
increase to a factor of 2 to 3 at the lowest mean energies. These two
cross sections, therefore, clearly need reassessment at low neutron
energies.

In Figure 4a, the ratios of calculated-to-measured helium production
cross sections for ^7Li show an irregularity that is probably due to a
combination of uncertainties in the ENDF data as well as uncertainties
in the exact content of ^6LiF (~0.007%). Although the expected contribu-
tion to the helium production for this ^6Li "impurity" has already been
subtracted from the data, the low energy data in Figure 4a suggest an
additional presence of this isotope. At higher energies, the ^7Li curve
indicates the evaluated cross section is 20 to 30% too high.

The other candidate HAFM sensor materials could also have impurities
of higher cross section helium-producing elements that could have con-
tributed significantly to the present results. For example, ^6Li or ^{10}B
impurities could produce a dramatic rise in the curves in Figs. 2 and 3
at low mean energies, and a corresponding drop in Figs. 4 and 5. This
trend appears only for ^7Li, indicating that the quality of the other
sensor materials is adequate for HAFM applications. The fact that the
data from separate compounds with common sensor elements were in agree-
ment, also suggests that impurity contributions were not important.

In general, some increased scatter is evident in the lowest energy
data points. This is consistent, however, with increased data scatter
observed in radiometric measurements at these and other far out-of-core
locations (e.g., Fig. 4, Ref. 9). The additional interpolations,
mentioned earlier, that were used to compare the HAFM data with the
radiometric results, also introduced uncertainties that are most notice-
able at the out-of-core locations, where the flux gradients are generally
steepest.

In summary, the results presented here from HAFMs irradiated in
EBR-II demonstrate that ^7Li, Be, N, O, F, S, Cl, K, and Ca, as well as
^6LiF and boron, can be used as effective HAFM sensors for dosimetry
measurements in fast breeder reactors. These measurements provide im-
portant integral cross section normalizations that can be used to improve
energy-dependent cross sections in energy ranges relevant to fast
breeder reactors. The integral cross sections themselves are also
valuable for prediction of helium production rates in alloys and other
fast breeder reactor materials.

ACKNOWLEDGEMENTS

REFERENCES

1. H. Farrar IV, W. N. McElroy, and E. P. Lippincott, "Helium Production Cross Section of Boron for Fast Reactor Neutron Spectra," Nucl. Technol. 25, 305 (1975).

2. H. Farrar IV and E. P. Lippincott, "Helium Production Measurements for Neutron Dosimetry and Damage Correlations," Proc. Second ASTM-EURATOM Symp. on Reactor Dosimetery, NUREG/CP-0004, Vol. 2, p 725 (1978).

3. H. Farrar IV, B. M. Oliver, and E. P. Lippincott, "Helium Generation Reaction Rates for ^{6}Li and ^{10}B in Benchmark Facilities," Proc. Third ASTM-EURATOM Symp. on Reactor Dosimetry, EUR 6813 EN-FR, Vol. 1, p 552 (1980).

4. B. M. Oliver, H. Farrar IV, E. P. Lippincott, and A. Fabry, "Spectrum-Integrated Helium Generation Cross Sections for ^{6}Li and ^{10}B in the Sigma Sigma and Fission Cavity Standard Neutron Fields," Proc. Fourth ASTM-EURATOM Symp. on Reactor Dosimetry, March 22-26, National Bureau of Standards, Gaithersburg, MD (1982).

5. W. N. McElroy, S. Berg, T. Crockett, and R. Hawkins, "A Computer-Automated Iterative Method for Neutron Flux Spectra Determination by Foil Activation, a Study of the Iterative Method," AFWL-TR-67-41, Vol. I, Air Force Weapons Laboratory, Kirtland Air Force Base, Albuquerque, NM (1967).

6. S. Berg and W. N. McElroy, "SAND-II (Spectrum Analysis by Neutron Detectors-II) and Associated Codes, A Study of the Iterative Method," AFWL-TR-67-41, Vol. II, Air Force Weapons Laboratory, Kirtland Air Force Base, Albuquerque, NM (1967).

7. S. Berg, "Modification of SAND-II," BNWL-855, Battelle-Northwest Laboratories, Richland, WA (1968).

8. C. L. Long, J. A. Ulseth, E. P. Lippincott, and N. J. Graves, "EBR-II Spectral Parameters, Run 75D," HEDL-TME 78-84, Hanford Engineering Development Laboratory (1979).

9. E. P. Lippincott and J. A. Ulseth, "High Flux-Fluence Measurements in Fast Reactors," Proc. Second ASTM-EURATOM Symp. on Reactor Dosimetry, NUREG/CP-0004, Vol. 1, p 271 (1978).

SPECTRUM CHARACTERIZATION IN A SIMULATED FR BLANKET REGION

VIA ACTIVATION OF THRESHOLD AND CONTINUOUS DETECTORS

M.Carta,A.De Carli,R.Martinelli,P.Moioli
C.S.N. Casaccia,CNEN
Rome,Italy
G.Daguzan,M.Salvatores,J.P.Trapp
C.E.N. Cadarache,CEA
St.Paul-Lez-Durance,France

ABSTRACT

The response of threshold and continuous activation detectors placed in the simulated blanket region fed by the fast source reactor Tapiro of C.S.N. Casaccia through a buffer fissile zone are analized and the differences with respect to transport calculations are evaluated.

The experiment, in the joint programme CNEN-CEA for fast reactors, has the purpose of studying blanket properties.

The C2 configuration experimental results together with the comparisons with transport and diffusion calculation are reported. The agreement is satisfactory, except for the high energy sensitive fission U^{238}/fission U^{235} index.

INTRODUCTION

Fast reactor fertile blanket neutronic properties have a direct influence on:
-total power output
-plutonium production during reactor life
-neutron spectrum at the core-shield boundaries.

The analysis of integral experiments performed in Masurca during R,Z[1] and Preracine[2] programmes evidenced the presence of considerable discrepancies between calculation and experiment affecting characteristic integral parameters of blanket. In particular,discrepancies of about 5-10% for U^{238} capture rates and U^{235} fission rates and of about 10% for U^{238} fission rates were observed.

The experimental programme NEFERTITI (<u>NE</u>utronique des regions <u>FERTI</u>-

les à Tapiro Interface) started in 1980 and still in course in the fast
source reactor Tapiro at C.S.N. Casaccia,is expected to supply a set of
experimental data which are needed to test -and possibly improve- the
calculational methods adopted in reactor design.

NEFERTITI PROGRAMME

The Nefertiti programme is based upon a parametric approach to the
above mentioned problems in which blanket properties are studied as a
function of:
-neutron spectrum entering into the blanket
-blanket composition
-composition of the reflector zone placed behind the blanket.

Experimental results obtained from this programme are expected to
allow validation of calculation methods utilized for the determination of
the spatial distribution,within blanket regions,of U^{238}capture rate,U^{235},
U^{238} and Pu^{239}fission rates and of the following spectral indexes:
-U^{238}fission/U^{235} fission   (F8/F5)
-Pu^{239}fission/U^{235}fission   (F9/F5)
-U^{238}capture/U^{235} fission   (C8/F5)

Fig.1 and table 1 show,respectively,the sequence of experiments and
the elementary cells of the blanket regions.
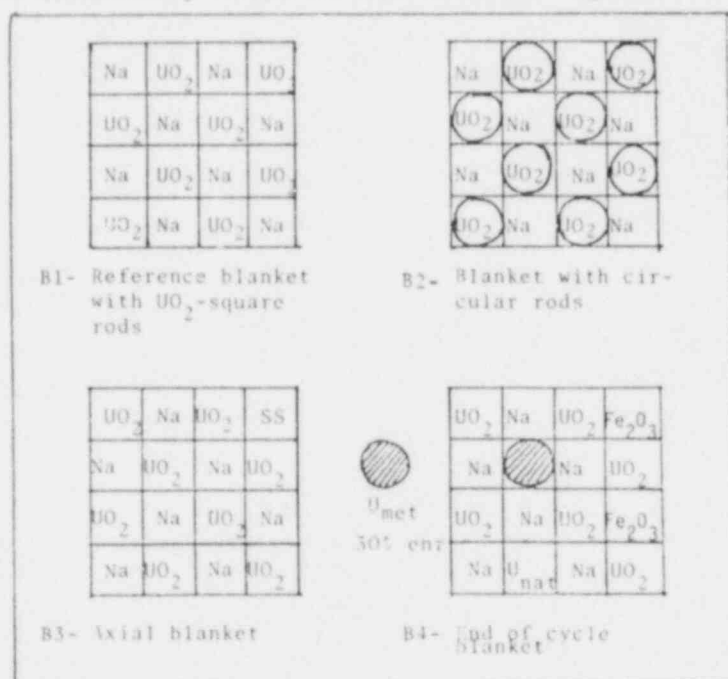
Fig. 1 Blanket elementary cells

Leakage spectra of different LMFBR cores were simulated at the blanket boundary by interposing spectral conversion zones between the source reactor and the blankets themselves. The three conversion zones,which replace a 60° sector of the copper reflector of Tapiro,are denominated R1,R2 and R3. They represente different U^{235}oxide fuel enrichment (respectively 18,25 and 15%).This type of media have spectra typical of large fast power reactor

core zones (fig.2). The results presented in this report have been obtained in C2 configuration which was fed by the R1 spectral conversion region.

The composition of the latter is given in fig.3.
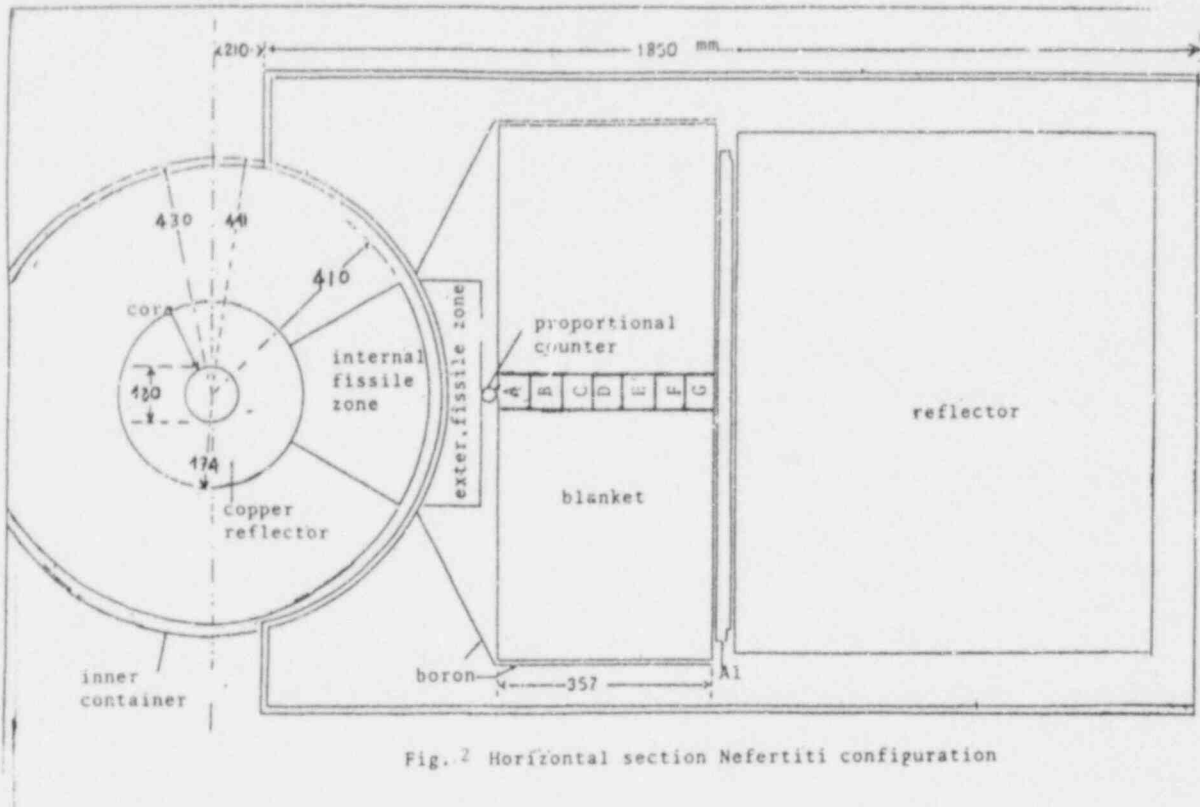
Fig. 2 Horizontal section Nefertiti configuration

Table 1-Nefertiti:experimental programme

Configuration	Spectral conversion zone	Blanket region	Reflector (Vol%)
C1	R1	B1	Na/SS(50/50)
C2	R1	B2	" "
C3	R1	B3	" "
C4	R1	B1	Na(100)
C5	R1	B4	Na/SS(50/50)
C6	R2	B1	" "
C7	R3	B1	" "
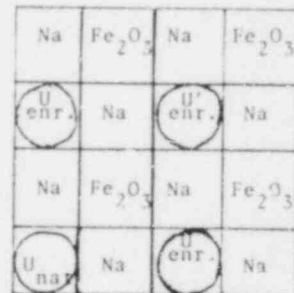
Fig.3 R1 cell

MEASUREMENT METHODS

Measurements of spectral indexes F8/F5,F9/F5 and C8/F5 have been performed by activation foil detectors(table 2)and by fission chambers.

The measurements procedure for F8/F5 and F9/F5 is:
- an index is measured in a reference point by flat fission microchambers. The deposits are put in a face-to-face arrangement.
- Relative reaction rates are measured for each isotope by irradiating foil detectors in the experimental channels.At the same time,a foil de tector for each isotope is irradiated,being placed in the same position (in a mock-up chamber) as the deposit of the pertinent fission chamber.
- Absolute values of reaction rate ratios are obtained by referring the activations of the detectors in the mock-up chambers to the counts from the fission chambers.

Table 2-Detectors characteristics

Detector	Composition	$\emptyset$(mm)	Thickn.
U-enr.	93% U^{235}	12.0	0.1 mm
U-dep.	.40% U^{235}	12.0	0.1 mm
Pu	2.22% Pu^{240} 0.07% Pu^{241}	11.7	0.2 mm

As far as C8/F5 is concerned, the procedure consists in si-multaneous irradiations of de tectors in experimental chan-nels and in a thermal flux po sition. Measurements have been performed radially along the neutron propagation axis, axially at two different ra - dial blanket penetrations and transversally in corrispondence of the cen-tral channel.

Experimental accuracies are $\pm$ 0.5% for all detectors.

CALCULATION METHODS

Neutronic library preparation for R1 and blanket media has been do-ne by cell code Hetaire coupled with Carnaval IV data[3](25 energy groups).

Calculation for the determination of reaction rates and spectral in dexes trends in the blanket have been performed by transport and diffu - sion theories in two dimensional cylindrical geometry by, respectively, Dot 3.5 and Citation codes. Transport calculations utilized S8 angular quadrature approximation. Fig.4 shows the system scheme utilized for Dot 3.5 and Citation calculations.

Table 3-Radial behaviour

Exper. channel	cm in blanket	F9/F5					F8/F5					C8/F5				
		D	$\frac{E-D}{D}$%	T	$\frac{E-T}{T}$%	E	D	$\frac{E-D}{D}$%	T	$\frac{E-T}{T}$%	E	D	$\frac{E-D}{D}$%	T	$\frac{E-T}{T}$%	E
A	2.625	9.636 -1 (")	-0.9	9.419 -1	1.4	9.547 -1	1.239 -2	-6.2	1.262 -2	-7.9	1.162 -2	1.244 -1	8.3	1.297 -1	3.9	1.347 -1
B	7.875	9.348 -1	-2.0	9.192 -1	-0.3	9.163 -1	8.860 -3	-9.2	9.050 -3	-11.1	8.049 -3	1.254 -1	5.0	1.293 -1	1.9	1.317 -1
C	13.125	9.151 -1	-2.1	9.040 -1	-0.9	8.956 -1	6.557 -3	-8.6	6.684 -3	-10.4	5.990 -3	1.256 -1	3.7	1.282 -1	1.6	1.303 -1
D	18.375	9.036 -1	-1.1	8.961 -1	-0.2	8.938 -1	5.024 -3	-8.2	5.153 -3	-10.5	4.611 -3	1.249 -1	3.1	1.265 -1	1.8	1.288 -1
E	23.625	9.015 -1	-1.2	8.964 -1	-0.6	8.909 -1	3.950 -3	-7.0	4.037 -3	-9.0	3.672 -3	1.230 -1	2.7	1.239 -1	1.9	1.263 -1
F	28.875	9.141 -1	-0.9	9.092 -1	-0.2	9.057 -1	3.096 -3	-4.9	3.179 -3	-7.4	2.945 -3	1.188 -1	2.8	1.195 -1	2.2	1.221 -1
G	34.125	9.554 -1	-1.5	9.429 -1	-0.2	9.407 -1	2.219 -3	4.0	2.337 -3	-1.3	2.307 -3	1.105 -1	7.7	1.124 -1	5.9	1.190 -1

D=Diffusion Calculation   T=Transport Calculation   E=Experience   (")Read 9.636 x 10^{-1}
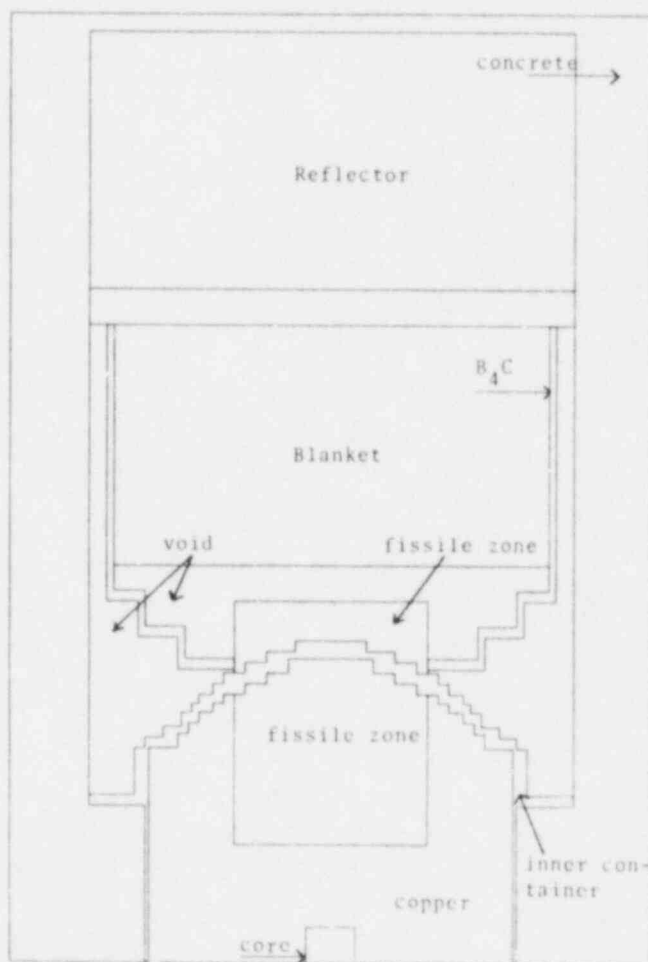
Fig.4 Calculation Model

C2 CONFIGURATION RESULTS

Radial behaviour of spectral indexes

Table 3 shows the experiment-calculation comparisons for the indexes F9/F5,F8/F5,C8/F5. The following conclusions can be drawn:
- Index F9/F5:experimental results for all the measurement points -with the exception of the first- are slightly overpredicted (within 1%) by transport calculations.As far as the first measurement point is concerned,it must be noted that it is very close to the P¹ᵗ blanket interface. Calculations are traditionally less accurate in interface regions, and our case is no exception. In fact,a 1.4% discrepancy is observed, the experiment being underestimated.
- Index F8/F5:the experimental results are systematically overestimated. The discrepancy is about 10% for most of the inner points,but decreases in the vicinity of interfaces,reaching 1.3% at the blanket-reflector boundary.
- Index C8/F5:the experimental results are underestimated and the differences,always below 6%,increase near the interface R1-blanket and blanket-reflector.

Effects of axial leakage

In order to determine the effects of the asymmetry of the experimental configuration,not representable in a two dimensional calculation, we have measured U^{235} and U^{238} fission rates at two different blanket penetrations.

The results which allowed to assess the effects of this asymmetry are summarized in table 4.

The decrease of F8/F5 values at the bottom of the blanket region is attributed to the strong thermalising effect of the reactor room floor.

Transversal behaviour

The blanket is surrounded by a boron carbide shield to minimize neutron reflection by concrete. Calculated and measured U^{235} fission rates at the traverse corresponding to the central channel are shown in table 5.

At the boundary the calculation-experiment deviation increases and

this is to be accounted to calculation model. In the central zone there is a good agreement and therefore the 2-D model looks suita̲ble to reproduce the system geometry.

Table 4- U^{235} and U^{238} fission rates: axial behaviour

Cm (")	Channel B		Channel F	
	F8	F5	F8	F5
-38.36	.234	.721	.442	.676
-28.67	.365	.804	.636	.779
-18.93	.651	.887	.798	.893
-13.69	.802	.927	.869	.944
- 6.49	.933	.983	.971	.988
0.78	1.000	1.000	1.000	1.000
6.89	.958	.980	.996	.985
14.21	.837	.922	.915	.938
22.84	.627	.854	.780	.852
32.36	.503	.732	.615	.738
42.07	.267	.625	.453	.658

"From system center (positive up)

Table 5- U^{235} fission rate:transversal behaviour at channel D quota

Transv. chann.	Cm(")	Exp.	Calc.	(E-C)/C%
1	-41.365	.494	.577	-14.4
2	-36.115	.589	.628	- 6.2
3	-30.865	.677	.691	- 2.0
4	-25.615	.761	.756	0.7
5	-20.365	.836	.829	0.8
6	-15.115	.J00	.892	0.9
7	- 9.865	---	.946	---
8	- 4.615	.981	.985	- 0.4
9	0.635	1.0	1.0	---
10	5.885	.982	.985	- 0.3
11	11.135	.947	.946	0.1
12	16.385	.891	.892	- 0.1
13	21.635	.823	.829	- 0.7
14	26.885	.747	.756	- 1.2
15	32.135	.662	.691	- 4.2
16	37.385	.571	.628	- 9.1
17	42.635	.475	.577	-17.7

"From channel D center

CONCLUSIONS

Calculation-experiment comparisons show systematical dif̲ferences for all indexes.

For F9/F5 this difference is very small,of the order of magnitude of experimental errors.

For F8/F5 and C8/F5 the differences are larger but still acceptable considering that these indexes are very sensiti̲ve to spectral changes.

Preliminary analysis of the discrepancies on these indexes indicates that the contribution of the fast region of the spec̲trum is seriously overestimated, while that of the intermediate region is slightly underestimated.

A detailed analysis is being performed, at present, in particular to assess what is the respective role of calculation methods and basic nuclear data.

Further experiments with different buffer regions - which are already planned - will be needed to validate improved calculation models, particularly for the interface regions.

REFERENCES

1. J.Y.Barrè,J.Boyer,J.C.Mougniot,B.Sicard,Reactor physics and fast po-
   wer breeders:MASURCA core R-Z program,Kiamesha Lake,September 1972.

2. Y.H.Bouget,R.Conversano,M.Cosimi,A.Desprets,P.Hammer,G.Humbert,F.Lyon,
   M.Martini,Physics studies of neutronics problems related to the hete-
   rog neous fast reactor core concept:experimental program PRE-RACINE
   performed on MASURCA,Gatlinburg,April 1978.

3. C.Tournier,P.Garnier,Private Communication

ANALYSIS OF BLANKET-PIN BURNUPS FOR DEPLETED-URANIUM-REFLECTED EBR-II CONFIGURATIONS

D. Meneghetti, E. R. Ebersole, D. A. Kucera, and R. H. Rempert
Argonne National Laboratory
Argonne, Illinois, U.S.A.

ABSTRACT

Calculations and measurements of burnup and plutonium buildup are described for EBR-II depleted-uranium blanket-pins irradiated near core at fixed and at non-fixed locations in the EBR-II blanket.

INTRODUCTION

In the original mode of operation of EBR-II as a demonstration sodium-cooled fast breeder reactor[1] and for the period through run 55 of its use as a fast reactor irradiation-test facility the core configurations were radially-reflected by blanket subassemblies of depleted-uranium metal pins. A radial blanket was retained (except during runs 25A through 29A which had the first two blanket rows replaced by steel-containing reflector subassemblies) through run 55B corresponding to about 54,407 megawatt-days-thermal of reactor operation during 120 loading configurations from August 1964 to April 1972. (Subsequently, the inner three to four rows of blanket subassemblies were replaced by steel-reflector subassemblies and about 142,473 megawatt-days-thermal of additional reactor operation from July 1972 through run 116C in December 1981 have been completed.)

A blanket subassembly contains 19 pins in a normal EBR-II hex duct. The hex duct of stainless steel has 5.82 cm (2.29 in.) flat-to-flat outside dimension and a wall thickness of 0.10 cm (0.040 in.). The depleted-uranium (0.22 wt. percent ^{235}U) pins of 1.10 cm (0.433 in.) outside diameter are sodium-bonded in stainless steel cladding of 1.25 cm (0.493 in.) outside diameter with 0.046 cm (0.018 in.) wall thickness. An un-irradiated blanket subassembly has about 60 volume percent depleted uranium, 17.6 volume percent steel, and 22.4 volume percent sodium.

Calculations and measurements of burnups and plutonium buildups in blanket pins irradiated in both fixed and non-fixed blanket locations near core boundaries are reported here. Burnup is defined as loss of fissile and fertile atoms by fission divided by initial fissile and fertile atoms. The results are reported in two groups. The first group comprises pins irradiated within runs 1 through 24 and having their irradiation locations unchanged during changes in core (and blanket) load-

ings. The second group comprises pins irradiated within runs 29B to 46B at various differing locations and orientations of their subassemblies as the irradiations progressed through the various core (and blanket) loading configurations.

PIN LOCATIONS AND IRRADIATION HISTORIES

The blanket subassembly locations and rotational orientations are shown in Fig. 1 for three of the runs included in the first irradiation group. The locations of the measured pins within their subassemblies are also shown. Some of the changes in run-to-run core periphery are illustrated by comparison of runs 4, 12, and 22. The subassemblies containing the measured pins are fixed in locations and orientations. The run-to-run core loadings and boundaries vary. Listed in the upper portion of Table 1 are the irradiation histories for these pins.

The various run-to-run locations and orientations of the subassemblies containing the pins of the second group are illustrated in Fig. 2. The core loading and periphery of run 36 is shown with all the locations and orientations of the blanket subassemblies of interest superimposed for simplicity. In the analyses, however, the changing run-to-run loadings are taken explicitly into account. Listed in the lower portion of Table 1 are the irradiation histories for these pins.

In both Figs. 1 and 2 only the first seven rows of core and blanket subassemblies are shown. During this range of operations approximately eight additional rows of blanket subassemblies external to those shown were present.

MEASUREMENTS

Burnup and plutonium analyses were made on samples cut from reactor midplane of depleted-uranium blanket pins.

Burnup analyses were made by isotope dilution mass spectrometry using ^{139}La as the burnup monitor with enriched ^{138}La as the internal standard. A measured quantity of the ^{138}La standard was added to a weighed aliquot of the sample solution and then lanthanum was separated chemically from the uranium and other fission products for mass spectrometry analysis. Burnup was determined for each sample from the mass spectrometry data and the effective fission yield of ^{139}La (5.95%) calculated from ^{139}La fission yields[2] for ^{238}U (5.94%), ^{235}U (6.76%) and ^{239}Pu (5.51%), and the respective fission rates of these materials. The accuracy of the burnup measurements is conservatively estimated to be ±3% of the reported values.
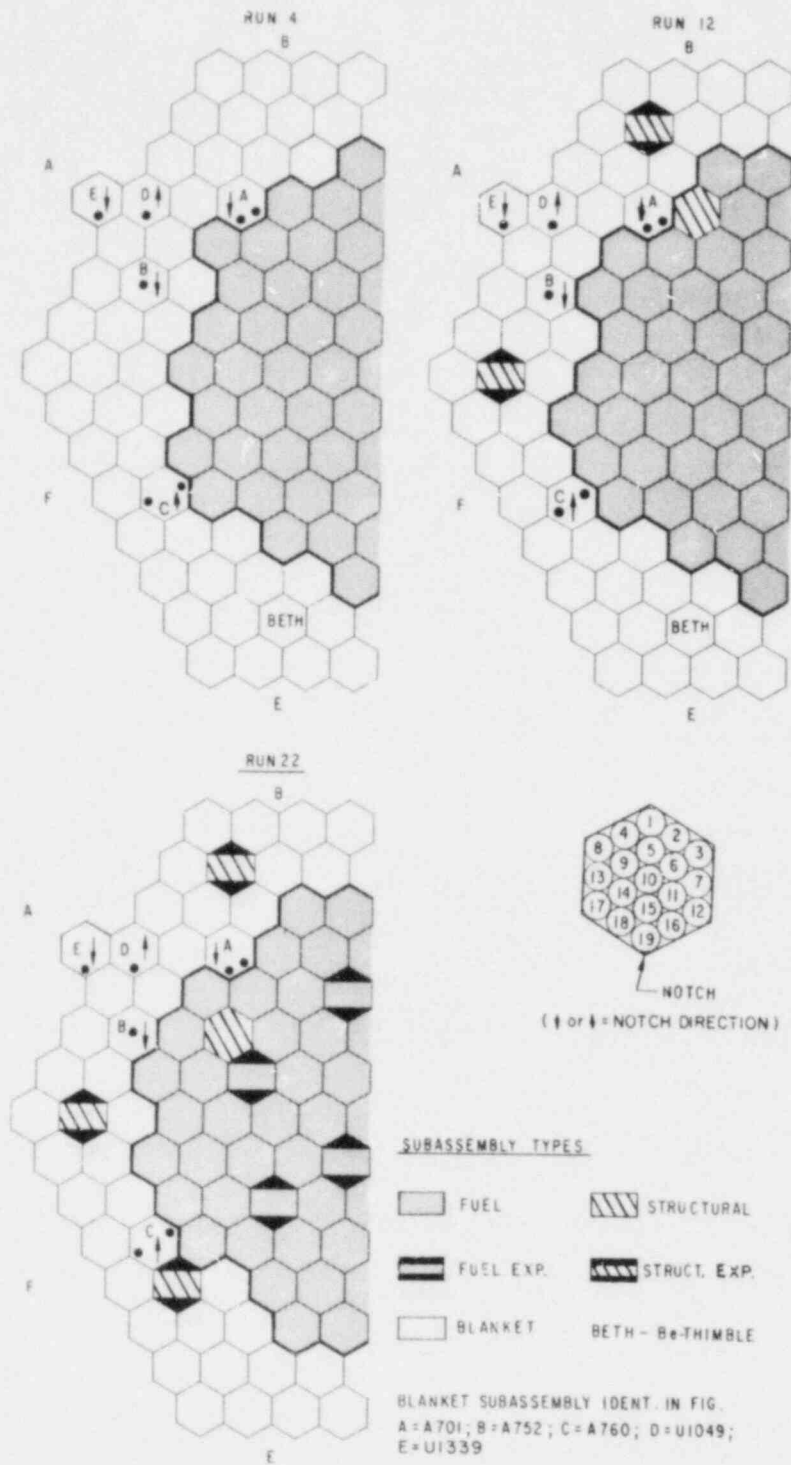
Fig. 1.   Locations of the Fixed-Location
              Blanket Pins.

Table 1. Irradiation Histories of the Blanket Pins

Subassembly Ident. (Pin No's.)[a]	Subassembly Location (Orientation)[a]	Run In	Run Out	MWd[b]
A701(19,12)	6A5 (↓)	1	23	11,615
A752(10)	7A3 (↓)	1	22	10,925
A760(17,3)	7F4 (↑)	1	24	12,245
U1049(1)	8A5 (↑)	1	24	12,245
U1339(19)	9A5 (↓)	1	24	12,245
U1124(10)	12E6	1	22	10,925
A795(19)	7B3 (↓)	29B	35	8,102
A795(19)	7D4 (↑)	36A	40B	6,504
A794(16,12,8)	7E5 (↑)	29B	35	8,102
A794(16,12,8)	7B4 (↓)	36A	41B	7,622
A787(3,2,10)	6C1 (↑)	27H	28A	456
A787(3,2,10)	7A5 (↑)	29B	33B	5,768
A787(3,2,10)	7C4 (↑)	34A	42	11,300
A897(3)[c]	7F6 (↓)	29B	44A	19,318
A896(19)	7C5 (↓)	29B	29C	229
A896(19)	6B5 (↓)	30D	30E	158
A896(19)	6C1 (↓)	37	38B	2,566
A896(19)	6D4 (↑)	39B	39C	600
A896(19)	7B5 (↓)	40A	46B	9,430

[a] Pin 10 is central pin of subassembly. Pin 19 is adjacent to the orientation-direction notch on the subassembly. Arrows show down or up notch direction relative to the loading diagrams such as shown in Figs. 1 and 2.

[b] Nominal powers. In the calculational analyses actual powers equal to nominal values for Runs 1-29D, 94% of nominal for Runs 30A-45B, and 96% of nominal from Run 46A are used.

[c] Irradiated at fixed-location during irradiation of second batch.

A measured quantity of ^{242}Pu, previously standardized against a National Bureau of Standards ^{239}Pu standard, was added to a weighed aliquot of the sample solution and then plutonium was separated chemically from the depleted uranium and fission products for isotope dilution mass spectrometry. Both the isotopic distribution and total plutonium production was determined for each sample from the mass spectrometry data. The precision and accuracy of the plutonium numbers are conservatively estimated to be ±2% of the reported values.
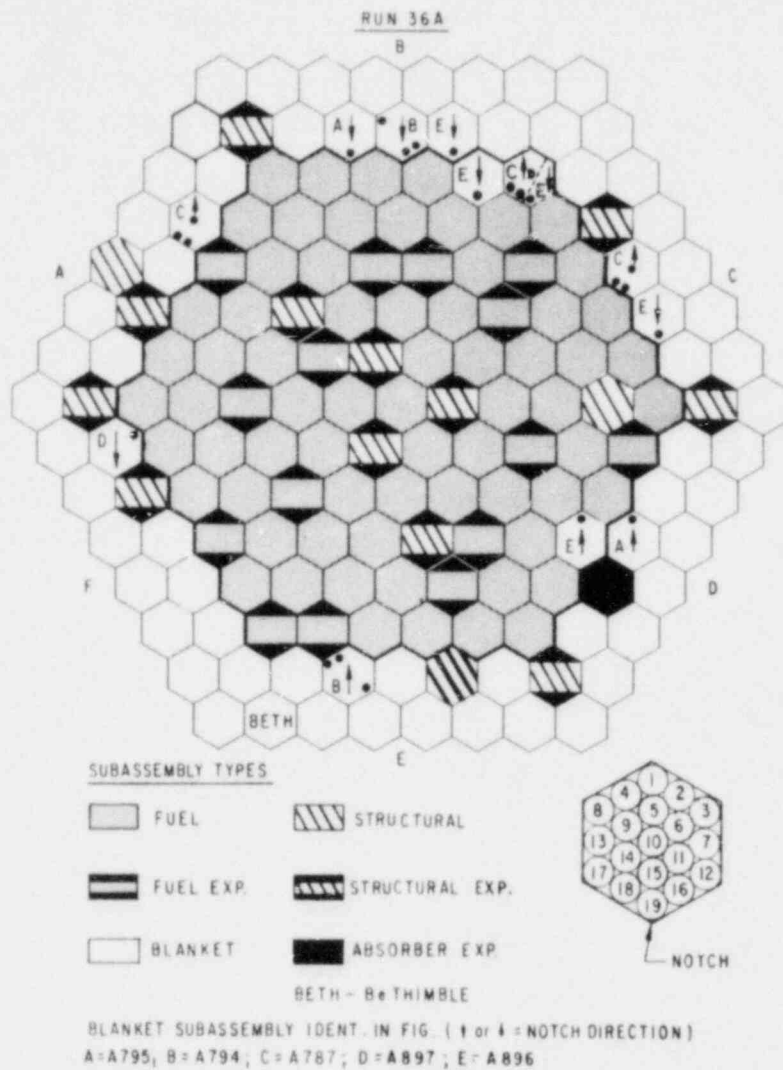
Fig. 2.   Locations of the Non-Fixed-Location
Blanket Pins.

CALCULATIONS

Comparison of calculated values with measured values for experimental fuel elements irradiated in the EBR-II core during this range of runs has been reported.[3] The computational procedure used for that comparison allows and compensates for changes in subassembly location and orientation. This procedure has been applied to the analysis of the present blanket pin study.

Computationally, compositional changes due to depletion and buildup are expressed by a heavy-isotope burnup matrix. A burnup matrix can be computed for each of the four mesh points about a pin location of interest, assuming initially the unirradiated blanket-material composition. The matrices at the mesh points are calculated using multigroup fluxes for 'ne run loadings from the EBR-II archival files[4] for this range of runs. (These 14-energy-group fluxes are from XY-geometry discrete-ordinate solutions, in S_4 approximation, having each hexagonal-shapeu core and blanket subassembly simulated by a rectangle of four mesh points and having each subassembly's average isotopic changes considered from run-to-run. The cross sections used are from a 14-energy-group set, which were collapsed from a 29-group set derived using the MC^2 code[5] with the ENDF/B-I cross section data used for many EBR-II calculations during those runs. They were collapsed sep rately for the core, inner blanket, outer blanket, and radial reflector regions. The lower energy values of the groups are 2.23 MeV, 1.35 MeV, 0.821 MeV, 0.302 MeV, 0.111 MeV, 40.9 keV, 15.0 keV, 5.53 keV, 3.35 keV, 2.03 keV, 0.454 keV, 0.101 keV, 13.7 eV, and 0.683 eV. The same cross section set has been used for the individual pin depletion and buildup reported herein.) For the location of the pins of interest the nearest four accumulated-burnup matrices, over all runs of interest, are spatially interpolated to the positions of the measured blanket pins.

Estimates of effects of using more recent ENDF/B libraries are subsequently described.

RESULTS AND DISCUSSION

Measured and calculated values of atom percent burnup, milligrams of plutonium per gram of original uranium, and atom percent plutonium-240 in total plutonium are listed in the upper and lower parts of Table 2, respectively, for the first and second groups of blanket pins. The blanket pins within each group have not been irradiated for the same megawatt-days; therefore, the calculated and measured values shown in Figs. 3 and 4 have all been normalized to 15,000 megawatt-days-thermal of energy before plotting the values as functions of megawatt-day-weighted radial distances from core center. The straight lines simply connect the points and should not be interpreted as radial interpolation functions.

Two aspects of the correlations should be considered. First, how does the envelope of calculated values compare in absolute value with the envelope of measured values, i.e., is there a general bias? Second, how do the individual ratios of calculations and measurements vary from pin-to-pin? If variations occur in the latter ratios then application of a general biasing factor may not suffice for predictions of non-measured pins in the irradiation.

Table 2. Burnup and Plutonium in the Blanket Pins

Subassembly Ident. (Pin No.)	Burnup (at.%)		Pu/U (mg/g)[a]		^{240}Pu/Pu (at. %)[b]	
	Meas.[c]	Calc.	Meas.	Calc.	Meas.	Calc.
A701(19)	0.218	0.23(1)	4.92	5.4(0)	0.36	0.27
A701(12)	0.209	0.22(4)	4.93	5.5(5)	0.38	0.28
A752(10)	0.087	0.091	3.51	3.8(3)	0.27	0.20
A760(17)	0.193	0.19(7)	4.59	5.0(5)	0.35	0.25
A760(3)	0.076	0.067	3.37	3.8(6)	0.27	0.21
U1046(1)	--	0.051	3.47	3.4(7)	0.27	0.19
U1339(19)	--	0.020	2.47	2.3(7)	0.20	0.13
U1124(10)	--	--	0.52	--	0.05	--
A795(19)	0.260	0.23(7)	5.32	5.7(6)	0.39	0.29
A794(16)	0.259	0.23(0)	5.58	6.2(2)	0.42	0.29
A794(12)	0.263	0.19(9)	5.80	6.0(3)	0.45	0.28
A794(8)	0.105	0.12(2)	4.94	5.7(5)	0.42	0.25
A787(3)	0.253	0.25(7)	5.80	6.8(8)	0.46	0.35
A787(2)	0.237	0.25(5)	5.74	6.8(7)	0.46	0.35
A787(10)	0.165	0.19(7)	5.24	6.4(8)	0.43	0.34
A897(3)[d]	0.294	0.29(8)	6.30	7.2(9)	0.48	0.37
A896(19)	0.177	0.22(7)	4.13	5.3(0)	0.33	0.26

[a]Total plutonium relative to initial total uranium.

[b]Atom percent ^{240}Pu in the plutonium.

[c]Using effective fission-yield of 5.95 at. % for ^{139}La.

[d]Irradiated at fixed-location during irradiation of second batch.

In Fig. 3 the comparisons for the first group show the calculated burnups to be within about ten percent of measured values. The plutonium-buildup calculated values are generally larger than measured by about 15 percent in near-core subassemblies, and the calculated plutonium-240 in plutonium about 30 percent smaller than measured.

In Fig. 4 comparisons for the second group show that the values of calculated plutonium-240 in plutonium are again about 30% smaller than measured and that the plutonium buildup values on the average are about 15 percent larger than measured. These exhibit some pin-to-pin variations. The burnup comparisons exhibit extremes of pin-to-pin error of about 25 percent smaller to about 30 percent larger than measured. These
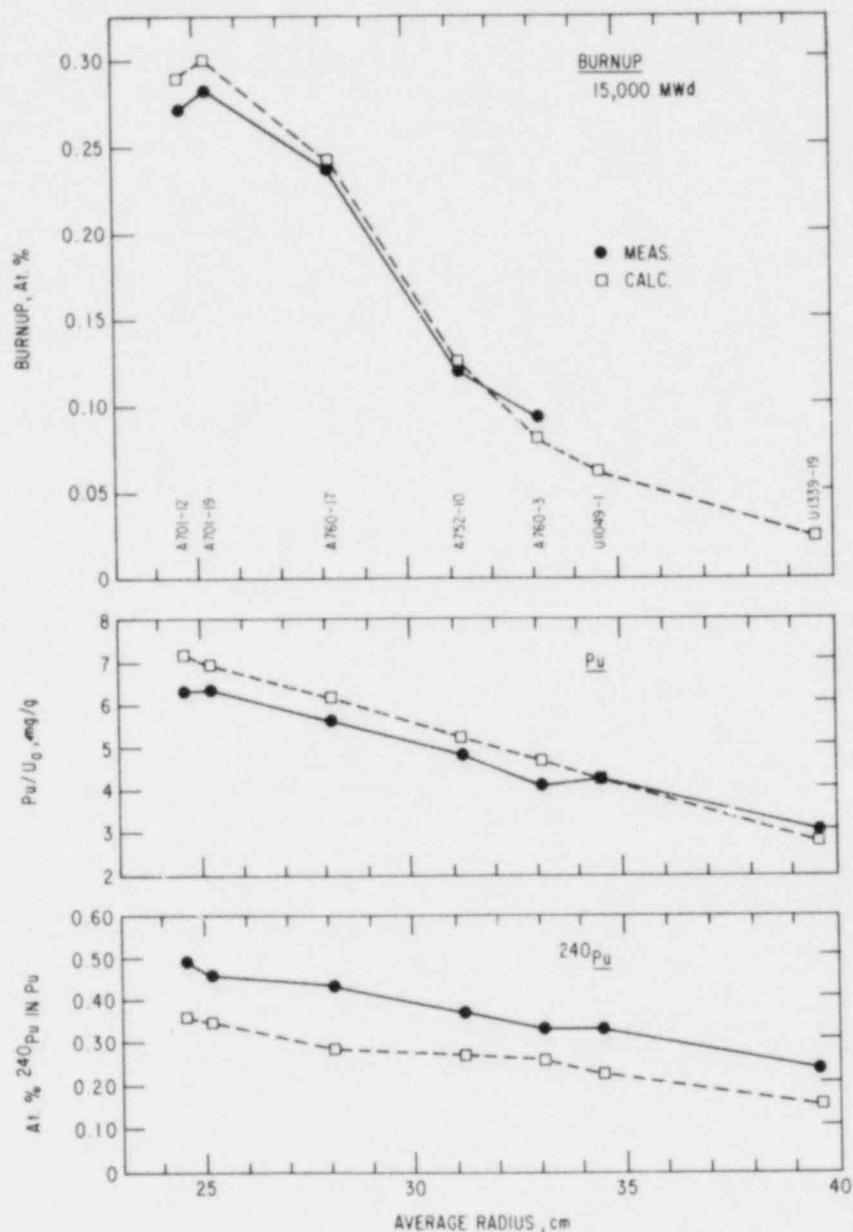
Fig. 3. Burnups and Plutonium Contents of the Fixed-
Location Blanket Pins.

large differences are in pin 12 of subassembly A794 and pin 19 of sub-
assembly A896, respectively. The causes (whether calculational, experi-
mental, or both) are not currently evident. The other pins of this
batch, however, are calculated within 20 percent of measured values.

The effects upon the overall bias levels of using more energy groups
and group cross sections based upon ENDF/B-III and ENDF/B-V cross section
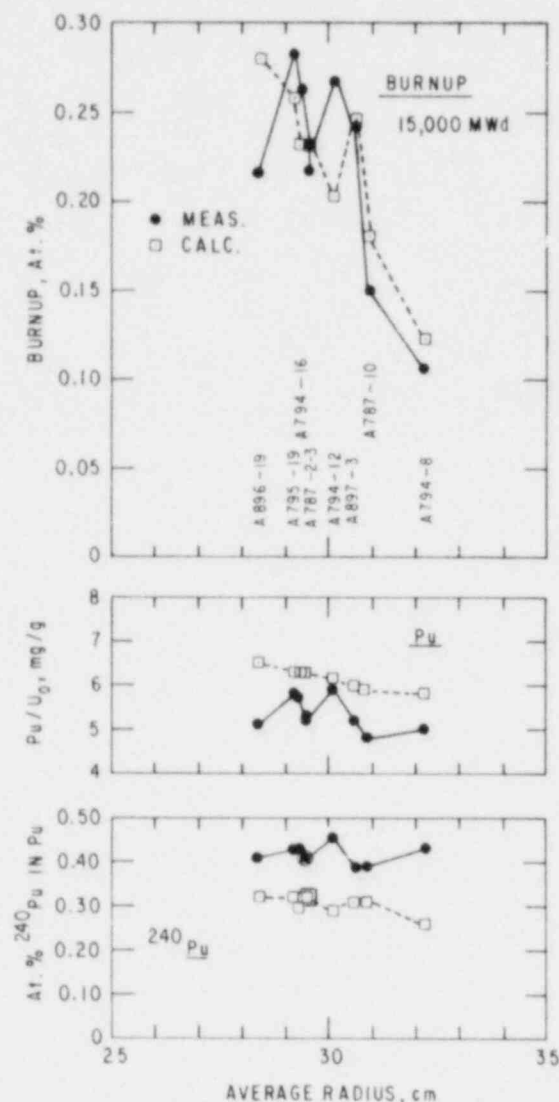
Fig. 4. Burnups and Plutonium Contents of the Non-Fixed-Location Blanket Pins.

libraries have been estimated by intercomparison calculations using a generic RZ-geometry representation for this range of runs. Thus, 29 groups instead of 14 groups would decrease burnup about five percent and retain about the same plutonium and plutonium-240 fraction. ENDF/B-III would increase burnup about five percent, decrease plutonium about five percent, and increase plutonium-240 fraction about 15 percent. ENDF/B-V relative to ENDF/B-III would increase burnup about 20 percent. If in the latter the Maxwellian fission spectrum of Version III (or I) is used instead of the Watt fission spectrum of Version V ENDF/B-V would instead increase burnup about ten percent.

REFERENCES

1. L. J. Koch, et al., Proc. 2nd UN Int. Conf. PUAE 9, 323 (1958).

2. "Fast Reactor Fission Yields for U-233, U-235, U-238, Pu-239, and Recommendations for the Determination of Burnup on FBR Mixed-Oxide Fuels: An Interim Project Report." Edited by W. J. Maeck, ICP-1050-1 (1955).

3. D. A. Kucera, D. Meneghetti, and E. R. Ebersole, "Analysis of Burnups in Experimental Fuel Elements Irradiated in EBR-II," Trans. Am. Nucl. Soc. 23, 573 (1976).

4. D. Meneghetti, E. R. Ebersole, and Phyllis Walker, "Analysis of Burnups in EBR-II Fuel Elements," Nucl. Tech. 25, 406 (1975).

5. B. J. Toppel, A. J. Rago, and D. M. O'Shea, "MC^2, A Code to Calculate Multigroup Cross Sections," ANL-7318 (1967).

DOSIMETRY WORK AND CALCULATIONS
IN CONNECTION WITH THE IRRADIATION OF LARGE DEVICES
IN THE HIGH FLUX MATERIALS TESTING REACTOR BR2

Ch. De Raedt, L. Leenders, H. Tourwé, SCK/CEN, Mol, Belgium
H. Farrar IV, Rockwell International Corporation, California, USA

INTRODUCTION

Since about fifteen years the high flux reactor BR2 is involved in the testing of fast reactor fuel pins. In order to simulate the fast reactor neutron environment most devices are irradiated under cadmium screen, cutting off the thermal flux component. Extensive neutronic calculations are performed to help the optimization of the fuel bundle design. The actual experiments are preceded by irradiations of their mock-ups in BRO2, the zero power model of BR2. The mock-up irradiations, supported by supplementary calculations, are performed for the determination of the main neutronic characteristics of the irradiation proper in BR2 and for the determination of the corresponding operation data. At the end of the BR2 irradiation the experimental results, such as burn-ups, neutron fluences, helium production in the fuel pin claddings, etc. are correlated by neutronic calculations in order to examine the consistency of the post-irradiation results and to validate the routine calculation procedure and cross-section data employed.

A comparison is made in this paper between neutronic calculation results and some post-irradiation data for MOL 7D, a cadmium screened sodium cooled loop containing a nineteen fuel pin bundle.

THE MOL 7D LOOP

The MOL 7D loop (fig. 1) was irradiated in BR2 from June 1975 till October 1976. It contained 19 sodium cooled UO_2-PuO_2 fuel pins (with Pu/(U+Pu) $\approx$ 30 % and $^{235}U/U \approx$ 83 %). The fuel pin claddings, with integral fins, were made of WN 4988 stainless steel. The fuel pin bundle was contained in a hexagonal AISI-316 stainless steel "wrapper tube" at the outer side of which vertical grooves had been machined. In these grooves thermocouples as well as - in one groove - a large number of neutron dosimeters and helium fluence monitors were located. As shown on the figure, the fuel pin bundle was further surrounded by pressure tubes, by a cadmium screen and by six small "driver" fuel elements located in a large cylindrical

aluminium plug, the whole occupying the central channel H1 of BR2.
The burn-up reached in the fuel pins amounted to about 75 000 MWd/t
UO_2-PuO_2.

EXPERIMENTAL TECHNIQUES EMPLOYED FOR THE CHARACTERIZATION OF THE
MOL 7D IRRADIATION

The dosimetry techniques applied in general to loops irra-
diated in BR2 are described in [1]. In the case of MOL 7D a
special feature was the presence of a large number of neutron dosi-
meters, helium accumulation fluence monitors (HAFM's) and stainless
steel samples - 58 in total - located in a stainless steel micro-
tube in one of the grooves of the wrapper tube, as mentioned above.
After the irradiation the activation of the dosimeters was counted
at SCK/CEN while helium production measurements were performed at
Rockwell International utilizing the technique described in [2].

The main SCK/CEN dosimetry results concern :
- the $^{54}Fe(n,p)^{54}Mn$ reaction in the dosimeters of the wrapper tube
  and in the pin cladding samples
- the $^{59}Co(n,\gamma)^{60}Co$ reaction in the dosimeters of the wrapper tube
  and in the pin cladding samples (as impurity in the claddings).
  Special 1 % Co/V alloys were developed by EURATOM, Geel, in order
  to resist the high irradiation temperature
- the $^{235}U(n,f)$, $^{239}Pu(n,f)$, $^{238}U(n,f)$ and $^{237}Np(n,f)$ reactions in
  the wrapper tube (by measuring the ^{137}Cs activity and taking into
  account the fission yields recommended in [3], when available).
  All fission dosimeters were made of well-characterized materials
  containing minimum amounts of impurities and were encapsulated in
  vanadium according to the technology described in [4]. These
  dosimeters were supplied by HEDL.

The cladding samples considered pertain to the pins shaded black on
fig. 1. They consist of small rings (1 mm thick) cut at various
axial levels.

The Rockwell International dosimetry results concern :
- the helium production in the ^{10}B and ^{6}Li of the natural boron and
  ^{6}LiF dosimeters (HAFM's)
- the helium production in the claddings (samples also pertaining
  to the pins shaded black on fig. 1). Moreover the boron content
  of the WN 4988 stainless steel used for the cladding was measured
  (4.0 weight ppm) after the irradiation of a sample in a nearly
  pure thermal neutron flux.

Gamma spectrometry results were obtained by measuring the
fission and the activation products accumulated in the pins during
the irradiation (these measurements are noted NDT, non-destructive
testing, in the tables).

Seven fuel pins were available in the BR2 hot-cells for the
non-destructive gamma spectrometry analysis as indicated in fig. 1.
At the time of the analysis (about five years after the irradiation),
the following isotopes were detected with a significant precision :

as fission products : - ^{106}Rh, fissions in plutonium

- ^{134}Cs, burn-up x $\emptyset$t

- ^{137}Cs, burn-up

- ^{154}Eu, complex formation.

^{106}Rh and ^{154}Eu are relatively stable within the fuel, while ^{134}Cs
and ^{137}Cs are volatile and migrate during irradiation. The ^{137}Cs
activities, when integrated over the whole length of the fuel pins,
remain nevertheless representative of the fissions in these pins,
as will appear in table 2.

as activation products : - ^{54}Mn, fast neutron flux

- ^{60}Co, epithermal neutron flux.

These measurements give axial distributions along the fuel pins
as well as pin to pin distributions. When adequate standards are
used for calibration, absolute values of given parameters can be
obtained. Techniques and features are detailed in [5]. One of the
objectives of the present work was to validate these non-destructive
techniques.

CALCULATION METHODS EMPLOYED FOR THE CORRELATION OF THE EXPERIMENTAL RESULTS IN THE MOL 7D IRRADIATION

The calculation methods employed for the analysis of the MOL 7D
irradiation were the same as those applied to the MFBS VI loop as
described in [6]. The basic code used to determine the neutron
field was the one-dimensional neutron transport code DTF-IV [7],
containing several improvements made at SCK/CEN and flanked by
preprocessing and postprocessing routines, the whole called the
MULCOS code system. This system is used together with a 40 energy
group cross-section library, including self-shielding factors (ABBN
formalism), elaborated at SCK/CEN for the study of coupled fast -
thermal systems. In all the calculations the geometrical data of
the experimental device were detailed as carefully as possible.

232

The intermediate and the outer annuli of fuel pins in the bundle were homogenized (fuel + cladding + coolant) taking into account the energy dependent local flux depressions, the resonance self-shieldings and the finite array character of these fuel pins, as explained in [8].

For the nuclides used as detectors, the ENDF/B V dosimetry file was used, reduced to the 40 energy group scheme of the SCK/CEN library and with an extension of 4 supplementary groups between 10.5 MeV and 20 MeV for the high energy detectors (the 40 energy group flux chart was prolonged beyond 10.5 MeV by a fission spectrum). For the helium production by threshold (n,α) reactions, the data given in [9] were utilized.

EXPERIMENTAL RESULTS OBTAINED FOR THE MOL 7D IRRADIATION. COMPARISON WITH CALCULATIONS

Two features of the MOL 7D experiment have first to be pointed out : the shape of the neutron spectrum and the high value of the burn-up. In the neutron spectrum, the epithermal part is important; most of the fissions occur in the resonance energy range and, from the dosimetry point of view, the significance of some measured data is not easy to assess accurately. This is the case for fission product measurements in highly burnt ^{238}U and ^{237}Np dosimeters. Helium production in pin cladding samples is also difficult to analyse by reason of the simultaneous contribution of epithermal and fast neutrons.

Four types of results are considered in this paper :

- quantities measured in and calculated for the dosimeters located on the wrapper tube : the values are given in table 1 in absolute units. For the calculations, the flux chart was normalized by equalizing the calculated ^{235}U fission rate to the experimental one, taking into account in the calculation the burn-up of the dosimeters during the irradiation (2.55 x 10^7s equivalent at full power). This normalization leads to a total neutron fluence of 2.17 x 10^{22}n/cm^2 corresponding to a total neutron flux of 8.51 x 10^{14}n/cm^{2}s. Once normalized, the calculated flux chart was kept as such for all reaction rate calculations.
The analysis of the ^{137}Cs activity measurements in the fissile dosimeters does not include correction for the burn-up of the dosimeters themselves. As for ^{235}U, the burn-up effect in ^{239}Pu, ^{238}U and ^{237}Np is included in the fission rate calculation. This correction is straightforward for ^{235}U and ^{239}Pu. For ^{238}U, neutron capture in ^{238}U and subsequent fission in ^{239}Pu are predominant whereas ^{237}Np is partially transformed into ^{238}Np, ^{238}Pu

and, to a smaller extent, into ^{239}Pu, all fissionable by low energy neutrons. The ^{137}Cs yields used in the experimental determination of the fission rates in the ^{238}U and ^{237}Np dosimeters were respectively 0.0676 ± 0.0024 (3.5 %) and 0.0650 ± 0.0065 (± 10 %), i.e. the yields for ^{239}Pu and ^{237}Np respectively, but with an uncertainty margin increased to take into account the influence of the other isotopes.

The helium production in ^{10}B and ^{6}Li was also calculated taking into account the burn-up of the targets, for direct comparison with the measured values.

The calculations are valid for the horizontal plane at about the maximum of the axial distribution. The axial distribution measured with ^{59}Co$(n,\gamma)^{60}$Co was used to convert experimental data obtained at other levels.

- radial distributions over the fuel pin bundle of the fissions in the fuel pins, of the helium production, and of the ^{59}Co$(n,\gamma)^{60}$Co and the ^{54}Fe$(n,p)^{54}$Mn reaction rates in the claddings are given in table 2, normalized for each reaction type to an average valu of 1.00 over all fuel pins.

- fuel pin bundle averaged absolute values of the helium production in the claddings and of the ^{59}Co$(n,\gamma)^{60}$Co and the ^{54}Fe$(n,p)^{54}$Mn reaction rates in the claddings are given in table 3.

- radial distributions over the fuel pin bundle and the wrapper tube are shown on fig. 2, with all distributions normalized to 1.00 in the wrapper tube. Fig. 2 also contains the measured and calculated distributions determined for the mock-up of MOL 7D in BR02 (the zero-power nuclear model of BR2) before the irradiation proper and presented in [1].

DISCUSSION OF THE RESULTS

Discussion of table 1

- An overall examination of the C/M values in table 1 indicates first a satisfactory agreement within the error margins for ^{235}U, ^{239}Pu, ^{10}B and ^{6}Li with respect to each other, and the reliability of the calculation of the low energy tail, more particularly around the cadmium cut-off. This is confirmed by previous measurements in BR02. Secondly, the responses of the ^{238}U, ^{237}Np and ^{59}Co dosimeters appear to be not consistent according to the calculation which overestimates these responses predominantly sensitive to epithermal (resonance) neutrons (see below). Finally, there is a general trend in the calculation to

underestimate by about 10 to 15 % the fast flux as measured with threshold reactions such as $^{54}Fe(n,p)$ with respect to the low energy flux. This is confirmed by the C/M values in table 3.

- The theoretical analysis of the response of the ^{238}U and ^{237}Np dosimeters gives the following results. The fissions in the ^{238}U dosimeters are due for about 10 % only to fast ^{238}U fissions and for about 90 % to fissions in ^{239}Pu. The ^{239}Pu producing (n,γ) reaction in ^{238}U is hence of capital importance. An explanation of the discrepancy in C/M could be that narrow dips in the neutron spectrum due to the presence of ^{238}U in the fuel pins are not well represented in the calculation, mainly at the $^{238}U(n,\gamma)$ resonance energies. An investigation of this problem is planned through $^{238}U(n,\gamma)$ measurements in BR02. Concerning the fission rate in the ^{237}Np dosimeters, the fissions occur, according to the calculation, for 41 % in ^{237}Np (fast energy domain), for 19 % in ^{238}Np (thermal + epithermal energy domain), for 36 % in ^{238}Pu (thermal + epithermal energy domain) and for 4 % in ^{239}Pu (thermal + epithermal energy domain); the formation chains of the fissile nuclides become longer and longer and moreover the cross-sections used are known with less precision (five-group cross-sections [10]) than those used for most of the other reactions considered in this paper.

From what precedes it may be concluded that the ^{238}U and ^{237}Np fissile dosimeters do not detect mainly fissions in the fast energy domain in an experiment such as MOL 7D and also that the interpretation of their results is not easy.*

- The $^{59}Co(n,\gamma)^{60}Co$ reaction rate is about 20 % higher in the calculations than measured. The 132 eV resonance (in an energy group contributing for 76 % to the whole) is probably unsufficiently shielded in the spectrum calculations.

Discussion of table 2

A very good consistency exists between the different techniques used to determine relative fission density distributions across the bundle. BR02 results have been added for comparison [1]; from these results, it was expected to obtain very similar distributions from ^{137}Cs measurements (U and Pu fissions) and from ^{106}Rh measurements (Pu fissions). The validity of the procedure applied for integrating the ^{137}Cs activity over the length of the pin must be emphasized. Fig. 3 shows clearly the effect of Cs migration and deposition at particular locations, depending on temperature variations (peaking at the extremities of the fuel column) or gaps between pellets (corresponding to narrow dips in the ^{106}Rh distribution).

---

*Note that in the ^{239}Pu dosimeter 93.8 % of the calculated fissions occur in ^{239}Pu, 0.2 % in ^{240}Pu and 6.0 % in ^{241}Pu.

The radial distributions measured for helium, ^{60}Co and ^{54}Mn agree in general with the calculations (the experimental errors are of pure statistical nature as the values are relative). The low value of the helium content and of the ^{60}Co activity (DT confirms the NDT results in this case) in the central pin cannot be explained at present.

Discussion of table 3

Considering first the ^{54}Fe(n,p)^{54}Mn reaction rate, it is observed that C/M (DT) = 0.87, just as in table 1. This means that the measurements of the Fe dosimeters located on the wrapper tube are fully consistent with the measurements of the cladding samples. This is illustrated in fig. 2 where the curves ^{54}Fe(n,p) and ^{115}In(n,n') - the latter obtained in BRO2 - agree with each other and are supported by the calculations.
The discrepancies C/M (DT) = 0.87 and C/M (NDT) = 0.81 suggest an underestimation of the fast flux component in the calculations. It must be remembered that the calculations are normalized on the ^{235}U fission rate measured on the wrapper tube (1σ = 7 %), which itself agrees with the helium production in ^{10}B (1σ = 3 %). This latter is a good reference, as well for the measurements as for the calculations.

The second series of results in table 3, the helium production measurements in the steel of the pin claddings, confirms this tendency. An important fraction of the helium production (77 %) is indeed due to the fast neutrons. The remaining discrepancy in C/M = 0.74 could be attributed to the fission spectrum averaged cross-sections for helium production in Fe, Cr, Ni and N used in the calculations. The nitrogen concentration, 710 ppm according to the fabrication certificate, is another source of uncertainty which requires further analysis. As to the boron concentration, as mentioned before, it was measured by Rockwell International with a sufficient accuracy for the present application : 4.0 ± 0.3 ppm; the resulting uncertainty is only 1 to 2 %.

Finally, the agreement of the DT and the NDT measurements of ^{54}Fe(n,p)^{54}Mn appears satisfactory : gamma scanning of entire fuel pins can provide the fast fluence on the cladding with an accuracy certainly better than 10 %.

CONCLUSIONS

The appraisal of the consistency of dosimetry results on the basis of detailed calculations is essential to assess the signifi-

cance and the reliability of experimental results in the analysis of experiments such as MOL 7D. Simple unfolding procedure is not applicable for different reasons :

- important space dependence, specially for the fission rates from the dosimeter position to the fuel pins, and therefore necessity to measure on fuel pin materials

- presence of multiple reactions in these fuel pin materials and also in some dosimeters (238U, 237Np), enhanced by the high burn-up.

The validity of the calculation, as to its ability to produce reliable spatial variation of reaction rates and flux spectra, is tested with the aid of BRO2 results. Further measurements are still necessary at present to clarify some discrepancies.

Taking into account the underestimation of the high to low energy flux ratio in the calculation, it is then expected to reach a global consistency of $\pm$ 10 %. The results presented in the present paper have to be completed by the analysis of the fuel burn-up data obtained from radiochemical measurements.

ACKNOWLEDGEMENTS

REFERENCES

[1] J. Debrue, G. De Leeuw-Gierts, S. De Leeuw, Ch. De Raedt, A. Fabry, L. Leenders, N. Maene, R.Menil, "Dosimetry work in connection with irradiations in the high flux materials testing reactor BR2," First ASTM-EURATOM symposium on reactor dosimetry, Petten, Sept. 22-26 (1975).

[2] H. Farrar IV, W.N. McElroy, E.P. Lippincott, "Helium production cross-section of boron for fast-reactor neutron spectra," Nuclear Technology, Vol. 25, N°2, p. 305 et seq. (Feb., 1975).

[3] W.L. Zijp, J.H. Baard, Nuclear data guide for reactor neutron metrology, EUR 7164 (1979).

[4] H.L. Adair, E.H. Kobisk, "Preparation and characterization of neutron dosimeter materials," Nuclear Technology, Vol. 25, N°2, p. 224 et seq. (Feb., 1975).

[5] Ch. De Raedt, J.-L. Genicot, L. Leenders, "Nuclear characterization of spent fuel by non-destructive examinations at SCK/CEN," Third ASTM-EURATOM symposium on reactor dosimetry, Ispra, Oct. 1-5 (1979).

[6] Ch. De Raedt, L. Fouarge, "Calculation methods applied to BR2 irradiations," Third ASTM-EURATOM symposium on reactor dosimetry, Ispra, Oct. 1-5 (1979).

[7] K.D. Lathrop, "DTF-IV, a FORTRAN-IV program for solving the multigroup transport equation with anisotropic scattering," LA-3373 (Nov.,1965).

[8] Ch. De Raedt, "Methods used for calculating radial power distributions in large fuel pin bundles irradiated in BR2. Comparison with experimental results," IAEA technical committee meeting on homogenization methods in reactor physics, Lugano, Nov. 13-15 (1978).

[9] E.P. Lippincott, W.N. McElroy, H. Farrar IV, "He production in reactor materials," Washington Conference (1975).

[10] B. Hinkelmann, "Microscopic neutron nuclear data and 5-group cross-sections for the actinides ^{231}Pa, ^{232}U, ^{234}U, ^{236}U, ^{237}U, ^{237}Np, ^{238}Np, ^{238}Pu, ^{241}Am, ^{242}Cu," KFK 1186, EANDC(E) 128 "U" (July, 1970).

Table 1. Dosimetry results in the wrapper tube

Quantity considered	Measured ($\pm$ 1σ in %)	Calculated	$\frac{C}{M}$	Remarks
Fission rate in the ^{235}U dosim. (10^{-9}s^{-1})	6.50 $\pm$ 7 %	6.50	1.00	(1) normalization
Fission rate in the ^{239}Pu dosim. (10^{-9}s^{-1})	9.40 $\pm$ 4 %	10.59	1.13	(1)
Fission rate in the ^{238}U dosim. (10^{-10}s^{-1})	4.62 $\pm$ 5 %	7.74	1.68	(1)
Fission rate in the ^{237}Np dosim. (10^{-10}s^{-1})	7.42 $\pm$ 10 %	8.69	1.17	(2)
He production in B$_{nat}$ dosim. [^{4}He]/[^{10}B]$_o$ (10^3 appm)	644 $\pm$ 3 %	647	1.00	(3)
He production in ^{6}LiF dosim. [^{4}He]/[^{6}Li]$_o$ (10^3 appm)	241 $\pm$ 3 %	230	0.95	(3)
^{59}Co(n,γ)^{60}Co reaction rate, burn-up corrected (10^{-9}s^{-1})	1.51 $\pm$ 2 %	1.83	1.21	
^{54}Fe(n,p)^{54}Mn reaction rate (10^{-11}s^{-1})	1.96 $\pm$ 3 %	1.70	0.87	

(1) in the calculations, spectrum averaged σ_f and σ_a values of ^{235}U and ^{239}Pu taken from the SCK/CEN 40-group library were adopted, σ_f but not σ_a being present in the ENDF/B V dosimetry file.

(2) in the calculations, the spectrum averaged σ_f and σ_a values of ^{237}Np, ^{238}Np and ^{238}Pu were calculated with the aid of the 5-group library [10].

(3) the total uncertainty includes the uncertainty on the He measurements and the uncertainty on the axial flux distribution utilized to reduce the experimental results to the maximum flux plane.

Table 2. Fission, helium production, ^{59}Co reaction and ^{54}Fe reaction distributions over the fuel pin bundle. Each row of data is normalized to a bundle-averaged value equal to 1.00

Pin position / Quantity considered	Central pin	Interme-diate pin	Outer pin Side	Outer pin Corner	Outer pin Average
Fissions in the fuel pin bundle measured(^{137}Cs)NDT	0.79±0.01	0.86±0.01	1.05±0.01	1.12±0.01	(1.08)
Pu fissions in the fuel pin bundle measured(^{106}Rh)NDT	0.79±0.01	0.85±0.01	1.05±0.01	1.13±0.01	(1.09)
Fissions in the fuel pin bundle measured in BRO2 mock-up [1]	0.81±0.01	0.87±0.01	1.04±0.01	1.12±0.01	(1.08)
He production in the fuel pin claddings					
measured (DT)	0.90±0.01	1.00±0.01	1.02±0.01	1.00±0.01	(1.01)
calculated	1.00	1.00			1.00
^{59}Co(n,γ)^{60}Co reaction rate in the fuel pin claddings					
measured on cladding samples (DT)	0.37±0.01	0.93±0.01	1.07±0.01	1.10±0.01	(1.09)
measured on fuel pins (NDT)	0.41±0.02	0.93±0.03	1.06±0.03	1.11±0.03	(1.09)
calculated	0.84	0.89			1.07
^{54}Fe(n,p)^{54}Mn reaction rate in the fuel pin claddings					
measured on cladding samples (DT)	1.06±0.02	1.03±0.02	1.00±0.02	0.96±0.02	(0.98)
measured on fuel pins (NDT)	1.06±0.03	1.07±0.02	0.98±0.02	0.93±0.02	(0.96)
calculated	1.07	1.05			0.97

Table 3. $^{59}Co(n,\gamma)^{60}Co$ reaction rate, helium production and $^{54}Fe(n,p)^{54}Mn$ reaction rate in the fuel pin claddings (bundle averaged values)

Quantity considered	Measured on cladding samples DT ($\pm$ 1σ in %)	Measured on entire pins NDT ($\pm$ 1σ in %)	Calculated	$\frac{C}{M(DT)}$	$\frac{C}{M(NDT)}$
$^{59}Co(n,\gamma)^{60}Co$ reaction rate ($10^{-9}s^{-1}$)	-	1.18* $\pm$ 3 %	1.25	-	1.06
He production in the claddings (appm)	11.79 $\pm$ 2 %	-	8.76**	0.74	-
$^{54}Fe(n,p)^{54}Mn$ reaction rate ($10^{-11}s^{-1}$)	2.39 $\pm$ 3 %	2.57 $\pm$ 3 %	2.09	0.87	0.81

* the strong dip measured in the central pin was not taken into account.

** threshold reactions in all constituents except N : 5.28 appm
threshold reactions in N : 1.58 appm
^{10}B reaction : 1.71 appm
two-step nickel reaction : $^{58}Ni(n,\gamma)^{59}Ni(n,\alpha)$: 0.19 appm.
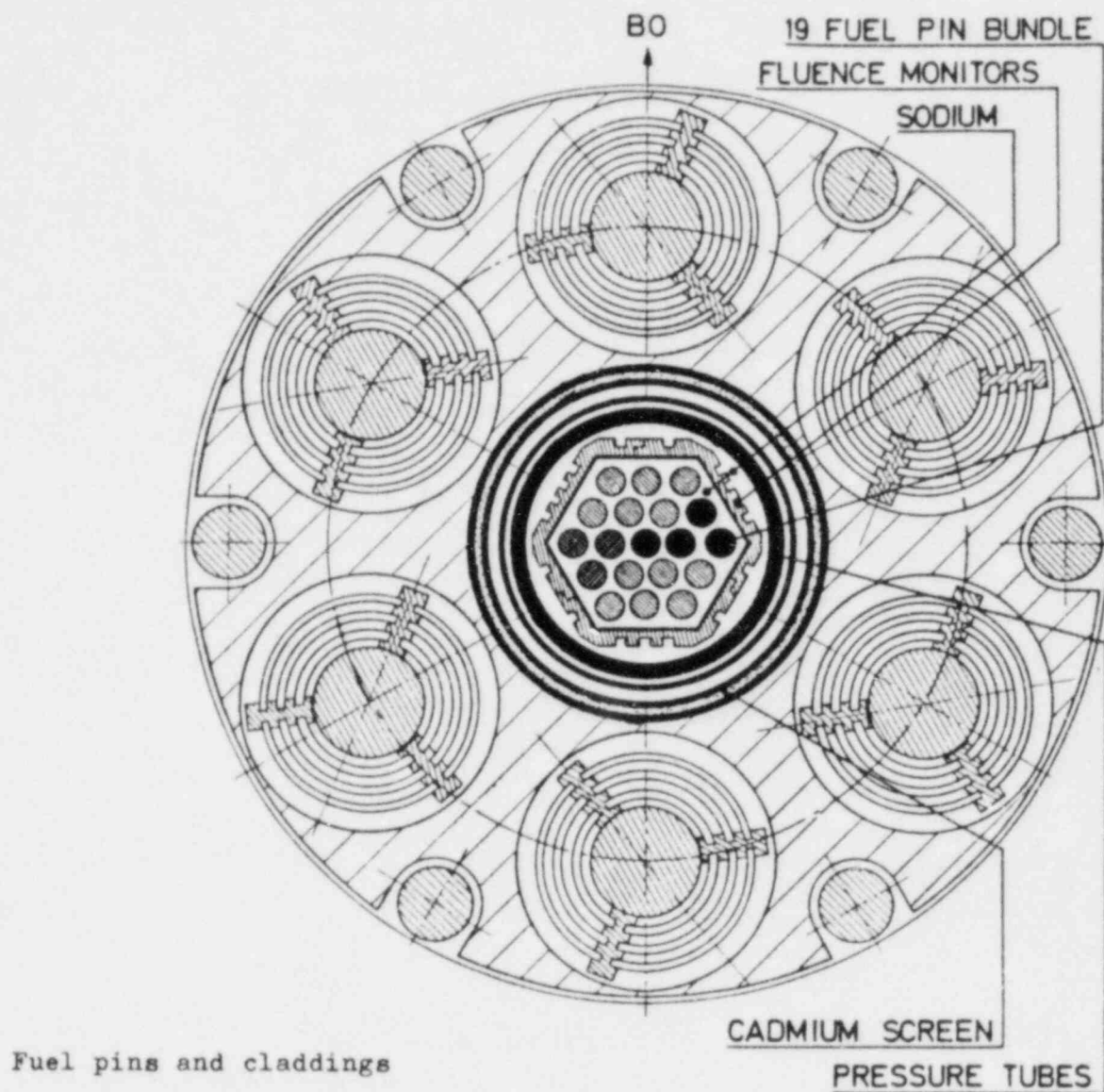
Fig. 1. Cross-section of the central channel H1 of BR2 containing the MOL 7D loop.
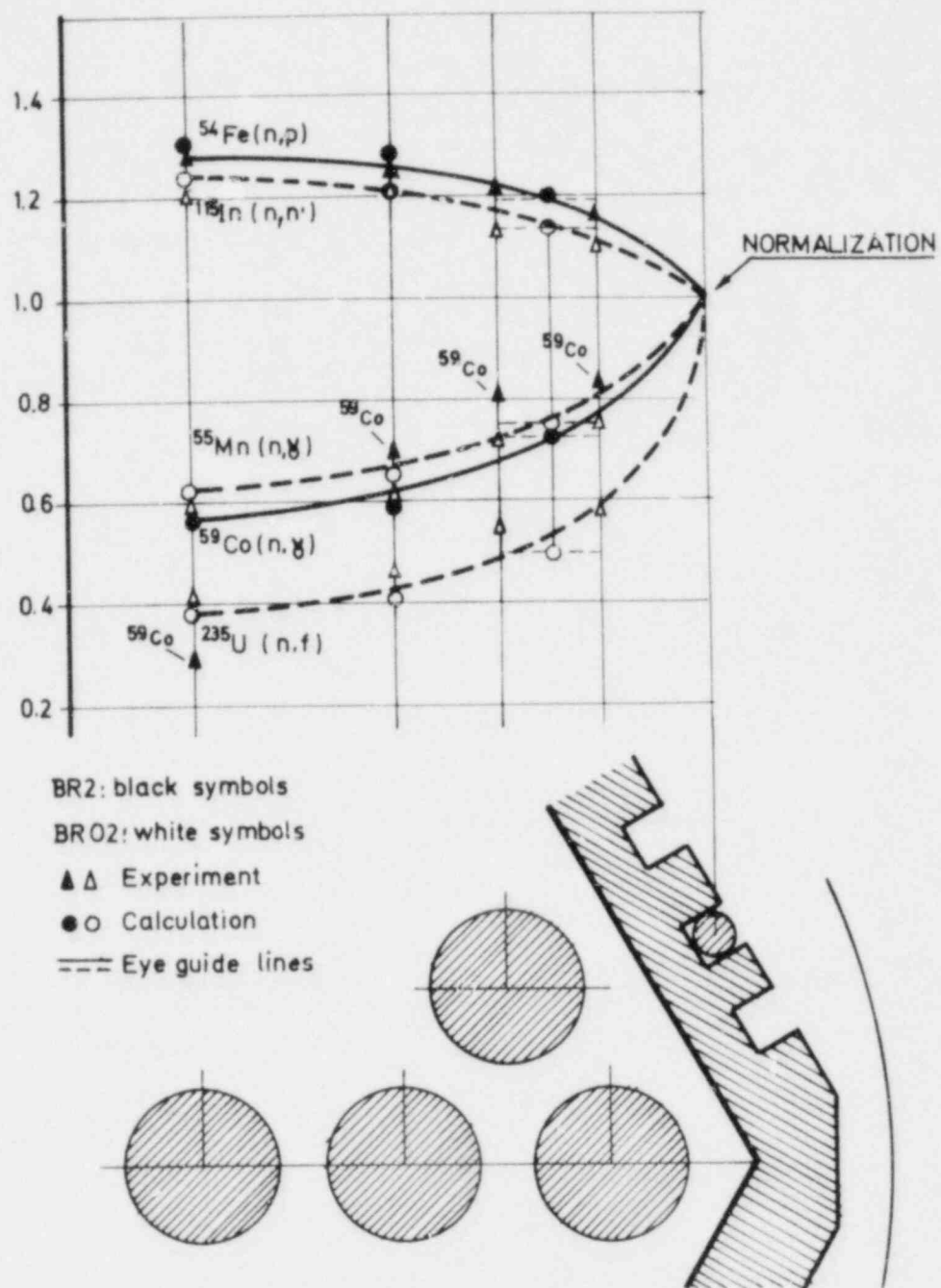
Fig. 2. Variation of reaction rates sensitive to low
($235U$, $55Mn$ and $59Co$) and high ($115In$ and $54Fe$)
energy neutrons from the position allocated to
the fluence monitors to different positions in
the fuel pin bundle.
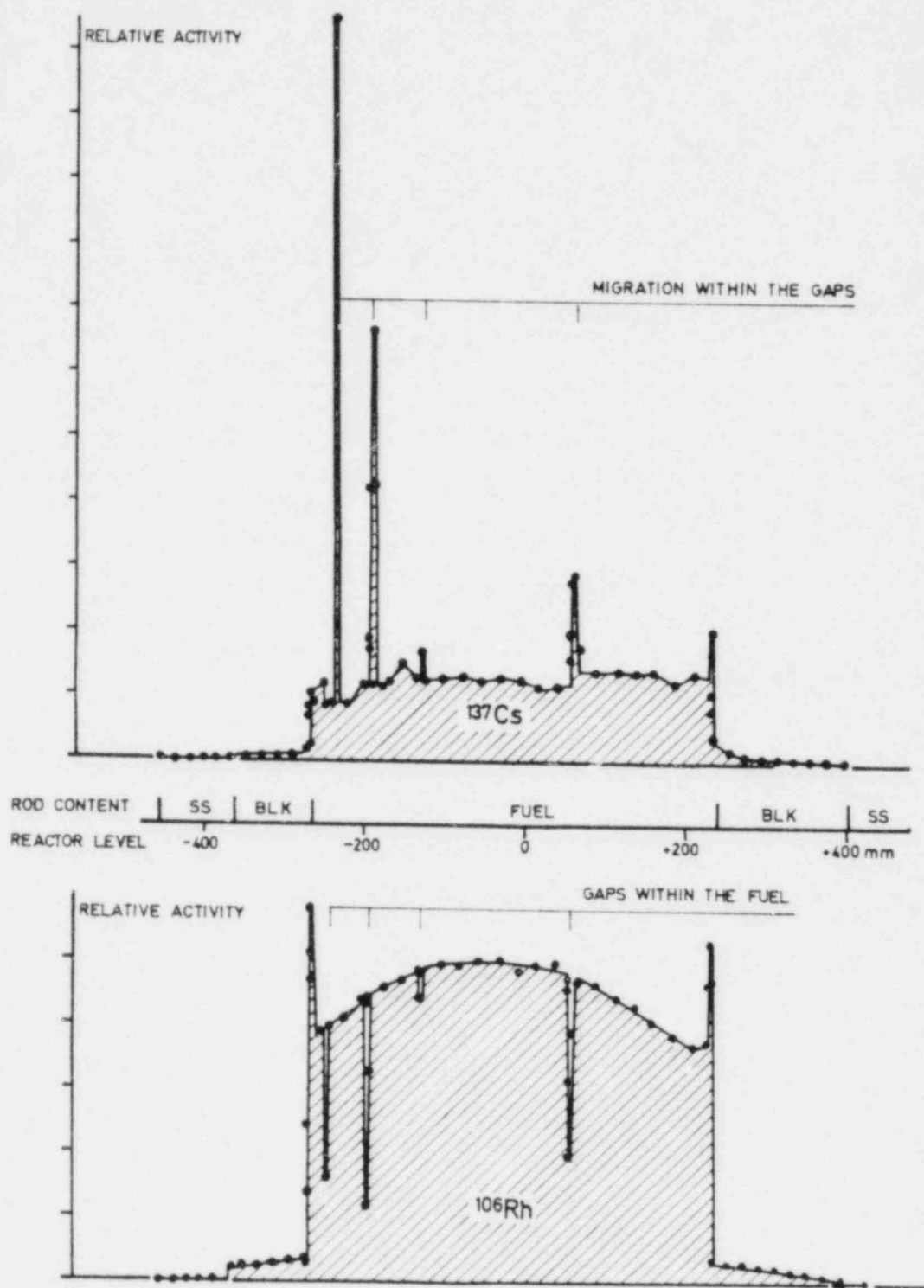
Fig. 3. Axial distributions of the ^{137}Cs and ^{106}Rh activities in a fuel pin, measured by NDT.

FFTF REACTOR CHARACTERIZATION PROGRAM REVIEW

J. A. Rawlins, J. W. Daughtry and R. A. Bennett
Hanford Engineering Development Laboratory
Richland, Washington, USA

ABSTRACT

This report summarizes the status of the Reactor Char-
acterization Program being conducted at the Fast Flux Test
Facility, a 400 MWth sodium-cooled fast reactor designed to
test fuels and materials for the United States' Liquid Metal
Fast Breeder Reactor Program. The program status is dis-
cussed in three parts. (1) A series of calibration experi-
ments was conducted in a dry, in-reactor thimble located near
the center of the reactor. As a result of the calibration
measurements, goal accuracies can be met for follow-on de-
tailed neutronic characterization. Quantities of interest
include fissionable nuclei fission and capture rates, non-
fission reaction rates, neutron flux spectra, power distri-
bution and burnup. (2) Ten characterizer assemblies were
irradiated for eight days at full power; test assembly
handling has been completed. Test fuel pins and dosimeters
from the full power irradiation are undergoing laboratory
analysis. Three characterizer assemblies were irradiated
at 1% power for one day; test fuel pins and dosimeters are
being examined. Current expectations are that all Phase 2
goal accuracies will be met. (3) Follow-on characterization
planning is under way.

INTRODUCTION

The Fast Flux Test Facility (FFTF), a 400 MW thermal sodium-cooled
fast test reactor, is located at the Hanford Engineering Development Lab-
oratory (HEDL) near Richland, Washington and operated for the U.S. De-
partment of Energy (DOE) by the Westinghouse Hanford Company. The pur-
pose of the FFTF is to test fuels, materials and components to support
the Liquid Metal Fast Breeder Reactor (LMFBR) program in the United
States. The FFTF Reactor Characterization Program (RCP)[1,2] was estab-
lished to provide high quality neutronic, gamma ray and thermal hydraul-
ic data to FFTF experimenters, to provide a basis for adjustment of cal-
culational tools used for FFTF analysis and to provide benchmark data
for the U.S. LMFBR Program.

The philosophy of the FFTF RCP is to conduct three phases of characterization:

Phase 1. A series of experiments to verify techniques to be used for routine neutron dosimetry, and to determine neutron and gamma ray characteristics that could only be measured prior to any power operation. The Phase 1 measurements were conducted in a special in-reactor thimble.

Phase 2. Two irradiations of prototypic characterizer assemblies containing a variety of dosimeters; these two irradiations were to be conducted prior to cycle one of routine operation. Ten characterizers were irradiated for eight days at full power, and three characterizers were irradiated at 1% power for 24 hours.

Phase 3. Ongoing characterization, to be achieved by piggybacking other experiments and by reirradiation of the characterizer assemblies used in Phase 2.

The first two irradiation phases have been completed and disassembly of the characterizer assemblies was completed. Test pin and dosimeter examinations are in progress.

The purpose of this report is to summarize the status of the neutronics portion of the FFTF RCP and to present some of the results obtained in the first phase of characterization. Although some details of the RCP plan have changed, the basic physics plans for the neutronics experiments are still as described in Reference 3. Gamma ray characterization measurements have been described in Reference 4 and will not be discussed here.

PHASE ONE EXPERIMENTS

The Phase one experiments were inserted into the reactor by hanging them from the reactor head inside a 14-meter-long, dry, cooled, in-reactor thimble (IRT).[5] Since the fuel assemblies are supported from the bottom, and the experiments were hung from the top, there is an uncertainty of about ±1 cm in the location of any experiment relative to the fuel column in surrounding assemblies. The IRT was located near the center of the core. Figure 1 shows the core map for the IRT irradiations. There are two fuel enrichment zones in the FFTF: the first four rows of fuel comprise the inner zone and the next two rows make up the outer zone. There are three rows of reflector elements. For purposes of discussion, the IRT neutronics measurements will be discussed in two categories: (1) fission rate experiments, and (2) neutron spectrum measurements.
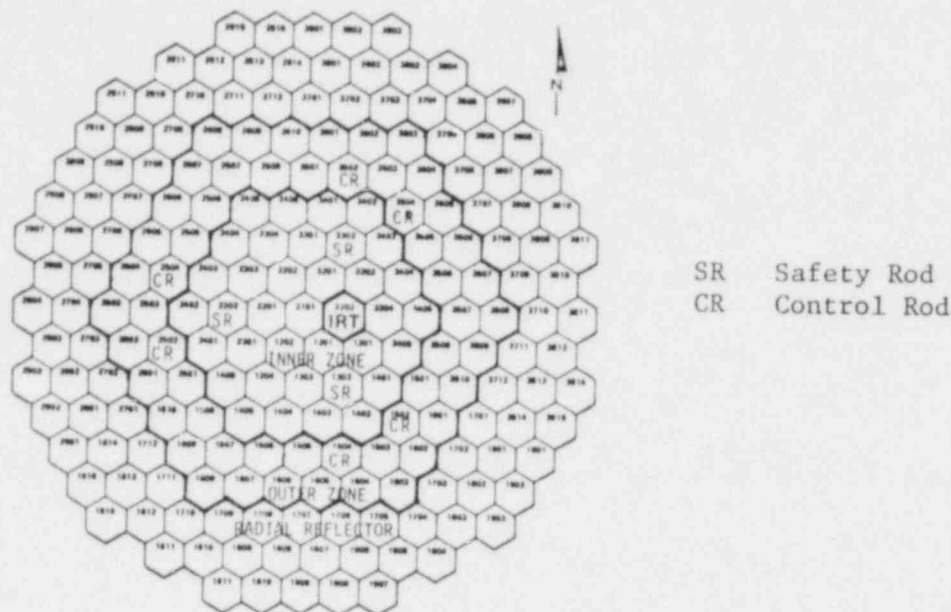
Figure 1.   FFTF Core Map With IRT Location.

Fission Rate Measurements

Two different kinds of IRT fission rate measurements were performed:
(1) detailed axial isotopic fission rate distributions measured with min-
iature traversable fission chambers, and (2) active and passive fission
rate measurements in modified National Bureau of Standards (NBS) absolute
fission chambers. The intent of the first kind of measurement was to
measure axial fission rate distributions in an environment resembling a
fuel test in the FFTF for comparison with calculation. The purpose of
the second set of experiments was to validate the use of vanadium-
encapsulated, oxide wire and powder dosimeters in Phases 2 and 3 of the
characterization program. Fission rate measurements using absolute fis-
sion chambers included the following:

1. Absolute fission rates using NBS deposits and electronic pulse
    counting.
2. Irradiation of high purity, fissionable foils of four isotopes
    in dummy fission chambers, and subsequent detection of fission
    product gamma rays with a calibrated counting system.
3. Irradiation of prototypic vanadium-encapsulated fissionable
    dosimeters and subsequent fission product gamma ray detection
    on calibrated counting systems.

Traversable Fission Chamber Experiment

The detailed fission rate axial profiles were measured by traversing miniature fission chambers from approximately 1 meter below core midplane to approximately 1 meter above core midplane.[6] The traversing chambers were surrounded by a can of frozen sodium to simulate the nuclear environment of a fuel test in the FFTF. Figure 2 shows the results for ^{239}Pu, which is typical of the curves obtained for ^{235}U, ^{233}U and ^{241}Pu. Figure 3 shows the fission rate profile measured for ^{238}U, which closely resembles the curves for ^{232}Th and ^{240}Pu. The fission rate profiles are similar to those measured in the FFTF Engineering Mockup Critical (EMC). The fissile isotope curves measured in the FFTF and the EMC measured data were also used to help establish the location of IRT experiments relative to the fuel in adjacent assemblies. The smooth curves in Figures 2 and 3 were calculated from a three-dimensional diffusion theory reactor calculation using 12 neutron energy groups and ENDF/B-III cross sections; the curves were preexperiment calculations and were used to judge the validity of the data when they were being taken. More extensive calculations using ENDF/B-V[7] cross sections are in progress. The discrepancies between measurements and precalculational results are similar to those observed for the FFTF EMC.
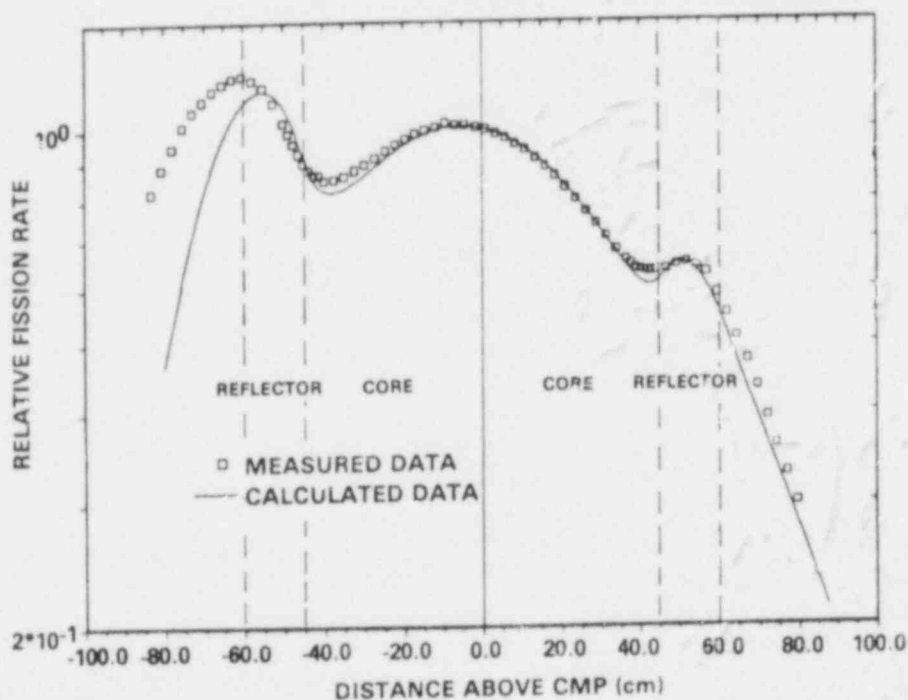
Figure 2. ^{239}Pu Fission Rate Profile.
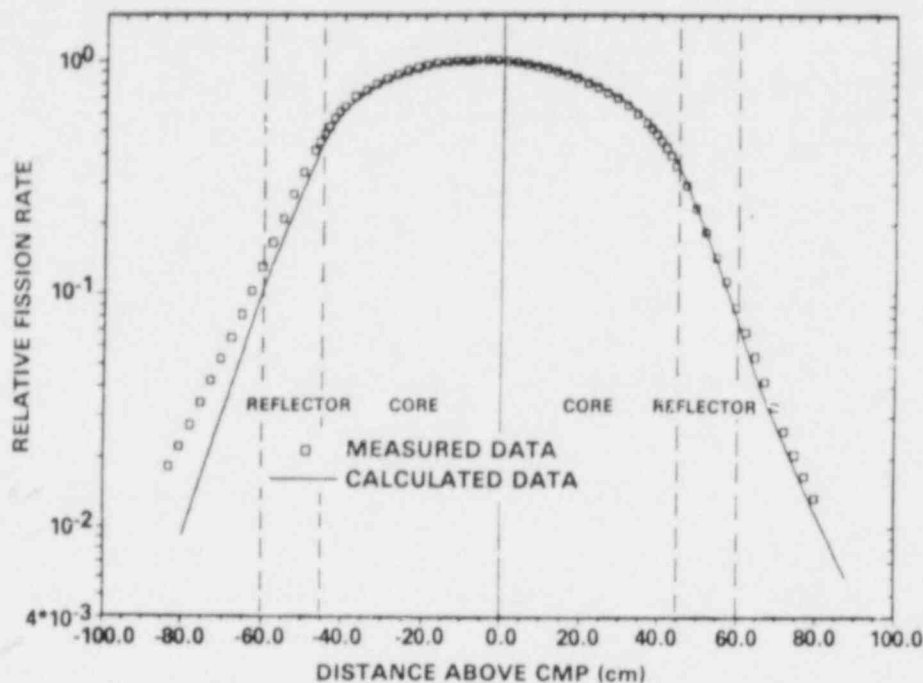
Figure 3. ^{238}U Fission Rate Profile.

Absolute Fission Chamber Experiment

To validate the radiometric method of fission rate measurements used during Phases 2 and 3 characterization, a series of experiments was performed in the IRT using modified NBS absolute fission chambers[8] as a basis. In each experiment, fission rates were measured at core midplane and at 54 cm above core midplane in the region of the FFTF upper axial reflector. A monitor absolute fission chamber with ^{239}Pu deposits was located 37.5 cm below midplane for all measurements.

The absolute fission chamber experiments determined the ratio of isotopic fission rates at two locations for the isotopes ^{232}Th, ^{233}U, ^{235}U, ^{238}U, ^{237}Np, ^{239}Pu, ^{240}Pu and ^{241}Pu. Tables 1 and 2 show the results and uncertainties obtained for the fission rates relative to the ^{239}Pu fission rate at each location. The different irradiations were normalized to each other using the same monitor absolute chamber with two ^{239}Pu deposits.

Table 1. Core Midplane Absolute Fission Rate Ratios

Isotope	Fission Rate/^{239}Pu Fission Rate	
^{232}Th	0.00556	(±2.7%)
^{233}U	1.513	(±1.7%)
^{235}U	1.038	(±1.1%)
^{238}U	0.0227	(±1.6%)
^{237}Np	0.1828	(±1.3%)
^{239}Pu	1.0	
^{240}Pu	0.2018	(±1.4%)
^{241}Pu	1.36	(±2.7%)

Table 2. Upper Axial Reflector Absolute Fission Rate Ratios

Isotope	Fission Rate/^{239}Pu Fission Rate	
^{232}Th	0.00145	(±4.3%)
^{233}U	1.513	(±1.7%)
^{235}U	1.015	(±1.1%)
^{238}U	0.00598	(±3.4%)
^{237}Np	0.0604	(±3.3%)
^{239}Pu	1.0	
^{240}Pu	0.0761	(±3.5%)
^{241}Pu	1.50	(±2.7%)

High Purity Foil Irradiation

The second fission rate measurement[9] utilized the same experiment insert to eliminate relative positioning errors. High purity fission foils[10] of ^{239}Pu, ^{235}U, ^{237}Np and ^{238}U were loaded into dummy fission chambers along with solid state track recorders (SSTR) and were irradiated for two hours at approximately 100 kW reactor power. Multiple foils were loaded into the chambers. One foil of each set was counted eight times at HEDL; the remaining foils were counted by other laboratories for comparison. Thirty-two gamma rays from 13 fission products were analyzed. The gamma ray counting system was calibrated to approximately 1% with NBS absolute gamma ray standards. Evaluated gamma ray branching intensities, ENDF/B-V cumulative fission product yields and the experimental data were combined in the FERRET generalized least-squares data adjustment code[11] to obtain adjusted values for the branching intensities and cumulative fission product yields, as well as a bias factor for each foil at each location.

Table 3 lists the fission products and gamma rays studied for the IRT foil irradiation and the initial and final uncertainty and percent adjustment for the gamma ray branching intensities. With the exception of the ^{132}Te gamma rays at 954 and 1399 keV and the ^{133}I gamma ray at 875 keV, branching intensity adjustments were within the initial uncertainty. Tables 4, 5, 6 and 7, list the cumulative fission product yield initial and final uncertainties, and the percent adjustments, for the samples at core midplane (CMP) and in the upper axial reflector (UAR) region (54 cm above midplane). Initial yields and uncertainties are from ENDF/B-V, and it was assumed in the FERRET analysis that the a priori yield for CMP and UAR locations was the same; the adjusted yield was not constrained to be location independent. The only case of a yield adjustment outside the initial uncertainties was for ^{106}Ru in the ^{235}U upper axial reflector foil, which implies a possible neutron energy dependence in the cumulative fission product yield. This is not unreasonable, since mass 106 lies on the high side of the first maximum in the mass-yield curve for ^{235}U. Table 8 lists the bias factor for each foil. For the CMP foils, only the ^{237}Np exhibits a possible bias. Both UAR foils show a bias significantly less than unity; the UAR bias for the fissile isotopes in the UAR was interpreted as a neutron self-shielding effect and was expected. The neutron energy response for ^{235}U and ^{239}Pu at CMP is primarily above the isolated resonance region in neutron energy, whereas the UAR response function is mostly in the isolated resonance region.

As a result of the analysis of the high purity foil irradiation, it was concluded that the counting system calibration contained no measurable bias, and the branching intensity and cumulative fission product yield adjusted data provide a consistent data set. The adjusted branching intensities, yields and covariance data for the four foil isotopes were used in the follow-on analysis of prototypic vanadium-encapsulated, high temperature fission dosimeters.

Table 3. Branching Intensity Adjustments

FISSION PRODUCT	GAMMA ENERGY	INITIAL UNCERTAINTY	FINAL UNCERTAINTY	PERCENT ADJUSTMENT
95Zr	724	1.1	.89	.06
	757	1.0	.84	-.02
	766	.03	.03	-.00
97Zr	658	.20	.20	-.03
	743	.30	.29	-.08
99Mo	181	9.3	2.9	3.7
	739	8.3	1.7	4.3
103Ru	497	3.3	1.4	.06
106Ru	512	2.9	1.7	-.27
	622	5.9	2.6	.40
131I	284	1.6	1.6	.
	364	1.4	1.1	.47
	637	1.6	1.3	.43
132Te	228	9.1	2.1	-.03
	773	2.4	1.4	-2.0
	954	3.3	1.4	-5.3
	1399	4.2	1.8	-5.3
133I	530	2.0	1.1	2.0
	875	2.1	1.3	6.1
	1298	2.2	2.2	.06
135I	1132	3.4	1.8	-.40
	1260	3.4	1.7	-1.7
	1457	3.3	2.2	1.2
137Cs	662	.50	.49	.06
140Ba	329	13.	1.7	-3.4
	487	7.0	1.6	-1.1
	1596	.10	.10	.006
	637	3.5	1.4	-1.3
143Ce	293	12.	1.4	-1.8
	351	15.	1.6	1.1
144Ce	133	2.0	2.0	-.17
	696	10.	1.8	2.4

Table 4. ^{235}U Fission Product Yield Adjustments

FISSION PRODUCT	INITIAL UNCERTAINTY	CORE MIDPLANE		UPPER AXIAL REFLECTOR	
		FINAL UNCERTAINTY	PERCENT ADJUSTMENT	FINAL UNCERTAINTY	PERCENT ADJUSTMENT
95Zr	1.4	1.2	.41	1.2	.56
97Zr	1.4	1.2	-.83	1.2	-1.1
99Mo	2.0	1.8	1.1	1.7	.32
103Ru	1.4	1.3	-.04	1.3	-.19
106Ru	4.0	3.0	-1.6	2.5	6.9
131I	1.0	1.0	.01	1.0	-.11
132Te	1.4	1.2	-1.3	1.2	-.88
133I	1.4	1.2	1.1	1.2	.77
135I	2.0	1.7	-.50	1.6	-1.5
137Cs	.70	.70	.03	.70	.05
140Ba	.70	.70	.04	.70	.23
143Ce	.50	.50	.01	.50	.04
144Ce	1.0	1.0	.13	1.0	.54

Table 5. ^{239}Pu Fission Product Yield Adjustments

FISSION PRODUCT	INITIAL UNCERTAINTY	CORE MIDPLANE		UPPER AXIAL REFLECTOR	
		FINAL UNCERTAINTY	PERCENT ADJUSTMENT	FINAL UNCERTAINTY	PERCENT ADJUSTMENT
95Zr	2.0	1.6	-.27	1.4	-1.1
97Zr	1.4	1.2	-.63	1.2	-.10
99Mo	2.8	2.6	.31	2.1	-.33
103Ru	1.4	1.3	-.04	1.3	.09
106Ru	1.4	1.3	.01	1.3	.45
131I	1.4	1.3	.36	1.3	.75
132Te	2.8	2.0	-2.4	1.7	-.63
133I	1.4	1.3	1.2	1.2	.73
135I	2.8	2.1	.50	2.0	-.36
137Cs	1.4	1.4	.01	1.3	.001
140Ba	1.4	1.3	-.33	1.2	-.56
143Ce	1.0	1.0	-.01	1.0	-.23
144Ce	1.0	1.0	-.01	1.0	-.23

Table 6. ^{238}U Fission Product Yield Adjustments

FISSION PRODUCT	INITIAL UNCERTAINTY	CORE MIDPLANE	
		FINAL UNCERTAINTY	PERCENT ADJUSTMENT
95Zr	1.4	1.2	-.40
97Zr	2.0	1.6	-.36
99Mo	2.8	2.3	-.79
103Ru	1.4	1.3	.21
106Ru	6.0	4.8	2.9
131I	1.4	1.3	-.53
132Te	2.8	2.0	-1.9
133I	2.0	1.7	1.1
135I	2.8	2.5	1.1
137Cs	1.0	1.0	.08
140Ba	1.0	.90	.31
143Ce	2.0	1.8	-.16
144Ce	2.0	2.0	-.17

Table 7. ^{237}Np Fission Product Yield Adjustments

FISSION PRODUCT	INITIAL UNCERTAINTY	CORE MIDPLANE FINAL UNCERTAINTY	PERCENT ADJUSTMENT
95Zr	2.8	2.3	-.41
97Zr	2.6	2.0	-1.9
99Mo	4.0	4.0	--
103Ru	2.8	2.3	-.40
106Ru	11.	11.	--
131I	2.8	2.4	2.2
132Te	4.0	2.4	-.68
133I	2.0	1.7	-.24
135I	6.0	3.8	.08
137Cs	2.8	2.7	.18
140Ba	2.0	1.6	.72
143Ce	4.0	2.8	-.56
144Ce	2.0	2.0	--

Table 8. High Purity Foil Neutron Self-Shielding Factors

	SELF-SHIELDING FACTOR	
Pu-239 CMP	1.0026	(± .96%)
U-235 CMP	1.0044	(± .69%)
U-238 CMP	1.0022	(± .91%)
Np-237 CMP	1.0160	(±1.40%)
Pu-239 UAR	.8408	(± .66%)
U-235 UAR	.9175	(± .48%)

Prototypic Dosimeter Irradiation

Two prototypic sets of fissionable dosimeters[9] were irradiated for four hours in dummy absolute fission chambers along with SSTR in the IRT at CMP and UAR locations at a power level of approximately 200 kW. The prototypic dosimeters were oxide wire- or powder-encapsulated in vanadium. Due to expected neutron self-shielding effects in the 100% oxide wire and powder dosimeters in regions outside the fuel, wires were also fabricated with a mass dilution of approximately 1%. The dosimeters were counted at least three times each on several calibrated counting systems, and many counts were made with the dosimeter close to the detector front face. Consequently, the calibration uncertainty for much of the data was larger than was the case for the foil experiment. All fissionable isotopes studied with the absolute fission chambers were studied in the prototypic dosimeter experiment. Table 9 lists the cumulative fission product yield adjustments made in the FERRET analysis for

three fission products expected to be used in most Phases 2 and 3 radiometric dosimetry work. No fission product yield was adjusted by an amount greater than the initial ENDF/B-V uncertainty, and some significant reductions in uncertainty are evident in Table 9. Gamma ray branching intensities were essentially unchanged as a result of the FERRET analysis. Table 10 lists the bias factors obtained for the prototypic dosimeters studied; the bias factors were interpreted as a combination of neutron self-shielding and composition effects. For example, the bias for ^{239}Pu at CMP is 0.993 (±1.9%), where no neutron self-shielding is expected; in the UAR, the bias for ^{239}Pu is 0.919 (±1.7%), where a neutron self-shielding effect on the order of 10-20% was expected. On the other hand, the ^{235}U 1% samples indicated a bias greater than unity for both locations, and no neutron self-shielding was expected for either location for dilute dosimeters. Therefore it appears that a composition bias should be assigned to the ^{235}U 1% dosimeters of approximately 1.05 (±2.5%). In summary, the composition biases were incorporated into the dosimeter data files for analysis of Phase 2 dosimetry, and the adjusted fission product yields are being used to determine isotopic fission rates. As a result of the IRT fission rate experiments, goal uncertainties of 2-5%^{2} can be achieved for fission rates measured during Phase 2 of the RCP.

Table 9. Dosimeter Fission Product Yield Adjustments

	^{96}Zr UNCERTAINTY			^{103}Ru UNCERTAINTY			^{140}Ba UNCERTAINTY		
	INITIAL	FINAL	ADJ	INITIAL	FINAL	ADJ	INITIAL	FINAL	ADJ
^{232}Th	6.0	4.7	.84				2.8	2.7	-.20
^{233}U CMP	4.0	2.9	1.5	16.	3.5	-1.9	2.8	2.4	-.73
^{233}U UAR	4.0	3.0	1.9	16.	3.7	-4.9	2.8	2.5	-.76
^{240}Pu	6.0	1.6	-2.3	8.0	4.9	.39	8.0	4.9	3.8
^{241}Pu CMP	2.0	1.9	.27	6.0	4.4	1.6	2.0	1.9	-.46
^{241}Pu UAR	2.0	1.9	.44	6.0	4.4	.87	2.0	1.9	-.53
^{239}Pu CMP	1.5	1.4	-.07	1.3	1.2	.63	1.3	1.2	-.53
^{239}Pu UAR	1.4	1.3	.16	1.3	1.2	.73	1.2	1.1	-.72
^{235}U CMP	1.2	1.1	.01	1.3	1.2	-.27	.67	.66	.07
^{235}U UAR	1.2	1.1	.27	1.3	1.2	.19	.66	.65	-.13
^{238}U	1.2	1.1	-.12	1.3	1.2	.12	.92	.88	.01
^{237}Np	2.3	1.9	1.4	2.3	1.9	.64	1.6	1.5	.34

Table 10. Dosimeter Irradiation Bias Factors

	CORE MIDPLANE	Δ%	UPPER AXIAL REFLECTOR	Δ%
^{232}Th	1.0075	3.9	.95170	6.1
^{233}U	.97747	3.0	.95261	3.0
^{233}U-1%	.90976	3.2	1.0097	3.8
^{235}U	.99002	1.6	.94156	1.5
^{235}U-1%	1.0690	2.6	1.0307	2.6
^{237}Np	1.0190	2.0	1.0122	3.0
^{238}U	.96382	1.7	.95270	3.0
^{239}Pu	.99343	1.9	.91912	1.7
^{239}Pu-1%	.99800	2.2	1.0393	2.2
^{240}Pu	1.0043	4.9	.97054	5.2
^{241}Pu	1.0059	3.6	1.0429	3.6

IRT Neutron Energy Spectrum Measurements

Neutron spectrum measurements with proton recoil techniques were made in the IRT at CMP and in the lower axial shield region (80 cm below midplane). The proton recoil experiments were made early in the IRT test sequence at subcritical reactor states prior to any power operation in order to obtain acceptable neutron-induced count rates and to minimize gamma ray background. The proton recoil measurements covered the neutron energy range of approximately 1 keV to 8 MeV at CMP, and 5 keV to 4.5 MeV at 80 cm below midplane. Cylindrical proportional counters[12] were used to obtain data below 2 MeV, and nuclear research emulsions[13] were used in the range from approximately 0.5 MeV up to the highest neutron energy stated. Since all four experiments (two techniques at two locations each) were made at different subcritical states and hence with different control rod configurations, there is a rather large uncertainty (about 15%) associated with correct normalization between the two techniques.

The last irradiation in the IRT testing included dosimeter packages at CMP and at 80 cm below midplane. The intent was to use calculation and data adjustment to infer the neutron spectrum for comparison with the proton recoil results. The four-hour irradiation was conducted at a power level of 1 MW. Since recovery time from shutdown to gamma ray counting of dosimeters was less than two hours, it was possible to measure some reaction rates involving short half-life ($\sim$2 hours) products. In the multiple dosimeter technique of determining neutron spectral data,[14] the measured reaction rates, differential reaction cross sections and covariances, and calculated neutron spectra and uncertainties, were combined using the FERRET code.[11] Neutron spectra in the IRT were calculated using three-dimensional diffusion theory[15] in 42 neutron energy groups; the calculated spectra were expanded to 53 neutron energy groups extending to 16.9 MeV by interpolation and extrapolation. The reactor calculation used ENDF/B-III

cross sections.[16] The dosimeter cross sections and covariances were taken from ENDF/B-V and HEDL evaluation. The dosimeter cross sections were prepared with in-group spectrum weighting typical of the dosimetry location. Table 11 lists the ratio of calculated-to-measured reaction rate for the reactions used in the FERRET evaluation. The dosimeter cross sections and calculated flux spectra were adjusced by FERRET; experimental data were not adjusted. Consistency is indicated in the adjusted ratios by obtaining Calculated/Experimental (C/E) values equal to unity, within the uncertainties. Figure 4 shows a priori (calculated) and adjusted flux spectrum at core midplane, and Figure 5 shows corresponding a priori and adjusted uncertainties. As expected, group flux uncertainties are reduced considerably from the estimated a priori values in the energy range in which significant response exists. The final adjusted uncertainties in the group fluxes range from 10-15% over most of the neutron energy range with significant response. However, the adjusted flux spectrum covariance matrix enables the calculation of various integral parameters of interest with uncertainties much less than 10%, as indicated in Table 12. Figure 6 compares the adjusted multigroup flux spectrum with normalized proton recoil data for the core midplane location; in general, the shape of the spectrum is well represented as a result of the FERRET multiple dosimeter analysis over the neutron energy range in which the two techniques are compared. Similar results were obtained for the 80 cm below midplane location, in spite of some difficulty with calculated spectrum uncertainties due to relatively high flux gradients and ±1 cm uncertainty in the experimental location relative to the calculational model.

In summary, it has been demonstrated that the type of multiple dosimeter technique used for neutron spectrum determination planned for Phases 2 and 3 can yield the goal uncertainties of 5-20% on group fluxes and 5-10% on important integral parameters.

Table 11. Core Midplane Dosimeter Adjustments

Reaction	C/E*	
	Initial	Adjusted
^{235}U(n,f)	0.973 (15%)	1.020 (3.1%)
^{239}Pu(n,f)	0.976 (15%)	1.006 (4.9%)
^{238}U(n,γ)	0.868 (15%)	0.994 (3.8%)
^{58}Fe(n,γ)	0.940 (19%)	1.039 (9.7%)
^{197}Au(n,γ)	0.821 (17%)	0.982 (7.3%)
^{23}Na(n,γ)	1.172 (22%)	1.049 (10%)
^{113}In(n,γ)	0.909 (19%)	1.001 (7.6%)
^{59}Co(n,γ)	0.856 (19%)	1.003 (9.0%)
^{45}Sc(n,γ)	1.209 (21%)	1.031 (8.6%)
^{237}Np(n,f)	1.006 (22%)	0.989 (8.3%)
^{115}In(n,n')	1.082 (28%)	1.063 (8.0%)
^{238}U(n,f)	1.082 (28%)	0.994 (5.3%)
^{58}Ni(n,p)	1.168 (40%)	0.995 (6.3%)
^{54}Fe(n,p)	1.155 (41%)	0.986 (6.3%)
^{27}Al(n,α)	2.000 (107%)	0.995 (9.4%)
^{6}Li(n,t)^{4}He	0.965 (16%)	1.003 (3.2%)
^{10}B(n,^{4}He)	0.873 (15%)	0.974 (2.7%)
^{81}Br(n,γ)	1.262 (64%)	0.996 (6.6%)
^{41}K(n,p)	0.981 (68%)	1.062 (13%)
^{46}Ti(n,p)	1.327 (65%)	1.002 (9.6%)
^{127}I(n,2n)	3.891 (147%)	1.002 (22%)

*Uncertainties include experimental (∿2-5%) and
calculational. Calculational uncertainties
include flux and cross section covariances.

Table 12. Integral Neutron Flux at Core Midplane,
1 MW Nominal Power

Quantify	A Priori	Adjusted
Total Flux	1.67×10^{13} (±16%)	1.68×10^{13} (±2.9%)
Flux >1 MeV	1.80×10^{12} (±25%)	1.70×10^{12} (±4.4%)
Flux >0.1 MeV	9.90×10^{12} (±18%)	9.42×10^{12} (±4.9%)
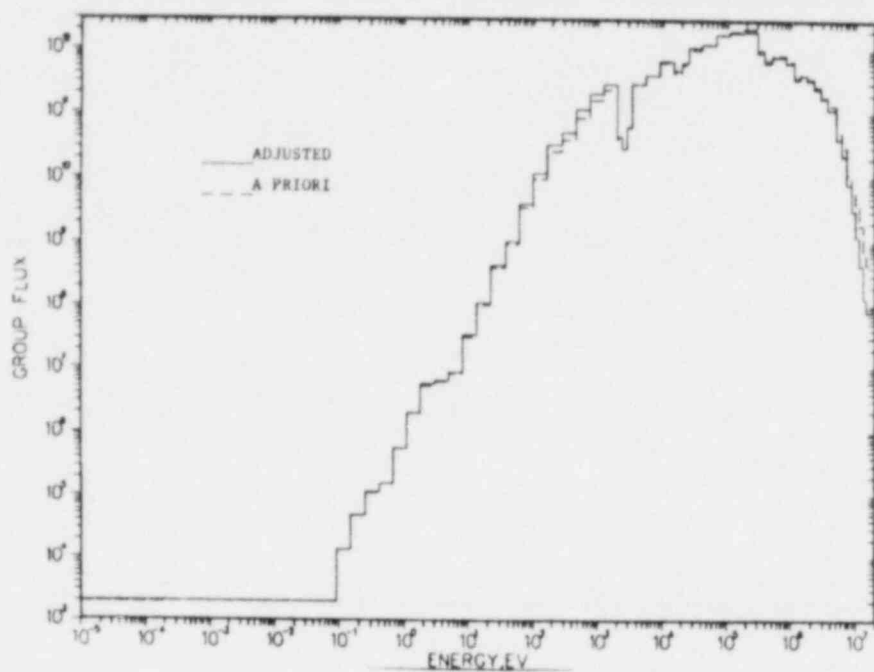
Figure 4.   IRT Core Midplane Flux Spectrum.
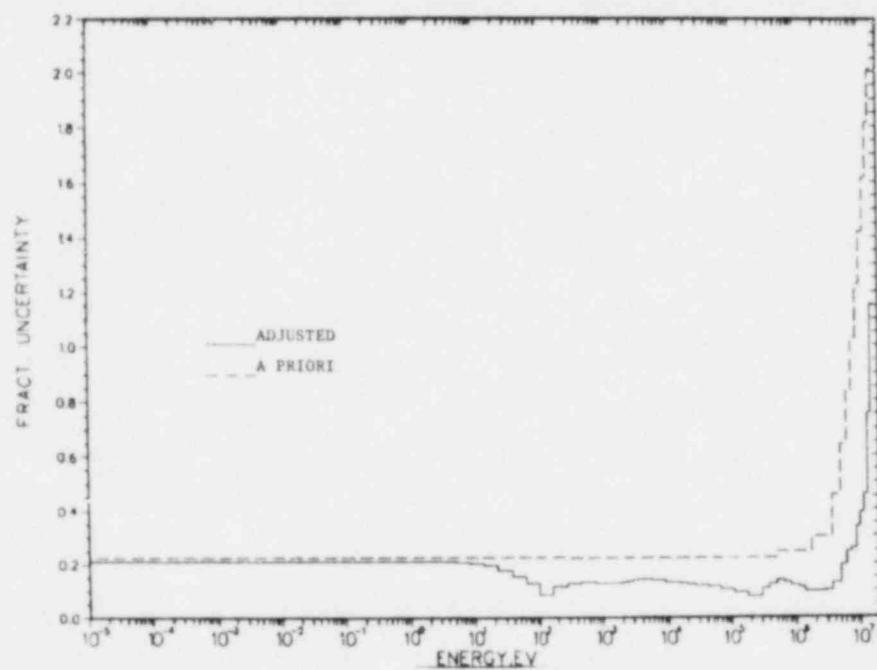
Figure 5.   IRT Core Midplane Flux Spectrum Uncertainty.
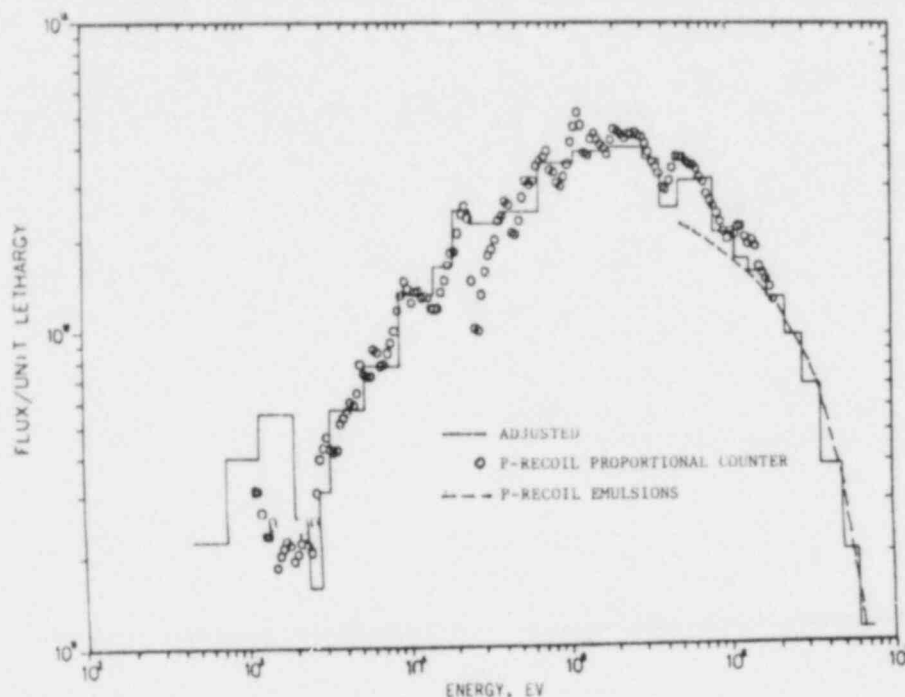
Figure 6. Comparison of Proton Recoil Spectrum with Ferret
Adjusted Spectrum, Core Midplane.

PHASE 2 CHARACTERIZATION STATUS

The high power (HP) irradiation of ten characterizer assemblies and reactor cavity samples was conducted during November 1981. The reactor power was nominally 400 MW (100% power), and the run consumed 8.6 equivalent full power days. Characterizer locations were as follows: two inner zone fuel assemblies in rows 1 and 4; two outer zone fuel assemblies in rows 5 and 6; three reflector assemblies in rows 7, 8 and 9; two sample holders in in-vessel storage locations; one in-core shim assembly in row 4. All assemblies were moved to the Interim Examination and Maintenance (IEM) Cell at the reactor site, where retrievable test pins were removed and shipped to other HEDL laboratories. The fuel pins are being gamma scanned with a high resolution GeLi detector/NaI Compton suppression system. The dosimeters are being counted with a CeLi detector coupled with an automatic sample changer/positioner.[17] Approximately half the 2000 HP dosimeters have been counted once on this system. It is expected that the fuel pin scanning and dosimeter counting will be 90% complete by October 1982. Other remaining laboratory work includes reaction rate determinations using mass spectrometric techniques, and SSTR analysis. The irradiation was conducted successfully, and the gamma scanning and dosimeter-related activities are proceeding well, so it is expected that all goal accuracy requirements will be met.

The low power (LP) irradiation of three characterizer assemblies was successfully performed during January 1982. The reactor power was approximately 4 MW (1% power), and the irradiation lasted 24 hours. Characterizer locations were as follows: one inner zone fuel assembly in row 4; one outer zone fuel assembly in row 6; one reflector assembly in row 7. All LP assemblies have been processed in the IEM cell, and the fuel pins have been gamma scanned. The 1500 LP dosimeters are being counted on a variety of high resolution systems, with completion expected around October 1982. A special part of the LP test included dosimeter foils sandwiched between fuel pellets in eight pins in the row 4 fuel assembly. This portion of the LP test could not have been performed at full power. The foils were successfully recovered, and excellent data are being obtained to determine the effect of measuring reaction rates in nonfueled pins in a fuel assembly. It is expected that all goal accuracy requirements for the LP irradiation will be met.

PHASE 3 CHARACTERIZATION STATUS

HEDL has a commitment for FY-82 to develop a program plan for follow-on characterization. Four special test fuel pins were included in two test assemblies planned for discharge at the end of Cycle 1. Planning has just begun for follow-on characterization. The characterizer assemblies were designed for reconstitution and reuse, but requalification concerns have arisen which may severely restrict their future use. Solid steel dummy pins were inserted into the assemblies in place of the Phase 2 test pins, and the assemblies are presently under sodium in interim decay storage.

Acknowledgments

Many people have been involved in various aspects of the FFTF RCP. In lieu of listing them all by name, an effort has been made to acknowledge outstanding contributions by listing references to their work where possible.

REFERENCES

1. J. W. Daughtry, R. A. Bennett, W. L. Bunch, W. N. McElroy, and T. L. King, "FFTF Reactor Characterization Program," p. 69 in Proceedings of Second International Symposium on Reactor Dosimetry, Vol. 1, NUREG/CP-0004 (1977).

2. T. L. King and J. A. Rawlins, "FFTF Characterization Program," Trans. Am. Nucl. Soc., 39, p. 892 (December 1981).

3. J. A. Rawlins, FFTF Reactor Characterization Program Neutronic Experiments, HEDL-TC 1904, Part I, Hanford Engineering Development Laboratory, Richland, WA (April 1981).

4. F. S. Moore, W. L. Bunch, B. J. Kaiser, and M. R. Wood, "Gamma Ray Measurements in the FTR," Trans. Am. Nucl. Soc., 39, p. 895 (December 1981).

5. A. T. Luksic, W. L. Bunch, and G. Felgate, "In-Reactor Thimble System for FTR Characterization," Trans. Am. Nucl. Soc., 39, p. 893 (December 1981).

6. K. D. Dobbin, J. P. McNeece, J. A. Rawlins, and J. W. Daughtry, "Summary of the FFTF Traversable Fission Chamber Experiment Results," Trans. Am. Nucl. Soc., 39, p. 899 (December 1981)

7. F. M. Mann, FTR Set 500, A Multigroup Cross Section Set for FTR Analysis, HEDL-TME 81-31, Hanford Engineering Development Laboratory, Richland, WA (February 1982).

8. D. M. Gilliam, J. L. Fuller, J. A. Grundl, and J. W. Daughtry, "Absolute Fission Rates in the FFTF," Trans. Am. Nucl. Soc., 39, p. 901 (December 1981).

9. D. W. Wootan, J. A. Rawlins, E. P. Lippincott, L. S. Kellogg, W. Y. Matsumoto, and J. W. Daughtry, "Fission Rate Assessments in the FFTF Using Passive Techniques," Trans. Am. Nucl. Soc., 39, p. 901 (December 1981).

10. H. L. Adair and E. H. Kobisk, "Preparation and Characterization of Neutron Dosimeter Materials," Nuclear Technology, 25, p. 224 (February 1975).

11. F. Schmittroth, FERRET Data Analysis Code, HEDL-TME 79-40, Hanford Engineering Development Laboratory, Richland, WA (September 1979).

12. W. R. Sloan, R. S. McBeath, E. F. Bennett, and T. J. Yule, "Proton Recoil Proportional Counter Measurements in the FFTF," Trans. Am. Nucl. Soc., 39, p. 896 (December 1981).

13. R. Gold and J. H. Roberts, "Nuclear Emulsion Neutron Spectrometry in the FFTF," Trans. Am. Nucl. Soc., 39, p. 896 (December 1981).

14. F. Schmittroth and J. A. Rawlins, "Dosimeter-based Adjustments of Fast Neutron Spectra," Trans. Am. Nucl. Soc., 28, p. 621 (June 1978).

15. R. W. Hardie and W. W. Little, Jr., 3DB, A Three-Dimensional Diffusion Theory Burnup Code, BNWL-1264, Battelle Northwest, Richland, WA (March 1970).

16. R. B. Kidman and R. E. Schenter, FTR Set 300-S Multigroup Cross
    Sections for FTR Shielding Calculations, HEDL-TME 71-184, Hanford
    Engineering Development Laboratory, Richland, WA (December 1971).

17. R. L. Daubert and W. Y. Matsumoto, "Automated Remote Positioning
    and Examination of FFTF Reactor Power Characterization Dosimeters,"
    Trans. Am. Nucl. Soc., 38, p. 699 (June 1981).

Session A.3
Data and Techniques

GAMMA-RAY SPECTROMETRY IN LIGHT WATER REACTOR ENVIRONMENTS

Raymond Gold, Bruce J. Kaiser, and James P. McNeece
Westinghouse Hanford Company
Handord Engineering Development Laboratory
Richland, Washington 99352

ABSTRACT

To satisfy the needs of the Light Water Reactor Pressure Vessel Sur-
veillance Dosimetry Improvement Program, differential and integral measure-
ments have been carried out in a light water reactor (LWR) pressure vessel
simulator (PVS) at the poolside critical assembly (PCA) in Oak Ridge
National Laboratory (ORNL). Within this framework, continuous gamma-ray
spectrometry was carried out using Compton Recoil Gamma-Ray Spectroscopy.
Advances in the state-of-the-art of this method are described with special
emphasis given to the capabilities of the new Janus spectrometer. This
new Janus spectrometer possesses many advantages and most notably extends
the domain of continuous gamma-ray spectrometry up to roughly 6 MeV.

Three different configurations of the LWR-PVS in the PCA have been
studied. Gamma-ray spectrometry measurements were conducted at different
midplane locations throughout the PVS for each configuration. Integral
gamma-ray dosimetry measurements were also conducted with thermoluminescent
dosimetry (TLD), ionization chambers and the method of Compton Recoil
gamma-ray spectrometry itself, which simultaneously provides absolute
gamma-ray dose. Comparison of results from these different experimental
methods are reported, as well as comparisons between theory and experiment.

INTRODUCTION

The radiation field found in nuclear reactors is comprised of two
components rather than just a single component, i.e., gamma-rays as well
as neutrons. The interdependence of these two neutral particle components
in reactor radiation fields has been recognized for some time[1] and has
been stressed in a review presented at the second of this series of inter-
national symposia.[2] In the LWR-PV Surveillance Dosimetry Improvement
Program, there is need for gamma-ray data in the design, control and analy-
sis of high power metallurgical irradiation tests. Gamma-ray data are also
needed to interpret fission neutron dosimetry in LWR-PV environments, where
non-negligible photofission contributions can arise.[3-6] Consequently, the
establishment of a low power LWR-PVS benchmark at the PCA has provided a
unique opportunity to obtain gamma-ray data heretofore unavailable.

Just as in reactor neutron metrology, gamma-ray spectometry and gamma-
ray dosimetry are techniques that complement each other at low power.

Gamma-ray spectrometry provides differential data, whereas gamma-ray dosim-
etry furnishes absolute integral data. Table 1 summarizes differential
and integral gamma-ray measurements carried out in different locations of
the LWR-PVS configurations studied at the PCA. All the nomenclature,
acronyms, etc., used herein conform with Reference 7, which can be con-
sulted for a more detailed description of the LWR-PVS. In fact, since
Chapter 5 of Reference 7 presents LWR-PVS gamma work through 1980, this
exposition need only focus on more recent developments.

Table 1. Test Matrix of LWR-PVS Gamma-Ray Measurements in the PCA*

In-Situ Location**	LWR-PV Configuration		
	8/7	12/13	4/12 SSC
TSB	S		
SSC			TLD
PVF	S		
1/4 T	S	S	S, I, TLD
1/4 T - Off Center	S		
1/2 T	S	S	S, I, TLD
3/4 T		S	S, I, TLD
VB		S	S, I, TLD

*S = Spectrometry, I = Ionization Chambers, TLD = Thermoluminescent
Dosimeter.
**Observations were restricted to midplane except for the 8/7 configura-
tion. For the 8/7 configuration, measurements were conducted at mid-
plane and also at 15.9 cm above midplane.

These gamma-ray efforts represent an effective collaboration between
groups at two major laboratories; namely, the Center for the Study of
Nuclear Energy, Mol, Belgium (CEN/SCK) and the Hanford Engineering Devel-
opment Laboratory (HEDL). The HEDL group carried out continuous gamma-ray
spectrometry and dosimetry with Si(Li) detectors, as well as ionization
chamber measurements.[7] The CEN/SCK group carried out TLD measurements
and coupled neutron-gamma transport calculations.[7] The CEN/SCK efforts
and results are described in a separate presentation at this symposium,[8]
as well as in Chapter 5 of Reference 7.

In the next section, the current status of Compton Recoil Gamma-Ray
Spectroscopy is described with particular focus upon the Janus spectro-
meter, Si(Li) dosimetry, and data analysis techniques. Experimental
results are presented in the final section, where comparisons with other
experimental methods as well as with theory are emphasized.

COMPTON RECOIL GAMMA-RAY SPECTROSCOPY

The basic principles underlying Compton Recoil Gamma-Ray Spectroscopy have been adequately documented.[1,9-14] However, since its inception rather than being static this method has continuously improved. Advances in this continuous gamma-ray spectrometry method were reviewed at the third of this series of international symposia.[15] Further developments as well as applications have been reported for fast breeder reactor (FBR) environments.[16,17]

This method continues to evolve so that even recently reported efforts, i.e., those in the LWR-PVS environment,[7] require updating. Consequently, the most recent improvements to date in the Janus spectrometer, Si(Li) dosimetry, and data analysis techniques are presented separately below.

Janus Spectrometer

The basic elements that comprise the Si(Li) gamma spectrometer Janus probe system are displayed in Figure 1a. This optimized system differs from that previously reported in four important ways:

(1) Two separate, but identical cooled 1 cm^3 Si(Li) detectors are placed face-to-face as shown in Figure 1a.

(2) Each detector output is fed into a reconfigured version of the ORTEC 142A preamplifier, in which the front end FET stage is cooled.

(3) The pulse processing instrumentation has been altered somewhat from the original Janus probe electronics.[7] Coincident counting between Si(Li) detectors is still possible, but no pulse shape discrimination is used.

(4) The detector vacuum enclosure has also been modified, as shown in Figure 1b, to reduce the probe perturbation on the LWR-PVS gamma field. Specifically, the detectors now are separated from the electronics below by a 0.254 cm steel plate. Steel plates have been used as well to reduce the vacuum voids beside and above the detector to 0.254 cm.

These modifications provide the following capabilities:

(1) Two complementary modes of operation.

The noncoincidence mode for low energy spectrometry ($\lesssim 3$ MeV).
The coincidence mode for high energy spectrometry ($\gtrsim 3$ MeV).

(2) Improved discrimination against neutron-induced events, since neutron interactions produce short-range events that are excluded in the coincidence-mode operation.
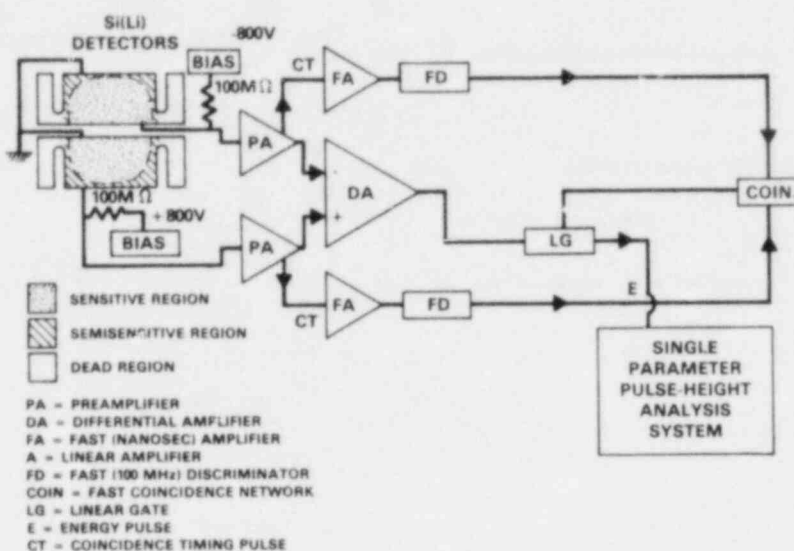
FIGURE 1a. CROSS-SECTIONAL VIEW OF THE JANUS DETECTOR
CONFIGURATION AND BLOCK DIAGRAM OF THE PULSE
PROCESSING INSTRUMENTATION.
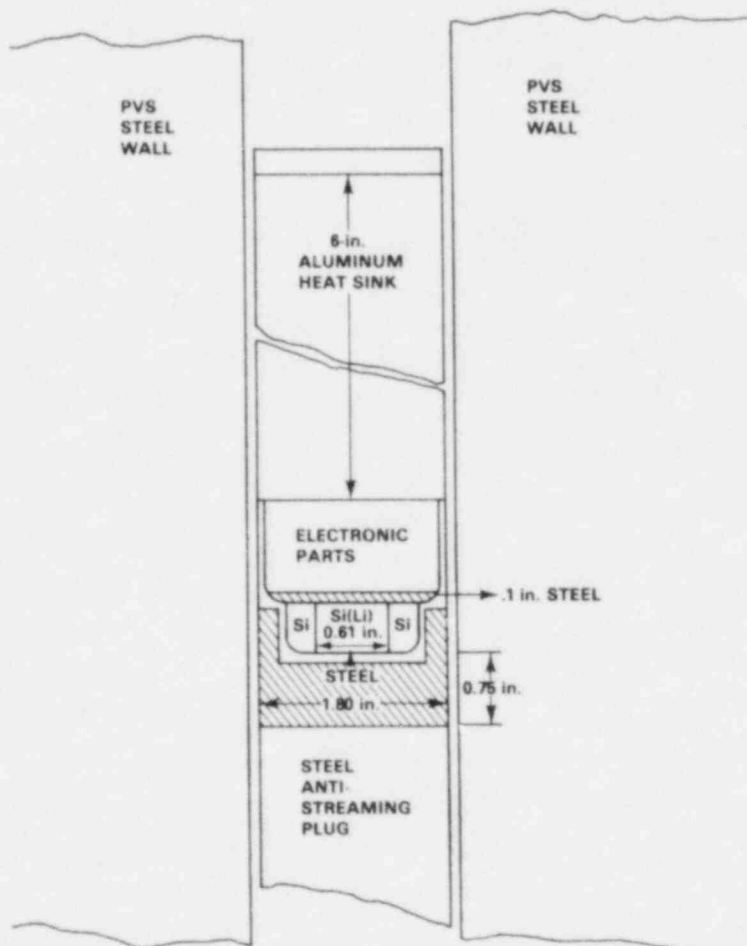
FIGURE 1b. IN-SITU IRRADIATION ENVIRONMENT OF THE Si(Li) JANUS
PROBE IN THE LWR-PVS.

HEDL 8008-104.1

(3) Improved high energy coincidence-mode response for unfolding analyses.

(4) Lower common mode noise and better resolution by utilizing a differential shaping amplifier, in place of the cascaded differential and linear amplifiers previously used.[7]

(5) Single parameter, rather than dual parameter analysis, reduces the complexity of the pulse processing instrumentation as well as the procedures necessary for data collection and unfolding.

The recent change from dual to single parameter pulse analysis was based upon a careful study of Si(Li) energy and rise time spectra as a function of gamma-ray energy, using monoenergetic gamma-ray sources in the 0.1 - 7.0 MeV energy region. The two most significant observations generated in this study were:

(1) Rise time spectra were found to be electron, hence gamma-ray, energy dependent.

(2) The variation of observed electron energy spectra was not adequately described by theory (Klein-Nishina formula). (These energy spectra were obtained from monoenergetic gamma-ray sources in the energy region 0.1 - 7.0 MeV using rise time discrimination to reject electron escape from the Si(Li) detectors.)

As a result of this study, the use of theory as the basis for response matrix construction, as practiced in earlier continuous gamma-ray spectrometry efforts,[18] was not appropriate for the Janus probe. Under these conditions, empirical response matrix construction affords greater accuracy, since systematic effects are automatically included in the observed monoenergetic responses which are used, in turn, to construct the response matrix. Moreover, the experimental technique is simplified considerably by use of single parameter as opposed to dual parameter pulse analysis. The success of this single parameter-empirical response matrix approach is demonstrated below.

Si(Li) Dosimetry

Use of Si(Li) detectors for gamma-ray dosimetry is not new, but dates back to the original work with these detectors for absolute gamma-ray continuum spectroscopy.[18-20] Consequently, only recent advances need be stressed in this presentation. Two different dose rates are available in Si(Li) dosimetry. The finite size dose rate $\dot{D}_{FS}$, arising in the Si(Li) detector, is given by:

$$\dot{D}_{FS} = \frac{F}{PTm} \sum_{i=n}^{k} c_i E_i , \qquad (1)$$

where:

E_i = Mid-bin electron energy of channel i (MeV)
C_i = Number of counts in the channel i bin
m = Mass of the sensitive volume of the Si(Li) detector (g)
T = Live time of the measurement (h)
P = Reactor power level maintained during the measurement (W)
F = 1.602×10^{-8} rad-g/MeV

The conversion factor, F, provides the finite-size rate $\dot{D}_{FS}$ in units of rad/(h·W). Note, according to Eq. (1), that the finite-size dose rate is defined in a specified electron energy range, namely $[E_n, E_k]$.

The mass of the sensitive volume of the Si(Li) detector, m, was determined experimentally. The detector integral count rate response was measured using a finely collimated beam of ^{54}Mn (0.8348 MeV) gamma rays. This fine beam (1.27 mm in diameter) was scanned across the detector surface, both diametrically and longitudinally, in 1.27 mm increments. Diametrical scans have verified that these Si(Li) detectors are cylindrically symmetric. These profile distributions have been used to obtain the effective volume of the Janus probe Si(Li) detectors. The observed volume of the redesigned Janus probe determined in this manner was 1.867 cm^3, which corresponds to a sensitive silicon mass of 4.350 ±0.22 g.

Unfolded absolute gamma-ray continua obtained from Si(Li) detectors can also be used to obtain gamma-ray dose rates. In this case, finite size effects have been properly accounted for in the empirical response matrix. Consequently, effects of electron escape or entry into the sensitive volume of the Si(Li) detector do not exist when using the absolute gamma continuum to determine dose. Hence, this dose rate has been called the infinite medium dose rate $\dot{D}_{IM}$.[18-20] The infinite medium dose rate in material M, $\dot{D}_{IM}$, is given by:

$$\dot{D}_{IM} = \frac{F}{PT} \sum_{i=n}^{k} \phi_i \cdot (\epsilon_0)_i \cdot M(\mu_{en}/\rho)_i \qquad , \qquad (2)$$

where:

$(\epsilon_0)_i$ = Mid-bin gamma-ray energy of channel i (MeV)

ϕ_i = number of gamma rays in the channel i bin

$M(\mu_{en}/\rho)_i$ = Mass energy absorption coefficient for material, M, at gamma-ray energy $(\epsilon_0)_i$

The other constants can be taken as defined earlier, so that $\dot{D}_{IM}$ possesses units of rad/(h·W). Note, according to Eq. (2) the infinite medium dose is defined in specified gamma-ray energy range, namely $[(\epsilon_0)_n, (\epsilon_0)_k]$, which normally corresponds to the measurement domain of the absolute gamma continuum.

Data Analysis

Empirical response matrix construction to date has only been performed in the low energy (non-coincidence) region. Hence, results reported here are necessarily confined to the energy region $\lesssim 3$ MeV.

The empirical response matrix was constructed from the measured responses of seven monoenergetic gamma ray sources. Monoenergetic gamma-ray energies ranged from 0.3208 MeV to 2.754 MeV. Table 2 lists the sources used. Column elements of the response matrix were generated by interpolation between these observed responses. The following sections describe data preparation and response matrix construction in detail.

Table 2. Monoenergetic Sources Used in the Response Matrix Construction

Radioisotope	Photon Energy (MeV)	Compton Edge Energy (MeV)
^{52}Cr	0.3208	0.1779
^{198}Au	0.4118	0.2541
^{64}Cu	0.511	0.3407
^{137}Cs	0.6616	0.4773
^{54}Mn	0.8348	0.6394
^{22}Na	1.275	1.0618
^{24}Na	2.754	2.5201

Initial Data Preparation. The first step in preparing the seven measured monoenergetic responses was to normalize each response to a fixed fluence at the center of the detector. Using absolute source strength together with geometric correction factors, each monoenergetic Compton recoil spectrum was normalized to 10^6 γ/cm^2 at the detector center. In addition the ^{22}Na and ^{24}Na spectra were corrected to remove secondary gammas (0.511 MeV for ^{22}Na and 1.3686 MeV for ^{24}Na).

At low energies, photopeaks represent a significant contribution to Si(Li) observed Compton continua. As gamma-ray energy increases, the photope k contribution becomes negligible and the double escape peak contribution from pair production becomes significant. Therefore, photopeaks and double escape peaks had to be treated with great care. The interpolation scheme used in generating the response matrix handled these peaks separately. Peaks were subtracted out of the normalized responses prior to interpolation. To superimpose these peaks onto the interpolated

responses, nonlinear least squares fits were made to the peak data to obtain energy dependent parameters for peak height, channel number, and width. These parameters were used to calculate photopeaks and double escape peaks for each column of the response matrix. The calculated peaks were then added to the column elements computed by the interpolation scheme.

To reduce the effect of statistical fluctuations on the response matrix, the normalized Compton recoil spectra were smoothed using a five point, weighted smoothing algorithm.

Response Matrix Generation. A (256 x 256) empirical response matrix was constructed. This matrix possessed 256 column (gamma energy) elements and 256 row (electron energy) elements, with the Compton edge energies lying along the main diagonal. A gamma energy range of 0.30 MeV to 2.75 MeV was covered. The following computational scheme (computer code) was used for the response matrix construction:

(1) Read the measured, normalized responses of the monoenergetic gamma ray sources.

(2) Compute the gamma ray energy for column, i, that has a Compton edge energy corresponding to electron energy row j=i. This creates a response matrix in which the Compton edge energies lie along the main diagonal. Adjust for energy broadening of the Compton edge.

(3) Use 3 point Lagrangian interpolation to generate the column elements from measured responses.

(4) Compute photopeak and double escape peak elements based on fitted parameters for electron energy, peak height, and width. Add these elements to the Compton column element.

(5) Repeat steps 2-4 until all 256 column elements are complete.

Unfolding. Compton recoil continua are obtained with iterative unfolding.[21] The arresting criterion for the iteration process was modified to account for not only the statistical fluctuation in the data, but also for the error, σ_E, in energy calibration. Hence, the standard deviation at each channel, σ_i, was computed as:

$$\sigma_i^2 = N_i + \left(\frac{\partial W}{\partial E}\right)_i^2 (\sigma_E)_i^2 \quad , \tag{3}$$

where:

N_i = Number of counts in channel i

$\left(\frac{\partial W}{\partial E}\right)_i$ = Slope of the spectrum at channel i

$(\sigma_E)_i$ = Error in electron energy at channel i

Iterative unfolding is arrested when the sum of the residuals decreases below a prescribed bound A. The initial estimate for A is taken as:

$$A = \sum \sigma_i^2 \qquad\qquad (4)$$

The arresting criterion is empirically refined by observing the results of unfolding a known gamma ray line-spectrum, such as ^{226}Ra.

To test the adequacy of this response matrix, data were collected with the Janus probe from a ^{226}Ra source. The observed ^{226}Ra electron data are shown in Figure 2a and the unfolded gamma-ray spectrum is shown in Figure 2b.

Obviously unfolding a line spectrum, such as ^{226}Ra, is a very rigorous test for a continuum spectrometry method. Nonetheless, as can be seen in Figure 2b, the unfolded gamma ray continuum is indeed a line spectrum. The energy of the unfolded peaks agree with known ^{226}Ra peaks to an uncertainty of less than 1%.

A comparison between the unfolded absolute peak intensities and peak intensities measured with a Ge(Li) spectrometer are shown in Table 3. Since the gamma-ray resolution of the continuum spectrometer is approximately 20 KeV, ^{226}Ra gamma-ray peaks having negligible interferences, i.e. no neighbors closer than ±30 KeV, were chosen for this comparison. As can be seen from Table 3, absolute results of the continuum spectrometer and Ge(Li) spectrometer agree to within approximately 10%.

Table 3. Comparison of Ge(Li) and Janus Probe Absolute ^{226}Ra Gamma-Ray Intensities*

Gamma-Ray Energy (MeV)	Ge(Li)	Janus	Janus/Ge(Li)
0.352	1.067	0.973	0.912
0.609	1.382	1.360	0.987
1.121	0.4261	0.4692	1.101
2.202	0.1364	0.1580	1.158

*Units of 10^6 gamma-rays/s.

Experimental Results

Progress in defining the gamma-ray component of the radiation field in the LWR-PVS environment has been exceptional. This progress can be attributed, in the main, to the synergistic collaboration between the CEN/ SCK and HEDL groups. At the outset, absolute gamma-ray spectral calculations performed by the CEN/SCK group for the 12/13 configuration were roughly an
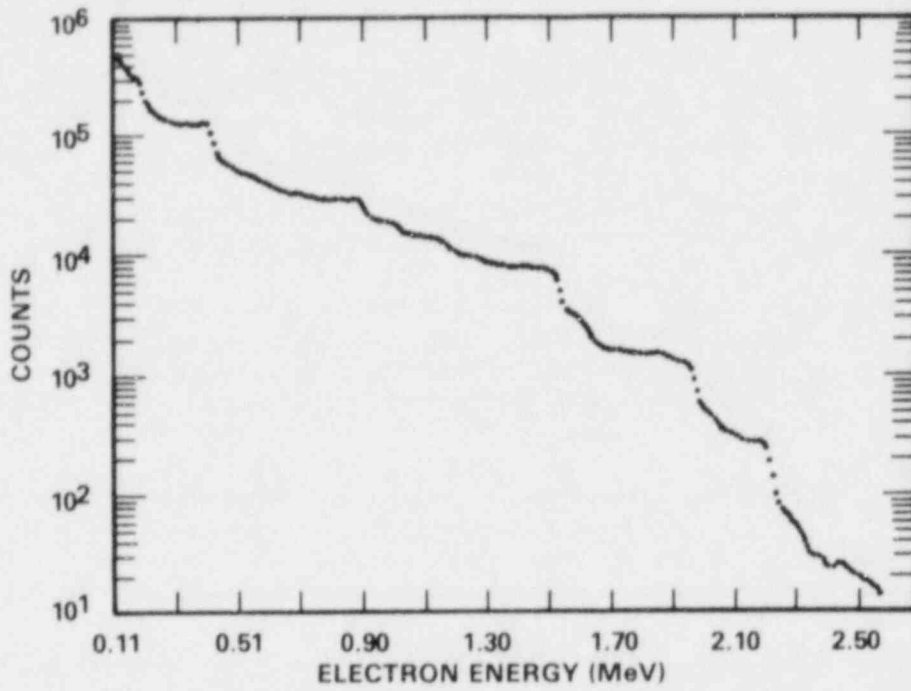
FIGURE 2a. ELECTRON ENERGY SPECTRUM OF 226Ra OBSERVED
WITH THE JANUS PROBE
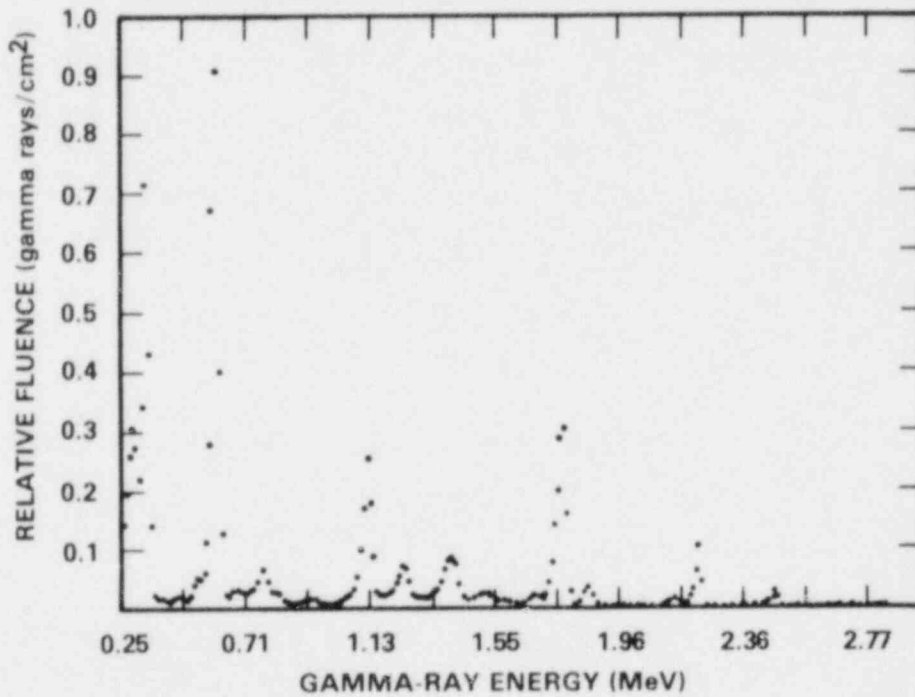
FIGURE 2b. UNFOLDED GAMMA-RAY LINE SPECTRUM OF 226Ra
OBTAINED FROM THE JANUS PROBE DATA

HEDL 8203-103.1

order of magnitude higher than continuous gamma-ray spectrometry carried out by the HEDL group in this (12/13) LWR-PVS configuration at the PCA.

This initial comparison provided the impetus for more detailed calculations as well as complementary TLD measurements by the CEN/SCK group. Subsequent comparisons in the 4/12 SSC configuration revealed that the absolute spectrometry measurements of the HEDL group were now a factor of two or so higher than these new calculations. Furthermore, Si(Li) gamma-ray dosimetry was roughly 35% higher than TLD measurement within the PV block.[7] The CEN/SCK group pointed out that the Si(Li) measurements could be high due to voids created upon insertion of the Janus probe into the PV block. The HEDL group concurred, noting that the gamma-ray intensity gradient in the PV block together with voids arising by introduction of the Janus probe could produce the higher absolute results observed in the Si(Li) measurements.

As a consequence, the Janus probe was redesigned to minimize voids. As shown in Figure 1b, this redesigned Janus probe was then subsequently used in the most recent LWR-PVS experiments. In addition, a miniature gamma-ray ionization chamber was developed to measure the perturbation introduced by the Janus probe. This ionization chamber, 2.41 cm length by 0.89 cm diameter, was small enough to use in a dummy Janus probe. Hence measurements could be carried out first with the LWR-PVS channels completely filled with steel and then in the same channel, but inside a dummy probe which represented the redesigned Janus spectrometer.

The resulting Janus probe perturbation factors for the 4/12 SSC configuration are enumerated in column 2 of Table 4. These perturbation factors have been applied to Si(Li) dosimetry data obtained with the redesigned Janus probe. Table 4 compares absolute Si(Li) dosimetry with both TLD results and calculations for the 4/12 SSC configuration.[7] The TLD and Si(Li) dosimetry results lie within experimental error, whereas Si(Li) dosimetry is roughly 35% higher than calculated gamma-ray dose rates in the PV block.

While it may be fortuitous, the difference between observed and calculated gamma dosimetry lies in the same direction and is roughly the same magnitude as the deviation between calculated and observed neutron fluxes for the LWR-PVS configurations studied in the PCA.[7] Further collaborative efforts are planned in forthcoming LWR-PV benchmark fields. On this basis, current differences between theory and experiment will hopefully be resolved.

ACKNOWLEDGMENTS

Table 4. Comparison of Gamma-Ray Dosimetry* For
the 4/12 SSC Configuration

Location	Perturbation Factor	$\dot{D}_{FS}$ 0.05-7.68 MeV	TLD	Calculation 0.02-14.0 MeV	$\dfrac{\dot{D}_{FS}}{TLD}$	$\dfrac{\dot{D}_{FS}}{Cal.}$
T/4	1.16	276	255	210	1.08	1.31
T/2	1.14	78	68	52	1.15	1.50
3T/4	1.11	23.5	21.5	19.1	1.09	1.23
VB	**	11.0***	11.5	2.20	0.96	5.0

---

*Dose rate in mrad/h at 1-W PCA power level, corrected for perturbation.
**Not measured.
***Perturbation correction assumed negligible for the VB location.

REFERENCES

1. R. Gold, "Compton Recoil Gamma-Ray Spectroscopy," Nucl. Instr. Methods 84, p. 173, 1970.

2. R. Gold, "Overview of Gamma Ray Energy Deposition and Spectra in Fast Reactor Environments," Proceedings of the Second ASTM-EURATOM Symposium on Reactor Dosimetry, NUREG/CP-0004, Vol. 1, Palo Alto, CA, p. 101, 1977.

3. C. D. Bowman, C. M. Eisenhauer and D. M. Gilliam, "Photofission Effects in Reactor Pressure Vessel Dosimetry," Proceedings of the Second ASTM-EURATOM Symposium on Reactor Dosimetry, NUREG/CP-0004, Vol. 2, Palo Alto, CA, p. 575, 1977.

4. G. L. Simmons, V. V. Verbinski, W. K. Hagan and C. G. Cassapakis, Measurement and Analysis of Gamma-Ray Induced Contamination of Neutron Dosimetry Procedures Used for Reactor Pressure Vessel Applications, EPRI NP-1056, Electric Power Research Institute, Palo Alto, CA, 1979.

5. R. Gold, "Estimates of High Energy Gamma and Neutron Flux from Continuous Gamma Ray Spectrometry," LWR Pressure Vessel Irradiation Surveillance Dosimetry Quarterly Progress Report, July - September 1978, NUREG/CR-0551, HEDL-TME 78-8, Hanford Engineering Development Laboratory, Richland, WA, 1979.

6. V. V. Verbinski, C. G. Cassapakis, W. K. Hagen, and G. L. Simmons, "Photointerference Corrections in Neutron Dosimetry for Reactor Pressure Vessel Lifetime Studies," Nucl. Sci. & Eng. 75, p. 159, 1980.

7. W. N. McElroy, Ed., LWR Pressure Vessel Dosimetry Improvement Program: PCA Experiments and Blind Test, NUREG/CR-1861, 1981.

8. N. Maene, et al., "Gamma Dosimetry and Calculations," _Proceedings of the Fourth International ASTM-EURATOM Symposium on Reactor Dosimetry_, National Bureau of Standards, Gaithersburg, MD (1982).

9. R. Gold, "Compton Continuum Measurements for Continuous Gamma-Ray Spectroscopy," _Bull. Am. Phys. Soc. 13_, p. 1405, 1968.

10. M. G. Silk, _Iterative Unfolding of Compton Spectra_, AERE-R5653, UK Atomic Energy Research Establishment, Harwell, UK, 1968.

11. M. G. Silk, "Energy Spectrum of the Gamma Radiation in the DAPHINE Core," _J. Nuclear Energy 23_, p. 308, 1969.

12. R. Gold, "Compton Recoil Measurements of Continuous Gamma-Ray Spectra," _Trans. Am. Nucl. Soc. 13_, p. 421, 1970.

13. H. E. Korn, _Measurement of the Energy Distribution of the Gamma Field in a Fast Reactor_, KfK 2211, Karlsruhe Nuclear Research Center, Federal Republic of Germany, 1975.

14. S. H. Jiang and H. Werle, "Fission Neutron-Induced Gamma Fields in Iron," _Nucl. Sci. Eng. 66_, p. 354, 1978.

15. R. Gold and B. J. Kaiser, "Reactor Gamma Spectrometry: Status," _Proceedings of the Third ASTM-EURATOM International Symposium on Reactor Dosimetry, Ispra (Varese), Italy, October 1-5, 1979_, EUR6813, Vol II, 1160 (1980).

16. R. Gold and B. J. Kaiser, "Status of Compton Recoil Gamma-Ray Spectroscopy," _Trans. Am. Nucl. Soc. 33_, p. 692, 1979.

17. R. Gold, B. J. Kaiser, F. S. Moore, Jr., W. C. Bunch, W. N. McElroy and E. M. Sheen, "Continuous Gamma Ray Spectrometry in the Fast Flux Test Facility," _ANS Topical Meeting on 1980 Advances in Reactor Physics and Shielding_, Sun Valley, Idaho, September 14-17, 1980. ISDN #0-89448-107-X, p. 803, 1980.

18. R. Gold and I. K. Olson, _Analysis of Compton Continuum Measurements_, ANL-7611, Argonne National Laboratory, Argonne, IL, 1970.

19. R. Gold, "Gamma-Continuum at the Air-Land Interface," _Health Physics 21_, p. 79, 1971.

20. A. M. Strash and R. Gold, "Absolute Gamma-Ray Dosimetry by Recoil Electron Spectroscopy," _Nature 234_, p. 260, 1971.

21. R. Gold, _An Iterative Unfolding Method for Response Matrices_, ANL-6984, 1964.

COMPUTER CONTROLLED SCANNING SYSTEMS FOR QUANTITATIVE TRACK MEASUREMENTS

Raymond Gold, James H. Roberts, Christopher C. Preston,
James P. McNeece and Frank H. Ruddy
Westinghouse Hanford Company
Handord Engineering Development Laboratory
Richland, Washington 99352

ABSTRACT

The status of three computer controlled systems for quantitative track measurements is described. Two systems, an automated optical track scanner (AOTS) and an automated scanning electron microscope (ASEM) are used for scanning solid state track recorders (SSTR). The third system, the emulsion scanning processor (ESP), is an interactive system used to measure the length of proton tracks in nuclear research emulsions (NRE). Recent advances achieved with these systems are presented, with emphasis placed upon the current limitations of these systems for reactor neutron dosimetry.

INTRODUCTION

A major inconvenience of track observation methods is the necessity of visual or manual measurement of tracks, a task which requires care, patience, and dedication. This drawback is clearly manifested in precision measurements, where inherent statistical limitations require the observation of large numbers of tracks for adequate precision and make the task time consuming as well as expensive. As a consequence, worldwide expertise in precision applications of NRE and SSTR methods is quite limited. A more detailed discussion of these requirements can be found in a critical review of the SSTR method, which was presented at the very first of this series of international symposia on reactor dosimetry.[1]

Elimination of the human element would be highly desirable for precise track measurements, since it would permit the introduction of more quantitative standards of track identification and background subtraction. Such standards would obviate problems of personal bias in manual track measurements, which can otherwise compromise experimental accuracy. Hence, such biases must constantly be guarded against in manual track scanning. Considerable interest exists, therefore, in the automation of this scanning task. A perhaps tacit, but certainly reasonable assumption is that any such automated system must provide at least comparable accuracy to manual scanning techniques. Only under such a condition can the high accuracy goals of current NRE and SSTR applications be maintained.

Present day minicomputers and microprocessors enable a range of automation, from partial to total, of tasks once thought beyond approach. Among the major considerations in the design and development of these track scanning systems were: (1) simplicity, (2) ease of operation, and (3) stability and reliability of performance. In all three systems, an attempt has been made to utilize the power and flexibility of computer control to the maximum possible extent.

In the next section, the recent upgrading of the AOTS system is outlined with emphasis on specific modifications that have been introduced to overcome limitations of the original AOTS system. The ASEM system, which is devoted to high power/high fluence SSTR experiments, is presented in the following section. In the last section, the interactive ESP system is described together with advances that have been effected in NRE neutron dosimetry.

AUTOMATED OPTICAL TRACK SCANNER (AOTS)

While many groups have attempted to automate SSTR scanning, the overall degree of success has been less than satisfactory. A spark counting method applicable with plastic SSTR such as Makrofol or Lexan has been successfully demonstrated,[2,3] but possesses severe limitations for precision work. Detailed investigations[4,5] reveal an accuracy of roughly 10-20% for this technique, provided track density is limited to less than $10^3/cm^2$.

A more sophisticated automation system, using an optical microscope under computer control, has been developed.[6-8] This automated optical track scanner (AOTS) system has demonstrated comparable accuracy to manual scanning for plastic SSTR of the polycarbonate resin variety such as Makrofol, Lexan, etc.[9]

Although this AOTS system did establish that SSTR automation was possible at an accuracy level comparable with human observations, severe limitations arose. Extreme difficulty was originally encountered using mineral track recorder materials such as mica with any degree of reliability or reproducibility. A track density limit of roughly 10^5 tracks/cm^2 was established, beyond which SSTR accuracy could be seriously compromised. System speed was approximately 10 hrs/cm^2, which provides a relatively slow processing rate of only one to two SSTR per day.

The AOTS system, originally developed at Argonne National Laboratory, (ANL), was the first microscope system ever built that possessed automatic focussing capability. It has been transferred to the Hanford Engineering Development Laboratory (HEDL) in order to meet the overall dosimetry needs of the US fast breeder reactor (FBR), light water reactor (LWR), and magnetic fusion reactor (MFR) energy programs. Since the AOTS system was fabricated over a decade ago, general upgrading of system components was warranted. While the difficulties encountered in scanning mica SSTR have apparently been solved[10], current improvements are intended to overcome earlier limitations in track density and slow processing speed.

Figure 1 displays the general block diagram of the present AOTS system. Components which comprise the upgraded AOTS system are summarized in Table 1. The video camera of the upgraded system replaces the photomultiplier readout of the original system, wherein, the photomultiplier viewed a 0.4 mm aperture located 20 cm above the microscope eyepiece.[8]

Since the quality of the video image scarcely compromises microscope resolution and contrast, significant improvement in pattern recognition accrues. As a consequence, this new videcon readout provides the AOTS system with equal processing capability for all types of SSTR, ranging from plastic to mineral. In fact, this new readout system facilitates applications that depend upon more detailed track observations, such as measurement of track structure or shape, e.g., track diameter, track range,....etc. An important example is the measurement of proton energy through track diameter observations in CR-39 SSTR.[11]

Improved speed and reliability accrue to the new AOTS system through reduced dependence upon mechanical motion. Now the microscope stage need only be moved from field-to-field. Video processing not only eliminates the need for mechanical (X,Y) motion within any given microscope field, but provides an estimated order of magnitude increase in system processing speed.

AUTOMATED SCANNING ELECTRON MICROSCOPE (ASEM)

An additional limitation in SSTR work arises because of the overlap of tracks at high track density. This phenomenon, which is generally called track pile-up, is especially prevalent in high power/high fluence applications due to the high sensitivity of the SSTR method. Optical microscopy cannot provide sufficiently high magnification to allay pile-up effects produced in such high power/high fluence experiments. Since the required levels of magnification for track scanning in high power/high fluence applications are more tractable for electron than optical microscopy, the logical outgrowth of earlier efforts is a second generation automated scanner using the higher magnification afforded by scanning electron microscopy. In view of the significance of in-situ SSTR experiments at high power/high fluence in U.S. FBR, LWR, and MFR energy programs, an automated scanning electron microscope (ASEM) system has been developed.

The block diagram of the ASEM system is displayed in Figure 2 and equipment components are summarized in Table 2. In scanning electron microscopy, the specimen (SSTR) is held stationary and a fine electron beam traces across the specimen surface in a television raster type scanning mode. Not only is all mechanical motion eliminated, but system speed is not longer inherently limited by the existence of mechanical motion. Hence SSTR processing rates should be significantly improved. Important improvements in stability and reliability accrue, since scanning electron microscopy possesses much greater depth-of-focus than optical microscopy. In contrast with the computer-controlled optical microscopy system, a SEM
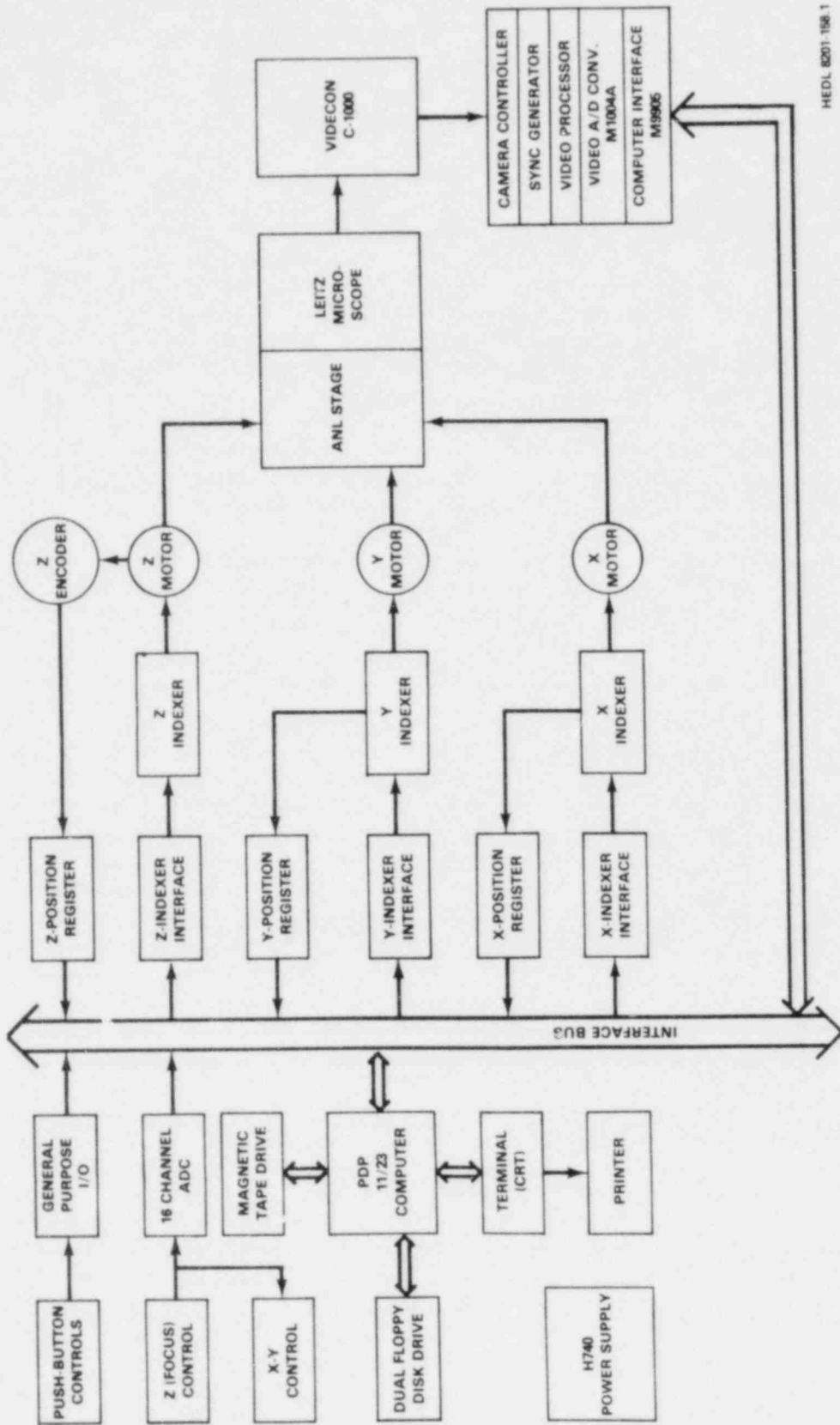
FIGURE 1. Block Diagram of the Automated Optical Track Scanner (AOTS) System.
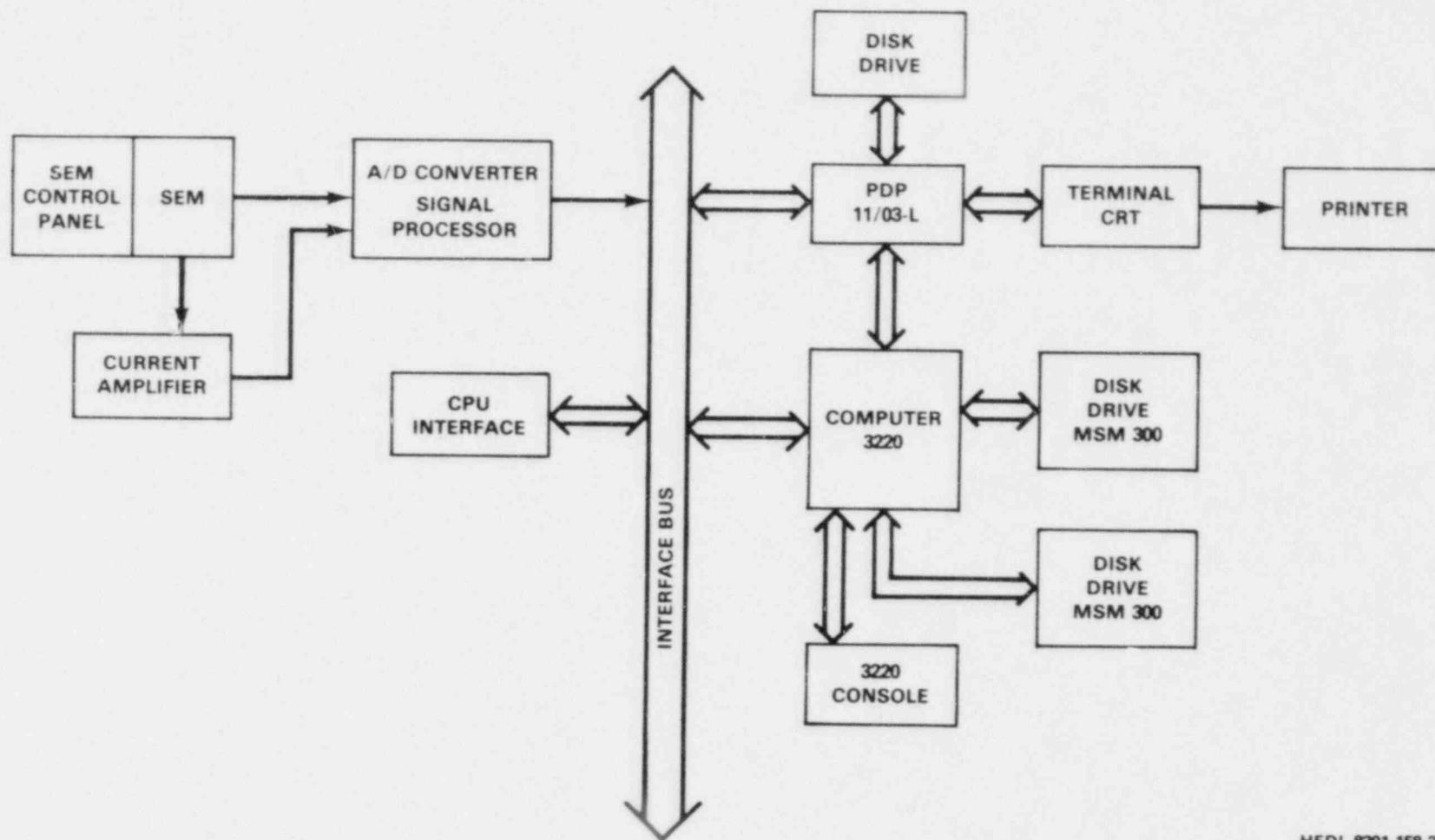
FIGURE 2. Block Diagram of the Automated Scanning Electron Microscope (ASEM) System.

TABLE 1

Automatic Optical Track Scanner (AOTS) System Equipment

Component	Manufacturer
Microscope System	Leitz
Computer Terminal VT100	Digital Equipment Corporation
Joysticks	Tektronix
PDP 11/23 Computer	Digital Equipment Corporation
Indexers SP153	Superior Electric
Interface/Bus	J. F. Microsystem
Bus Expander	HEDL
H740d Power Supply	Digital Equipment Corporation
Stepper Motors HDUM-16-100-5	Harmonic Drive Div/United Shoe Machinery Corporation
Magnetic Tape Drive - CIPER	Aviv Corporation
Dual Floppy Disk Drive	Charles River Data Systems
X, Y, Z Stage	ANL
Support Table	ANL
TV Monitor, DM 14/C	COHU, Inc.
Video Camera, C-1000	Hamamatsu Systems, Inc.
Camera Controller, C-1000	Hamamatsu Systems, Inc.
Graphics Controller, MLSI-512	Matrox Electronic Systems, Ltd.
Phase Lock Loop Module, PLL-01	Matrox Electronic Systems, Ltd.
RAM (24X80), 2480	Matrox Electronic Systems, Ltd.
Light Pen, LP-600	Matrox Electronic Systems, Ltd.

under computer control would be much simpler in that no need for automatic focusing adjustments would exist. Elimination of automated mechanical motion and focus control in the SEM system should, in principle, provide quantitative data of higher accuracy for many differnet types of track recorder materials.

A significantly larger domain of track density can be covered by the ASEM system. In view of inherent track pile-up effects in high power/high fluence SSTR experiments, it is obviously desirable to restrict track size as much as possible. Owing to the range of magnification available with a SEM, it should be possible to adjust etching conditions so that extremely high track densities can be quantified. Our work to date indicates that it should be possible to accurately determine track density up to 10^8 tracks/cm^2 and perhaps even higher by use of the Buffon needle method.[12,13]

TABLE 2
Automated Scanning Electron Microscope (ASEM) System Equipment

Component	Manufacturer
Scanning Electron Microscope, 1200A	American Metals Research Corp.
Current Amplifier, 427	Keithley
PDP 11/03-L Computer	Digital Equipment Corporation
Terminal, 2644A	Hewlett-Packard
Printer 440	Integral Data Systems
H740d Power Supply	Digital Equipment Corporation
Interface/Bus	J. F. Microsystems
Duel Floppy Disk Drive	Charles River Data Systems
Video A/D Converter, TV8B	Datel Interfil
Computer, 3220	Perkin-Elmer
Terminal, 520	Perkin-Elmer
Disk Drive MSM 300	Perkin-Elmer
Bus Expander	HEDL

EMULSION SCANNING PROCESSOR (ESP) SYSTEM

Because of the enormous utility of NRE, many groups have developed special instrumentation systems to aid in the task of emulsion scanning. A review text[14] on NRE summarizes these activities through 1961. More recently, a Russian group has developed an emulsion scanning instrumentation system for fast neutron measurements.[15]

Our applications of NRE in neutron dosimetry and spectrometry have motivated the development of a computer-based interactive system for scanning emulsions. This system, which is called the Emulsion Scanning Processor (ESP), has been developed to measure the lengths of proton-recoil tracks in NRE as well as to store, process, and analyze track data so obtained. To date, this system has been successfully used for neutron dosimetry and spectrometry in FBR and LWR environments.[16,17]

In the ESP system, the X, Y, and Z (focus) stage motion of a motorized Universal Zeiss microscope is controlled by a PDP 11/03-L computer. The computer receives all operator instructions, moves the stage as directed, and stores positional information on command. Software programs, stored on floppy disks, provide the flexibility needed to conveniently tailor operating, storage, and data presentation formats to fit different scanning situations. The motorized stage possesses a travel of 75 mm in the X-direction, 25 mm in the Y-direction, and 4 mm in the Z (focus) direction. Digital motion step size is 0.25 μm in the X and Y directions, whereas the Z direction step size is 0.05 μm.

Figure 3 displays the operational block diagram of the ESP system. An operator must interact with the system to obtain the desired results. The joystick and pushbutton controls are used to set parameters and boundaries, focus, locate tracks, measure track lengths, categorize, and store track data. Major equipment components of the ESP system are summarized in Table 3.

To our knowledge, the ESP system is the first truly interactive system developed and used for emulsion scanning. This system possesses interfaces between all three fundamental constituent elements, namely man, microscope, and computer. Of equal significance is our reliance upon computer control to the maximum extent possible. For these reasons, the ESP system provides a substantial advance in the state-of-the-art of emulsion scanning systems in terms of both accuracy and cost-effectiveness.

While the Russian system[15] represents the first system ever built which responded to hardware instructions, only motion in the (X, Y) plane could be controlled through two specific hardware instructions, namely (1) return to the center of field and (2) go to the next field. Consequently such a system does not constitute a fully interactive system between man and computer. Indeed, there was no computer.

The ESP system is fully interactive and possesses automated (X, Y, Z) control, where Z is the depth coordinate in the emulsion, which is controlled by changing microscope focus. Consequently as opposed to the 2-dimensional Russian system, our 3-dimensional ESP system provides the full automation required of scanning 3-dimensional entities (tracks) in emulsions. While the Russian system responds only to two specific hardware instructions, our fully interactive system responds to computer software. This is a crucial distinction, since through appropriate computer software the ESP system can carry out, in principle, infinitely more tasks of greater sophistication and/or complexity. This feature provides the power and capability to use our system for many different applications.

To date, the ESP system has been used exclusively for observation of proton-recoil tracks in neutron dosimetry measurements. On the basis of these efforts, the power and flexibility of this system has been demonstrated by the development of computer codes to handle three completely different scanning tasks. These different tasks are:

1. Track length measurements in 4π irradiated emulsions for differential neutron spectrometry.

2. Track length measurements in 4π irradiated emulsions for integral neutron dosimetry.

3. Track length measurements in emulsions irradiated in collimated or unidirectional neutron beams for differential neutron spectrometry.
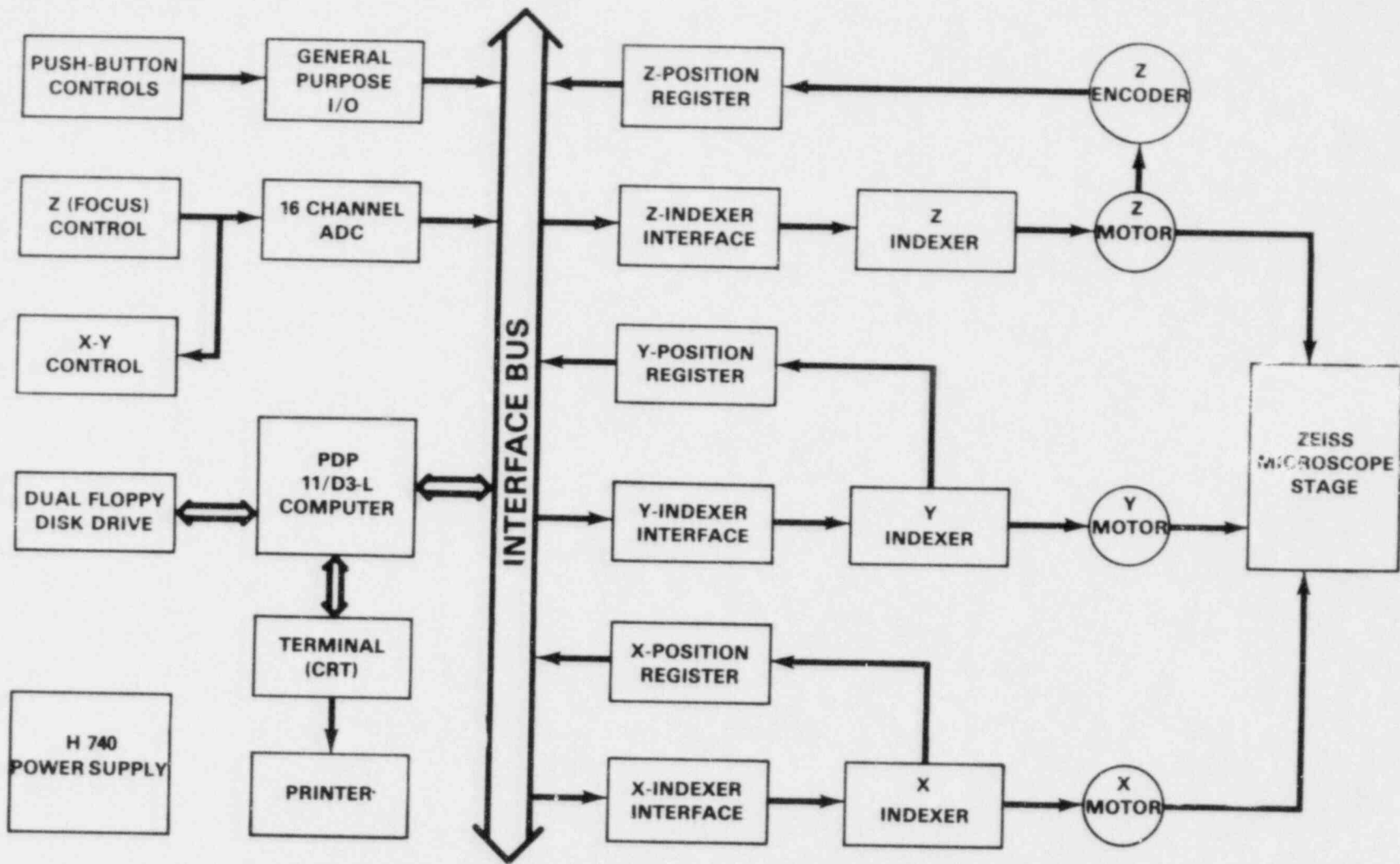
FIGURE 3.   Block Diagram of the Emulsion Scanning Processor (ESP) System.

289

TABLE 3
Emulsion Scanning Processor (ESP) System Equipment

Component	Manufacturer
Universal Microscope System	Carl Zeiss
Computer Terminal	Beehive International
Joysticks	Tektronix
PDP 11/03-L Computer	Digital Equipment Corporation
H740d Power Supply	Digital Equipment Corporation
Dual Floppy Disk Drive	Charles River Data Systems
Indexers SP153	Superior Electric
Interface	J. F. Microsystem
Bus Expander	HEDL

These scanning tasks correspond to operation of the ESP system in different modes, namely differential mode scanning, integral mode scanning, and end-on scanning, respectively. Differential mode scanning has been used for NRE differential neutron spectrum measurements in the Fast Flux Test Facility (FFTF) at startup.[16] Indeed, these efforts led to the first experimental confirmation of the existence of angular anisotropy in the neutron field within a reactor core. Integral mode scanning has been used for NRE integral proton-recoil reaction rate measurements in the LWR pressure vessel mockup at the pool critical assembly (PCA) in Oak Ridge National Laboratory (ORNL).[18] The end-on scanning mode has been applied with NRE exposed in the standard ^{252}Cf fission neutron benchmark field maintained at the National Bureau of Standards (NBS). These NRE spectral measurements of the standard ^{252}Cf fission neutron field will be reported in sequel.

The ESP system provides a substantial advance in the state-of-the-art of emulsion scanning in terms of both accuracy and cost-effectiveness. The uncertainty in track length measurements with this system is approximately $0.52\mu m$ (1σ), which is an improvement of about a factor of 4 over earlier automation efforts.[15] While emulsion scanning rates vary for the different modes of system operation, scanning rates of 30 to 40 tracks/hour have been typically obtained. This rate represents an increase by a factor of 3 to 4 over scanning rates attained in earlier work.[15]

ACKNOWLEDGEMENTS

REFERENCES

1. R. Gold, "Critical Requirements of the SSTR Method," 1st ASTM-EURATOM Symposium on Reactor Dosimetry, Petten (1975), EUR5667, Part II, 175 (1977).

2. N. G. Cross and L. Tommasino, Proc. Intern. Topical Conf. on Nuclear Track Registration in Insulating Solids and Applications, Univ. of Clermont, Clermont-Ferrand, France, Vol. I, 73, (1969).

3. N. L. Lark, "Spark Scanning for Fission Fragment Tracks in Plastic Foils," Nucl. Instr. Methods 67, 137 (1969).

4. F. J. Congel, et al., "Automatic System for Counting Etched Holes in Thin Dielectric Plastics," Trans. Am. Nucl. Soc. 13, 419 (1970).

5. F. J. Congel, et al., "Automatic System for Counting Etched Holes in Thin Dielectric Plastics," Nucl. Instr. 100, 247 (1972).

6. C. E. Cohn, R. Gold, and T. W. Pienias, "Computer-Controlled Microscope for Scanning Fission Track Plates," Trans. Am. Nucl. Soc. 12 68 (1969).

7. R. Gold and C. E. Cohn, "Analysis of Automatic Fission Track Scanning Data," Trans. Am. Nucl. Soc. 14, 500 (1971).

8. C. E. Cohn and R. Gold, "A Computer-Controlled Microscope for Automatic Scanning of Solid State Nuclear Track Recorders," Rev. Sci. Inst. 43, 12, (1972).

9. R. Gold and C. E. Cohn, "Analysis of Automatic Fission Track Scanning in Solid State Nuclear Track Recorders," Rev. Sci. Inst. 43, 18 (1972).

10. C. E. Cohn and R. J. Armani, "Automatic Scanning of Mica Track Recorders," Rev. Sci. Inst. 46, 18 (1975).

11. E. V. Benton, C. C. Preston, F. H. Ruddy, R. Gold, and J. H. Roberts, "Proton and Alpha Particle response Characteristics of CR-39 Polymer for Reactor and Dosimetry Applications," Proceedings of the Tenth International Conference on Solid State Nuclear Track Detectors, Lyon (1979), Pergamon Press, Oxford, 459 (1980).

12. R. Gold, F. H. Ruddy and J. H. Roberts, "Buffon Needle Method of Track Scanning at High Track Density," Bull. Am. Phys. Soc. 25, 484 (1980).

13. R. Gold, F. H. Ruddy, and J. H. Roberts, "Buffon Needle Method of Track Counting," Solid State Nuclear Track Detectors, Proceedings of the Eleventh International Conference on Solid State Nuclear Track Detectors, Bristol (1981), Pergamon Press, Oxford, 891 (1982).

14. W. H. Barkas, Nuclear Research Emulsions, Vol. 1, Techniques and Theory, Academic Press, New York and London (1963).

15. G. E. Belovitskii, A. E. Voronkov, L. N. Kolesnikova, R. A. Latypova, L. V. Sukhov, and I. V. Shtranikh, "Measurements of the Spectra of Fast Neutrons (14 MeV) with High Energy Resolution with the Aid of Nuclear Emulsions. Automation of the Measurements," Proceedings (Trudy) of the P. N. Lebedev Physics Institute, Nuclear Reactions and Interaction of Neutrons and Matter, Vol. 63, p. 109 (1972).

16. R. Gold and J. H. Roberts, "Nuclear Emulsion Neutron Spectrometry in the Fast Flux Test Facility," Trans. Am. Nucl. Soc. 39, 896 (1981).

17. R. Gold, J. H. Roberts, C. C. Preston, and F. H. Ruddy, "Neutron Spectrometry with Nuclear Research Emulsions," Section 3.3 in LWR Pressure Vessel Surveillance Dosimetry Improvement Program: PCA Experiments and Blind Test, W. N. McElroy, Editor, NUREG/CR-1861, HEDL-TME 80-87 (1981).

18. R. Gold, J. H. Roberts, F. H. Ruddy, C. C. Preston, and C. A. Hendricks, "Proton-Recoil Emulsion Observations for Integral Neutron Dosimetry," Proceedings of the IAEA Advisory Group Meeting on Nuclear Data for Radiation Damage and Safety, Vienna (1981).

LIGHT WATER REACTOR -
PRESSURE VESSEL NEUTRON SPECTROMETRY WITH
SOLID STATE TRACK RECORDERS

Frank H. Ruddy, Raymond Gold, and James H. Roberts
Hanford Engineering Development Laboratory
Richland, Washington, U.S.A.

ABSTRACT

Solid State Track Recorders have been used to measure absolute fission rates in the Light Water Reactor - Pressure Vessel Simulator at the Oak Ridge Pool Critical Assembly. Measurements were made in the 12/13 configuration with ^{237}Np, ^{238}U, and ^{235}U at the TSF, TSB, PVF, 1/4 T, 1/2 T, and 3/4 T locations. To avoid relative power normalization uncertainties, all locations were measured simultaneously in a single run for each isotope.

Comparisons of SSTR results are made with the results of measurements performed by NBS and CEN/SCK using benchmark referenced fission chambers and with the trends of theoretical calculations.

INTRODUCTION

Fission rate measurements using Solid State Track Recorders (SSTR) have been continued at the Pool Critical Assembly (PCA) Light Water Reactor-Pressure Vessel Simulator (LWR-PVS) at Oak Ridge.[1] In addition to the previously reported[2,3] PCA 8/7* and 12/13 fission rates for ^{232}Th, ^{235}U, ^{238}U, and ^{237}Np, additional measurements have been carried out in the PCA 4/12 (SSC), PCA 8/7, and PCA 12/13 configurations. A summary of these additional PCA runs completed to date is contained in Table 1.

This paper presents data taken in November 1981 for the 12/13 configuration when fission rates were measured for all seven radial locations simultaneously in separate runs for ^{237}Np and ^{238}U. These data represent the only PCA radial traverses where relative fission rates can be obtained without power normalization uncertainties for the seven radial locations. Data taken during the other runs listed in Table 1 are being reduced and will be reported in sequel.

---

*Nomenclature and acronyms conform to those already introduced in Reference 1.

Experimental Procedures

Mica SSTR were placed in contact with deposits of the appropriate fissionable materials. Thin vacuum deposits of ^{238}U, ^{235}U and ^{237}Np on 5 mil stainless steel backings were used. These deposits were calibrated before use using alpha spectrometry and were simularly recalibrated after they had been used in the PCA to insure against loss of deposit material during the measurements. The deposit, surrounded by two 3/4-in. diameter mica SSTR wafers, was placed between two 10 mil Cd wafers in the cases of ^{238}U and ^{237}Np. Iron wafers were used to center the deposits in the measurement locations in the pressure vessel simulator and to fill all voids and aluminum was used to center the deposits in the void box measurement location. The ^{235}U and ^{237}Np deposits were surrounded by a cylindrical 10 mil Cd liner. In the case of the ^{235}U measurements, iron or aluminum wafers were used in place of the cadmium discs and liner. For the measurements in the SSC, cadmium capsules were used in place of the discs and liners. The deposits in the water positions (TSF, TSB, PVF) were placed between two mica SSTRs which were in turn placed between two polyethylene plastic discs to protect the mica and attached with waterproof tape to lucite sheets which were held at the proper distances from the core in the water with a rigid aluminum frame. Cadmium could not be used in the water positions, so ^{235}U measurements were done to assess any contributions to the fission rates from the ^{235}U impurities in the ^{238}U and ^{237}Np deposits. Care was taken to avoid cross-contamination between deposits when loading or unloading the SSTR dosimeters. The exposed mica SSTR were etched for 90 minutes in 49.2% HF at 22.7°C and manually scanned using optical microscopy to a statistical accuracy of about 3% (1σ) by at least two independent scanners. The integrated power during each run was obtained with an NBS calibrated fission chamber run-to-run monitor.[4]

Results and Discussion

The SSTR fission rates measured in the PCA for ^{237}Np and ^{238}U are listed as a function of radial position for the 12/13 configuration in Table 2. These data are plotted in Figure 1 for ^{237}Np and Figure 2 for ^{238}U. These fission rates display the pseudologarithmic decrease as a function of distance within the PVS block that is characteristic of threshold reactions. The departure of the ^{237}Np fission rates in Figure 1 from linearity in the water locations is due to contributions to the fission rate from sub-threshold fission. The cross section for neutron induced ^{237}Np fission shows resonances in the epithermal energy range and the relative number of epithermal neutrons increases as the core is approached. In the case of the ^{238}U data plotted in Figure 2, a straight line with a slope slightly less than the slope in the PVS is obtained in the water positions. These lines intersect at the PVS-H_2O boundary. The contribution to the measured fission rate from ^{235}U in the ^{238}U foils is appreciable in the water positions. A 14.6% correction was required in the PVF position and a 30% correction

was required at the TSB location. The thermal fission correction resulted in an overall uncertainty of 15% for the TSB ^{238}U fission rate, and although this point has been plotted in Figure 2, it has been omitted from Table 2 because of its large uncertainty. In the TSF position, the ^{238}U fission rate could not be accurately measured even with ^{238}U deposits containing as little as 6 ppm ^{235}U due to the extremely high thermal to fast neutron ratio at this location. The relative uncertainties (1σ) have been obtained by combining the sources of error tabulated in reference 3 in quadrature. Uncertainties in power normalization do not enter into the calculation of the relative uncertainties, since a single run was used for ^{238}U or ^{237}Np. To obtain the absolute uncertainties from the relative uncertainties of Table 2, the 4.1% uncertainty in the absolute power normalization must be combined in quadrature with the tabulated values. The absolute uncertainties in these data are generally 5% (1σ) or less.

Previous SSTR fission rate data have been compared with the corresponding NBS and CEN/SCK fission chamber measurements.[5] Tables 3 and 4 are comparisons of the most recent ^{238}U and ^{237}Np fission rates measured in the PCA 8/7 and 12/13 configurations respectively with the corresponding fission chamber measurements.* Note that the more recent SSTR ^{237}Np fission rates are 15% lower than the SSTR fission rates measured in October 1978 which are tabulated in reference 5. This difference must be due to a mispositioning of the PCA 12/13 configuration during the earlier measurements as a 15% error is far to large to be accounted for by any other experimental error. The new results are about 6% lower than NBS as are the October 1978 results for both ^{237}Np and ^{238}U in the 8/7 configuration. The new SSTR results for ^{238}U in the 12/13 configuration are also lower than NBS by about 6%. The overall ratio for the six ^{237}Np results is 0.940 ± 0.031 and for the six ^{238}U results is 0.940 ± 0.016. The smaller standard deviation for the ^{238}U ratio reflects the fact that the SSTR ^{238}U fission rates have lower uncertainties than the ^{237}Np fission rates. Although a 6% discrepancy is within the range of the relative uncertainties of the SSTR and fission chamber measurements, the SSTR to fission chamber ratios are consistently about 0.94 for all of the measurements to date suggesting that there is a systematic bias between the two types of measurements. A possible explanation for this bias is the fact that the void introduced by the fission chamber causes some uncertainty as to the effective position of the fission rate measurement. The fact that the fission chamber measurements are consistently higher would indicate that the fission chamber measurements correspond to a position closer to the core side of the void rather than the assigned central position.[4] The results of additional SSTR measurements in the 8/7 and 12/13 configurations (See Table 1) will be compared to existing SSTR and fission chamber measurements to attempt to resolve this matter.

---

*The NBS ^{237}Np fission rates have been increased by 2.2% due to recalibration of the mass of the NBS ^{237}Np fission deposit.

Comparisons of theoretical calculations to experimental estimates[6] lead to calculated results that are systematically lower than experiment for both ^{238}U and ^{237}Np (see, for example, Figure 7.1.1. and 7.1.4. of Reference 6). If the lower SSTR experimental values are compared to these calculations, calculated to experimental ratios closer to unity would result. These higher ratios would be more consistent with the ratios reported for other dosimeter reactions.[6]

Acknowledgements

We gratefully acknowledge the assistance of F. B. K. Kam, S. Hurt, and the operating crews of the PCA. We thank J. VanAudenhove and his staff at CBNM, Geel and K. M. Glover and her staff at the Chemistry Division, Harwell for providing high quality calibrated fissionable deposits. We thank L. Dunn, L. Icayan, M. Heffner, and J. Smart for assistance with optical scanning. Special thanks are due to A. Fabry for experimental assistance and for carrying out several of the exposures and to C. C. Preston for experimental assistance. This work is supported by the U. S. Nuclear Regulatory Commission.

References

1. F. B. K. Kam, "Description of Experimental Facility," in LWR Pressure Vessel Surveillance Dosimetry Improvement Program: PCA Experiments and Blind Test, W. N. McElroy (Ed.), NUREG/CR-1861, 1981, p. 1.1-1.

2. F. H. Ruddy, R. Gold, and J. H. Roberts, "Solid State Track Recorder Measurements in the Pool Critical Assembly," in Dosimetry Methods for Fuels, Cladding and Structural Materials, Proceedings of the Third ASTM-Euratom Symposium on Reactor Dosimetry, Ispra (Varese) Italy, EUR 6813 Vol. II, 1980, p. 1069.

3. F. H. Ruddy, R. Gold, and J. H. Roberts, "Solid State Track Recorder Measurements" in LWR Pressure Vessel Surveillance Dosimetry Improvement Program: PCA Experiments and Blind Test, W. N. McElroy (ed.), NUREG/ CR-1861, 1981 p. 2.5-1.

4. E. D. McGarry and A. Fabry, "Fission Chamber Measurements" in LWR Pressure Vessel Surveillance Dosimetry Improvement Program: PCA Experiments and Blind Test, W. N. McElroy (ed.), NUREG/CR-1861, 1981, p. 2.3-1.

5. A. Fabry, R. Gold, F. H. Ruddy, J. H. Roberts, E. D. McGarry, and F. W. Stallman, "Comparison Between Solid State Track Recorder and Fission Chamber Measurements," in LWR Pressure Vessel Surveillance Dosimetry Improvement Program: PCA Experiments and Blind Test, W. N. McElroy (ed.), NUREG/CR-1861, 1981, p. 4.3-1.

6. W. N. McElroy, E. P. Lippincott, A. Fabry, F. W. Stallmann, and F. B. K. Kam, "Overview Analysis of Neutronic Calculations and Measurements" in LWR Pressure Vessel Surveillance Dosimetry Improvement Program: PCA Experiments and Blind Test, W. N. McElroy, (ed.), NUREG/CR-1861, 1981, p. 7.0-1.
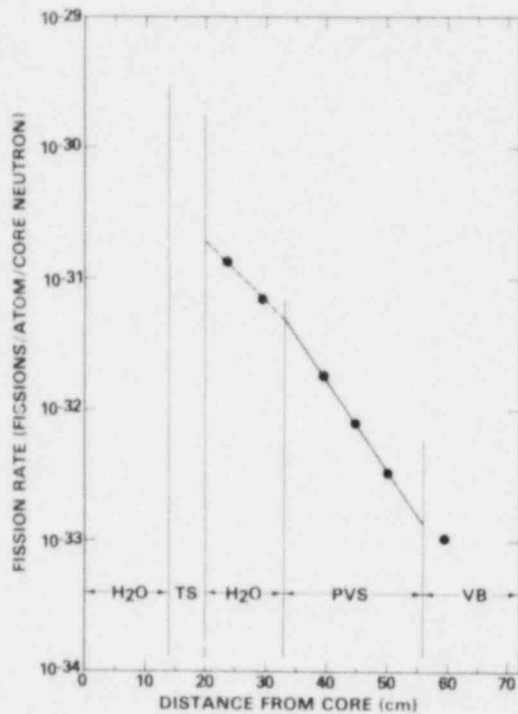
Figure 1. Radial fission rate distribution for ^{237}Np in the PCA 12/13 configuration.
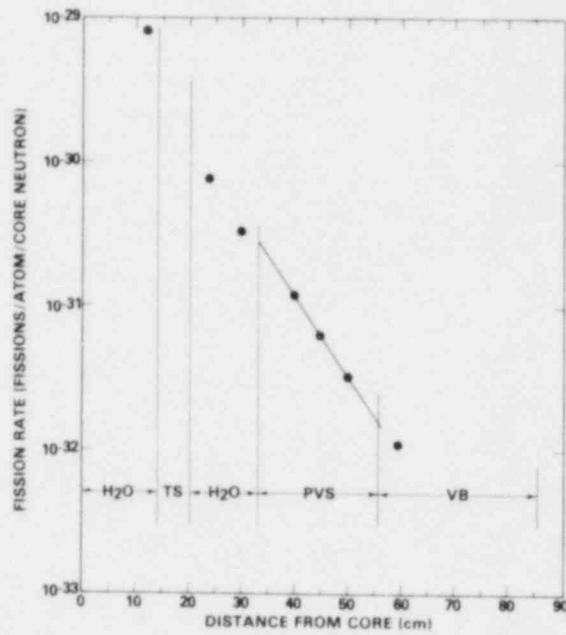
Figure 2. Radial fission rate distribution for ^{238}U in the PCA 12/13 configuration.

Table 1. Schedule of PCA Solid State Track Recorder Measurements

Run Number	Date	Configuration	Isotope	Positions[a]
PCA37	01/14/81	4/12(SSC)	^{237}Np	SSC (+75mm, MP, -75mm), 1/4 T (+75mm, MP, -75mm), 1/2T (MP)
PCA38	01/14/81	4/12(SSC)	^{238}U	SSC (+75mm, MP, -75mm), 1/4 T (+75mm, MP, -75mm), 1/2 T(MP), 3/4 T(MP)
PCA39	10/15/81	8/7	^{238}U	1/4 T, 1/2 T, 3/4 T, VB (all MP)
PCA40	10/15/81	8/7	^{237}Np	1/4 T, 1/2 T, 3/4 T, VB (all MP)
PCA41	10/15/81	8/7	^{238}U	1/4 T (MP)
PCA42	10/16/81	12/13	^{238}U	1/4 T, 1/2 T, 3/4 T, VB (all MP)
PCA43	10/16/81	12/13	^{237}Np	1/4 T, 1/2 T, 3/4 T, VB (all MP)
PCA44	10/16/81	12/13	^{238}U	1/4 T (MP)
PCA45	10/19/81	12/13	^{237}Np	1/4 T (MP)
PCA51	11/18/81	12/13	^{238}U	TSF, TSB, PVF, 1/4 T, 1/2 T, 3/4 T, VB (all MP)
PCA52	11/18/81	12/13	^{237}Np	TSF, TSB, PVF, 1/4 T, 1/2 T, 3/4 T, VB (all MP)
PCA53	11/19/81	12/13	^{235}U	TSF, TSB, PVF, 1/4 T, 1/2 T, 3/4 T, VB (all MP)
PCA54	11/19/81	12/13	^{238}U	TSF, TSB, PVF (all +75mm, MP, and -75mm)

a. 1/4 T, 1/2 T, and 3/4 T refer to depths in a PVS of total thickness, T. The other acronyms are defined as follows: Simulated Surveillance Capsule (SSC); Thermal Shield Front (TSF); Thermal Shield Back (TSB); Pressure Vessel Front (PVF); Void Box (VB); and Mid Plane (MP).

298

Table 2. <u>SSTR Fission Rates Measured in the PCA 12/13 Configuration</u>

| Location | Distance From Core (cm)* | Fission Rate f/atom/(core neutron) | |
		^{237}Np	^{238}U
TSF	12.0	$8.23 \times 10^{-30} \pm 3.2\%$	---
TSB	23.8	$7.78 \times 10^{-31} \pm 3.2\%$	---
PVF	29.7	$3.23 \times 10^{-31} \pm 3.2\%$	$6.75 \times 10^{-32} \pm 4.0\%$
1/4 T	39.5	$1.23 \times 10^{-31} \pm 3.5\%$	$1.82 \times 10^{-32} \pm 2.6\%$
1/2 T	44.7	$6.45 \times 10^{-32} \pm 5.4\%$	$7.81 \times 10^{-33} \pm 2.6\%$
3/4 T	50.1	$3.46 \times 10^{-32} \pm 3.2\%$	$3.36 \times 10^{-33} \pm 2.6\%$
VB	59.1	$1.01 \times 10^{-32} \pm 3.3\%$	$1.01 \times 10^{-33} \pm 2.6\%$

---

*Distance from inner face of core aluminum simulator (or window).

Table 3. Comparison of SSTR and Fission Chamber Measured Fission Rates for the PCA 8/7 Configuration.

Isotope	Location	Fission Chamber	SSTR		Ratio (SSTR/Fission Chamber)*
		f/atom/(core neutron) x 10^{31}			
^{237}Np	1/4 T	7.83 ± 2.9%	7.45 ± 4.6%		0.951 ± 0.052
	1/2 T	4.34 ± 2.9%	4.20 ± 5.4%		0.968 ± 0.060
	3/4 T	2.29 ± 2.9%	2.05 ± 4.4%		0.895 ± 0.047
				Ave.	0.938 ± 0.038
^{238}U	1/4 T	1.04 ± 2.8%	0.951 ± 2.5%		0.918 ± 0.034
	1/2 T	0.451 ± 3.0%	0.421 ± 2.8%		0.933 ± 0.038
	3/4 T	0.187 ± 3.0%	0.178 ± 2.6%		0.952 ± 0.038
				Ave.	0.934 ± 0.017

---

*The uncertainties on individual ratios were obtained by combining the uncertainties on the SSTR and fission chamber measurements in quadrature. The uncertainty on the average is the standard deviation of the mean of the three ratios.

Table 4. Comparison of SSTR and Fission Chamber Measured Fission Rates for the PCA 12/13 Configuration.

Isotope	Location	Fission Chamber	SSTR	Ratio (SSTR/Fission Chamber)*
		f/atom/(core neutron) x 10^{32}		
^{237}Np	1/4 T	12.6 ± 2.9%	12.3 ± 3.5%	0.976 ± 0.044
	1/2 T	7.06 ± 3.1%	6.45 ± 5.4%	0.914 ± 0.062
	3/4 T	3.70 ± 3.1%	3.46 ± 3.2%	0.935 ± 0.045
				0.942 ± 0.032
^{238}U	1/4 T	1.92	1.82 ± 2.6%	0.948
	1/2 T	0.842	0.781 ± 2.6%	0.928
	3/4 T	0.350	0.336 ± 2.6%	0.960
				0.945 ± 0.016

*See footnote for Table 3.

AMELIORATIONS DES CALORIMETRES
POUR LA MESURE DES PUISSANCES SPECIFIQUES
DEPOSEES DANS LES REACTEURS NUCLEAIRES

H.PETITCOLAS, J-J.BONNIN, P.CHENAVAS
CENTRE D'ETUDES NUCLEAIRES DE GRENOBLE
SERVICE DES PILES
85 X
F 38041 GRENOBLE.

ABSTRACT

IMPROVEMENTS OF CALORIMETERS

TO MEASURE THE SPECIFIC POWERS RELEASED IN NUCLEAR REACTORS

Several improvements have been carried out on some calorimeters, manufactured at CEA/CEN-GRENOBLE, to answer three main objectives :

- warrant the absolutness of measurements,
- stabilize the response,
- adapt the sensitivity and the characteristics to the various conditions.

Several types of products are described, particularly :

- a highvolumic sensitivity calorimeter, used for absolute calibration of thermoluminescent dosimeters, able to measure, in spite of its small volume, a value of 2 mWg^{-1} with a 4% accuracy and 2% precision.

- a calorimeter with a magnesium jacket and sample.

RESUME

Plusieurs améliorations sont apportées aux calorimètres fabriqués au CEN-G pour répondre à 3 objectifs principaux :

- garantir le caractère absolu des mesures,
- stabiliser la réponse de l'appareil,
- adapter la sensibilité et les caractéristiques aux multiples conditions.

Diverses réalisations sont décrites, en particulier :

- un calorimètre à grande sensibilité volumique, servant à l'étalonnage absolu de détecteurs thermoluminescents, capable, malgré son petit volume, de mesurer 2 mWg^{-1} avec une exactitude de 4% et une précision de 2%.

- un calorimètre à paroi et à échantillon en magnésium.

==

Avertissement : Ce document est la reproduction d'une affiche

1° OBJECTIF : MESURER EN ABSOLU LA PUISSANCE SPÉCIFIQUE GAMMA

SÉLECTIVITÉ : MINIMISER LA SENSIBILITÉ AUX NEUTRONS

thermiques : échantillons et enveloppes à faibles sections efficaces de capture ;
rapides : échantillons à nombre de masse A élevé (corrections si A faible).

MINIMISER LES PERTURBATIONS PAR L'ENVELOPPE

Épaisseur et numéro atomique Z faibles pour ne pas affaiblir
le champ gamma ni l'appauvrir en basses énergies.
Échantillon et enveloppe si possible de même nature pour avoir
l'équilibre électronique (sinon, corrections).

NATURE ET GÉOMÉTRIE DES ÉCHANTILLONS
INFLUENT SUR LA PUISSANCE SPÉCIFIQUE →
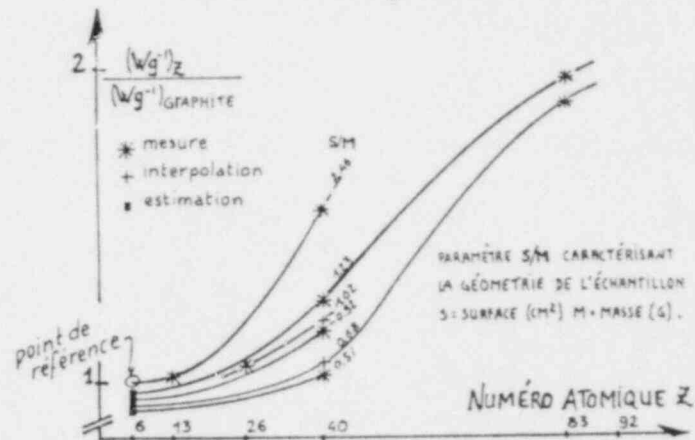
PUISSANCE SPÉCIFIQUE RELATIVE MESURÉE DANS DIVERS ÉCHANTILLONS
dans le réflecteur du réacteur SILOÉ.

les écarts sont accentués dans un spectre γ plus riche en basses énergies.
Pour éviter l'hypersensibilité aux basses énergies γ, utiliser des échantillons à Z faible.

2° OBJECTIF · STABILISER LES CALORIMÈTRES

QUAND LA TEMPÉRATURE AUGMENTE,
LA CONSTANTE DE TEMPS DIMINUE.

Causes : les échanges thermiques par conduction dans le gaz
et les supports, et par convection et par rayonnement,
croissent avec la température.

Solutions : minimiser la convection et le rayonnement ;
utiliser des couples échantillon-isolant tels
que $T(\theta) =$ Constante (Mg-Ne ; Mg-He).

AU COURS DE LA DURÉE D'IRRADIATION,
LA SENSIBILITÉ DIMINUE.

Causes : dégazage (surtout hydrogène) de l'échantillon et de l'enveloppe,
augmentation du pouvoir émissif ε.

Solutions : utiliser des matériaux fondus sous vide et les dégazer ;
diminuer le pouvoir émissif (polissage, dorure) ;
isoler par des gaz rares ;
remplacer le graphite (poreux, ε élevé) par du MAGNÉSIUM.

3ᵉ OBJECTIF ADAPTER AUX MULTIPLES CONDITIONS

puissance spécifique γ : de 15 à 10^{-5} W/g⁻¹.
géométrie de l'échantillon ou du calorimètre.
nature des échantillons.
constante de temps $T_{(\theta)}$ maximale
 (durée d'une mesure, évolution du champ γ à mesurer)
instabilité de θ_0 imposant un $\Delta\theta$ minimal.

CONDITIONS JOUANT SUR LA SENSIBILITÉ

influence des
pouvoirs émissifs
$F = f(\varepsilon_e, \varepsilon_t, \text{géométrie})$

SENSIBILITÉ
°C/Wg⁻¹

	0,02	0,02	} VIDE
	0,1	0,1	
	0,2	0,2	

KRYPTON
ARGON

1000

NEON

ajustement
de la
Sensibilité
(°C/Wg⁻¹)
par la
géométrie
et l'isolement.

HELIUM

100

GAZ
ISOLANT

évaluation
pour le
graphite
à 30°C.

10

DIAMÈTRE DES
THERMOCOUPLES
0,5 mm
1 mm

hypothèse:
pas de
convection.

2   4   8   16 MM

DIAMÈTRE DE L'ÉCHANTILLON

Sensibilité (°C/Wg⁻¹)
Constante de temps (s)

BISMUTH
PLOMB
ZIRCONIUM
FER
ALUMINIUM
MAGNÉSIUM
GRAPHITE

400

200

0

6   12 13   26   40   82 83 Z

CONDITIONS LIÉES AU TYPE DE RÉACTEUR :
ESSAIS & PUISSANCE

température, pression, vibrations, fluide de refroidissement :
→ adapter la nature et l'épaisseur des matériaux, les soudures.

enveloppe acier

isolant thermique
He, Ne, Ar, Kr ou vide.

échantillon graphite, ou
Mg, Al, Fe, Zr, Pb, Bi

thermocouples chromel-alumel
température extérieure θ_0
température de l'échantillon θ

câble coaxial chauffant.
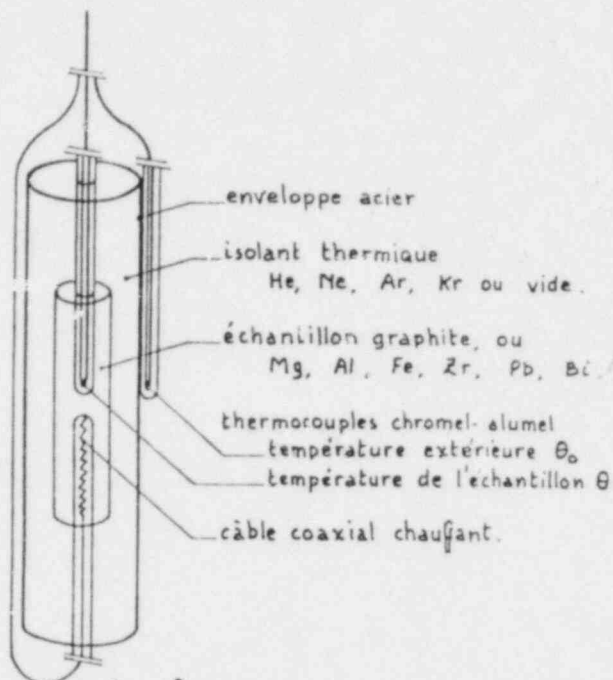
CALORIMÈTRES TG type GRENOBLE
BREVET No. P.V. 910-201

acier ⌀ 19.0.3
azote
thermocouples ⌀ 1
graphite ⌀ 6.35
s/m : 3.6

200 °C/W/g⁻¹

150 S

graphite ⌀ 2.5
s/m = 9.1

15 °C/W/g⁻¹
10 S

enveloppe ⌀ 4.5 . 0.25
isolant argon +
feutre de graphite
thermocouples ⌀ 0.5
0 10 20 mm

zirconium ⌀ 2.5
s/m = 2.5

30 °C/W/g⁻¹
10 S

CALORIMÈTRE TM
à participé aux intercomparaisons
internationales de calorimètres
au CEN GRENOBLE FRANCE
1970 - réacteur Mélusine
à SWIERK, POLOGNE
1972 - réacteur EWA 10
avec 6 autres états.

CALORIMÈTRES MINIATURISÉS

enveloppe Ø 9.05
isolant variable
suivant échantillon

divers échantillons Ø 5

nature	s/m
graphite	4.6
aluminium	3
fer	1
zirconium	1,23
bismuth	0,82

0 10 20 mm

enveloppe Ø 15.05
feutre de graphite
+ hélium
Zirconium Ø 12
$s/m = 0,52$
105 °C/Wg⁻¹
30 s

Zirconium Ø 8/12
$s/m = 0,92$
60 °C/Wg⁻¹
17 s

enveloppe Ø 9.05
feutre de graphite
+ hélium
thermocouples Ø 0.5

bismuth Ø 3.3
$s/m = 1,23$
55 °C/Wg⁻¹
7 s

bismuth Ø 4/6
$s/m = 1,23$
40 °C/Wg⁻¹
5 s

bismuth Ø 6
$s/m = 0,68$
70 °C/Wg⁻¹
9 s

CALORIMÈTRES D'ÉTUDES

— NSM 21 S   Ø 8,6/10,2
— feutre de graphite
— graphite Ø 5,6

dans le CO_2
à 40 bars et 350 °C
de 0,1 à 0,3 Wg⁻¹

sensibilité ~ 100 °C/Wg⁻¹
constante de temps ~ 70 s.

0 10 20 mm

— NSMC Ø 22,6/24,2
— feutre de graphite
— graphite Ø 16

dans le CO_2
à 20 bars et 350 °C
~ 0,2 Wg⁻¹

sensibilité ~ 300 °C/Wg⁻¹
exactitude ~ 12%
précision ~ 1%
Constante de temps ~200 s.

BUGEY 1 FRANCE.

WAGR WINDSCALE UKAEA.

CALORIMÈTRES pour RÉACTEURS de PUISSANCE.

CALORIMÈTRE
POUR LE RÉACTEUR ESSOR
CCR ISPRA

enveloppe Ø 12/14
krypton

fer Ø 9
1750 °C/Wg⁻¹
760 s.

Zirconium Ø 9
1430 °C/Wg⁻¹
400 s.
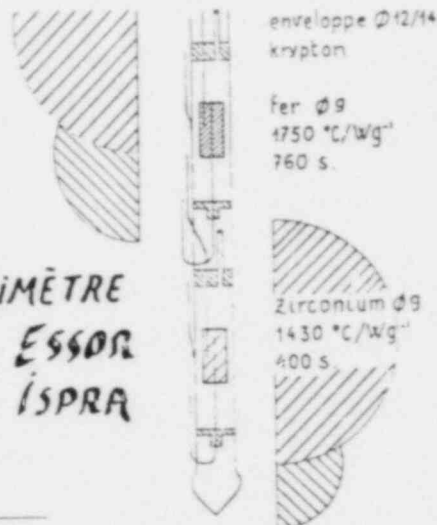
enveloppe Ø 31/32
krypton
graphite Ø 25
1700 °C/Wg⁻¹ 1200 s.

CALORIMÈTRE À
GRANDE SENSIBILITÉ

enveloppe Ø 16/17
krypton
échantillon Ø 12 : Pb, Fe et Al.
3200 °C/Wg⁻¹ 730 s.

CALORIMÈTRE À NOYAU COMPOSITE
POUR MAQUETTE PAHR

CALORIMÈTRE EN MAGNÉSIUM

acier
jonction acier-magnésium
argon
feuille anti-convection
échantillon en magnésium (Ø 5)
enveloppe en magnésium

sensibilité ~80 °C/Wg⁻¹.
constante de temps ~80 s.

0 10 20 mm

enveloppe Mg

remplace avantageusement le graphite

PEU DE PERTURBATION
du champ γ incident.
car densité et Z
faibles

PLUS SÉLECTIF
peu sensible aux neutrons

SENSIBILITÉ
ÉGALE AUX γ.
car même densité (1,75)
et Z proches (12-5)

MESURE ABSOLUE
EXCELLENTE.
car échantillon et enveloppe
de même nature
(équilibre électronique)

PLUS STABLE

échantillon Mg

CALORIMÈTRE À ULTRA-VIDE

prise et câble
haute tension

pompe ionique

boitier étanche

POUR ÉTALONNAGE ABSOLU DE
DÉTECTEURS THERMOLUMINESCENTS
ET DE CHAMBRE D'IONISATION
dans divers spectres gamma de réacteur.

puissance spécifique imposée
compatible avec les D.T.L: 0.002 Wg⁻¹
exactitude 4%   précision 2%

vide 10^{-8} torr

sensibilité
~4000 °C/Wg⁻¹

sensibilité
~4000 °C/Wg⁻¹
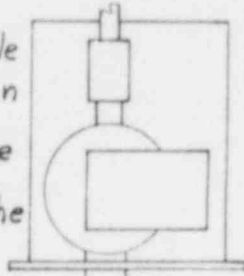
tube poli Ø 14.1

échantillon
graphite doré Ø9

thermocouples Ø1

FER

GRAPHITE

constante
de temps
30 mn

constante
de temps
50 mn.

tube poli Ø 10.1

échantillon
fer doré Ø 5.2

thermocouples Ø1

0 10 20 mm
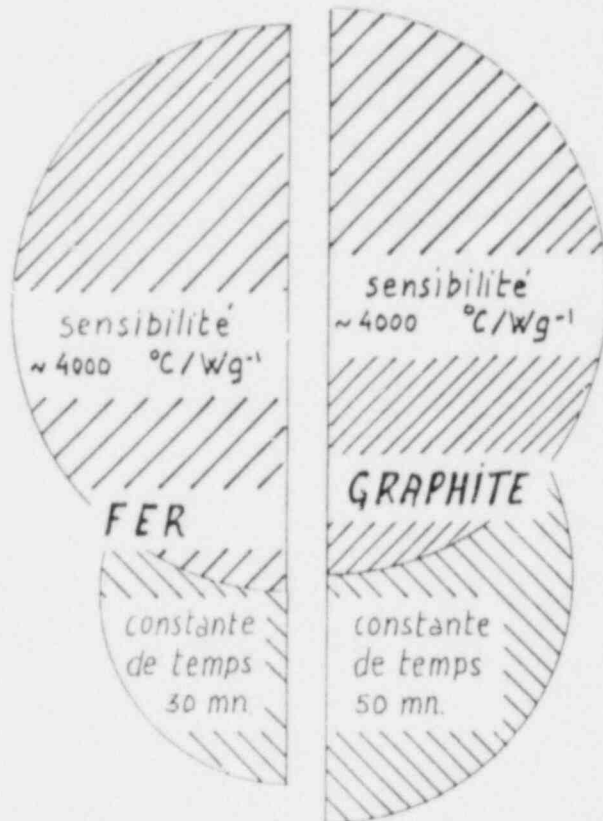
CHAMBRE
D'IONISATION
en fer.

D.T.L.
dans poudre
de fer. •

RAPPEL SUR LE PRINCIPE DE FONCTIONNEMENT

La puissance spécifique P/m (en Wg^{-1}), déposée par les rayonnements dans l'échantillon, élève sa température θ de θ_0 (température extérieure de refroidissement) à θ_e (température à l'équilibre).

- Voir la planche "Calorimètre type GRENOBLE" -

On montre que :

$$\frac{P}{m} = \int_{\theta_0}^{\theta_e} \frac{C(\theta)}{T(\theta)} \, d\theta$$

avec $C(\theta)$ chaleur spécifique de l'échantillon (en $Jg^{-1} \, °C^{-1}$).

$T(\theta)$ constante de temps du calorimètre (en seconde), mesurée après un échelon de puissance électrique ou nucléaire.

REFERENCES

1. International intercomparison of calorimeters. A report of measurements made in the reactor MELUSINE at CEN/GRENOBLE. A.W.BOYD, mars 1970 - I.A.E.A.128.

2. Intercomparison of reactor calorimeters. Proceedings of an international seminar at Institute of Nuclear Research - Swierk, POLAND 15/27 mai 1972.
   Czechoslovak atomic energy commission nuclear information centre Prague - 1974.

3. Mesure par calorimètrie de la dose absorbée dans le graphite dans le réacteur de recherche MELUSINE (8 MW), SILOE (35 MW) et dans le réacteur de puissance BUGEY 1 (1900 MW).
   H.PETITCOLAS,J-J.BONNIN,P.CHENAVAS, First ASTM-Euratom Symposium on reactor dosimetry - Petten 1975 - EUR 5667 e.f. Part I.

4. Nouveaux développements en calorimétrie au Centre d'Etudes Nucléaires de GRENOBLE.
   H.PETITCOLAS, 3ème Symposium ASTM-Euratom, ISPRA(Ital   1-5 Oct. 1979.

5. H.PETITCOLAS, J-J.BONNIN. Calorimètre à grande sensibilité pour la mesure de rayonnement auprès de réacteur nucléaire.
   44ème réunion du Groupe de Travail EURATOM sur la dosimétrie des rayonnements de réacteur. PETTEN - 29 avril 1980.

TOMOGRAPHIE D'ELEMENTS COMBUSTIBLES OBTENUE PAR GAMMAMETRIE

G. Simonet, Services des Piles de Saclay
T. Pineira, Laboratoire d'Etude des Combustibles Irradiés

C.E.N./Saclay, 91191 Gif Sur Yvette, France

RESUME

A partir de mesures transversales gamma d'un élément combustible cylindrique, le programme TOMOGAM reconstitue la distribution des produits de fissions dans une section.

Cette méthode directe, rapide, non destructive, permet à tout moment d'avoir accès au comportement du combustible :

. les produits de fission solubles dans la matrice représentent le combustible lui-même et la répartition des fissions ;

. les éléments migrants renseignent sur les températures atteintes selon les puissances permises ;

. les nucléides volatils s'accumulent en des points particuliers où les phénomènes physico-chimiques d'interaction combustible-gaine sont susceptibles de corroder cette dernière.

Ainsi, la spectrométrie gamma étend ses possibilités d'analyse relatives aux performances des éléments de réacteurs.

PRESENTATION

La compréhension des mécanismes entraînant les ruptures de gaines et la connaissance du comportement du combustible sont l'un des centres d'intérêt actuels, inhérents à l'optimisation des performances des éléments de réacteurs. Il est donc nécessaire de surveiller l'évolution des températures dans le combustible et les modifications de structures.

Si ces informations existent dans le combustible et si l'on peut les mesurer, on saura répondre aux questions posées. Si ces renseignements peuvent être obtenus au long de la vie en pile, sans démantèlement ni séparation chimique, on connaîtra la dynamique rigoureuse des phénomènes.

Or, il se crée, par fission, toute une gamme de produits de fissions ayant leurs propriétés spécifiques ; certains sont corrosifs; d'autres gazeux peuvent induire des contraintes mécaniques. La plupart sont caractérisés par des isotopes radioactifs émetteurs gamma, pénétrants et d'énergie sélective ; leur localisation dans l'espace et l'évolution dans le temps peut être connue par spectrométrie gamma. En particulier, la répartition au sein d'une section droite peut être connue par une transposition des procédés de tomographie médicale à la gammamétrie. Tel est le but du programme TOMOGAM développé à Saclay et présenté dans ce rapport.

REALISATION

Les réacteurs expérimentaux sont équipés d'installations de gammamétrie.

A Saclay, sur un mur de la piscine OSIRIS, un support pour dispositifs expérimentaux est animé de mouvements continus alternés devant un collimateur d'ouverture variable. Un calculateur coordonne le déplacement de la table et l'acquisition des données [1]. A tout moment, il est aisé d'y mesurer, localiser et suivre l'évolution des produits de fission, en corrélation avec les variations de puissance et la combustion massique maximum possible.

Des mesures longitudinales sont réalisées couramment. Les inhomogénéités sont directement décelables et facilitent le choix des zones à étudier.

Des mesures transversales sont effectuées et notre propos est d'obtenir la cartographie des produits de fission dans une section.

La façon la plus concrète de prouver la validité du code nous a semblé être la comparaison de ces examens avec les mesures destructives des mêmes échantillons réels. A cet effet, le LECI dispose d'installations performantes qui ont permis d'assumer complètement cette qualification.

METHODE

Etant donné un combustible cylindrique d'axe vertical, on effectue un balayage horizontal.

L'activité gamma détectée pour un nuclide, à chaque pas de scrutation, résulte de la concentration locale élémentaire recherchée mais aussi du volume émetteur vu par le collimateur, qui change à chaque pas (Fig. 1), de l'auto-atténuation pour ce volume et de l'atténuation dans les structures.

Un code est donc nécessaire pour évaluer la répartition des émetteurs gamma dans la section à partir de projections mesurées sous différentes incidences.

Dans l'hypothèse d'une symétrie de révolution, la concentration de chaque élément peut être calculée depuis les couches extérieures vers l'intérieur avec une seule exploration [2, 3, 4].

Dans le cas d'anisotropie, plusieurs balayages à différents angles de vue sont nécessaires, ainsi qu'un traitement plus complexe. Ce travail a été réalisé en tomographie médicale [5, 6].

La nature des crayons combustibles permet d'émettre des hypothèses simplificatives qui ont facilité l'élaboration du code pluridimensionnel TOMOGAM [7] :

. la géométrie est connue et le faisceau gamma est parallèle (détecteur loin du combustible),

. la migration ne concerne que la localisation d'émission des P.F. dans le milieu qui est considéré comme homogène pour le calcul d'autoatténuation.

Le nombre des projections nécessaires est alors réduit. En effet, nous abandonnons les méthodes analytiques, classiques et rigoureuses, qui exigent un grand nombre de projections, pour utiliser une méthode itérative de moindres carrés, nécessitant moins de mesures.

L'algorithme est basé sur la minimisation des écarts entre les projections mesurées $P(k,\theta)$ et celles calculées $R(k,\theta)$. A titre d'exemple, à la $n^{ième}$ itération :

$$R^{(n)}(k,\theta) = \sum_{i,j \in k} A^{(n)}_{i,j} \times f^{\theta}_{i,j}$$

où, suivant la figure 2 :

θ est l'angle d'un examen

k   est l'indice courant d'une projection

$A_{i,j}$ est l'activité de la cellule concentrée au point de coordonnées (i,j) ; elle sera considérée ou non dans la projection selon que le centre appartient ou non à la bande délimitée par la collimation

$f^{\theta}_{i,j}$ est le facteur d'atténuation qui entre dans la contribution de la cellule (i,j) à la projection

Considérant l'ensemble de toutes les projections, la somme des écarts s'écrit :

$$T^{(n)} = \sum_{\theta} \sum_{k} \frac{[P(k,\theta) - R^{(n)}(k,\theta)]^2}{\sigma^2(k,\theta)}$$

où $\sigma(k,\theta)$ représente l'écart-type dans la mesure de $P(k,\theta)$.

Le passage aux valeurs $A^{(n+1)}_{i,j}$ de la $(n+1)^{ième}$ itération s'effectue en deux temps.

Tout d'abord, prenant isolément la cellule courante d'activité $A_{i,j}^{(n)}$, on recherche la correction d'activité $\Delta^{(n)} A_{i,j}$ à lui apporter pour rendre minimale la somme partielle des écarts des projections qui, dans $T^{(n)}$ se trouvent seulement concernées par la cellule de coordonnées (i,j). Le calcul est alors effectué successivement pour toutes les cellules. En-suite, pour arriver aux activités des cellules de la $(n+1)$ième itération.

Posant :

$$A_{i,j}^{(n+1)} = A_{i,j}^{(n)} + \delta \times \Delta^{(n)} A_{i,j}$$

on recherche, pour l'ensemble des cellules, la valeur de δ qui rend minimal l'ensemble des écarts $T^{(n+1)}$ sur la totalité des projections. δ est un coefficient dit d'amortissement qui, permettant de lier les activités des cellules entre elles, accélère la convergence.

Pour démarrer le processus itératif, une répartition initiale d'activités est introduite. Elle peut être élaborée à partir d'une analyse transversale traitée en révolution symétrique. Une répartition homogène donne de bons résultats en convergeant très rapidement.

Des travaux similaires sont développés par le Service des Piles de Grenoble [8].

RESULTATS (Fig. 4)

Le résultat est une matrice de répartition de densité pour chaque point du réseau découpé dans la section. La représentation graphique, sous forme de courbes d'isoconcentration, facilite l'interprétation et est directement comparable aux résultats éventuellement obtenus par méthodes destructives (Fig. 3).

On peut obtenir le tracé d'un profil dans une direction quelconque prise sur la section du combustible. On dispose des valeurs numériques des concentrations de 24 profils pris tous les 15°, ainsi que les profils moyens.

QUALIFICATION

Le but est de confronter les résultats des mesures non destructives obtenues par le code avec ceux des examens destructifs portant sur des échantillons prélevés après tronçonnage aux mêmes cotes et effectués au Laboratoire d'Etude des Combustibles Irradiés [9].

Gammamétrie transversale

Les courbes d'isoconcentration du ^{137}Cs (Fig. 3a) obtenues par TOMOGAM, à partir de 2 projections à 90°, révèlent :

. la zone centrale, très appauvrie en Cs,
. en périphérie de l'oxyde, le ^{137}Cs est présent avec des concentrations variables suivant les rayons. C'est le phénomène majeur relevé par ces analyses ; en effet, l'un des objectifs recherché dans la scrutation transversale pluridimensionnelle est de mettre en évidence les hétéro-généités de concentration des P.F. volatils au voisinage de la gaine.

Examens destructifs

Macrographie et spectrométrie gamma de section obtenues par déplacement devant la section d'un collimateur (0,5 x 0,5 mm) et reconstitution de la répartition d'activité dans la section par le code ISOPROF. Les examens destructifs (Fig. 3b, 3c) confirment les résultats et permettent d'établir certaines corrélations :

. la zone centrale, appauvrie en ^{137}Cs, correspond à la zone restructurée en grains allongés,

. la suraccumulation de ^{137}Cs est localisée au droit d'une fissure gaine .

Par ailleurs, plusieurs types de distribution ont été testés au cours de la qualification. La comparaison des profils moyens, dont la figure 3d est un exemple représentatif, amène les commentaires suivants :

. TOMOGAM donne, dans tous les cas, une bonne évaluation de la zone centrale désertée en césium,

. les rapports d'activités périphérie/centre sont généralement bien calculés,

. de légers écarts, dans la zone radiale intermédiaire, restent encore à expliquer.

EXEMPLES ET APPLICATIONS [10]

Interaction combustible-gaine : accumulation de ^{132}Te-I (Fig. 4)

A partir des images relevées sur deux balayages à 90° (Fig. 4a), la reconstitution de la répartition de ^{132}Te-I dans la section (Fig. 4b) révèle une accumulation sur la gaine. L'observation de la gaine dévoilera effectivement un début de corrosion à ce niveau.

Migration du ^{137}Cs selon la température (Fig. 5)

Les différents niveaux de puissance relatifs aux différentes cotes d'un crayon PWR permettent d'apprécier l'évolution des migrations.

Dépression du flux de neutrons à l'intérieur du combustible

Le cas des produits de fissions solubles dans la matrice est représentatif du combustible, d'éventuelles densifications, et permet d'avoir accès à la répartition des fissions. Ainsi, ^{95}Zr donne une répartition sans migration dont le profil moyen est celui du flux dans le cas d'irradiation de courte durée, ou représente la densité de fission des derniers mois d'irradiation.

CONCLUSION

Le code a donc été validé par des mesures destructives. Des perfectionnements sont à aménager mais dès à présent ces mesures directes, rapides, non destructives, permettent de multiplier les tests et de progresser rapidement, à moindre frais, dans la connaissance de la tenue des crayons combustibles et de certaines causes de rupture de gaine.

REFERENCES

[1] G. Simonet, Application of reactor gamma scanning to fuel irradiation, CEA.CONF.3992, 2nd Symposium ASTM-EURATOM, Palo Alto, October 1977

[2] F. Michel, M.L. Pointud, Méthodes spécifiques de la gammamétrie en pile, Communication personnelle, 1979

[3] J.R. Phillips, Nucl. Techn. 28, 1976

[4] B.K. Barnes, J.R. Philipps, G.R. Waterbury, J.N. Quintana, J.R. Netuschill, A.S. Murray, Journal of Nuclear Materials 81 1979

[5] T.F. Budinger, G.T. Gullberg, Three dimensional reconstruction in nuclear medecine emission imaging, IEE - Transactions on Nuclear Science, vol. NS 21, 1974

[6] T.F. Budinger et G.T. Gullberg, Three dimensional reconstruction in nuclear medicine by iterative least - squares and Fourier transforme technique, UC 48 Biology and Medicine, 1974

[7] A. Schwartz, T. Pineira, TOMOGAM : une méthode de reconstruction dimensionnelle de la répartition de nucléïdes dans un combustible irradié à partir de scrutations gamma transversales à différentes incidences, Note CEA.N. 2272 , 1980

[8] G. Ducros, Programme ISARD : méthode itérative de reconstruction de sources gamma dans un crayon combustible à partir de plusieurs projections, Communication personnelle

[9] T. Pineira, Méthode non destructive de reconstruction de la répartition spatiale des émetteurs gamma dans un combustible nucléaire irradié. Développements et applications, à paraître

[10] G. Simonet, J. Locard, Connaissance des éléments combustibles par tomographie d'émission gamma. Exemples de dépression de flux, migrations et accumulations de produits de fission, Communication personnelle, 1981
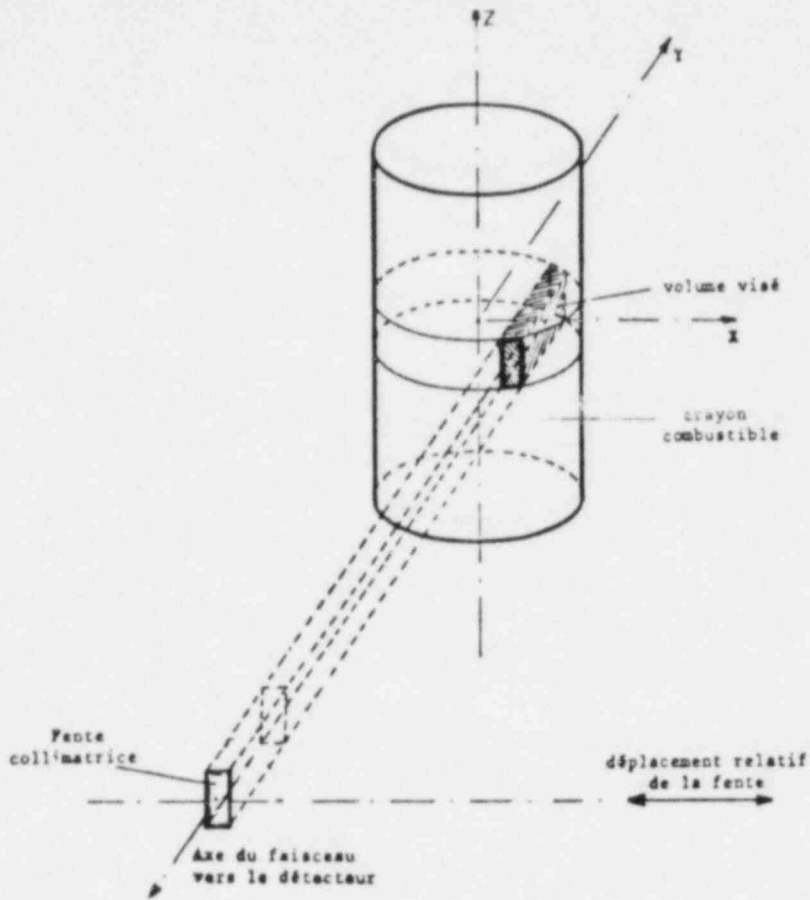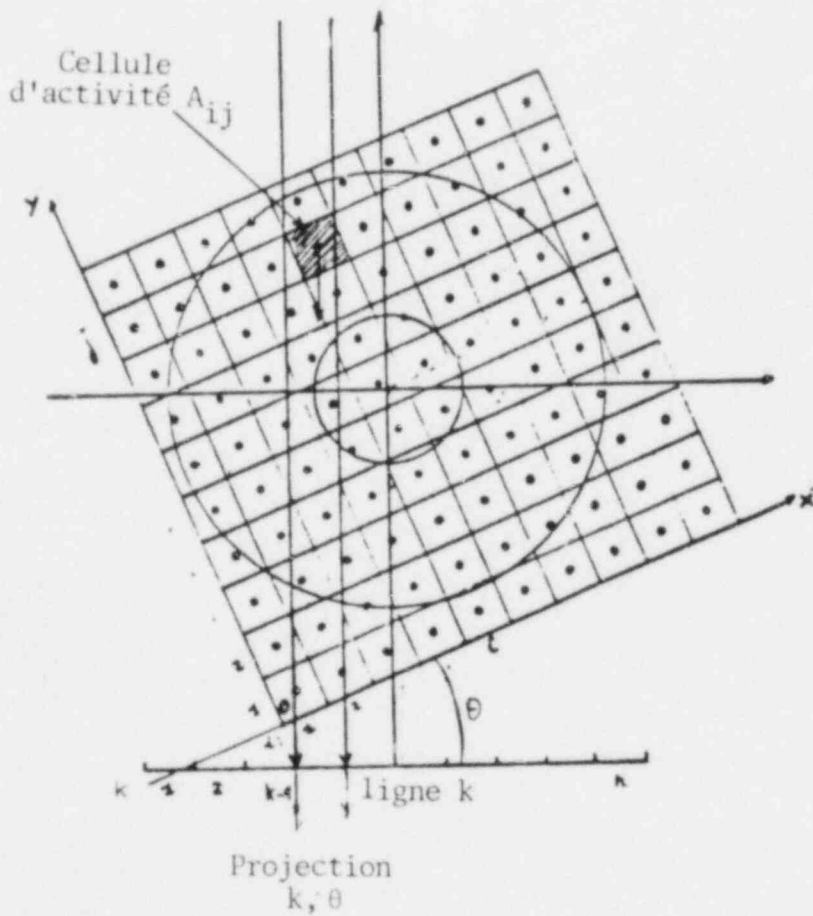
Fig. 1
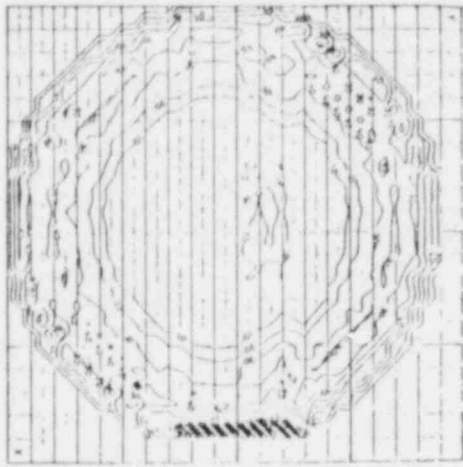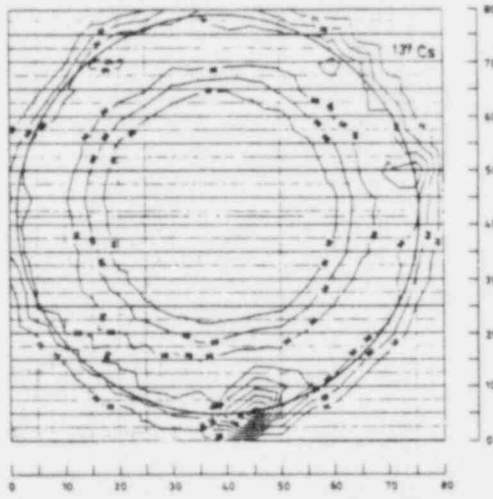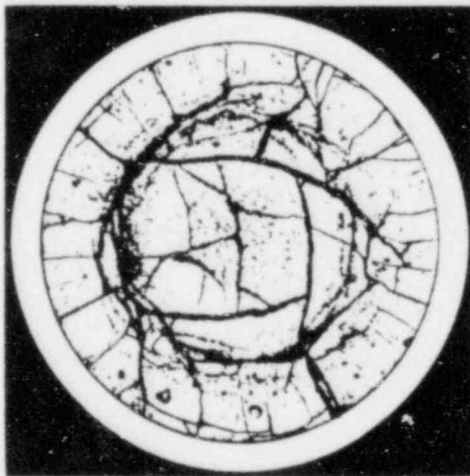
Spectrométrie transversale

Fig. 2 -

Répartition des cellules
vues par les projections
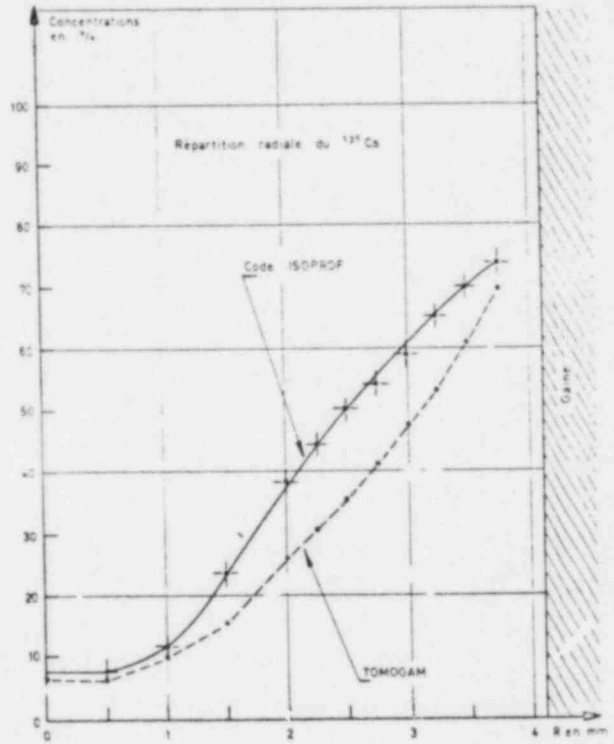
a) TOMOGAM (2 génératrices à 90°)

b) spectrométrie gamma destructive (ISOPROF)

ANALYSES DESTRUCTIVES _ EXPÉRIENCES _

c) macrographie

d) COMPARAISON ISOPROF _ TOMOGAM (profils moyens)
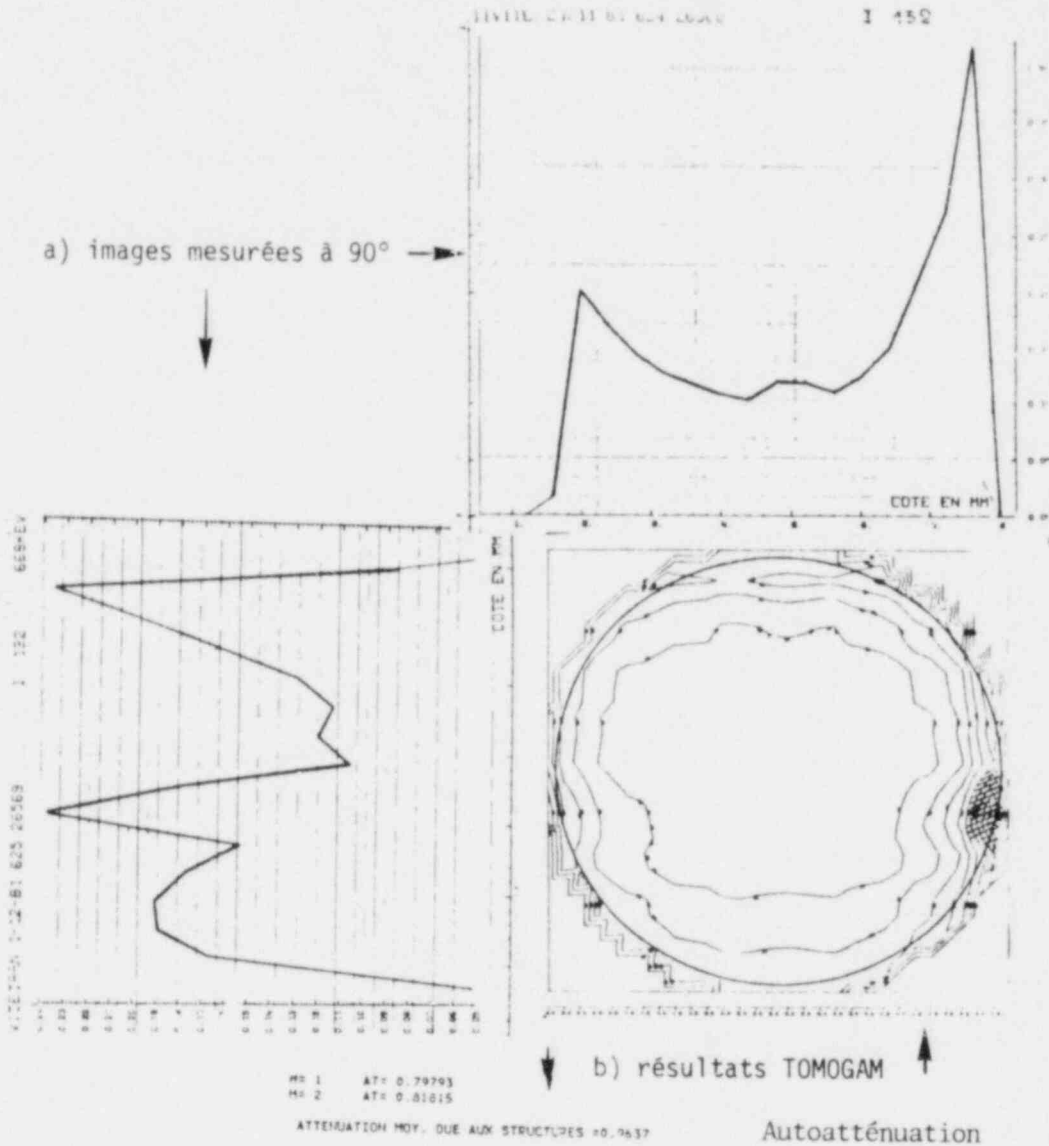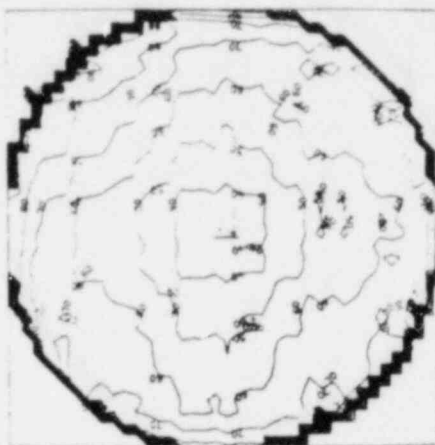(P_{MAX} = 330 W /cm)

Fig. 3 - Qualification

a) images mesurées à 90° →

COTE EN MM

COTE EN MM

Hª 1   AT= 0.79793
Hª 2   AT= 0.81815

ATTENUATION MOY. DUE AUX STRUCTURES =0.7637

b) résultats TOMOGAM

Autoatténuation

Fig. 4 -

Accumulation ^{132}Te

TABLEAU DE COMPTAGE
CENTRE   X= 2.900   Y= 2.900

* RAYONS * ANGLES *	0.0	0.50	1.00	1.25	1.50	1.75	2.00	2.25	2.50	2.75
0.0 *	0.0	0.0	0.0	0.198	2.653	8.069	12.245	20.798	40.844	50.387
15.0 *	0.0	0.0	0.0	0.0	1.456	6.724	9.900	17.527	32.309	52.973
30.0 *	0.0	0.0	0.0	0.0	0.547	5.181	10.733	14.377	22.502	39.793
45.0 *	0.0	0.0	0.041	1.366	1.726	2.655	7.952	17.254	20.256	34.717
60.0 *	0.0	0.0	0.0	0.0	0.412	6.434	11.971	15.771	23.615	36.001
75.0 *	0.0	0.0	0.0	0.0	3.117	8.555	10.980	17.532	27.441	26.167
90.0 *	0.0	0.3	0.0	0.0	4.693	9.910	13.602	20.682	33.896	25.778
105.0 *	0.0	0.0	0.0	0.0	2.911	7.747	9.830	15.630	24.783	24.264
120.0 *	0.0	0.0	0.0	0.0	0.448	6.194	10.837	13.383	18.840	27.536
135.0 *	0.0	0.0	0.3	1.125	1.651	2.101	6.262	12.536	17.218	20.865
150.0 *	0.0	0.0	0.0	0.0	0.447	4.049	7.093	8.577	12.340	19.932
165.0 *	0.0	0.0	0.3	0.0	0.882	4.037	5.327	9.147	15.646	23.198
180.0 *	0.0	0.0	0.030	0.133	1.900	4.955	7.047	11.509	20.019	32.209
195.0 *	0.0	0.0	1.510	2.418	5.413	10.028	12.415	17.898	26.964	37.204
210.0 *	0.0	0.0	2.833	4.110	5.008	8.643	11.356	12.166	16.858	25.849
225.0 *	0.0	0.000	0.972	4.742	4.247	4.641	9.456	16.443	21.459	24.435
240.0 *	0.0	0.202	1.637	0.935	2.126	9.056	13.932	15.497	19.420	24.981
255.0 *	0.0	0.752	2.091	1.372	5.027	10.392	11.414	15.483	20.766	25.278
270.0 *	0.0	0.999	2.367	2.072	7.352	12.344	14.451	18.509	24.985	27.369
285.0 *	0.0	0.935	2.439	1.690	8.533	11.104	12.134	16.041	20.942	24.902
300.0 *	0.0	0.588	2.025	1.098	2.099	9.118	14.409	16.461	20.830	26.393
315.0 *	0.0	0.201	0.971	4.766	4.473	5.352	10.675	19.934	27.502	32.145
330.0 *	0.0	0.0	2.779	4.593	6.447	11.411	16.306	18.166	26.799	43.489
345.0 *	0.0	0.0	1.335	3.021	7.024	15.609	21.612	34.413	58.876	93.317

MOY.CIRC.   0.0   0.159   0.875   1.591   3.235   7.702   11.359   16.479   25.045   33.299

Faible migration
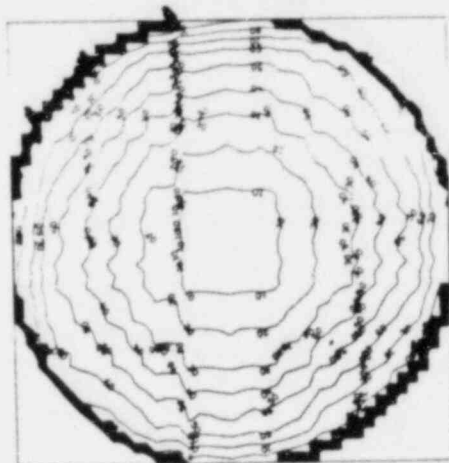
P MAX 310 W cm

Cote 310 mm
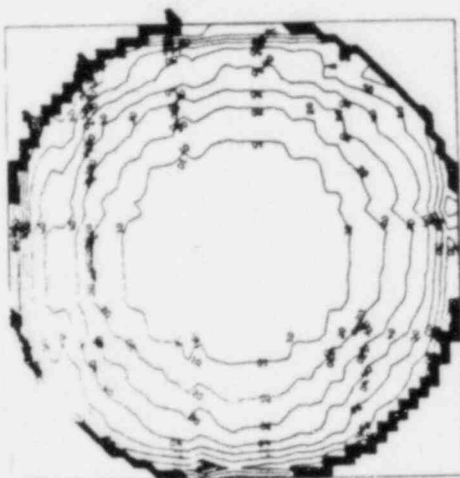
P MAX 330 W cm

Migration importante
homogène

Cote 83 mm

P MAX 370 W cm

Fig. 5 - Migration ^{137}Cs

NOUVEAUX DEVELOPPEMENTS DE LA DOSIMETRIE DES DOMMAGES
PAR TECHNIQUE TUNGSTENE (W)

A. Alberman, J.P. Genthon,
SPS, CEN/Saclay, 91191 Gif Sur Yvette, France

H.J. Nolthenius, W.L. Zijp
ECN, PB 2, 1755 ZG Petten, Netherlands

RESUME

La bonne cohérence entre les réponses des détecteurs de dommages à
variation de résistivité électrique GAMIN et Tungstène, et leurs
fonctions de dommages théoriques (dpa), avait été montrée au 3ème
Symposium ASTM-EURATOM (Ispra, 1979). Les résultats obtenus depuis
sur maquettes de cuve PWR indiquent que l'effet des neutrons de
basses énergies (< 1 MeV) est sous estimé dans le cas du tungstène.
Après avoir rappelé les principaux résultats expérimentaux obtenus
dans différents réacteurs, on donne la meilleure évaluation, à ce
jour, de la fonction de dommages applicable au détecteur W, obtenue
par ajustement mathématique. Cette fonction correspond à un seuil
effectif de dommages de 0,3 MeV environ.

SUMMARY

Good consistency between GAMIN and tungsten damage monitors (based
upon electrical resistivity change) and corresponding theoretical
damage models was given at the 3rd ASTM-EURATOM Symposium (Ispra,
1979). Results obtained since then in pressure vessel mock-ups show
enhanced contribution of low energy neutrons (< 1 MeV) in tungsten.
Main results in various reactor positions are summarized. We give
best estimate of mathematically adjusted damage function applicable
so far to the W detector. Corresponding effective damage threshold
worth about 0.3 MeV.

DOSIMETRIE DES DOMMAGES

LA FLUENCE DE NEUTRONS INTEGREE
DANS UNE IRRADIATION EN PILE DE MATE-
RIAUX DE STRUCTURE EST GENERALEMENT
MESUREE PAR DETECTEURS D'ACTIVATION.

LA TECHNIQUE PRESENTEE ICI CONSISTE
A ETALONNER CES DETECTEURS A FAIBLE
NIVEAU PAR DES DOSIMETRES DE DOMMA-
GES A EFFET PHYSIQUE (VARIATION DE
RESISTIVITE ELECTRIQUE) DANS TOUT
SPECTRE DE NEUTRONS.

DU RAPPORT MESURE DOMMAGES / ACTI-
VATION ON DEDUIT DIRECTEMENT LA FLU-
ENCE DE DOMMAGES (D.P.A.) DANS LE DIS-
POSITIF D'IRRADIATION.

LE DOSIMETRE TUNGSTENE COMPLEMENTAIRE
DE CELUI AU GRAPHITE (G.A.M.I.N.) EST RE-
PRESENTATIF DES EFFETS D'IRRADIATIONS
DANS LES METAUX ET EN PARTICULIER
LES ACIERS.

DAMAGE DOSIMETRY

INTEGRATED NEUTRON FLUENCE
RECEIVED BY IRRADIATED STRUCTURAL
MATERIALS IS USUALLY MEASURED BY
MEANS OF ACTIVATION MONITORS.

THE PRESENTED TECHNIQUE CONSISTS
IN A LOW-LEVEL CALIBRATION OF THESE
MONITORS THROUGH RADIATION SENSITIVE
DAMAGE DOSIMETERS (ELECTRICAL RESISTI-
VITY CHANGE) IN EACH NEUTRON SPECTRUM
FROM ACTUALLY MEASURED DAMAGE/
ACTIVATION RATIO, THE DAMAGE FLUENCE
(OR D.P.A.) IS DIRECTLY DERIVED IN THE
IRRADIATION DEVICE.

THE TUNGSTEN DOSIMETER, AS A
COMPLEMENT OF PREVIOUS GRAPHITE DOSI-
METER (G.A.M.I.N.), IS REPRESENTATIVE OF
RADIATION EFFECTS IN METALS, PARTICU-
LARLY IN STEELS.
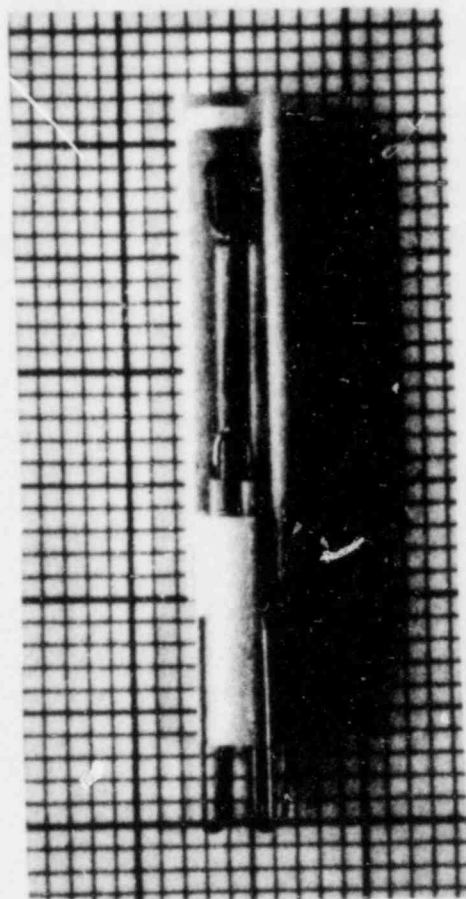
TUNGSTENE (W)

FIG. 1 DETECTEURS DE DOMMAGES

PRINCIPE

LE DOSIMETRE W EST UNE RESISTANCE
ELECTRIQUE (1Ω) A 4 BORNES, RECUITE
ET ENCAPSULEE SOUS VIDE DANS UNE
ENVELOPPE EN ALUMINE (*FIG 1*)

LA VARIATION RELATIVE DE RESISTIVITE
SOUS FLUX :

$$\Delta R / R$$

EST MESUREE PAR DIFFERENCE, AVANT ET
APRES IRRADIATION DANS UN LABORATOI-
RE SPECIALEMENT EQUIPE A SACLAY
    _ ENCEINTE THERMOSTATEE
    _ BAIN D'HUILE REGULE (10^{-3} °C)
    _ COMPARATEUR AVEC ETALONS ($10^{-6} \Omega$)
    _ "CONDUCTIMETRE" SPECIAL

LA FLUENCE DE NEUTRONS EST MESUREE
PAR L'ACTIVITE EN CO^{58} DES DOSIMETRES
NICKEL A_{Ni} : REACTIONS (n,p) /ATOME CIBLE
ON OBTIENT UN RAPPORT EXPERI-
MENTAL SANS DIMENSION :

$$S = 10^{-5} \frac{(\Delta R/R)}{A_{Ni}}$$

CARACTERISTIQUE DE L'EMPLACEMENT
D'IRRADIATION.

PRINCIPLE

THE W DOSIMETER IS A 4 CONTACTS
ELECTRICAL RESISTANCE (1Ω), ANNEALED
AND VACUUM SEALED INSIDE AN ALUMINA
COVER (FIG 1)

RELATIVE RESISTIVITY CHANGE
$$\Delta R / R$$

IS MEASURED BEFORE AND AFTER IRRADIA-
TION IN A SACLAY LABORATORY
    _ THERMALLY INSULATED ROOM
    _ CONTROLLED OIL BATH (10^{-3} °C)
    _ ELECTRICAL COMPARATOR ($10^{-6} \Omega$)
    _ SPECIAL MEASUREMENT DEVICE

NEUTRON FLUENCE IS MEASURED
THROUGH NICKEL FOILS (CO^{58} ACTIVITY)

A_{Ni} : (n,p) REACTIONS / TARGET ATOM
WHENCE EXPERIMENTAL DIMENSIONLESS
RATIO :

$$S = 10^{-5} \frac{(\Delta R/R) corr.}{A_{Ni}}$$

TYPICAL OF IRRADIATION POSITION.

DESCRIPTION

	DOSIMETRE W	CONTENEUR (FACULTATIF)
LONGUEUR	31 mm	39 mm
ϕ	5 mm	6,5 mm

GAMME D'UTILISATION

_ TEMPERATURE
    AUCUN EFFET ENTRE : 25 - 300 °C

_ VARIATION DE RESISTIVITE

$$4.10^{-4} \leqslant \Delta R / R \leqslant 4.10^{-3}$$
ou $400 \mu\Omega \leqslant \Delta R \leqslant 4000 \mu\Omega$

_ FLUENCE DE DOMMAGES CORRESPON-
DANTE

$$7.10^{15} \leqslant \phi W \leqslant 7.10^{16} \ n.cm^{-2}$$

_ COMPATIBLE SIMULTANEMENT AVEC
LE DOSIMETRE GRAPHITE (G.A.M.I.N)

_ PRECISION MOYENNE $1\sigma < 5\%$
(6 DOSIMETRES)

_ ENVIRON 300 DOSIMETRES W ONT ETE
UTILISES A CE JOUR.

DESCRIPTION

	DOSIMETER	CONTAINER (OPTIONAL)
LENGTH	31 mm	39 mm
ϕ	5 mm	6,5 mm

RANGE

_ TEMPERATURE
    NO DEPENDANCE UP TO 300 °C
_ RESISTIVITY CHANGE
$$4.10^{-4} \leqslant \Delta R/R \leqslant 4.10^{-3}$$
OR $400 \mu\Omega \leqslant \Delta R \leqslant 4000 \mu\Omega$

_ DAMAGE FLUENCE
$$7.10^{15} \leqslant \phi_W \leqslant 7.10^{16} \ n.cm^{-2}$$
_ SIMULTANEOUS COMPATIBILITY WITH
THE GRAPHITE DOSIMETER (G.A.M.I.N.)
_ CCURACY $1\sigma < 5\%$ (6 SAMPLES)

OVER 300 "W" DOSIMETERS HAVE
BEEN USED UNTIL NOW.

REACTEURS	SPECTRES	REPONSES	
		"S" TUNGSTENE	"Γ" G.A.M.I.N.
OSIRIS /ISIS (SACLAY)	COEUR	4.97	3.18
	BERYLL.	6.76	4.28
	REFLECT.	4.41	2.92
E.L.3 (SACLAY)	COEUR	5.32	4.04
TRITON DOMPAC (FONTENAY)	SURVEILL.	6.29	3.40
	POS. AV.	5.53	3.86
	" 1/4	6.86	4.94
	" 1/2	9.84	6.81
O.R.R PSF (OAK-RIDGE)	SURVEILL.	8.48	7.00
	POS. 1/4	11.78	9.24
	POS. 3/4	27.60	24.16
MELUSINE (GRENOBLE)	STANDARD	5.39	-
	SPECIAL	11.04	-
FRJ 2 FRJ 1 (JÜLICH)	COEUR	5.88	4.04
	SPECIAL	*	*
H.F.R (PETTEN)	10 EXP.	*	*

* EN COURS

Tableau I - Résultats de dosimétries

QUALIFICATION DE LA REPONSE "S"

LE TABLEAU 1 RECAPITULE LES PRINCIPALES DOSIMETRIES.

LA BONNE COHERENCE ENTRE REPONSES GRAPHITE & TUNGSTENE DANS DES SPECTRES NEUTRONIQUES $\varphi(E)$ DIFFERENTS PERMET DE VALIDER UNE FONCTION DE DOMMAGES $W(E)$:

$$DAR = \frac{\phi_W}{\phi_{Ni}} = \frac{\int_0^\infty W(E)\,\varphi(E)\,dE}{\int_0^\infty \overline{\sigma}_{Ni}(E)\,\varphi(E)\,dE} \cdot \frac{\overline{\sigma}_{Ni}^F}{\overline{W}^F} = \beta \cdot S$$

A PARTIR DU FLUX DE FISSION EQUIVALENT GRAPHITE (REFERENCE) :

$$DAR = \frac{\phi_G}{\phi_{Ni}} = 0.50\ (\pm 0.01) \cdot \Gamma$$

LA FIGURE 2 MONTRE LES REPONSES S = fonction DE Γ EN GEOMETRIE P.W.R. $W(E)$ DOIT VERIFIER CETTE RELATION DE SORTE QUE β = CONSTANTE.
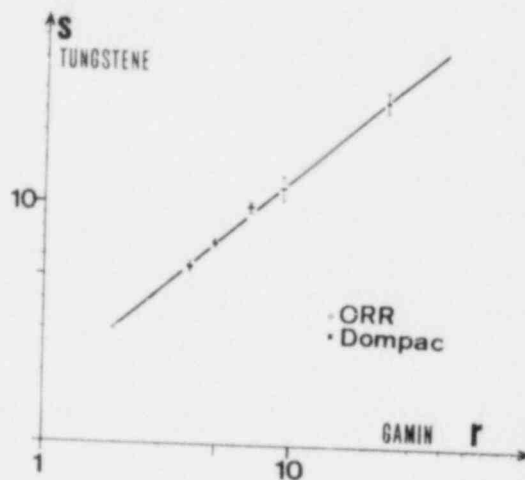
QUALIFICATION OF RESPONSE "S"

MAIN DOSIMETRY RESULTS ARE SUMMARIZED IN TABLE 1.

GOOD CONSISTENCY OF GRAPHITE AND TUNGSTEN RESPONSES IN DIFFERENT SPECTRA $\varphi(E)$ ALLOWS DAMAGE FUNCTION $W(E)$ VALIDATION :

$$DAR = \frac{\phi_W}{\phi_{Ni}} = \frac{\int_0^\infty W(E)\,\varphi(E)\,dE}{\int_0^\infty \overline{\sigma}_{Ni}(E)\,\varphi(E)\,dE} \cdot \frac{\overline{\sigma}_{Ni}^F}{\overline{W}^F} = \beta \cdot S$$

CONSIDERING EQUIVALENT FISSION FLUENCE IN GRAPHITE AS A REFERENCE :

$$DAR = \frac{\phi_G}{\phi_{Ni}} = 0.50\ (\pm 0.01) \cdot \Gamma$$

PRESSURE VESSEL MOCK-UPS RESPONSES S VERSUS Γ ARE SHOWN IN FIG. 2

$W(E)$ SHOULD FIT THIS CURVE PROVIDED β = CONSTANT

Fig. 2 - Réponses dans les simulateurs de cuve P.W.R.

FONCTION DE DOMMAGES POUR LE DETECTEUR W

Fonction de dommages théorique (dpa) :

La corrélation des résultats du tableau I avec le modèle théorique de déplacements atomiques (W dpa) aboutit à la valeur moyenne de la constante :

$$\beta_{dpa} = 0,247$$

La dispersion moyenne sur tous les spectres est de 6 % (1 σ). Elle est nettement plus élevée dans les spectres de maquettes de cuve PWR.

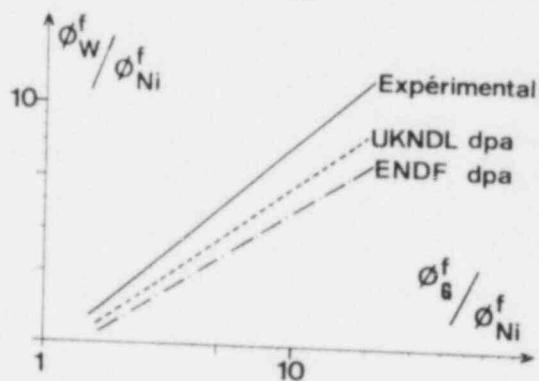La figure 2 montre clairement que la dosimétrie par utilisation des rapports dommages/activation est conservative mais aussi que la fonction théorique sous-estime l'efficacité relative des neutrons de basses énergies (inférieures à 1 MeV).

Fonction de dommages ajustée :

Les spectres calculés retenus pour valider une procédure d'ajustement sont ceux qui, précisément pour les dosimétries, conduisent aux rapports dommages/activation effectivement mesurés dans le graphite (fluence de dommages de référence). Le choix de spectres différents permet de discriminer telle ou telle fonction de dommages. Le meilleur jeu de spectres retenu est ainsi :

TRITON-DOMPAC (3 cas)	ISIS-COEUR	FRJ.2 COEUR
Calcul : TRIPOLI (MONTE CARLO)	APOLLO	ANISN

Les 2 modèles d'ajustement décrits ci-dessous sont indiqués sur la figure 3.

a) modèle semi-empirique :

On corrige la fonction W dpa par addition d'un terme proportionnel à la fonction graphite G dpa. L'optimisation (σ < 1%) conduit à :

$$W_{S.E.}(E) = 0,38 \ G_{dpa}(E) + 0,62 \ W_{dpa}(E)$$

et $\beta_{S.E.} = 0,28$.

b) modèle mathématique par déconvolution :

On utilise le code SAND II avec, pour fonction d'essai, W dpa. Le calcul est effectué sur 640 groupes d'énergies avec une optimisation (valeurs expérimentales retrouvées à mieux que 1 % sur les spectres) sur 40 itérations.

La fonction résultante $W_{exp}(E)$ est très cohérente avec la précédente (fig.3) et peut être considérée comme la meilleure évaluation actuelle de la fluence de dommages dans le tungstène. On aura ainsi pour tous les spectres :

$$\frac{\emptyset \ W_{exp}}{\emptyset \ Ni} = 0,27 \ (\pm \ 0,01) \ . \ S$$

La répartition énergétique de la fonction $W_{exp}(E)$ normalisée sur spectre de fission ($<W_{exp}(E)>^f = 1$) est donnée dans le tableau II (découpage en énergie standard MUFT). Elle correspond à un seuil effectif de dommages de 0,3 MeV environ.
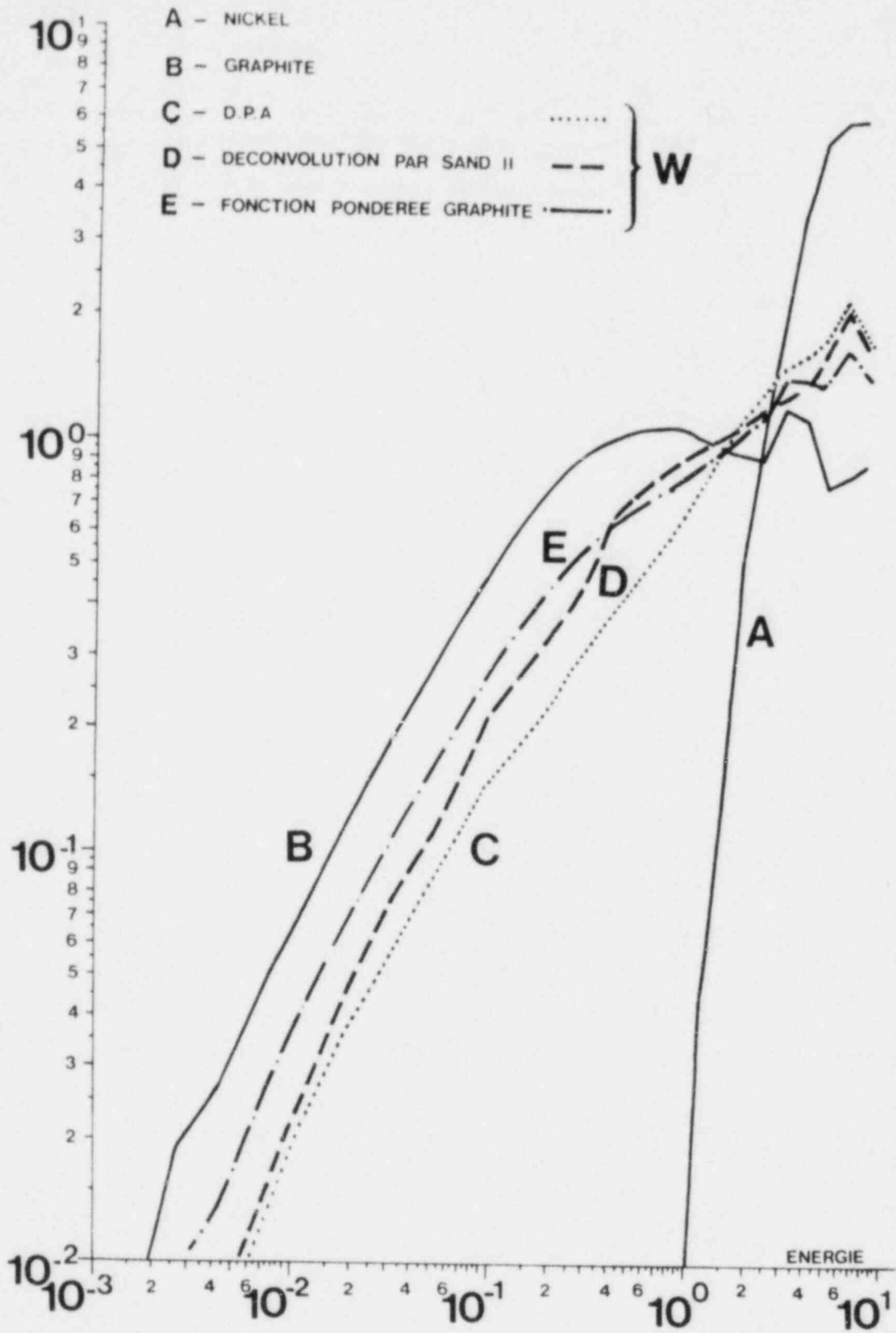
Fig. 3 - Fonctions de dommages normalisées sur le spectre de fission
(sans dimension)

Groupe N°	Δu	Energie (limite inférieure)	Fonction résultante SAND II W_{exp} (E)
		14 MeV	
0	0,338	10	1,1595
1	0,25	7,788	1,6034
2	0,25	6,0653	2,0617
3	0,25	4,7237	1,6090
4	0,25	3,6788	1,3999
5	0,25	2,8650	1,3075
6	0,25	2,2313	1,1682
7	0,25	0,7377	1,0290
8	0,25	1,3533	1,0540
9	0,25	1,0540	0,8704
10	0,25	0,8208	0,8448
11	0,25	0,6393	0,7293
12	0,25	0,4979	0,6843
13	0,25	0,3877	0,6712
14	0,25	0,3020	0,5106
15	0,25	0,2352	0,4229
16	0,25	0,1832	0,3553
17	0,25	0,1426	0,3033
18	0,25	0,1111	0,2528
19	0,25	86,52 keV	0,2206
20	0,25	67,38	0,1452
21	0,50	40,87	0,1015
22	0,50	24,79	0,0709
23	0,50	15,03	0,0419
24	0,50	9,12	0,0227
25	0,50	5,53	0,0123
26	0,50	3,35	0,0063
27	0,50	2,03	0,0014
28	0,50	1,23	0,0007
29	0,50	0,75	0,0003
30	0,50	0,45	0

Tableau II - Fonction de dommages pour le détecteur W normalisée sur le spectre de fission

CONCLUSION

Les résultats de dosimétrie présentés montrent la validité de la technique des détecteurs de dommages à variation de résistivité électrique pour déterminer expérimentalement une fluence de dommages.

La précision des mesures a permis de déterminer une fonction de dommage applicable au détecteur W par méthode de déconvolution. La corrélation des effets d'irradiation dans les métaux irradiés et particulièrement les aciers, dans des environnements neutroniques différents, à l'aide de cette fonction, doit permettre sa qualification en tant que paramètre d'exposition.

REFERENCES

A. Alberman, M. Cance, J.P. Genthon, ...
Le détecteur de dommages miniaturisé au tungstène. CEA.CONF.4734
3ème ASTM/EURATOM sur la Dosimétrie, Ispra, 1979 (EUR.6813)

A. Alberman, M. Faure, M. Thierry,...
Expérience de dosimétrie DOMPAC. Simulation neutronique de l'épaisseur de la cuve d'un réacteur PWR. CEA.CONF.4741
3ème ASTM/EURATOM sur la Dosimétrie, Ispra, 1979 (EUR.6813)

A. Alberman, M. Thierry, W. Schneider, L. Weise
Mesure du rapport dommages/activation dans FRJ.2   CEA.CONF.4735
3ème ASTM/EURATOM sur la Dosimétrie, Ispra, 1979 (EUR.6813)

A. Alberman, M. Benoist, M. Thierry
Mesure et interprétation des flux de dommages dans le simulateur de cuve PWR d'Oak Ridge (ORR-PSF). CEA.CONF.6209
Communication présentée à ce 4ème symposium ASTM/EURATOM

W.N. Mc Elroy, ...
SAND II neutron flux spectra determinations ...
RSIC collection CCC 112   ORNL   (May 1969)

An Investigation into the use of Sapphire
as a Fast Neutron Damage Monitor

G.P. Pells, A.J. Fudge, M.J. Murphy,
and M. Wilkins

Metallurgy and Chemistry Divisions
A.E.R.E., Harwell, United Kingdom.

Abstract

The thermal stability of aluminium vacancies (V centres) and interstitials in $\alpha\text{-}Al_2O_3$ (sapphire) has led to the consideration of this material as a pressure vessel steel damage monitor. Polished sapphire blocks have been fast neutron irradiated to fluences of $10^{17} - 2 \times 10^{19}$ n./cm^2 ($E_n > 1$ MeV) at temperatures of 60, 250 and 290°C and in different neutron spectra. Measurements of optical absorption in the V band gave a non-linear response with dose which was independent of irradiating temperature and for dose expressed in dpa, was independent of the irradiating neutron spectrum. The sensitivity and sources of error of this technique for measuring neutron dose in steels are discussed as are the conditions required to develop a practical reader.

1. Introduction

The final damage state of any material subjected to fast neutron irradiation is governed by the following factors; neutron energy spectrum, neutron fluence, the irradiation temperature, the chemical composition of the material and possibly the neutron flux or dose rate. The spectrum and fluence are the major determinants of the number of displacements per atom (dpa) that occur in the irradiated material, although the final damage state can be influen. . by quite small variation in the chemical composition and irradiation temperature as well as dose rate by varying the recombination rate of Frenkel defects and by altering the stability of the various sinks for interstitials and vacancies.

The simple statement of d̠ a neutron fluence greater than some arbitrary energy is now consia. o be inadequate and it is thought that dpa should be used as the measure of damaging dose received by irradiated materials[1]. Solid state devices for the measurement of dpa are being increasingly studied and in this paper we show that sapphire (single crystal α-Al_2O_3) has a suitable combination of physical and chemical properties, coupled to its radiation damage behaviour, to allow its use as a dpa monitor for steel.

Sapphire is available with high purity at moderate cost. It is very hard, (9·on the Mohr scale of hardness where diamond is 10), is mechanically strong and does not have any cleavage planes. It is very inert chemically such that polished surfaces are unaffected by heating in vacuum, oxidising or reducing atmospheres at temperatures up to 1500°C. Aluminium and oxygen nuclei are equally stable to neutron irradiation; each has a very small capture cross-section for pile neutrons and specimens may be safely held in the hand within a few days of irradiation to 10^{20} n./cm^2. All of these properties make sapphire an ideal material for use in the hostile environment of a nucl. r reactor.

The radiation damage behaviour of sapphire exhibits equally valuable features. Doran and Graves[2] show that iron and aluminium have similar displacement cross-sections as a function of neutron energy and there is considerable evidence that most of the defects produced by displacement damage are immobile at moderate temperatures. Isochronal annealing of radiation induced colour centres has shown that most centres are stable below 250°C except for the F centres (two electrons trapped at an oxygen vancancy) which start to anneal at ~ 200°C and then proceed to anneal out in several stages until annealing is complete at ~ 700°C [3]. The aluminium vacancy centres (V centres) are much more stable. They do not start to anneal until temperatures > 400°C have been reached and have not fully annealed at 1100°C [4,5]. There is also evidence from electron microscope studies of irradiated sapphire that point defects do not aggregate below ~ 500°C for damaging doses of < 1 dpa.[6,7] Wilks[8] has examined sapphire by electron microscopy following reactor irradiation at 150 and 650°C. After irradiation at 150°C to 5 x 10^{19} n./cm^2 (~ 0.05 dpa) no damage at all could be seen in the microscope and anneals of > 1200°C were required to produce dislocation loops of 2-10 μm diameter.

These results from reactor and HVEM irradiated sapphire suggest that below 10^{19} n./cm^2 (0.01 dpa) and 500°C the displacement damage on the aluminium sublattice remains as discrete vacancies and interstitials.

There are a number of techniques by which the presence of aluminium vacancies or interstitials may be monitored. X-ray lattice parameter measurements have been extensively used to follow radiation damage in oxides [9] and in the case of high purity sapphire, precision lattice parameter measurements capable of resolving changes of 1 part in 10^6 would allow radiation damage changes to be observed from $\sim 10^{17}$ n/cm^2 upwards. Unfortunately such measurements would also reflect changes in the oxygen sublattice which are expected to be temperature sensitive above 200°C.

Two types of paramagnetic, aluminium ion defect pairs have been detected by electron spin resonance in reactor irradiated sapphire [10] using the ^{27}Al hyperfine structure but it was thought that the aluminium ion pairs were probably related to some impurity as the defect concentration saturated after neutron doses of 3×10^{17} n./cm^2.

Optical spectroscopy may be used to detect the aluminium vacancy centre (V centre) and has the advantage that, although several types of V centre are thought to exist, they overlap and are all summed in one broad absorption band - the V band. In the following sections we shall present the results of experiments in which the effects of neutron dose, neutron spectrum, irradiation temperature and post-irradiation behaviour upon a limited region of the optical absorption spectrum of sapphire are examined.

2. Experimental Procedure

Specimen preparation and irradiation

The sapphire specimens were obtained from the Union Carbide Corp. in the form of 2mm x 3mm x 10mm rectangular blocks cut from a U.V. grade, single crystal boule. Two opposing 3mm x 10mm faces were polished to an optical finish to give an optical path length of 2mm. The sapphire specimens were wrapped in aluminium foil and sealed in a helium filled stainless steel can along with Ti, Fe and Ni fast neutron activation monitors. The aluminium foil wrapping served to provide good thermal contact between the sapphire and stainless steel can. The cans were irradiated in the HERALD swimming pool reactor at Aldermaston over the dose range $3 \times 10^{16} - 2 \times 10^{17}$ n/cm^2 (E > 1 meV) at positions of known neutron spectrum. The irradiations were performed at the reactor pool temperature of 60°C and in gamma-heated copper and iron blocks at 250°C or 290°C. Fifteen similar sapphire blocks were cut and polished at Harwell for irradiation in the Oak Ridge pool-side-facility (PSF) irradiation positions. This was part of the LWR Pressure Vessel Surveillance Dosimetry improvement programme. To date, specimens from the 19 day test irradiation have been examined from the surveillance capsule, 1/4T, 1/4T (offset), 1/2T and 3/4T positions. As well as

encountering differences of neutron energy spectrum in these positions, differences in dose rate of up to about 100 also occurred. These irradiations were carried out at 290°C. A few specimens have been gamma-irradiated in the spent fuel pond at Harwell to doses of ~ 1000 Mrad. to investigate any gamma ray damage effects.

Neutron dosimetry

The Ti, Fe and Ni foils included in the irradiation capsules give only a small range of neutron activation energy responses. The induced radioactivity in the dosimeter materials was measured using a Ge (Li) detector and suitable pulse processing equipment. The gamma ray spectrum obtained for each dosimeter material was analysed by using GAMANAL computer code and the absolute disintegration rate was evaluated by comparison with calibrated sources of the same nuclides. To convert these activities into fluences it was first necessary to compute an integral cross-section for each reaction using the differential neutron reaction cross-section and a calculated neutron energy spectrum for each irradiation position. The integrated dose or fluence was taken as the mean value for the Fe^{54} n,p Mn^{54}, Ni^{58} n,p Co^{58} and Ti^{46} n,p Sc^{46} reactions. Displacement cross-sections were calculated for sapphire using the RECOIL code. The fluence is calculated from the measured activities using the following relationship:-

$$\emptyset_{Total} = \frac{A}{N_o \, \sigma_{Eff} \, (1 - e^{-\lambda t})}$$

where $\emptyset_{Total}$ is the fluence of neutrons in the energy range specified

A   is the activity or disintegration rate of the monitor nuclide measured and corrected for decay

N_o is the number of atoms of the target nuclide originally present assuming that the change in the number of atoms during the irradiation is small.

σ_{Eff} is the effective integral cross-section for the nuclear reaction over the specified energy range for the neutron spectrum existing at the irradiation position.

λ the decay constant of the radioactive product nuclide

$(\lambda = \frac{0.693}{T_{\frac{1}{2}}}$ where $T_{\frac{1}{2}}$ is the half-life of the nuclide)

t   is a composite time-power factor for the irradiation.

Optical measurements

The optical absorption spectra of the polished sapphire blocks were measured in a Cary 14 dual beam, spectrophotometer. The optical density is given by $\log_{10} (I_o/I)$, where I_o is the incident light intensity and I is the intensity remaining after the light has passed through the specimen. The dimensions of the sapphire blocks were chosen so that there would be no obstruction of the spectrophotometer light beam at full aperture. The specimens were accurately positioned

by a purpose built holder that also prevented stray light from by-passing the specimens. The reproducibility of the absorption measurements was ± 0.002.

Before canning and neutron irradiation the absorption spectrum of each specimen was recorded over the wavelength range of 185-750nm. A few samples also had the near infra-red spectra measured from 750-2500nm. Following neutron irradiation the specimens were decanned and exposed to daylight for a few weeks to allow optical equilibrium to be reached before remeasuring the absorption spectrum as it has been shown by Turner and Crawford[4] that some of the absorption bands could be affected by exposure to light. The strength of the F bands in the post-irradiation measurements were so great that the absorption spectra were limited to wavelengths of 300-750 nm. The specimens were then X-irradiated at 90 kV, 25 mA for 1 hour (~ 1 Mrad) to saturate the colour centres and the optical absorption remeasured within a few minutes of the cessation of X-irradiation.

3. Results

The effects of reactor irradiation upon sapphire is to change it from a clear crystal to a yellow/brown colour and the optical absorption spectrum for a specimen fast neutron irradiated at 250°C is shown in Fig.1. It can be seen that below 400 nm the ultraviolet absorption rises rapidly to unmeasurably high values. This is thought to be due to the F-type centres. The broad V-centre absorption in the visible part of the spectrum has other absorption bands of unknown origin superimposed upon it which peak at 455, 570 and 690 nm. The strength of these narrow bands, particularly those at 455 and 570 nm , are affected by irradiation temperature. Fig.1 also shows the spectrum obtained after X-irradiation. It can be seen that the strength of the broad underlying V band is considerably increased whilst that of the narrow bands at 455 and 570 nm are decreased. In the narrow part of the spectrum between 600 nm and 650 nm the V band is least affected by interfering bands and the measurements of optical density presented in this paper have been restricted to this region.

The optical density at 600 nm for both as-received and X-irradiated specimens is shown as a function of fast neutron fluence in Fig.2 where it can be seen that a common non-linear curve describes the results for the three irradiation temperatures 60, 250 and 290°C. When the optical densities of the sapphire specimens from the short P.S.F. run at Oak Ridge are plotted against neutron fluence for neutron energies > 1 MeV a markedly different set of curves are obtained as shown in Fig.3. However the specimens irradiated in HERALD were all exposed to fairly similar neutron spectra whereas the P.S.F. irradiation involved widely varying neutron spectra because of the different thickness of steel between the specimens and the neutron source. The dose in terms of dpa was derived from the displacement cross-sections for aluminium in sapphire which had been calculated for the various neutron spectra in the P.S.F. array and the HERALD irradiation positions. Fig. 4 shows that reasonable agreement is obtained between the HERALD and P.S.F.

optical data when plotted against dpa.

Specimens that had been gamma-irradiated to 1000 Mrad in the spent
fuel pond at Harwell showed no change in optical absorption for wave-
lenghts above 400 nm.

4.   Discussion

The fact that the experimental points in Fig.2, for sapphire
neutron irradiated at various temperatures up to 290°C, all fall on a
common curve justifies the prediction that the aluminium defects
could be stable at PWR operating temperatures and hence sapphire may
be used to monitor radiation damage at these temperatures. The response
curves are sublinear even at the relatively low fluence of 10^{17} n./cm^2.
The oxygen vacancy centres (F-type centres) have been shown by Levy [3]
to follow a linear growth up to ~ 5 x 10^{17} n./cm^2 after which further
growth becomes sublinear suggesting an approach to saturation. No
growth measurements have been reported for the V bands in sapphire
although measurements in MgO[11] show the V bands to be still growing at
10^{20} n./cm^2, the highest reported dose.

In the present heavily irradiated sapphire specimens it is
difficult to identify the broad V bands with certainty because of other
overlapping bands. Levy [3] and Turner and Crawford[4] have shown that
the peak of the V band occurs between 400-450 nm. They note that the
peak shifts with annealing temperature which suggests that there are
several overlapping V bands. The effects of X-irradiation on the
optical spectrum is largely to make all of the various types of aluminium
vacancy centre optically active by displacing electrons from the oxygen
ions surrounding the vacancy. At the same time it would appear to bleach
some of the unknown bands such as those peaking at 455 and 570 nm as shown
in Fig.1. The overall effect of X-irradiation produces very little change
in the response of the optical absorption to neutron fluence but
significantly reduces the scatter for the data.

The scatter shown in Fig.2 arises from two principle sources,
although there are small but not insignificant errors from spectral
variations between HERALD irradiation rig positions. Firstly the neutron
dose measurements using activation monitors have errors which derive from
neutron spectrum calculations, inaccuracies in the activation cross-
sections, and radioactivity measurements. These are estimated to give a
total uncertainty of ~ ± 15%. Secondly there are errors in the optical
measurements caused by fading of the V centres. The scatter in the as-
received measurements are largely due to fading as the time interval
between removal from the reactor and optical measurement varied over
several weeks. The intense gamma flux in the reactor would have ensured
that all the V centres were optically active but, on removal from the
reactor, electron-hole recombination at the oxygen ions surrounding the
aluminium vacancies would make some centres optically inactive, i.e.
they will not absorb light and so be undetected by the absorption
measurements. It was expected that after an interval of a few weeks the
V centre concentration would have reduced to a metastable level so as to

give reproducible results, but measurements over a period of several months showed that this was not so. Consequently X-irradiation was used to reactivate the V centres.

Unfortunately X-irradiation did not completely solve all the problems as the initial decay following X-irradiation is quite rapid (approximately a rate of change of optical density of 0.001/min), therefore the V centres were decaying at the same time as they were being pumped up by the X-rays and ~ 1 Mrad was required to produce saturation in the present work although with a more intense beam a lower dose would be required. The V centre decay meant that errors of 2-10% accumulated in the time required to make an optical measurement after X-irradiation. In a purpose built reader it would be easy to arrange for X-irradiation and optical interogation to occur simultaneously therefore eliminating fading as a problem. It should be stressed that the fading phenomena, whether thermally or optically induced are purely electronic effects and the basic defect, the aluminium vacancy, remains perfectly stable at all temperatures below 400°C and may always be reactivated by X- or gamma-irradiation.

The sensitivity of the present optical measurements were limited by the accuracy and reproducibility of the spectrophotometer to ~ 5% for a neutron fluence of 10^{17} n./cm^2 and to < 1% at 10^{19} n./cm^2. Variations in thickness of the specimen were ~ ± 1% about an average value of 1.99mm but the optical absorption value can be adjusted in proportion to the thickness deviation. If the optical measurements were the only limitation, then, for a response given by the upper curve in Fig.2, the sapphire monitor would be capable of giving a value for neutron dose to an accuracy of ± 1.5% at 2 x 10^{19} n./cm^2 reducing to ± 4.5% at 10^{17} n./cm^2. Increasing the optical path length from 2mm to 10 mm would reduce the error to less than ± 1% at all fluences > 10^{17} n./cm^2, although it must be remembered that a true measure of neutron dose will always be dominated by errors in the activation monitor measurements used at present for calibration.

Apart from the temperature stability of the V centre, the most important aspect of sapphire as a dosimeter is its ability to take account of variations in neutron spectrum as demonstrated in Fig.4, where the optical density of specimens irradiated in different neutron spectra produced a uniform response in terms of dpa. The displacement cross-section for iron and aluminium show reasonable agreement and Fig.5 shows the calculated number of displacements per neutron as a function of neutron energy for iron in steel and aluminium in sapphire using the displacement damage cross-sections of Doran and Graves[2]. The displacement threshold energy E_d was taken as 40 eV for iron and 18 eV for aluminium in sapphire. It can be seen that displacements of aluminium in sapphire would tend to overestimate the dose for iron in the important 10^5 - 10^6 eV neutron energy range, but the value of 18 eV for E_d^{Al} taken from Pells and Phillips[6] may be too low when averaged over all crystal orientations. Nevertheless the overall agreement is sufficiently good for sapphire to be considered as a potential dosimeter for PWR steels.

5. Conclusions

Fast neutron irradiation of high purity sapphire produces damage on the aluminium sublattice which may be measured by optical absorption in the V band. The absorption at 600 nm shows a reproducible but non-linear response with neutron fluence ($E_n > 1$ MeV) and the response was shown to agree for irradiation in different neutron spectra when neutron dose was expressed in dpa. The response was also shown to be invariant with irradiation temperature between 60°C and 290°C. Calculation of the number of displacements per neutron for aluminium in sapphire shows reasonable agreements with iron over a wide neutron energy range which in conjunction with the experimental results demonstrates the potential of sapphire as a dpa monitor for steel.

The necessity for X-irradiation prior to the measurement of optical absorption complicates the readout procedure and experiments are in hand to explore alternative methods. Work is also planned to investigate the effects of a wider range of neutron spectra, radiation temperature, and dose rate on reproducibility; the nature of the optical absorption bands on either side of 600 nm and the effects of impurities.

Acknowledgements

REFERENCES

1. C.Z. Serpan Jr., "Review of Metallurgical Papers for Session B - Workshop on The Metallurgy & Dosimetry Interface" Proc. 3rd ASTM - Euratom Symp. on Reactor Dosimetry, Ispra, Italy 1-5 Oct. 1979, Vol.1, p47, (1980)

2. D.G. Doran & N.J. Graves, "Neutron Displacement Damage Cross Sections for Structural Metals", Irradiation Effects on the Microstructure & Properties of Metals, ASTM STP 611, American Society for Testing & Materials, p463, 1976.

3. P.W. Levy, "Annealing of the Defects & Colour Centres in Unirradiated and in Reactor Irradiated Al_2O_3", Disc. Faraday Soc. 31, 118, (1961)

4. T.J. Turner and J.H. Crawford, "Nature of the 6.1 eV Band in Neutron-irradiated Al_2O_3 single crystals", Phys. Rev. B., 13, 1735, (1976)

5. G.P. Pells, unpublished work.

6. G.P. Pells and D.C. Phillips, "Radiation Damage of α-Al_2O_3 in the HVEM:I. Temperature Dependence of the Displacement Threshold", J. Nucl. Mat., 80, 207, (1979)

7. G.P. Pells and D.C. Phillips, "Radiation Damage of α-Al_2O_3 in the HVEM:II. Radiation Damage as High Temperature and High Dose", J. Nucl. Mat., 80, 215, (1979)

8. R.S. Wilks, J.A. Desport and R. Bradley, "Transmission Electron Microscopy of Neutron Irradiated α-Al_2O_3 Single Crystals" AERE-R5103 (1965)

9. R.S. Wilks, "Neutron-induced Damage in BeO, Al_2O_3 and MgO - a Review", J. Nucl. Mat., 26, 137, (1968)

10 R.T. Cox, "Electron Spin Resonance Studies of Aluminium Ion Defect Pairs in Reactor Irradiated Al_2O_3", Phys. Lett., 21, 503, (1966)

11 B. Henderson and D.H. Bowen, "Radiation Damage in Magnesium Oxide", J. Phys C., 4, 1487, (1971)
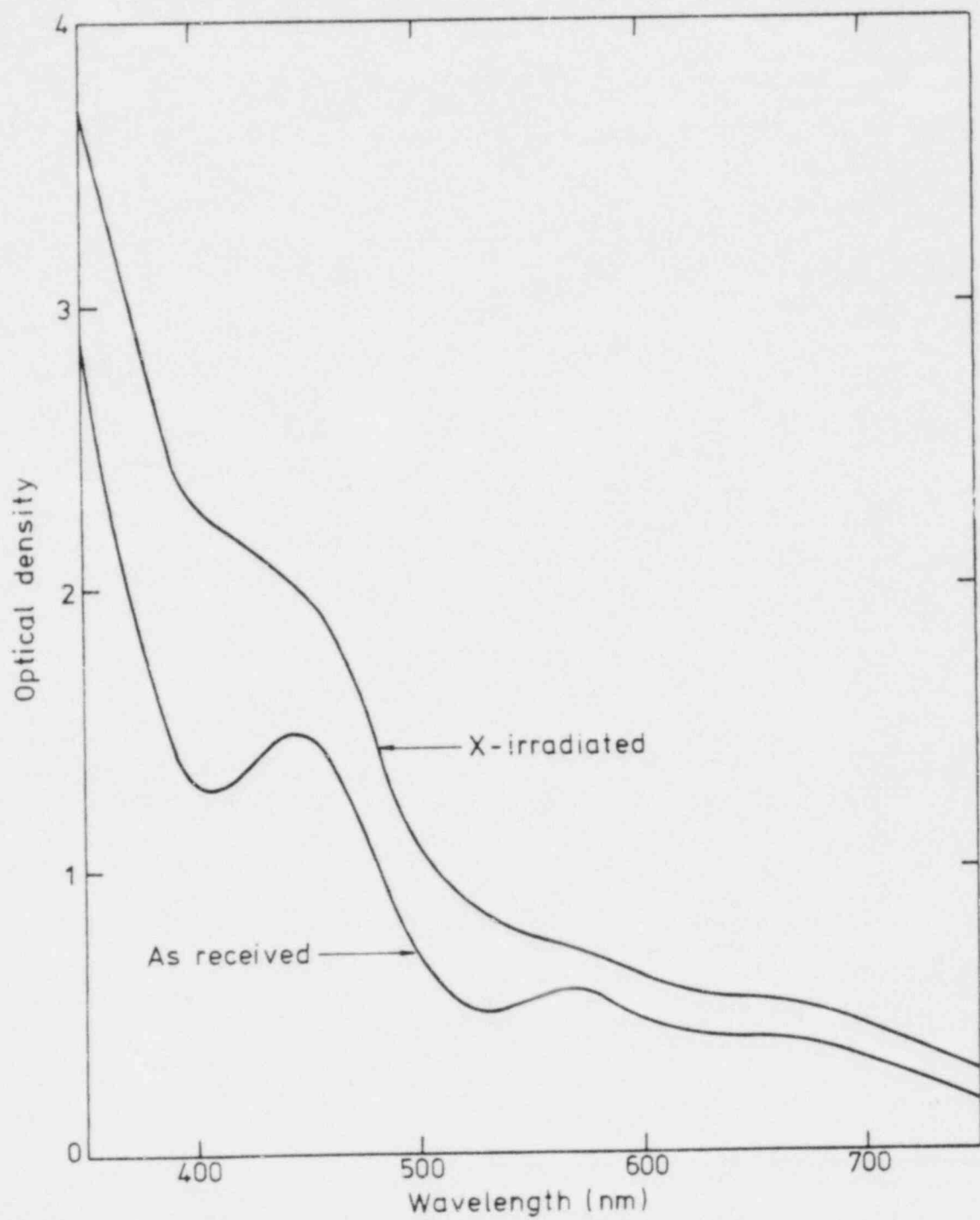
Fig.1.   OPTICAL DENSITY/WAVELENGTH FOR AN IRRADIATED SAPPHIRE SPECIMEN

Fig.2. OPTICAL DENSITY/NEUTRON FLUENCE ($E_n > 1$ MeV) AT 600 nm FOR SAPPHIRE IRRADIATED IN HERALD REACTOR AT 60°C, 250°C, and 290°C

Fig.3. OPTICAL DENSITY/FLUENCE (E_n > 1 MeV) FOR SAPPHIRE IRRADIATED IN
OAK RIDGE P.S.F. EXPERIMENT
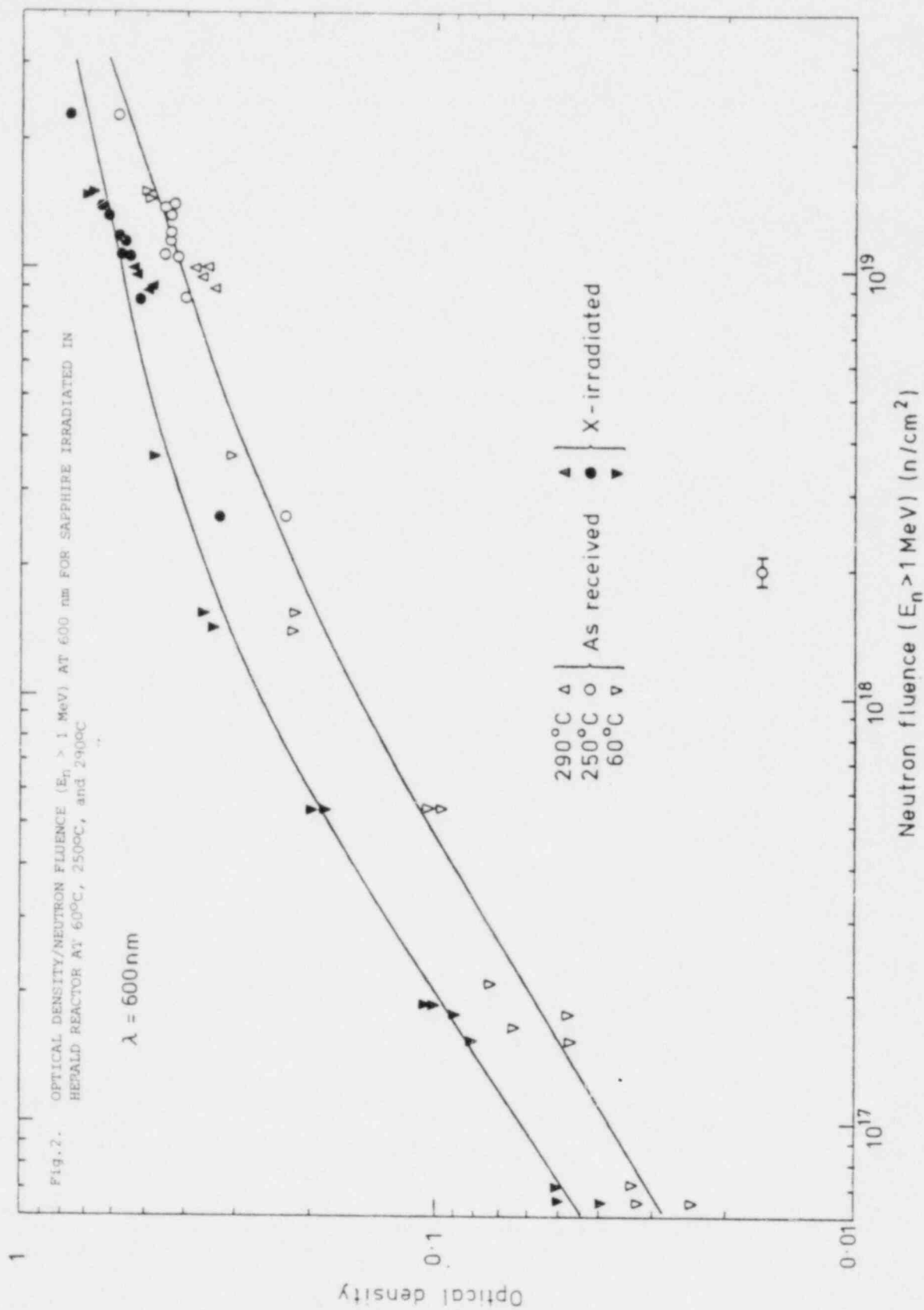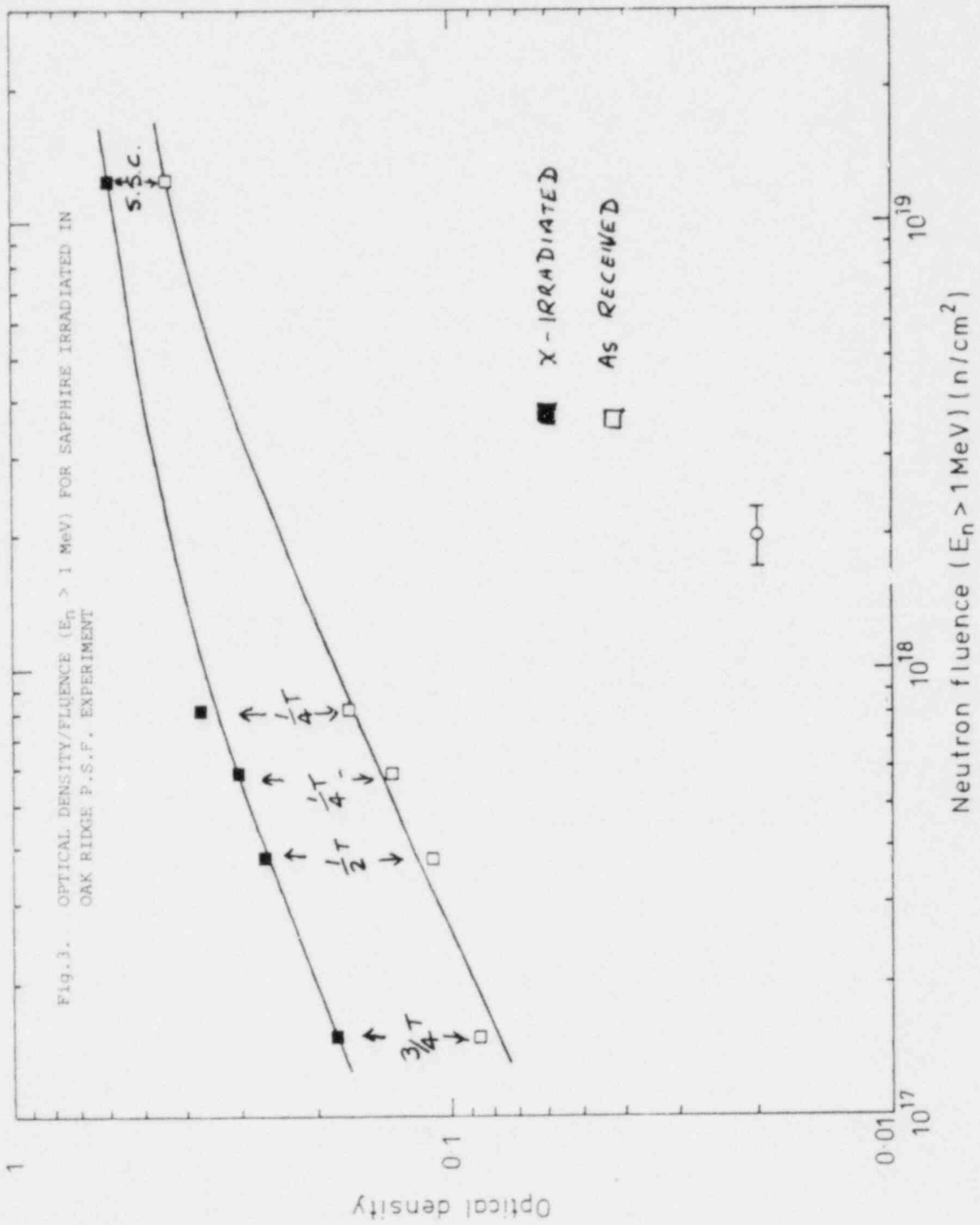
Fig. 4. OPTICAL DENSITY/DISPLACEMENTS PER ATOM IN SAPPHIRE

Fig.5. DISPLACEMENT DAMAGE CROSS SECTIONS FOR IRON AND ALUMINIUM IN α-ALUMINA (DORAN and GRAVES[2])

PHOTOFISSION OBSERVATIONS IN REACTOR ENVIRONMENTS USING SELECTED FISSION PRODUCT YIELDS

Raymond Gold, Frank H. Ruddy, and James H. Roberts
Westinghouse Hanford Company
Hanford Engineering Development Laboratory
Richland, Washington, U. S. A.

ABSTRACT

A new method for the observation of photofission in reactor environments is advanced. It is based on the in-situ observation of fission product yield. In fact, at a given in-situ reactor location, the fission product yield is simply a weighted linear combintation of the photofission product yield, Y_γ, and the neutron induced fission product yield, Y_n. The weight factors arising in this linear combination are the photofission fraction and neutron induced fission fraction, respectively. For the fission product yield to be a sensitive index of photofission, the selected fission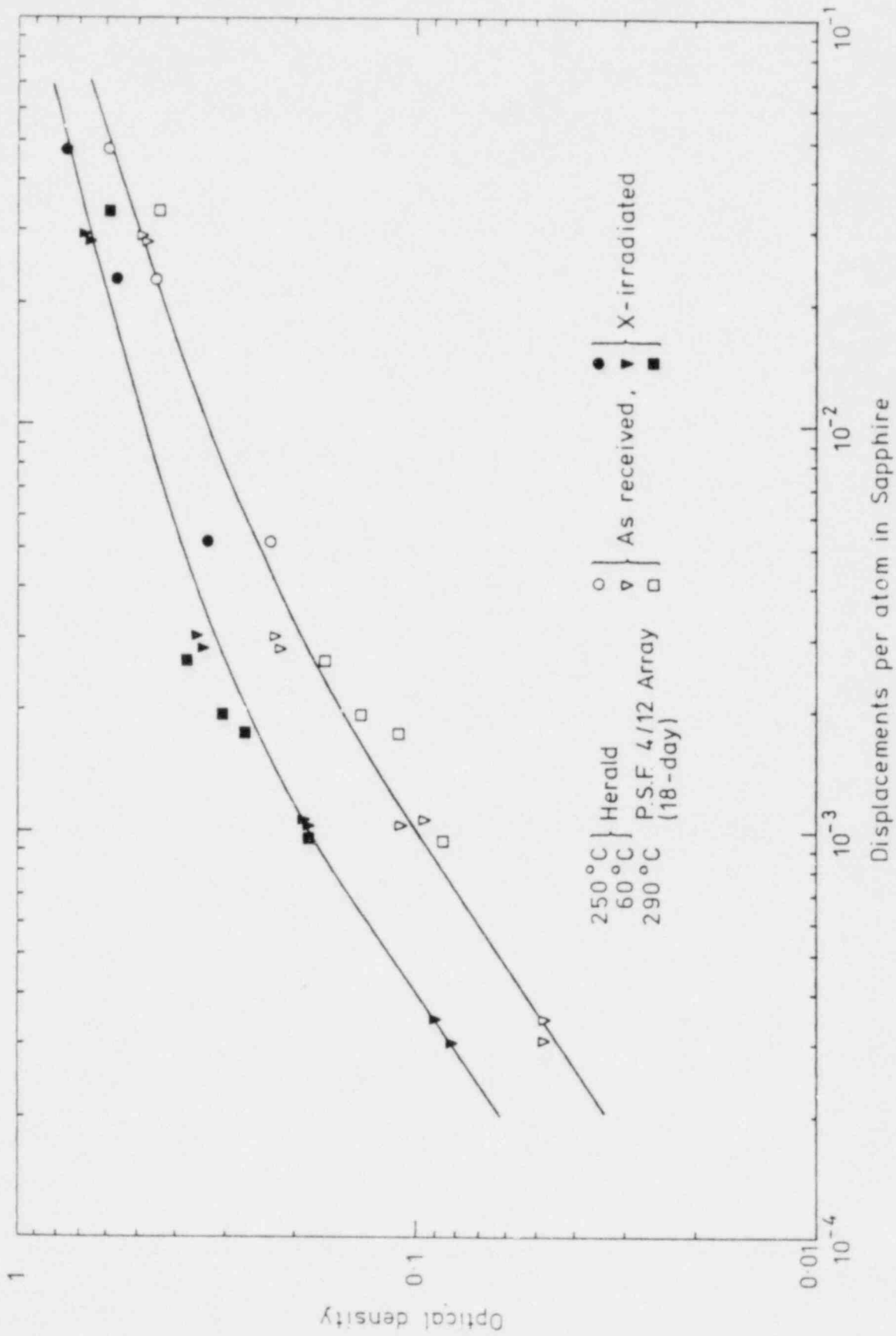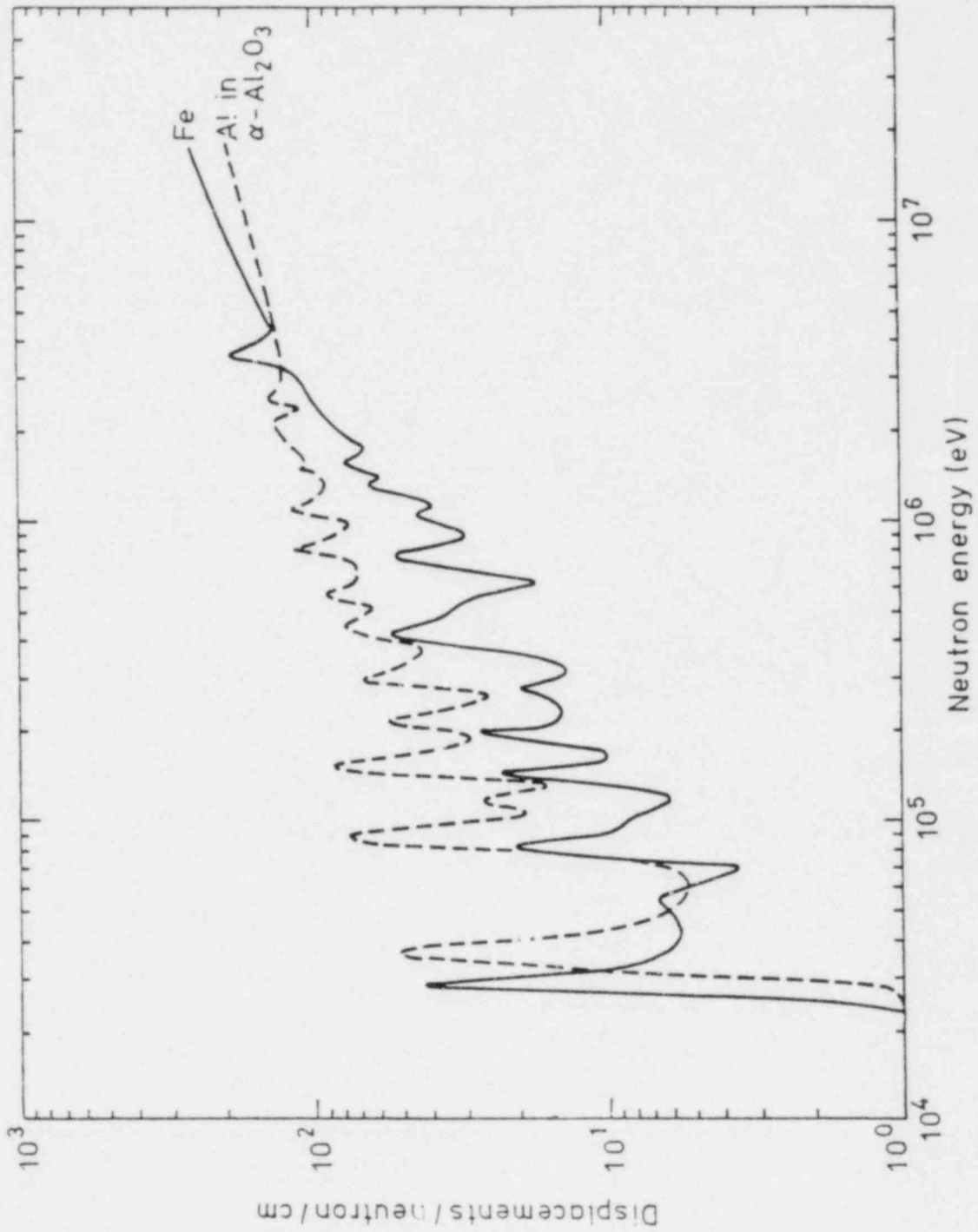 product must satisfy the condition: $Y_\gamma \gg Y_n$. Fortunately, a number of fission products exist which satisfy this general condition. For example, fission products on the light mass side of the low mass fission product peak, in the region near approximately 75 a.m.u., generally fulfill this condition.

This method can be readily implemented with established techniques for measuring in-situ reactor fission product yield. For example, one can use the method based on simultaneous irradiation of radiometric (RM) and solid state track recorder (SSTR) fission monitors. The sensitivity and accuracy of the method are estimated using state-of-the art experimental accuracy and current knowledge of fission product yields. Unique advantages of this method for reactor applications are emphasized.

INTRODUCTION

Fission neutron dosimetry has been used extensively in reactor applications. Fission product yield (FPY) monitors can determine absolute fission rates based on the knowledge of the absolute fission product yield of selected radiometric or stable fission products. Fission chambers and solid state track recorders (SSTR) are more direct methods of absolute fission rate measurements that have been used for reactor applications. However, difficulties arise for all these fission neutron dosimetry techniques in certain reactor environments, when fission induced by the gamma-ray component of the radiation field, commonly called photofission, is non-negligible.

Concern with possible photofission contributions in fission monitors used for reactor neutron dosimetry has existed for some time. Indeed, the significance of photofission in the environment of the pressure vessel (PV) of light water reactors (LWR) was formally emphasized in the second of this series of international symposia devoted to reactor dosimetry.[1,2] Subsequently, a method using a tungsten "photofraction" gauge was successfully developed and used. [3,4] These measurements as well as calculations[5] reveal that the photofission contribution apparently exhibits large changes for different fission nuclei, ^{232}Th, ^{238}U, ^{237}Np, ... etc., that are candidates for fission neutron dosimetry in the LWR-PV environment. It is interesting to note that the use of SSTR for photofission estimates was presaged at the second of these international symposia on reactor dosimetry.[2]

This new method, which is called the fission product yield determination of photofission fraction (FPY-PFF), is described by the next section. The accuracy and sensitivity of this new method is then estimated. In the concluding section, the unique advantages of the FPY-PFF method for reactor neutron dosimetry are stressed.

THE FISSION PRODUCT YIELD-PHOTOFISSION FRACTION (FPY-PFF) METHOD

In-situ FPY measurements have been carried out in reactor environments using appropriate combinations of SSTR and radiometric (RM) fission monitors.[6-8] In the FPY-PFF method, an appropriate fission product is chosen so that the photofission yield Y_γ is considerably greater than the neutron induced fission product yield Y_n. Although photofission product data is rather sparse,[9] fission products exist which satisfy this criterion. In particular, fission products in the region near 75 a.m.u., which represent very asymmetric mass divisions, generally meet the condition $Y_\gamma >> Y_n$.

Let Y_i be the fission product yield of such a candidate nuclide as measured in the in-situ reactor environment with a suitable combination of RM and SSTR fission dosimeters. The total in-situ fission rate, F, observed with the SSTR is composed of a neutron induced component, F_n, and a gamma-ray induced component, F_γ, so that

$$F = F_n + F_\gamma. \tag{1}$$

Hence the fraction of fissions induced by neutrons and gamma-rays is simply

$$n = F_n/F \tag{2a}$$

and

$$\gamma = F_\gamma/F, \tag{2b}$$

respectively. Consequently, Equation (1) can be written in the form

$$\gamma + n = 1 \qquad . \qquad (3)$$

The observed fission product yield Y_i can also be expressed in terms of these neutron and gamma-ray fractions. One can write

$$\gamma Y_\gamma + nY_n = Y_i \qquad . \qquad (4)$$

where Y_n is the neutron-induced FPY and Y_γ is the gamma-induced FPY.

Equations (3) and (4) furnish a simple (2X2) system of equations which can be written in matrix form as

$$\begin{pmatrix} 1 & 1 \\ Y_\gamma & Y_n \end{pmatrix} \begin{pmatrix} \gamma \\ n \end{pmatrix} = \begin{pmatrix} 1 \\ Y_i \end{pmatrix} \qquad . \qquad (5)$$

The solution of this system can be obtained by applying the inverse of the matrix

$$M = \begin{pmatrix} 1 & 1 \\ Y_\gamma & Y_n \end{pmatrix} \qquad , \qquad (6)$$

which is given by

$$M^{-1} = (Y_n - Y_\gamma)^{-1} \begin{pmatrix} Y_n & -1 \\ -Y_\gamma & 1 \end{pmatrix} \qquad . \qquad (7)$$

Consequently the solution of Equation (5) is, in matrix form

$$\begin{pmatrix} \gamma \\ n \end{pmatrix} = (Y_n - Y_\gamma)^{-1} \begin{pmatrix} Y_n & -1 \\ -Y_\gamma & 1 \end{pmatrix} \begin{pmatrix} 1 \\ Y_i \end{pmatrix} \qquad . \qquad (8)$$

From Equation (8), the gamma and neutron fractions are simply

$$\gamma = \frac{Y_i - Y_n}{Y_\gamma - Y_n} \qquad , \qquad (9a)$$

and

$$n = \frac{Y_\gamma - Y_i}{Y_\gamma - Y_n} \qquad . \qquad (9b)$$

It is clear that both the photo-fission fraction γ as well as the neutron fraction n depend very simply upon the observed FPY, Y_i. The conditioning of this 2 x 2 system of equations depends upon the absolute value of the determinant of M, which is given by

$$\left| \det M \right| = \left| Y_\gamma - Y_n \right| . \qquad (10)$$

Consequently one can anticipate that the accuracy of this correction method will improve by selecting FPY which increase $\left| Y_\gamma - Y_n \right|$. In addition, it is highly desirable that FPY be selected so that $Y_\gamma \gg Y_n$. Satisfying this latter condition obviously implies good sensitivity of this method for the photo-fission fraction relative to the neutron fraction. It has already been emphasized that such a characteristic is obviously desirable in order to generate accurate correction of the photo-fission fraction.

Further comment on the benchmark experiments to measure Y_n and Y_γ is warranted. The neutron yield Y_n should be determined in a neutron spectrum which is representative of the in-situ reactor environment. One thereby attempts to render negligible any change in Y_n arising between the in-situ neutron spectrum and the benchmark neutron spectrum. In this vein, it is obviously desirable to use FPY that are less dependent upon neutron energy while still fulfilling the general condition $Y_\gamma \gg Y_n$.

As for the photofission benchmark experiments, information on Y_γ could be obtained from targets that have been used in electron accelerators to generate intense photoneutron sources. Amusingly enough, such discarded targets could prove valuable provided the electron energy used at the accelerator produced a bremsstrahlung spectrum which is representative of the in-situ gamma spectrum (above the given photofission threshold).

ACCURACY AND SENSITIVITY

The experimental error in the deduced fractions, n and γ, can be derived from Equations (9a,b) in terms of the errors in the known FPY, Y_γ and Y_n, as well as the error in the observed in-situ FPY, Y_i. For the respective variances of γ and n, namely $(\delta\gamma/\gamma)^2$ and $(\delta n/n)^2$, one finds the expressions

$$\left(\frac{\delta\gamma}{\gamma}\right)^2 = \frac{1}{(1-Y_n/Y_i)^2}\left(\frac{\delta Y_i}{Y_i}\right)^2 + \frac{(1-\gamma)^2\,(Y_n/Y_i)^2}{(1-Y_n/Y_i)^2}\left(\frac{\delta Y_n}{Y_n}\right)^2 + \frac{\gamma^2\,(Y_\gamma/Y_i)^2}{(1-Y_n/Y_i)^2}\left(\frac{\delta Y_\gamma}{Y_\gamma}\right)^2, \quad (11a)$$

and

$$\left(\frac{\delta n}{n}\right)^2 = \frac{(Y_i/Y_\gamma)^2}{(1-Y_i/Y_\gamma)^2}\left(\frac{\delta Y_i}{Y_i}\right)^2 + \frac{n^2\,(Y_n/Y_\gamma)^2}{(1-Y_i/Y_\gamma)^2}\left(\frac{\delta Y_n}{Y_n}\right)^2 + \frac{(1-n)^2}{(1-Y_i/Y_\gamma)^2}\left(\frac{\delta Y_\gamma}{Y_\gamma}\right)^2 . \quad (11b)$$

Using Equations (2a,b) the variances of F_γ and F_n are simply

$$(\delta F_\gamma/F_\gamma)^2 = (\delta\gamma/\gamma)^2 + (\delta F/F)^2 , \tag{12a}$$

and

$$(\delta F_n/F_n)^2 = (\delta n/n)^2 + (\delta F/F)^2, \tag{12b}$$

respectively.

Error estimates for the FPY-PFF method have been obtained from Equations (11 and 12) using state-of-the art experimental accuracy. Thus the relative error* of the in-situ FPY observation has been assumed to be 5 per cent, i.e. $(\delta Y_i/Y_i) = 0.05$, whereas the relative errors of Y_n and Y_γ are assumed to be 3 percent. This assumption is reasonable, since more careful calibration/benchmark type experiments can be conducted to determine Y_γ and Y_n than is usually possible in in-situ reactor measurements. In addition, the relative error of the absolute SSTR fission rate measurement has been assumed to be 3 percent i.e. $\delta F/F = 0.03$.

The relative error in n and F_n obtained under these assumptions are shown in Figures 1 and 2, respectively, for (Y_γ/Y_n) values of 2, 5, 10, and 100. As could have been anticipated, these relative errors decrease rapidly with both increasing n and increasing (Y_γ/Y_n). Although these data indicate that accurate correction of photointerference is possible with the FPY-PFF method, the actual accuracy attained must obviously await experimental confirmation. Indeed, it must be stressed that error estimates have only been forecasted herein, whereas in the actual course of experimental effort unforeseen sources of experimental error invariably arise.

The sensitivity of the FPY-PFF method corresponds directly to the sensitivity available for in-situ FPY observations. This latter domain of sensitivity is enormous, since both SSTR and RM fission monitors can be accurately applied over many orders of flux/fluence magnitude. In fact, this enormous range of applicability has already been demonstrated through measurements in low power critical assemblies[6] as well as in high power research reactors.[7,8]

---

*Relative error throught this treatment refers to the 1σ level.

FIGURE 1. The relative error ($\delta n/n$) as a function of n for the FPY-PFF method under the assumptions: ($\delta Y_i/Y_i$) = 0.05 and ($\delta Y_n/Y_n$) = ($\delta Y_\gamma/Y_\gamma$) = ($\delta F/F$) = 0.03
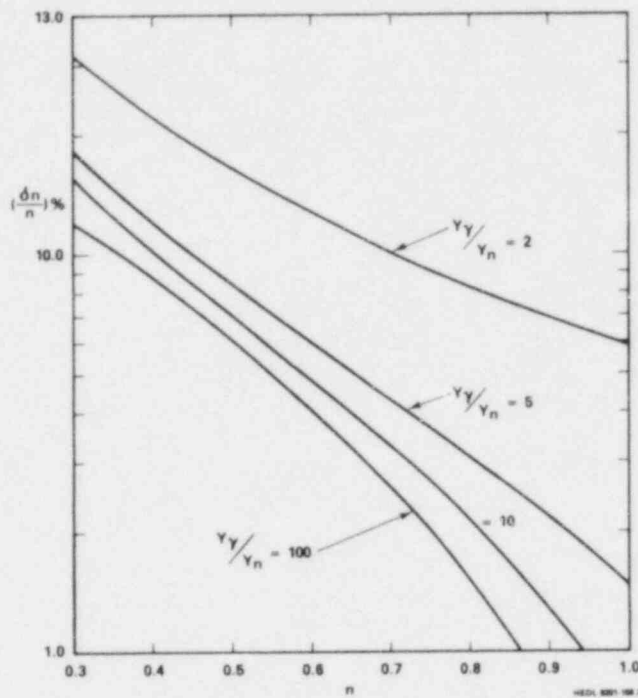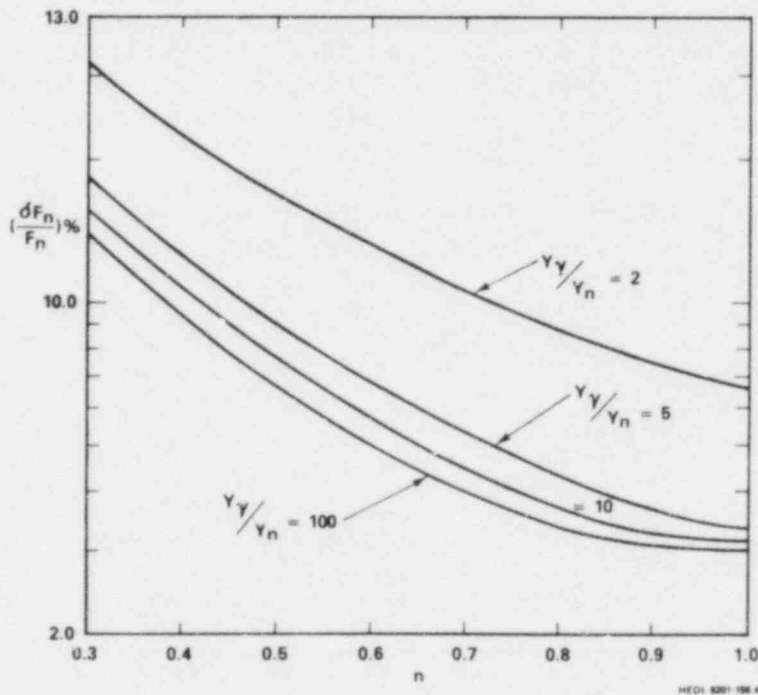

FIGURE 2. The relative error ($\delta F_n/F_n$) as a function of n for the FPY-PFF method under the assumptions: ($\delta Y_i/Y_i$) = 0.05 and ($\delta Y_n/Y_n$) = ($\delta Y_\gamma/\gamma$) = (F/F) = 0.03.

ADVANTAGES

Bootstrap Applications

It may be possible to use the FPY-PFF method to obtain approximate photointerference corrections in already irradiated RM fission dosimeters. In this bootstrap application of the FPY-PFF method, one can no longer use SSTR to measure the total in-situ fission rate F since the actual irradiation has already been concluded (perhaps many years ago). However for many candidate fission monitor nuclides, FPY in the neighborhood of the heavy mass peak (e.g. ^{137}Cs) can be used to provide the total fission rate F. Not only is the FPY in the neighborhood of the heavy mass peak almost independent of neutron energy for many actinide fission monitors, but photofission yields in this region are approximately the same as fission neutron induced FPY.[9]

Under these conditions, if the RM fission dosimeter still exists then Y_i can be measured and F can be determined, in principle, from measurements of fission products in the neighborhood of the heavy mass peak. Obviously Y_γ and Y_n must still be determined in separate benchmark experiments. At the same time, these benchmark field measurements will provide an opportunity to assess the validity of this FPY total fission rate measurement. In these experiments use of FPY from the neighborhood of the heavy mass peak can be directly compared with SSTR observations. In fact, such comparisons will help quantify the component of experimental error introduced through this FPY measurement of F in bootstrap applications. While this latter error could be significantly larger than SSTR observations, this would be small penalty to pay for the ability to correct already conducted reactor neutron dosimetry experiments. Perhaps the most obvious example of such experiments would be fission monitors from already irradiated LWR-PV surveillance capsules.

Passive Techniques

In that this method combines two well established passive fission rate measurement techniques, namely RM and SSTR methods, the FPY-PFF method possesses the advantages of passive techniques for reactor dosimetry. In particular, this method can generally be applied with negligible perturbation of the in-situ reactor environment. Hence this method can be implemented in virtually all reactor regions of interest. Moreover, both flux and fluence measurements are possible. In fluence measurements, F would represent the total number of in-situ fissions.

Radiometric/Stable FPY

In the FPY-PFF method, stable FPY can be used to provide results that are independent of the power-time history of reactor operations.

Stable FPY are of particular interest for bootstrap applications. On the other hand, radiometric FPY provide comparable accuracy at considerably less cost. By appropriate selection of FPY, the FPY-PFF method can provide adequate accuracy even for substantial photofission fractions. (See Figures 1 and 2.)

Gamma-Ray Dosimetry

Since the FPY-PFF method quantitatively assesses the photo-fission component, it can also be used, in principle, for high energy gamma-ray dosimetry. However, practical applications would be restricted to in-situ reactor environments where the high energy gamma-ray intensity is significantly larger than the neutron intensity.

ACKNOWLEDGEMENTS

REFERENCES

1. C. D. Bowman, C. M. Eisenhauer, and D. M. Gilliam, "Photofission Effects in Reactor Pressure Vessel Dosimetry," Proceedings of the Second ASTM-EURATOM Symposium on Reactor Dosimetry, Vol. 2, 575, NUREG/CP-0004, Palo Alto, 1977.

2. J. H. Roberts, and R. Gold, "SSTR and Emulsion Techniques and Their Applications for FBR, LWR, and MFER Programs," Proceedings of the Second ASTM-EURATOM International Symposium on Reactor Dosimetry, Vol. 2, 739, NUREG/CP-0004, Palo Alto, 1977.

3. G. L. Simmons, V. V. Verbinski, W. K. Hagen, and C. G. Cassapakis, "Measurement and Analysis of Gamma-Ray Induced Contamination of Neutron Dosimetry Procedures Used for Reactor Pressure Vessel Applications," EPRI NP-1056 (1979).

4. V. V. Verbinski, C. G. Cassapakis, W. K. Hagen, and G. L. Simmons, "Photointerference Corrections in Neutron Dosimetry for Reactor Pressure Vessel Lifetime Studies," Nucl. Sci. & Engng. 75, 159 (1980).

5. E. D. McGarry, C. M. Eisenhauer, and G. Minsart, "Gamma-Ray Response of Integral Neutron Dosimeters," in LWR Pressure Vessel Surveillance Dosimetry Improvement Program: PCA and Blind Test, Ed. W. N. McElroy NUREG/CR-1861 (1981).

6. R. J. Armani, R. Gold, R. P. Larsen, and J. H. Roberts, "Measured Fission Yields of ^{99}Mo and ^{140}Ba in Fast Neutron-Induced Fission of ^{239}Pu, Trans. Am. Nucl. Soc. 13, 90 (1970).

7. R. P. Larsen, N. D. Dudey, R. R. Heinrich, R. J. Armani, R. Gold, R. D. Oldham, and R. J. Popek, "^{235}U, ^{238}U, and ^{239}Pu Fast Fission Yields of Short-Lived Gamma-Active Nuclides, Trans. Am. Nucl. Soc. 15, 483 (1972).

8. R. P. Larsen, N. D. Dudey, R. R. Heinrich, R. D. Oldham, R. J. Armani, R. J. Popek, and R. Gold, "The Yield of Short-Lived Gamma-Ray Emitting Nuclides from Fast- and Thermal-Neutron Fission," Nucl. Sci Eng. 54, 263 (1974).

9. E. K. Hyde, "The Nuclear Properties of the Heavy Elements, Volume III: Fission Phenomena," Prentice-Hall, Inc., Englewood Cliffs, N. J. (1964).

GAMMA DOSIMETRY AND CALCULATIONS

N. Maene, R. Menil, G. Minsart, SCK/CEN, Mol, Belgium
L. Ghoos, CORAPRO, Mol, Belgium

SUMMARY

A procedure was developed to improve the accuracy of gamma dose measurements with ^{7}LiF thermoluminescent dosimeters. By repeatedly exposing a set of dosimeters to a uniform gamma dose, followed by readout and subsequent release a more homogeneous subset may be selected. It was found that a reader equipped with three hot nitrogen jets yielded very accurate relative dose values because of the excellent short-term stability. Monitoring with aid of dosimeters exposed near a ^{60}Co source remains necessary.

The technique was applied to determining the nuclear heating in the mock-up of a nuclear fast power reactor and also to check calculated gamma dose over neutron flux ratios in a mock-up of the pressure vessel of a PWR reactor (PCA). The procedure of calculation, after validation in a particular PCA configuration, can be used to provide photofission and photoactivation corrections related to measurements in other configurations [1].

CHARACTERISTICS OF THE TLD READER

When using TLDs to determine the gamma dose in a critical assembly it is highly desirable that stable readout equipment be available. The automatic TLD reader used in this series of experiments was designed by TNO[*]; it is equipped with three hot N_2 gas jets aiming at the centre of a cylindrical cavity (see fig. 1). This provides perfect thermal contact and ensures fast reproducible heating of the samples. These samples are sucked up at the tip of a vacuum needle which turns over 180° along an horizontal axis and is pushed upwards into the cavity (see fig. 2).

This system has one limitation related to the fast heating : it is not possible to start the integration at an arbitrary temperature level. In practice this difficulty may be circumvented by a pre-readout of all samples at a fixed lower temperature of the oven (12 seconds at 130°C). This erases the low-temperature defects

---

[*]Organisatie voor Toegepast Natuurwetenschappelijk Onderzoek, Arnhem, The Netherlands.

which are responsible for differences in fading among dosimeters.
This is very useful as measurements are always made relative to a
set of calibrating dosimeters exposed to a known gamma field near
a ^{60}Co source. This usually takes place at a date which does not
coincide with the experiment.

SELECTION OF THE ^{7}LiF DOSIMETERS

A batch of 380 pure ^{7}LiF dosimeters (diameter = 1 mm; length =
6 mm) was used for the irradiations. The dosimeters, which were
new (unirradiated), were first annealed in an oven during one hour
at 400°C. This was followed by rapid cooling and by a second anneal
during two hours at 100°C. The whole batch was exposed four times,
at a distance of 150 cm from a ^{60}Co source, to a uniform dose of
about 5 Rad. Each run was followed after about three days by the
readout of the individually numbered dosimeters on the automatic
TLD reader. The light output was integrated by the photomultiplier
during 12 seconds at 220°C. All readings belonging to one run
were renormalized by dividing them by the average reading and thus
represent deviations from the batch average. This means that one
counts on the short-term stability of the equipment only.

In the course of these and other measurements it was observed
that the statistical distribution of the results gradually approached
a Gaussian distribution after a few exposures. In fig. 3 this is
illustrated for a batch of 185 dosimeters, exposed eight times to
a dose of 8 Rad. In order to improve the statistics the results
of the irradiations were lumped together into two groups. This
effect was interpreted as an indication that the heating cycle in
the reader was more reproducible than the first annealing in the
oven. After the last test exposure each sample was kept for 60
more seconds in the reader at 220°C after readout in order to enhance
this annealing effect.

For each sample the average over the four exposures was taken
as a measure of the intrinsic sensitivity.

By combining the estimates of the standard deviation of one
readout, derived for every single dosimeter, and assuming that the
mean value of the standard deviation is the same for all dosimeters
a sufficiently accurate estimate is obtained for this parameter

$$\sigma = 3.2 \% ;$$

75 dosimeters located within a deviation less than 3 % from the
average intrinsic sensitivity were finally selected for further
use.

APPLICATION TO IRRADIATIONS IN PCA

The results of irradiations in PCA (Pool Critical Assembly) configuration 4/12 SSC in November 1980 are given as an example of the application of this technique. In the wooden dosimetry tower five TLDs were irradiated in a pure gamma field under 0.5 mm of steel at a distance of 150 cm from the ^{60}Co source. The exposure was 100 Roentgen in air which corresponds to a calculated dose of 82.7 Rad in steel.

Thirty dosimeters were irradiated at five locations in PCA 4/12 SSC : SSC, 1/4 T, 1/2 T, 3/4 T and VB at the maximum axial flux level (see fig. 4). The TLDs were always placed in mild steel sample holders, generally located inside ferritic steel boxes which provided for an essentially unperturbed environment.
The power level was chosen to keep the doses in each run well within the linear region of the TLD response curve ($\sim$ 80 Rad for calibration and 20 to 40 Rad for PCA).

All the TLDs were read on January 7, 1981 with the TNO reader in the following way

* First, a pre-reading of 12 seconds at 130°C
* Second, the real reading of 12 seconds at 220°C.

The corrections for fading of the TLD signals were kept small by performing the PCA and Mol Wooden Tower calibrations approximately at the same date and also by the pre-reading which erases low-temperature defects in the ^{7}LiF.

With six dosimeters in each position the standard deviation on a dose value is generally less than 3 %.

TRANSPORT THEORY CALCULATIONS

The neutron and gamma flux maps were computed for the PCA 4/12 SSC geometrical configuration in which TLDs were exposed, using exactly the same calculational procedure as for the blind test cases PCA 8/7 and PCA 12/13[2]. The neutron and gamma fluxes obtained at the locations where measurements were performed were then used to deduce reaction rates and gamma-to-fast-neutron flux ratios, and these results were combined to absolute fast flux values obtained with the 2D DOT calculation to yield "absolute" theoretical results to be compared to the TLD responses scaled to the same core power [1].

Neutron Field Computation

A one-dimensional 40-group neutron problem was run along the Y coordinate using the modified DTF-IV program, part of the SCK/CEN MULCOS Code system, in S8 approximation. The geometrical model was identical to the one adopted for the 171-group S8/P3 ANISN calculation. The macroscopic effective cross sections for each region were prepared by the PREPROCESSING part of the MULCOS Code system, starting from the SCK/CEN MOL-BR2 40-group library and using a ABBN-type formalism. Since this set does not contain scattering expansions up to P3, the PO diagonal transport correction has been adopted as the standard option; the MOL-BR2 set contains a detailed energy group structure for the thermal and epithermal neutrons.

The buckling terms are computed on the basis of Σ_{tr} (for D), and space-dependent B^2 values are provided in the input; these B2 values were deduced from measurements for the vertical components [the same values as in the DOT (X,Y)], and the lateral ones were computed from the flux map provided by the 2D calculation.

The space-dependent fixed-fission source is provided by the core power study, as for the ANISN and DOT problems [3].

Gamma Field Computation

An ancillary program (GAMPREP) is used to compute :

* Gamma sources in each mesh point (deduced from capture and fission rates); for gamma emission, fission products are assumed to be in equilibrium

* Macroscopic gamma cross sections in each region (based on the compositions used in each zone of the model), with scattering matrix expansion up to P3

The basic data for this step are :

* The flux map provided by the neutron DTF-IV run

* The self-shielded microscopic 40-group neutron cross sections for reaction rate computations

* The gamma production cross sections derived from the EURLIB-3 coupled library, after the collapse of the original 100-neutron groups into the actual 40-group structure of the MOL-BR2 library

* The 20-group gamma interaction cross-sections, as they are in the EURLIB-3 set

The output of GAMPREP is the full data set needed for running a gamma problem in S8/P3 approximation (ANISN or DTF-IV); the same geometrical model and space-dependent bucklings as for the neutron run are used.

As for the neutron problem, pointwise convergence criteria are applied in order to obtain a good flux map stabilization. Since no scaling was applied in the gamma part of the work, gamma fluxes and neutron fluxes are at the same scale.

Additional Processing of the Results

From the neutron flux map, reaction rates and equivalent fission fluxes were computed for several threshold detectors $[^{115}In(n,n'), \, ^{58}Ni(n,p), \, ...]$ at the measured locations. The effect of fast neutrons on the TLD material was also calculated in order to provide corrections to be applied to the TLD readings.

With the gamma-ray map, energy deposition rates in Fe were calculated. Ratios between these results and nickel equivalent fission flux were then obtained and applied to the nickel fission fluxes yielded by the 2D DOT run scaled to the core power, in order to obtain normalized theoretical energy deposition rates at the different positions (see fig. 4); due to the P3 expansion and the better modelling, 2D DOT (X,Y) neutron results are a good basis for flux magnitudes. The assumption made here is that the ratios: gamma energy deposition/fast neutron flux, which should be deduced from the refined 2D model, are not very different from the ones yielded by the present 1D calculations; this assumption is supported by the good agreement between these theoretical ratios and the experimental ones.

CONCLUSION

The TLDs yield sufficiently accurate results when they are preselected as indicated. As can be seen from fig. 4, the agreement between the calculated and the experimental TLD results is generally better than 20 %; it is thus believed that the theoretical estimates made for the other PCA configurations with the same procedure and basic data are sufficiently accurate as far as photofission and γ,γ' corrections are concerned.

REFERENCES

[1] LWR pressure vessel surveillance dosimetry improvement program : PCA experiments and blind test, NUREG/CR-1861, HEDL-TME 80-87/R5 (July, 1981).

[2] G. Minsart, "Theoretical analysis of the PCA experiment," Proc. of the 3th ASTM-EURATOM symposium on Reactor Dosimetry, Ispra (October 1-5, 1979).

[3] F.B.K. Kam et al., "The core power of the pool critical assembly light water reactor pressure vessel benchmark," Proc. of the 3th ASTM-EURATOM symposium on Reactor Dosimetry, Ispra (October 1-5, 1979).
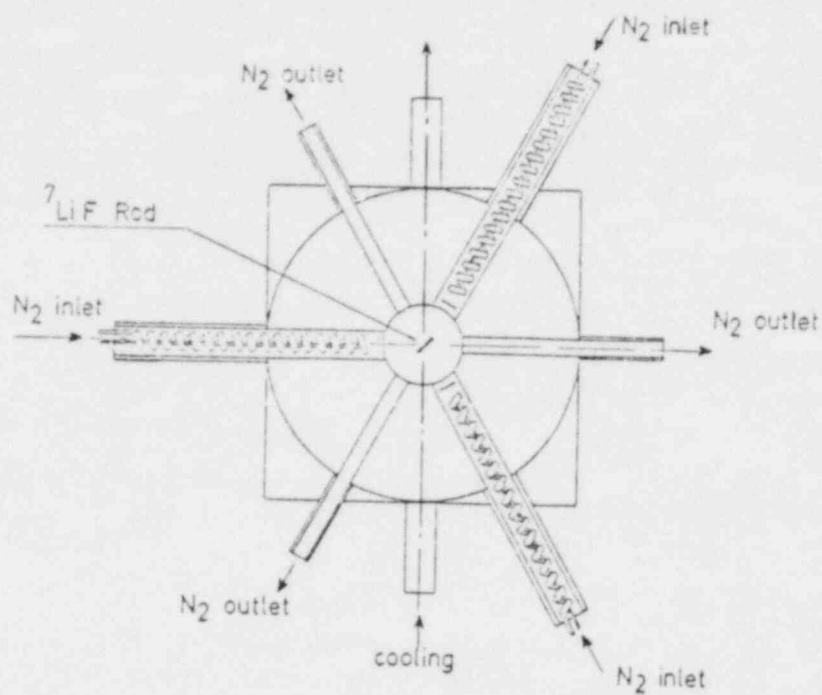
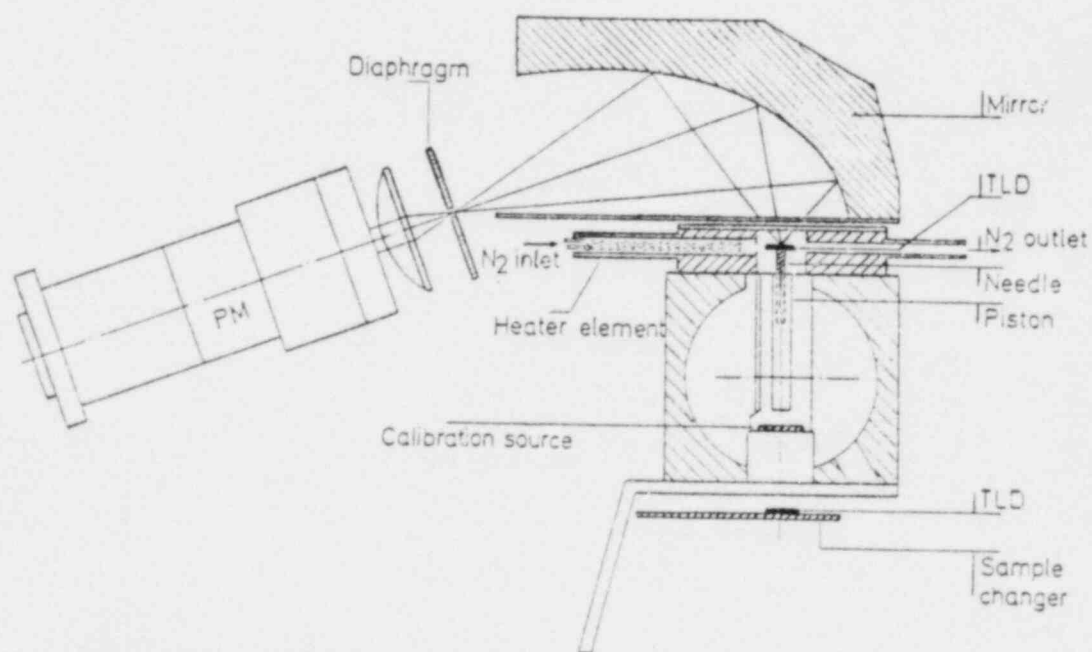Fig. 1. TLD (^{7}LiF rod) in centre of heating cavity, exposed to three jets of hot nitrogen gas.

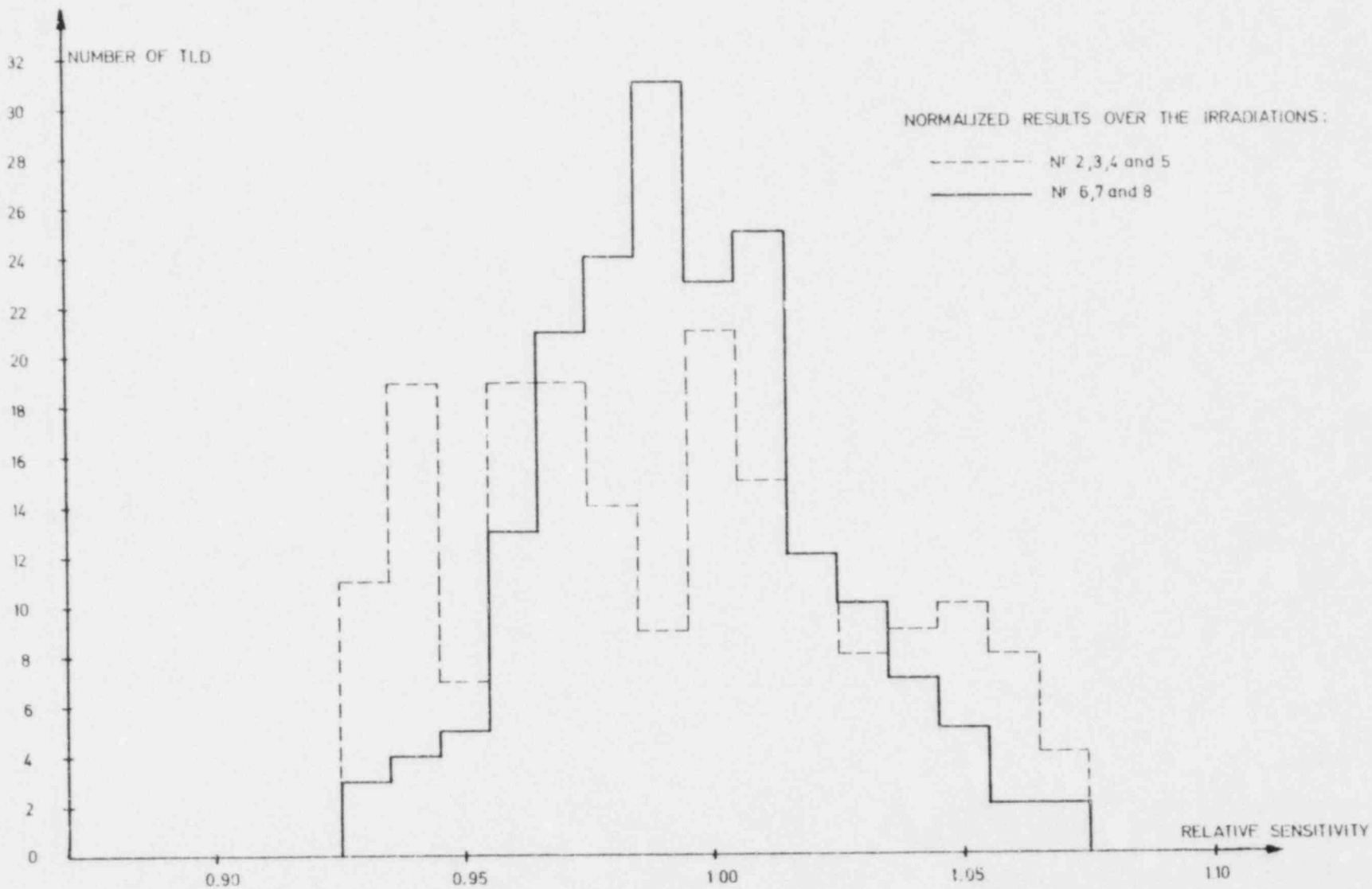Fig. 2. Schematic diagram of the rsader.

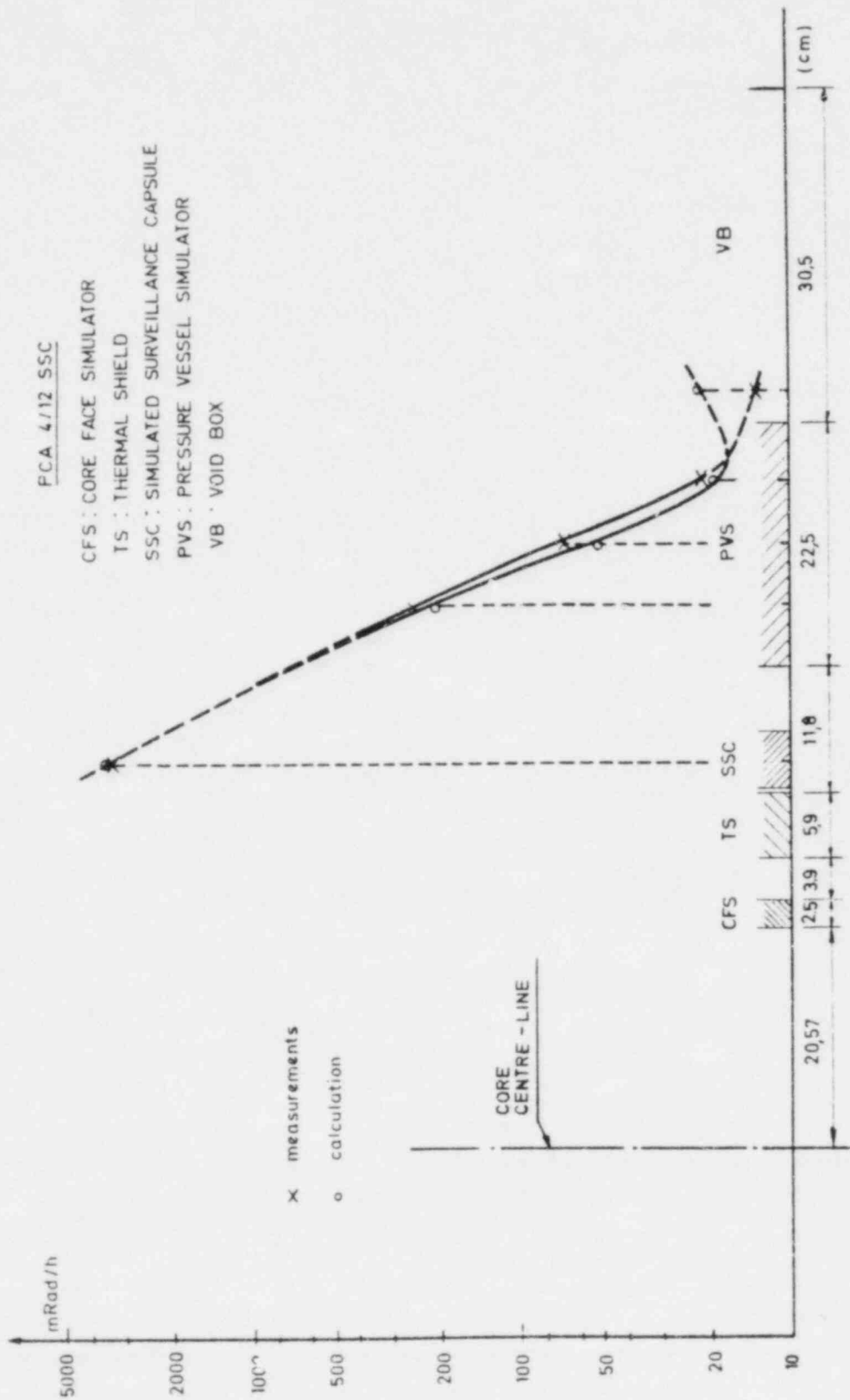Fig. 3. Evolution of the relative sensitivity with increasing number of exposures.

362

Fig. 4. Energy deposition in steel in mRad/h at 1 W core power.

DEVELOPMENT OF SENSITIVE MICROCALORIMETERS FOR ABSORBED DOSE MEASUREMENTS IN BENCHMARK RADIATION FIELDS

J.A. Mason
Imperial College and the University of London Reactor Centre,
Silwood Park, Ascot, Berkshire, England

ABSTRACT

The present paper describes the development of sensitive adiabatic graphite and aluminium microcalorimeters designed for dose rate measurements in low power benchmark radiation fields. The calorimeters are both small and portable and they are controlled by a microcomputer.

Results are reported for measurements in two radiation fields. Dose rates of a few tens of milligray per second have been measured in a core tube of the Consort II reactor and, in the Imperial College ^{60}Co irradiation facility, accurate dose rate measurement of a few milligray per second have been achieved. These latter measurements are compared with the results of ionization chamber measurements.

INTRODUCTION

The principal limitation in the use of absorbed dose calorimetry has been the lack of sensitivity. The technique has therefore been unsuitable for measurements in zero energy benchmark fields. The aim of the present work has been to improve the calorimeter sensitivity and therefore extend the application of the technique to low dose measurements.

Certain conditions must be observed in the measurement of absorbed dose if the result is to be meaningful. First, the incident or primary radiation field must not be significantly perturbed or attenuated by the presence of the dosimeter. Second, the electronic and photonic equilibrium must exist between the detector and its surroundings. If these conditions are observed, the measured absorbed dose rate will be the ideal dose rate[1] or KERMA rate.

In order to achieve greater measurement sensitivity, the adiabatic mode of calorimeter operation was chosen[2]. Using this method, the rate of temperature rise is measured in a sample which is surrounded by a jacket whose temperature is maintained at the sample temperature. As a result of the presence of the jacket, the rate of temperature rise of the sample is due solely to the deposition of energy by radiation.

CALORIMETER DESIGN

A block diagram of the calorimeter system appears as Fig. 1. In addition to the calorimeter, the system consists of amplifiers, a multiplexer, a digital voltmeter (DVM) and a CAMAC electronic-based control and data-logging system.
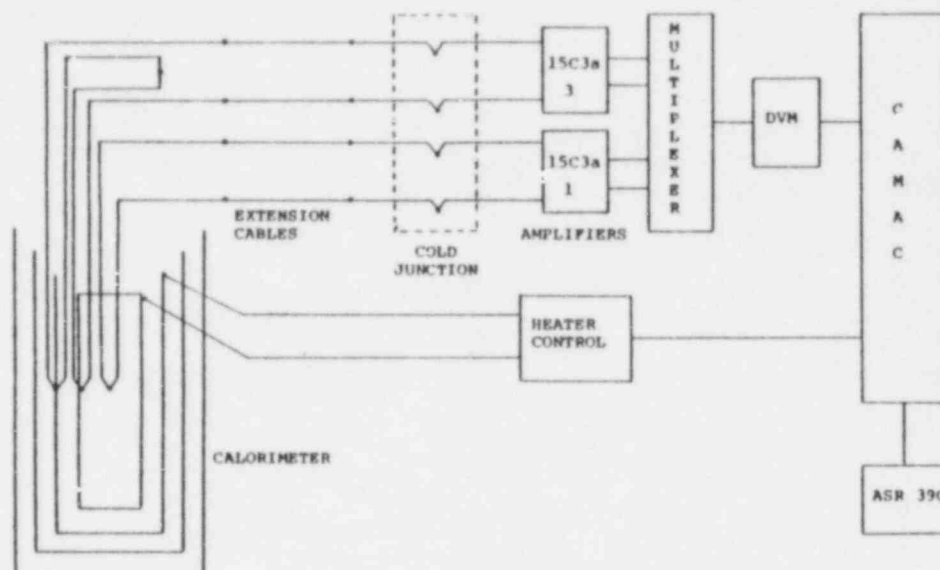
Fig. 1. MKII Adiabatic Calorimeter System

Mechanical Construction

The calorimeters consist of a set of two cylindrical jackets or baffles surrounding a central cylindrical sample. The jackets are made of the sample material, either graphite or aluminium. The jacket wall thickness of 1.5 mm was chosen in order to achieve electronic equilibrium between the jackets and the sample. The sample is 1 cm in diameter.

Surrounding the sample and jackets is an external aluminium can and lid. The can thickness is 1 mm and the lid is extended in a stem from which the calorimeter is supported. The sample, jackets and outer can are electrically and thermally insulated from one another by means of air gaps and PTFE spacers or supports which have been designed in such a way that the contact area and hence the heat transfer between the spacers and calorimeter components is minimized. Although PTFE is subject to radiation damage, this is not a problem in the dose range where the calorimeters are employed. The separate calorimeter components and an assembled calorimeter may be seen in Fig. 2. The calorimeters are 42 mm in diameter and 93 mm high, not including the mounting stem.
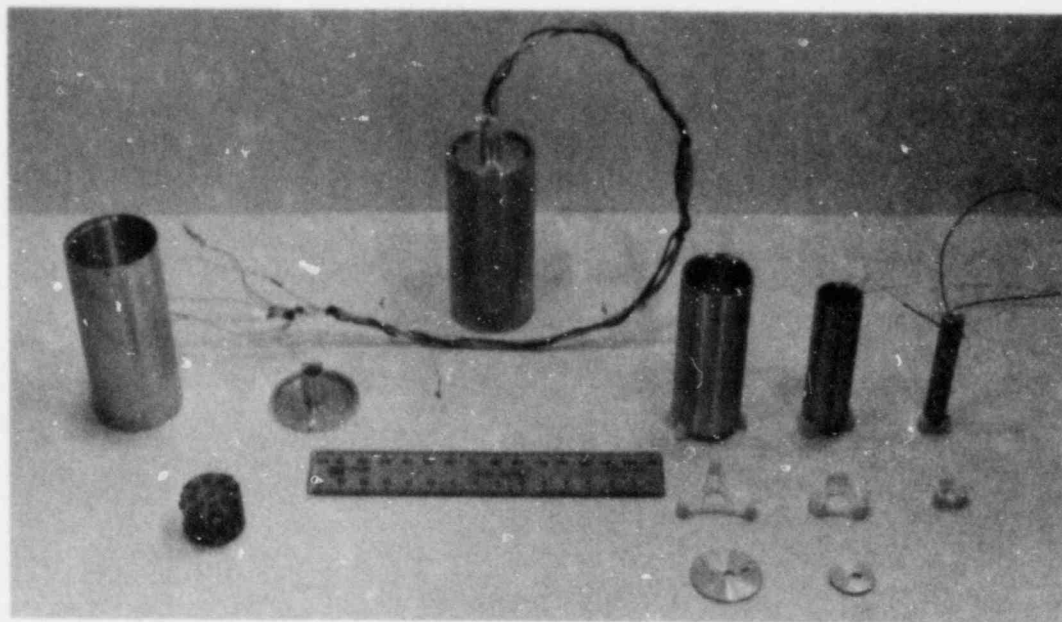
Fig. 2. MKII Calorimeter and its Component Parts

Three thermocouples are employed in each calorimeter as temperature sensors. They are constructed of insulated 46 SWG chromel-constantan in order to minimize the transmission of heat along the thermocouple wires. Two are placed in channels at the mid-plane in the sample: one is on the central axis and the other is near the surface and opposite the third thermocouple which is fixed to the inside of the inner jacket. All these thermocouples pass out of the calorimeter through holes in the jacket lids and spacers and are clamped at the top of the support stem.

The electrical calibration and adiabacic control of each calorimeter is achieved by means of helical electrical heating coils wound around the sample and inner jacket respectively. The 40 SWG heater wires are provided with a resin insulation coating. The positions of the heater coils, thermocouples and the calorimeter component parts may be seen in Fig. 3 which illustrates a cross-section through a calorimeter.

A multi-terminal connection block is provided immediately external to the calorimeter in order to connect both the thermocouples and heater wires to their respective extension cables. In this connection block a differential thermocouple is formed between the inner jacket and outer sample thermocouples. Extension cables of 30 SWG continue the thermocouples to a cold junction several metres away. The cold junction consists of a constant temperature water bath which is at room temperature.

Fig. 3. Calorimeter in Cross-
Section

The figure labels read (top to bottom):

THERMOCOUPLE WIRES

HEATER WIRES

ADIABATIC HEATER

CALIBRATION HEATER

DIFFERENTIAL THERMOCOUPLE

OUTER CAN

SAMPLE THERMOCOUPLE

SAMPLE

INNER BAFFLE

OUTER BAFFLE

SUPPORTS

Adiabatic Heater Control and Data Logging

A novel feature of the calorimeter system is that both adiabatic heater adjustment and data acquisition are controlled by the same microcomputer based CAMAC electronic equipment. This is accomplished using the thermocouple voltages derived from the calorimeter. The voltages from both the sample and differential thermocouples are amplified by low drift, low noise chopper stabilized amplifiers. These voltages are small, generally of only a few microvolts in magnitude, and small changes in the voltages are of interest.

The amplifier output signals are multiplexed by a multichannel reed relay multiplexer which is controlled from CAMAC. The output of the multiplexer is in turn passed to a high resolution DVM which is also controlled from CAMAC. The amplified and digitised thermocouple signals are then passed to the CAMAC system for processing and analysis.

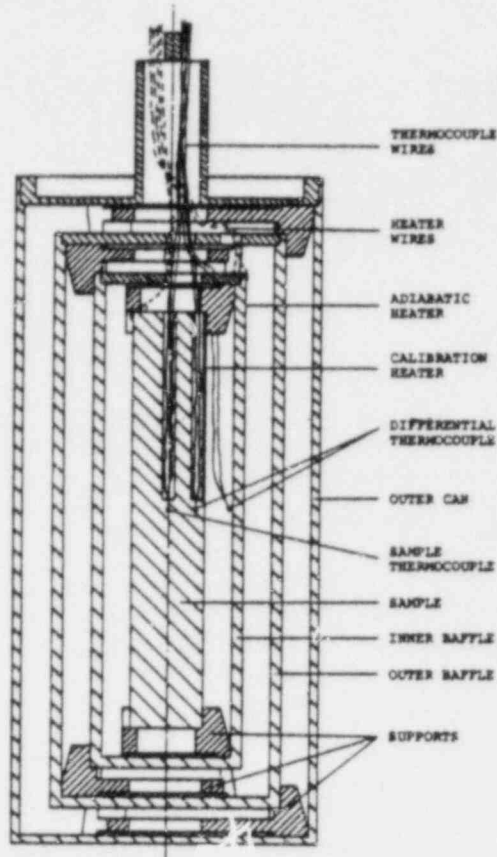The heart of the CAMAC electronic equipment is the Harwell 7025 programmed dataway controller. The 7025 is a treble width CAMAC module which serves as the central processing unit for a single crate CAMAC based computer. CAMAC serves as the peripheral device highway. The 7025 employs the 24-bit CAMAC word length, and it is programmed using an assembly language. Although less sophisticated, the capabilities of the 7025 may be compared with those of current microprocessors even though it predates them by several years.

The 7025 controller performs two basic functions. By monitoring the differential thermocouple it determines if a temperature difference exists between the sample and its surrounding jacket. Both the presence and the magnitude of the heater current are controlled in order to match the jacket temperature to that of the sample. Heater current adjustments may be made every half second and an algorithm is included in the software so that the controller may anticipate and avoid the injection of excessive heat into the jacket.

The second controller function is that of data logging. With an adjustable period the controller prints the time of the measurement and the magnitudes of the amplified thermocouple voltages on the input chan-

nels. The data is normally punched on paper tape for subsequent analysis. The system may be interrogated at any time between the predetermined scans of all channels.

MEASUREMENTS

Preliminary calorimetry measurements have been performed in a core tube of the CONSORT II reactor and in the Imperial College ^{60}Co irradiation facility. The measurement procedure consists of determining the calorimeter sample temperature drift immediately before and after nuclear or electrical calibration heating. The energy deposition or heating rate is determined by correcting the rate of sample temperature rise using the average sample temperature drift rate.

CONSORT II Reactor Measurements

Measurements in the CONSORT II reactor were performed at low power, and always following a weekend shutdown. The calorimeter was lowered into a vertical irradiation tube to a position of low neutron and gamma ray flux above the core. At this position the background temperature drift rate was measured. Measurements of nuclear heating were accomplished by lowering the calorimeter to the core mid-plane. At the end of each heating measurement the device was raised back to the position above the core, the reactor power was raised, and the sequence was repeated.

The results of the CONSORT II experiments are tabulated in Table 1.

Reactor Power (W)	Graphite		Aluminium	
	$(mGy\ s^{-1})$	Error s %	$(mGy\ s^{-1})$	Error s %
10	-	-	44.4	2.3
50	56.1	4.0	50.9	2.6
100	61.6	4.0	59.3	2.6
200	76.0	6.4	74.6	1.5
400	-	-	101.3	2.0
500	109.1	6.3	-	-
600	-	-	131.2	2.7
800	158.6	4.2	162.9	10.1
1K	170.3	5.8	192.5	2.7
2K	288.4	14.5	-	-

Table 1. CONSORT Reactor Measurements

The errors in the table are one standard deviation expressed as a percentage of the measured value. The results of a typical heating rate experiment for the aluminium calorimeter are plotted as Fig. 4. The displayed errors represent a range of two standard deviations.
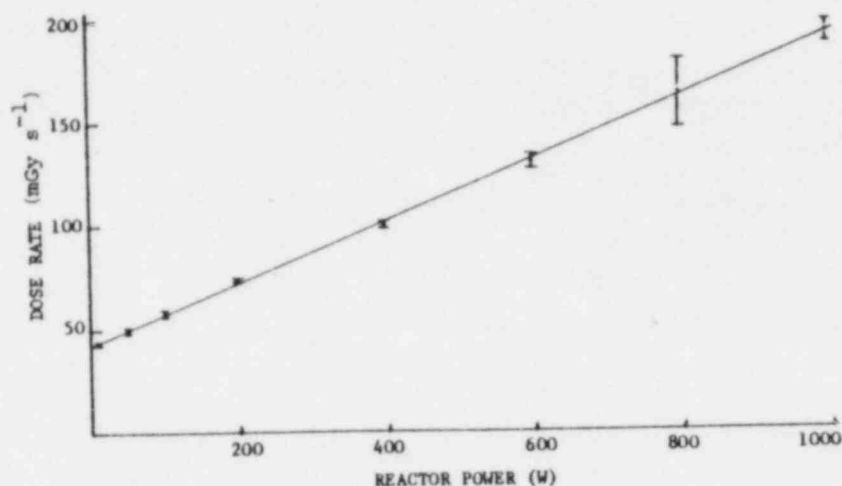
Fig. 4. Aluminium Calorimeter CONSORT Reactor Measurements

^{60}Co Gamma Ray Measurements

Calorimetry measurements in the Imperial College ^{60}Co facility have been performed in a manner similar to those for the CONSORT II reactor. The calorimeters have been placed at various distances from a source of approximately 1500 Ci. The experimental sequence proceeds by moving the calorimeter successively closer to the source following each measurement of initial background temperature drift, nuclear heating and final background temperature drift.

POSITION	IONIZATION CHAMBER EXPOSURE RATE		CALORIMETER			
			Graphite		Aluminium	
(cm)	(R/sec)	Error s%	(R/sec)	Error s%	(R/sec)	Error s%
20	11.8	1.2	10.37	4.9	10.94	3.0
30	5.51	1.3	4.86	4.8	5.08	3.0
40	3.61	1.3	2.86	4.6	2.87	2.6
60	1.45	0.9	1.30	4.4	1.32	2.1
100	0.537	0.9	-	-	0.477	6.2

Table 2. ^{60}Co Measurements

Calibrated ionization chamber measurements have been made using the same experimental geometry. The results of these measurements and the calorimetry measurements have been converted to units of exposure rate, assuming monoenergetic ^{60}Co gamma rays of energy 1.25 MeV. These results are tabulated in Table 2, where again, the errors correspond to one standard deviation expressed as a percentage of the measured value.

DATA ANALYSIS AND RESULTS

The analysis procedure is based on the assumption that the calorimeters undergo adiabatic or nearly adiabatic heating. The temperature drifts before and after a heating rate measurement are a measure of the deviations from adiabatic equilibrium. The linear rate of sample temperature rise is corrected using the linear sample temperature drift rates. An error is determined for each heating rate measurement and, where a statistical measure of the uncertainty is not available, two thirds of the absolute error is used as one standard deviation.

The electrical calibration was intended to be the principal means by which the performance of the device was assessed, and the calibration established. Unfortunately, at this preliminary stage of calorimeter development, difficulties have been experienced with the electrical calibration procedures. An alternative calibration factor has been established through a knowledge of the calorimeter and measurement system parameters, such as the sample specific heat, amplifier gain and sample mass. All of these parameters have been accurately measured and calibration factors have been determined.

In order to assess the performance of the calorimeters, measurements of the dose rates in the ^{60}Co facility have been compared with calibrated ionization chamber measurements. The results of the comparison, expressed in units of exposure, have been tabulated in Table 2. The ratios of calorimeter to ionization chamber derived exposure rates have been plotted as a function of measurement position in Fig. 5. The error bars, which for convenience are displayed in boxes to the right of the measured points, correspond in length to two standard deviations.

In Fig. 5 it may be seen that the calorimeter performs in a consistent manner with a systematic bias of about 10%. Indeed, weighted averages of the ratios yeild 0.89 for graphite and 0.91 aluminium. With these results revised calibration factors may be determined which permit the use of the calorimeter for relative measurements at low dose rates.
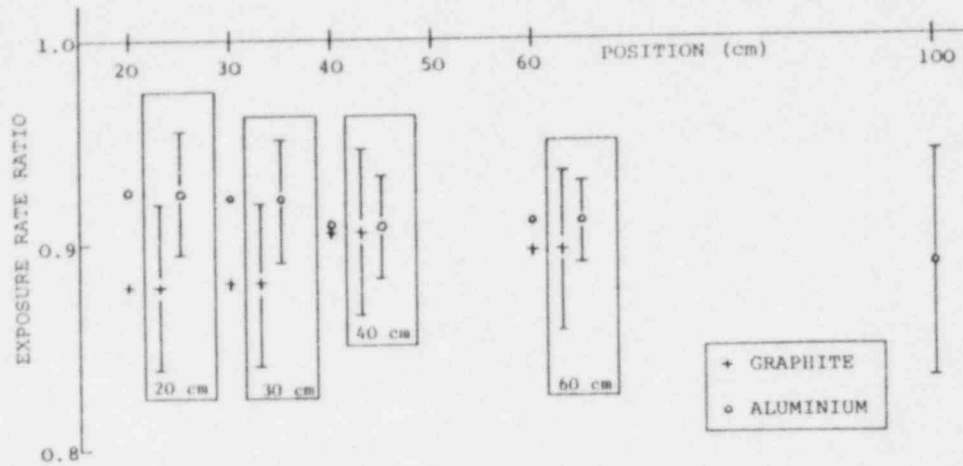
Fig. 5. Exposure Rate Ratios

CONCLUSIONS

Microcalorimeters have been developed which are capable of accurate dose rate measurements at the level of a few milligray per second. The calorimeters perform consistently and with a bias of about 10% when compared with calibrated ionization chamber measurements. The discrepancy is attributed to imperfect adiabatic control, and work is underway to overcome this difficulty, thus permitting absolute calorimetry measurements.

REFERENCES

1. J.K. Linacre and R.B. Thomas, "Calorimetric Dosimetry for Reactor," Irradiation Experiments Part I, UKAEA Report AERE-R4805 (1965).

2. J.A. Mason, "Microcalorimetry in Benchmark Mixed Radiation Fields," ULRC/RES/10, Internal Report, University of London Reactor Centre (1976).

Use of New Threshold Detector ^{199}Hg(n,n')^{199m}Hg for Neutron Spectrum Unfolding

Kiyoshi SAKURAI
Japan Atomic Energy Research Institute
Ibaraki-ken, Japan

Abstract

The nuclear data for the ^{199}Hg(n,n')^{199m}Hg reaction are reviewed and the data are used for neutron spectrum unfolding. The neutron spectrum of the YAYOI glory-hole is unfolded by SAND II with 10 nuclear reactions including the ^{199}Hg(n,n')^{199m}Hg reaction. The ratio of the measured reaction rate to the calculated reaction rate is about 1 ∿ 1.1 for the guess spectrum. The ^{199}Hg(n,n')^{199m}Hg, ^{115}In(n,n')^{115m}In, ^{103}Rh(n,n')^{103m}Rh reactions should be useful threshold detectors for the neutron dosimetry with low level fast neutron flux.

1. Introduction

Many activation detectors are being used for neutron spectrum unfolding. Evaluated neutron cross sections for the activation and/or fission reactions are available, for example the ENDF Dosimetry File is often used for neutron spectrometry. Application of the threshold detector reaction rate of ^{199}Hg(n,n')^{199m}Hg for unfolding has not yet been described, because the evaluated neutron cross sections for the reaction were not available. The author has tried to apply the result of the detector to an unfolding procedure.

This paper describes a verification experiment of new threshold detector ^{199}Hg(n,n')^{199m}Hg on YAYOI standard neutron field.

2. Nuclear Data for the ^{199}Hg(n,n')^{199m}Hg Reaction

2.1 Abundance

We have used natural mercury sample (HgO), because enriched ^{199}Hg sample is very expensive (about 100$/1mg). The mercury element consists of seven isotopes. Each abundance is as follows[1]; ^{196}Hg(0.15%), ^{198}Hg(10.1%), ^{199}Hg(16.9%), ^{200}Hg(23.1%), ^{201}Hg(13.2%), ^{202}Hg(29.7%) and ^{204}Hg(6.8%).

2.2 Half-life and gamma branching ratio of ^{199m}Hg

The excited state of ^{199}Hg is shown in Fig. 1[2]. The threshold energy of the ^{199}Hg(n,n')^{199m}Hg reaction is about 530 keV, the isomer

half-life is 42.6±0.2 minutes and the transition from the isomer state to the 158 keV energy level is M4 and that from 158 keV energy level to the ground state is E2[2]. The branching ratios are 52.3±0.5% and 12.3± 0.5% for the 158 and 374 keV gamma-rays, respectively[2].

2.3 Cross section for the $^{199}Hg(n,n')^{199m}Hg$

Energy dependent cross sections for the $^{199}Hg(n,n')^{199m}Hg$ reaction are not available[3]. Swann and Metzger[4] measured the cross sections from the threshold energy to 2.1 MeV. Bornemisza et al.[5] measured the cross section at 2.8 MeV. Hankla et al.[6] measured the cross section at 14.4 MeV. From these data, it is impossible to evaluate a reliable neutron cross section for neutron spectrum unfolding. Therefore, Sakurai et al.[7] measured the cross sections from 0.78 to 6.3 MeV. The neutron cross section for neutron spectrum unfolding was evaluated from data from Refs. 6 and 7.

3. Verification Experiment of Threshold Detector $^{199}Hg(n,n')^{199m}Hg$ on YAYOI Standard Neutron Field

The validity of the $^{199}Hg(n,n')$ reaction for reactor neutron dosimetry has been examined through an irradiation experiment using the standard neutron field (glory-hole) in the YAYOI. The neutron spectrum had been accurately evaluated by repeated measurements and by calculation[8].

The irradiation of foils in the YAYOI glory-hole was performed at a reactor power of 500 W and an irradiation time of 30 minutes. The measured reaction rates of the $^{199}Hg(n,n')^{199m}Hg$, $^{27}Al(n,\alpha)^{24}Na$, $^{24}Mg(n,p)^{24}Na$ and $^{115}In(n,n')^{115m}In$ reactions are given in Table 1[9]. The reaction rates of the $^{59}Co(n,\alpha)^{56}Mn$, $^{56}Fe(n,p)^{56}Mn$, $^{27}Al(n,p)^{27}Mg$, $^{27}Al(n,\alpha)^{24}Na$, $^{24}Mg(n,p)^{24}Na$, $^{23}Na(n,\gamma)^{24}Na$, $^{47}Ti(n,p)^{47}Sc$, $^{48}Ti(n,p)^{48}Sc$ and $^{115}In(n,n')^{115m}In$ reactions measured by Tokyo Univ. dosimetry group are also given in Table 1[9].

The unfolding code SAND II[10] was used for neutron spectrum unfolding. Newtron cross section library was compiled the program CSTAPE which is a sub-program of the SAND II package. The 620 groups energy structure was applied in the calculations. The neutron cross sections for the library are given in Table 1. The guess spectrum[11] for neutron spectrum unfolding was one which was calculated with a one dimensional transport code ANISN[12]. The uncertainty of the guess spectrum was about 30% from 0.3 to 3 MeV and about 50% outside this range[11].

The unfolded neutron spectrum is shown in Fig. 2. The ratio of the measured reaction rate (M) to the calculated reaction rate is given in Table 2. The ratio in the zeroth and in the final iteration is given in the same table.

More quantitative analysis will give information concerning the usefulness of the threshold detector $^{199}Hg(n,n')^{199m}Hg$. Therefore, characteristic neutron flux density value was calculated from the guess spectrum and from the unfolded spectrum. The total neutron flux density calculated from the guess spectrum is 1.614×10^{11} n/cm^2·sec. The value calculated from the unfolded spectrum is 1.826×10^{11} n/cm^2·sec. The value calculated from the evaluated spectrum[8] is 1.875×10^{11} n/cm^2·sec. Using the $^{199}Hg(n,n')^{199m}Hg$ reaction rate, the total neutron flux density was

1% smaller than that calculated from the neutron spectrum unfolded without the ^{199}Hg(n,n')^{199m}Hg reaction rate.

4. Discussion

We have used natural mercury sample. Therefore, the activity of the ^{199m}Hg is produced by the ^{198}Hg(n,γ)^{199m}Hg and the ^{200}Hg(n,2n)^{199m}Hg reactions, and also generated by following decay of ^{199}Au that is produced by the ^{199}Hg(n,p)^{199}Au reaction. As the neutron spectrum of the YAYOI glory-hole is very hard, the influence of the ^{198}Hg(n,γ)^{199m}Hg reaction is negligibly small. The fission spectrum averaged cross section of the ^{200}Hg(n,2n)^{199m}Hg reaction is 5.5 mb[13]. Therefore, the influence of the ^{200}Hg(n,2n)^{199m}Hg reaction is about 2%. The fission spectrum averaged cross section of the ^{199}Hg(n,p)^{199}Au is 0.009 mb[13]. The influence of beta decay of the ^{199}Au is negligibly small.

We had compiled the neutron cross sections for the ^{199}Hg(n,n')^{199m}Hg reaction. One is compiled by using the cross section data that were measured by Swann and Metzger[4], Bornemisza et al.[5] and Hankla et al.[6], another is compiled by using the cross section data that were measured by Sakurai et al.[7] and Hankla et al.[6]. When the former cross sections are used for neutron spectrum unfolding, the ratio of M/C for the zeroth iteration is about 3. The value is about 1∿1.1 when the latter cross sections are used for the unfolding.

The calculated fission spectrum averaged cross section is 238.3 mb[7]. The half-life of the isomer is 42.6 minutes[2]. It means that the activity is easily produced by the irradiation with low level fast neutron flux. We have used the reaction in the experiment at the critical assembly of the Japan Materials Testing Reactor. As the threshold energy of the reaction is as low as that of the ^{115}In(n,n')^{115m}In reaction. Therefore, the ^{199}Hg(n,n')^{199m}Hg, ^{115}In(n,n')^{115m}In, ^{103}Rh(n,n')^{103m}Rh reactions should be useful threshold detectors for the neutron dosimetry with low level fast neutron flux.

References

1) W. Seelmann-Eggebert, G. Pfennig and H. Münzel, Nuklidkarte, (1974).
2) C. Michael Lederer and Virginia S. Shirley, Table of Isotopes (Seventh Edition), John Wiley and Son, Inc. (1978).
3) M.F. Vlasov, et al., "Review of Differential Neutron Data for Important Reactions not yet included in ENDF/B-V Dosimetry File", NUREG/CP-0004, II (1977) 855.
4) C.P. Swann and F.R. Metzger, "Production of ^{89m}Y, ^{137m}Ba and ^{199m}Hg by Inelastic Neutron Scattering", Phys. Rev., 100, 5 (1955) 1329.
5) P. Bornemisza, J. Károlyi and G. Peto, "Measurements on the Excitation Cross Section of Isomeric States by Scattering of 2.8 MeV Neutrons", Atomiki Kozlemenyek, 10 (1968) 112.
6) A.K. Hankla, R.W. Fink and J.H. Hamilton, "Neutron Activation Cross Sections at 14.4 MeV for Some Naturally Occurring Heavy Elements in the Region 76≤Z≤82", Nucl. Phys., A180 (1972) 157.
7) K. Sakurai, et al., "Cross Section Measurement for the ^{199}Hg(n,n') ^{199m}Hg Reaction from 0.78 to 6.3 MeV", J. Nucl. Sci. and Technol. (to be published).

8) A. Sekiguchi, et al., "Several Dosimetry Studies in the Fast Neutron Source Reactor YAYOI", NUREG/CP-0004, II (1977) 1223.

9) M. Nakazawa, et al., "The YAYOI Blind Intercomparison on Multiple-Foil Reaction Rate Measurements", UTNL-R-0099 (1981).

10) W.N. McElroy, et al., "A Computer-Automated Iterative Method for Neutron Flux Spectra Determination by Foil Activation", I and II, AFWL-TR-67-41 (1967).

11) D.E. Gullen, "Summary of ORR and YAYOI data for the REAL-80 Project Distributed 6 Feb. 1981", IAEA-NDS-33 (1981).

12) W.W. Engle, "A User's Manual for ANISN", K-1693 (1967).

13) J.C. Roy and J.J. Hawton, "Table of Estimated Cross Sections for (n,p), (n,α) and (n,2n) Reactions in a Fission Neutron Spectrum", CRC-1003 (1960).
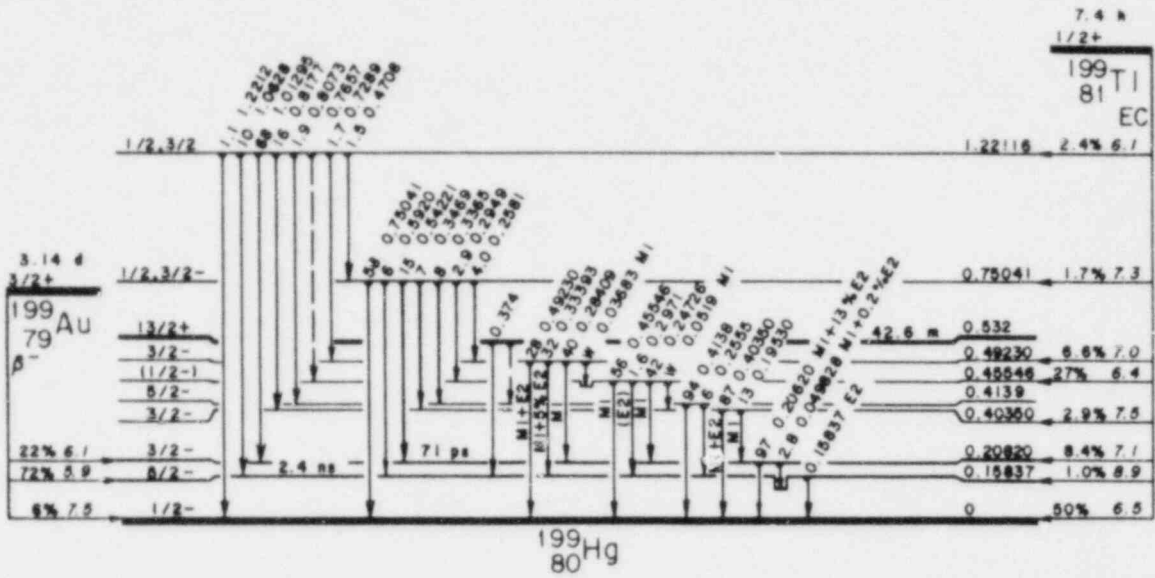
Fig. 1 Excited state of ^{199}Hg[2]
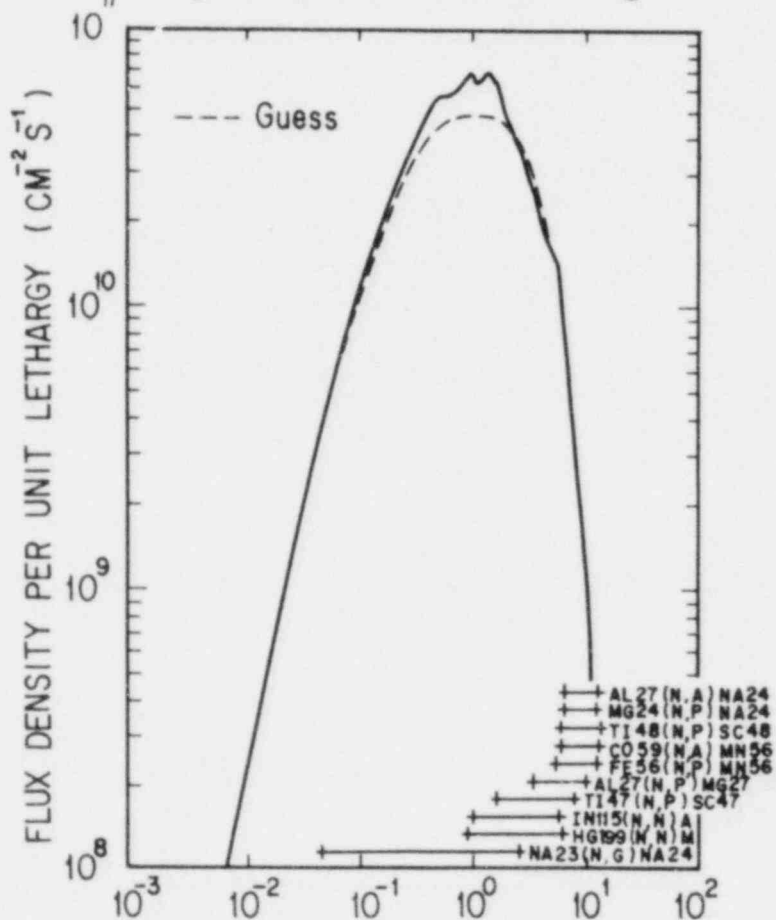
Fig. 2 Unfolded neutron spectrum of YAYOI glory-hole

Table 1 Experimental reaction rate[9] and neutron cross sections

Reaction	YAYOI glory-hole reaction rate(dps/atom)		Neutron cross section for unfolding
	Sakurai's data set[9]	Tokyo Univ. dosimetry group[9]	
$^{119}Hg(n,n')^{119m}Hg$	2.89-14[+] (±4%)	——	Ref. 7)
$^{59}Co(n,\alpha)^{56}Mn$	——	1.47-17 (±2.4%)	ENDF/B-V
$^{56}Fe(n,p)^{56}Mn$	——	1.00-16 (±2.8%)	"
$^{27}Al(n,p)^{27}Mg$	——	3.87-16 (±8.4%)	"
$^{27}Al(n,\alpha)^{24}Na$	6.91-17 (±3%)	6.74-17 (±2.9%)	"
$^{24}Mg(n,p)^{24}Na$	1.40-10 (±3%)	1.47-16 (±3.1%)	"
$^{23}Na(n,\gamma)^{24}Na$	——	7.85-17 (±4.1%)	"
$^{47}Ti(n,p)^{47}Sc$	——	1.68-15 (±11.5%)	"
$^{48}Ti(n,p)^{48}Sc$	——	2.57-17 (±3.8%)	"
$^{115}In(n,n')^{115m}In$	2.14-14 (±3%)	2.12-14 (±3.9%)	"

+ 2.89-14 means 2.89×10^{-14}.

Table 2 M/C ratios after the zeroth and the fuel
iterations in SAND II analyses

Reaction	Reaction rate M/C	
	Guess spectrum	10 iteration spectrum
$^{59}Co(n,\alpha)^{56}Mn$	0.9582	1.0264
$^{56}Fe(n,p)^{56}Mn$	1.0144	1.0498
$^{27}Al(n,p)^{27}Mg$	1.0497	1.0750
$^{27}Al(n,\alpha)^{24}Na$	0.8895	0.9690
$^{24}Mg(n,p)^{24}Na$	0.9139	0.9850
$^{47}Ti(n,p)^{47}Sc$	0.8491	0.8721
$^{48}Ti(n,p)^{48}Sc$	0.8819	0.9463
$^{115}In(n,n')^{115m}In$	1.2210	1.1380
$^{23}Na(n,\gamma)^{24}Na$	1.2070	0.9941
$^{199}Hg(n,n')^{199m}Hg$	1.0164	0.9466

MULTICOMPONENT WIRE ACTIVATION DETECTOR SYSTEM
FOR NEUTRON SPECTROMETRY ON POWER REACTORS

H.-C. Mehner, I. Dennstädt, U. Hagemann. S. Nagel,
and M. Schöne
   Zentralinstitut für Kernforschung Rossendorf,
   German Democratic Republic

ABSTRACT

A measuring system based on a multicomponent
wire activation detector is presented, which is
applied for neutron spectrometry inside PWR.
The detector consists of the basic material nickel
alloyed with gold, manganese and tungsten. The
masses of the components are in such proportions
that the neutron spectrum in the thermal, epi-
thermal, and fast energy regions is determined by
one gamma-ray spectrum measurement. Preliminary
results are given from experiments in dry channels
of the WWER-440 reactor at the Greifswald NPS.

INTRODUCTION

Knowledge of the neutron spectrum in a nuclear reactor
is steadily gaining greater importance from the point of
view of reactor physics calculation and safety predictions.
Nowadays it is generally accepted that sophisticated
neutron spectrum measurements inside power reactors can
increase the economic rates of reactors and the relia-
bility of reactor material components. An accurate deter-

mination of spectral parameters of the neutron flux makes
it possible to enlarge the accuracy of fixed installed
incore detectors for power distribution measurements and
to improve radiation damage estimates.

Up to now, incore measurements of the neutron field in
power reactors have mainly been carried out with the
multiple foil activation method. The axial interpolation
across the core was performed with activation wires. In
order to make these measurements simpler and faster a new
system was developed by combining the multiple foil tech-
nique with the activation wire method.

On the basis of a multicomponent wire activation detec-
tor (MWAD) a travelling incore system consisting of the
MWAD, the mechanical measuring equipment, the control unit,
a Ge(Li) detector, a multichannel analyzer, and a mini-
computer was designed to measure the axial neutron flux
density as well as its spectral distribution in WWER-440
type pressurized water reactors.

MULTICOMPONENT WIRE ACTIVATION DETECTOR

First of all a multicomponent wire activation detector
was designed for determining the neutron spectrum in diffe-
rent energy regions with a single gamma-ray spectrum mea-
surement.[1] The MWAD is made as a metallic alloy in wire
form. In the course of our investigations Aarnio[2] proposed
to combine several activation detector materials in quartz
glass, but this arrangement has technical imperfections
similar to those of the multiple foil method.

The choice of an appropriate MWAD for incore measurements
is closely connected with the PWR conditions and the con-
struction of the measuring device. Materials in the MWAD
should meet the known demands on usual foils such as res-

ponse to different neutron energies and special criteria like the following ones: (i) Detector materials should be homogeneously alloyable to a wire, (ii) the alloyed wire has to be resistant   corrosion and temperatures up to 700 K, (iii) reaction products should have simple decay schemes and small half-lives (reuse).

Taking these requirements into account a multicomponent detector with the basic material nickel alloyed with gold, manganese and tungsten has been developed (Table 1).

Table 1. Composition of the MWAD

Element	Mass fraction (%)
Gold	0.284 ± 0.005
Manganese	1.16 ± 0.14
Nickel	95.87 ± 0.72
Tungsten	2.67 ± 0.10

As basic material nickel was preferred for metallurgical and neutron physical reasons. Manganese is mainly responsible for thermal neutrons while gold and tungsten are also responsible for epithermal neutrons. The fast neutron density is determined by the reaction ^{58}Ni(n,p) ^{58}Co.

Fig. 1 shows the response curve $R_{gi} = I_i \sigma_{gi} \phi_g$ of the single materials contained in the MWAD together with the total response curve $R_g = \sum_i I_i \sigma_{gi} \phi_g$ for a typical WWER-440 neutron spectrum, where I_i represents the mass
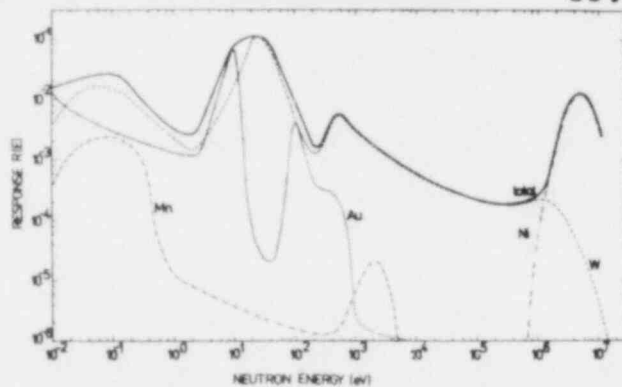
Fig.1: Response curve of the MWAD for a WWER-440 neutron spectrum

fraction of the element i in the MWAD, σ_{gi} the group cross section and ϕ_g the group flux (normalized to $\sum_g \phi_g = 1$). The response region of the MWAD covers the whole energy region without the region from 10^4 to 10^6 eV. The half-lives of the avtivated nuclides are smaller than 3 days with the

exception of ^{58}Co so that a residual activation has to be taken into account in the case of ^{58}Co, only.

The mass composition of the MWAD has been chosen in order that (i) the activities of the different nuclides can be measured with approximately the same accuracy if the irradiation time is some minutes and the cooling time is some hours, and (ii) the self-shielding corrections for epithermal neutrons in the main resonances is smaller than 10 %.

MEASURING EQUIPMENT ON THE PWR

The measuring system consists of the MWAD, the mechanical apparatus, the control unit, the Ge(Li) detector coupled with a multichannel analyzer and a minicomputer. The wire driving mechanism, the position indicator, the Ge(Li) detector, and the collimator are installed in a box on the top of the reactor shielding (Fig. 2).

The collimator has an an aperture of 10 x 10 mm and a length of 380 mm. The gamma-rays are registrated by means of a well shielded Ge(Li) detector connected with the box of the mechanical apparatus. For an absolute calibration of the system a ^{137}Cs source is used, which also gives a reference line in every gamma-ray spectrum.

Usually the wire is rolled on a drum. For

1. reactor shielding
2. pressure vessel
3. core
4. mechanical measurement equipment
5. Ge(Li)-detector with Dewar vessel
6. control unit, multichannel analyzer, minicomputer and data output
7. dry tube

Fig.2: General scheme of the experimental setup.

measurements the wire with a length of 22m and a diameter
of 0.9 mm is driven into the core within a small tube in-
stalled in a dry channel of the reactor. After irradiation
and the cooling time the activated part of the wire of
2.5 m length is moved continuously or step by step in front
of the collimator.

The control unit consists of the components position
indication and evaluation, processor, and drive controller.
The conversion of the distance covered by the wire into
digital signals is performed by an angle measuring system,
which gives $2 \cdot 10^6$ information per 1000 rotations and
provides a position accuracy < 1 cm. In addition, a photo-
electric relay is installed in the middle of the colli-
mator to indicate the wire end and to adjust the position
indication. The processor controls the irradiation and
measurement cycles. The multichannel analyzer NTA- 1024
is connected with the minicomputer EMG- 666/B to analyze
the gamma-ray spectra and to calculate the reaction rates.

EXPERIMENTAL RESULTS

The measuring system was tested on the Rossendorf Re-
search Reactor in order to determine axial neutron flux
profiles in irradiation channels. Some probes of the MWAD
of 10 mm length were also irradiated in dry channels of
the third and fourth units of the Greifswald NPS[1] to check
the applicability of the material combination chosen for
measurements of neutron spectra. The gamma-ray spectrum
(Fig. 3) shows well-isolated single peaks at 412 keV(^{198}Au),
480 keV (^{187}W), 811 keV (^{58}Co), and 847 keV (^{56}Mn). Due
to the several well-known gamma-ray transitions the nuclide
^{187}W is appropriate for the determination of the relative
efficiency of the Ge(Li) detector from the measured gamma-
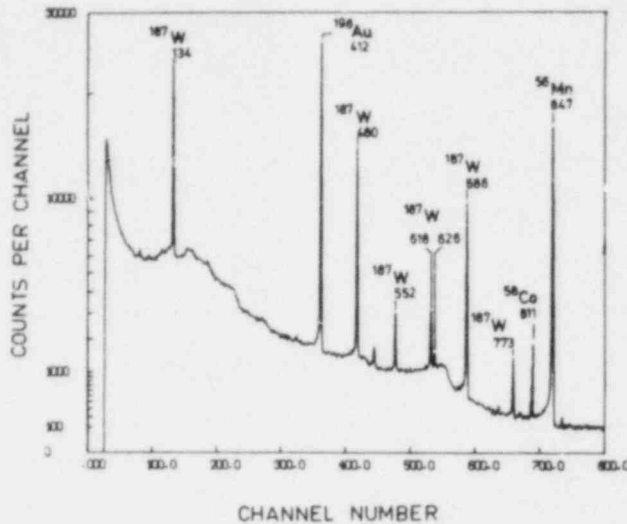
Fig. 3: Gamma-ray spectrum of the MWAD (irradiation time 4 min, cooling time 11 h, counting time 2000 s).
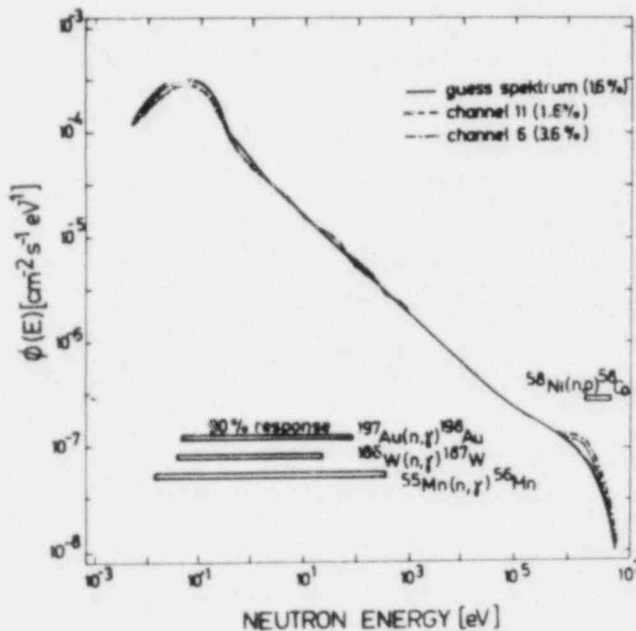
Fig. 4: Neutron spectra in a WWER-440 reactor of the Greifswald NPS for different enriched fuel assemblies.

ray spectrum. The peak areas can be calculated with standard summing procedures on the mini-computer.

By using the decay data[3] the reaction rates of the irradiated probes were calculated to feed the unfolding code SAND-II.[x] The guess spectrum was taken from a 34 group reactor physics programme. The unfolded neutron spectrum shown in Fig. 4 is a typical one for a PWR. In energy regions covered by the detector materials the unfolded spectrum differs from the guess spectrum. Comparing the neutron spectra for the reactor channel with 1.6 % enriched fuel assembly it can be concluded that the guess spectrum seems to be too soft. As expected the unfolded neutron spectrum is harder in a fuel assembly with 3.6 % enrichment compared to one for 1.6 %. The mean square deviation between the measured reaction rates and the re-

x) The unfolding of the neutron spectra was kindly carried out by B. Osmera, UJV Rez, Czechoslovakia.

action rate reproduced by the SAND-II code is 6.8 % for
channel 11 and 4.8 % for channel 6.

Furthermore, an intercomparison with commonly used acti-
vation detectors was carried out by irradiations in two
different neutron spectra[4]. Through such an intercompari-
son and unfolding the neutron spectra with the RFSP code
the MWAD was verified as a useful tool for incore neutron
spectrometry in the whole energy region.

REFERENCES

1. I. Dennstädt and H. -C. Mehner, Messung der Neutronen-
flußdichte mit einer Mehrkomponentensonde an Leistungs-
reaktoren des KKW "Bruno Leuschner" Greifswald, German
Report ZfK-449 (July, 1981).

2. P. Aarnio, M. Koskelo, P. Lund, K. Maunula, J. Routti,
J. Sandberg and H. Takala, Multicomponent Activation
Detectors: I. Design, Optimization and Fabrication,
Finnish Report TKK-F-A435 (December, 1980).

3. W. L. Zijp and H. J. Baar, Nuclear Data Guide for Re-
actor Neutron Metrology, Part I: Activation Reactions,
Netherlands Report ECN-70 (August, 1979).

4. I. Dennstädt, H.-C. Mehner, J. Vegh, and I. Vidovszky,
Intercomparison of two neutron spectrometric activation
measurement techniques, German Report ZfK-450 (August,
1981).

SILICON P.I.N. DIODE NEUTRON DAMAGE MONITORS

S. De Leeuw, R. Menil
SCK/CEN, Boeretang 200, B-2400 Mol, Belgium

INTRODUCTION

In a previous paper [1] the use of silicon P.I.N. diodes as
fast neutron damage monitors was described. While these diodes
were successfully used for several years as personnel dosimeters
[2, 3, 4, 5] the accuracies achieved (10 - 15 %) were insufficient
for reactor physics purposes. By careful selection this range
could be reduced to 8 - 10 % and it was suggested [1] that indivi-
dual calibration could still improve this. The idea proved false
because re-irradiation followed by pre-read anneal changes the
characteristics. However, a considerable improvement in accuracy
to 5 % or better has been obtained by :

- combination of forward voltage and recovery time measurement in
  the fluence range where ΔV_f and $\Delta 1/T_r$ are linearly related

- selection of diodes with matched pre-irradiation values of for-
  ward voltage and recovery time

- improved control of the characteristics by the manufacturer
  (types 5430-C)

- reduced Joule heating by the recovery time monitor.

The effect of high temperature anneal (280°C), in view of reusing
the diodes, is also investigated. Besides the fact that the epoxy
coating does not withstand temperatures above 250°C, the results
indicate that the un-annealed fraction perfectly memorizes the ir-
radiation history. The effect is not too pronounced for diodes
that were irradiated at moderate fluences ($\leq 5 \cdot 10^{10}$nvt) but even
in that case the quoted accuracy cannot be maintained for re-
irradiated diodes.

MEASUREMENT METHODS AND IRRADIATION FACILITIES

- The principles of operation have been discussed elsewhere [1, 2,
  3, 4]. The diode readers used are a STUDSVIK 3809 A model for
  forward voltage monitoring used with 25 mA - 10 ms pulses for all
  measurements and a recovery time monitor of own design using a
  100 mA forward current pulse and a steady 10 mA reverse current.

An important difference with the reader previously used [1] is the reduction of pulse duration from 10 ms to 1.5 ms in order to minimize Joule heating.

The irradiation facilities used for calibration, pre-read anneal and high temperature anneal are the fission spectrum facility [6] installed in the vertical thermal column of the BR1 reactor and the MOL-$\Sigma\Sigma$ benchmark spectrum [7]. The diodes were applied for monitoring fast neutron damage in conjunction with other techniques in the PCA-PWR Pressure Vessel Mock-up (configuration 8/7 and 4/12) [10].

PRE-IRRADIATION DIODE CHARACTERISTICS

All data quoted are relative to STUDSVIK type 5430 diodes of which three different batches were used. These diodes have a nearly cube structure (1.2 mm side) and a wide base of high resistivity material (about 4.5 diffusion lengths as deduced from the pre-irradiation values of the recovery time using a high level diffusion constant of 22 cm^2/sec). In figure 1 the pre-irradiation values of recovery time T_{r_0} versus forward voltage V_{f_0} have been plotted for two representative batches (labelled C and D). Within a given batch the variations about the nominal values of forward voltage and recovery time are within $\pm$ 1 % and $\pm$ 2 % respectively, not exceeding twice these values from batch to batch. The figure further reveals that despite the high degree of control a strong correlation exists between both parameters. This behaviour is expected for diodes with a well controlled base width : the variations are directly related to the diffusion length, the more, if to improve uniformity, the diode chips have been pre-irradiated at a low dose - not necessarily neutrons - and high temperature annealed.

Hence, it is important to select the diodes for matched values of "both" forward voltage and recovery time to ensure identical behaviour under neutron irradiation.

EFFECT OF FAST NEUTRON IRRADIATION ON THE CHARACTERISTICS

The forward voltage for high injection current is a complex function of base width (W) and diffusion length (L) [8, 9], while the relation between fast neutron fluence φ and high level injected carrier life-time - hence recovery time - is well known to be :

$$\frac{1}{T_r} - \frac{1}{T_{r_0}} = K \varphi$$

at fluences below 10^{14} nvt.

For "wide" base diodes i.e. when the base is at least a couple of diffusion lengths wide ($w = W/L \geq 2$) the behaviour is much easier to understand : when the forward voltage exceeds the diffusion threshold i.e. :

$$V_f \geq V_1 \sim 2 \ U_T \left(e^{w/2} + \frac{w}{2} \right)$$

and $w < 3$, the diffusion currents penetrating the base will be sufficient to sustain the injected current flow and $V_W \approx V_1$. The voltage drop over the highly doped injecting junctions will remain important in this region. With decreasing diffusion length a field will develop over the middle section of the base to sustain the current. The field and carrier densities will not vary much for moderate base widths ($w \lesssim 12$) and a voltage

$$V_W' \approx U_T \frac{(W - 2 \alpha L)^2}{L^2} \left(\frac{I}{I_o} \right)^n \quad \text{with } \alpha \approx 1 \quad n = 0 \text{ to } 0.5$$

will develop over this part of the base and add up to the diffusion current term. At some point where L has sufficiently decreased and when

$$V_f - V_W' < V_1$$

this term will dominate. Hence for $5 \lesssim w \lesssim 12$ we expect to find a region where

$$V_f T_r \sim V_f L^2 = c^t \ .$$

In figure 2 the variation of $V_f T_r / V_{f_o} T_{r_o}$ versus T_r / T_{r_o} has been drawn for type 5430-B diodes irradiated from about 5 10^{10} up to 2 10^{12} nvt. The behaviour is exactly as predicted and for about halve a decade in fluence starting at $\sim 2 \ 10^{11}$ nvt this ratio increases with decreasing T_r / T_{r_o} varying by not more than 10 %. In this part of the characteristic ΔV_f and $\Delta 1/T_r = K \varphi$ are linearly related and both types of measurements can be simply combined for improved accuracy. The dependence on initial values evidences the importance of matching "both" parameters. Figure 3 displays the dependence of ΔV_f on $\Delta 1/T_r$ for the 5430-C diodes.

READ OUT TEMPERATURE SENSITIVITY AND FADING

- The forward voltage sensitivity to temperature is given by STUDSVIK as :

$$\frac{V_f}{V_{f\ 22.5}} \simeq \frac{1 - 8.82 \ 10^{-3} \times (\theta°C - 22.5) \times V_{f\ 22.5}^{-1}}{1 - 0.0063 \ (\theta°C - 22.5)}$$

and is <u>dose dependent</u>

The sensitivity of the recovery time to temperature is found to be <u>dose independent</u> and is given by :

$$\frac{T_r}{T_{r\,22.5}} \simeq 1 + 0.005 \times (\theta°C - 22.5) \quad \text{below } 60°C$$

With these low sensitivities of about 0.5 % per degree centigrade Joule heating of the diodes is likely to be the most important cause of error due to temperature. It is minimized by pulsed operation of the readers.

- Room temperature anneal or fading is the main source of errors. Typical curves are given for $\Delta\,1/T_r$ and $\Delta\,V_f$ (fig. 4). Fading curves cannot be relied upon :

  * because of ambiguities about the fraction annealed during ir- radiation

  * despite all precautions internal Joule heating can never be completely avoided, especially at higher fluences ($V_f \geq 5$ V) : an unknown fraction, depending on the fluence integrated, is annealed.

To avoid errors introduced by fading the unstable signal com ponent should be removed !

PRE-READ ANNEAL

- Pre-read anneal for 2 minutes at 100°C (recommended by STUDSVIK). While this procedure seems adequate for recovery time and indeed removes most of the unstable component in $\Delta\,V_f$ shortly after ap- plication of the procedure, a steady increase in $\Delta\,V_f$ has been observed during the hours following the anneal : up to 7 % after 9 days. Hence, this procedure is inadequate.

- Pre-read anneal for 48 hours at 45°C (fig. 5.a). Repeated measurements have shown that this procedure effectively removes the fading effect : $\Delta\,1/T_r$ remains stable, $\Delta\,V_f$ still fades but this is unpercep- tible for all practical purposes : < 10 % 2 years ! after anneal.

Re-irradiation for calibration purposes followed by a second pre-read anneal (fig. 5.b)

  * recovery time : the fluences cumulate within the obtainable accuracy, linearity is conserved.
    This can avoid the need to rely upon the cali- bration characteristics of the whole batch.

* forward voltage : no real advantage :

> * an accurate calibration curve is always
> needed
>
> * ΔV_f versus cumulated fluence did not com-
> pletely match the original calibration
> curve (up to 10 % difference).

HIGH TEMPERATURE ANNEAL

The epoxy coating of the diodes used does not resist to tem-
peratures of 250°C and above excluding reuse of coated diodes for
mechanical reasons.

Annealing for 1 H at 280°C reveals the following :

- A non-negligible fraction ($\sim$ 20 % - 30 %) of the response remains
having a perfect memory of the previous irradiation history
(fig. 6.a).

- Re-irradiating the H.T. annealed diodes to a known fluence, ta-
king as initial values those obtained after the anneal, can
lead to the false believe that reuse is possible (fig. 6.b)

  * before pre-read anneal the values seem to cluster although with
  considerable spread

  * however : the situation deteriorates the more the higher the
  fluence previously received. After pre-read anneal no impro-
  vement is observed indicating that the effect does not stem
  from the unstable component

  * referring forward voltage and recovery time to the original
  pre-irradiation values reveals the influence of the previous
  irradiations.

Conclusion : reuse of the diodes after H.T. anneal is unpossible,
not only for mechanical reasons but because of the
un-annealed remaining fraction contaminating the
measurement memorizes the previous irradiation his-
tory.

ACCURACY OBTAINABLE AND TYPICAL RESULTS

- The precision of the readers is ΔV_f : $\pm$ 1 mV ; $\Delta 1/T_r$: $\pm$ 50 ns
the latter is affected by the shape of the pulse and can rise to
$\pm$ 200 ns if the pulse has no sharp edge (about 10 % of the
diodes tested).

- The influence of temperature is less than 2 % as fading is eliminated by pre-read anneal and elevation of the junction temperature is minimized by pulsed operation.

- Statistical errors are : $\pm$ 1 % (1 σ) on V_{f_o} , $\pm$ 2 % (1 σ) on T_{r_o} for the pre-irradiation values.
  After irradiation to a known fluence a spread of $\pm$ 2 % is still observed for matched diodes.

- The flux calibration error is estimated to be less than $\pm$ 2 % (1 σ).

- Over a restricted range of $\sim$ 2 10^{11} to 10^{12} nvt the combined error (1 σ) does not exceed $\pm$ 5 % .

Typical results obtained in PCA (Pool Critical Assembly) configurations 4/12 SSC [10] and 8/7 are given in tables I and II.

REFERENCES

[1] S. De Leeuw et al., "Reactor damage monitors and their application," Proc. of the 3th ASTM-EURATOM symposium on Reactor Dosimetry, Ispra (October 1-5, 1979).

[2] G. Kramer, "The semiconductor fast neutron-dosimeter its characteristics and applications," IEEE-NS, 104-118 (February, 1962).

[3] J.C. Lanore, "Etude de l'irradiation aux neutrons rapides du silicium au moyen de jonctions P.I.N.," CEA-R 3061.

[4] S. De Leeuw, Internal report N.B.C.-S.C.K./C.E.N. (1969).

[5] J.C. Bauduin, Internal report N.B.C.-S.C.K./C.E.N. (1976).

[6] A. Fabry, J.A. Grundl and C. Eisenhauer, "Fundamental integral cross section ratio measurements in the thermal-neutron-induced Uranium-235 fission neutron spectrum," Proc. Nuclear Cross Sections and Technology Conference, NBS Special Publication 425, Vol. I, 254 (1975).

[7] A. Fabry, G. De Leeuw and S. De Leeuw, "The secondary intermediate energy standard neutron field at the MOL-$\Sigma\Sigma$ facility," Nuclear Technology, Vol. 25, nr 2 (February, 1975).

[8] A. Rose, "Comparative anatomy of models for double injection of electrons and holes into solids," Journ. of Appl. Ph., Vol. 35, N9, 2664-2678 (September, 1964).

[9] J.M. Swartz and M.D. Thurston, "Analysis of the effect of fast neutron bombardement on the current-voltage characteristic of a conductivity-modulated P.I.N. diode," Journ. of Appl. Ph., Vol. 37, N2, 745-755 (February, 1966).

[10] LWR pressure vessel surveillance dosimetry improvement program : PCA experiments and blind test, NUREG/CR-1861, HEDL-TME 80-87/R5 (July, 1981).

Table 1. Results of P.I.N. irradiations in the PCA 4/12 SSC configuration

PCA 4/12 ($T_{irr.}$ = 40 min.)						
POSITION	POWER (KW)	Before indiv. calibr. $1000 \times \left(\Delta \frac{1}{T_r}\right)^{\mu s^{-1}}_{PCA}$	ΔV_f^V PCA	After indiv. calibr. : $\frac{(nvt)_{PCA}^{*}}{(nvt)_{cal}}$ From $\Delta \frac{1}{T_r}$	From ΔV_f	Theor/exp[+] (norm. at 1/4 T)
SSC	0.2	42.4	1.326	0.822	0.80	1.041
1/4 T	2.5	47.2	1.567	0.955	0.95	1
1/2 T	4	45.7	1.470	0.895	0.89	1.015
3/4 T	7.5	48.4	1.636	0.965	0.99	0.976

* $(nvt)_{cal}$ = 3.78 10^{11} n cm^{-2} . fission   [+] Damage functions : P.C. DULIEU, CEA-R 3228 (1967)

Table 2. Results of P.I.N. irradiations in the PCA 8/7 configuration

POSITION	POWER (KW)	IRR. TIME (Min.)	ΔV_f^V	$1000 \times \Delta \frac{1}{T_r}^{\mu s^{-1}}$	$(nvt)_{PCA}/(nvt)_x$ (x : 35' at 600 KW) From ΔV_f (linear dep.)	From $\Delta \frac{1}{T_r}$
TSF	0.1	40	1.725	47.30	1.17	1.17
PVF-TSB	1	46	1.704	45.01	1.16	1.116
1/4 T	2.5	41	1.550	44.72	1.091	1.107
1/2 T	4	40	1.485	42.06	1.061	1.042
3/4 T	7	40	1.4807	42.81	1.059	1.060
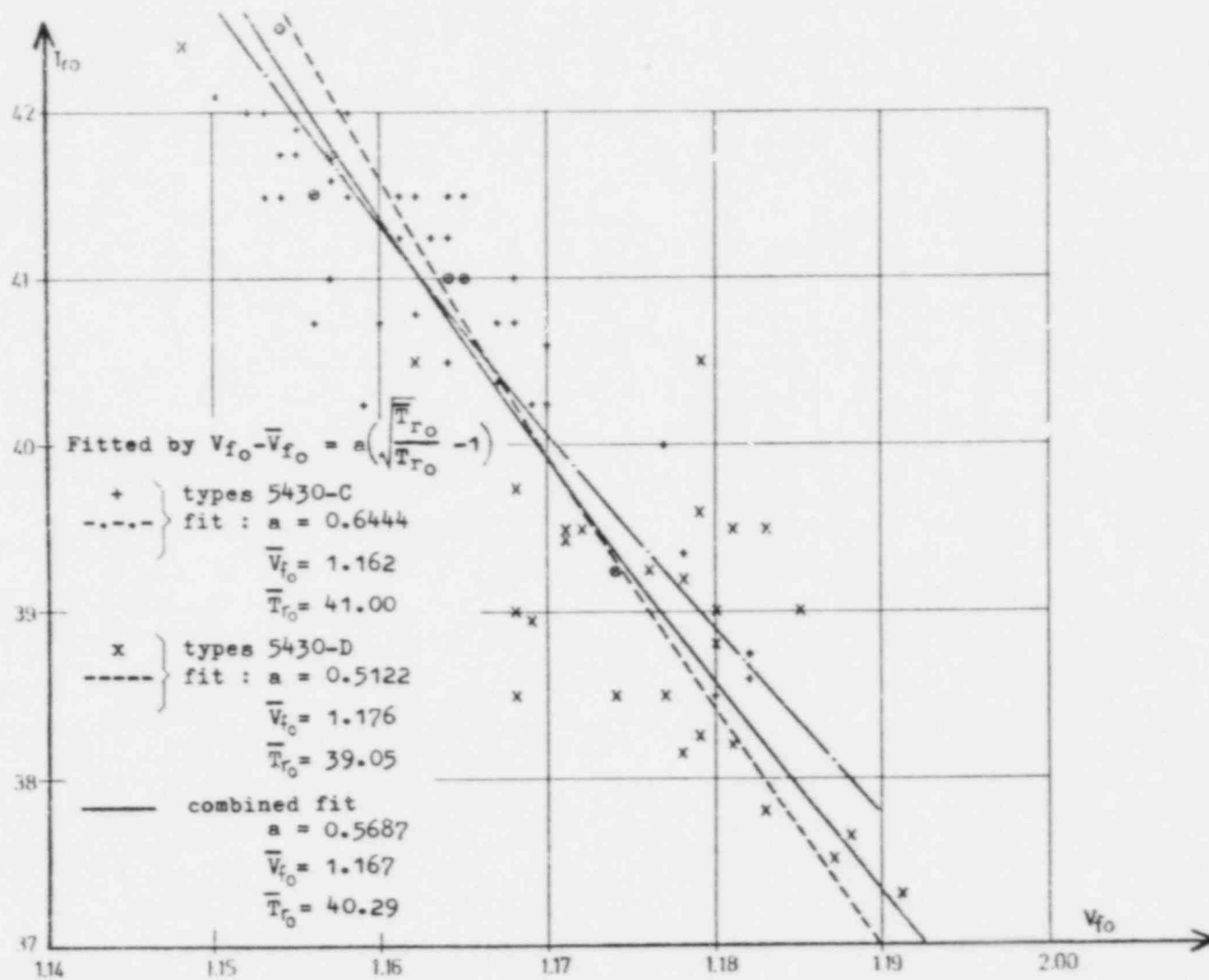
Fig. 1. Correlation between the pre-irradiation values of forward voltage V_{fo} and recovery time T_{ro}.

396
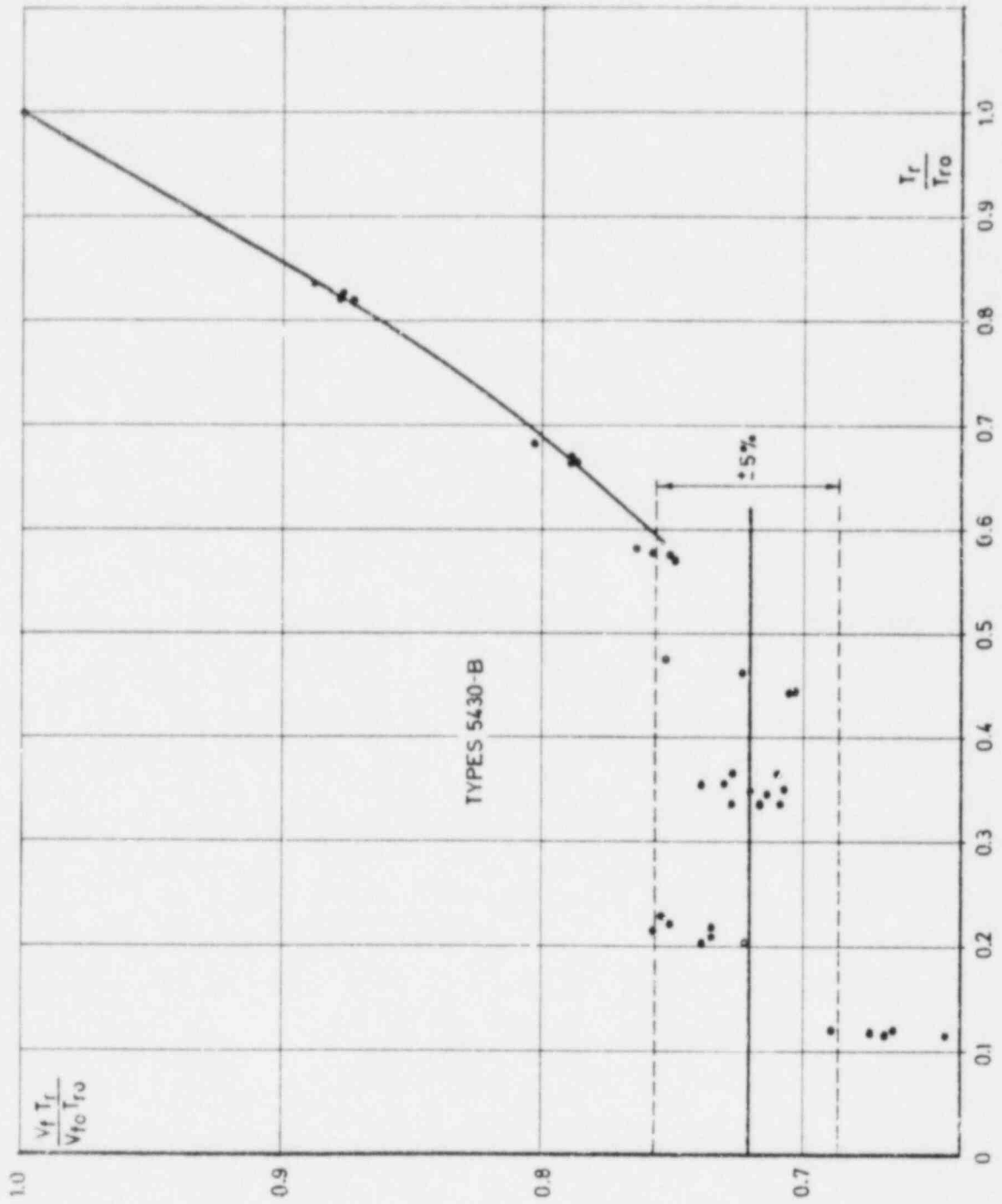
Fig. 2. Relation between forward voltage and recovery time after neutron irradiation.
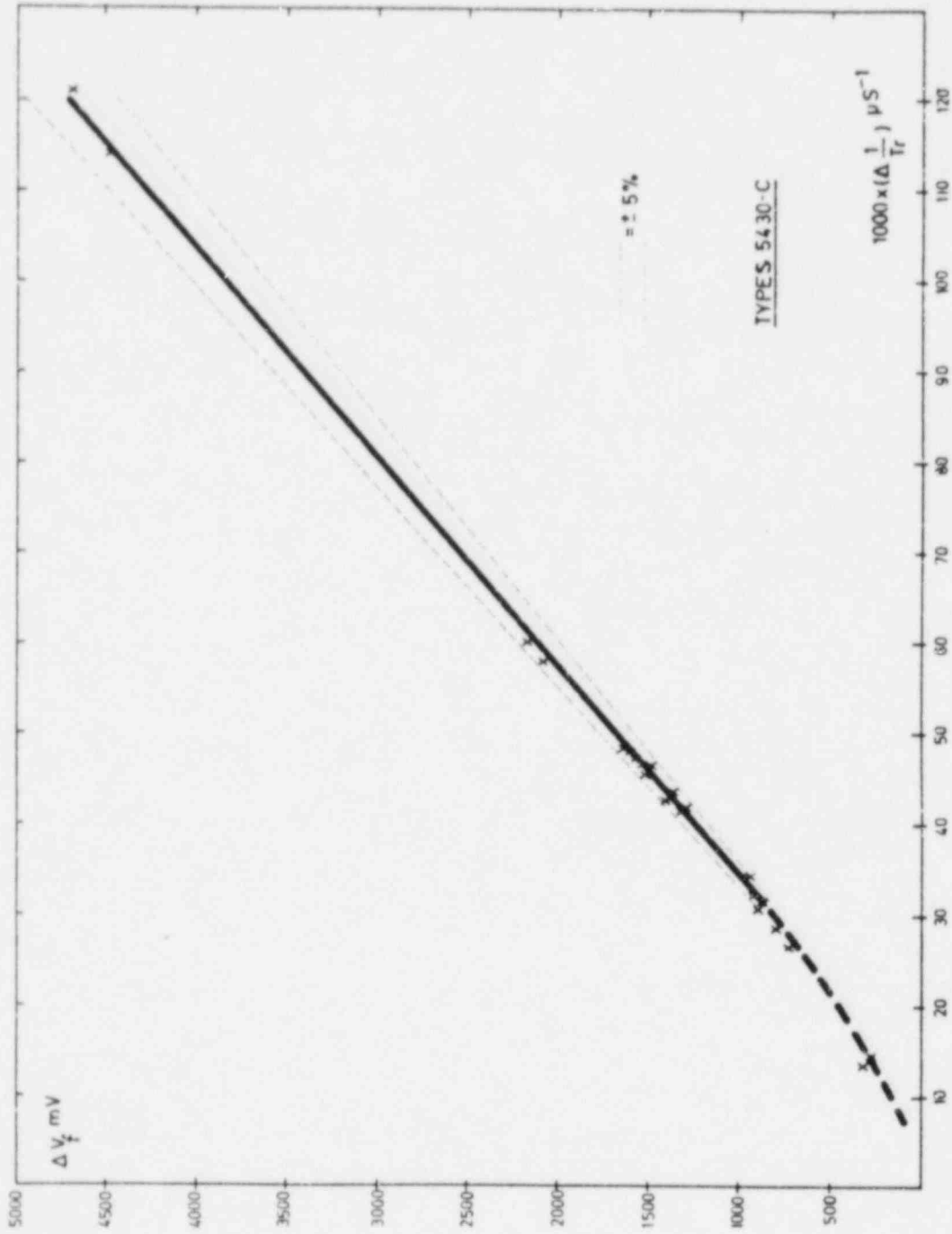
Fig. 3. Interdependence of ΔV_f and $\Delta \frac{1}{T_r}$ after neutron irradiation.
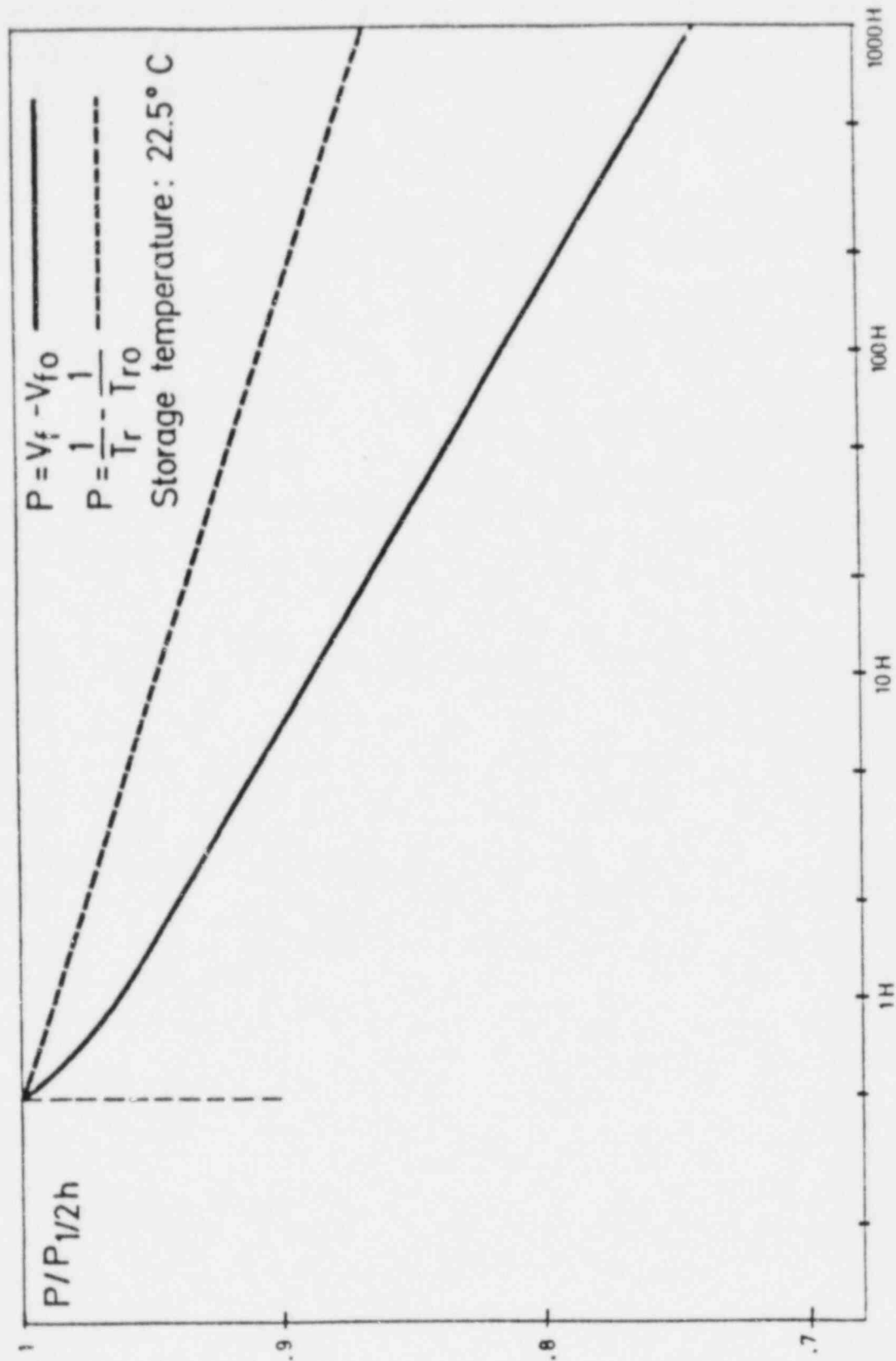
Fig. 4. Typical fading curves.

Diodes irradiated once and
pre-read annealed

Diodes reirradiated and
pre-read annealed

ΔV_f^v

$\Delta \frac{1}{T_r} \mu S^{-1}$

----- no pre-read anneal
(1/2 H after irr.)

―――― pre-read annealed
48 H @ 45°C

TYPES 5430-C

Min. @ 100 kW - fission sp.

ΔV_f^v

Parameters in function of
cumulated fluence

1 min @ 100 kW = 1.26 10^9 n.cm^{-2}

――― First irradiation

Min. @ 100 kW - fission sp.
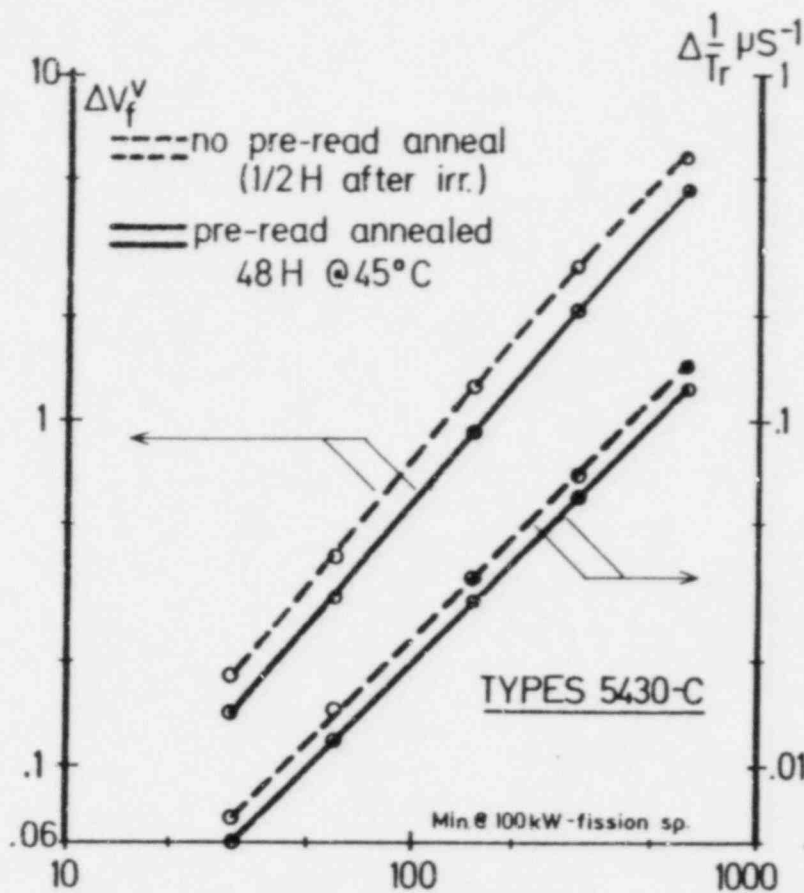
Fig. 5.a. Influence of pre-read anneal
for 48 h at 45°C.
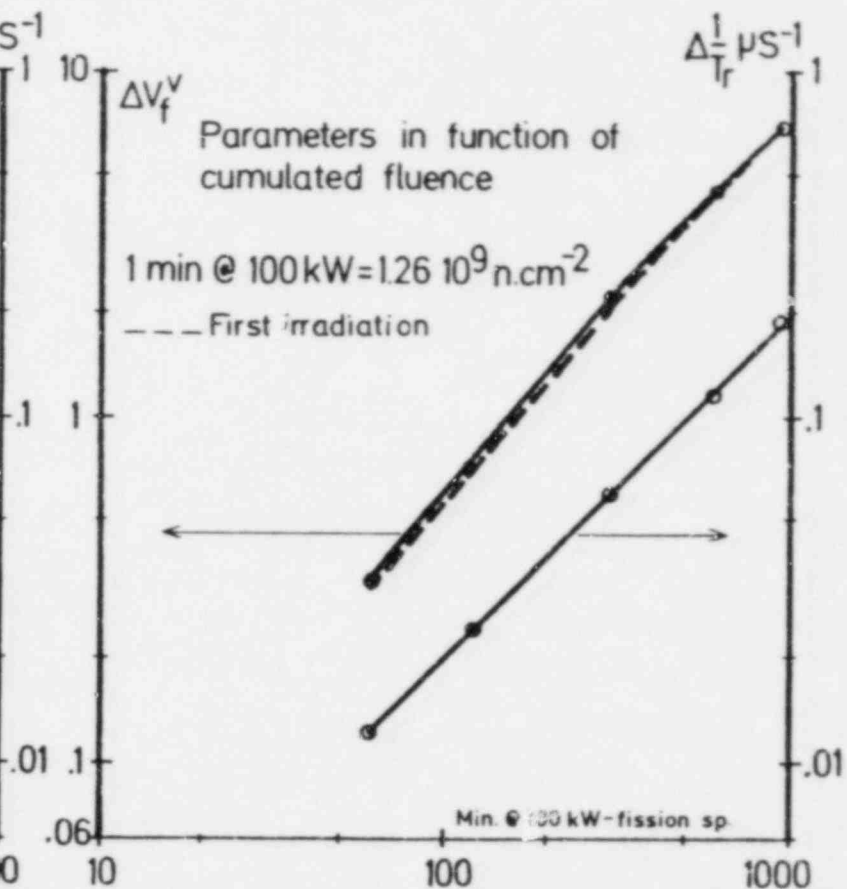
Fig. 5.b. Reirradiation followed by
second pre-read anneal.

399

Fig. 6.a. Response curves and memory after H.T. anneal.

Fig. 6.b. Response in function of previous history.

NIOBIUM DOSIMETRY INTERCOMPARISON IN EBR II AND BR2

H. Tourwé, SCK/CEN, Mol, Belgium
W.H. Taylor, AEE, Winfrith, United Kingdom
D. Reher, R. Vaninbrouckx, CBNM, Geel, Belgium
R. Lloret, CEN, Grenoble, France
H.J. Nolthenius, ECN, Petten, Netherlands
P. Wille, GKSS, Geesthacht, Germany
R. Schweighofer, KWU, Erlangen, Germany

INTRODUCTION

Niobium has been used more and more in recent years to perform fast neutron flux and fast neutron fluence measurements in LWR and fast reactors. The major advantages of this type of detector are its long half-life and its relative low threshold (< 1 MeV).

In order to evaluate the actual state-of-the-art of niobium dosimetry, an interlaboratory comparison was organized under the responsability of the SCK/CEN in EBR II. The EBR II niobium foils were supplemented by foils irradiated in the BR2 reactor at Mol, since some niobium material was damaged during the EBR II irradiation.

Reaction rate and/or activity measurements were performed by seven different laboratories :

- Atomic Energy Establishment, Winfrith, United Kingdom   (P1)

- Central Bureau for Nuclear Measurements, Geel, Belgium   (P2)

- Centre d'Etudes Nucléaires, Grenoble, France   (P3)

- Energieonderzoek Centrum, Petten, Nederland   (P4)

- GKSS Forschungszentrum, Geesthacht, Germany   (P5)

- Kraftwerk Union, Erlangen, Germany   (P6)

- Studiecentrum voor Kernenergie, Mol, Belgium   (P7)

The work of these laboratories is discussed in this document.

EXPERIMENT DESCRIPTION AND IRRADIATION CONDITIONS

The EBR II dosimeter rig was irradiated in row 2 for one reactor cycle from September 30, 1978 till November 13, 1978. The

niobium foils were stacked in stainless steel capsules with 25 μm thick Ti spacers between them. The niobium needles were mounted into holes drilled axially in small stainless steel cylinders. The dosimetry rig and dosimetry capsules were filled with helium gas. A more detailed experiment description is given in reference [1].

The BR2 niobium foils (thicknesses of 20 μm and less) were irradiated in a core position along the axis of a fuel element. The dosimeters were packed in aluminium boxes and separated by 40 μm thick aluminium spacers. The dosimeter rig was irradiated for one reactor cycle from October 31, 1978 till November 24, 1978.

The irradiated niobium material was sent to the different laboratories for counting in the summer 1979. All distributed EBR II niobium material contained a high Ta content (Kawecki : 586 ppm Ta), while the distributed BR2 foils contained different Ta impurities (Max Planck Institute : 4 ppm Ta; Highways : 209 ppm Ta; Goodfellow Metals : 510 ppm Ta).

BEHAVIOUR OF NIOBIUM IN EBR II

All niobium foils having a thickness equal or less than 20 μm were damaged during irradiation. Only some niobium powder could be recuperated. Activity measurements confirmed that this powder was composed for the largest part of niobium material. The Ti spacers were undamaged. A loss of weight of 4 % to 5 % was noted for 80 μm thick niobium foils. The weight of niobium wires remained unchanged. So there seems to be a correlation between the damage and the material thickness. There is no correlation with the impurities in the foils since all thin foils of different origin were damaged. The damage mechanism, that takes place under conditions of high neutron fluence (equivalent iron fission fluence in the range of $5.1 \cdot 10^{19} n \, cm^{-2}$ to $1.3 \cdot 10^{21} n \, cm^{-2}$) and under conditions of high temperature (400 °C to 500 °C), is not quite well understood. The observations in EBR II do not confirm the observations made by R. Lloret in RAPSODIE. Thin foils (20 μm) were irradiated in similar conditions in RAPSODIE and no loss of weight and no damage was noted when using helium or argon as a filling atmosphere.

WEIGHT VERIFICATION

The detectors were weighted by SCK/CEN prior to distribution. Five participants verified these weights. The results of this verification are shown in table 1. The maximum observed deviation

TABLE 1. WEIGHT VERIFICATION OF THE Nb DOSIMETERS

LOCATION/LEVEL (cm)	WEIGHT DIFFERENCE IN % $\frac{P7 - Pi}{P7} \times 100$																
	EBR II / -1.2	EBR II / -37.8	BR2 / -5	BR2 / -15	BR2 / +5	BR2 / -15	EBR II / -1.2	EBR II / -37.8	BR2 / +5	BR2 / -5	BR2 / -15	EBR II / 0	BR2 / +5	BR2 / -15	BR2 / +5	BR2 / -15	EBR II / 0
P1	0.0	+0.1	+1.5	+1.0													
P2					+0.1	+1.2	-0.2	+0.7									
P4									0.0	-0.5	+0.8						
P5												+1.2	-0.3	+0.4			
P6															-0.3	+0.3	+0.5

is 1.5 %. One can conclude that in general the weight accuracy (1σ) is about 0.6 %.

The participants P3 and P7 used the original SCK/CEN weights; P1, P2, P4 and P6 used the values determined in their own laboratory; P5 used average values. The results given in this report were not rescaled to the original SCK/CEN weights.

COUNTING TECHNIQUE

Most participants measured the Nb-93m activity with a Si(Li) detector, while P4 measured the Nb-93m activity with a hyperpure Ge low energy photon detector. P2 used besides two Si(Li) detectors also the liquid scintillation technique.

The area of the Nb K_α and Nb K_β peaks of Nb-93m were taken to calculate the absolute activities, except by P6 who used only the Nb K_α peak areas. The Nb K_α peak was also considered by P3 when comparing the activity of the Nb detectors with a Nb-93m fluence reference source. P2 stated that, when measuring the EBR II/-37.8 cm detector, the Nb K_α peak was distorted by the overlapping from W L(X) peaks, so that only the Nb K_β peak was used for the count rate determination.

SOURCE PREPARATION

The technique of dissolving the irradiated niobium material is most widely spread. The Nb is dissolved in HF and HNO_3. Part of the solution is evaporated on filter paper or equivalent material. A list with the characteristics of the deposits used by different participants in this intercomparison is shown in table 2. The pycnometer method is the most accurate technique to determine the niobium weight on the deposits. Moreover this method is less time consuming than the use of tracers (e.g. Nb-94) for mass determination. The niobium X-ray selfabsorption in these deposits is of the order of 0.1 % per 100 $\mu g/cm^2$ niobium material on the deposit, so that in some cases X-ray selfabsorption corrections may be required.

P3 and P4 applied a non-destructive technique by measuring directly the Nb-93m activity emitted by the detector. This method was also applied by P7 on some BR2 niobium foils (this is however not the P7 routinely used technique). This is the most simple technique but it can only be applied on thin niobium foils with a low Ta content.

Two containers per dosimeter were prepared by P2 for the liquid scintillation counting technique. One container was prepared with Lumagel and one with a scintillator based on dioxane.

TABLE 2. CHARACTERISTICS OF THE THIN SOURCE DEPOSITS

	SOURCE THICKNESS	NUMBER OF DEPOSITS PER DOSIMETER	BACKING	FRONT COVER	WEIGHT DETERMINATION	UNCERTAINTY ON DEPOSIT WEIGHT (2)
P1	MAX. 60 $\mu g\ cm^{-2}$	2	COPPER	ADHESIVE POLYETHYLENE FILM	PYCNOMETER METHOD (1)	0.5 %
P2		3	VYNS COATED GLASS DISCS		PYCNOMETER METHOD (1)	0.03 %
P5	MAX. 950 $\mu g\ cm^{-2}$	2 - 5	GLASS	PLASTIC FOIL	^{94}Nb ACTIVITY MEASUREMENT ON Ge(Li)	1.5 %
P6	MAX. 30 μg	12			PIPET	0.7 %
P7	MAX. 70 $\mu g\ cm^{-2}$	5 - 10	ALUMINIUM	PLASTIC	PYCNOMETER METHOD (1)	0.6 %

(1) PYCNOMETER METHOD : THE PYCNOMETER IS WEIGHTED ON A MICROBALANCE BEFORE AND AFTER THE DROPS HAVE BEEN EXPELLED

(2) THE LARGEST ENCOUNTERED UNCERTAINTY IS QUOTED

CALIBRATION

Different types of sources were used by the participants to calibrate the Si(Li) crystal. An overview is given in table 3. Deposits made of standard solutions have the advantage that the equipment can be calibrated in exactly the same geometrical conditions as these wherein the niobium deposits are measured. The use of "solid" sources in the form of radioactif material (evaporated solution or powder) sandwiched between polyethylene foils is less time consuming. However when the use of "solid" calibration sources is combined with measurements on thin Nb deposits corrections may be required for : the X-ray absorption in the polyethylene foils of the calibration source, the difference in diameter between the niobium deposits and the standard source when measurements are performed in a close-to-detector geometry, the Nb X-ray absorption in the niobium material on the deposit and the Nb X-ray absorption in the filter paper tissue or equivalent material. Corrections for the absorption of the Nb K(X) rays have to be applied when performing

TABLE 3. Si(Li) DETECTOR CALIBRATION

PARTICIPANT	ISOTOPE (1)	RADIATION ENERGY (EMISSION PROBABILITY IN %)	CALIBRATION UNCERTAINTY (1 σ)
P1	Am-241 (DE)	11.9(.86 ± .03); 13.9(13.2 ± .35); 17.8(19.25 ± .6); 20.8(4.85 ± .2); 26.35(2.4 ± .1)	3 %
	Cd-109 (DE)	22.1(84.4 ± 3.0); 25.0(17.8 ± .7)	
P2	Nb-93m (DE)	16.6 + 18.6 (not applicable)	1 %
P3	Nb-93m (P)	16.6 + 18.6(11.6)	
	Nb-93m (RF)	16.6 (not applicable)	
P4	Am-241 (P)	26.35(2.40 ± .05)	3 %
	Co-57 (P)	14.41(9.54 ± .13)	
P5	Nb-93m (DI)	16.6 + 18.6(12.0)	2 %
	Y-88 (DE)	14.14 + 15.86(61.6)	
P6	Sr-85(DE); Y-88(DE) Co-57(DE); Mo-99(DE) Rh-103m(DE)		5 %
P7	Am-241 (P)	13.76-13.94(13.2 ± .3); 15.9-18.6(19.2 ± .4) 20.1-22.2(4.9 ± .2); 26.35(2.40 ± .05)	5 %
	Co-57 (P)	14.42(9.54 ± .13)	

(1) DE = DEPOSITS; P = MATERIAL BETWEEN POLYETHYLENE FOILS; DI = DISCS;
RF = REFERENCE FLUENCE SOURCE

measurements directly on the Nb discs in case the Si(Li) is cali-
brated by means of thin standard sources or by means of standard
niobium discs with a different thickness. Such corrections were
applied by P3, P4 and in a few cases by P7. For a not too low
solid angle geometry the formula for radiation perpendicular to the
foil is a good approximation :

$$T = \frac{1 - e^{-\mu d}}{\mu d}$$

Here is μ the attenuation coefficient (P3 and P7 : 167.12 cm^{-1} for
Nb K$_\alpha$ and 119.98 cm^{-1} for Nb K$_\beta$ [2]; P4 : 155.54 cm^{-1} for Nb K(X))
and d the foil thickness.

P2 calibrated the Si(Li) detectors for the Nb-93m desintegra-
tion rate by means of deposits from Nb-93m solutions that were stan-
dardized with the liquid scintillation technique. This approach does
not imply the use of decay scheme parameters such as I_{KX} or $I_{K\beta}/I_{K\alpha}$
with the exception of the case of the EBR II dosimeter where only
the K$_\beta$ peak was measured.

A standard fluence source was used by P3 to determine the
fission equivalent fluence greater than 1 MeV. This standard disc
was irradiated in a fast neutron fluence, determined by means of
the Ni-58(n,p) reaction, in the core of a MTR type reactor. This
means that the activity of the standard fluence source corresponds
to a certified equivalent fission fluence > 1 MeV. In this way
the neutron fluence was determined by P3 without using the Nb K(X)
ray emission probability.

The values quoted by the participants for the uncertainty (1σ)
on the Si(Li) spectrometer calibration are mentioned in table 3.
The major contributions to the total uncertainty are in most cases
the uncertainties on the emission probabilities of the used iso-
topes.

FLUORESCENCE CORRECTIONS

Fluorescence corrections could be neglected for all types of
niobium foils when performing measurements on deposits. P1 made a
deposition of Mn-54 activity plus a typical amount (40 μg) of un-
irradiated Nb. Mn-54 was chosen to simulate the Nb-94 + Nb-95 +
Ta-182 activity since it has a 100 % β emission and the energy of
its γ rays is an approximate average of the Nb and Ta activities.
No fluorescence effect was observed. P5 verified the Ta-182
fluorescence by means of the following formula [3] :

$$\Delta I = 0.05 \times t \times \frac{A \ (Ta-182)}{A \ (Nb-93m)}$$

where ΔI is the ratio of the X ray fluorescence induced by Ta-182 and the X ray emission by Nb-93m, t the sample thickness in mg/cm^2, and A the corresponding activities. A value of 0.2 % was calculated in the worst case. P7 verified the Ta-182 fluorescence by means of the formula [4] :

$$\Delta I = 3 . 10^{-5} \times P \times \frac{\text{area W L}_{\beta}}{\text{area Nb K}_{\alpha}}$$

Here is P the weight of the deposit in μg; area W L_{β} and area Nb K_{α} are the areas of the W L_{β} peak and the Nb K_{α} peak measured with the Si(Li) detector. This is an empirical formula, that was developed for a given type of deposit ($\emptyset$ 13 mm) and a given type of Si(Li) detector (80 mm^2, 3 mm thick, 1 mil Be window). The Ta-182 fluorescence was less than 0.1 % in all cases.

Fluorescence corrections have to be applied when performing measurements directly on Nb foils. P3 corrected for Nb-94, Nb-95 and Ta-182 fluorescence by measuring their absolute activities. P4 calculated the ratio between the peak area of Ta-182 ($\sim$ 68 keV) and the peak area of Nb K_{α} . Both participants applied empirical proportionality factors. The largest applied correction was 2 % (all measured discs contained 209 ppm or less Ta).

DECAY SCHEME PARAMETERS OF Nb-93m

The decay scheme parameters that were used by the different participants are summarized in table 4.

TABLE 4. DECAY SCHEME PARAMETERS OF Nb-93m

PARTICIPANT	Nb-93m HALF-LIFE (YEAR)	Nb X-RAY EMISSION PROBABILITY	
P1	15.9 ± 0.6	K(X)	0.116 ± 0.004
P2	16.0 ± 0.5	K(X)	0.116 ± 0.004
		K_{β}/K_{α}	0.188 ± 0.002
P3	16.4 ± 0.4	K(X)	0.116 ± 0.004
P4	16.4 ± 0.4	K(X)	0.116 ± 0.004
P5	15.0	K(X)	0.12
P6	13.6 ± 0.3	K_{α}	$(0.116 \pm 0.004) \times (0.841 \pm 0.002)$
P7	16.4 ± 0.4	K(X)	0.116 ± 0.004

All results (activities, reaction rates) given in this document are rescaled using a half-life of 16.4 ± 0.4 year [5], a Nb K(X) emission probability of 0.116 ± 0.004 [5] and an emission probability ratio of Nb K_α to Nb K_β of 0.189 ± 0.003 [5]. This was done for reasons of comparison.

Nb-93m ACTIVITY

The absolute Nb-93m activities as measured by the different participants are summarized in table 5. The activities are expressed in Bq g^{-1} and are given at the end of the irradiation time. In table 6 all results within a laboratory are related to sample BR2/-15 since this sample was measured by all laboratories. Several systematic uncertainties and especially the most important one, that for the calibration of the counting device, are usually

TABLE 5. ^{93m}Nb ACTIVITIES (Bq g^{-1}, END OF IRRADIATION)

REACTOR	LEVEL (cm)	AEE Winfrith	CBNM Geel	CEN Grenoble	ECN Petten	GKSS Geesthacht	KWU Erlangen	SCK/CEN Mol
EBR II	0					2.92×10^9	3.26×10^9	2.89×10^9
EBR II	-1.2	2.89×10^9	3.01×10^9					2.88×10^9
EBR II	-37.8	2.48×10^8	2.67×10^8					2.57×10^8
BR2	+5		7.86×10^8	7.85×10^8	8.16×10^8	8.15×10^8	8.44×10^8	7.84×10^8
BR2	-5	7.77×10^8		7.99×10^8	8.21×10^8			7.90×10^8
BR2	-15	7.45×10^8	7.70×10^8	7.54×10^8	8.03×10^8	7.54×10^8	8.38×10^8	7.65×10^8

TABLE 6. "BEST" ACTIVITIES OF THE DIFFERENT EBR II AND BR2 SAMPLES

REACTOR	LEVEL (cm)	ACTIVITY RELATIVE TO THAT OF SAMPLE BR2/-15									ACTIVITY OF THE SAMPLES ON THE BASIS ACT. BR2/-15 = 7.76 10^8 Bq g^{-1}	OVERALL UNCER-TAINTY
		AEE Winfrith	CBNM Geel	CEN Grenoble	ECN Petten	GKSS Geesthacht	KWU Erlangen	SCK/CEN Mol	MEAN	UNCER-TAINTY (1)		
EBR II	0					3.87	3.89	3.78	3.85	0.9 %	2.99×10^9	1.8 %
EBR II	-1.2	3.88	3.91					3.76	3.85	1.2 %	2.99×10^9	2.0 %
EBR II	-37.8	0.333	0.347					0.336	0.339	1.3 %	2.63×10^8	2.1 %
BR2	+5		1.02	1.04	1.02	1.08	1.01	1.02	1.03	1.0 %	7.99×10^8	1.9 %
BR2	-5	1.04		1.06	1.02			1.03	1.04	0.8 %	8.07×10^8	1.8 %
BR2	-15	1.00	1.00	1.00	1.00	1.00	1.00	1.00	1.00		7.76×10^8	1.6 %

(1) UNCERTAINTY $= \sqrt{\dfrac{\Sigma (x_i - u)^2}{n(n-1)}}$

the same for all samples measured at one laboratory. Therefore, the ratios of the activities of the same samples measured at the various laboratories relative to the activity of sample BR2/-15 should be more or less independent from the laboratories involved, and a mean ratio can be deduced for each of the samples. The "best" activities of the different samples can be calculated by multiplying these mean ratios with the activity of the sample BR2/-15 (table 6). The overall uncertainties on these values are about 2 % . Fig. 1 shows the differences between the measured values per laboratory and per position and the "best" corresponding activities.

An overview of the different types of uncertainties that contribute to the total uncertainty, in case of the techniques using dissolved samples, is given in table 7. Error calculations are carried out in different ways by the participants. So an attempt was made in table 7 to find a consensus for reasons of comparison, that should be acceptable to each individual participant. Orders of magnitude for the different types of uncertainties are indicated as quoted by the participants. Uncertainties due to the Nb-93m half-life and the Nb-93m K(X) ray emission probability are not given since all results in table 5 were rescaled with the same $T_{1/2}$ and the same $I_{K(X)}$. The figures given in table 7 are in good agreement with the data in fig. 1.

From the intercomparison one can conclude that at present the specific Nb-93m activity in routine niobium dosimetry procedures can be determined with an accuracy of 4 % (using the Wagner method for error propagation). The most inaccurate parameters are the calibration of the counting equipment and the Nb K(X) ray emission probability. An error of 2.4 % on the Nb-93m half-life (16.4 ± 0.4) does not contribute significantly to the total uncertainty : a decay over a period of 5 year for example will only contribute for about 0.5 % .

Fig. 1. Comparison of the measured Nb-93m activities.

TABLE 7. UNCERTAINTIES IN % THAT CONTRIBUTE TO THE TOTAL UNCERTAINTY ON THE Nb-93m ACTIVITY

TYPE (1)	P1	P2	P5	P6	P7	ACHIEVABLE ACCURACIES AT PRESENT FOR Si(Li) MEASUREMENTS
WEIGHT OF THE DOSIMETER (R)		0.03	0.3	0.6	0.5	0.5
WEIGHT OF THE DEPOSIT (R)	0.5	0.03	1.5	0.7	0.6	0.6
STATISTICAL (R)	0.5	0.2	0.2	0.9	0.5	0.5
Nb X-RAY ABSORPTION IN DEPOSIT, FILTER PAPER, ... (S)	0.1	NEGL.	0.5		0.1	0.1
CALIBRATION OF COUNTING DEVICE (S)	3	1	2	5	5	3
GEOMETRY CORRECTION (S)		NEGL.			0.2	0.2
FLUORESCENCE (S)	NEGL.	NEGL.	0.2		0.1	0.1
[LIQUID SCINTILLATION (S)]		[1]				

(1) R : RANDOM   S : SYSTEMATIC

Nb-93(n,n') REACTION RATES

Nb-93(n,n') reaction rates were provided by P1, P3, P4, P6 and P7. The reaction rates of P1, P4, P6 and P7 were deduced from the measured Nb-93m activities (table 5). The observed differences between the Nb-93(n,n') reaction rates of P1, P4, P6 and P7 are within 0.8 % equal to the differences observed between the measured Nb-93m activities. So the calculation procedure to deduce reaction rates from the measured activities introduces only a small error ($1\sigma \approx 0.3$ %). For this reason and also because only 4 of the 7 participants calculated in this way the reaction rates, the Nb-93(n,n') reaction rates were deduced from all individual activities in table 5 with the SCK/CEN procedure in order to calculate the recommended values. The SCK/CEN procedure is using the following formulas :

EBR II $\sigma\phi = 3.673 \ 10^{-20}$ x activity (Bq g^{-1} at end of irradiation)

BR2 $\sigma\phi = 6.382 \ 10^{-20}$ x activity (Bq g^{-1} at end of irradiation)

P3 measured the equivalent fission fluence > 1 MeV using a Nb-93m reference fluence source. The corresponding P3 reaction rates, which are considered as a set independent data, are given in table 8. These values differ by about 3 % from the reaction rates deduced directly from the Nb-93m activities measured by P3.

The recommended values in table 8 were calculated with a similar procedure as the "best" activities in table 6. The total uncertainties on these values were calculated taking into account : the uncertainty on the Nb-93m activities, the uncertainty on the

TABLE 8.   Nb-93 (n,n') REACTION RATES AT NOMINAL POWER

REACTOR	LEVEL (cm)	P3 REACTION RATES (s^{-1})	RECOMMENDED REACTION RATES (s^{-1})	σ
EBR II	0		$1.10 \ 10^{-10}$	2.4 %
EBR II	-1.2		$1.10 \ 10^{-10}$	2.5 %
EBR II	-37.8		$9.66 \ 10^{-12}$	2.6 %
BR2	+5	$5.21 \ 10^{-11}$	$5.10 \ 10^{-11}$	2.5 %
BR2	-5	$5.20 \ 10^{-11}$	$5.15 \ 10^{-11}$	2.4 %
BR2	-15	$4.97 \ 10^{-11}$	$4.95 \ 10^{-11}$	2.2 %

calculation procedure to convert activities into reaction rates
(0.3 %) and the uncertainty on the Nb-93m desintegration constant
(2.4 %). The accuracy obtained on the EBR II and BR2 Nb-93(n,n')
reaction rates is of the order of 2.5 %. One can conclude that in
routine niobium dosimetry procedures (not in the frame of an in-
ternational comparison) Nb-93(n,n') reaction rates can be deter-
mined with an accuracy of the order of 6 %.

CONCLUSIONS

The technique of dissolving the irradiated niobium material in
HF and HNO_3 is most widely spread. The pycnometer method is the
most accurate method to determine the niobium weight on the depo-
sits. The fluorescence corrections due the Nb-94 + Nb-95 + Ta-182
activities were very small and they had little influence on the
observed differences. This indicates that, when irradiations are
performed in a high neutron flux environment and when the dissolving
technique is applied, the quality of commercial niobium is suffi-
cient. Direct foil measurements are only feasible on pure niobium
material (low Ta content) and when correction factors for fluores-
cence were established.

Most of the countings are performed with a Si(Li) detector.
Suitable calibration sources are : Am-241, Cd-109, Y-88, Co-57 and
Nb-93m. The calibration uncertainty, together with the uncertainty
on the K(X) ray emission probability, determines the accuracy on
the Nb-93m desintegration rate.

As a result of this niobium intercomparison reaction rates in EBR II and BR2 were determined with an accuracy of the order of 2.5 %. It was shown to be possible in routine dosimetry procedures that accuracies of 4 % and 6 % respectively on the Nb-93m activities and on the Nb-93(n,n') reaction rates are achievable.

ACKNOWLEDGEMENTS

REFERENCES

[1] C.L. Long, J.A. Ulseth, E.P. Lippincott, "As-built description of the EBR II, RUN 97 dosimetry experiment," HEDL/TC-1262 (December, 1978).

[2] R. Lloret, "Utilisation du niobium comme intégrateur de fluences élevées de neutrons," Technical CEA-CENG note PI/DOS n° 321-68/73 (Mars 27, 1973).

[3] Private communication of F. Hegedüs to P. Wille.

[4] H. Tourwé, N. Maene, "Fast neutron fluence measurements with the Nb-93(n,n') reaction and the application to long-term irradiations," Proc. 3th ASTM-EURATOM symp. on Reactor Dosimetry, Ispra (October 1-5, 1979).

[5] W.L. Zijp, J.H. Baard, "Nuclear data guide for reactor neutron metrology," ECN-70 (August, 1979).

DEVELOPPEMENTS RECENTS DES CHAMBRES A FISSION
DANS LE DOMAINE DE LA DOSIMETRIE DES REACTEURS

G. Daguzan - C. Fiche - H. Lupo - P. Menessier
Commissariat à l'Energie Atomique - Centre d'Etudes Nucléaires de CADARACHE
BP. N° 1 - 13115 SAINT-PAUL-LEZ-D''RANCE (FRANCE)

ABSTRACT

This paper described some fission chambers applications, in neutron dosimetry, both for research and power reactors.
1 - Miniature pulse fission chambers ($\emptyset \geqslant 1,5$ mm), equiped with transsactinium isotopes deposits.
With this nuclides we can improve the knowledge of the neutron spectrum, for basic experiments in characteristic lattices.
2 - High sensibility pulse fission chambers with reduce volume. In particular they were used in the realization of an equipment to follow the fusion of a fuel pin in a safety experiment.
3 - Pin chamber ($\emptyset$ 1,5 mm) designed for continus neutron flux measurements in power reactors, in order to point out power peaks during electric load follow transients.

Le principal moyen pour effectuer des mesures neutroniques au sein des réacteurs a été, pendant longtemps, l'usage de détecteurs d'activation.

Le principal défaut de ces derniers est de fournir une mesure différée, ce qui est un défaut rédhibitoire lorsqu'il s'agit de suivre des phénomènes évoluant rapidement dans le temps.

D'autres types de détecteurs ont donc été mis au point, comme par exemple les compteurs à protons de recul, les ensembles scintillateur - photomultiplicateur et, notamment, les chambres à fission qui, en plus de leur rôle classique dans l'instrumentation de base des coeurs, sont mises à contribution dans de nombreux domaines.

C'est ainsi que différents laboratoires du CEA ont été amenés à développer, ces dernières années, différents types de chambres à fission adaptés à des problèmes spécifiques.

Seront ainsi décrites les techniques utilisées :
1 - Pour la fabrication de chambres à fission miniatures, utilisées pour la mesure de paramètres neutroniques de base dans des maquettes de réacteurs de faible puissance, et utilisant une très grande variété de dépôts fissiles.

2 - Pour la réalisation de chambres à dépôts de neptunium, entrant en grand nombre dans la fabrication d'un dispositif conçu pour suivre les phénomènes associés à la fusion d'une aiguille de combustible.

3 - Pour la réalisation d'une chambre-aiguille prototype destinée à la mesure du flux en continu dans les réacteurs de puissance.

CHAMBRES A FISSION MINIATURES CONCUES POUR LA DOSIMETRIE DANS DES REACTEURS DE FAIBLE PUISSANCE

Deux types principaux de chambres à fission sont fabriqués, prévus pour fonctionner en impulsions.

A - Chambres d'un diamètre de 4 mm, associées à un prolongateur de longueur variable dont elles peuvent être séparées.

B - Chambres d'un diamètre de 1,5 mm, intégrées à leur prolongateur, dont elle ne peuvent être séparées.

Pour chacune de ces deux chambres seule l'anode reçoit, habituellement, le dépôt fissile.

Son diamètre est de 2,5 mm pour les chambres de $\emptyset$ 4 mm et de 0,7 mm pour les chambres $\emptyset$ 1,5 mm.

La longueur de dépôt, partie sensible, étant de 10 mm dans les deux cas, les surfaces actives sont donc respectivement de 0,78 cm^2 et 0,22 cm^2.

La matière fissile est généralement déposée par électrolyse, la masse superficielle ne devant pas dépasser 1 mg/cm^2 si l'on désire discriminer correctement les impulsions de fission des impulsions parasites (bruit de fond et alphas).

La limite inférieure, pour la masse déposée, est de l'ordre de 10^{-5} mg/cm^2.

Description des chambres[1]

A - Chambres $\emptyset$ 4mm (Fig. 1)

Ces chambres se présentent sous la forme d'un cylindre de 4 mm de diamètre et 23 mm de longueur, sortie axiale non comprise.

Le passage étanche, du type alumine-titane, a une sortie axiale flexible afin d'éviter les contraintes dangereuses sur la brasure céramique-métal lorsque la chambre est couplée à son prolongateur.

L'anode et la cathode peuvent être réalisées en acier inoxydable, en inconel, en titane ou en zircalloy si une faible absorption neutronique

.../...

est exigée.

La distance anode - cathode est de 0,5 mm, le gaz de remplissage (argon le plus souvent) étant introduit sous une pression de 12 bars.

La capacité est d'environ 5 pF, les impulsions ayant une durée inférieure à 100 nanosecondes.

Moyennant un dégazage approprié, la température de fonctionnement peut atteindre 300 à 400 °C.

La tension généralement appliquée est de 300 V, mais le palier haute-tension débute le plus souvent entre 50 et 100 V.

La canne coaxiale servant de prolongateur a un diamètre de 5 mm, sa capacité étant de 40 pF par mètre. Sa longueur peut atteindre plusieurs mètres, la limite supérieure étant fixée par l'augmentation du bruit de fond résultant de la capacité appliquée au préamplificateur.

B - Chambres Ø 1,5 mm (Fig. 2)

Dans ce modèle, chambre et canne coaxiale sont solidaires et remplies du même gaz.

L'ensemble se présente sous la forme d'une aiguille de 1,5 mm de diamètre, très flexible, dont la longueur est habituellement de l'ordre du mètre mais peut atteindre facilement six mètres et plus si l'on fonctionne en courant.

Une prise coaxiale est adaptée à l'extrêmité de ce tube pour le raccordement au préamplificateur.

La partie sensible (dépôt de matière fissile) est centrée à 10 mm de l'extrêmité et son support (anode) est maintenu par deux pièces en rubis synthétique.

Un fil de 0,1 mm, isolé par des tubes d'alumine, relie l'anode à la prise de sortie.

Les matériaux utilisés sont les mêmes que ceux adoptés pour les chambres Ø 4 mm.

La distance inter-électrodes est de 0,3 mm , le gaz de remplissage (argon) étant introduit sous une pression de 15 bars.

Pour une longueur de chambre de 1,00 m la capacité est de 60 pF, les impulsions ayant une durée de l'ordre de 50 nanosecondes.

La température de fonctionnement peut atteindre 350 °C.

Ce type de chambre est extrêmement peu sensible au rayonnement gamma, une ambiance de 10^7 R/h ne créant pas d'impulsions parasites génantes.

Problèmes posés par l'utilisation de ces chambres

Les chambres Ø 4 et Ø 1,5 mm dont les principales caractéristiques viennent d'êtres données sont destinées à fonctionner dans des flux neutroniques souvent peu élevés (10^3 à 10^9 n/cm^2/s).

Leur sensibilité est le plus souvent suffisante car il est possible, pour un grand nombre de corps fissiles, et dans certaines limites, d'adapter la masse du dépôt aux caractéristiques du spectre neutronique mesuré.

Dans la majorité des cas l'amplitude des impulsions dues à l'émission des produits de fission par le dépôt est nettement supérieure à celle des impulsions issues du bruit de fond et des alphas émis par l'isotope fissile.

Ceci n'est vrai cependant que si le taux d'émission alpha est suffisamment faible pour qu'il ne se produise pas d'empilements.

Pour des chambres à fission réalisées avec un isotope fort émetteur alpha cette dernière condition n'est plus remplie, et des précautions particulières doivent être prises pour la mise en oeuvre de la chaîne électronique amplificatrice.

Les isotopes fissiles pour lesquels le problème se pose en terme aigus sont :

^{241}Am $\longrightarrow$ Période : 462 ans $\longrightarrow$ Activité : 1,2 10^{11} α/s/g

^{238}Pu $\longrightarrow$ Période : 86,4 ans $\longrightarrow$ Activité : 6,43 10^{11} α/s/g

^{244}Cm $\longrightarrow$ Période : 18,1 ans $\longrightarrow$ Activité : 3,00 10^{12} α/s/g

L'électronique utilisée, très classique , se compose d'un amplificateur de charge, placé le plus près possible de la chambre, relié par une ligne coaxiale basse impédance à un amplificateur admettant des impulsions à temps d'établissement rapide.

Cet amplificateur est lui-même relié, soit à une échelle de comptage soit le plus souvent à un analyseur multicanaux permettant de définir avec une meilleure précision l'intégrale du "spectre de fission" délivré par la chambre.

Pour les dépôts fort émetteurs alpha il est nécessaire, soit d'adapter très correctement la liaison préamplificateur-amplificateur soit, dans les cas extrêmes, de mettre en place dans la chaîne de mesure un amplificateur à seuil destiné à éliminer les impulsions alpha avant qu'elles ne soient appliquées à l'amplificateur final (Fig. 3, Fig. 4).

CHAMBRES DE HAUTE SENSIBILITE, A DEPOT DE NEPTUNIUM

Dans le cadre d'études de sûreté des réacteurs, effectuées sur le réacteur CABRI à CADARACHE, et relatives à la connaissance des mouvements de combustible liés à une surpuissance volontairement provoquée, une instrumentation a été mise au point par des spécialistes du réacteur concerné [2].

Ce dispositif de surveillance des mouvements de combustible, appelé hodoscope, met en oeuvre un grand nombre de chambres à fission ayant une bonne sensibilité pour la détection des neutrons de fission.

Principe de l'hodoscope (Fig. 6)

La position du combustible est déterminée à tout moment par la détection des neutrons rapides émis par celui-ci lors des fissions dont il est le siège.

Le but est d'isoler les neutrons de fission issus d'un élément de volume du matériau fissile, avec une certaine direction, de ceux provenant du coeur nourricier, diffusés par différentes structures, et constituant la principale source de bruit de fond.

Les deux éléments constitutifs principaux d'une installation du type hodoscope sont :
a) Le collimateur
b) Les détecteurs.

a) Le collimateur

Celui-ci permet d'assigner à chaque détecteur une zone d'observation spatiale déterminée au niveau du combustible et d'empêcher, dans la mesure du possible, la détection des particules issues des régions voisines.

Le collimateur est un bloc prismatique de 3 mètres de long, comprenant 3 colonnes de 51 canaux de section rectangulaire. Chaque canal permet d'observer une zone de 10 mm de large et 20 mm de haut.

Après un parcours d'environ 4 mètres dans le vide, les neutrons atteignent un ensemble double de détecteurs, placés l'un derrière l'autre en face de chaque canal du collimateur.

b) Les détecteurs

La plage de puissance à laquelle est soumise l'hodoscope étant très grande, deux jeux de compteurs, d'efficacités différentes, ont été adoptés, à savoir détecteurs à protons de recul et chambres à fission à dépôts de ^{237}Np.

Seules ces dernières sont évoquées ci-après.

Le principal problème à résoudre était de pouvoir déposer la plus grande masse possible de Neptunium sans augmenter exagérément les dimensions de la chambre, ceci en respectant une masse superficielle de dépôt ≤ 1 mg/cm^2 afin que ceux-ci soient bien adhérents.

La forme adoptée a été celle d'une chambre cylindrique renfermant un assez grand nombre d'électrodes planes, ce qui a conduit à un espace inter-électrodes faible ($\sim 0,7$ mm), d'où la nécessité d'obtenir des électrodes

porte-dépôts très planes.

Cette condition s'est révélée d'autant plus difficile à remplir que, lorsque le dépôt est réalisé, sur chacune des deux faces de l'électrode, cette dernière est chauffée à plusieurs centaines de degrés pour l'étuver et qu'une cambrure se produit de façon presque systématique.

Caractéristiques générales (Fig. 5)

. Diamètre extérieur : 35 mm
. Longueur de la chambre 115 mm
. Matière utilisée : Acier inoxydable
. Isolateurs : Alumine haute pureté
. Nombre d'électrodes porte-dépôts : 94, soit 188 dépôts par chambre
. Electrodes acier inoxydable, épaisseur : 0,1 mm
. Distance inter-électrodes : $\sim$ 0,7 mm
. Gaz de remplissage : Argon U + 0,2 % N_2U
. Pression de remplissage : $\sim$ 6 bars
. Capacité totale : 420 pF
. Isolement : $\sim$ 2,5 10^{10} Ω (mesuré avec dépôts Np réalisés)
. Densité des dépôts : 1 mg/cm^2, réalisés par électrolyse
. Masse de chaque dépôt : 2 mg de ^{237}Np
. Forme des dépôts : rectangulaires (1 x 2 cm)
. Activité γ au contact (dépôts de Np) : $\sim$ 6 mRad/h
. Tension de fonctionnement : 350 V

Les pièces sont nettoyées par ultra-son et un dégazage est effectué avant remplissage de gaz, à 400 °C sous une pression de 10^{-6} Torr.
Les soudures sont faites à l'arc, sous argon.
Ces chambres peuvent fonctionner jusqu'à une température de 250°C.
Les impulsions délivrées ont une largeur d'environ 80 ns.

Des chambres identiques, quant à la conception, au volume et à la masse de matières fissile déposée, ont été réalisées avec de l'uranium 235.

Leur sensibilité, dans un spectre thermique, atteint 0,3 impulsion / neutron/cm^2/s.

CHAMBRE AIGUILLE PROTOTYPE POUR LA MESURE DU FLUX
DANS LES REACTEURS DE PUISSANCE

Si l'on demande aux Centrales électronucléaires d'adapter la puissance qu'elles débitent à celle, variable, demandée par le réseau de distribution électrique, il en résulte des transitoires de puissance pouvant entraîner une déformation du flux, donc l'apparition de points chauds.

La connaissance permanente du flux neutronique en un maximum de points du coeur est donc souhaitable.

L'existence de détecteurs filiformes et de faible dimensions, qui

pourraient être introduits à poste fixe en assez grand nombre, à différents niveaux du coeur dans des canaux de mesure, afin de donner en permanence le profil du flux, serait donc bienvenue.

Ces détecteurs devraient répondre aux conditions principales suivantes :
. Etre peu sensibles au rayonnement γ
. Avoir une réponse ne dépendant pas de leur temps de séjour dans le flux neutronique (consommation du dépôt)
. Fonctionnement correct pendant au moins la durée d'un cycle.

Les chambres à fission miniatures possèdent des caractéristiques qui, moyennant des améliorations dans certains domaines, peuvent résoudre le problème posé.

Il s'agit des chambres-aiguilles, d'un diamètre de 1,5 mm, déjà mentionnées précédemment.

De nombreux essais ont démontré leur insensibilité au rayonnement γ.

En ce qui concerne l'usure du dépôt au fur et à mesure de l'augmentation de la fluence neutronique, qui est de l'ordre de quelques $1.10^{21} n/cm^2$ pour un cycle de fonctionnement, la combustion de la matière fissile du dépôt ^{235}U peut atteindre 50 %.

Une solution possible, à cette disparition de la matière sensible, est celle de la fabrication d'un dépôt régénérable en matière fissile tout au long de l'irradiation.

Cette régénération s'effectue par l'apport d'un corps fissile vierge, à partir de la capture neutronique d'un corps fertile, compensant la disparition par fission de l'isotope fissile d'origine.

Plusieurs combinaisons de mélanges : corps fissile - corps fertile existent, conduisant à des durées de vie variables et à une plus ou moins grande sensibilité aux variations de spectre neutronique.

Pour les essais effectués au CEA un mélange de ^{235}U et de ^{234}U a été choisi [3].

Des expériences réalisées dans un réacteur expérimental, avec une fluence de 10^{21} n/cm^2, ont montré que la compensation d'usure du dépôt réalisée était très bonne.

Mais la température de fonctionnement ne dépassait pas 70 °C.

D'autres essais sont actuellement en cours, dans des coeurs dont la température est de 300 °C, afin de vérifier la tenue dans le temps de ce type de chambre et de mettre en évidence des phénomènes parasites éventuels susceptibles de nuire à la qualité du signal.

Ces chambres ont une technologie identique à celle décrite dans la première partie de ce rapport, seule leur longueur est portée à 8 mètres.

Elles subissent un dégazage préalable très soigné (600 °C pour les pièces métalliques, 1200 °C pour les alumines).

Compte- tenu de leur capacité électrique un fonctionnement en courant est adopté, 50 µA environ étant débités pour la puissance nominale (dépôt de 40 µg de ^{235}U).

REFERENCES

1. MM.Guéry - Jarrige, "Chambre à fission miniature pour les mesures des taux de fission dans les réacteurs de recherche", Revue de Physique Appliquée, Tome VI - 06. 1971

2. K. Böhnel and H. Blum,"First results of the CABRI neutron hodoscope", Proceeding International Meeting on Fast Reactor Safety Technology, SEATTLE - 1979 - P. 2261

3. F. Berger, "Mesures neutroniques effectuées avec des chambres à fission miniatures", Thèse présentée à l'université de Paris-Sud, soutenue le 11 Octobre 1977.
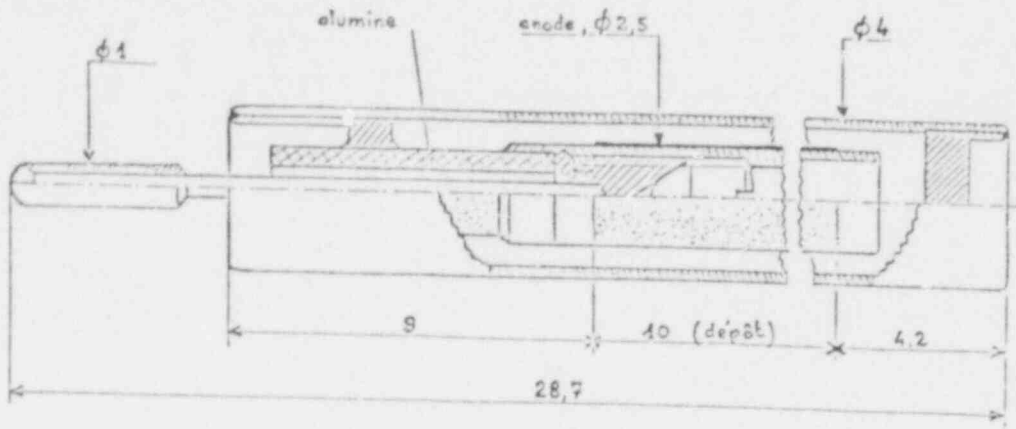
Chambre ⌀ 4 mm

Figure 1
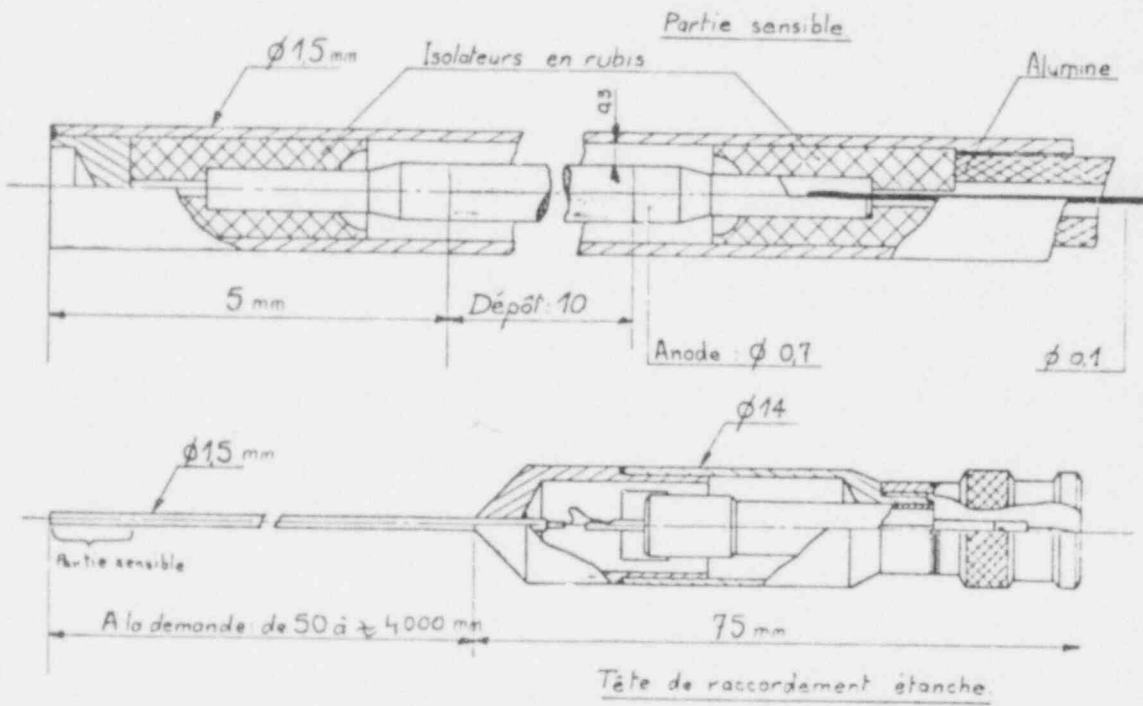
Chambre-aiguille ⌀ 1,5 mm

Figure 2
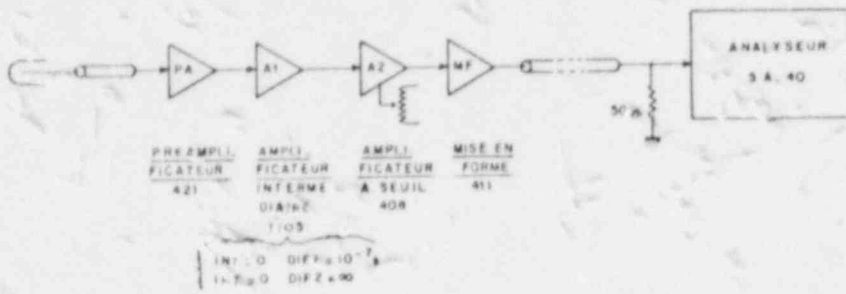
SCHEMA DE PRINCIPE DE LA
CHAINE DE MESURE POUR LES CHAMBRES
avec dépôts ayant une forte émission α
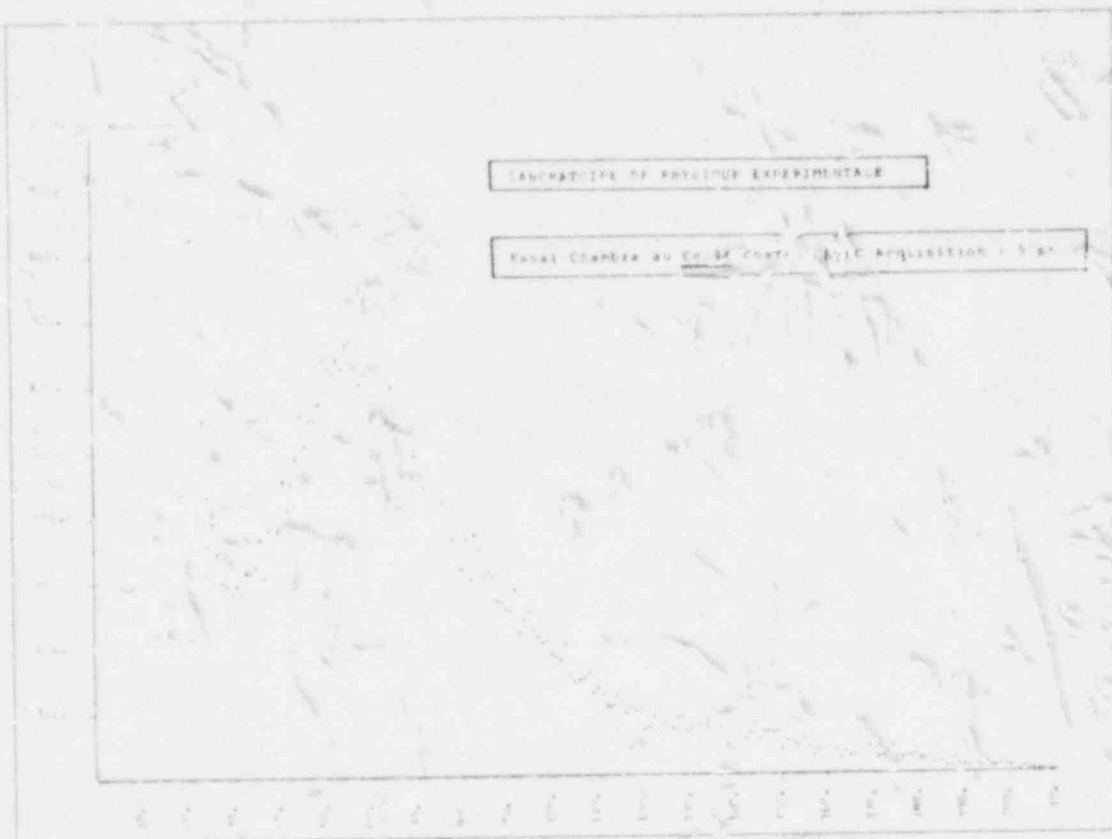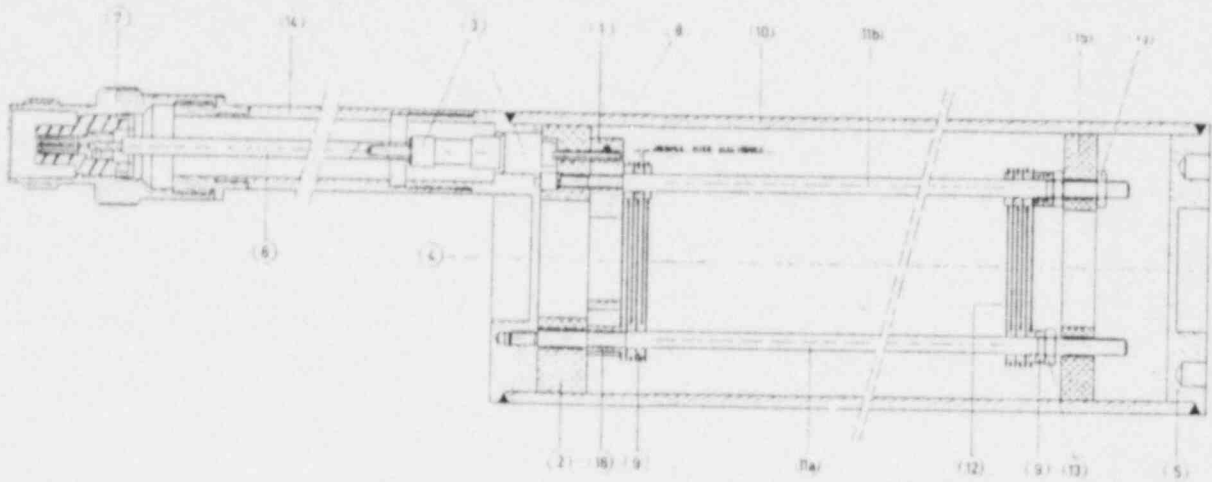
Figure 3

Figure 4

Chambre Hodoscope

Figure 5
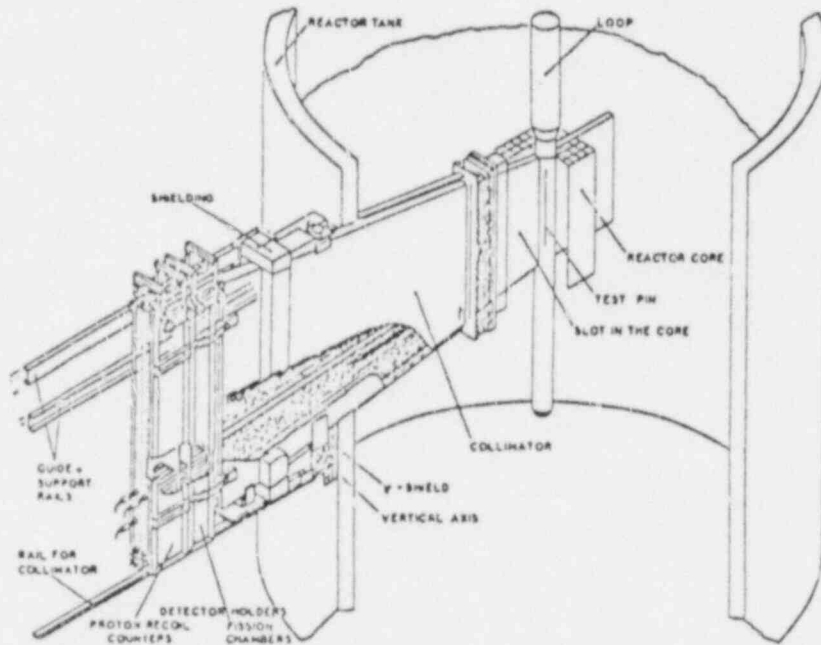
: Cut-off view of the hodoscope installation in
the reactor building.

Figure 6

ON THE NEUTRON SPECTRUM MEASUREMENT BY MULTIPLE FOIL ACTIVATION METHOD . A PARTICULAR CHOICE OF DETECTORS AND OF COUNTING TECHNIQUE.

A. Cesana, V. Sangiust, M. Terrani
Politecnico di Milano, Istituto Ingegneria Nucleare - CESNEF
Milano, Italy
G. Sandrelli
ENEL, Centro Ricerca Termica e Nucleare
Milano, Italy

ABSTRACT

The use of (n,fission) reactions only and the determination of the fission rates by delayed neutron counting is proposed for neutron spectra measurement by multiple foil activation technique. A set of detectors suitable for nuclear reactor dosimetry could be: ^{232}Th, ^{233}U, ^{235}U, ^{238}U, ^{237}Np, $^{238/239/240/241}Pu$ and ^{241}Am. The results of a measurement performed with these monitors are presented. Advantages and drawbacks of this technique are discussed.

INTRODUCTION

In neutron spectrum measurement by multiple foil activation technique, the reaction rates per atom of a number of nuclear reactions: (n,γ), (n,p), $(n,\alpha)$, $(n,fission)$ etc. are usually determined by counting the β or γ radiation from the reaction products. Starting from those rates and a guess spectrum, through appropriate adjustment techniques(e.g. SAND II or STAY'SL codes) the desired solution is obtained. Our proposal is :
1) to use only fissionable nuclides as flux monitors,
2) to determine the fission rates per atom by delayed neutron counting.

The main advantages should be :
a) the longest delayed neutron half life being about 55 s, the measurement can be performed in a short time;
b) raw data handling in order to estimate the reaction rates is very simple;
c) problems connected with counting efficiency determination are greatly simplified, hence an accurate determination of the delayed neutron activity is expected. In particular

the efficiency is the same for all the monitors.

EXPERIMENTAL

The reaction rates per atom of the ten isotopes listed in Table 1 were experimentally determined in a known neutron spectrum and compared with the values computed in it.

Monitors

The fissionable materials (each a few milligrams of oxide powder), sealed in small Zircaloy vials, 4-mm-diam, 8 to 14-mm-long, were furnished by the Oak Ridge National Laboratory and the Radiochemical Centre of Amersham.

The monitors were transferred to and from the irradiation and counting positions by a pneumatic system. The pneumatic tube was 10-mm-diam, 10-m-long. The transit time was about 0.6 s.

Table 1. Fissionable monitors and related nuclear data

ISOTOPE	GROUP 1		GROUP 2		GROUP 3	
	$\lambda(s^{-1})$	y	$\lambda(s^{-1})$	y	$\lambda(s^{-1})$	y
^{232}Th *	0.0124	1.85 E-3	0.0334	8.18 E-3	0.121	8.45 E-3
^{233}U °	0.0128	7.10 E-4	0.0356	2.18 E-3	0.143	1.84 E-3
^{235}U *	0.0127	6.45 E-4	0.0317	3.62 E-3	0.115	1.59 E-3
^{238}U *	0.0132	5.86 E-4	0.0321	6.17 E-3	0.139	7.30 E-3
^{237}Np °	0.0127	4.90 E-4	0.0318	3.10 E-3	0.123	2.51 E-3
^{238}Pu °	0.0140	2.68 E-4	0.0317	1.11 E-3	0.140	1.19 E-3
^{239}Pu *	0.0129	2.49 E-4	0.0311	1.83 E-3	0.134	1.42 E-3
^{240}Pu °	0.0128	2.65 E-4	0.0317	2.63 E-3	0.115	1.26 E-3
^{241}Pu °	0.0128	2.76 E-4	0.0317	3.70 E-3	0.137	2.98 E-3
^{241}Am °	0.0122	1.92 E-4	0.0310	1.16 E-3	0.126	6.55 E-4

*From Ref. 1·
° From Ref. 2.

Irradiation Position

It was inside a B4C filter situated near the L54 reactor core. The neutron spectrum resulting from a multiple foil activation measurement[3] is shown in Fig. 1.
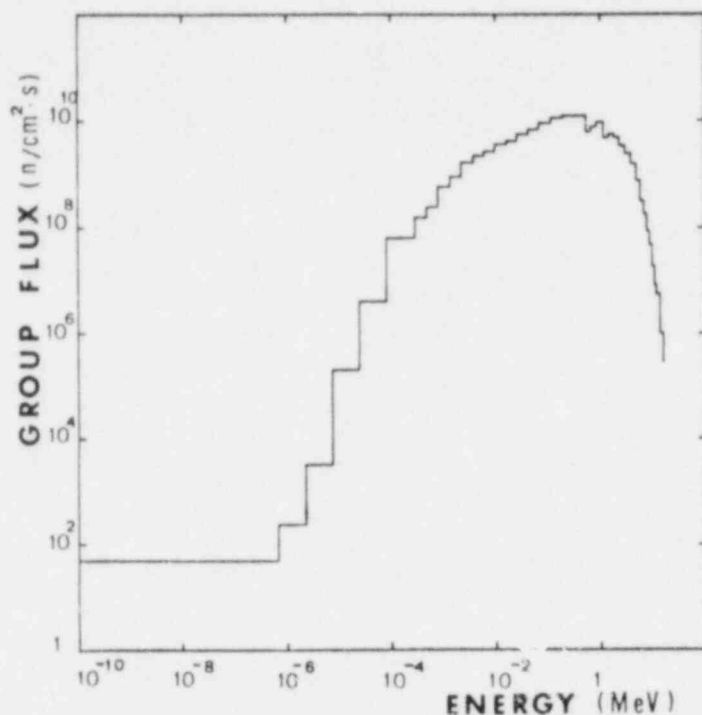
Fig.1. Neutron spectrum inside the B4C filter.

Counting Position

It was placed at the centre of a 40-cm-diam, 80-cm-long paraffin cylinder. Neutrons were detected by a 5-cm-diam, 50-cm-long BF_3 proportional counter embedded in paraffin parallel to the cylinder axis.

The neutron detection efficiency was $\varepsilon_n = 0.076 \pm 0.002$, independent of the delayed neutron group considered.

Fission Rate Determination

The monitors were irradiated ten times each. The time schedule of the runs was: irradiation time 180 s, waiting time 60 s, counting time 120 s, so that only the first and second delayed neutron groups were considered (see Table 1).

Since the monitors are themselves weak sources of neutrons (produced via spontaneous fission and/or (α,n) reaction on oxigen), the background was separately determined for each of them.

The reaction rate per atom was obtained from:

$$R = \int_0^\infty \sigma(E)\Phi(E)dE = \frac{C - C^\circ}{\varepsilon_n \sum_{i=1}^{2} \frac{y_i}{\lambda_i}\left(1 - e^{-\lambda_i t_{irr}}\right)\left(1 - e^{-\lambda_i t_c}\right) e^{-\lambda_i t_w}} \qquad (1)$$

where:

C = total neutron counts

C° = correction for background and contributions from fissionable impurities.

The yields y_i and the decay constants λ_i were those reported in Table 1.

Time required

The determination of the ten values of R, each one measured ten times, required the work of one operator for less than two days.

Results

In Table 2 the experimental reaction rates per atom are compared with the values calculated in the spectrum of Fig.1.

The cross section library (40 group energy structure as reported in Table 3) was derived from ENDFB/IV for all the nuclides but for ^{232}Th, for which these data were derived from ENDF B/V.

The original 620 group cross section library was furnished by Centro Calcolo CNEN-Bologna (Italy).

Taking into account the errors on the cross sections, the agreement can be considered very good.

Table 2. Comparison between calculated and measured
reaction rates per atom.

| Nuclide | Reaction Rate (x 10^{15}) | | Deviation % |
	Measured	Calculated	
^{232}Th	2.56 ± 0.14	2.61	+ 2
^{233}U	323.1± 17.0	299.5	- 8
^{235}U	210.9± 11.0	216.6	+ 3
^{238}U	10.21± 0.51	10.93	+ 7
^{237}Np	67.2 ± 3.6	72.4	+ 7
^{238}Pu	164.7± 10.7	165.9	+ 1
^{239}Pu	223.3± 12.0	217.0	- 3
^{240}Pu	80.3 ± 5.0	77.5	- 4
^{241}Pu	279.4± 17.0	282.2	+ 1
^{241}Am	71.7 ± 4.4	69.4	- 3

Table . Energy limits of
40 group structure

Group	Lower Limit
1	1 (-4)*eV
2	0.69
3	2.30
4	7.60
5	25.5
6	84.0
7	0.30 keV
8	0.50
9	0.80
10	1.35
11	2.20
12	3.80
13	6.00
14	10.0
15	17.0

DISCUSSION AND CONCLUSIONS

The proposed technique is
attractive from many points of
view, in particular from the
experimental one. Nevertheless,
some drawbacks must be consi-
dered.

A) A constraint on the choice
of the monitors implies ne-
cessarily the loss of some
amount of information. An
"improvement factor", defin-
ed as the ratio of the "old"
to the "new" errors in group
fluxes, computed by STAY'SL
for our set of fissionable
detectors is shown as a
broken line in Fig.2, where
the full line represents the
integral normalized flux. It

Table 3. (cont.d)

Group	Lower Limit
16	27.0 keV
17	45.0
18	72.0
19	0.12 MeV
20	0.20
21	0.32
22	0.55
23	0.69
24	0.88
25	1.20
26	1.50
27	1.90
28	2.40
29	3.10
30	4.0
31	5.0
32	6.0
33	7.0
34	8.0
35	9.0
36	10.0
37	11.0
38	12.0
39	14.0
40	16.0→18.0

*Read: 1×10^{-4}

is clear that, in spectra like that one considered, this set of fissionable detectors cannot add a substantial amount of information to that contained in the guess spectrum in the low (E<1.5 KeV) and high (E>5 MeV) energy regions. The situation in the first region is common to any other set of detectors; in the high energy region an improvement could be obtained by adding to the present set some threshold detectors such as ^{231}Pa or ^{234}U, which however are difficult to obtain and for which nuclear parameters such as cross sections and delayed neutron yields are poorly known.

Looking at the integral flux distribution one can conclude that in this kind of spectra the proposed set of detectors gives a response in the most significant energy region.

B) Serious interference from photofission is expected in some cases. Photofission effect is important for threshold detectors (^{232}Th, ^{238}U etc.) irradiated next to intense sources of capture gamma radiation: e.g., for ^{232}Th contributions of the photofission to the total fission rate up to 40% were measured near the pressure vessel of a reactor[4]. The same problem arises for some reactions of commoner use, e.g. (n,n') reactions.

Due to uncertainties in the photon spectra and photofission cross sections, an accurate determination of the correction is at present impossible. However in our case, as well as in several situations, typically at the boundary or inside the core, this correction is negligible.

C) Fission yields are energy dependent, so that in principle one should use a set of fission yields for each spectrum. The dependence of delayed neutron yields on neutron energy is not well established.
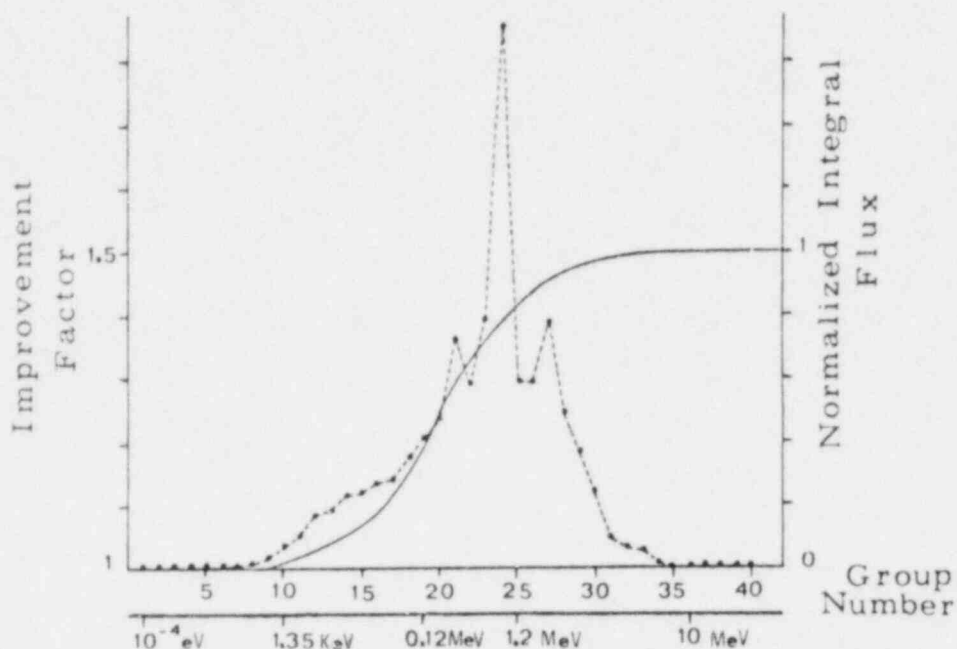
Fig.2. Detector response versus group numbers.

They are believed to be practically constant for neutr-
on energies up to 4 ÷ 5 MeV, whereas at higher energies
they decrease and, at about 7 MeV, they reach a new pla-
teau which extends up to 14MeV at least. Since most of
the neutrons in reactor spectra are included in the first
energy interval (e.g., in our spectrum only about 1% of
the neutron flux is above 4 MeV), one can take the value
corresponding to the first plateau as yield value. This
procedure required in our case a correction of less than
5% for ^{232}Th and ^{238}U and less than 1% for all the other
monitors.

D) Delayed neutron decay constants and yields (and their de-
pendence on neutron energy) are at present quoted with
rather great uncertainties and for many fissionable nu-
clides they are not known at all.

Considering the quoted errors, relatively great un-
certainties in the fission rate determination were expect-
ed. Our results indicate that the situation is not worse
for the set of fissionable detectors used than for other
sets of detectors commonly employed.

However, a better knowledge of the necessary nuclear
parameters (yields and cross sections for neutron and pho-
ton induced fission) is advisable. In our opinion the

advantages offered by this technique justify some effort
in this field.

REFERENCES

1. R.J.Tuttle,"Delayed Neutron Data for Reactor Physics
   Analysis", Nucl.Sci.Eng.,56,37(1975)

2. G.Benedetti,A.Cesana,G.Sandrelli,V.Sangiust,M.Terrani,
   "Delayed Neutron Yields from Fission of U-233,Np-237,
   Pu-238/240/241,Am-241",Nucl.Sci.Eng. (to be published)

3. A.Cesana,G.Sandrelli,V.Sangiust,M.Terrani,Characteriz-
   ation of the Radiation Environment in Fission Reactors
   by the Activation Technique and Optimization of the Set
   of Nuclear Reaction of Possible Use,IAEA Advisory Group
   Meeting on Nuclear Data for Radiation Damage Assessment
   and Related Safety Aspects, Vienna(October 1981)

4. V.V.Verbinski,C.G.Cassapakis,W.K.Hagan and G.L.Simmons,
   "The Effects of Photoreactions on Neutron Dosimetry for
   Reactor Pressure Vessel Lifetime Studies",Proceedings
   3rd ASTM-Euratom Symposium on Reactor Dosimetry,Ispra
   (Varese),Italy(October 1979)

5. Samson A.Cox, Delayed Neutron Data-Review and Evaluation,
   USA report ANL/NDM-5(April,1974)

MEASUREMENTS WITH THE NIOBIUM NEUTRON FLUENCE DETECTOR AT THE PTB

W.G. Alberts, R. Hollnagel, K. Knauf, M. Matzke, W. Peßara
Physikalisch-Technische Bundesanstalt
D-3300 Braunschweig, Fed.Rep. Germany

ABSTRACT

The emission probability for X_K radiation from $^{93}Nb^m$ was determined to be $p_K = 0.107 \pm 0.003$. The activity of thick metallic niobium foils after irradiation with ^{252}Cf spontaneous-fission neutrons was derived by measuring the emitted $X_{K\alpha}$-rays with a calibrated Ge detector considering self-absorption in the foils. From these measurements a fission spectrum-averaged cross section of (149 ± 10) mb for the $^{93}Nb(n,n')^{93}Nb^m$ reaction was derived.

INTRODUCTION

The importance of the niobium activation detector in reactor neutron metrology is underlined by various publications on this subject presented at previous ASTM-EURATOM Symposia on Reactor Dosimetry[1-5]. The increasing practical use of this detector is documented by another paper presented in this symposium[6]. The well-known advantages of this detector are the low energy threshold of the reaction $^{93}Nb(n,n')^{93}Nb^m$ and the long half-life of the generated nuclide which allows long irradiation times for neutron fluence determination.

The reliability of reaction rate measurements was, however, undermined by the fact that several of the nuclear parameters involved were not well known, leading to quoted uncertainties in the order of 30 %. It was only recently that the half-life of $^{93}Nb^m$, for which published values had varied from 11.4 a [2] to 19.1 a [7], was established by two working groups in Geel and Grenoble who measured (15.9 ± 1.0) a [8] and (16.11 ± 0.19) a [10], respectively. For the present work we use an adopted value of (16.0 ± 0.5) a [9,12]. For neutron flux density determination by Nb activation the reaction rate in the Nb detector has to be derived: $N_oR = N_o\sigma\phi$ (N_o number of Nb atoms in the detector, R reaction rate per atom, σ reaction cross section, ϕ neutron flux density). The derivation of a neutron fluence from a reaction-rate measurement thus requires the knowledge of the cross section of the reaction. The activity of the irradiated sample is given by $A = N_oR (1-\exp(-\lambda t))$ (λ decay constant of $^{93}Nb^m$, t irradiation time), introducing the decay constant as the second important quantity. The activity is usually determined by the measurement of the X_K-radiation following internal conversion of the M4 transition of the 30 keV level to

ground state in ^{93}Nb. According to $A = \dot{N}/(\varepsilon_K \cdot p_K)$ ($\dot{N}$ count rate and ε_K efficiency of the X-ray detector, p_K emission probability for the X_K-radiation), the emission probability is the third significant parameter.

It is the aim of this paper to present a new determination of the emission probability p_K as well as a measurement of the spectrum-averaged cross section in the ^{252}Cf spontaneous-fission neutron field.

EMISSION PROBABILITY FOR ^{93}Nb^m X-RAYS

Experimental Equipment

The X_K-radiation of the ^{93}Nb^m was measured with a cooled high-purity germanium detector of 16.6 mm diameter and 5 mm depth. The efficiency curve was carefully measured in the standard geometry (source-detector distance: 60 mm). In this geometry the spectrometer is furnished with two collimators (Fig. 1). The source collimator prevents scattered photons from impinging on the detector (Path 1), and the detector collimator prevents photons from hitting the edge of the germanium crystal where charge collection is incomplete (Path 2). This arrangement together with calibration sources on thin VYNS (polyvinylchloride-polyvinylacetate co-polymer) foils leads to proper line shapes in the spectra.

Fig. 1. Detector arrangement in the standard geometry

For the efficiency calibration in the energy region 6 to 35 keV the X_K-radiations from the nuclides ^{57}Co, ^{65}Zn, ^{85}Sr, ^{88}Y, ^{109}Cd and ^{125}I and the gamma radiations from ^{241}Am and ^{125}I were used. The activity of all samples except ^{109}Cd was determined by the $4\pi\beta$-γ-coincidence method. The most frequently used 14.4 keV ^{57}Co-γ and the ^{241}Am X_L radiations were excluded because they do not match the resulting efficiency curve[11].

The efficiency ε is determined according to $\varepsilon = \dot{N}/(p \cdot A)$ ($\dot{N}$ measured pulse rate in the peak, p emission probability, A activity). The measured points were corrected for absorption in air, in the Be window of the cryostate, in the Au layer in front of the crystal, and for the escape of the germanium-X_K photons. This procedure leads to an energy-independent

efficiency curve in the energy region where the intrinsic efficiency of the detector is 1, allowing a good interpolation (Fig. 2).
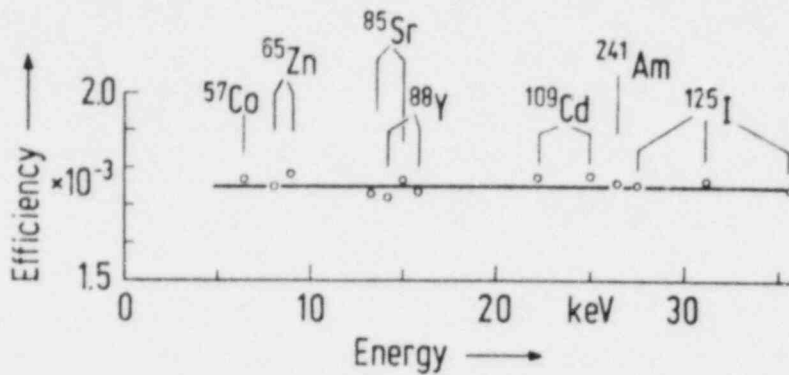
Fig. 2. Corrected efficiency curve for the standard geometry

X_K Emission Probabilities for $^{93}Nb^m$

Using the well-established efficiency curve, the emission probability p_K for X_K-radiation from $^{93}Nb^m$ could be determined[11] according to the relation $p_K = \dot{N}_K/(\varepsilon_K \cdot A)$. The $^{93}Nb^m$ sources were produced by dropping onto VYNS and polyester foils weighed amounts of a solution of known specific activity determined by CBNM Geel[12] with the liquid scintillation method. The results of measurements with the high-purity germanium detector are listed in Table 1. The uncertainties are standard deviations; the relative standard deviations of the components are 0.3 % for $\dot{N}_K$, 2.5 % for ε_K, and 1.3 % for A, yielding 2.8 % for p_K by quadratic summation.

Table 1. Emission probabilities
for $^{93}Nb^m$ X_K-radiation

p_K	$= 0.107 \pm 0.003$
$p_{K\beta}/p_{K\alpha}$	$= 0.195 \pm 0.001$
$p_{K\alpha}$	$= 0.0892 \pm 0.0025$
$p_{K\beta}$	$= 0.0174 \pm 0.0005$

MEASUREMENT OF THICK NIOBIUM FOILS AT LOW DISTANCE

The low reaction rate which is unaviodable in irradiation experiments with a californium neutron source (see next chapter) yields a low activity. Two things can be done to raise the count rate. First, the mass of the

sample can be increased thus increasing the induced activity. This makes necessary the consideration of self-absorption effects of the 16.6 X_K-radiation within the foil. Secondly, the sample-detector distance can be decreased. In this case self-absorption and soild-angle calculation can no longer be handled separately.

The calculation was performed using a program DODE which was originally developed for the very similar situation when measuring the 20 keV X-rays of an activated Rh foil[13]. With this program a "detection probability" is caluclated, which is defined as the ratio of photon current impinging on the detector to the photon emission rate within the foil. This definition requires the assumption that the intrinsic efficiency of the detector is 1. (For a thin source without self-absorption the detection probability is equal to the efficiency ϵ_K.) The program also considers the absorption of the X_K-radiation in the Be window in front of the detector. Photon scattering within the foil as well as the influence of the foil rim are taken into account in this calculation. The mass attenuation coefficient at 16.6 keV ($X_{K\alpha}$) was taken from Ref. 14 as 18.219 cm^2/g (155.8 cm^{-1}). Calculations were performed to judge the influence of various parameters on the detection probability. Fig. 3 shows the variation according to the diameter of the sample and Fig. 4 that according to the distance between sample and detector, each for three foil thicknesses of 0.1 μm (standard sample, no self-absorption), 28 μm and 56 μm.
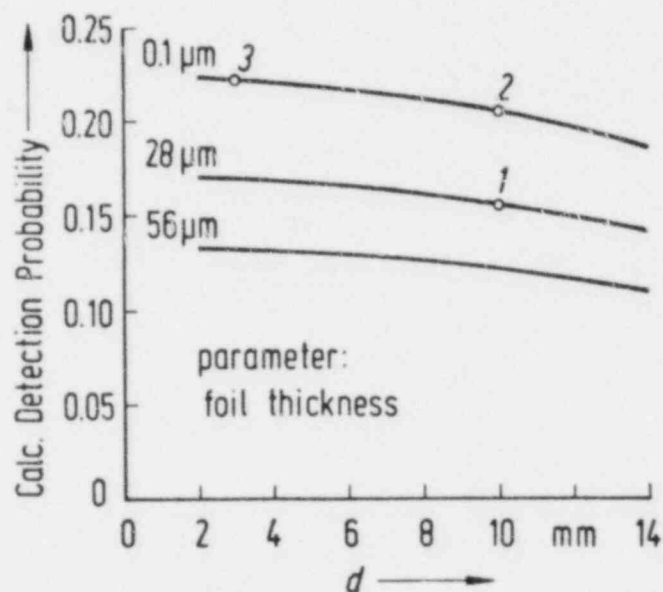
Fig. 3. Variation of the detection probability
with the foil diameter d. Foil-detector
distance 5 mm, detector diameter 16.6 mm.
Numbered points referred to in the text.
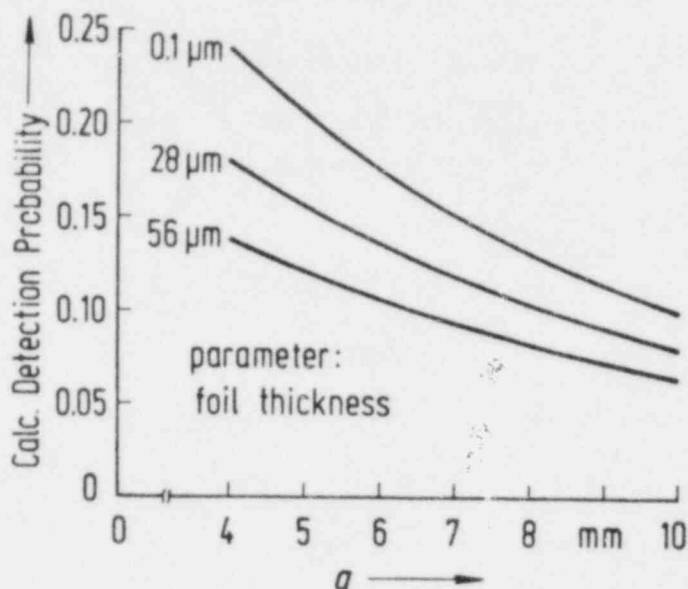
Fig. 4. Variation of the detection probability
with the foil-detector distance a. Foil
diameter 10 mm, detector diameter 16.6 mm.

CROSS SECTION OF ^{93}Nb(n,n')^{93}Nb^m AVERAGED OVER
THE ^{252}Cf SPONTANEOUS FISSION NEUTRON SPECTRUM

Irradiation Experiment

An irradiation experiment was performed in the PTB's ^{252}Cf sponta-
neous-fission standard neutron field[15,16]. Metallic niobium foils of
10 mm diameter and 28 µm thickness were irradiated close to the ^{252}Cf
source which had a neutron source strength of $2.3 \cdot 10^8$ s^{-1}. This neutron
field has a well-known spectrum with a negligible proportion of thermal
and epithermal neutrons. Therefore negligible activation of impurities
(180 µg/g of tantalum) was expected, which is an advantage compared to
reactor-irradiated Nb samples[3].

The flux density during the irradiation was monitored by indium foils
(thickness 50 µm) in sandwich geometry (Fig. 5) using the ^{115}In(n,n')^{115}In^m
reaction. The ^{115}In^m activity was determined by measuring the 336 keV
γ-rays with a calibrated Ge(Li) detector. The neutron fluence in the
indium foils was calculated based on a spectrum-averaged cross section of
(195 ± 5) mb measured earlier with the same source[16]. The decay of ^{115}In^m
(half-life 0.1869 d) as well as that of ^{252}Cf (half-life 2.65 a) during
the irradiation period was taken into account. The irradiation time was
about 40 days and the neutron fluence $1.2 \cdot 10^{14}$ cm^{-2}.
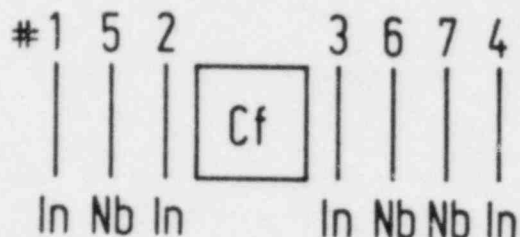
Fig. 5. Schematic view of the source-
sandwich configuration

$^{93}Nb^m$ Activity Determination

The $^{93}Nb^m$ activity of the metallic foils was determined measuring the
$X_{K\alpha}$-radiation of 16.6 keV relative to that of a standard sample of the type
described before, both at a 5 mm distance to the Ge detector. Since the
activity of the foils was only about 3 Bq a measuring period of 160 000 s
was taken in the middle of which the
sample was reversed to minimize the
distance uncertainty. Fig. 6 shows
the pulse-height spectrum from which
the peak area of the $X_{K\alpha}$-ray could
be evaluated with a standard devia-
tion of 3 %. The long-period measure-
ments were performed inside a lead
shield in order to reduce the back-
ground and the external excitation
of X-fluorescence radiation in Nb.

Fig. 6. Pulse height spectrum
of Nb Foil 5 obtained
with the Ge detector
after 80 000 s.

Using the curves in Fig. 3
the count rate of the foil could be
corrected to make it comparable to
that of the standard sample. Start-
ing from Point 1 and going to
Point 2 we find that due to self-
absorption the detection probabili-
ty is a factor of 1.32 smaller for
28 µm than for 0.1 µm. This
correction contains only a 0.5 %
contribution from scattering and rim
effects. It has a relative uncertainty of 1.5 % derived from an assumed
5 % uncertainty of the attenuation coefficients used in the calculation
and an additional 3 % uncertainty arising from an assumed ± 1 µm uncertain-
ty of the foil thickness due to inhomogeneities which were not investigated.

In a second step, going from Point 2 to 3 in Fig. 3, we find an in-
crease in the detection probability for a smaller source diameter of a
factor 1.082, for which the uncertainty was assumed to be negligible. Now

the count rate can be compared directly to that of the standard sample of which the activity is known, as mentioned before.

Spectrum-Averaged Cross Section Determination

Two foil packs were irradiated on opposite sides of the source (Fig.5). The Nb Foils 6 and 7 were disregarded because inconsistencies in the evaluations of the respective In monitor Foils 3 and 4 did not allow the derivation of a flux density for the Nb foils. From the activity of Nb Foil 5 and a decay parameter $\lambda = 1.1861 \cdot 10^{-4}$ d^{-1} (half-life 16 a) a reaction rate per Nb atom $R = 5.5 \cdot 10^{-18}$ s^{-1} was calculated. Using the average result of the two In Foils 1 and 2 yielding a flux density $\phi = 3.7 \cdot 10^7$ cm^{-2} s^{-1}, we obtain a spectrum-averaged cross section for the ^{93}Nb(n,n')^{93}Nb^m reaction of $\bar{\sigma} = R/\phi = 149$ mb. The uncertainty of this value was calculated by quadratic summation of the contributions listed in Table 2 which were estimated as standard deviations.

Table 2. Uncertainty determination for the cross section

Source of Uncertainty	Rel.Std.Dev. in %
Count rate of Foil 5	3.0
Count rate of standard	0.5
Activity of standard	1.3
Sample-detector distance	0.8
Self-absorption	3.3
^{93}Nb^m half-life	3.1
Indium cross section	2.5
Indium activity	2.5
Syst. uncertainty of flux determination at Nb foil position	2.0
Total	7.0

SUMMARY AND DISCUSSION

Little information is available on the energy-dependent cross section for the formation of the metastable state in ^{93}Nb. A recent measurement in the energy range from 0.85 to 5 MeV was performed by Williams[17], who evaluated this cross section as the sum of all γ-ray production cross sections which feed the isomer level. Strohmaier performed statistical model calculations which are the basis for a set of evaluated group cross sections[18] shown in Curve 2 of Fig.7. Hegedüs[19] proposed a set of group cross sections (Curve 1) which was obtained from Nb activation measurements in reactor neutron spectra. This cross section was derived as being proportional to that of the reaction ^{103}Rh(n,n')^{103}Rh^m and contains scaling factors due to decay constant and X_K emission probability of ^{93}Nb^m. Spectrum-averaged cross sections were calculated from the above cross sections using a Watt expression[20] for ^{235}U and the NBS evaluation[21] for the ^{252}Cf fission neutron spectra. Due to the low energy threshold of the reaction, there is only a small difference between the values for both spectra (see caption of Fig. 7).
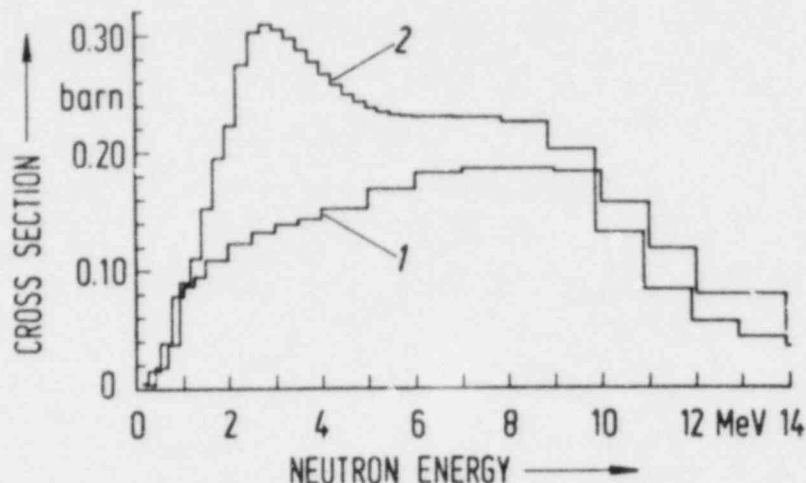
Fig. 7. Cross section for the activation of ^{93}Nb proposed by (1) Hegedüs[19] and (2) Strohmaier et al.[18]. Averaging these cross sections over fission neutron spectra (see text) one obtains:

fission spectrum	^{235}U	^{252}Cf
$\overline{\sigma}_1$	97 mb	99 mb
$\overline{\sigma}_2$	158 mb	162 mb

Table 3. Fission spectrum-averaged cross sections for ^{93}Nb(n,n')^{93}Nb^m

Reference		Cross Section (mb)
Hegedüs	1971 [19]	155 + 55
Kobayashi	1979 [24]	164 + 12[+]
Strohmaier	1980 [18]	158 + 16[+]
Sakurai	1981 [25]	177 + 40
Present work		149 + 10

[+]Uncertainty does not include contributions from λ and p_K.

In order to compare our cross section result with those of other authors it is necessary to agree upon a common set of nuclear decay data. For the half-life of ^{93}Nb^m we take the value of (16.0 ± 0.5) a as adopted in Ref. 9. The $\overline{X}_K$ emission probability was redetermined as $p_K = 0.107 ± 0.003$. Previous values used by other authors were 0.129 [22], 0.122 [19] and 0.116 [23].

Table 3 shows various ^{235}U fission spectrum-averaged cross sections, rescaled to our set of decay data with the exception of Strohmaier's value which was derived by a different method. The uncertainties in the table are those given by the authors and accordingly rescaled. The uncertainties of the results obtained by Hegedüs and Sakurai contain large contributions from the uncertainties of λ and p_K and are therefore not representative for the actual situation. The only known measurement in a ^{252}Cf fission neutron spectrum, performed by Shani[26], was not included in the table, because no proper rescaling was possible from the given data. Moreover, his use of the competing reaction ^{93}Nb(n,2n)^{92}Nb^m as the only fluence monitor seems to be doubtful because of the high threshold (9 MeV) and the unsatisfactory knowledge about the cross section. As a by-product we have determined this cross section as (0.7 ± 0.2) mb measuring the

935 keV γ-ray with very low counting statistics. Another value found in the literature is (0.88 ± 0.04) mb [27]. This cross section may be remeasured in a future experiment.

Acknowledgement: The authors gratefully acknowledge the measurement of the $^{115}In^m$ and $^{92}Nb^m$ activities by Dr. U. Schötzig.

REFERENCES

1. R. Lloret, 1st ASTM-EURATOM Symposium in Reactor Dosimetry, Petten 1975, EUR 5667 e/f, Part I (1977) 747.
2. F. Hegedüs, ibid. p. 757.
3. F. Hegedüs, 2nd ASTM-EURATOM Symposium on Reactor Dosimetry, Palo Alto 1977, NUREG/CP-0004 (1978) 825.
4. W.H. Taylor, ibid. p. 831.
5. H. Tourwé, N. Maene, 3rd ASTM-EURATOM Symposium on Reactor Dosimetry, Ispra 1979, EUR 6813 en-fr (1980) 1245.
6. H. Tourwé et al., "Niobium Dosimetry Intercomparison in EBRII and BR2", this symposium.
7. R. Lloret, PI(NT) 527-126, Petten 1971, cited by P. Wille, Atomkern-energie 29 (1977) 166.
8. D. Reher, R. Vaninbroukx, Annual Progress Report on Nuclear Data 1980, CBNM Geel, p. 40.
9. D. Reher, R. Vaninbroukx, ibid. p. 57.
10. R. Lloret, Radiochem. Radioanal. Letters 50 (1981) 113.
11. W. Peßara, to be published.
12. D. Reher, R. Vaninbroukx, W. Zehner, Document CBNM/RN/36/80, Geel (1980).
13. R. Hollnagel, K. Knauf, German Report PTB-FMRB-77 (1980) and paper submitted for publication to Atomkernenergie/Kerntechnik 1982.
14. W.H. McMaster et al., Compilation of Xray cross sections. Section II. Revision 1, UCRL-50174 (1969).
15. W.G. Alberts, E. Günther, M. Matzke, G. Rassl, Proc. First ASTM-EURATOM Symposium on Reactor Dosimetry, Petten 1975, EUR 5667 e/f, Part I (1977) 131.
16. W. Mannhart, W.G. Alberts, Nucl. Sci. Eng. 69 (1979) 333.
17. G.H. Williams, The Energy Levels of ^{93}Nb Through a Study of the $^{93}Nb(n,n'\gamma)^{93}Nb$ Reaction, Dissertation, Austin, Texas 1975.
18. B. Strohmaier, S. Tagesen, H. Vonach, Physik Daten - Physics Data 13 (1980) 62.
19. F. Hegedüs, Swiss report EIR-Bericht Nr. 195 (1971).
20. B.E. Watt, Phys. Rev. 87 (1952) 1037.
21. J.A. Grundl, C.M. Eisenhauer, 1st ASTM-EURATOM Syposium on Reactor Dosimetry, Petten 1975, EUR 5667 e/f Part I (1977) 425.
22. C.M Lederer, V.S. Shirley, Table of Isotopes, J.Wiley, New York 1978.
23. W.L. Zijp, J.H. Baard, Nuclear Data Guide for Reactor Neutron Metrology (1979 Edition), EUR 7164 EN (1981).
24. K. Kobayashi, I. Kimura, Proc. 3rd ASTM-EURATOM Symp. on Reactor Dosimetry, Ispra 1979, EUR 6813 en-fr (1980) 1004.
25. K. Sakurai, I. Kondo, Nucl. Instr. Meth. 187 (1981) 649.
26. G. Shani, Nucl. Technology 51 (1980) 83.
27. Z. Dezsö, J. Csikai, Proc. IV All Union Conf. Neutron Physics, Kiev 1977, Atomizdat Moscow (1977) 32.

GAMMA-RAY INDUCED RANGE CONTRACTION IN POLYMERIC NUCKLEAR TRACK DETECTORS;
ACTIVATION ENERGIES, DIFFUSION COEFFICIENTS AND JUMP FREQUENCIES.

A. Aframian

Atomic Energy Organization of Iran

NRC. P.O. Box 3327 Tehran-Iran

ABSTRACT

Dielectric Nuclear Track Detectors (DNTDs) are used for the detection
and identification of charged particles $1 \le Z \le 92$ for such measurements as
absolute fission rates and fission cross sections in reactor cores, and
high background γ-ray fields. Comparative range measurements and simula-
tions employing accelerators have been made showing that above certain γ-
ray dose level, reduced particle registration sensitivities lead to erro-
neous results in ranges. A prospective study based on the effect of Co-60
γ-rays on Am-241 alpha-particles (5.48MeV) is made predicting variations
in sensitivities. Activation energies of 0.44-0.5ev and diffusion coeffi-
cients for γ-ray induced annealing and range contraction are calculated.

INTRODUCTION

Examples of charged particle induced annealing in dielectric mate-
rials were first observed in mineral crystals[1,2] and plastic dielectrics[3].
Thus samples irradiated with charged particles were either pre-or-post ir-
radiated with doses of up to 10^{17} protons/cm^2 at 10Mev/nuc, causing reduc-
tions in nuclear track registration and retension efficiencies. Energy
resolution of various detectors is generally dependent on the stopping

power of a material and the critical energy loss rate, $(dE/dx)_{critical}$[4]. Under normal conditions of track registration, the lightest particles ${}^A_Z X$ have an entrance energy at the detector surface that is $\geq$ the threshold energy $(dE/dx) \geq (dE/dx)_{crit}$. As such stopping power and $(dE/dx)_{crit}$ data are used for charge Z, and energy E, determination. The ensuing γ-ray induced annealing and the accompanying changes in $(dE/dx)_{crit}$ have been measured for He-4, in a cellulose nitrate detector, CA80-15*, $(C_6H_8O_9N_2)$. An attempt is made to account for the processes resulting in range contraction; this often causes difficulties and ambiguities attendant to the numerical specification of the effect[5]. A greater difficulty is that the complex reactions of the activated species (electron-holes) created by polymeric chain breakage due to secondary electrons, implicate too many free parameters to allow valid conclusions. These difficulties are reduced or eliminated if one considers a dose-LET relation for the energy loss in a nuclear track. In this case there is no need to find or construct a numerical scale of effect for predicting the extent of γ-ray annealing, as one asks by definition only, for equality of the effect. Therefore both coordinates in a graph of dose versus percentage track retention Fig(1) refer explicitly only to physical quantities.

Experimental Procedures

Samples of the detector CA80-15, 100μm, thick and one cm^2 area were exposed to 5.48MeV, Am-241 alpha-particles. Irradiations were made in a vacuum chamber at 45° and 90° to the detector plane using a collimator. Detectors were then exposed to Co-60 γ-rays for various exposure times and doses. Etching solutions were 25% NaOH at 60°C. Following selective chemical etching the ranges were measured using an optical microscope at 900X.

Annealing (range-contraction) and empirical relations

The use of an appropriate detector with an optimum sensitivity to

*CA80-15 made by Kodak Pathe' France

light charged particles e.g. 1=Z, is a powerful tool in terms of charge and energy resolution. Thus quantitative data about such parameters as E_{crit} (critical energy of registration) and R_{max} (maximum etchable range) are necessary for charge and energy identification. Hence the etching velocity along the track V_t increases exponentially with (dE/dx) such that

$$V_t = V_b \exp \quad a \quad \{ (dE/dx) - (dE/dx)_{crit} \} \quad /Kt \qquad (1)$$

V_b is the bulk etching rate, $(V_t = V_b/Sin\ \theta)$, θ is the angle of incidence and a, is a constant, for the etching solution. Therefore tracks will not be etched in the detector where particle energy E exceeds E_{crit}. Therefore, particles will register at the detector surface only when $E_0 = E_{crit}$ and a particle with $(E_{crit} + \Delta E)$ will need to cross a thickness Δx and lose energy ΔE, so that after a given etching time $t = \Delta x\ sin\theta/V_b$ tracks may be revealed. Empirically, Δx can be defined as $\Delta x = (E_0 - E_{crit}/(dE/dx)_{ave}$. Hence γ-ray annealing affects the track length by increasing ΔE. For a given γ-ray dose, ΔE_{max}, is the maximum sub-ionization energy lost before the particle can be observed, after a required etching time t,

$$(\Delta E)_{max} \simeq (V_b t/Sin\ \theta) \quad (-dE/dx)_{average} \qquad (2)$$

Ploting the range-energy curves, (dE/dx) average for alpha-particles in CA80-15 have been measured[3] as 1.4Mev $mg^{-1}\ cm^2$.

Results

Figures (1 and 2) show the effect of γ-ray doses, for Am-241 alpha-particles and comparative values for the different quantitative parameters are provided in table (1). The sudden increase in V_b at 30MRad corresponds to a change in the irregular layered structure of the polymer chains becoming more ordered[3]. The probable threshold for Co-60 γ-annealing can be set at around 300K Pads, and the extrapolated upper limit lies around 75 MRad whence tracks are completely annealed and the detector is increasingly crystalline. Thus E_{crit}. for Am-241, α-particles at
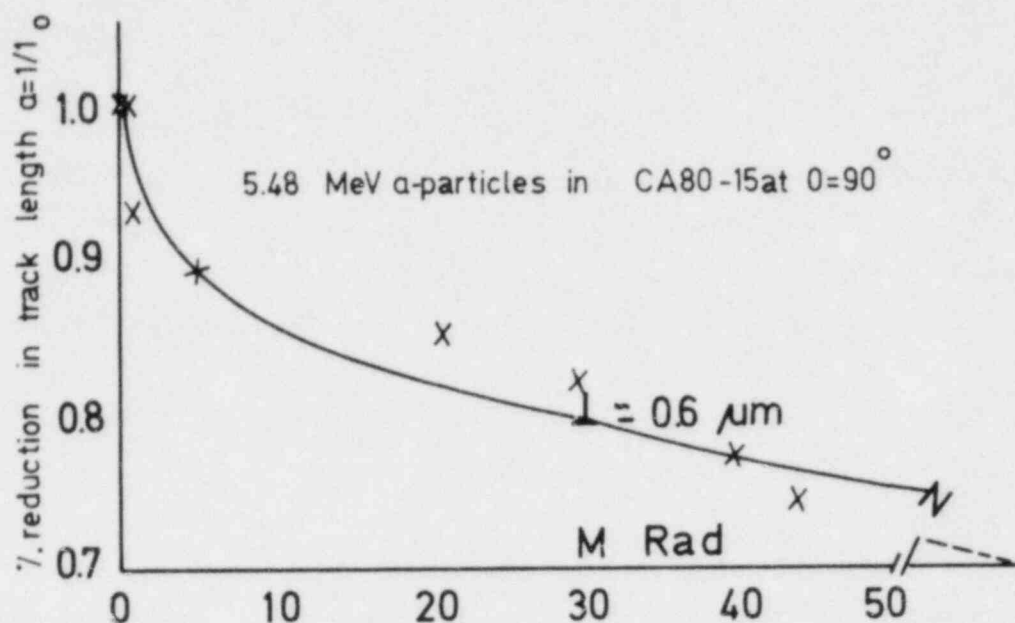
Fig.(1). percentage retension in track length as a function of gamma-ray dose.

$\theta=90^o$ is reduced from 5.48 MeV at some 500 KRads to 4.13MeV, at 43.6 MRad, corresponding to a decrease in sensitivity $(dE/dx)_{crit}$ (at $E_o=5.48MeV$) of 0.84 to 0.98MeV mg^{-1}, cm^2, and at $E_o=0$, of 0.7 to 0.88MeV mg^{-1} cm^2, with roughly a third of the range observable.

Quantitative considerations and stimulated range-contraction

Amongest the various processes[5] involved in stimulated γ-ray annealing, the potentials affecting such positive or negative charges within an overall framework of compton electron tracks are considered. Average spacings of 100-500A^o have been obtained for electron holes (and/or activated
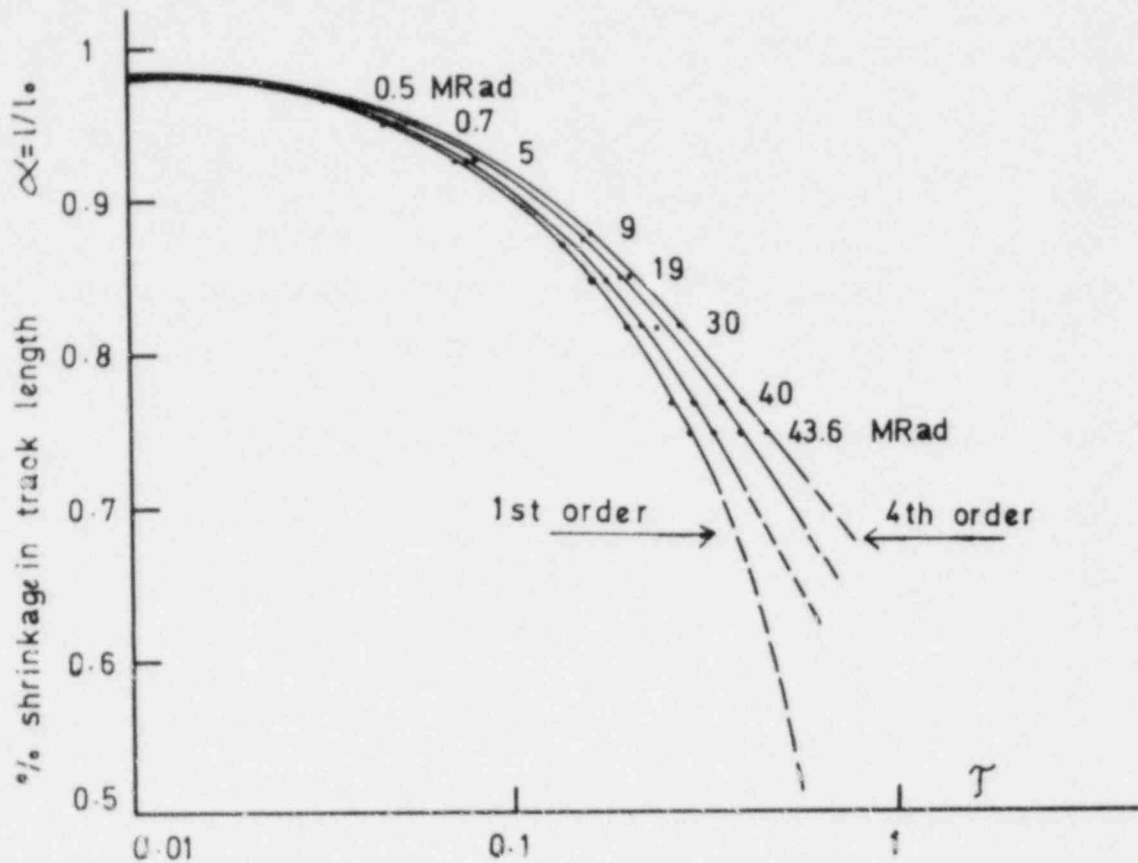
Fig.(2) Co-60, γ-ray annealing of α-tracks in CA80-15 at θ=90° and 300°K for 1st to 4th order rates, n=1 to n=4.

radical species), and F-centers of 4500Å°, for an absorption of one Rad. Such energy deposition interrupts the overall equilibrium and electrical neutrality of the latent track by creating an abundant supply of carriers needing small activation energies, for reorientation and further recombinations. This will in turn set up small indigenous electric fields predominantly in the peripheral regions of the track leading to preferential annealing. With a rough approximation the field set up by a pair of charge carriers at equilibrium and some 100Å° apart (ε=2 for CN at 27°c), is $E=K q/\varepsilon r^2=7.2X10^5$ Vm^{-1}, where $K=1/4\pi\varepsilon_0=9X10^9$, and $e=1.6X10^{-20}$emu. Assuming that positive and negative charge carriers have a Maxwell-Boltzman distribution of energies and velocities when considered as particles, the RMS of such a distribution is $V_T=\sqrt{3kt/m}$, m being the effective mass of the carrier, (i.e. the free electron). Thus at 300°K, $V_T=1.1X10^5$m. sec^{-1},

yielding an induced charge mobility $\mu = \bar{V}/E = 0.153$ m^2. V^{-1} sec^{-1}. Based on Fick's law, this leads empirically, to a diffusion coefficient $D = (KT/q)\mu = 3.96X10^{-2} m^2$. sec^{-1}, and an electron jump frequency, $\gamma = 3D/2r^2 = 5.94X10^{14}$ sec^{-1}. With Co-60, yielding compton recoil electrons of $E_{ave} = 577$ KeV[6], the total energy deposited/cm^3 from one Rad is $8.74X10^{10}$ KeV/cm^3. Assuming a value, $N = 5X10^{11}$ active centers/cm^3 in a latent track at equilibrium, it will be observed that even though the field sustained is somewhat decreased $(2.88X10^6$ $V.m^{-1})$ by a dose of one Rad the jump frequency is not significantly affected at this dose, being $\gamma = 5.93X10^{12}$ Sec^{-1}. The density of the active centers however increases from $5X10^{11}/cm^3$ at one Rad to $2.2X10^{19}$ at 44 MRad. Indeed the increased track annealing potential (decreased registration efficiency) at high γ-doses are related to increased charge mobility. Suzuoki, have suggested that oxidation products, such as the main carbonyl (C=O) stretching mode in the IR region[11] at 1720 cm^{-1} act as localised centers and deep traps by which the hopping transport of the "injected electrons occur". Hence according to the simple hopping transport theory, the mobility μ, can now be expressed as: $\mu \alpha$ E^{-1} $sinh$ $(q\lambda/2KT)$, where E is the field induced and λ the hopping distance. Using an applied field of 2-$6X10^5 V.cm^{-1}$, Fischer[9], have obtained a hopping distance of some $10\overset{o}{A}$ for a plot of $\log$ $\mu Vs.E$ whose slope indicated λ. This is the value employed by us[5], assuming a radical concentration of $5X10^{18} cm^{-3}$ in a track with a monomer diameter of $10\overset{o}{A}$ or a mean ion spacing assuming uniform distribution of 10 nm after a dose of one MRad. This and our diffraction studies[3], comfirm our assumed dimensions, indicating an essential correlation with the results of Hannay[6], that tracks have not been found in semiconductors having mobilities above 150 cm^2 V^{-1}. Sec^{-1}, and between 35 to 150cm^2 V^{-1} Sec^{-1}, for track forming thin films[7], of $MoSe_2$, $MoTe_2$ and WTe_2. All higher doses, (greater % crystallinity) injected electrons and the thermal release of space charges captured by physical traps in the crystalline regions[8], are likely to move across these regions and counter, track registration. Thus we have calculated[10], activation energies for annealing of α-particles at $300\overset{o}{K}$, of 0.46 eV to 0.5eV for γ-doses of 0.5 to 44 MRads at $\Theta = 90^o$, and 0.4 eV to 44eV at $\Theta = 45^o$.

Table (1) Characteristic Range Contraction for Am-241 α-particles in CA80-15, at θ=90°, etched in 25% NaOH at 60°C.

Dose MRad	V_b μm/min	ΔX Expt. μm	E_c MeV	E_o-E_c MeV	ΔX_{max} Mev	ΔX Theo. μm	Range Annealed at E_o 5.84 μm	at E_o 0 μm	Increase in $(dE/dx)_c$ at E_o=5.48 MeV cm²/mg	at E_o=0 MeV cm²/mg	Observed Track length μm	α=t/L_o
43.5	0.39	6	4.13	1.35	0.617	6.89	6	1.5	0.98	1.22	22.5	0.75
40	0.36	5.4	4.35	1.13	0.54	5.76	5.4	1.4	0.96	1.18	23.2	0.77
30	0.29	4.2	4.64	0.84	0.42	4.3	4.2	1.1	0.91	1.03	24.7	0.82
21	0.24	3.5	4.94	0.65	0.36	3.32	2.5	0.9	0.9	0.88	25.6	0.85
9.7	0.2	2.9	5.07	0.47	0.29	2.4	2.9	0.6	0.88	0.78	26.5	0.88
5	0.18	2.6	5.16	0.38	0.26	1.94	2.6	0.5	0.88	0.64	26.9	0.896
1	0.14	2	5.27	0.26	0.20	1.33	2	-	0.88	0.64	28	0.93
0.7	0.13	1	5.38	0.1	0.1	0.5	1	-	0.86	0.64	29	0.966
0.5	0.13	-	5.48	0	0	-	-	-	0.84	0.64	30	1.00

The following parameters relate to table (1)

$\Delta x=(E_o-E_{crit})<-(dE/dx)>$ ave. $\Delta x_{max} = (v_bt/Sin\theta)/<-dE/dx>$ ave.

$E_o=E_{critical}$ $(dE/dx)_c = (dE/dx)_{critical}$

$t=12$ mint. $(-dE/dx)ave = 1.4$ Mev mg⁻¹. cm²

Conclusion

The onset of γ-ray induced annealing of particle tracks in SSNDTs is found to be some 400 KRads. Thus in studies of (n,f), (n,α), particle recoil/intrinsic neutron dosimetry and/or γ-heating monitors in γ-ray fields the necessary corrections for particle or enhanced, reductions in ranges and/or track registration efficiences should be carried out.

Reference

1. S.A, Durrani, H.A., Khan, S.R. Malik. A. Aframian. Proc Lunar Sci. Conf. 4th, P.2291-2305 (1973)

2. A. Aframian, Lunar and Planetary Sci. 10th Abs. Pt. I,P. 4-5 (1979)

3. A. Aframian, Appl. Phys, 19. P-353-358 (1979).

4. H.A. Bethe, Ann. Physick, 5, 325 (1930).

5. A. Aframian, Appl. Phys. 25,337-345 (1981).

6. N.B. Hannay (ed) "Semiconductors", New York: Reinhold Press (1959)

7. J.A. Wilson and A.D. Yolf. Adv. Phys. 18,193-335. (1969)

8. T. Mizutani, and M. Idea. J.Phys. D: Appl. Phys. 11,185-91, (1973) and 12,291-6, (1979).

9. P. Fischer and P. Rohl J. Polym Sci. Polym Phys. Ed. 14,531 (1977)

10. A. Aframian. Radiat Eff. 23, 95. (1977).

11. Y. Suzuoki, K. Yasuda, T. Mizutani and M. Ieda, J. Phys. D: Appl Phys 10, 1985-90 (1977).

12. J.P. Moliton, C. Boutinaud, J.L. Decossas , J.C. Vasielle, J.L. Teyssier and B. Delunay. Proc. 10th. Int. Conf. Solid State Nuclear Track Detectors, Lyon, 2-6 July (1970) France.

ENERGY DEPENDENT SENSITIVITIES FOR NEUTRONS
OF SOLID STATE RECOIL TRACK DETECTORS

MASAKUNI NARITA, FUMIYUKI FUJITA, KEN-ICHI WADA,*
    Hokkaido University, Sapporo, 060 Japan
KATSUHISA KUDO, TAICHI MICHIKAWA
    Electrotechnical Laboratory, Ibarakiken, 305 Japan

ABSTRACT

Energy dependent absolute sensitivities for neutrons of solid
state recoil track detectors (polycarbonate and cellulose nitrate
foils) were measured with monochromatic neutrons(the energy range of
1.9 MeV to 5 MeV) from D(d,n)He reaction with the ETL Van de Graaff
accelerator. After irradiation and chemical etching, an automatic
track counting system, Luzex 450, counted the number of etched tracks.
The theoretical energy dependent sensitivities were calculated using
the local energy loss theory by R. Katz and E. J. Kobetich and good
agreement with the observed results was obtained.

INTRODUCTION

Polycarbonate and cellulose nitrate foils are capable of detecting
fast neutrons by recording recoil carbon, oxygen and nitrogen atoms
from neutron elastic collisions as well as alpha and recoil particles
from (n,α) reactions. The neutron energy dependent sensitivities of
the recoil track detectors are more complex than those of fission
track detectors, which are determined from the fission cross section.
K. Józefowicz and others have measured energy dependent sensitiv-
ities[1-5]. F. Spurný and K. Turek tried to determine them theoretically
by conducting an experiment at several points of neutron energy.[2]
Their results seemed to show a discrepancy between theoretical and
experimental sensitivities in lower energies (<4 MeV) of neutrons.

The present report describes an experimental determination of the
neutron energy-dependent sensitivities of polycarbonate and cellulose
nitrate foils in detail in the energy range of 1.9 - 5 MeV. These
results were compared with the sensitivities calculated from the
threshold energy for track formation, which were determined by the
local energy loss theory by R. Katz and E. J. Kobetich.[6]

---

* present address ; Japan Atomic Power Co., Tokai-mura, Ibaraki-ken,
  319-11 Japan

EXPERIMENT

Several sheets (2.5 cm x 52cm) of polycarbonate (Teijin Takiron PC-1600, 500 μm) and cellulose nitrate (Kodak LR-115 type II, 13 μm) were mounted on an aluminum ring holder and placed at a distance of 10 cm from a deuteron target on the Van de Graaff accelerator at Electrotechnical Laboratory as shown in Fig. 1. Consisting of TiD on a
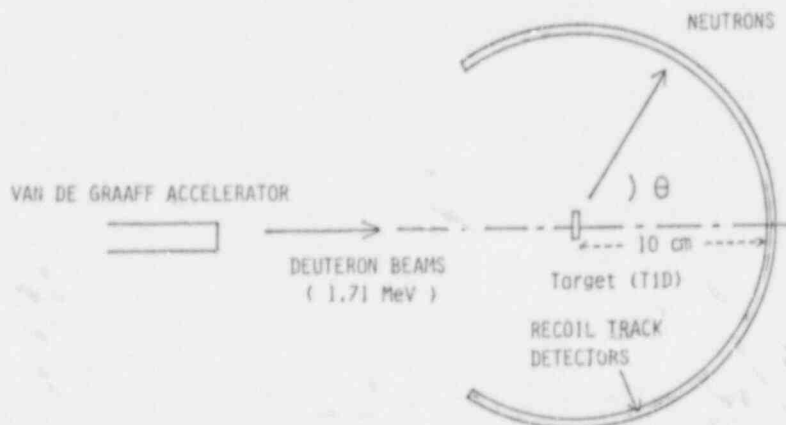
Fig. 1 Experimental arrangement for the sensitivity determination of recoil track detectors.

0.25 mm Ta backing, the target has a thickness of 270 μg/cm². Deuteron beams of 1.71 MeV from the accelerator were bombarded with the target. The energy of neutrons emitted at an angle θ to the direction of the motion of the deuteron beams is given by

$$ En = [\frac{\sqrt{2Ed}}{4} \cos\theta + (\frac{1}{8} Ed \cos^2\theta + \frac{3}{4}(Q + \frac{1}{3} Ed))^{1/2}]^2 , \quad (1) $$

Where Ed is the energy of the deuterons and Q is the Q value of D(d,n)He reaction (3.26 MeV). A standard neutron yield was measured by a semiconductor detector with a polyethylene radiator, which is the Japanese standard measurement system of fast neutrons.[7] The emitted neutron energy and the fluence are 4.935 ± 0.0085 MeV and 1.535 x 10^12 n/sr respectively at θ = 0°. The equation (1) shows that the measurable neutron energy range in this experiment is 1.9 - 5 MeV. The neutron yields of the D(d,n)He reaction were calculated from the differential cross section at Ed = 1.71 MeV(Fig. 2).

After irradiation, the polycarbonate sheets were etched at 70°C in 30% KOH solution for 15 minutes. The cellulose nitrate films received a 300 minutes etch at 50°C in 10% NaOH, enough to make through etched tracks. The diameters of the tracks on PC-1600 were nearly 1 μm and those of LR-115 holes, 1-10 μm.

The number of etched tracks were counted with an automatic track counting system, Luzex 450, manufactured by Nihon Regulator Co., LTD (through-etched tracks only for LR-115).

The measured energy dependence of the neutron sensitivity K(E) is
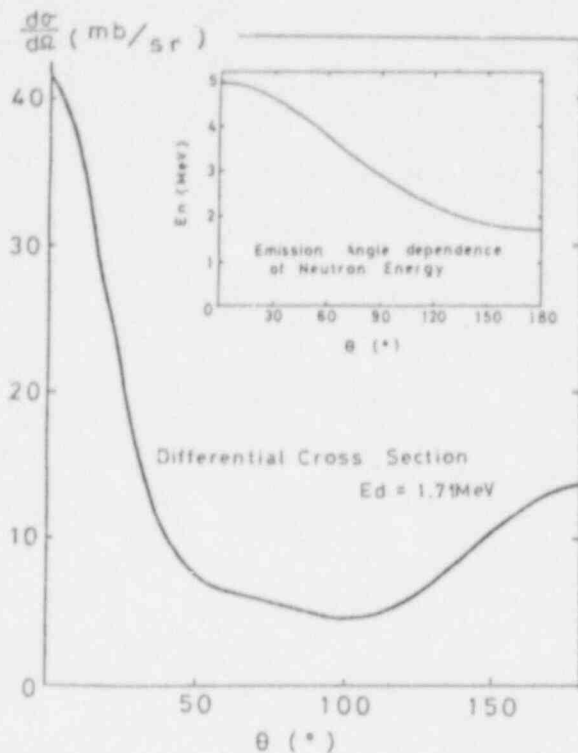
Fig.2 D(d,n)He differential cross section and the emission angle dependence of the neutron energy Ed = 1.7 MeV.

shown by the broken line for the polycarbonate PC-1600 in Fig. 3 and for the cellulose nitrate LR-115 in Fig. 4.

THEORETICAL ESTIMATION OF THE SENSITIVITIES

The detectable ion density $R^*(E)$ of the recoil track detectors is given by

$$R^*(E) = \sum_i Pi(E) \cdot Ri(E) \quad (2)$$

where $Ri(E)$ is the secondary particle density of the i-th type generated in the reactions caused by neutrons with an incident energy E, and $Pi(E)$ denotes the probability that the secondary ion of the i-th type has a kinetic energy capable of forming an etchable track.

In their local energy loss theory, R. Z. Katz and E. J. Kobetich have proposed the

Table I Minimum and Maximum Energies of Detectable Secondary Particles Estimated by Katz and Kobetich's Theory

		Minimum Energy Emin (MeV)		Maximum Energy Emax (MeV)
POLYCARBONATE				
C-12		0.32	(1.14) *	43.2
O-16		0.37	(1.66)	96.0
He-4 }	O(n,α)	C.22	(3.65)	1.24
C-13 }		0.35		46.8
CELLULOSE NITRATE				
C-12		0.24	(0.85)	149.
O-16		0.32	(1.44)	320.
N-14		0.28	(1.13)	216.
He-4 }	N(n,α)	0.10	(1.02)	4.95
B-11 }		0.22		88.0
He-4 }	O(n,α)	0.10	(3.65)	4.95
C-13 }		0.26		161.

* (---) : Lower limit of the neutron energy corresponding to Emin.

criterion for determining etchable track formation using several ion species in plastic detectors. According to the criterion, the secondary ions can produce etchable tracks only when their kinetic energies lie in a range between the maximum and the minimum values shown in Table I. Detectable neutron energies are determined from the $P_i(E)$ corresponding to these energy ranges of ions in Table II.

From these results the detectable densities $R^*(E)$ were calculated and also shown by curved lines in Fig. 3 for PC-1600 and Fig. 4-(a),(b) for LR-115.

Table II Probability that the Secondary Particle Generated from i-th Type Reaction Has a Kinetic Energy Capable of Forming Etchable Track

Neutron Energy E	Elastic Scattering — Detectable Neutron Energy $E-E_{max} < E < E-E_{min}$	$P_i(E)$
(a) $E < \dfrac{E_{min}}{1-\alpha_i}$	$P(E \cdot E')$ graph with level $\dfrac{1}{(1-\alpha_i)E}$; axis marks $E-E_{max}$, $E-E_{min}$, $\alpha_i E$, E	0
(b) $\dfrac{E_{min}}{1-\alpha_i} \le E \le \dfrac{E_{max}}{1-\alpha_i}$	$P(E \cdot E')$ graph with level $\dfrac{1}{(1-\alpha_i)E}$; axis marks $E-E_{max}$, $\alpha_i E$, $E-E_{min}$, E	$1 - \dfrac{E_{min}}{(1-\alpha_i)E}$
(c) $\dfrac{E_{max}}{1-\alpha_i} < E$	$P(E \cdot E')$ graph with level $\dfrac{1}{(1-\alpha_i)E}$; axis marks $\alpha_i E$, $E-E_{max}$, $E-E_{min}$, E	$\dfrac{E_{max} - E_{min}}{(1-\alpha_i)E}$
All neutron energy	(n,α) Reaction $\cos\theta_1 = \dfrac{M_a(E_{min}(1+\frac{M_R}{M_a}) - E(1-\frac{M_R}{M_a}) - Q)}{2\sqrt{M_a E\, M_a E_{min}}}$ $\cos\theta_2 = \dfrac{M_a(E_{max}(1+\frac{M_R}{M_a}) - E(1-\frac{M_R}{M_a}) - Q)}{2\sqrt{M_a E\, M_a E_{max}}}$ sufix M_a:neutron mass, a:α-particle, R:residual nucleus	$\dfrac{\int_{\theta_1<\theta<\theta_2} \frac{d\sigma}{d\Omega}\, d\Omega}{\int_{4\pi} \frac{d\sigma}{d\Omega}\, d\Omega}$ Isotropic Scattering $\dfrac{\cos\theta_1 - \cos\theta_2}{2}$

DISCUSSION AND CONCLUSION

Figure 3 shows the energy dependence of the measured sensitivity and the detectable ion density $R^*(E)$ of the polycarbonate detector. The theoretical values agree well with the observed results in the experimental energy range; Józefowicz's results (En < 2.2 MeV) are shown by the cross in the same figure. His data also show a shape similar to our calculation except for the absolute values, which depend on etching conditions. The sensitivity K(E) increases with neutron energy E when E < 3.8 MeV and decreases gradually above this energy.

For cellulose nitrate LR-115, shown in Fig. 4(a), the experimental sensitivity obtained from the through-etched tracks does not agree with the theoretical $R^*(E)$, which was calculated for all kinds of the secondary particles (Z ≧ 2) produced. The through-etched track can be produced by secondary charged particles with a long range. Alpha particles generated from $^{14}N(n,\alpha)^{11}B$ and $^{16}O(n,\alpha)^{13}C$ reaction in cellulose nitrate are responsible for the through-etched tracks in our experiment.[8] The $R^*(E)$ obtained by using only α-particle is shown in Fig. 4(b); as shown, the agreement of the theoretical and experimental sensitivities for LR-115 is good in this case. Detailed discussion of the through-etched track considering the foil thickness will be reported by T. Sawamura in the near future.[11]
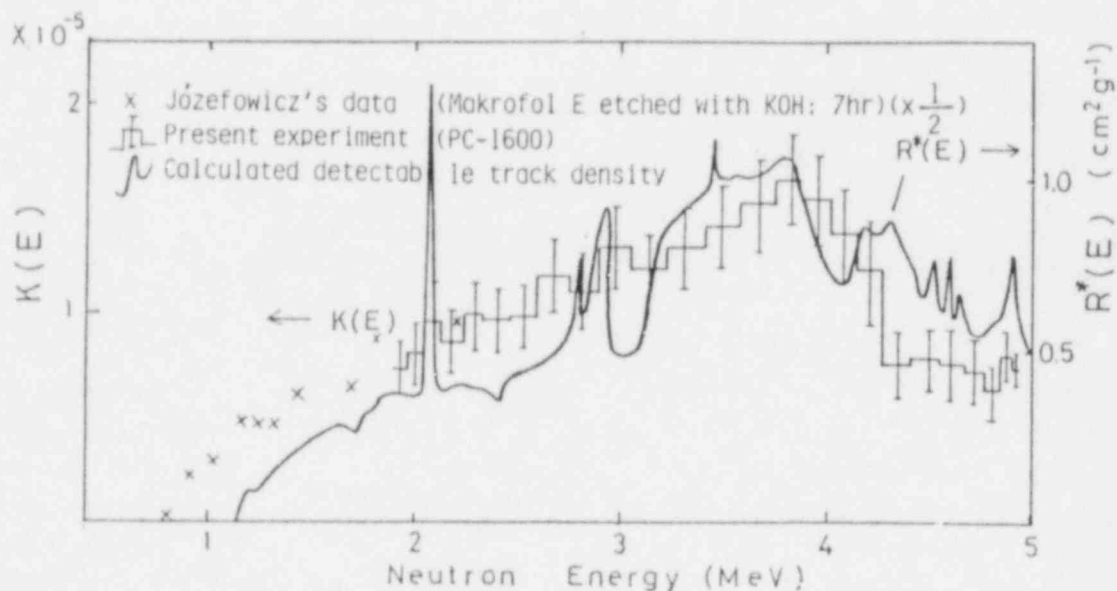
Fig. 3 Experimental sensitivity K(E) and detectable track density R*(E) for polycarbonate PC-1600.
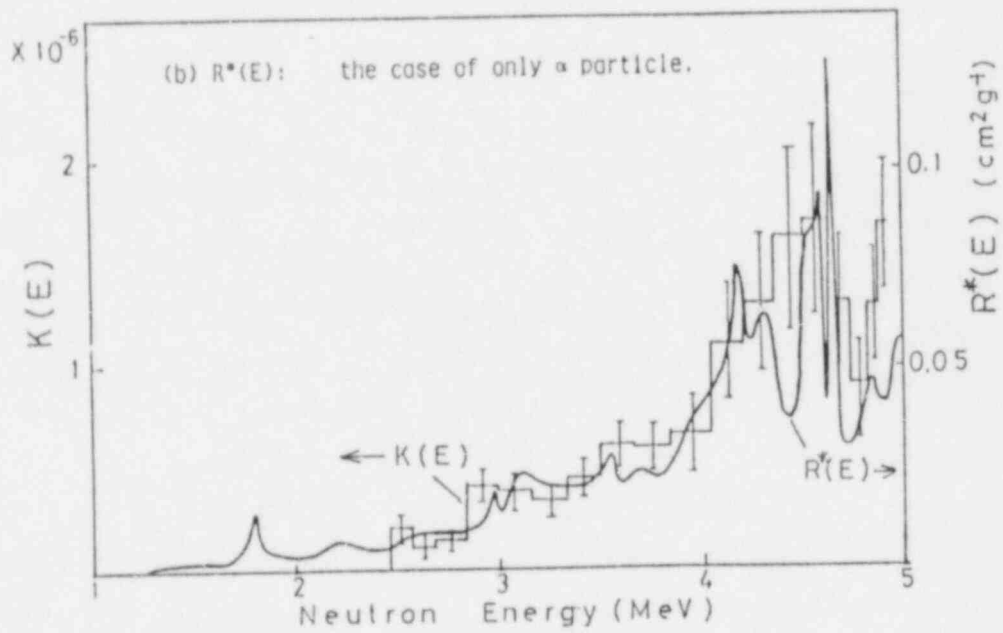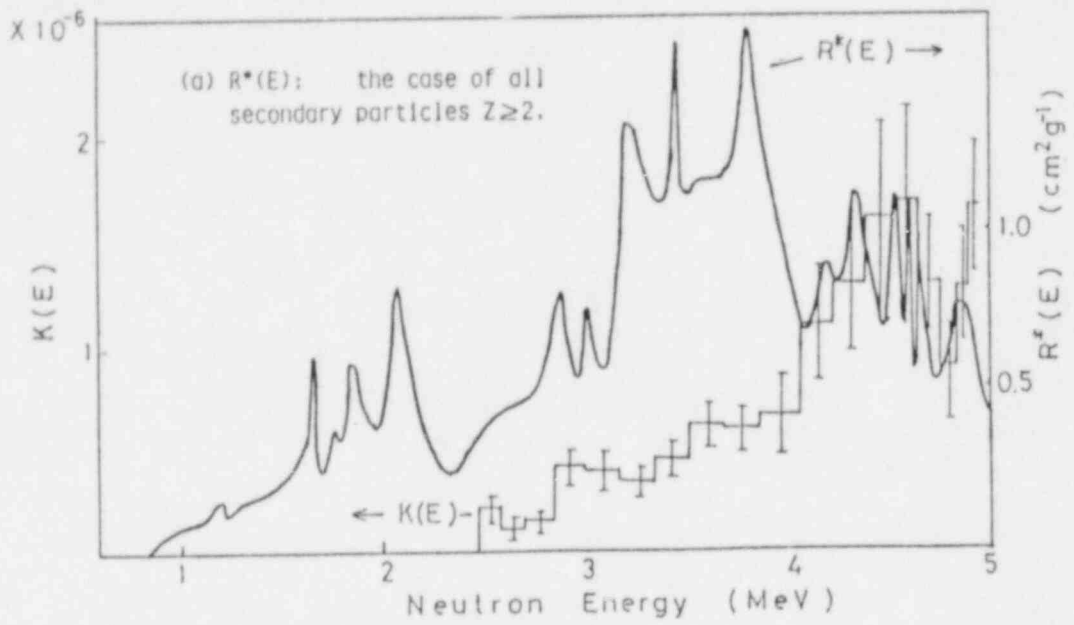
Fig. 4 Experimental sensitivity K(E) and detectable track densities
R*(E) for cellulose nitrate LR-115.
(a) R*(E):   the case of all secondary particles Z≥2.
(b) R*(E):   the case of only α particle.

The difference of the absolute sensitivities between various counting methods is shown in Fig. 5. This value suggests that for absolute fluence determination such as neutron dosimetry, it is advisable to compare results with a reference detector exposed in a standard neutron field.

Though F. Spurný and K. Turek selected several lower threshold energies of the secondary ions arbitrarily, the present experiment and results show that the minimum and maximum energies obtained by R. Katz and E.J. Kobetich's theory are accurate indicators and can be used reliably.

We have successfully used the solid state recoil track detectors for reactor physics experiments using the fast neutron source reactor "YAYOI" installed in the university of Tokyo.[10]
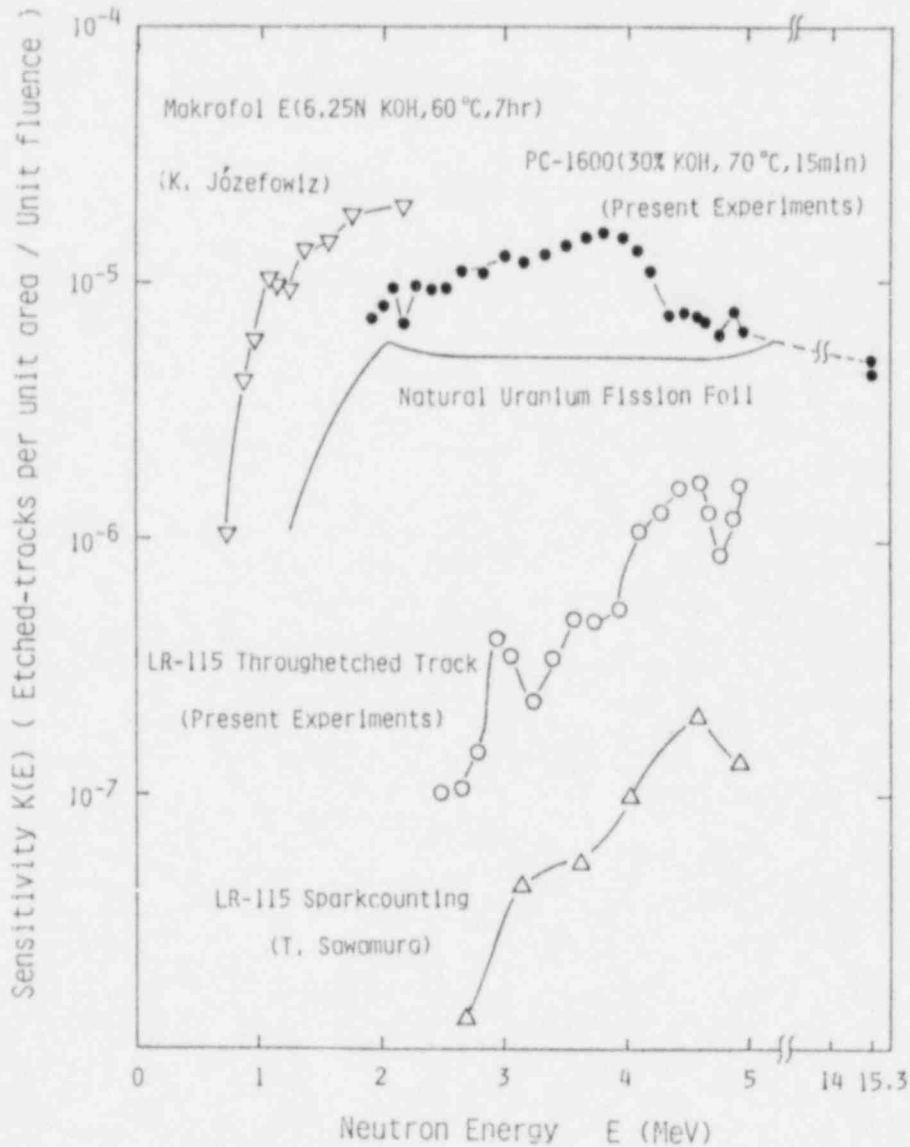
Fig. 5 Comparison of absolute sensitivities for several detectors and counting methods.

REFERENCES

1. K. Józefowicz, Proc. IAEA Symp. on Neutron Monitoring for Radiation Protection Purposes, Vienna, Vol. II 183 (1973).

2. F. Spurný and K. Turek, Nuclear Track Detction, 1, 189 (1977) and also Proc. 9th Conf. SSNTD Vol. 2, Pergamon 863 (1976).

3. G. M. Hassib, S. A. Kasim and E. Piech, Radia i /n Effects, 45 57 (1979).

4. Y. Eisen, Z. Karppinowitz et al., Health Physics 38 479 (1980).

5. M. Narita, on Solid State Nuclear Track Detectors, - Neutron Sensitivities and Applications to Reactor Physics - , Nucl. Eng. Research Lab. Univ. of Tokyo, Report UTNL-R-0084 12 (1977) (in Japanese).

6. R. Katz and E. J. Kobetich, Phys. Rev. 170 401 (1969).

7. E. Teranishi, T. Michikawa et al., Bul. Electrotech. Lab. 41 693 (1977).

8. T. Sawamura and H. Yamazaki, Nuclear Tracks 5 (1981) to be published.

9. T. Sawamura, M. Nomura et al., J. Nucl. Soc. Tech. 18 766 (1981).

10. M. Narita, F. Fujita et al., Bul. of Faculty of Eng. Hokkaido Univ. 103 27 (1981) and 107 73 (1982) (in Japanese).

11. T. Sawamura, private communication.

Session B.1
Light Water Reactors-II

SENSE OF DIRECTION: AN OBSERVATION OF TRENDS IN MATERIALS DOSIMETRY IN THE UNITED KINGDOM

M Austin
Rolls-Royce & Associates Ltd
Derby, England.

"Materials Dosimetry" requires no epic discoveries to be made before its successful implementation in relevant areas of nuclear plant evaluation. Rather it needs only the careful and standardised application of existing techniques, underpinned by a rigorous uncertainty analysis. Such application makes it possible to set targets for dosimetry programmes which will be consistent with the uncertainties inherent in other materials evaluation variables.

In spite of this apparently promising prognostic, such an approach does not yet exist for dosimetry applications within the UK. This is not to say that UK dosimetry evaluation is left in the hands of the calculator. Much valuable and detailed experimentally-based analysis has been carried out on UK reactor systems, but to date this has been largely "project based". Little attempt has yet been made to "pool" the experience so gained for the general benefit of UK workers in the field.

This paper therefore summarises important UK dosimetry applications to date and reviews the major areas of present development and investigation. Connections with current international programmes and the advantages of a higher level of interaction among UK workers are discussed. It is argued in conclusion that this increase could be achieved by the establishment of a forum for UK dosimetry comprised of specialists from all projects and reactor types. Besides providing an opportunity for discussion such a Group would allow for the effective dissemination of the results of the development work already referred to, and the definition of standardised techniques. A more effective UK presence on associated international bodies should also result from such an arrangement.

BACKGROUND

The objective of this paper is not to attempt an exhaustive review of British dosimetry practice, but rather to present an observation of its important trends. Originating as it does from one of the smaller organisations within the UK nuclear industry, this view cannot pretend to be entirely representative of the industry. However it is hoped that the experience gained by Rolls-Royce and Associates from significant project commitment to dosimetry studies, as well as collaborative involvement in recent international programmes, serves as a relevant credential for the presentation of a constructive assessment of the UK situation. Similarly suggestions for change in this situation rest upon the observation of their successful application in a wider external sphere.

In considering the international emergence of "dosimetry" (or more correctly, "materials dosimetry") as an established branch of radiation metrology and the markedly different emphasis in its development within the United Kingdom it is more than important to consider the divergence between the UK and other national nuclear programmes and the correspondingly different design problems posed. Before 1979 the UK programme was unique in its overwhelming investment in gas-cooled reactor systems, with a line of development from Magnox through AGR plant. It was only in an early (but continued) interest in the exploitation of the fast-reactor concept that an international point of convergence seemed apparent.

Of the world's production of nuclear power, 70% comes from Light-Water reactor (LWR) systems and of this proportion 10% was installed before 1970. It is the continued safety justification of these older LWR plants, or more particularly their pressure vessels (PV), which has produced the incentive to invest in dosimetry program nes since the mid-seventies. It will be seen that the British system, with different materials problems, has adopted an alternative approach to "dosimetry".

To judge from the recently published literature on the subject one might be forgiven for assuming that the "dosimetrist" was not native to the shores of Great Britain and that all radiation quantities of interest to the materials scientist were calculated to a high degree of confidence by the reactor physicist. (1) (2) From the perspective of the rest of the "nuclear" world, tackling the problems associated with the performance of low-alloy steel pressure vessels, and producing in the process a wealth of published information on materials-related dosimetry development, this may seem to be a fair judgement. However, such a conclusion would underrate the amount of work, from the earliest days of the British programme, which has been carried out in support of the materials problems specific to the UK systems. In particular, in the parallel example to that quoted for low-alloy steel, significant work was carried out to investigate the irradiation effects to be expected from the use of graphite including the production of energy-dependent neutron damage models. (3) The translation of Materials Test Reactor (MTR) data to operating systems by means of these models was made possible by comprehensive radiation field definition both in mock-up assemblies and operating plant, and by making use of calculational as well as experimental techniques.

Thus it would be a mistake to assume that UK "dosimetry" studies were not carried out in the period preceding the 1st ASTM Symposium on Reactor Dosimetry. To the observer, progress in the subject in the UK has been masked by two further factors. Firstly, the investigatory work which has been done has been carried out on a "project" basis; thus work which may be termed dosimetry has been sponsored by specific design and operation groups within the industry (Magnox, AGR, Fast reactor) but little attempt has yet been made to coordinate these efforts for more general outside application. In the second place, the rather flippant earlier reference to the "dosimetrist" in the UK contains more than a grain of truth. In a very relevant opening paper to the Second ASTM-EURATOM Conference (4), Farinelli drew a detailed picture of the overlap between the disciplines of shielding and dosimetry, (and by implication between the shielding physicist and the dosimetrist). Now, nearly five years after that paper was written, the overlap may be judged to be almost complete, with the materials dosimetry problem a special case of the shielding problem in respect of calculational methods and experimental verification. This coincidence is perhaps less apparent in the USA but has to all intents and purposes always existed in the UK, where the problem of defining radiation environments of interest has been the almost exclusive preserve of radiation physics and shielding design groups. Thus as much information on the progress of UK dosimetry may be found in the proceedings of shielding conferences as in those gatherings dedicated to "materials dosimetry" as such. (5) (6) (7).

Having observed a number of differences which have served apparently to isolate British workers from their "LWR-based" colleagues abroad, it should now be noted that there has been a slow but discernible change in emphasis in the UK within the last three to four years. In fact, it is most useful to discuss UK work in the area in two phases: before 1978-9, and since that date. The events which mark this artificial but noticeable division are twofold. The first was a step-change in support and investment in dosimetry development via international programmes, such as the Nuclear Regulatory Commission (NRC) sponsorship of the US Surveillance Dosimetry Improvement Programme (US-SDIP) and European-sponsored PV and shielding benchmark exercises. The collaborative nature of programmes such as these provided fresh opportunities for information exchange. The second event, in 1979, was the declared intention of the British Government to pursue a design of PWR reactor system as an alternative to the AGR design should it be required. With this decision British workers are increasingly coming to terms with what have long been international preoccupations and of these dosimetry is a relevant example.

While seeking to give a broad explanation of the reasons for the somewhat isolated position of UK dosimetry development, as an observer it is also possible to see some of the shortcomings of that position, particularly from the vantage point of collaborative experience from international programmes. Thus in pointing out the project-based nature of the British investigations it is also pertinent to indicate the resulting lack of coordination, standardisation and documentation of techniques which is necessary if new workers are to benefit from past developments. Similarly, in discussing the increased tempo of materials irradiation programmes in British MTR's it is relevant to note that one consequence of this overall lack of direction was the realisation that the standard of characterisation of the neutron spectrum in such facilities was not always consistent with that required by current materials evaluation procedures. Before proceeding to further discussion of these problems it will be informative to review, in broad terms, the scope of the UK dosimetry effort before 1978-9 and more particularly to identify several interesting lines of development since that date.

THE HISTORICAL BASIS OF UK DOSIMETRY

Given the basic differences in the British approach to dosimetry it should also be said that there has always been a strong leaning towards a calculational methodology in assessing neutron field characteristics. These techniques have been subject to careful validation, using zero-energy assemblies (in-core) and shield mockup and benchmark arrays (out of core). This is in marked contrast to the more "international" approach to dosimetry where a great reliance on direct experimental measurement can be observed. Thus while given early consideration in the UK, the development of multiple-foil activation techniques as embodied in the original SAND code (8), was not pursued in the UK where accurate calculational prediction of a few relevant and experimentally-measured reaction-rates was preferred.

This general approach to field characterisation was applied consistently to the various generations of plant design where materials data have been required. In the first Magnox design, which incorporated a steel pressure vessel, estimates of damage fluence were made from calculations employing the developing removal-diffusion method by way of the COMPRASH code. Checks of the calculation were made with a range of threshold foil measurements, both within the vessel and in the cavity. It was concluded that no limiting steel damage problem existed due mainly to the size of the graphite reflector and the consequently low vessel-wall fluxes (5). Surveillance specimens of PV steel were included in the early Magnox plants but details of these or, indeed, associated dosimetry are not freely available. A recent reanalysis of vessel exposure using a cavity 'long-wire' activation detector, and compared with Monte-Carlo calculation, has confirmed the earlier predictions.

The change to a concrete vessel design in the later Magnox plants confirmed the performance of graphite (as an in-core material) under irradiation to be the principal UK material problem. The introduction of the AGR design, still with concrete vessel but with significantly increased core power-rating, served only to increase the emphasis on its investigation. Extensive studies of the AGR system have been, and continue to be, carried out. Once again the materials evaluator has been able to rely on a strong calculational base linked to measurements in low-power core mockups, shield test assemblies and direct experiment on the operating plant. These studies have brought with them significant developments in calculational methods including more flexible extensions of 'adjusted' diffusion theory and multi-dimensional Monte-Carlo techniques. It is these developments which form the basis of the codes currently used in UK dosimetry analysis. (9) (10). Investigation of the graphite damage problem produced the earliest theoretical and semi-empirical damage models. The model now regarded as the international standard was due to Thompson and Wright (11), the latter providing damage fluence estimates for the DIDO test irradiations by way of nickel activation measurements and a spectrum analysis in which the Monte-Carlo code, SPEC, was used.

It is with the adoption and continuing development of the Fast-reactor system that the closest points of convergence between the UK and other international nuclear interests may be observed, as far as dosimetry is concerned. In general, the British approach has been consistent: faced with novel materials-effects problems in the new environment, particularly in-core, comprehensive calculational techniques have been developed which, linked with extensive zero-power studies in the ZEBRA mockup at the Atomic Energy Establishment, Winfrith (AEEW) are capable of producing high-confidence estimates of relevant damage parameters. By the mid-seventies a considerable amount of work had been carried out by Nelson and others (12) based on atomic displacement models, and these were considered adequate to account for the observed material property changes in the structural components of the fast-reactor core. Thus by the time of the 1st ASTM-EURATOM Symposium a British contribution to "reactor dosimetry" was heralded by a paper on fast-reactor damage analysis by Etherington. (1) However, this paper did much at the time to condition a view that, in British terms at least, dosimetry was a subject wholly amenable to treatment by calculation within the currently-defined target accuracies, provided that the important link between method and zero-energy validation was maintained. This approach was reiterated at the 2nd ASTM-EURATOM Symposium by Sanders (2), although by this time it was more fully accepted that such apparent confidence could be extended only to problems within the core boundary. Beyond this point it would be necessary to have recourse to a combination of calculation and passive dosimetry measurement, since the geometrical complexity introduced by the presence of reactor structures made impractical the calculational prediction of damage or flux parameters to the required accuracy. More stringent definition of target accuracies for fast-reactor damage analysis, coupled with the probable requirement for validated dosimetry within the experimental Demountable Sub-assemblies (DMSA) of the Prototype Fast Reactor, (possibly by 'outside customers'), has led to a reappraisal of dosimetry needs within the project. Perhaps the clearest published statement of the problem and its resolution is contained in the paper by Butler et al (13), to the BNES Conference on 'Radiation Protection

and the Fuel Cycle'. The paper reported extensive experimental work carried out in the PFR and made use for the first time of spectrum-adjustment techniques by way of the SENSAK code. In discussing the 'complementary roles' of calculation and experiment in the new situation of tighter target accuracies Butler defined a revised approach to the dosimetry problem in which the techniques employed would be dependent on the location of interest. With the exception of 'in-core' locations it was concluded that only by a judicious combination of calculation, measurement and adjustment of the two where necessary, could the required assessment be made of flux and damage parameters and their associated uncertainties.

Nine months before the conference the NRC-sponsored Surveillance Dosimetry Improvement Programme had been launched; within a year of the conference the British Government had announced its intention to pursue a PWR design as a possible alternative system for the third phase of the UK nuclear programme.

PRESENT DIRECTIONS

From the time of the Petten Symposium there has been a growing awareness of the need for a more formalised approach to dosimetry application within the UK nuclear industry. Despite this, the only attempt to coordinate resources has been the establishment of a Fast-Reactor Working Group on Dosimetry; other initiatives have therefore continued along independent lines. In reviewing the directions being taken by the British groups, it will be convenient to consider the work involved under five headings:-

(i)   Development of Calculational Techniques
(ii)   Benchmark Validation of Techniques
(iii) The NESTOR Dosimetry Improvement Programme
(iv)   Radiation Sensor Development
(v)   Reactor Environment Characterisation

Development of Calculational Techniques.

Maintaining that the practice of modern dosimetry involves the application of existing techniques of calculation (and measurement) to a more tightly-defined situation rather than the development of entirely novel solutions, British workers have been fortunate in being able to draw on the results of twenty years of radiation physics and shielding methods expertise. Originating mainly in the Radiation Physics and Shielding Group at the Atomic Energy Establishment, Winfrith (AEEW), the methods development has followed a route which (again for historical reasons) is different in character from similar developments in Europe and the USA. British techniques rest on a base of computer codes embodying three-dimensional Monte-Carlo and 'adjusted' diffusion theory methods rather than the more universally adopted discrete-ordinates. These methods have been adopted for and adapted to the needs of dosimetry application by groups such as AEEW and Rolls-Royce and Associaties (RR&A) using experience gained in shield design studies. The recent development of a cross-section sensitivity processor to the Monte-Carlo shielding code MCBEND (14) has enabled the RR&A and AEEW groups to embark upon a revised technique for the estimation of through-life PV damage accumulation, within which the high quality neutron flux calculation will be tied to activation measurements of neutron spectrum which may be made in a pressure vessel cavity.

RR&A have been participating since its inception in the NRC-SDIP and techniques referred to above were used in a joint RR&A/AEEW submission to the PCA "Blind Test" exercise. (15) A similar exercise remains to be completed for the dosimetry/metallurgy irradiation being carried out in the Poolside Facility (PSF) of the Oak Ridge Reactor. As mentioned above, and in addition to their work on transport calculational techniques, McCracken of AEEW has produced a "third generation" spectrum-adjustment code, SENSAK (16), broadly equivalent to STAY'SL (17) and LSL (18). This code has been used by RR&A to produce an entry for the IAEA Spectrum Adjustment exercise, code named "REAL-80" (19). Since the computer codes described can be, and have been, used in the most complex of reactor situations, it is considered that the principal calculational tools required for dosimetry evaluation within the UK are available and are in a well-developed state.

Benchmark Validation of Techniques

The confidence expressed in the status of calculational methods development rests squarely on the thoroughness with which the codes concerned have been validated against high-quality "benchmark" measurements in directly-relevant materials arrays. A series of benchmark or mock-up experiments has been established in the ASPIS facility of the NESTOR reactor at AEE, Winfrith during the past ten years, including most reactor materials and configurations of interest. Based on a 'clean' fission-plate source, the facility is extremely flexible in use, and is amenable to the accurate measurement of neutron and gamma-ray spectra. Thus the Winfrith group were able to contribute a comprehensive study on penetration of fast-neutrons in iron to a European exercise on Shielding Benchmarks. (20) Such measurements have thus made possible the validation of calculational techniques now in use in British shielding and dosimetry programmes.

In addition to the source penetration benchmark facility, ASPIS, a standard neutron field has been established by AEEW on the NESTOR reactor. This facility, known as NESSUS, is situated in the centre of the annular NESTOR core and its schematic arrangement is shown in Figure 1. On completion of characterisation studies the facility will provide a high-flux, benchmark standard field which will be available for a wide range of reference applications from methods-testing to quality control.

The NESTOR Dosimetry Improvement Programme (NESDIP)

As an example of the flexibility of the NESTOR facilities, work is currently proceeding on a dosimetry benchmark experiment (code named NESDIP) which will seek to extend the range of the Pool Critical Assembly (PCA) measurements made at Oak Ridge. The initial phase of the programme (for which measurements are about to begin) will comprise a replica of the PCA array. Components have been
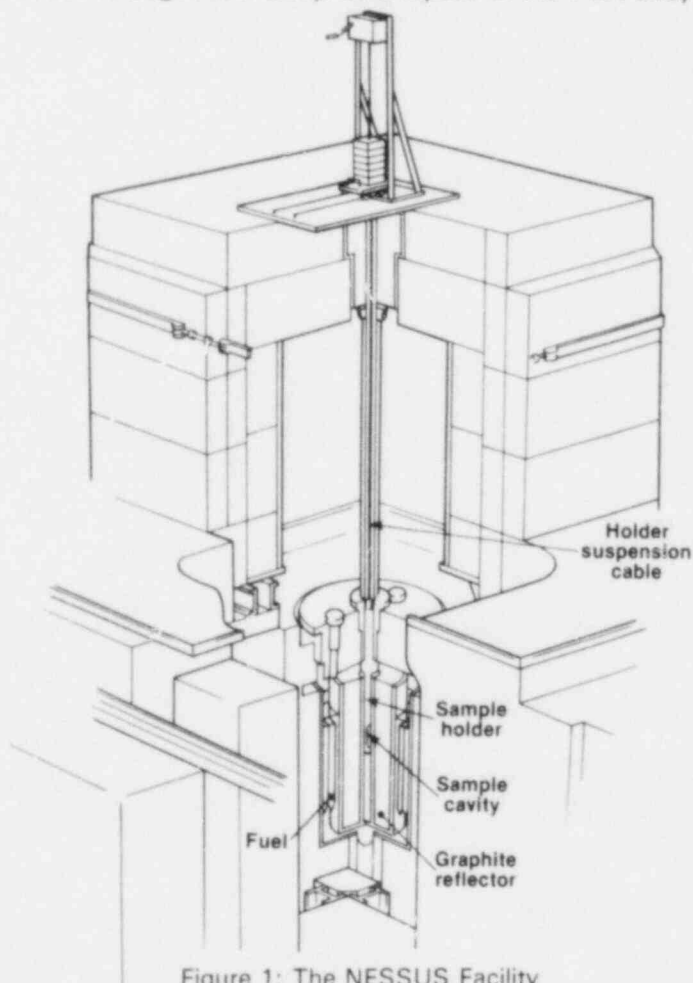
Figure 1: The NESSUS Facility

manufactured in accordance with the original ORNL drawings and a schematic view of the assembly is shown in figure 2. The significant difference between the two arrays however is the replacement of the PCA core by the ASPIS fission-plate. Although the plate has been designed so as to present a cross-section identical to the relevant face of the PCA, this approach will remove from the analysis of the experiment errors due to the representation of the 'core source'.

The objective of the programme is to extend, not duplicate the Oak Ridge work and this will be achieved in two senses. Firstly, in producing measured data, the accent will be on the provision of high-quality spectral information throughout the array making use of well-established Winfrith spectrometry techniques. Inclusion of NE213 scintillator measurements will extend the spectral data well into the MeV range. Secondly, the basic array is obviously capable of flexible extension to investigate a wide range of problems of interest up to and including a full representation of the reactor vessel cavity. The possibility of such extensions will be discussed on the successful completion of the first phase of the programme.

Radiation Sensor Development

In this area significant work is being carried out not only by the established radiation metrology groups within the industry, but also within the universities. Interpreting 'dosimetry' in its widest sense, current projects range from the production of 'tailored' packaging for conventional activation detectors to the measurement of total energy deposition by means of micro-calorimeters. There is space only to summarise the main lines of research and development.

In developing activation detectors for routine irradiation applications, Fudge and co-workers at the Atomic Energy Research Establishment, Harwell, (AERE) have produced a range of specific package designs covering the monitoring of metallurgical specimens in MTRs to spectrum measurement in the PV cavity. Figure 3 shows the package developed for the UK monitoring of the PSF experiment. In the special case of the niobium threshold reaction, the analysis technique originally proposed by Tourwe at Mol in Belgium has now been established as a routine measurement by Taylor at Winfrith. (21) The AEEW group have also carried out closely-controlled irradiations of niobium in different reactor spectra.

Pells and Fudge, at AERE, have completed preliminary feasibility studies on a 'Damage' or 'dpa' monitor based on single crystals of alumina, or 'Sapphire'. The monitor may also be seen in the package of Figure 3, as installed for irradiations in the PSF. Early results of exposure in a variety of environments has shown the device to be extremely stable to effects such as temperature and high gamma-ray background. The energy-dependence of the monitor is demonstrated in Figure 4 where the results of irradiations to date are plotted as a function of 'dpa' in sapphire, using a theoretical displacement cross-section (22). Similar
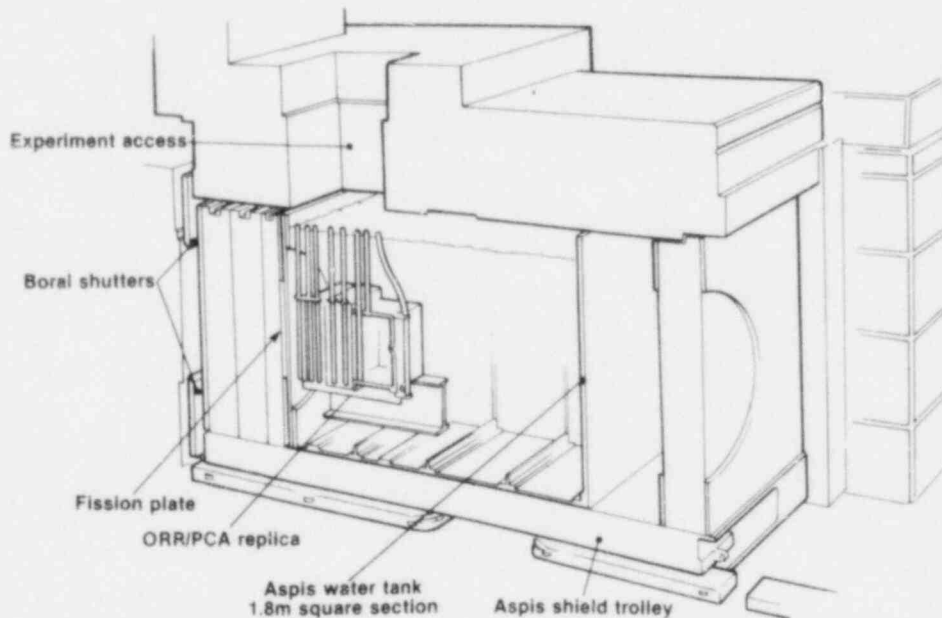
Figure 2: The ASPIS/PCA Replica

attempts at direct damage dosimetry using silicon PIN diodes being carried out at the University of London will be reported at this conference by Mason. (23).

In the field of gamma-radiation detection, several groups are working on the application of thermoluminescent dosimetry (TLD) techniques to the measurement of gamma-ray energy deposition in mixed, neutron and gamma fields. An original exercise carried out by Knipe (24) to measure the gamma-energy distribution within the ZEBRA core, has been followed by similar studies by Lewis, of the Central Electricity Generating Board (25), using beryllium oxide phosphor to measure gamma-ray energy-deposition in AGR graphite reflector material, and a joint project between the Royal Naval College, Greenwich and Rolls-Royce and Associates Ltd, developing a 'thin-film' dosimeter of lithium fluoride in a polyether sulfone matrix. (26). A further, but independent approach to the measurement of total energy deposition has been adopted by Mason and Curl of the University of London, who have developed a micro-calorimeter technique; this work will be the subject of a paper at the present conference (27). Finally, in reviewing the work being carried out by British University groups, mention should be made of the work of Durani et al, of the University of Birmingham, whose developments of solid-state track recorder techniques include current studies aimed at producing a device capable of obtaining spectral information in low-level neutron fields. This device is for use mainly in shield performance monitoring.
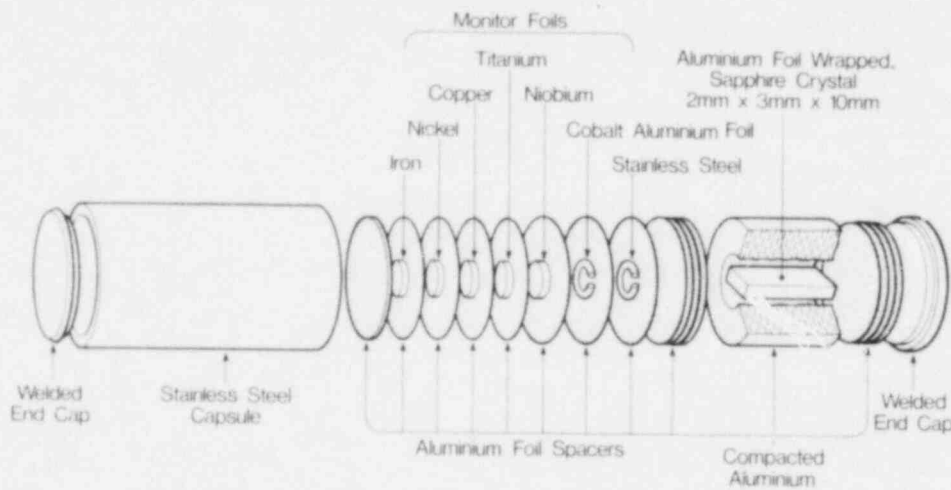
Figure 3: Sapphire Damage Monitor and Activation Monitors Irradiation Capsule
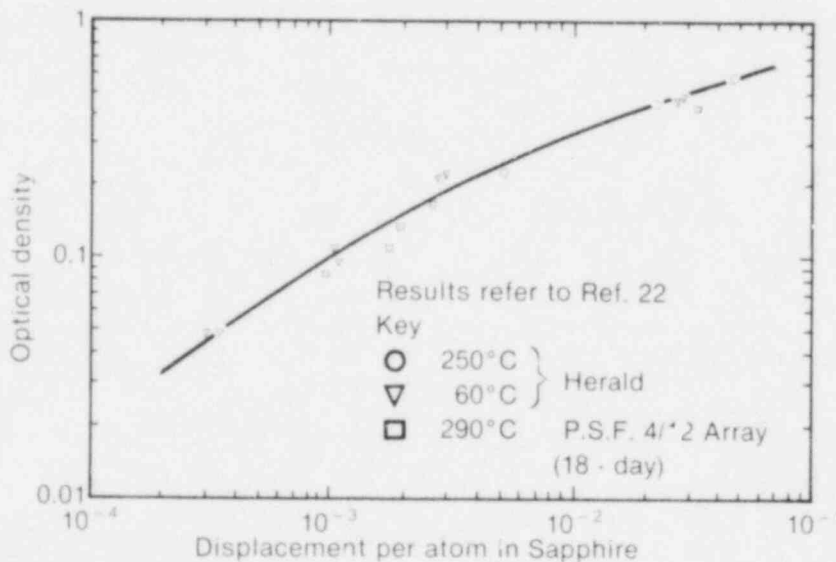
Figure 4: Irradiation Response of Sapphire Damage Dosimetor

Characterisation of Reactor Fields

A consequence of the project-based nature of British dosimetry development has been the level of resources applied to the definition of the radiation environment in the widely-used British MTRs. Thus while these reactors or experimental assemblies (such as ZEBRA), which were of prime importance in a project sense, were extremely well-defined, it has apparently not been possible to keep the basic dosimetry and radiation field data in the "commercial" MTRs abreast of the requirements of present-day materials evaluation programmes. Thus in steels' irradiation studies in DIDO, PLUTO and HERALD, significant work has been carried out by the user groups at Rolls-Royce & Associates and AERE itself in order to define the radiation conditions within the rigs and facilities used. (28). In addition to these studies work has now been started by the DIDO/PLUTO Physics Group which will extend these analyses to include a wider range of facilities. Similar analysis of the neutron spectrum in the irradiation locations used in HERALD are also being carried out by the RR&A/AERE/AWRE group and will be reported as part of the British contribution to the IAEA PV Steels' Irradiation Programme later this year.

This necessarily brief summary of recent UK dosimetry development studies hopefully serves to demonstrate a convergence of interest in the broader applications of the subject. This is in part due to increased collaboration and a recognition of the parallel interests of workers in other countries, but has also been influenced by the decision to proceed with a design study for a British PWR plant. Although in its early stages this project has already taken cognisance of the changes in international materials requirements and has made some preliminary comments on the surveillance standards which would be required of such a project design. This statement included a preliminary definition of the dosimetry and temperature sensor specification for such a surveillance package.

QUO VADIMUS?

In attempting to survey with such brevity a subject of such breadth the establishment of a proper perspective is difficult. The evidence suggests that dosimetry studies at each stage of the UK nuclear programme have been carried out using established techniques of core and shield design and evaluation, and that the information tended to be specific to particular projects. These techniques, referenced to detailed measurements in core and shield mockup assemblies, placed a heavy emphasis on calculation and the accurate prediction of a relatively few activation measurements. This was in marked contrast to other international groups which tended to work with multiple-foil activation and spectrum-adjustment techniques. Only with the more stringent materials performance requirements imposed on the fast-reactor programme has there been a need to broaden the basis of UK dosimetry. The coincidence of this requirement with a general increase of the tempo of dosimetry development programmes internationally over the past few years, and the possibility of a "PWR-component" in the British nuclear programme, has resulted in a corresponding increase in collaborative activity on the part of UK "dosimetrists". The efficient resolution of materials effects problems, within limited resources, cannot but be aided by such exchange of information, and the continuation of international "benchmark" studies, providing as they do invaluable reference points in the application and validation of design techniques, is to be applauded.

As a worker with considerable project commitment in the dosimetry area, such convergence and broadening of emphasis is to be welcomed. However, it is the conclusion of this study at least that this increased interest and activity amongst British workers would be more efficiently consolidated if some form of coordination was to be applied across the divisions imposed by project boundaries. The establishment of a forum for discussion would enable the experience from past, but independent, developments to be effectively coupled with the knowledge gained from increasing international collaboration to produce standardised and validated procedures. In this respect such a forum could deal more rationally with the nomination of UK representatives to the various international working groups dealing with the subject. This representation could then in itself be made more effective in terms of the dissemination of basic information to interested parties.

It has been a main premise of this paper that dosimetry consists of the application of existing calculational and experimental techniques to new problems with more tightly-defined standards of accuracy. The ever-increasing cost of materials evaluation programmes and the resultant trend towards the pooling of resources and results requires high standards of execution and documentation of such experiments if their results are to be accepted and used with confidence. In the specific case of dosimetry the adoption and validation of standard procedures is a prerequisite and it is along this path, it is suggested, that the UK has to stride more purposefully.

ACKNOWLEDGEMENT

REFERENCES

1. E W Etherington — 'The Calculation of Atomic Displacement Dose in Fast Reactors' (Proceedings of 1st ASTM-EURATOM Symposium on Reactor Dosimetry EUR 5667 e/f, Part 1, p375)

2. J E Sanders — 'The Zero-power Basis of Fast Reactor Dosimetry' (Proceedings of the 2nd ASTM-EURATOM Symposium on Reactor Dosimetry, NUREG/CP-0004; vol. 1, p85)

3. M W Thompson & S B Wright — Nuclear Materials 16 (1965) 146

4. U Farinelli — 'Dosimetry and Shielding' (Proceedings of the 2nd ASTM-EURATOM Symposium on Reactor Dosimetry; Palo Alto, 1977)

5. I G Pugh et al — 'Shielding Performance of Magnox Stations in the Light of Operating Experience' (Proceedings of Conference on 'Physics Problems of Reactor Shielding', Harwell, UK, 1968)

6. R A Stewart et al — 'Shielding Problems Associated with Commercial AGR Power Stations' (ibid)

7. K W Brindley — 'Shielding of Commercial Fast Reactors' (Proceedings of the 4th International Conference on Reactor Shielding; Paris 1972)

8. W N McElroy et al — 'A computer-automated iterative method for neutron flux spectra determination' (AFWL-TR-67-41; Sept. 1967)

9. D E Bendall & S J Cripps — 'A Modified form of Diffusion Theory for use in Calculating Neutron and Gamma-ray Penetration in Practical Shields' (Proceedings of the 4th International Conference on Reactor Shielding; Paris, 1972)

10. D E Bendall & R H Brissenden — 'MCBEND Programme User's Guide (CRSD/147, AEE, Winfrith 1980)

11. — ''Recommendations on Radiation Damage in Graphite' (IAEA Specialists Meeting on Damage Units; Nucl. Eng. and Design, Vol. 33 (1975) No. 1, p10)

12. R S Nelson et al — 'Recommended Iron Atomic Displacement Cross-Sections for use in Fast Reactors' (TRG Report 2152 (D) 1972)

13. J Butler et al — 'Utilization of Radiation Measurements made during the Commissioning and Operation of the PFR' (Proceedings of BNES Conference: 'Radiation Protection in Nuclear Power Plants and the Fuel Cycle' 1978)

14. M C G Hall — 'DUCKPOND — a Monte-Carlo Perturbation Code and its applications' (Paper to NEA Specialists' Meeting on Nuclear Data and Benchmarks for Reactor Shielding; Paris, October 1980)

15. Rolls-Royce & Associates Limited/Atomic Energy Establishment, Winfrith (Contribution to NUREG/CR-1861 'Blind Test' Document, July 1981)

16. A McCracken — 'Few Channel Unfolding in Shielding — the SENSAK Code' (EUR 6813, EN-FR Vol. 2, p732)

17. F G Ferey — 'Least Squares Dosimetry Unfolding: the Program STAY'SL' (ORNL-6062; October 1967)

18. F Stallman — 'LSL: A Least-Squares Unfolding Code' (to be published)

19. C Ertek — 'International Intercomparison on the Neutron Flux Density Spectra just before the REAL-80 Exercise' (IAEA-RL-82; June 1981)

20. M D Carter & A. Packwood — 'The Winfrith Benchmark Experiment in Iron — Experimental Results' (Proceedings of OECD Specialists' Meeting on Sensitivity Studies and Shielding Benchmarks; Paris, 1975)

21. W H Taylor — 'Some Studies of the Nb93 (n,n') Nb93m Reaction' (Proceedings of the 2nd ASTM-EURATOM Conference on Reactor Dosimetry; Palo Alto, USA; 1977)

22. P Pells & A J Fudge — 'The Use of Single-Crystal Alumina (Sapphire) as a Damage Monitor for Fast Neutron Damage Irradiations' (To be presented at the 4th ASTM-EURATOM Conference on Reactor Dosimetry, Washington, March 1982)

23. J A Mason — 'Silicon PIN Diode Dosimetry in a Standard Fast Neutron Field' (To be presented, 4th ASTM-EURATOM Conference)

24. A Knipe — 'Gamma-ray Energy Deposition in Fast Nuclear Reactors' (Thesis, University of London, 1976)

25. T Lewis — (Central Electricity Generating Board, UK; Private Communication)

26. D Lowe — 'Thermoluminescent Dosimetry at Interfaces in Mixed Radiation Fields' (Thesis: Royal Naval College, Greenwich, 1980)

27. J A Mason & I. Curl — 'Development of Sensitive Micro-calorimeters for Absorbed Dose Measurements in Benchmark Radiation Fields' (To be presented at the 4th ASTM-EURATOM Conference on Reactor Dosimetry; Washington, 1982)

28. M Austin — 'Experience from Materials Test Irradiations of RPV Steels in DIDO, PLUTO and HERALD' (Proceedings of an IAEA Technical Committee Meeting; (CAPRICE); Julich, Sept. 1979)

SURVEILLANCE CAPSULE PERTURBATION STUDIES IN THE
PSF 4/12 CONFIGURATION

H. Tourwé, G. Mingeart
SCK/CEN, Boeretang 200, B-2400 Mol, Belgium

INTRODUCTION

Calculational estimates and physics considerations suggest that fluxes measured within a surveillance capsule significantly differ from those which would have been obtained without the presence of the capsule. Since these perturbations, created by the fact that the capsule displaces water, are important, two dimensional neutron spectrum calculations taking into account the geometrical description of the surveillance capsule are necessary to interpret the neutron dosimetry measurements performed for the surveillance programmes of the PWR plants. A validation of such calculation techniques is requested.

To provide experimental data for comparison with analytical predictions, a perturbation/dosimetry experiment was irradiated in the PSF high power LWR pressure vessel mock-up facility (configuration 4/12) at ORNL. Appropriate dosimetry was supplied by SCK/CEN and HEDL to measure perturbed and unperturbed reaction rates.

The measured unperturbed to perturbed reaction rate and neutron flux ratios are reported in this paper. A comparison between experimental results and theoretical calculations indicates that perturbations in surveillance capsules can be calculated with a good accuracy.

GEOMETRICAL DESCRIPTION OF THE PERTURBATION/DOSIMETRY EXPERIMENT

The experiment mock-up design is shown in fig. 1 [1]. The surveillance capsules consist of an aluminium outer container (25.4 mm square ; 1.59 mm wall thickness). The container is filled with 22.2 mm square iron blocks.

The surveillance capsule mock-ups are positioned by means of a rig designed by ORNL. This rig positions the thermal shield capsule 101.6 mm to the right of the centerline and touching the thermal
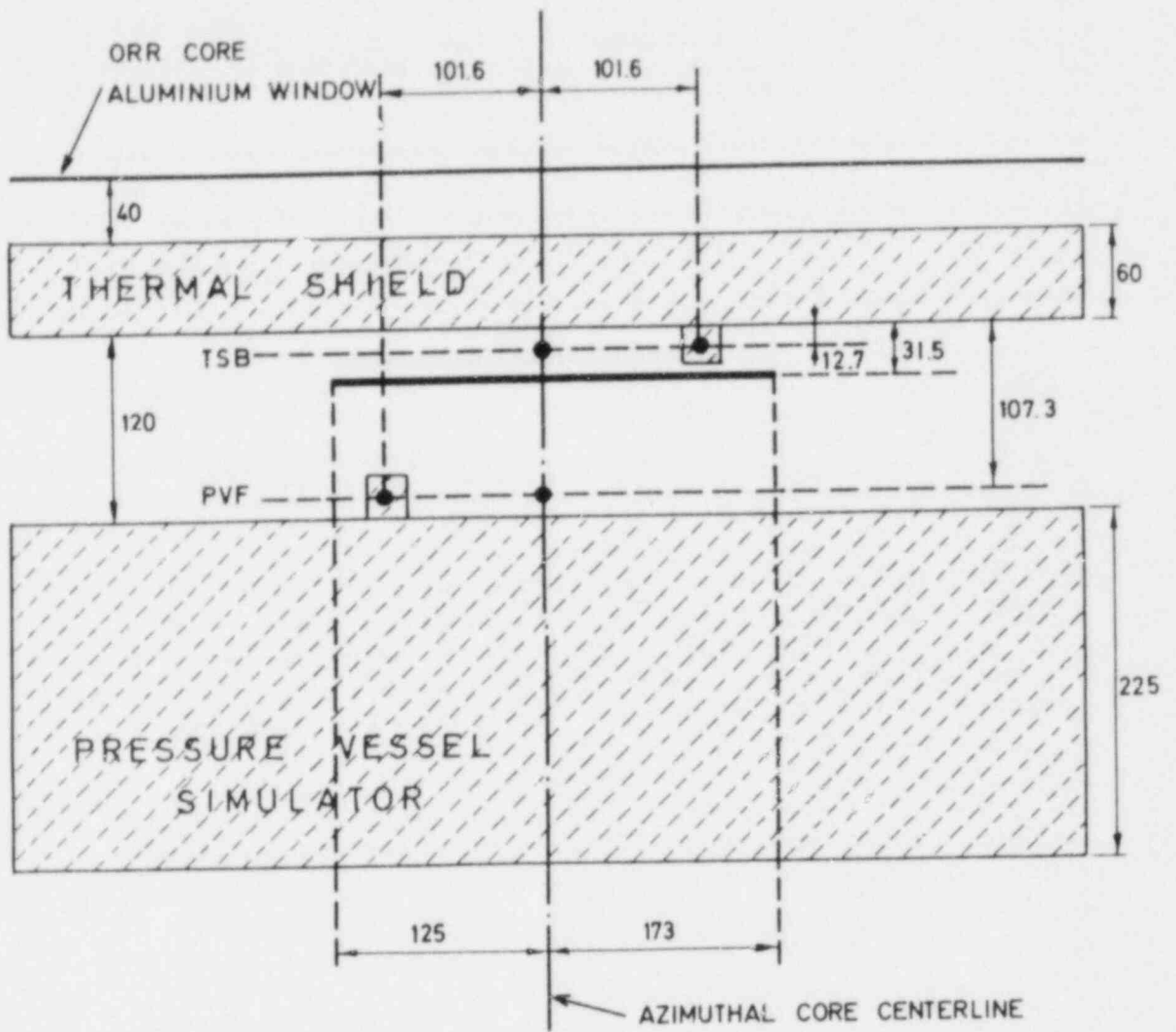
Fig. 1. LWR Surveillance capsule perturbation experiment :
location of dosimeters.

shield. Similarly the pressure vessel surface capsule is positioned 101.6 mm to the left of the centerline. Each 355.6 mm long mock-up has its centerline located 50.8 mm below the reactor centerline and near the position of flux symmetry.

The SCK/CEN and HEDL dosimetry capsules were inserted in a 6.4 mm central vertical hole in the surveillance capsules. Bare detector sets and gadolinium covered detector sets were irradiated.

Also three stainless steel microtubes (O.D. : 4.5 mm; I.D. : 4.0 mm), containing free-field dosimeters, were inserted. Two microtubes were positioned vertically to measure the unperturbed reaction rates respectively in the TSB and PVF position. Both microtubes contained the same type of detectors as the corresponding surveillance capsules. The 3th microtube lies parallel to the thermal shield, in the horizontal plane through the maximum axial flux. This microtube contains Ni, Fe and Al/Co wires, all co-axially centered within an inner steel sleeve.

IRRADIATION HISTORY

The irradiation can be considered to have a square wave profile at a nominal power of 30 MW. The irradiation started on January 31, 1980 (3:30 pm EST or 9:30 pm Mol time) and ended on February 9, 1980 (3:30 pm EST or 9:30 pm Mol time). The total irradiation time at a nominal power of 30 MW is $7.776 \ 10^5$s.

COUNTING TECHNIQUES

Relative countings were performed with a NaI. For the determination of the absolute activities some foils or needles of each dosimeter type were counted with a calibrated Ge(Li) detector. The efficiency as a function of the gamma energy was determined by means of ^{152}Eu reference sources. The analysis of the simple gamma spectra was made using the SPECTRAN software developed by CANBERRA, while the more complex gamma spectra (fission dosimeters) were analysed using the SAMPO programme.

All ^{93}Nb^m activities were measured with a Si(Li) detector, calibrated by means of ^{241}Am and ^{57}Co reference sources. The X-ray spectra were analysed with the SAMPO programme.

The decay scheme parameters that were considered to calculate the absolute activities are taken from reference [2] . The fol-

lowing fission yield values were used [3] :

^{237}Np : $^{95}Zr(0.0593)$, $^{103}Ru(0.0589)$, $^{137}Cs(0.0650)$, $^{140}Ba(0.0574)$

^{238}U : $^{95}Zr(0.0519)$, $^{103}Ru(0.0634)$, $^{137}Cs(0.0600)$, $^{140}Ba(0.0600)$.

COUNTING RESULTS

The experimental results in the unperturbed and perturbed TSB and PVF position are summarized in the tables 1 and 2. Parabolic curves $A_2 y^2 + A_1 y + A_0$, wherein y is the distance in mm to the reactor midplane, were fitted through the measuring points when at least 4 measuring points were available. The SCK/CEN measurements in the perturbed TSB and the perturbed PVF position were supplemented by HEDL measurements taken from reference [4] in order to increase the accuracy. The quoted uncertainties in tables 1 and 2 take only into account these types of uncertainties that contribute to the overall uncertainty when calculating unperturbed to perturbed ratios, namely the statistical uncertainties and the uncertainties on the ^{58}Co and $^{58}Co^m$ burnup corrections of the Ni detectors.

The azimuthal flux distributions were measured by means of Ni and Fe wires. Parabolic curves were fitted through the ^{58}Co and ^{54}Mn specific activities :

$$^{58}Co : (-0.3732 \ 10^{-4} \ x^2 + 0.01065 \ x + 2.583) \ 10^8 \ \ Bq \ g^{-1}$$

$$^{54}Mn : (-0.5828 \ 10^{-4} \ x^2 + 0.01666 \ x + 3.975) \ 10^6 \ \ Bq \ g^{-1}$$

In this formula is x the wire length in mm (x = 0 corresponds with the left-hand side of the microtube in fig. 1). The maximum azimuthal fast neutron flux is situated 18 mm to the right of the ORR core azimuthal centerline. From the fitted curves the following unperturbed fast neutron flux ratios are deduced :

$$\frac{ORR \ azimuthal \ core \ centerline \ (x = 125)}{PVF \ surveillance \ capsule \ (x = 23.4)} = 1.1864 \ \ (\sigma = 0.6 \ \%)$$

$$\frac{ORR \ azimuthal \ core \ centerline \ (x = 125)}{TSB \ surveillance \ capsule \ (x = 226.6)} = 1.0817 \ \ (\sigma = 0.4 \ \%)$$

It was supposed to calculate these ratios that the shape of the neutron spectrum in free-field conditions does not change in the azimuthal direction. This hypothesis was confirmed by means of theoretical calculations. Calculations showed that the fast

TABLE 1. EXPERIMENTAL RESULTS IN THE UNPERTURBED AND PERTURBED TSB POSITION

		^{237}Np(n,f)	^{93}Nb(n,n')	^{238}U(n,f)	^{58}Ni(n,p)	^{54}Fe(n,p)	^{46}Ti(n,p)	^{63}Cu(n,α)
UNPERTURBED TSB	A_2		$-0.6212 \cdot 10^2$		$-0.4029 \cdot 10^4$	$-0.529/ \cdot 10^2$	$-0.5042 \cdot 10^2$	
	A_1		$-0.8230 \cdot 10^4$		$-0.4708 \cdot 10^6$	$-0.6084 \cdot 10^4$	$-0.5674 \cdot 10^4$	
	A_0		$9.407 \cdot 10^6$		$4.490 \cdot 10^8$	$6.920 \cdot 10^6$	$5.971 \cdot 10^6$	
	MAX. (mm)		-66.2		-58.4	-57.4	-56.3	
	ACT* (Bq g^{-1})		$9.663 \cdot 10^6$		$4.624 \cdot 10^8$	$7.092 \cdot 10^6$	$6.129 \cdot 10^6$	$9.282 \cdot 10^4$
	σφ* (n^{-1})	$1.582 \cdot 10^{-11}$	$1.432 \cdot 10^{-12}$	$2.594 \cdot 10^{-12}$	$7.867 \cdot 10^{-13}$	$5.737 \cdot 10^{-13}$	$8.393 \cdot 10^{-14}$	$4.377 \cdot 10^{-15}$
	UNCERTAINTY (%)	1.6	0.3	2.0	1.4	0.3	0.3	0.4
PERTURBED TSB	A_2				$-0.3281 \cdot 10^4$	$-0.1360 \cdot 10^3$	$-0.5599 \cdot 10^2$	-0.6044
	A_1				$-0.4530 \cdot 10^6$	$-0.1167 \cdot 10^5$	$-0.7341 \cdot 10^4$	$-0.8940 \cdot 10^2$
	A_0				$4.505 \cdot 10^8$	$7.144 \cdot 10^6$	$5.608 \cdot 10^6$	$7.943 \cdot 10^4$
	MAX. (mm)				-69.0	-42.9	-65.6	-74.0
	ACT* (Bq g^{-1})		$1.072 \cdot 10^7$		$4.650 \cdot 10^8$	$7.388 \cdot 10^6$	$5.835 \cdot 10^6$	$8.238 \cdot 10^4$
	σφ* (n^{-1})	$1.935 \cdot 10^{-11}$	$1.589 \cdot 10^{-12}$	$2.813 \cdot 10^{-12}$	$7.911 \cdot 10^{-13}$	$5.976 \cdot 10^{-13}$	$7.990 \cdot 10^{-14}$	$3.884 \cdot 10^{-15}$
	UNCERTAINTY (%)	1.8	3.5	2.0	0.7	1.9	0.6	1.4

TABLE 2. EXPERIMENTAL RESULTS IN THE UNPERTURBED AND PERTURBED PVT POSITION

		^{93}Nb(n,n')	^{58}Ni(n,p)	^{54}Fe(n,p)	^{46}Ti(n,p)
UNPERTURBED PVT	A_2	$-0.1485 \cdot 10^2$	$-0.8540 \cdot 10^3$	$-0.8478 \cdot 10^1$	$-0.9894 \cdot 10^1$
	A_1	$-0.1850 \cdot 10^4$	$-0.1083 \cdot 10^6$	$-0.1116 \cdot 10^4$	$-0.1209 \cdot 10^4$
	A_0	$1.591 \cdot 10^6$	$9.151 \cdot 10^7$	$1.452 \cdot 10^6$	$1.434 \cdot 10^6$
	MAX. (mm)	-62.3	-63.4	-65.8	-61.1
	ACT* (Bq g^{-1})	$1.646 \cdot 10^6$	$9.479 \cdot 10^7$	$1.486 \cdot 10^6$	$1.470 \cdot 10^6$
	σφ* (n^{-1})	$2.439 \cdot 10^{-13}$	$1.613 \cdot 10^{-13}$	$1.202 \cdot 10^{-13}$	$2.013 \cdot 10^{-14}$
	UNCERTAINTY (%)	0.8	0.7	1.4	1.3
PERTURBED PVT	A_2		$-0.6107 \cdot 10^3$	$-0.1422 \cdot 10^2$	$-0.1709 \cdot 10^2$
	A_1		$-0.7824 \cdot 10^5$	$-0.1802 \cdot 10^4$	$-0.1953 \cdot 10^4$
	A_0		$8.065 \cdot 10^7$	$1.282 \cdot 10^6$	$1.212 \cdot 10^6$
	MAX. (mm)		-64.1	-63.4	-57.1
	ACT* (Bq g^{-1})	$1.550 \cdot 10^6$	$8.304 \cdot 10^7$	$1.337 \cdot 10^6$	$1.267 \cdot 10^6$
	σφ* (n^{-1})	$2.297 \cdot 10^{-13}$	$1.413 \cdot 10^{-13}$	$1.082 \cdot 10^{-13}$	$1.735 \cdot 10^{-14}$
	UNCERTAINTY (%)	1.0	0.8	1.4	1.0

*ACTIVITY AT THE END OF IRRADIATION; VALUES AT A DISTANCE OF -50 mm TO THE REACTOR MIDPLANE.

azimuthal neutron flux distribution, measured by means of Ni and Fe
wires that were irradiated in the presence of the TSB surveillance
capsule, is disturbed by maximum 3 % in the vicinity of the TSB
surveillance capsule. This influence is however negligible on the
fitted azimuthal curves. The largest contribution to the uncer-
tainty is the uncertainty on the positioning of the detector wires
($\pm$ 2 mm).

The counting results of the thermal neutron detectors were
only used to correct for ^{58}Co and ^{58}Co^m burnup in the Ni dosimeters
and to correct for disturbing fissions in the ^{237}Np and ^{238}U dosi-
meters.

THEORETICAL CALCULATIONS OF THE DOSIMETRY/PERTURBATION EXPERIMENT

Two dimensional discrete ordinate transport DOT calculations
of the perturbation experiment were performed in a 17 group energy
structure. These calculations employed the S8-P3 approximation
and the 171-group cross section sets of VITAMIN-C, based on
ENDF/B-IV and collapsed on average spectra computed with ANISN for
each zone of the PCA 4/12 SSC (simulated surveillance capsule) con-
figuration. The ENDF/B-V fission spectrum was used for all these
calculations. The ORR core configuration was replaced by the PCA
(low power LWR pressure vessel mock-up facility) core configura-
tion described in reference [5]. The surveillance capsules were
represented by means of 5 meshes in both directions : 1 mesh re-
presenting the 6.4 mm central hole, 2 meshes representing the iron
material on both sides of the central hole and 2 meshes to repre-
sent the aluminium capsule container. The ORR azimuthal centerline
was considered as an axis of symmetry. Three calculations runs
were performed : one without the surveillance capsules, one in-
cluding the TSB surveillance capsule and one including the PVF
surveillance capsule. The calculated unperturbed and perturbed
neutron spectra above 0.1 keV in the TSB and the PVF position are
shown in fig. 2; they are all scaled on a same fission neutron
source strength in the core. The perturbation effect is parti-
cularly pronounced in the neutron energy region between 100 keV
and 3 MeV.

The ENDF/B-V cross section data* were condensed into the 17
group energy structure using local ANISN spectra of the PSF 4/12
SSC configuration as weighting functions in order to calculate
reaction rates and spectrum averaged cross sections. The choice
of the ANISN weighting spectra is not very critical : e.g. the

*Hegedüs cross section data for ^{93}Nb(n,n') + biasfactor of 1.37 [6].

477
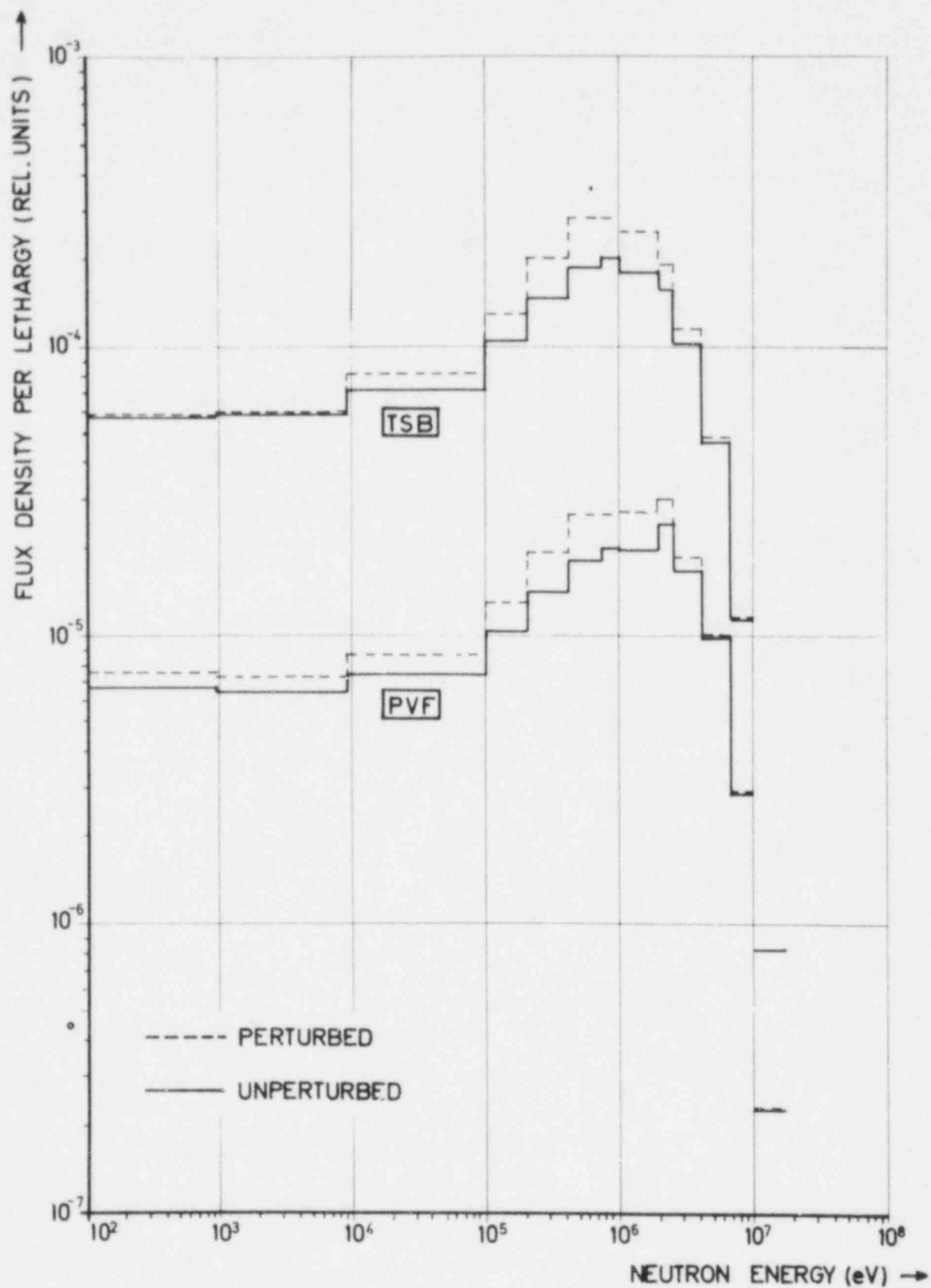
Fig. 2. Calculated perturbed and unperturbed neutron spectra in the TSB and the PVF surveillance position.

perturbed PVF reaction rates were calculated with both a ANISN SSC spectrum and a ANISN 1/4 T spectrum. The differences in calculated reaction rates were smaller than 0.5 % for all types of reactions, except for ^{46}Ti(n,p) and ^{63}Cu(n,α) where differences of respectively 1 % and 3 % were observed.

COMPARISON BETWEEN EXPERIMENT AND THEORETICAL CALCULATIONS

Based on the measured reaction rates and on the measured azimuthal flux distribution and with the aid of spectrum averaged cross sections calculated according the principles shown in the previous section, fluxes > 1 MeV were derived in the perturbed and unperturbed TSB and PVF position. The results are shown in fig. 3. The neutron flux values of the ^{237}Np(n,f), ^{238}U(n,f), ^{58}Ni(n,p), ^{54}Fe(n,p) and ^{46}Ti(n,p) detectors agree within 5 %. The spectrum averaged ^{63}Cu(n,α) cross sections are somewhat overestimated in the TSB position, while the spectrum averaged ^{93}Nb(n,n') cross sections are somewhat underestimated in the PVF position.

The measured unperturbed to perturbed reaction rates and flux ratios are compared with calculated values in table 3. The agreement between experiment and calculation is excellent, better than 5 % for all ratios except ^{93}Nb(n,n'). The somewhat different behaviour of the calculated ^{93}Nb(n,n') data can only be explained by
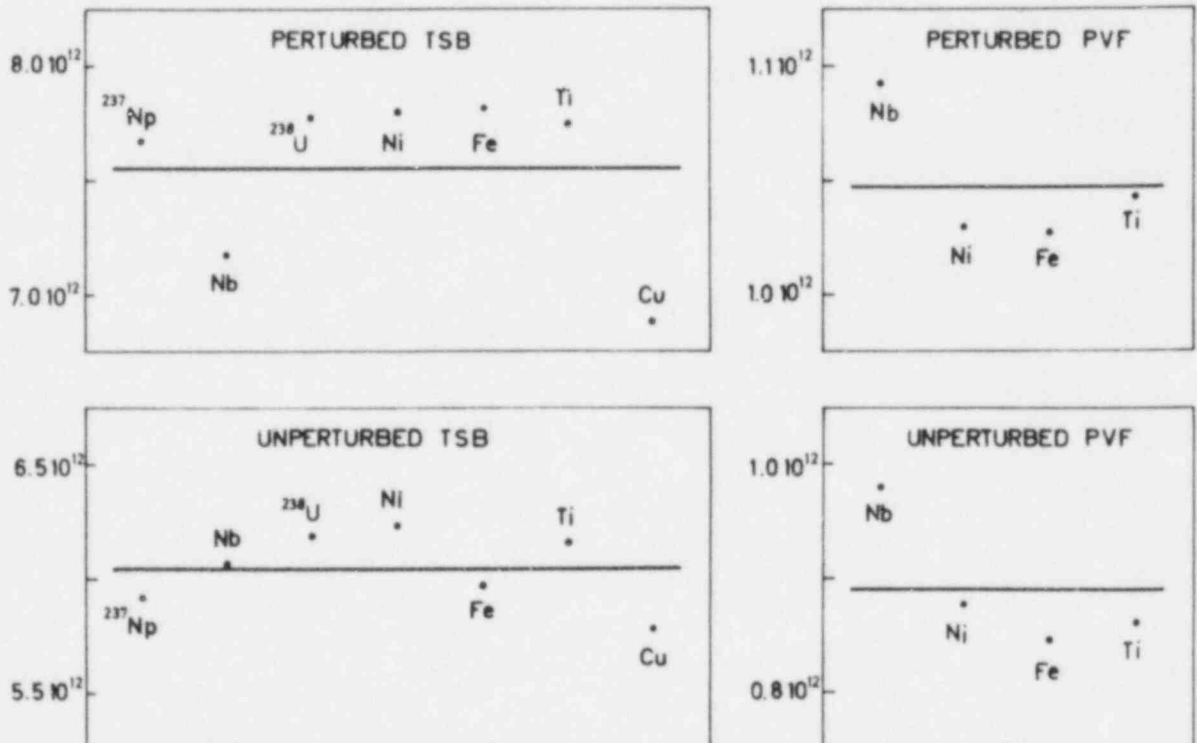
Fig. 3. $\emptyset$(> 1 MeV) in n s^{-1}cm^{-2} at the TSB and PVF position.

TABLE 3.   UNPERTURBED TO PERTURBED RATIOS IN THE TSB AND THE PVF POSITION

	TSB POSITION				PVF POSITION			
	M	σ (%)	C	C/M	M	σ (%)	C	C/M
^{237}Np(n,f)	0.756	2.4	0.781	1.03			0.830	
^{93}Nb(n,n')	0.833	3.5	0.786	0.94	0.895	1.4	0.821	0.92
^{238}U(n,f)	0.852	2.9	0.853	1.00			0.879	
^{58}Ni(n,p)	0.919	1.6	0.919	1.00	0.962	1.2	0.931	0.97
^{54}Fe(n,p)	0.887	2.0	0.928	1.05	0.936	2.1	0.937	1.00
^{46}Ti(n,p)	0.971	0.8	0.975	1.00	0.978	1.7	0.976	1.00
^{63}Cu(n,α)	1.042	1.5	0.990	0.95			0.990	
Ø (> 1 MeV)	0.800	5.7	0.798	1.00	0.851	7.6	0.824	0.97
Ø (> 98 keV)	0.756	5.7	0.753	.00	0.803	7.6	0.779	0.97

a non adequate shape of the employed ^{93}Nb(n,n') cross section data.
The perturbation effect becomes more important with decreasing ef-
fective energy threshold, the experimental ^{54}Fe(n,p) values and the
theoretical PVF ^{93}Nb(n,n') value being the only exceptions. The
fact that the perturbation effect increases with decreasing thres-
hold energy is in agreement with the tendency shown on fig. 2.
The fast neutron flux perturbation is more important in the TSB
position than in the PVF position.

The damage ratios, calculated by means of the ASTM E 693-79
data, are 0.848 and 0.939 respectively for the TSB and the PVF
position. Niobium is apparently a good damage monitor since both
damage ratios and both measured ^{93}Nb(n,n') ratios agree within
5 % .

CONCLUSIONS

Accurate experimental data of the perturbation/dosimetry
experiment in the PSF high power LWR pressure vessel mock-up fa-
cility were provided for the validation of reactor codes, which
are used to calculate the neutron spectrum and the neutron flux
perturbations created by LWR surveillance capsules.

Two dimensional calculations performed by SCK/CEN demonstrated that neutron spectrum and neutron flux perturbations can be calculated with an accuracy better than 5 % .

REFERENCES

[1] H. Tourwé, SCK/CEN Reactor Physics Technical Document, HT/eu - 380/81-27 (June 15, 1981).

[2] W.L. Zijp, J.H. Baard, "Nuclear data guide for reactor neutron metrology. Part 1 : Activation reactions," ECN-70 (August, 1979).

[3] W.L. Zijp, J.H. Baard, "Nuclear data guide for reactor neutron metrology. Part 2 : Fission reactions," ECN-71 (August, 1979).

[4] Minutes of the 6th LWR-pressure vessel surveillance dosimetry program meeting, NBS (October 27-31, 1980).

[5] W.N. McElroy, "LWR pressure vessel surveillance dosimetry improvement program : PCA experiments and blind test," NUREG/CR-1861 (July, 1981).

[6] H. Tourwé, N. Maene, "Fast neutron fluence measurements with the $^{93}Nb(n,n')$ reaction and the application to long-term irradiations," Proc. of the 3th ASTM-EURATOM symposium on Reactor Dosimetry, Ispra (October 1-5, 1979).

CALCULATION OF THE FAST NEUTRON FLUX AND DAMAGE
IN THE PRESSURE VESSEL OF THE BR3 REACTOR

G. Minsart, H. Tourwé, J. Debrue
SCK/CEN, Boeretang 200, B-2400 Mol, Belgium

INTRODUCTION

Due to the high fluence accumulated in the pressure vessel of the BR3 reactor, it is necessary to determine it with the best accuracy. Dosimetry capsules were irradiated in the reflector during the cycles 4 A and 4 B and very detailed calculations were performed in order to relate these measurements with the core power distribution and to yield fast fluxes and spectra for various positions, at the surface and through the pressure vessel.

One-dimensional and two-dimensional problems were run with ANISN and DOT 3.5 respectively, using the DLC/41B VITAMIN-C data set based on ENDF/BIV, and the ENDF/BV fission spectrum. In order to avoid the repetition of costly 2-Dim. runs for flux integration over the whole BR3 history, a perturbation-like method was applied to a "reference calculation" performed for 1/6th of the cycle 4 B core loading.

PROCEDURE OF CALCULATION

The procedure adopted for this study is the same as for the analysis of the PCA experiments (Blind test, PCA 4/12 SSC, PSF 4/12 with perturbation experiment).

- Using the ANISN code [1], a one-dimensional fixed source calculation is performed in S8, P3 approximation with the 171-group VITAMIN-C cross-section library [2] and the ENDF/BV fission spectrum. The processing of the library is made by the code system MARS [3] : the modules AIM, AJAX, BONAMI and NITAWL were used to produce effective microscopic cross-sections; macroscopic cross-section in group-independent format were then obtained with the programme AXMIX, part of the AMPX-II code system [4].

- The average spectra produced by the ANISN run for each region or subregion are used for collapsing the macroscopic cross-sections into a 17-group set, whose energy structure is given in table 1.

Table 1. 17-group energy structure

Broad group	VITAMIN-C* groups	Energy groups	Fission spectrum (ENDF/B V)
1	1 - 13	17.333 - 10.513 MeV	1.3035 E-03
2	14 - 22	10.513 - 6.59 MeV	1.6404 E-02
3	23 - 31	6.59 - 4.066 MeV	9.0302 E-02
4	32 - 39	4.066 - 2.466 MeV	1.9911 E-01
5	40 - 47	2.466 - 1.92 MeV	1.1879 E-01
6	48 - 59	1.92 - 1.00 MeV	2.7271 E-01
7	60 - 65	1.00 MeV - 742.7 KeV	8.9850 E-02
8	66 - 75	742.7 - 407.6 KeV	1.1429 E-01
9	76 - 89	407.6 - 207.4 KeV	6.0861 E-02
10	90 - 102	207.4 - 98.04 KeV	2.4052 E-02
11	103 - 124	98.04 - 9.12 KeV	1.2609 E-02
12	125 - 138	9.12 - 0.96 KeV	3.6790 E-04
13	139 - 147	0.96 KeV - 101.3 eV	1.2627 E-04
14	148 - 156	101.3 - 10.68 eV	4.3220 E-07
15	157 - 163	10.68 - 1.855 eV	1.4205 E-08
16	164 - 168	1.855 - 0.5316 eV	9.3924 E-10
17	169 - 171	0.5316 - 0.001 eV	1.6305 E-10

*DLC-41B

- After addition of the DB² terms, this 17-group set is introduced
  as input for a fixed source two-dimensional R-θ calculation (code
  DOT 3.5 [5]), also with the discretisation levels S8, P3, in order
  to obtain a detailed flux map across the system.

The ENDF/BV dosimetry file is the basic set selected for com-
puting average cross-sections used in the determination of the ex-
perimental flux values. It has been collapsed into the 171-group
structure, using the DETAN 74 code [6] and a Watt spectrum analy-
tical model ($\overline{E}$ = 2 MeV). For its use with the DOT fluxes, an
additional, space-dependent, collapsing has been performed with the
local ANISN spectra in order to include fine group structure infor-
mation into the computed results.

GEOMETRICAL MODELS

The geometry of the BR3 reactor installation is illustrated on
fig. 1, where only 1/6th of the horizontal cut is represented. For
the basic calculations, it has been assumed that the core configu-
ration has this order of symmetry.

The one-dimensional model is cylindrical, and the core is
represented by five rings, each corresponding to one row of assem-
blies (7 assemblies for the central one); the 2nd and 4th rows are
made up by mixing fuel assemblies and moderator cells. In this
operation, volumes are preserved and the outer core boundary is at
an average radius equal to 43.4 cm rather close to the center of
the corner assembly in the outer row.

The two-dimensional model, designed in Rθ geometry, has been
refined in order to represent, as well as possible, the assembly
boundaries, particularly the core outer border. The sixty 1° angles
and the variable mesh spacing along the R axis are shown on fig. 2,
where the exact shapes of the fuel assemblies have also been indi-
cated for the two outer rows. Outside the core, meshes about 1 cm
thick were adopted up to the outer surface of the pressure vessel;
the system modelling extents up to a radius of 158 cm, far inside
the water tank surrounding the vessel thermal insulation.

FISSION NEUTRON SOURCE DISTRIBUTIONS

The BR3 reactor is mainly operated for testing fuel assemblies
and fuel pins of different designs e.g. mixed oxide fuels, gadoli-
nium bearing fuels; its core loading is thus rather intricated and

the detailed models adopted for computing power distributions and
burnups are more detailed than those generally used for the analysis
of current power plants. The power distribution is calculated in
each pin over the whole core at selected operation times. For the
reference calculation of the complete neutron flux map around the
core, leading to the determination of the flux spectrum in the
vessel and at the dosimeter locations, the power density per fuel
pin was only considered in the two outer rings of fuel assemblies.
In the central zone, the consideration of the average power in each
assembly appeared to be adequate.

The power densities (averaged over the height of the core) were
translated into fission neutron sources, taking into account the
number of neutrons emitted per fission in the uranium and plutonium
isotopes, as well as the corresponding energy amounts deposited in
the fuel pins; the resulting conversion coefficient has been re-
lated to the burnup for its application to the different mixed oxide
fuel compositions and the upper value corresponding to ^{239}Pu has
been used for Pu enriched natural uranium pins.

The reference calculation modelled 1/6th of the BR^3/4 B core
loading, facing locations where measurements were performed (HF 4,
thermocouple guide, ...). The neutron source distribution, ob-
tained as indicated hereabove, has been shared amongst the many
meshes representing the fuel zones (see fig. 2), uniformly on
each assembly in the inner core part, and pinwise in the two outer
rows. For the one-dimensional run aimed at preparing the 17-group
cross-sections sets, the fission neutron source intensity averaged
over the assembly rows was given as input.

REFERENCE CALCULATION

The fixed-source DOT Rθ problem where the most detailed avai-
lable information was given in the input (including space-dependent
vertical buckling terms), provided a complete multigroup flux map
on which several postprocessing analyses were applied. Fluxes
above 1 MeV and above 98 keV were computed at many locations :
measurement positions, radial traverses, azimuthal traverses at
a radius corresponding to 1/4 T (1/4th of the pressure vessel
thickness). Spectra were also examined for several meshes, and
the analysis extended up to the outer water tank.

Some of the results are illustrated on figs 3 to 5. On
fig. 3 for example, it can be seen that the radial traverse of
$\emptyset > 1$ MeV yielded by the 1-Dim. 171 gr. ANISN calculations has a
shape very similar to those given by the DOT run; the absolute
level is different according to the considered DOT angle, due to

the different distances between the core border and the surrounding structures (thermal shield, vessel ...). All results are given for the horizontal reactor midplane. The axial shape factor (1.27) was obtained from several measurements with threshold detectors at two different radii in the radial reflector.

Fig. 4 shows that the azimuthal fast flux distribution at 1/4 T is very smooth, with respect to large power plants. The peak-to-minimum ratio is around 1.185. The iron damage response plotted on fig. 5 was computed with the ANISN flux map, in order to keep the maximum of spectral information, and the ASTM damage function [7].

Knowing the absolute fission source strenghts (scaled to the reactor power), all the computed results (fluxes, reaction rates) are easily normalized to yield absolute values, and the load diagram of the reactor operation enables to calculate fluences.

APPLICATION OF THE REFERENCE CALCULATION TO DIFFERENT CORE LOADINGS

In order to avoid the costly and lengthy repetition of the 2-Dim. Rθ DOT study for other parts of the core 4 B and for other core loadings, a perturbation-like procedure was developed. The goal was to obtain absolute fast fluence values at the 1/4 thickness of the pressure vessel for all the BR3 core loadings, particularly at the location of the longitudinal weld, which is the most sensitive to neutron damage.

It must first be pointed out that modifications of fuel reloading strategy, more specifically change of burnup at BOL in the outer fuel assemblies, have a small impact on the azimuthal neutron flux distribution in the vessel. A perturbation calculation is therefore acceptable. Moreover, a modification of the fuel composition due to burnup or different enrichments does not affect significantly the transport of fast neutrons in the fuel assemblies. Starting from a detailed calculation for a particular core (or 1/6th core), it is thus sufficient to introduce the variation of the neutron source in each fuel assembly to calculate fast flux values in the vessel for other cores.

The flux at any location in the vessel is the superposition of the contribution of each fuel assembly. Several DOT problems were run with a unique composition and fixed fission sources uniformly distributed in one fuel assembly at a time. Owing to the symmetry, four cases are sufficient to cover the two outer rows (7 assemblies in 1/6th of the core). The contribution of these 7 assemblies to the fast flux at 1/4 T represents 80 to 85 % of the

total response; the 5 assemblies of the outer row yield 60 to 65 % of the total response. It was thus assumed that it is sufficient to account for the variations of the fission source in the two outer rows for providing reasonably accurate results for the other core loadings : even if a 10 % change of the fission source inte- grated over the central core zone had to be considered, it would affect the flux at 1/4 T by not more than 1.5 %.

Having checked this point, the procedure was applied in a dif- ferent way, which tends to minimize the errors and the influence of the modelling by a flat source in each assembly : the reference calculation results were used to provide the basic term, and this one was modulated by addition of the contributions coming from each assembly weighted by the difference of fission sources between the considered configuration and the reference case. This opera- tion has been made for each azimuthal position at 1/4 T and for each BR3 core loading.

According to the calculations, the flux above 1 MeV at the 1/4 T in the weld, averaged over the duration of a cycle, does not vary by more than ± 5 % from one cycle to the other.

COMPARISON OF CALCULATION WITH EXPERIMENTAL RESULTS

Three sources of information are available to confirm the validity of the calculations.

Numerous post-irradiation examinations of individual fuel pins indicate that the discrepancy between measured and calculated pin power densities practically never exceeds 10 %. The uncer- tainty on the power per assembly is estimated at ± 5 %.

Dosimetry measurements were performed during cycles 4 A and 4 B in positions HF and TC-A (fig. 1). In position HF, reaction rates obtained with different threshold reactions provide a check of the DOT neutron spectrum calculated at this location when using the ENDF/BV dosimetry file for the detector cross-sections (except for niobium), as shown in table 2.

If one excepts ^{237}Np(n,f), all data are in good agreement to define the flux above 1 MeV : this confirms the calculated spectral shape.

Table 2. Test of validity of the neutron spectrum
at the periphery of the core (HF position)

Reaction	$\bar{\sigma}_{1\ MeV}(mb)^{(a)}$	$\phi_{>1\ MeV}\ (10^{13}n/cm^2s)^{(c)}$
$^{93}Nb(n,n')$	$221.3^{(b)}$	1.00
$^{237}Np(n,f)$	2107	1.10
$^{58}Ni(n,p)$	156.5	0.99
$Ti(n,x)$	17.95	1.01
$^{54}Fe(n,p)$	121.1	1.01
		Average : 1.02×10^{13}

(a) Calculated reaction rate/calculated flux > 1 MeV.

(b) Calculated from Hegedüs cross-section [8] multiplied
by 1.37; this bias factor was deduced from several
comparisons of niobium with other threshold monitors
in BR2 and BR3.

(c) Experimental reaction rate divided by $\bar{\sigma}_{1\ MeV}$.

Table 3. Comparison of measured and calculated flux values
at two locations in the radial reflector

Cycle	Position	Flux > 1 MeV (n/cm^2s)		Calc.
		Measured	Calculated	Meas.
4 A	HF	1.01×10^{13}	1.09×10^{13}	1.08
4 B	HF	1.01×10^{13}	1.15×10^{13}	1.14
4 A	A	1.45×10^{12}	2.24×10^{12}	1.54
4 B	A	1.70×10^{12}	2.44×10^{12}	1.44

In table 3, absolute flux values deduced from ^{54}Fe(n,p) measurements are compared with calculations.
The calculations agree with the measurements at position HF if one takes into account the uncertainty on the input data (power distribution and neutron sources). At a greater distance in the reflector (position A is roughly at 12 cm from the core boundary), a significant discrepancy of about 50 % exists.

A third source of information, extremely important as to the validation of the procedure using ANISN/DOT and the VITAMIN-C library as applied to BR3, is the analysis of the PCA experiments [9]. The calculation of the configurations 8/7 and 12/13 indicates that no systematical deviation appears between calculations and measurements over the distance separating the core periphery and the 1/4 thickness of the vessel ($\sim$ 27 cm in configuration 8/7 and $\sim$ 37 cm in configuration 12/13). The discrepancy of 50 % at position A in BR3 is therefore considered as an anomaly which will require further investigation : it is planned to remove the core basket at next BR3 shutdown in order to take off steel samples at different azimuthal positions and to measure the ^{54}Fe(n,p) activation rate in these samples.

The importance of neutron dosimetry and calculations must be stressed in the present situation of BR3. The maximum allowable fluence in the longitudinal weld being determined on the basis of the irradiation embrittlement of the weld material, the knowledge of the actual fluence determines whether the operation of the reactor can be pursued with or without undertaking major actions such as complete inspection of the weld or annealing.

As explained briefly in this paper, the determination of the fluence in the weld relies mainly upon calculations supported by experimental validation. A global uncertainty of 25 % is estimated by combining individual sources of discrepancies; a margin of 25 % is therefore added to the nominal value for operational evaluations (pressure-temperature diagram of the primary circuit). It is not expected to reduce significantly this margin. However if dosimetry results (for instance, examination of the core basket) demonstrated the existence of a systematic bias in the calculation and confirmed the trend observed in table 3, a relatively small adjustment could modify significantly operational decisions and the schedule of the fuel irradiation programme (10 % readjustment corresponds to about 8000 hour operation e.g. one operation cycle).

REFERENCES

[1] ANISN-C, A one-dimensional discrete ordinates transport code, Computer Code Collection CCC-82, Radiation Shielding Information Center, Oak Ridge, TN.

[2] VITAMIN-C, 171 neutron, 36 gamma-ray group cross sections in AMPX and CCCC interface formats for fusion and LMFBR neutronics, Data Library Collection DLC-41, Radiation Shielding Information Center, Oak Ridge, TN.

[3] MARS, Collection of computer codes for manipulating multigroup cross section libraries in AMPX or CCCC formats, Computer Code Collection PSR-117, Radiation Shielding Information Center, Oak Ridge, TN.

[4] AMPX-II, Modular code system for generating multigroup neutron gamma-ray cross sections libraries from data in ENDF format, Computer Code Collection PSR-63, Radiation Shielding Information Center, Oak Ridge, TN.

[5] DOT 3.5, A two-dimensional discrete ordinates radiation transport code, Computer Code Collection CCC-276, Radiation Shielding Information Center, Oak Ridge, TN.

[6] C. Eisenhauer and A. Fabry, "DETAN 74, a computer code for calculating detector responses in reactor neutron spectra".

[7] ASTM standard E 693-79.

[8] F. Hegedüs, "Détecteur de fluence de neutrons rapides basé sur la réaction $^{93}Nb(n,n')^{93m}Nb$," EIR-Bericht Nr. 195 (März,1971).

[9] LWR pressure vessel surveillance dosimetry improvement program : PCA experiments and blind test, NUREG/CR-1861, HEDL-TME 80-87/R5 (July, 1981).

490

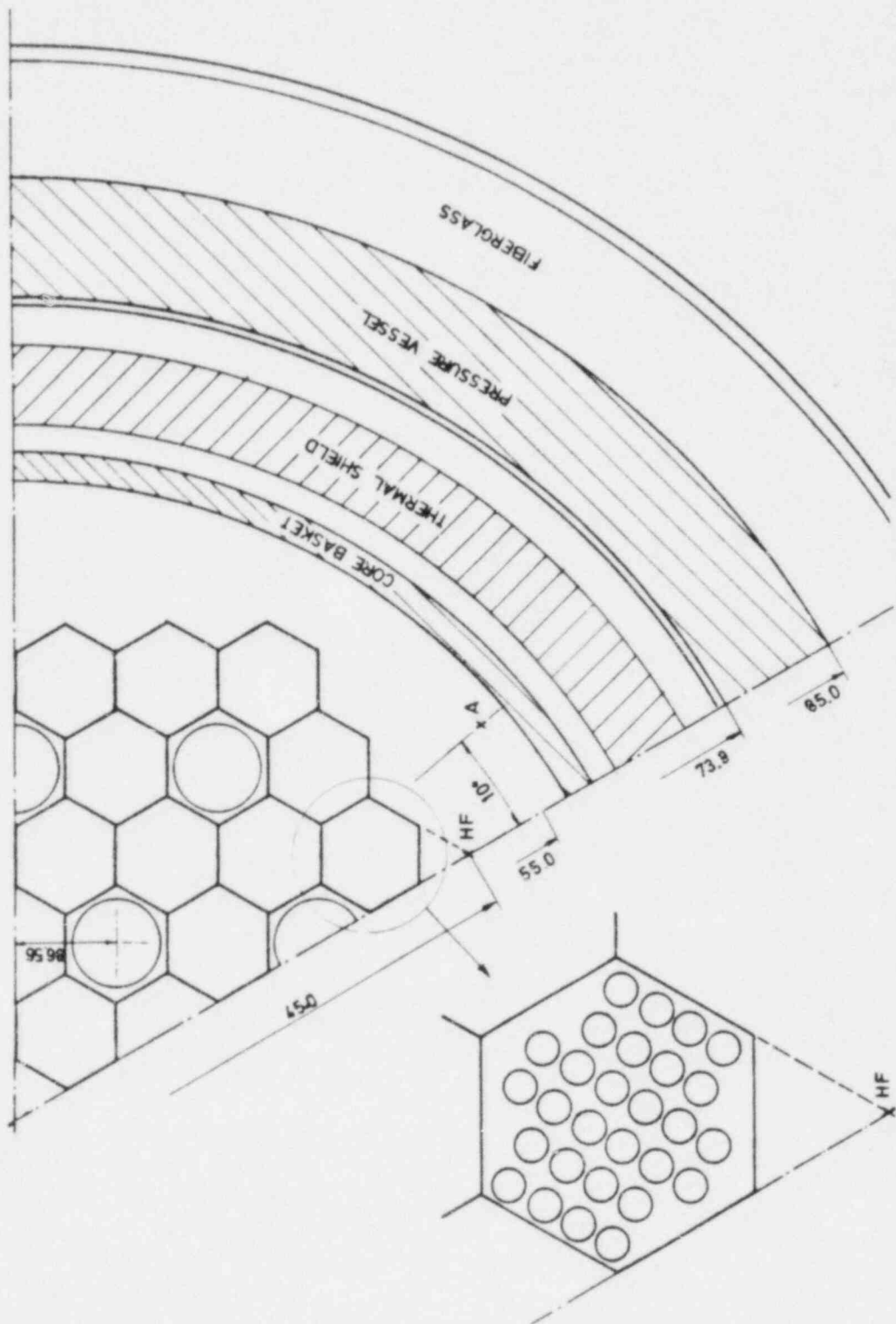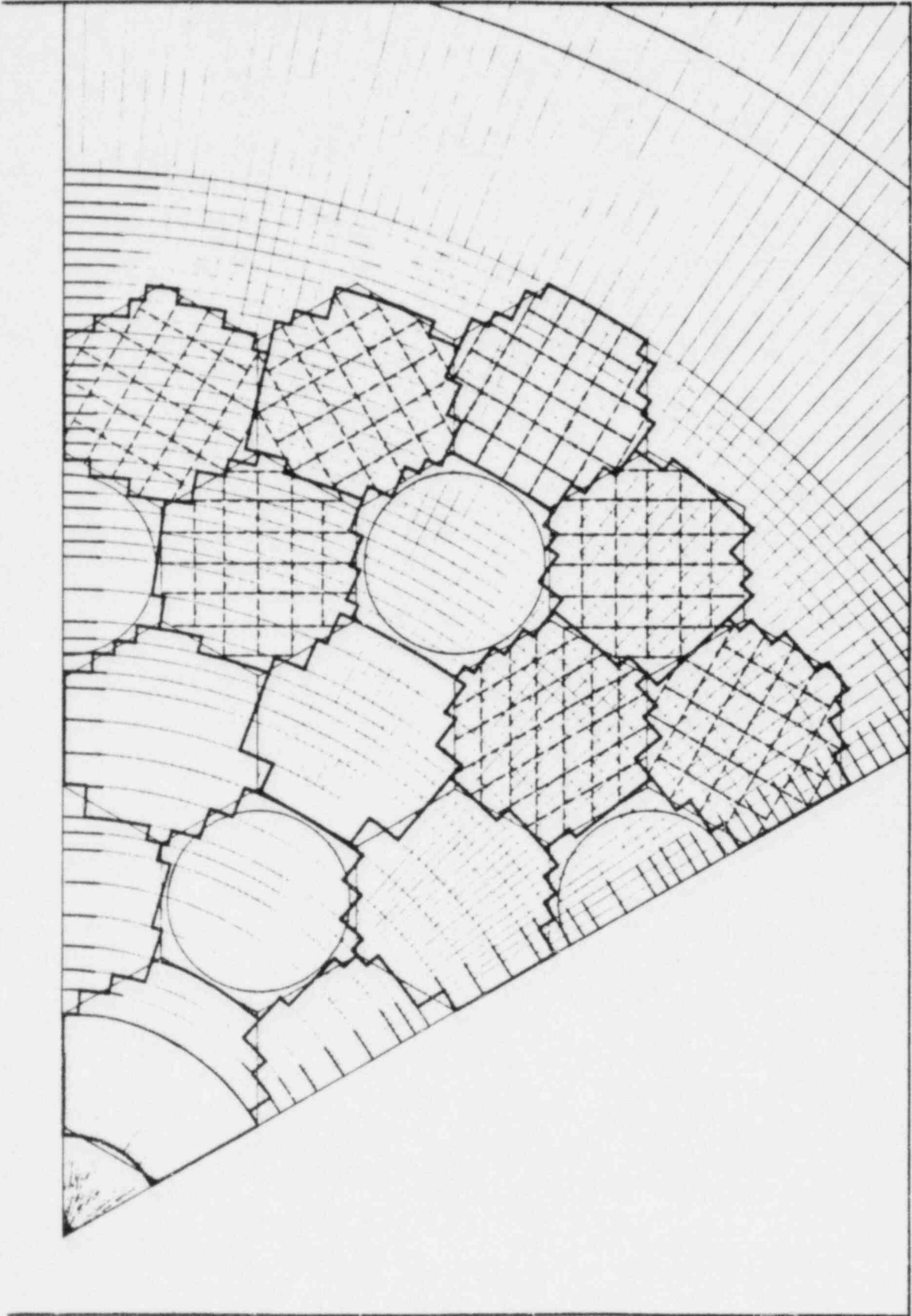Fig. 1. Horizontal cut of the BR3 reactor, with the positions of measurements HF 4 and TC-A.

Fig. 2. RΘ core model.

492
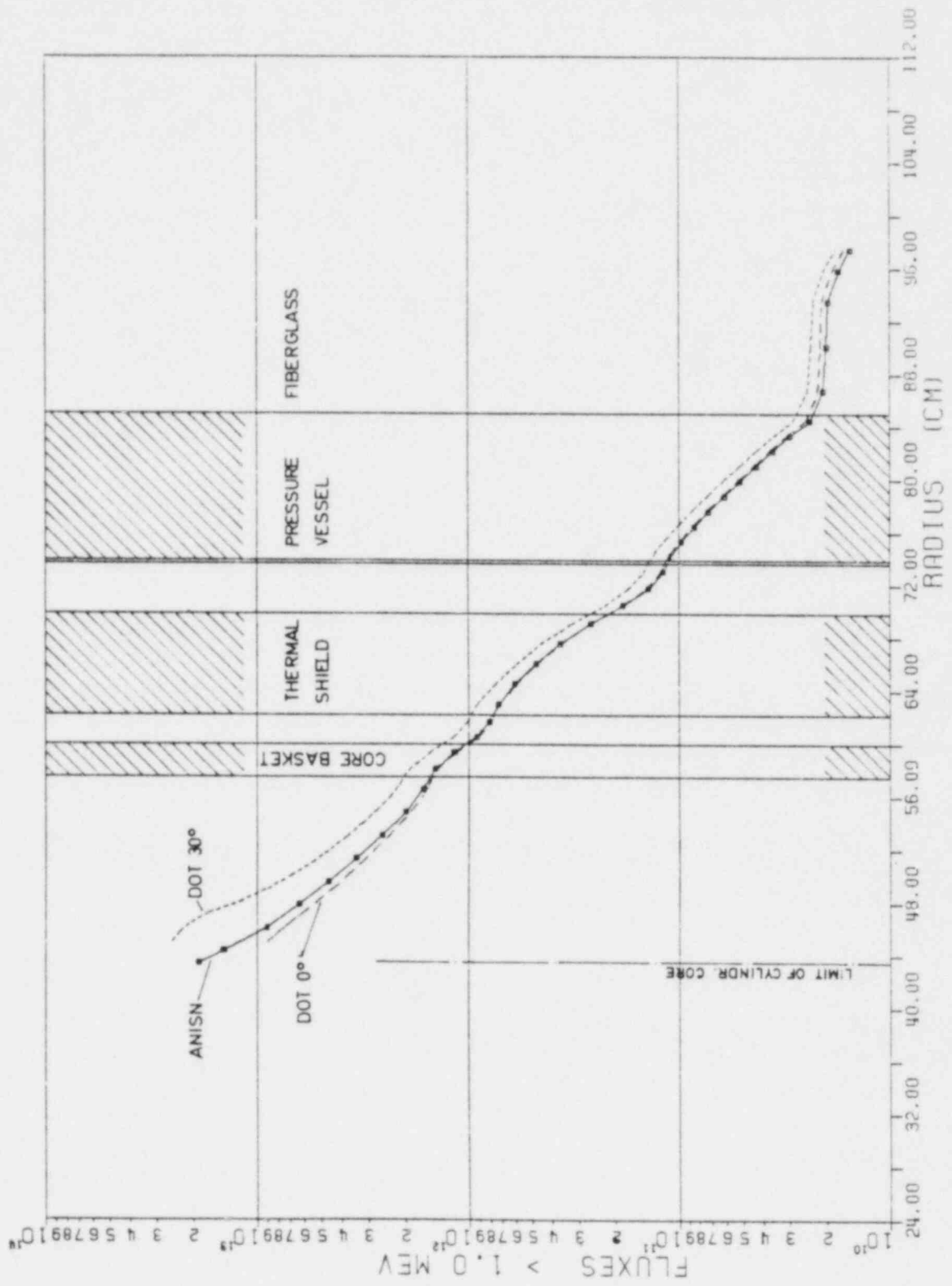
Fig. 3. COMPAR. ANISN 171GR - DOT17GR
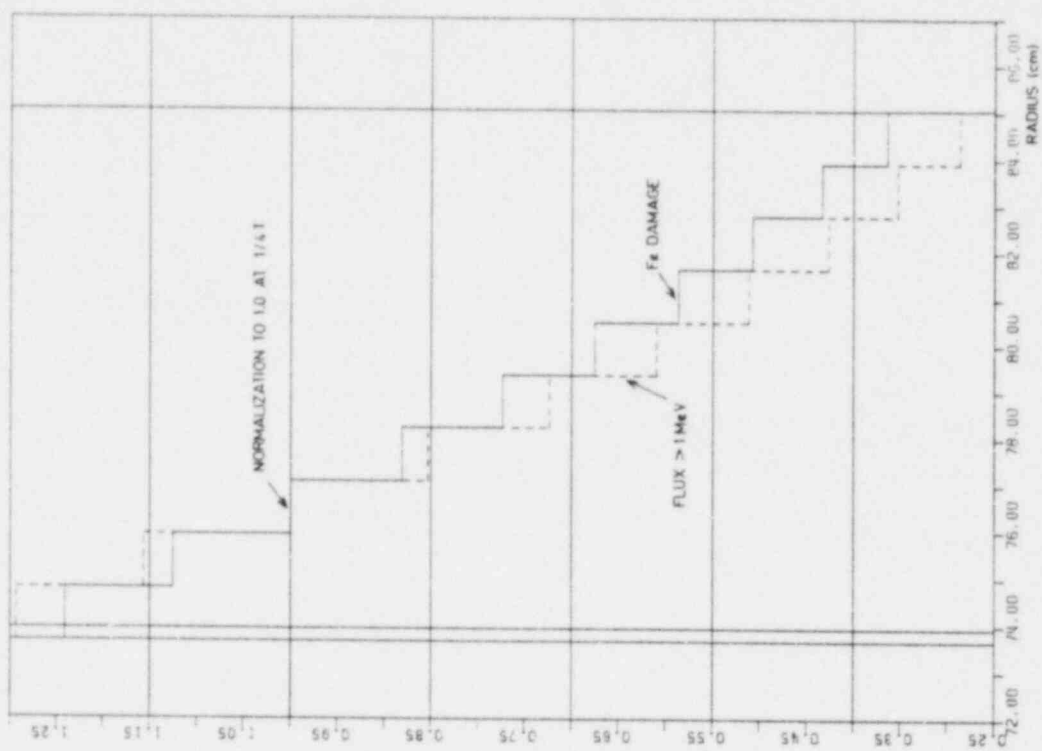
Fig. 5. 8R348. DAMAGE FE ASTM AND FLUX ABOVE 1 MEV
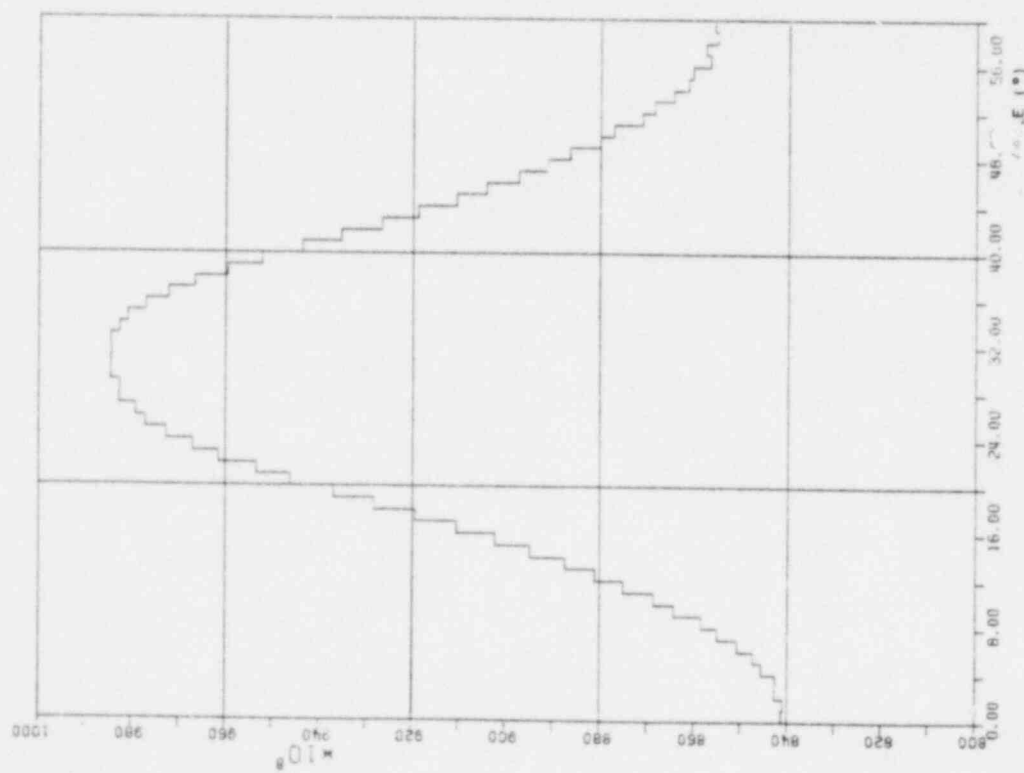
Fig. 4. FLUX ABOVE 1 MEV AT 1/4 T

NEUTRON FLUX DENSITY CALCULATIONS
FOR THE BR3 REACTOR

R. M. Rubin
Radiation Research Associates, Inc.
Fort Worth, Texas, U. S. A.

ABSTRACT

As part of an extensive experimental and analytical program sponsored by the Electric Power Research Institute on LWR pressure vessel irradiation surveillance dosimetry, extensive discrete ordinates calculations have been performed in one and two dimensions to determine the neutron flux density distribution in the core midplane of the BR3 reactor system. Beginning of life calculations were performed for the BR3 Core 4A and Core 4B in one dimension. Both beginning of life and end of life calculations were performed for Core 4B in two dimensions. The one dimensional calculations used the computer code XSDRNPM; the two dimensional calculations used DOT 3.5. The calculations were for P_3 and S_8. The neutron flux density calculations are in reasonable agreement with available data from CEN/SCK.

We find the maximum flux greater than 1 MeV at the 1/4T position in the pressure vessel to be 1.258×10^{11} n/cm^2 sec.

INTRODUCTION

Light water reactor pressure vessels change mechanical characteristics under long term bombardment by neutrons. Estimation of the change is important in estimating the safe operating life of the reactor. Under current operating conditions, the neutron fluence is monitored at a surveillance position outside the pressure vessel. The recommended practice for extrapolating to the pressure vessel combines the measured fluence at the surveillance position with analytical calculations of the fluence in the pressure vessel. The Electric Power Research Institute is cooperating with laboratories in this country and abroad to improve radiation damage dosimetry and calculational methodology. EPRI has sponsored computational and experimental programs for this purpose. As part of the EPRI program, Radiation Research Associates has cooperated with the Centre d'Etude de L'Energie Nucleaire (CEN/SCK) in Mol, Belgium to determine the flux density in the Belgian reactor system, BR3. RRA has performed neutron flux density calculations for comparison with calculations and experiments performed by CEN/SCK. This paper describes the calculations.

DESCRIPTION OF BR3 REACTOR SYSTEM

BR3 is a 40 MW (th) pressurized water reactor operated by CEN/SCK in Mol, Belgium. The reactor has been in operation for over 20 years.

Figure 1 shows a plan view of the BR3 reactor system.[1] The reactor core is hexagonal shaped with hexagonal fuel assemblies. The assemblies labeled with letters or numbers are water filled moderator tubes. Several cylindrical regions surround the core. They are in order: water, core basket, water, thermal shield, water, pressure vessel, a fiberglass-air region and a neutron shield tank.

Figure 2 shows a plan view of the reactor core.[1] The shaded region is the section of core for which data is provided. Elements 63, 65, 80, and 82 are water filled moderator tubes. Material data are given for individual fuel assemblies in zone A. Materials in zone B are homogenized.

CALCULATIONAL RESULTS

RRA performed both one and two dimensional discrete ordinates calculations of the flux density in the BR3 system. The calculations were for P_3 and S_8 in both cases.

Figure 3 illustrates the power distribution in the BR3 reactor core. The power distribution was provided to EPRI and RRA by CEN/SCK.[2] The data is given as neutrons per sec per unit length. Data was provided for beginning of life for Core 4A and beginning and end of life for Core 4B. Pin by pin data is given for zone A, and assembly average data is given in zone B. The calculations required 1) development of a cross-section set suitable for the problem at hand and 2) performance of one and two dimensional discrete ordinates calculations of the flux density outside the reactor core.

One Dimensional Calculations

Figure 4 illustrates the zones used in the one dimensional calculations. Materials were homogenized within zones maintaining volume fractions of each element in a zone. The power distribution was averaged over the zone.

Figure 5 shows the scheme used to prepare the cross sections. We used the 171 group neutron cross sections from the DLC 41 library. The AMPX[3] modules AIM, AJAX, BONAMI, and NITAWL were used for BCD to binary conversion, selection of nuclides, resonance self shielding using the
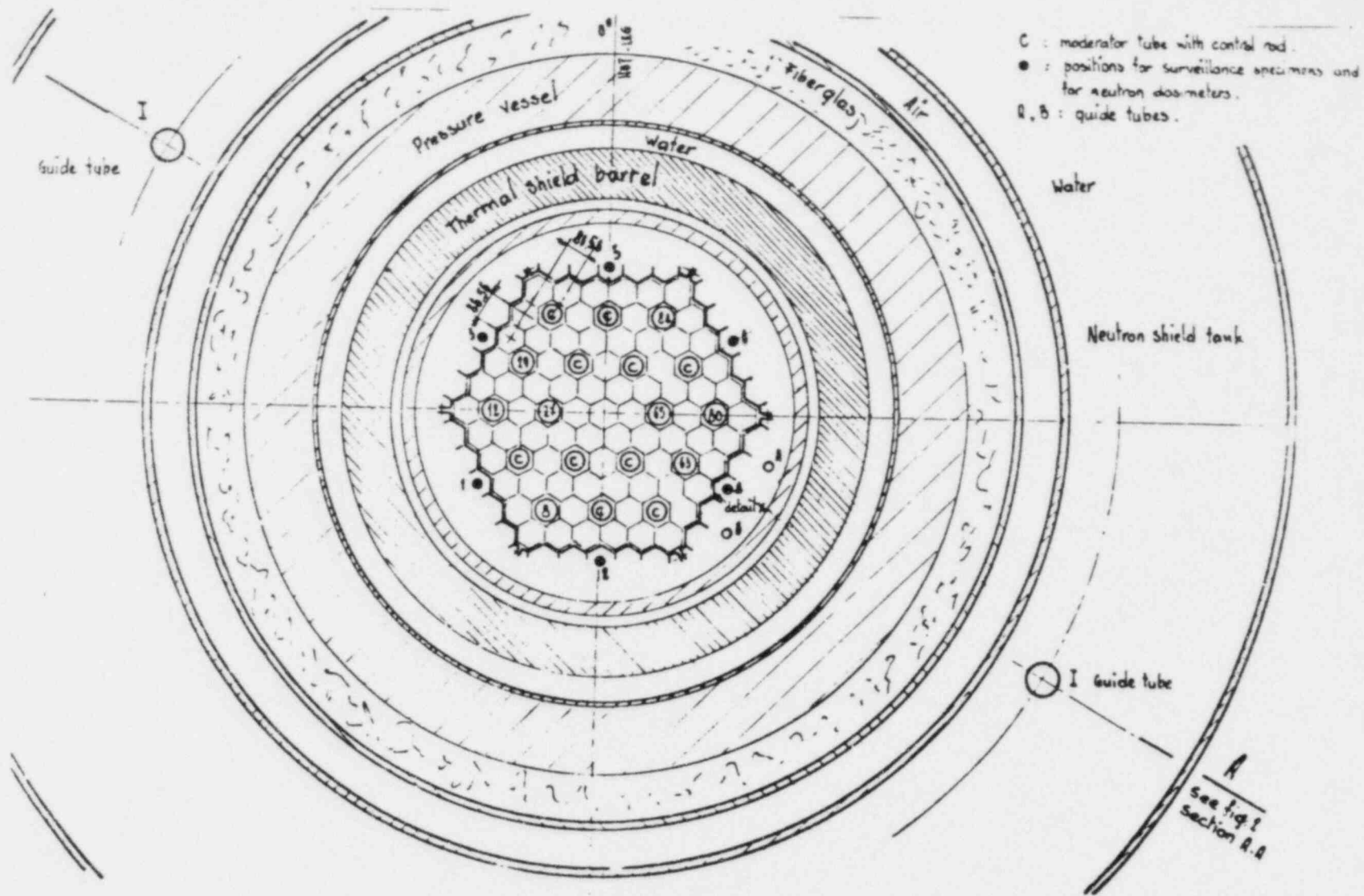
Fig. 1.   Plan View of the BR3 Reactor System
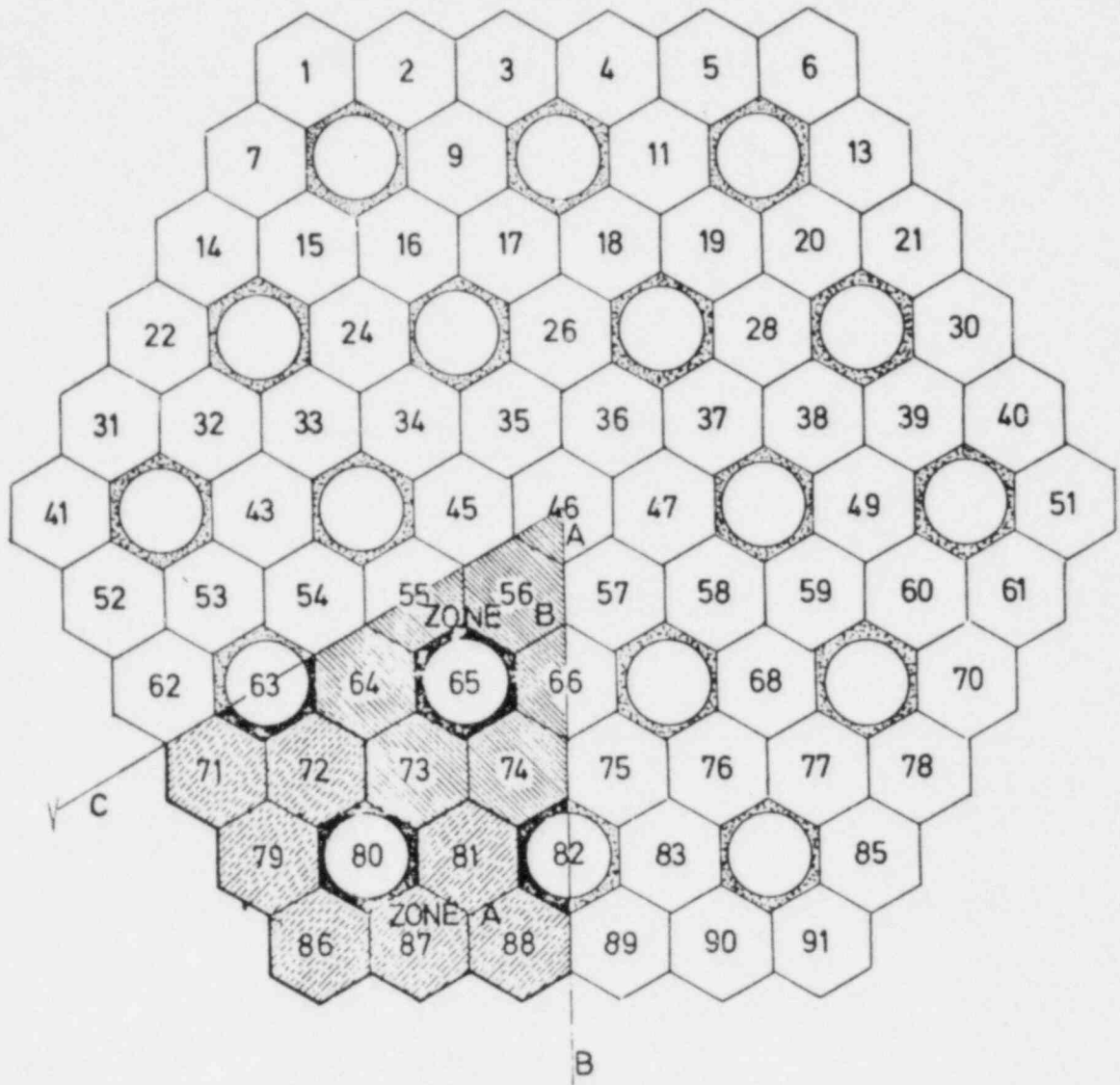
Fig. 2. Plan View of BR3 Reactor Core

499
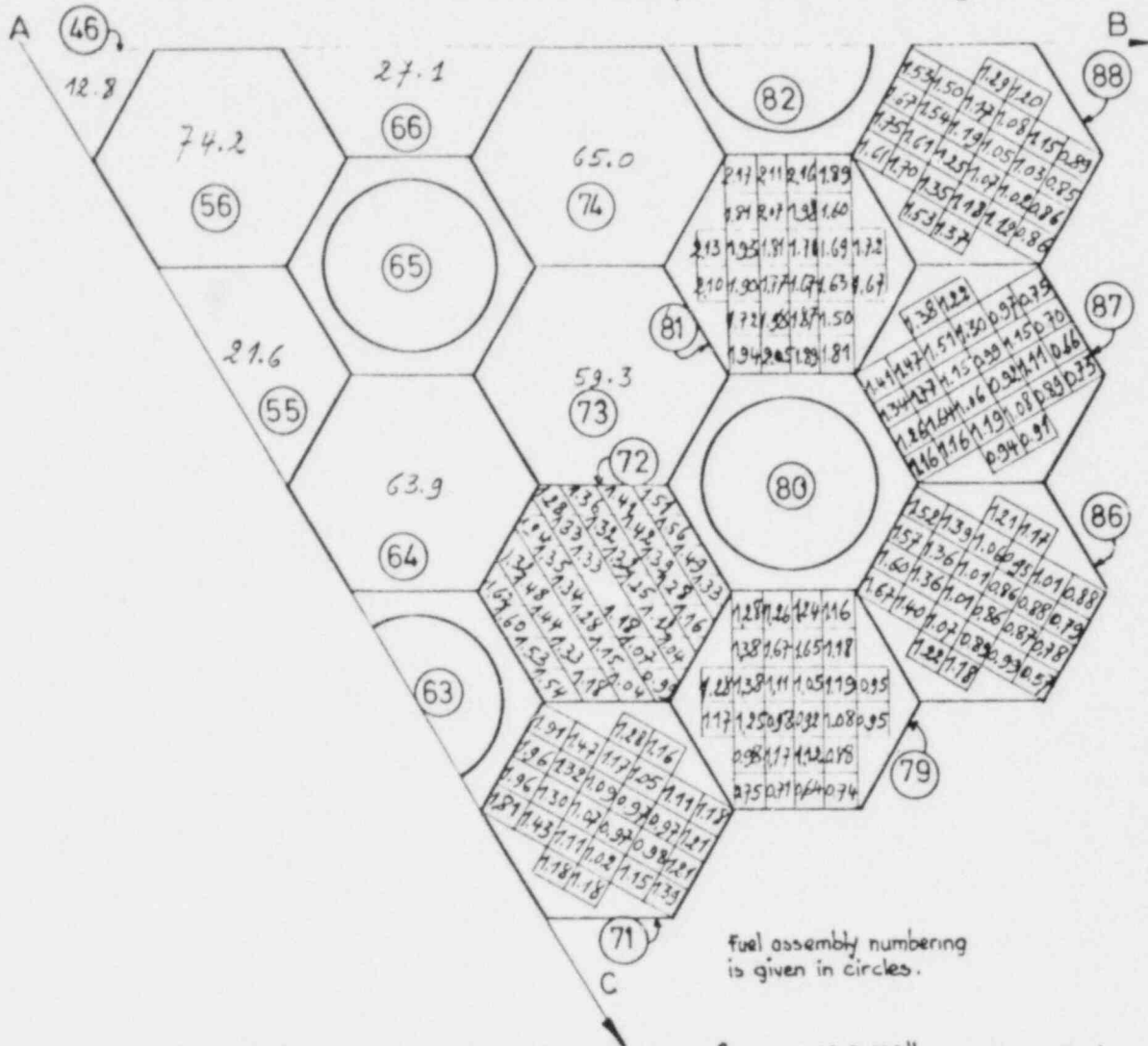
Fig. 3.   Power Distribution for BR3/4B End of Life Core
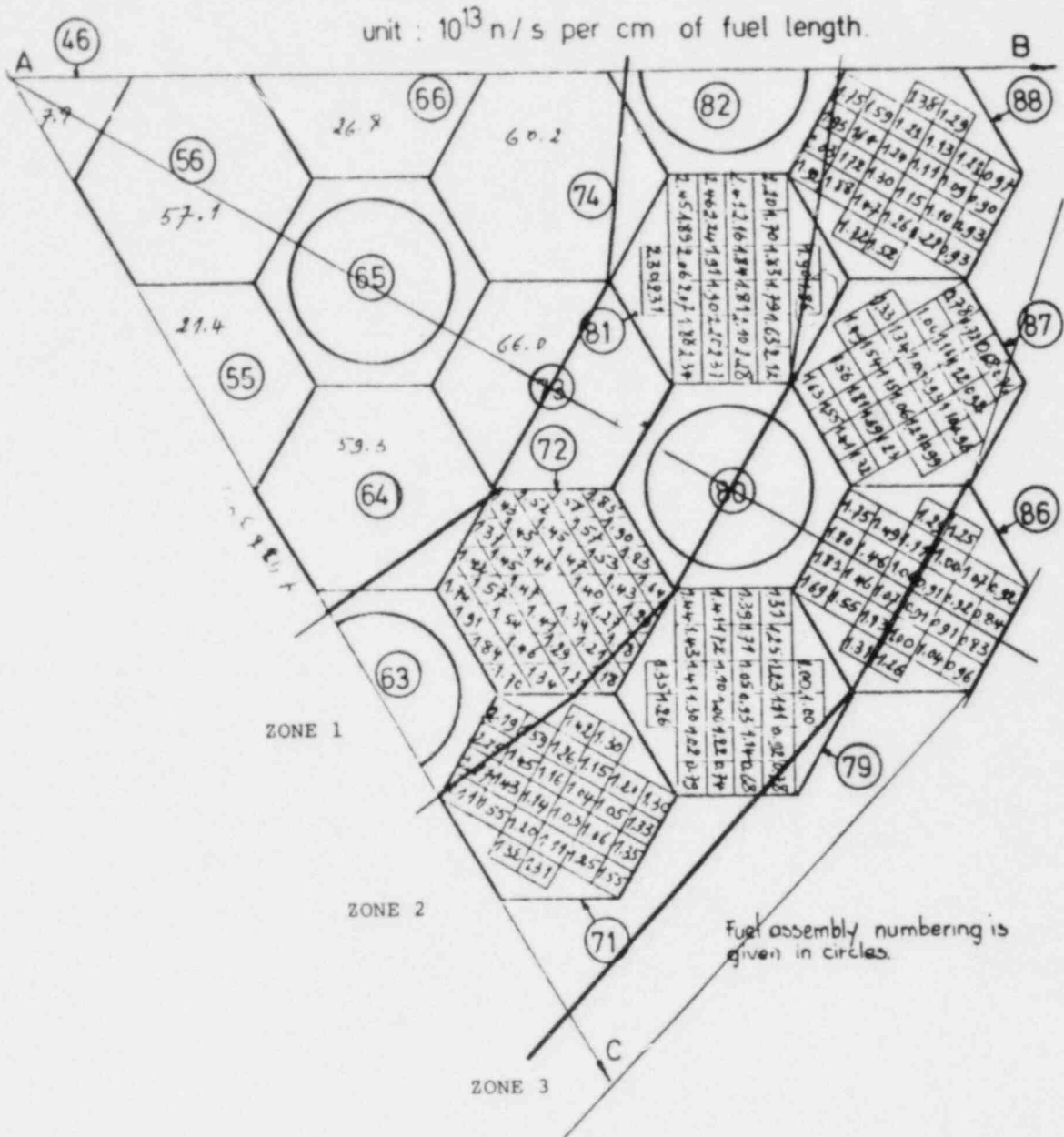
Fig. 4. Zones in the BR3 Core that were Homogenized for use in the One Dimensional Cylindrical Geometry Representation of the Core Region
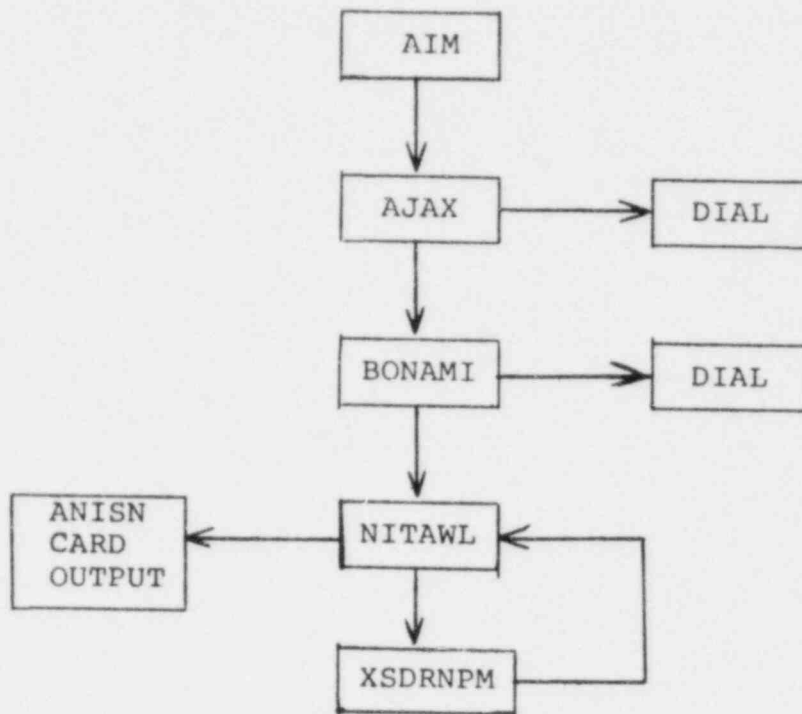
Fig. 5. Flow Diagram for AMP Cross Section Processing

Bondarenko method and putting data into AMPX working format, respectively. The XSDRNPM[3] computer code was used for the one dimensional discrete ordinates calculations and to collapse the 171 group library to 25 groups for subsequent two dimensional calculations with DOT 3.5.[4] The cross sections were collapsed using zone weighting.

Flux Greater Than 1 MeV and Flux Greater Than 0.098 MeV

Figure 6 illustrates the one dimensional results for flux greater than 0.098 MeV and flux greater than 1.0 MeV. We also show results provided to RRA by CEN/SCK. The RRA results are approximately 15 to 20 percent higher than those of CEN/SCK. The difference is due at least in part to differing modeling techniques. The RRA one dimensional model extends further into the water than does the CEN model. However, additional study is required to determine the full reasons for the differences.

Energy Spectra Exterior to the Reactor Core

Figure 7 illustrates one dimensional results for the energy spectrum in the water outside the core and at the 1/4 T position in the pressure vessel. In the energy range .1 to 1.2 MeV, we see the change in the spectrum caused by absorption of neutrons in the pressure vessel.

Figure 8 shows the one dimensional spectra continued up to 11. MeV. Here we see spectral changes again in the range 1 to about 3 MeV. Above 3 MeV, we find principally a magnitude change in the spectrum in going from the water to the 1/4 T position.

Two Dimensional Calculations

Flux Greater Than 1 MeV and Flux Greater Than 0.098 MeV

Two dimensional results for flux greater than 0.098 MeV and flux greater than 1.0 MeV for core 4B are shown in Figure 9 for $\theta=0$. (θ is measured from a line going through core center and center of fuel assembly 86.) Both beginning and end of life data are given. The beginning of life results are parallel to and 6 percent higher than the end of life results for both cases.

Figure 10 shows the ratio of the flux greater than 0.1 MeV to the flux greater than 1.0 MeV. The ratio varies from about 2 near the core to about 5 in the pressure vessel.

Effect of Geometry

Figure 11 shows the effect of geometry on the flux greater than 1.0 MeV. Data for $\theta=30$ degrees corresponds to radial variations along
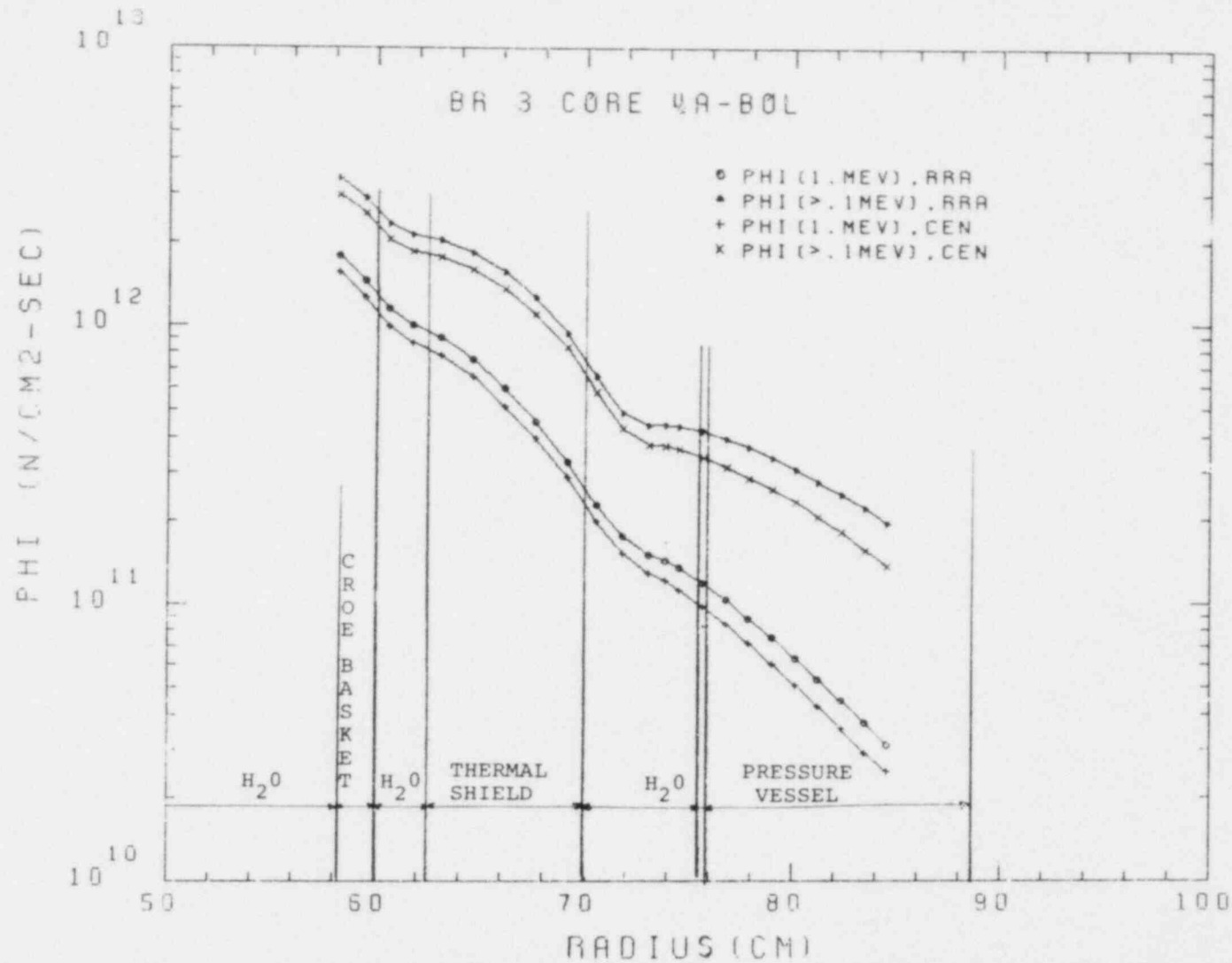
Fig. 6.   Comparison of the RRA and CEN/SCK Calculations of the Neutron Fluxes Greater than 0.098 and 1.0 MeV Versus Radius: Core 4A - BOL

503
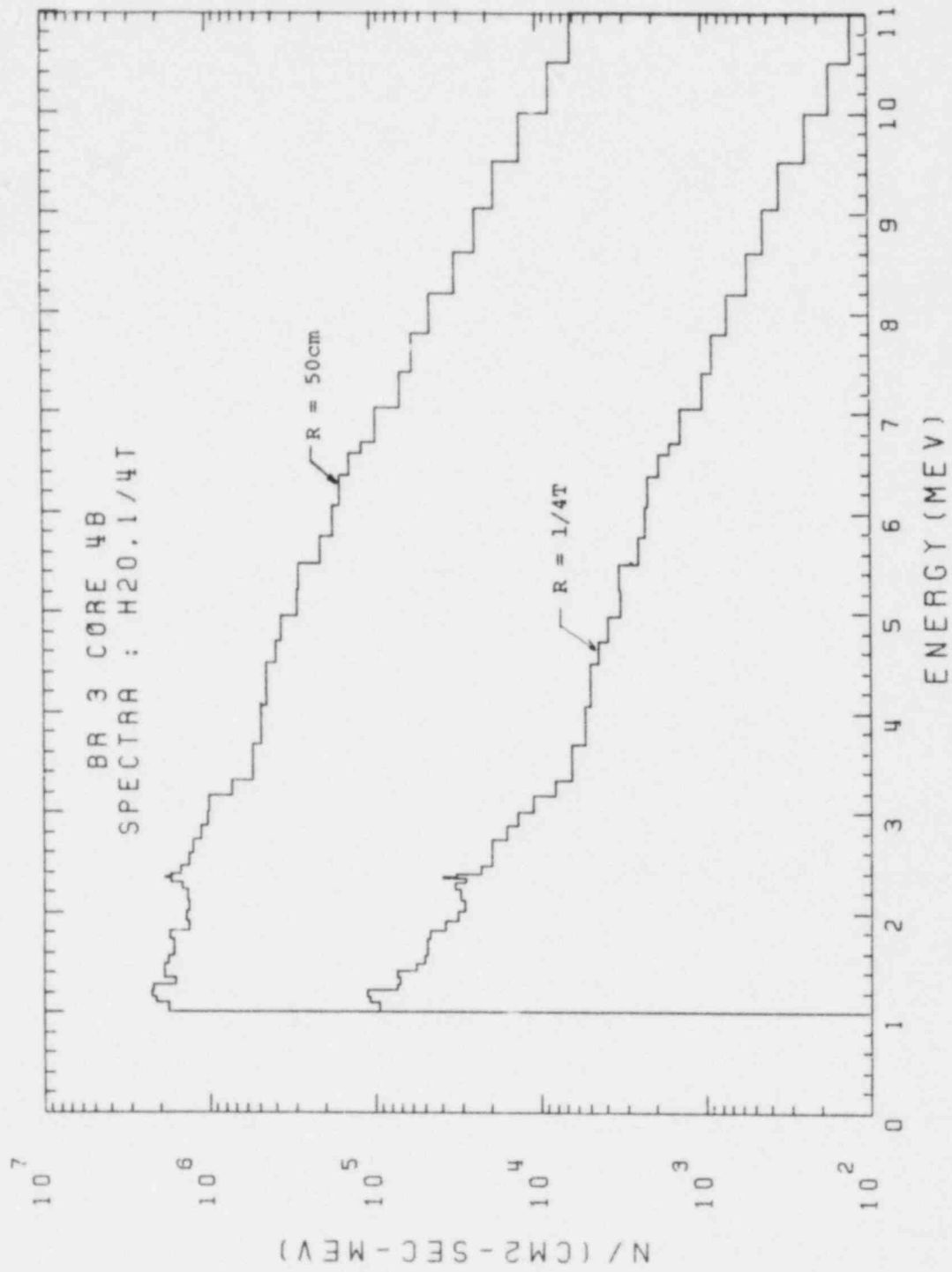
Fig. 7. Neutron Energy Spectra at 50cm and 1/4T for Energies Between 1,0 and 11 MeV: Core 4B-BOL
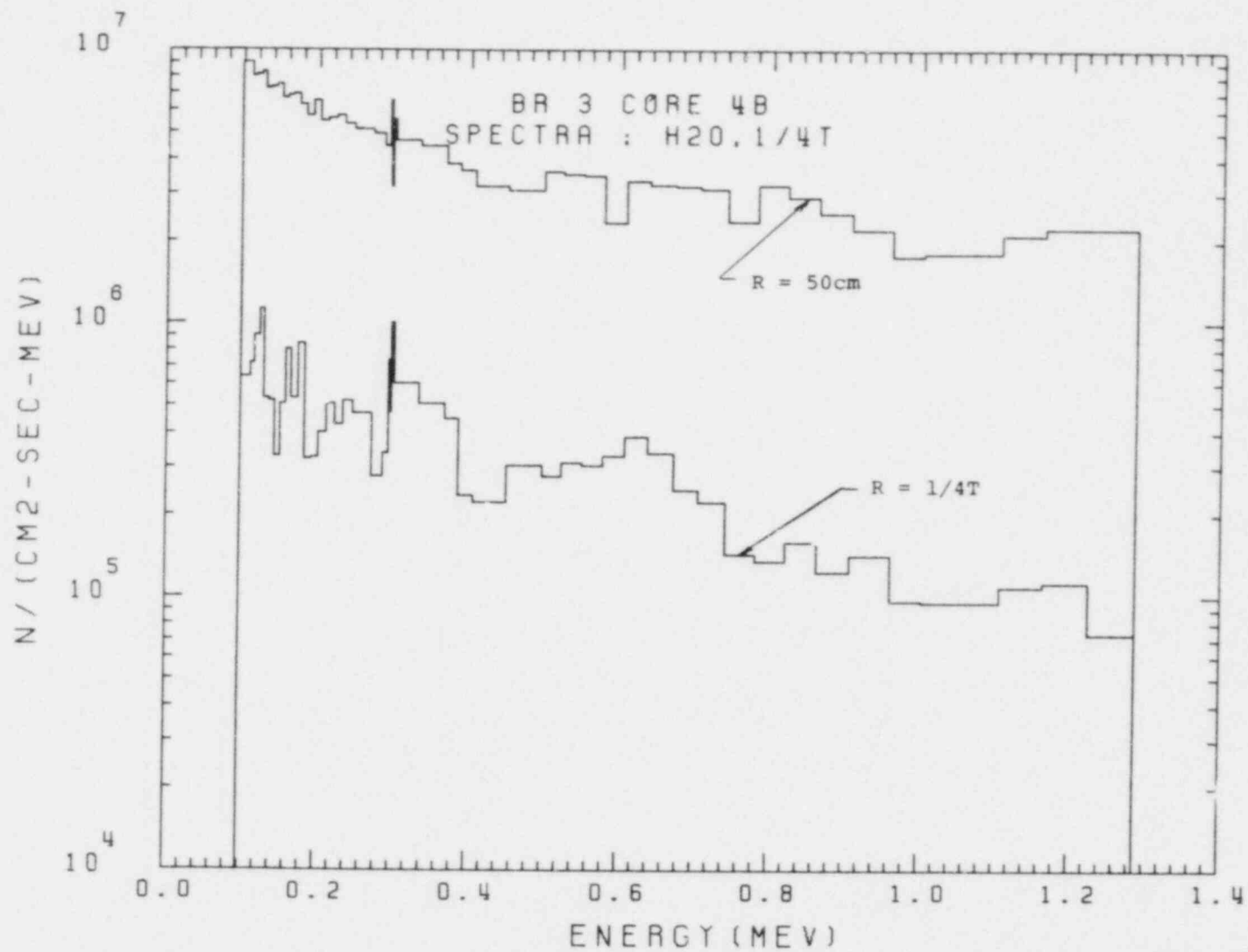
Fig. 8.   Neutron Energy Spectra at 50cm and 1/4T for Energies Between 0.098 and
          1.225 MeV: Core 4B-BOL
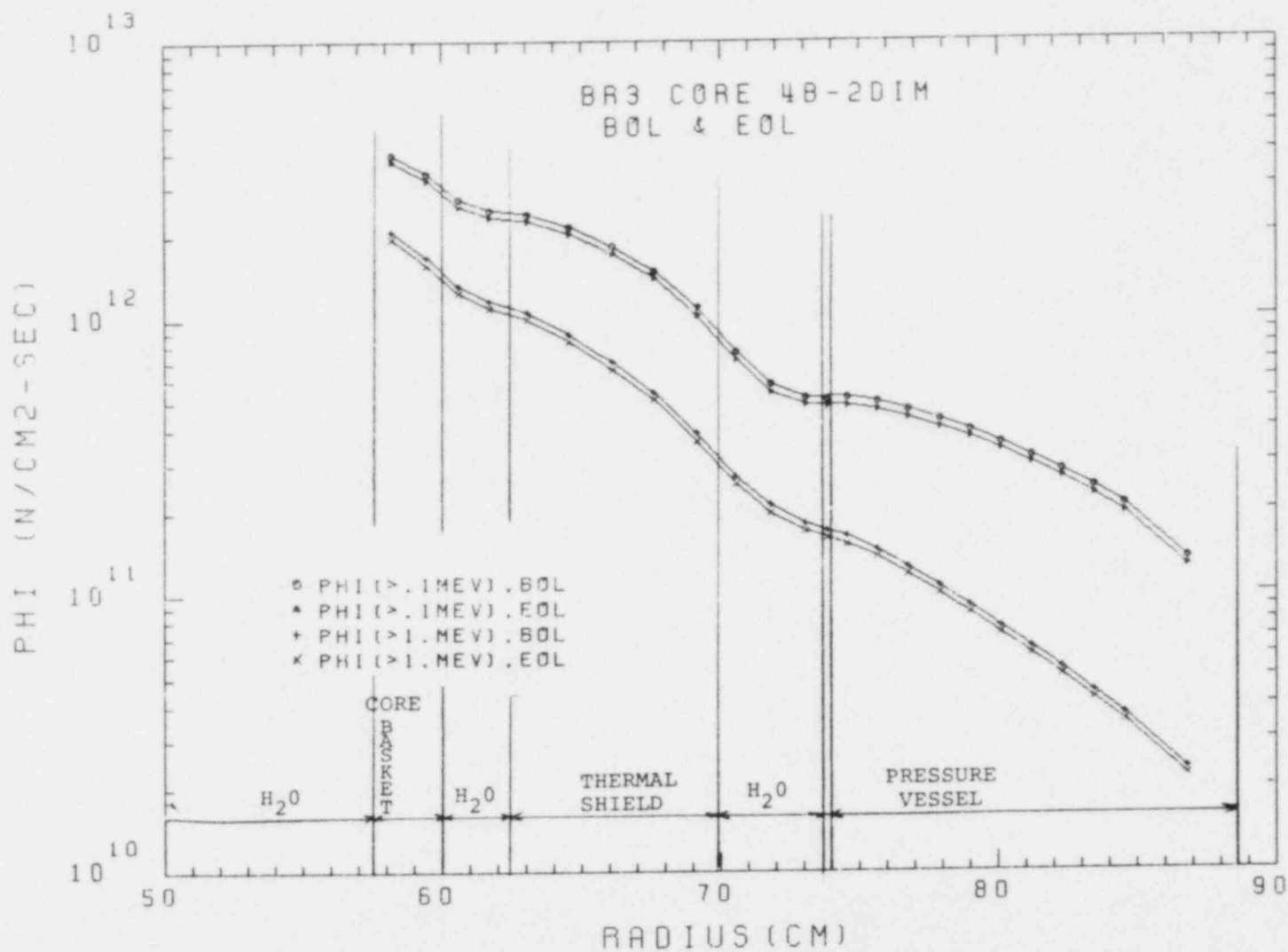
Fig. 9. $\Phi(>1\text{MeV})$ and $\Phi(>0.098\text{ MeV})$ - Results of Two Dimensional Calculations, BR3 Core 4B, BOL and EOL. $(\theta=0)$
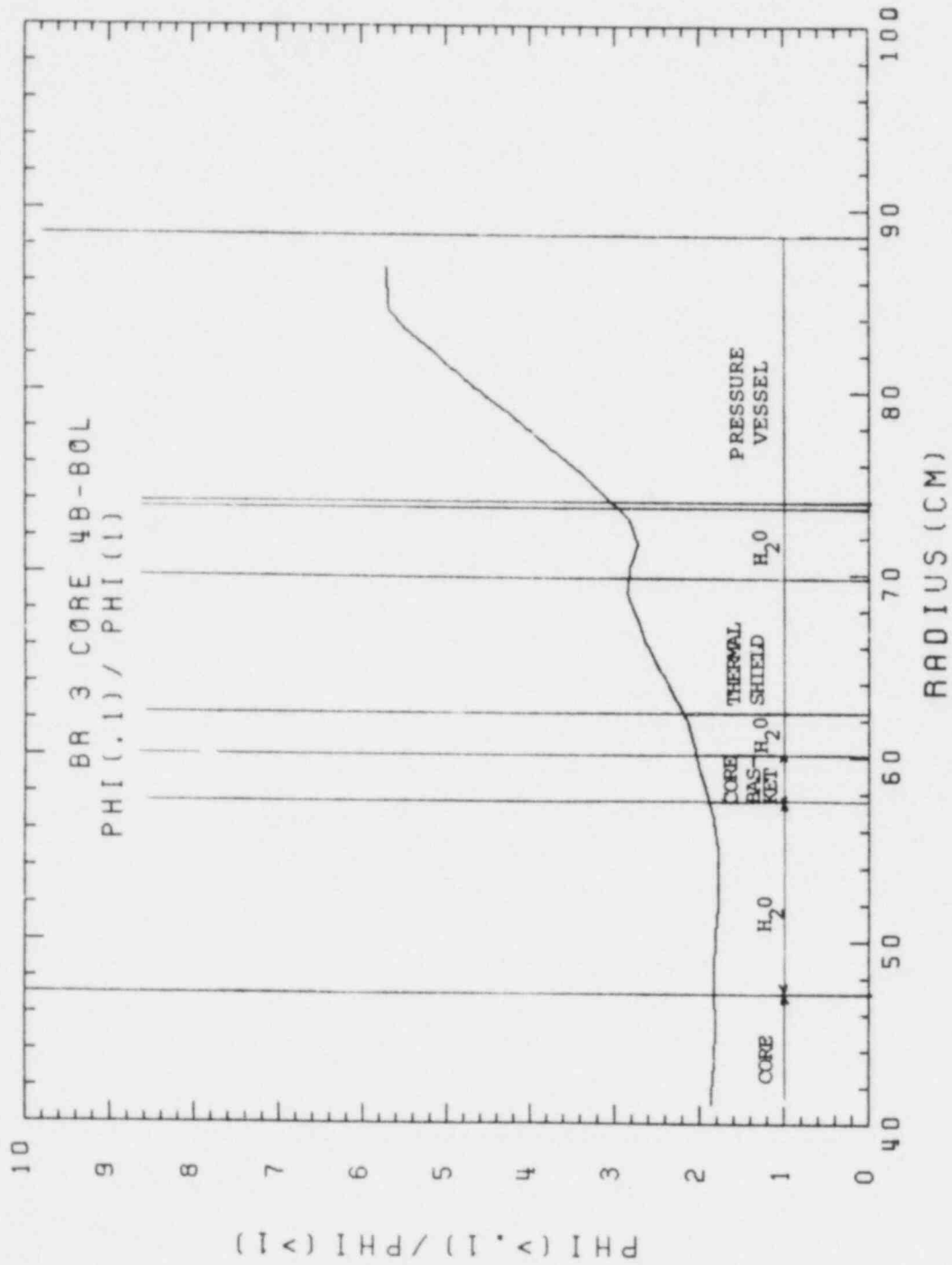
Fig. 10. Ratio of Flux Greater Than 1 MeV to Flux Greater Than 0.098 MeV Versus Radius, BR3 Core 4B, BOL and EOL ($\theta=0^o$).
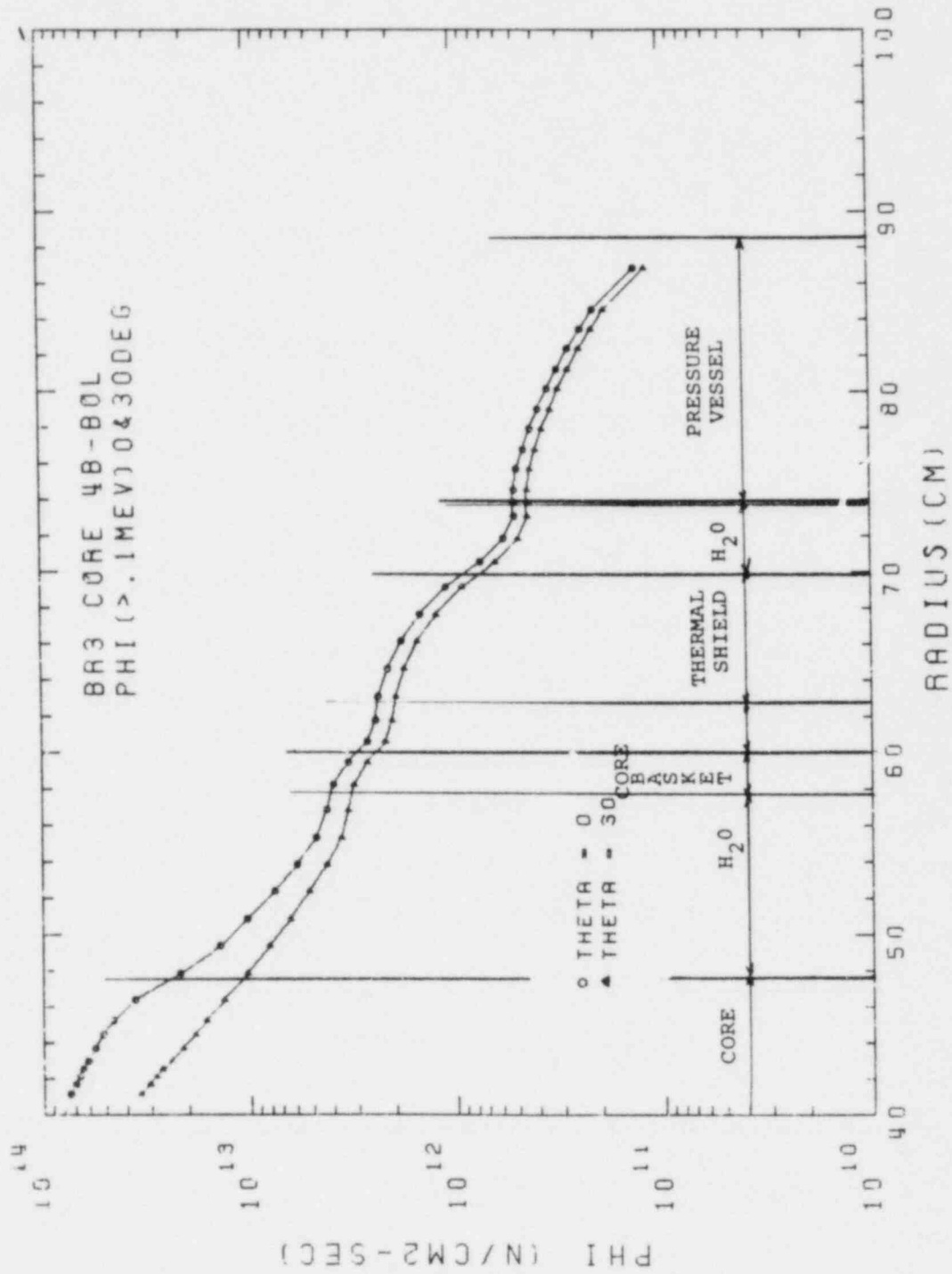
Fig. 11. Flux Greater Than 1 MeV at the 1/4T Position in Pressure Vessel - Azimuthal Variation

a radius passing through the middle of reactor side. The edge of the core is farther from the remainder of the system, and results near the core are lower for 30 degrees as expected. As we move from near the core to the pressure vessel, the effects of geometry are not as strong. Once in the thermal shield, the results for $\theta=0$ and $\theta=30$ degrees are parallel.

COMPARISON WITH EXPERIMENT

Table 1 gives a comparison of RRA calculated ratios of flux greater than .1 to flux greater than 1 MeV with data provided by CEN/SCK for selected positions. The results are in reasonable agreement.

Table 2 gives a comparison of results for flux greater than 1 MeV calculated by RRA, recent calculations by CEN/SCK[5], and recent experimental measurements at CEN/SCK. We find the calculational results in good agreement at positions A and HF. Calculations also agree reasonably well with experiment at position HF. However, calculations and experiment do not agree at position A. Further study is required to determine the reasons for disagreement.

TABLE 1. RATIO OF FLUX GREATER THAN .1MEV TO FLUX GREATER
THAN 1 MEV AT SELECTED POSITIONS IN THE BR3
REACTOR SYSTEM AS COMPUTED BY RRA AND CEN/SCK

POSITION	RRA	CEN/SCK**
1. Surveillance Position*	1.8	1.9
2. Dosimetry Position in Reflector	1.8	1.8
3. PVF (in water)*	2.7	2.9
4. PVF (in steel)*	2.9	3.1
5. PV - 1/4T	3.7	3.6

*RRA values are chosen at positions believed to be those used
by CEN/SCK. Exact CEN locations are not known at this writ-
ing.

**Data from CEN/SCK is calculated for Core 4A.

TABLE 2. VALUES OF FLUX GREATER THAN 1 MeV AT THE
LOCATIONS OF BR3 EXPERIMENTS (CORE 4B)

Position			Measured	Calculated RRA	CEN/SCK[+]
Location	R (cm)	θ (deg)	$(n/cm^2 sec)$	$(n/cm^2 sec)$	
HF	45.0	30	1.01+13	9.254+12	1.15+13
A	55.0	20	1.70+12	2.170+12	2.24+12
Outside Core Barrel	61.1	0	NA*	1.176+12	NA
Outside Core Barrel	61.1	30	NA	1.007+12	NA

*NA = not available at this date

[+]Reference 5

REFERENCES

1. "Neutron Dosimetry Programme in The BR3 Reactor Core 4B Neutrons Calculations: Geometrical Description and Composition of the Outer Regions," document from CEN/SCK, Mol dated September 29, 1977.

2. "BR3/4B - Fission Neutron Source Distribution and Isotopic Compositions at the End of Life," document from CEN/SCK (313/79-03) dated July 26, 1979.

3. N. M. Greene, et al, AMPX, A Modular Code System for Generating Coupled Multigroup Neutron-Gamma Libraries from Data in ENDF Format Oak Ridge National Laboratory Report, PSR-63 (December, 1978).

4. DOT 3.5 - Two Dimensional Discrete Ordinates Radiation Transport Code, Radiation Shielding Information Center, Oak Ridge National Laboratory Code Package CCC-276 (1977).

5. G. Minsart, et al, "Calculation of the Fast Neutron Flux and Damage in the Pressure Vessel of the BR3 Reactor," a paper presented at the Fourth ASTM-Euratom Symposium on Reactor Dosimetry in Washington, D. C., March 22-26, 1982.

BROWN'S FERRY AND ARKANSAS NUCLEAR ONE
PRESSURE VESSEL NEUTRON FLUENCE BENCHMARKS

Robert A. Shaw
Electric Power Research Institute
Palo Alto, California, USA

ABSTRACT

A brief overview of the EPRI program on reactor vessel
pressurized thermal shock is given, including thermal
hydraulics testing and analysis, integrity assessment
analysis, plant analysis and technology transfer,
remedial action evaluation, and neutron dosimetry.
The particular efforts in the latter, the neutron
dosimetry program, are emphasized. This program
includes experimental and analytical work associated
with the neutron fluence for the reactor vessels at
Brown's Ferry-3 and at Arkansas Nuclear One-1 and -2.

INTRODUCTION

The nature of this paper has changed since the abstract was sub-
mitted. The title is not descriptive of the entire paper.

The broad scope of the EPRI program on reactor vessel pressurized
thermal shock will be described. Following this, the particular emphasis
on neutron dosimetry and fluence calculations at and near the pressure
vessel boundary will be characterized. Other papers being presented
at this meeting will discuss in more detail the particular issues and
results of the EPRI-supported dosimetry work.[1-4]

EPRI REACTOR VESSEL PRESSURIZED THERMAL SHOCK PROGRAM

EPRI has been supporting research on reactor vessel integrity for
the past several years. This work has focused on materials and dosimetry.
However, in June of 1981, thermal hydraulics research was expanded and
accelerated. In addition, EPRI has initiated cooperative programs for
utilities to evaluate reactor vessel pressurized thermal shock for
specific plants. This effort is particularly aimed at assisting in
the application and transfer of technology to the utilities and to the
PWR vendors.[8]

The five principal elements of the EPRI coordinated program are:

- thermal hydraulics testing and analysis
- integrity assessment and analysis
- plant analysis and technology transfer
- remedial action evaluation
- neutron dosimetry

Each of these will be discussed briefly in the following paragraphs with neutron dosimetry being emphasized in the remainder of the paper.

In the area of thermal hydraulics testing and analysis, EPRI has completed scoping tests of fluid and thermal mixing using one-fifth scale transparent models of cold legs and downcomers representative of current PWRs. The analysis effort includes modeling of the turbulent flow mixing and heat transfer and fluid stratification. The results to date indicated substantial mixing of the loop flow with high pressure injection water by the time the mixture reaches the downcomer which potentially limits the extent of thermal shock. Tests at higher pressure and in a larger scale facility are planned for this year. These will help to validate the methods being used to predict the transient temperatures at the pressure vessel wall.

The efforts in integrity analysis are divided into four topics:

(1) the prediction of radiation damage
(2) the measurement of fracture toughness of irradiated materials
(3) the measurement of crack arrest conditions for irradiated materials
(4) methods of annealing embrittled reactor vessels

The objective of these is to integrate the results from EPRI efforts and from other organizations into a state-of-the-art procedure to estimate safe and reliable vessel lifetimes.

The area of plant analysis and technology transfer emphasizes the application of R&D technology to particular plants. Particular parameters such as the thermal shock transient scenario, the fluid and thermal mixing, composition of critical welds, the stress intensity calculations, and the fracture toughness profiles for the various materials present will be incorporated. The results for the selected thermal transient would be an estimate of (a) the operational time available before crack initation is expected; and (b) the operational time available before initiation and arrest of such cracks is expected.

The remedial action evaluation has particularly dealt with the evaluation of the following possible remedial actions: modified operational strategies; raising the safety injection water temperature; neutron flux reduction; and reactor vessel annealing. The thermal annealing research results have included the following: (a) complete

material properties recovery is anticipated for an annealing temperature of 850°F for one week; (b) reimbrittlement rates are less than for the original annealment rates; (c) recovery of the fracture toughness transition can be monitored with tensile or hardness measurements; (d) the practicality of vessel annealing and continuing licensability of an annealed vessel remains to be established.

EPRI DOSIMETRY PROGRAM

It is necessary to characterize the neutron flux and energy spectrum for the purpose of assessing radiation induced embrittlement in nuclear power plant pressure vessels. Primary reliance is placed on a combination of analytical calculations and a series of experimental foil measurements. The comparison of the analytical calculations and the foil activities is used to gain better measurement of the total neutron fluence that has been absorbed by the reactor pressure vessel. These fluences are in turn used to predict material toughness, which is particularly sensitive to material composition, such as copper in weld materials.

An analytical program is underway at Oak Ridge National Laboratory under EPRI sponsorship to develop and use an advanced methodology for reducing the uncertainties in the estimate of the spectrum and the total fluence determined from dosimetry measurements.[5] The approach is to combine differential cross section and dosimetry data, both measured and calculated in a consistent fashion using information from various benchmark fields of increasing complexity, eventually including fields of operating power reactors. In addition to obtaining improved estimates of the fluence and the spectrum, the methodology can be used to determine the uncertainties associated with these quantities.

In the experimental portion of this program, foils have been exposed in operating power reactors. In-vessel foil experiments have been carried out by General Electric and ex-vessel measurements under an EPRI project at Tennessee Valley Authority's Brown's Ferry-3.[1,6] PWR experiments have been carried out at Arkansas Power and Light's Nuclear One-1 by the University of Arkansas.[2] These measurements could be conducted only ex-vessel. A set of measurements at ANO-2 is presently being planned. This work would include in-vessel as well as ex-vessel foil measurements. Supporting neutron transport calculations are being conducted at the University of Missouri, Rolla for ANO-1 and -2.[3] In addition, analytical measurements have been performed to calculate the neutron fluence in the BR-3 reactor located in Belgium for direct comparison with the analytical and experimental results.[4]

A number of recommendations and observations have resulted from the EPRI Dosimetry Program:

(1) The primary role of dosimetry measurements conducted
     through foil activation is to verify the calculational
     techniques at operating power reactors. This assesses
     the ability to predict the total fluence that various
     regions of a particular pressure vessel have received
     by calculations using neutron transport codes.

(2) The best basis for comparison of the neutron transport
     calculational results and the experimental foil
     activities is a direct comparison of the foil activities.
     It is preferred that the neutron transport calculations
     be carried to the point where foil activities are
     predicted, rather than for foil activities to be used
     to develop an unfolded neutron spectrum.

(3) The susceptibility to pressure vessel thermal shock
     must be conducted for each individual nuclear power
     plant. This is true for neutron fluence determinations
     as well as the other characteristics such as pressure
     vessel embrittlement, thermal mixing, and the stresses
     associated with the thermal shock.

(4) The uncertainty associated with the materials properties
     and the determination of thermal stresses is sig-
     nificantly greater than the uncertainties associated
     with dosimetry. The scatter associated with the
     fracture toughness in the unirradiated as well as
     the irradiated case, is quite substantial. On the
     other hand, the uncertainty associated with foil
     determinations of total neutron fluence on the pressure
     vessels, appears to be less than 50%, and many
     observers suggest it is less than 30% for specific
     analysis of a particular reactor vessel.

(5) It is hard to perceive how advances in dosimetry research
     will benefit the operators of nuclear power plants as
     they strive to relieve themselves of the concerns of
     pressure vessel embrittlement. The development of
     new foil techniques for dosimetry, as an example,
     would be expected to take years before being accepted
     by operating and regulatory staffs.

(6) It is likely that new fuel arrangements which are devised
     to reduce neutron fluence at the pressure vessel would
     require verification of calculational techniques and,
     hence, would be treated in a conservative fashion by
     those determining the reduction in embrittlement
     susceptibility.

(7) An increasing emphasis on using displacements per atom (dpa)
     certainly appears to be a better basis for evaluation of

total fluence than either fast fluence above 1 Mev or
fluence greater than 0.1 Mev. Nonetheless, one must
consider the inherent uncertainties involved in the
calculations that determine the total dpa to a given
structure.

(8) Neptunium's usefulness as an activation foil stems from
its' neutron spectral response, being the most similar
to that of dpa of any of the foils that are presently
being used. Nonetheless, for some as yet undetermined
reason, the variations in the neptunium foil activities
are substantially greater than those of other foils.
Until the causes of these variations can be determined
and corrected, reliance on neptunium as a fluence and
dpa indicator is in question.[7]

(9) Niobium-93 may offer an attractive alternative to
neptunium. It has an attractive half-life of 12.6
years. Its' sensitivity to neutrons covers an energy
spectrum that is close to that of dpa and its'
mechanical and emission properties appear to be
appropriate. It has been used in Europe for some
time. Despite the consideration raised in Item 5
above, irradiation of new foil materials, or the
testing of new fluence monitoring techniques, is
of value to utilities. When acceptability is
achieved for certain techniques, the utility which
has used this technique will have this additional,
more significant data.

EPRI will continue to emphasize two areas in neutron dosimetry:
1) the reduction of and the determination of uncertainties in spectral
estimates, and 2) direct measurements of total fluence at operating
power reactors through the use of foil activations and direct comparison
of these results with the calculated neutron spectra. The nine items
cited above are an expression of some of the observations and concerns
we have regarding dosimetry and its' applications to the pressure
vessel thermal shock issue.

REFERENCES

1. G. C. Martin, Jr. and R. A. Shaw, "Brown's Ferry Unit-3 Cavity
   Neutron Spectrum Analysis", Fourth ASTM-EURATOM Symposium on
   Reactor Dosimetry, Washington, DC (March 1982).

2. R. A. Shaw, W. E. Brandon, C. O. Cogburn, R. R. Culp, J. L. Meason,
   W. W. Sallee, "Neutron Dosimetry in the Pressure Cavity of Two
   Pressurized Water Reactors", Fourth ASTM-EURATOM Symposium on
   Reactor Dosimetry, Washington, DC (March 1982).

3. N. Tsoulfanidis, D. R. Edwards, D. Frankenbach, R. Lemaster, K. Wincell, R. A. Shaw, "Calculations of Neutron Fluxes at the Pressure Vessel and the Cavity of a PWR", Fourth ASTM-EURATOM Symposium on Reactor Dosimetry, Washington, DC (March 1982).

4. R. M. Rubin, "Neutron Flux Density Calculations for the BR-3 Reactor", Fourth ASTM-EURATOM Symposium on Reactor Dosimetry, Washington, DC (March 1982).

5. Development and Demonstration of an Advanced Methodology for LWR Dosimetry Applications, EPRI Report NP-2188 (December 1981).

6. Brown's Ferry Unit-3 Cavity Neutron Spectral Analysis, EPRI Report NP-1997 (August 1981).

7. J. Grundl, C. Eisenhauer, G. Lamaze, E. D. McGarry, C. Cogburn, N. Tsoulfanidis, L. Kellogg, W. McElroy, NRC-EPRI Studies of Pressure-Vessel-Cavity Neutron Fields, Presented at the NRC Ninth Water Reactor Safety Information Meeting, Washington, DC (October 1981).

8. T. Marston, B. Sun, B. Chexal, EPRI Pressurized Thermal Shock Program: Status and Review, Presented at the Ninth Water Reactor Safety Review Meeting, Gaithersburg, MD (October 1981).

CALCULATION OF NEUTRON SPECTRA AT THE PRESSURE VESSEL AND CAVITY OF A PWR

N. Tsoulfanidis, D.R. Edwards, D. Frankenbach,
L. Kao, R. Lemaster, and K. Wincel

ABSTRACT

Transport calculations of the neutron flux have been performed in the region extending from the center of the core to the concrete wall forming the cavity behind the pressure vessel of a Pressurized Water Reactor. The transport codes XSDRNPM and DOT-IV were used in 1-D and 2-D geometries, respectively. A $45°$ slice of the reactor divided into 52 angular intervals formed the basis of a R-θ model for DOT-IV. The neutron source distribution for the R-θ calculation was obtained from information provided by the Performance Data Output (PDO) report which is produced by the plant computer based on in-core measurement of the power distribution. The R-θ flux was corrected for leakage along the Z axis by combining results of a 1-D and a 2-D R-Z calculation. The results are compared with a neutron spectrum measured at one point in the cavity. For E>300keV the result of the calculation is lower than that of the experiment; for E<300keV, the opposite is true. In front of the Pressure Vessel the flux for E>1MeV is 9.16×10^9 n/cm^{2}s. Assuming a 40 year lifetime and a 80% capacity factor, the neutron fluence with E>1MeV hitting the pressure vessel will be 9.24×10^{18} n/cm^2.

INTRODUCTION

This work presents calculations of neutron energy spectra in a Pressurized Water Reactor (PWR) in the space that extends from the center of the core up to the end of the cavity surrounding the Pressure Vessel (PV). Knowledge of the radiation field to which critical components such as the PV and support structures are subjected is important because it provides us with a more accurate estimate of the radiation dose and its effect-radiation damage-imparted upon these components. Since radiation damage changes the strength of materials, knowing the radiation field enables us to predict radiation-induced changes with greater accuracy and thus increase the margin of safety during operation of a nuclear power plant.

In all nuclear power plants PV surveillance dosimetry programs have been established providing useful experimental data. The Nuclear Regulatory Commission (NRC) is supporting these efforts and furthermore is attempting to standarize the dosimetry procedures employed[1]. The Electric Power Research Institute (EPRI) is also supporting the effort and this report is a part of this program.

Calculations of neutron energy spectra in PWR's have been reported in the past. A brief but comprehensive review of the problem was given by Rahn[2] and by Gritzner et al[3]. The proceedings[4] of a special session during the American Nuclear Society meeting of November 1978 also constitute an excellent review. Finally, the report on the PCA blind test[5] provides valuable insight into this problem.

The calculations presented in this report are compared with experimental results obtained by Dr. C. Cogburn and his co-workers of the University of Arkansas. The experiments were performed at the Arkansas Power and Light Company, Arkansas Nuclear One (ANO) plant.

METHOD OF CALCULATION

Neutron Spectra have been calculated for the ANO-1 reactor using 1-D and 2-D transport codes. The 1-D calculations were performed using the transport code XSDRNPM with cylindrical geometry and reflective boundary conditions on the left and vacuum boundary conditions on the outer surface of the concrete wall. The following equation was used to obtain the source normalizacion for the 1-D calculation (parameter XNF in XSDRNPM)

$$XNF = \frac{Power \ (Mwt) \ x \bar{\nu} \ x 2.989 x 10^{16} \ (fissions/Mwt\text{-}s)}{core \ height \ (cm)} = 5.22 x 10^{17} n/cm\text{-}s \quad (1)$$

For ANO-1 P=2599.6 Mwt and core height = 366 cm, $\bar{\nu}$=2.46=average number of neutrons per fission

For our study, the basic cross section data came from ENDF/B version IV in the form of the VITAMIN-C[6] library. Two libraries that were obtained by collapsing the VITAMIN-C cross sections are the BUGLE-80[7] and SAILWR[8] which consist of 47 neutron and 20 gamma energy groups. The SAILWR library is a variation of BUGLE-80.

We used the cross sections for ^{238}U and the plutonium isotopes from the SAILWR library. The cross sections for all the other isotopes were obtained by collapsing the 171 group cross sections of VITAMIN-C into the 26-neutron group structure shown in Table 1, using the code XSDRNPM. All the calculations (1-D and 2-D) were executed using a P_3 expansion of the scattering cross section and a S_8 angular quadrature.

Table 1. The 26-Neutron Group Energy Structure

Group	E Upper	Group	E Upper
1	17.33 Mev	14	183.2 Kev
2	12.21 Mev	15	111.1 Kev
3	10.00 Mev	16	67.4 Kev
4	7.41 Mev	17	31.8 Kev
5	4.97 Mev	18	26.1 Kev
6	3.01 Mev	19	24.2 Kev
7	2.47 Mev	20	15.0 Kev
8	2.31 Mev	21	7.1 Kev
9	1.65 Mev	22	454.0 ev
10	1.00 Mev	23	101.3 ev
11	742.7 Kev	24	1.86 ev
12	497.9 Kev	25	0.414 ev
13	297.2 Kev	26	0.100 ev

The 2-D calculations were performed using DOT-IV in R-θ geometry. The R-θ model of ANO-1 used in DOT is shown in Fig. 1. One eighth of the reactor (a 45°slice) was modeled, divided into 52 angular intervals. Along the radial direction, the calculation was accomplished in two steps. The first step covered the region from the core center up to the PV whereas the second covered the area from the water region in front of the PV up to the end of the concrete wall forming the cavity around the PV. The output of DOT from the first step was introduced into the same code as a neutron source for the second step employing bootstrapping. Sixty-five radial intervals were used for the first step and 49 for the second. Reflective boundary conditions were applied along the 0° and 45° lines from the center of the core up to and including the PV. Vacuum boundary conditions were employed beyond that point.

The neutron source used in the calculation was obtained from information contained in the Performance Data Output (PDO) report that is produced by the plant computer. All the numbers in the PDO have their origin in the signal generated by the Self-Powered Neutron Detectors (SPND) placed inside the instrumented assemblies of the reactor core. Every instrumented assembly contains seven SPND's which, essentially, divide the assembly into seven segments and provide a signal that depends on the thermal power produced by the corresponding segment. Thus, every instrumented assembly provides seven numbers which give the Z-distribution of the power generated in it. Using symmetry and other information, the power distribution for all 177 assemblies in the core is obtained from the data provided by the instrumented ones. The neutron source is given by

$$n = 2.989E16 \frac{P}{V} \bar{\nu} \ (n/cm^3 \cdot s) \qquad (2)$$

where P = total power (Mwt) (or assembly power)

V = core volume (or assembly volume)

Since the R-θ calculation is based on two dimensions, a correction has to be applied for the leakage along the third dimension (Z-axis). The correction was accomplished by executing a 2-D R-Z DOT and a 1-D XSDRNPM calculation. Axial leakage factors were obtained by dividing the DOT R-Z flux by the corresponding XSDRNPM flux. Thus, for every group g, a 3-D flux was determined from the equation

$$\phi_g(r,\theta,z) = \phi_g(r,\theta \ DOT) \ X \frac{\phi_g(r,z)_{DOT}}{\phi_g(r)_{XSDRNPM}} \qquad (3)$$

RESULTS

Since this work concentrates on the fluence hitting the PV, most of the results refer to that position. Fluxes at the foil position in the cavity are also presented for comparison with experiment. Figure 2 shows the change of the energy spectrum as the neutrons traverse the PV. The neutron spectrum at the foil location (cavity) is presented in Fig. 3. The experimental result shown in Fig. 3 is that of experiment #7 performed by the University of Arkansas group. Tables 2 and 3 give the numerical values of group fluxes. For neutron energy larger than 1 MeV, the difference between experiment and calculation is less than 10% for the first eight groups, 16% for group eight and 33% for group nine.

Because the shape of the neutron spectrum does not change with angle, Fig. 2 and 3 show the flux at 23°only. The variation of the neutron flux as a function of the angle θ is shown in Fig. 4, for the first neutron group. As the neutron energy decreases, the angular variation, in general, is smoother. There is considerable variation of the flux in front of the PV and at T/4, but at the foil position the flux looks much more even. We conclude that it would be difficult to check experimentally the angular variation of the flux at the position of the PV by placing foils at different angles but at a position inside the cavity.

To investigate how the flux changes from cycle to cycle, the DOT-IV R-θ calculation was repeated using data from ANO-1 cycle 5. The results that the position and power generated by the assemblies of the last row may change significantly the angular variation of the flux of the PV position, from cycle to cycle.

Table 2. Group Fluxes at Four Different
Locations (Corrected for Axial Leakage)

Group	In Front of PV	At 1/4 T of PV	At 3/4 T of PV	Behind the PV
1	3.24E7	1.28E7	2.03E6	7.57E5
2	8.22E7	3.08E7	4.45E6	1.59E6
3	3.57E8	1.30E8	1.68E7	5.65E6
4	1.07E9	3.62E8	3.93E7	1.22E7
5	1.63E9	5.76E8	6.66E7	2.00E7
6	1.08E9	4.62E8	6.12E7	1.81E7
7	4.90E8	2.18E8	2.97E7	8.70E6
8	1.86E9	1.10E9	1.98E8	5.63E7
9	2.54E9	2.07E9	5.28E8	1.59E8
10	1.40E9	1.22E9	3.79E8	1.34E8
11	2.08E9	2.78E9	1.30E9	4.40E8
12	2.10E9	3.59E9	2.08E9	6.39E8
13	1.49E9	1.45E9	7.40E8	3.16E8
14	1.35E9	1.94E9	1.14E9	3.75E8
15	1.11E9	1.53E9	9.45E8	2.81E8
16	1.31E9	7.60E8	3.90E8	1.96E8
17	3.17E8	8.96E7	4.73E7	3.50E7
18	1.98E8	5.33E8	3.42E8	1.50E8
19	7.66E8	7.33E8	4.80E8	2.45E8
20	1.10E9	3.58E8	1.69E8	1.50E8
21	4.00E9	1.82E9	6.37E8	4.73E8
22	2.23E9	9.66E8	3.02E8	2.31E8
23	6.25E9	2.24E9	5.28E8	4.90E8
24	2.18E9	4.60E8	8.65E7	1.42E8
25	3.66E9	1.81E8	2.17E7	1.56E8
26	1.85E10	1.21E8	8.27E6	6.03E8

The radial variation of the flux is shown in Fig. 5 and 6. Fig.
5 shows the change of the flux as a function of distance from the
center of the core, for three neutron groups. The effects of the
heterogeneity at the end of the core are clearly shown, especially
for the thermal flux. Fig. 6 shows integral fluxes as a function of
distance.

Table 4 gives the numerical values of the integral fluxes at
three locations: in front of PV, at T/4 of PV and at the foil location.

Table 3. Calculated and Measured Neutron
Energy Spectra at the Foil Position

Group	Experiment #7	R-θ Calculation	Leakage Factor	Flux Corrected for Leakage	Difference %
1	4.477E5	5.225E5	0.83	4.35E5	3
2	9.528E5	1.085E6	0.84	9.15E5	4
3	3.371E6	3.847E6	0.85	3.28E6	3
4	8.392E6	8.579E6	0.86	7.40E6	12
5	1.446E7	1.529E7	0.85	1.30E7	10
6	1.260E7	1.440E7	0.84	1.21E7	4
7	6.513E6	6.983E6	0.84	5.85E6	10
8	4.450E7	4.506E7	0.83	3.73E6	16
9	1.695E8	1.401E8	0.80	1.13E8	33
10	2.025E8	1.289E8	0.79	1.01E8	50
11	4.934E8	4.319E8	0.76	3.29E8	33
12	5.927E8	6.814E8	0.75	5.10E8	14
13	3.663E8	4.045E8	0.73	2.96E8	19
14	2.997E8	4.561E8	0.72	3.30E8	-10
15	2.164E8	3.591E8	0.71	2.56E8	-18
16	1.843E8	2.939E8	0.70	2.06E8	-12
17	5.962E7	4.444E7	0.70	3.10E7	48
18	6.008E7	1.356E8	0.74	1.01E8	-68
19	1.918E8	2.706E8	0.76	2.06E8	-7
20	1.413E8	2.519E8	0.73	1.83E8	-29
21	4.921E8	7.693E8	0.70	5.40E8	-10
22	1.453E8	3.743E8	0.70	2.61E8	-80
23	4.360E8	7.842E8	0.70	5.48E8	-26
24	1.296E8	2.166E8	0.71	1.53E8	-18
25	9.636E7	2.068E8	0.72	1.49E8	-55
26	1.970E8	6.219E8	0.72	4.48E8	-127

CONCLUSIONS

Transport calculations of the neutron energy
spectrum have been performed and compared with a neutron spectrum
measured at one position in the cavity. The difference between
measured and calculated spectrum is less than 16% for neutron energy
greater than 2.3 MeV (Table 4). For lower energies the differences
are larger with the most significant being the flux difference at 1 MeV
(group 10) and at 0.743 MeV (group 11). In general, the result of the
calculation is lower than that of the experiment for E>300keV, and
higher for lower energies.

The maximum of the neutron flux for E>1MeV in front of the PV at
23° is equal to 9.16×10^9 $n/cm^2 s$. Assuming a 40 year lifetime and a 80%
capacity factor, the neutron fluence with E>1 MeV hitting the PV is

9.24×10^{18} n/cm^2.

The R-θ calculation shows that there is a considerable variation of the flux hitting the pressure vessel as a function of angle, variation which may change from cycle to cycle and, as a result, move the maximum of the flux hitting the PV to a different angle. Since the lifetime of the PV is decided on the basis of the maximum and not of the average fluence, it would be prudent to study ways by which the angular variation of the flux hitting the PV becomes more even.

Table 4. Integral Fluxed at Three Different
Locations. Experimental Results Also Shown

	$E_n > 1$MeV	$E_n > 67$KeV	E Total
In front	1.01E10	2.07E10	6.40E10
of P.V.	*9.16E9	*1.87E10	*5.92E10
T/4 of	5.32E9	1.92E10	2.80E10
P.V.	*4.96E9	*1.75E10	*2.57E10
Foil	2.36E8	2.70E9	6.67E9
Position	*1.93E8	*2.02E9	*4.84E9
Foil Position (Experiment)	2.607E8	2.432E9	4.565E9

*Flux Corrected for Leakage

REFERENCES

1. C.Z. Serpan, "NRC Light-Water-Reactor Pressure Vessel Surveillance Dosimetry Improvement Program", Nucl. Safety 22, 449 (1981).

2. F.J. Rahn, "Power Reactor Pressure Vessel Benchmarks: An Overview", EPRI NP-380-SR, Electric Power Research Institute (1976).

3. M.L. Gritzner, G.L. Simmons, T.E. Albert, and E.A. Straker, "PWR and BWR Radiation Environments for Radiation Damage Studies", EPRI NP-152, Electric Power Research Institute (1977).

4. "Radiation Streaming in Power Reactors", G.P. Lahti, R.R. Lee, and J.C. Courtner, Editors, ORNL/RSIC-43, Radiation Shielding Information Center (1979).

5. "LWR Pressure Vessel Surveillance Dosimetry Improvement Program: PCA Experiments and Blind Test", W.N. McElroy, Editor, NUREG/CR-1861, July 1981.

6. R.W. Roussin, C.R. Weisbin, J.E. White, N.M. Greene, R.Q. Wright, and J.B. Wright, "VITAMIN-C: The CTR Processed Multigroup Cross Section Library for Neutronic Studies", ORNL/RSIC-37 (1980) (available from RSIC as DLC-41C/VITAMIN-C).

7. R.W. Roussin, "BUGLE-80 Couples 47-Neutron, 20-Gamma-Ray, P_3 Cross Section Library for LWR Shielding Calculations", Informal Notes, ORNL and ANS - 6.1.2 (June 1980).

8. G.L. Simmons, SAI Company, LaJolla CA, (Private Communication)

THERMAL SHIELD
CORE BARREL
CORE SHROUD

FOILS

CONCRETE

CAVITY

PRESSURE VESSEL

FUEL ASSEMBLY

23°

98.20 120.03 141.85 163.58 165.49 184.15 186.69 179.07 191.77 217.77 239.08 323.85 345.44

distance (cm) from core center
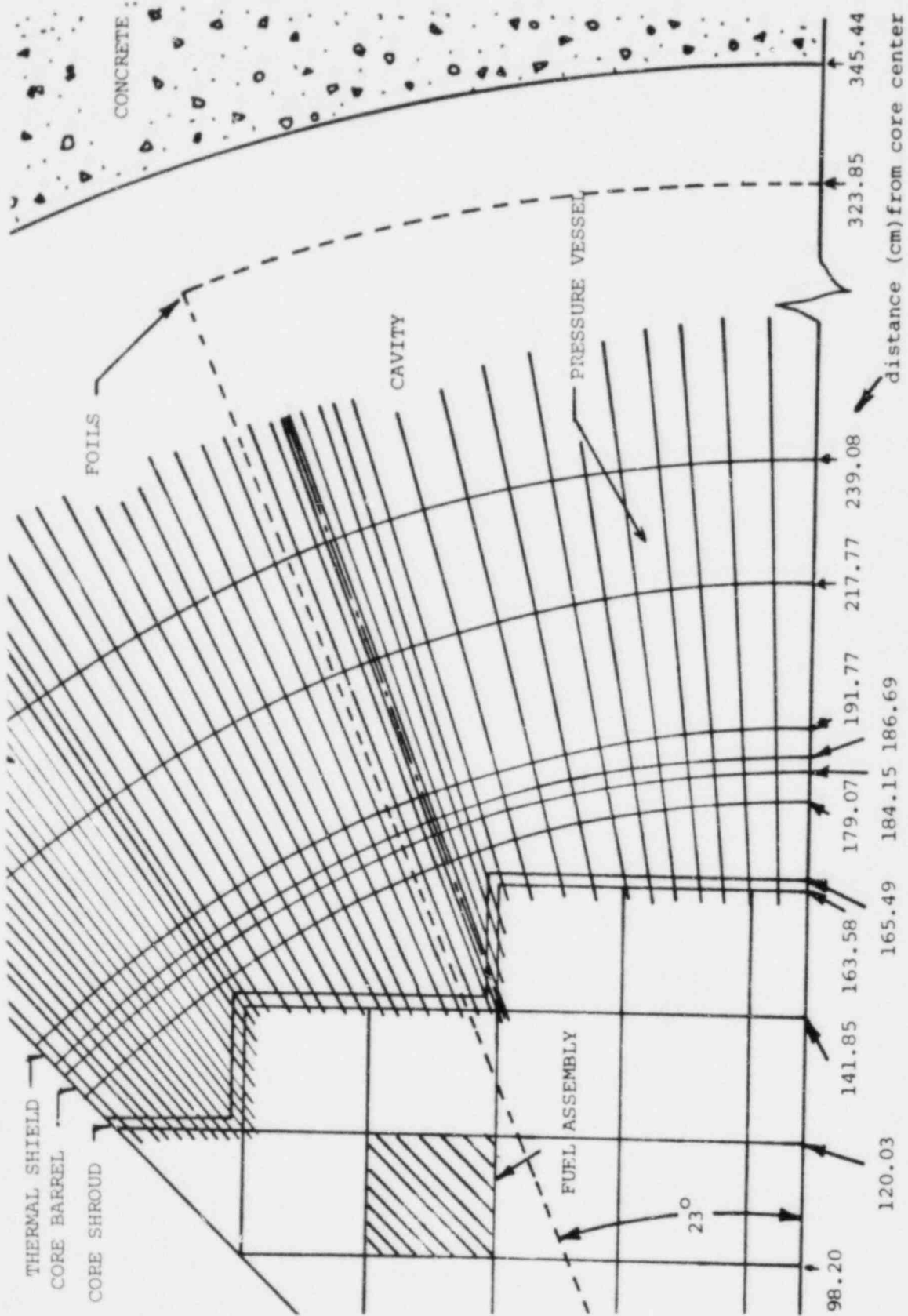
Figure 1 . The R-θ model of ANO-1. Details of the
angular intervals and space beyond the pressure vessel.
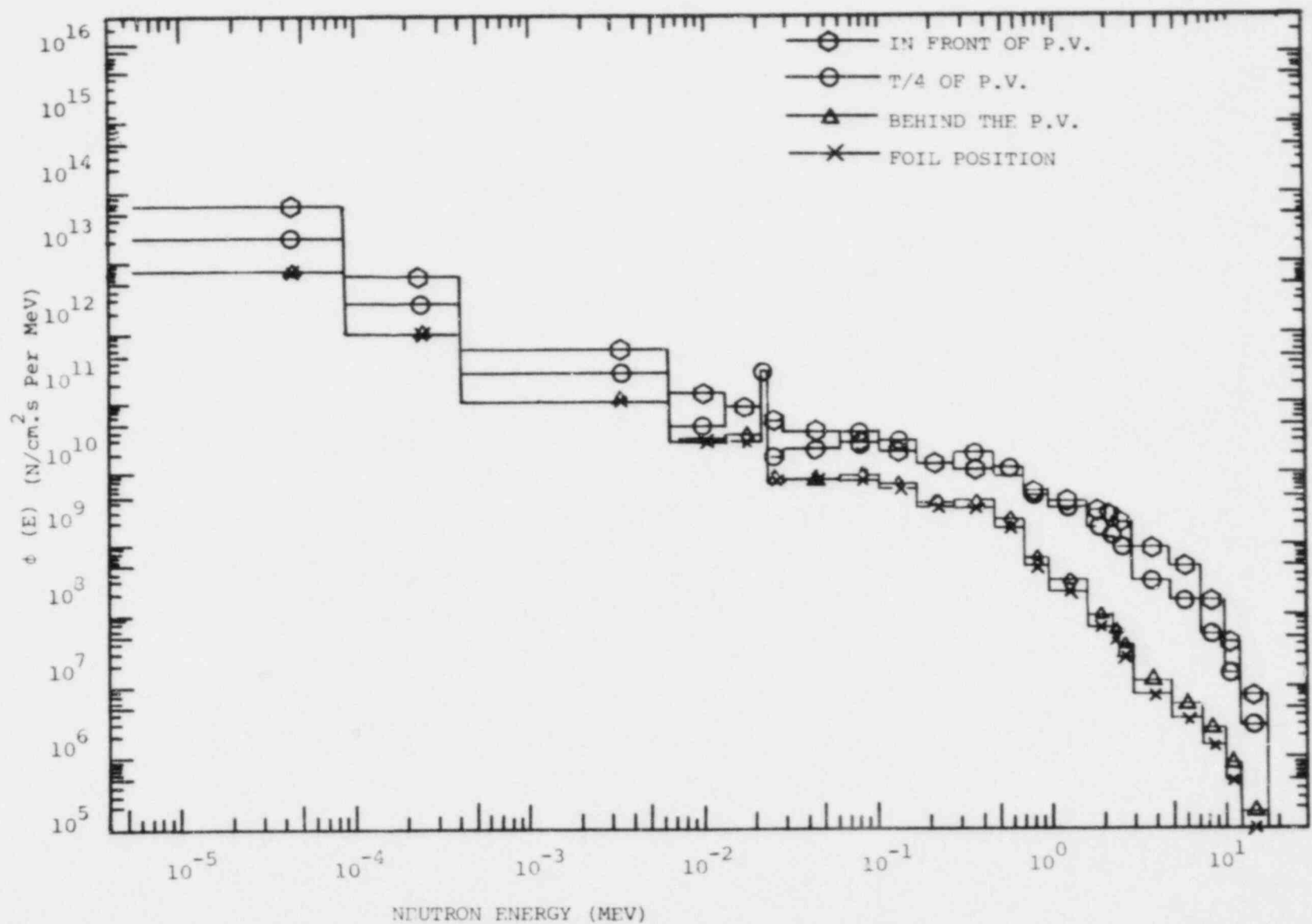
Fig. 2. Change of the energy spectrum as the neutrons traverse the PV.
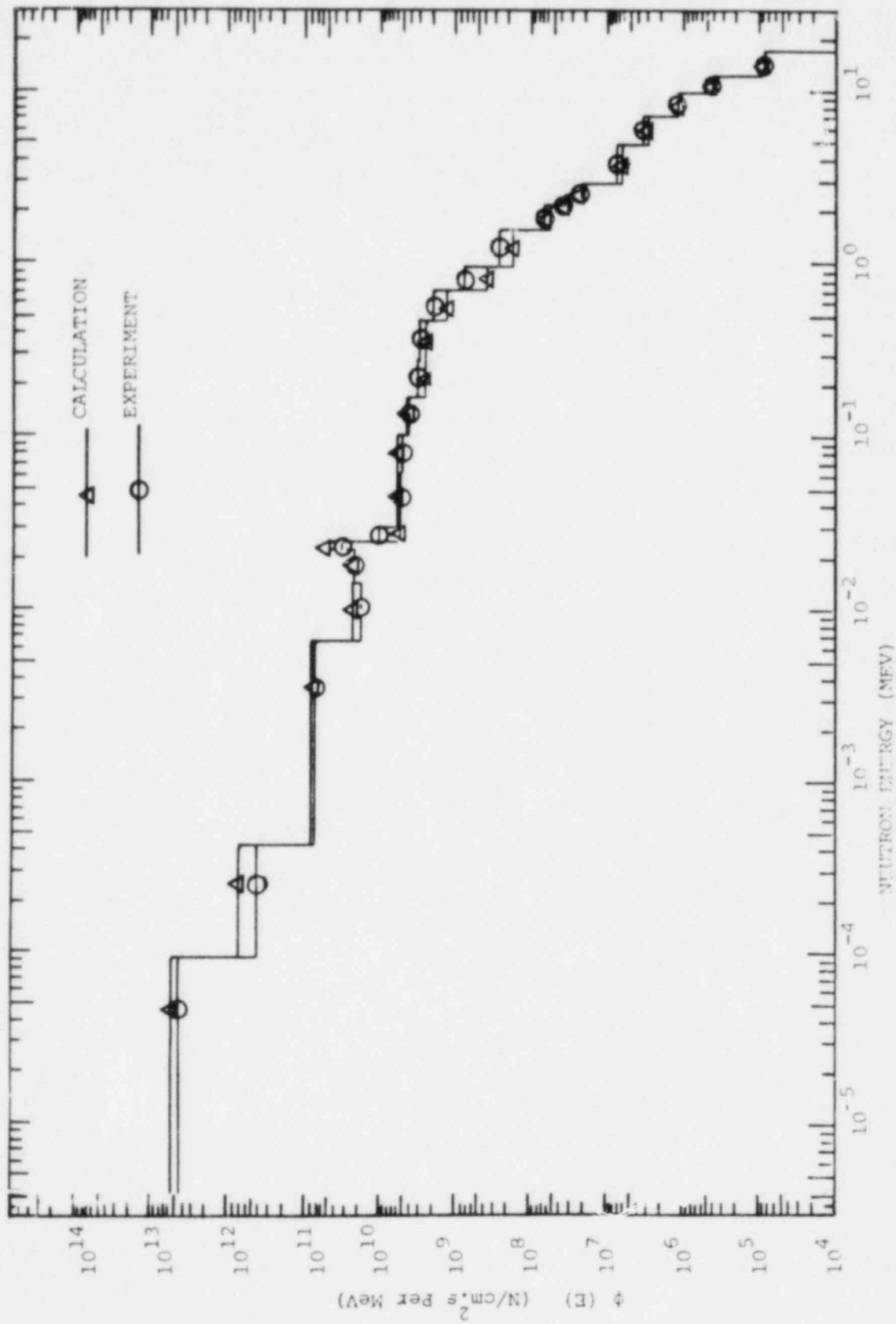
Fig. 3. Comparison between the calculated and the measured energy spectrum

Group 1
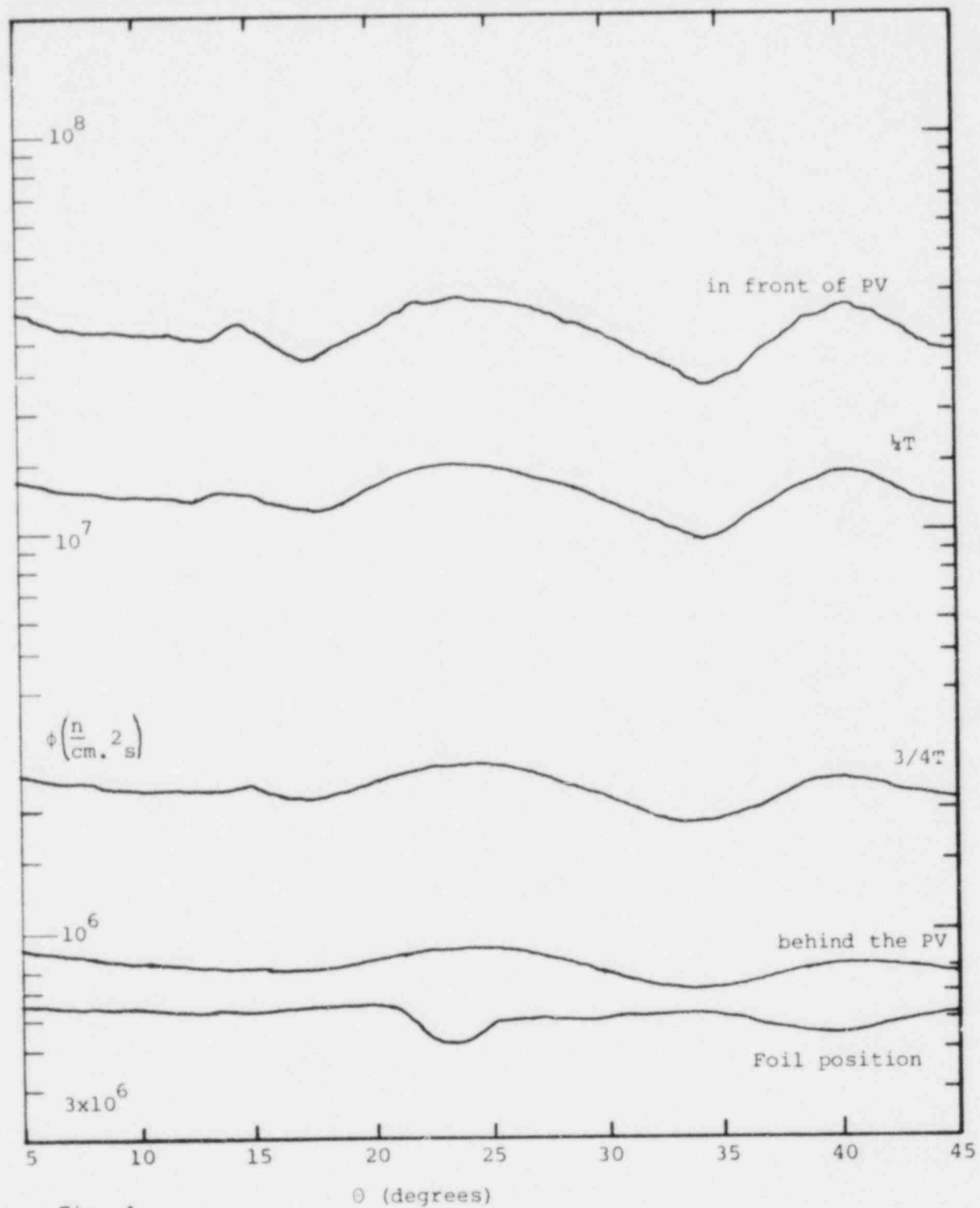
Fig. 4.

Angular variation of the flux (group 1) at four different locations
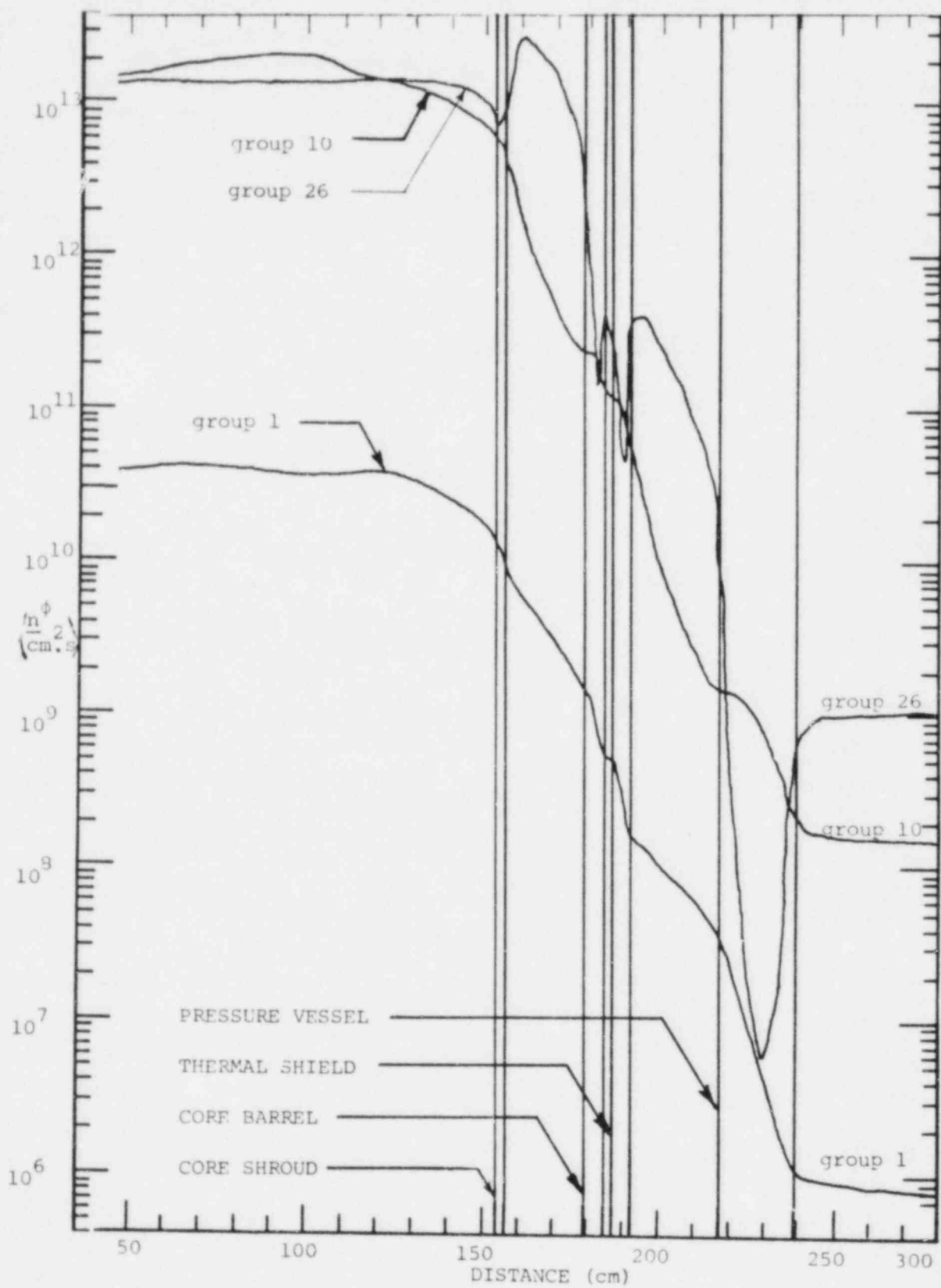
Fig. 5. The neutron flux as a function of radial distance, at $\theta=23^{\circ}$.
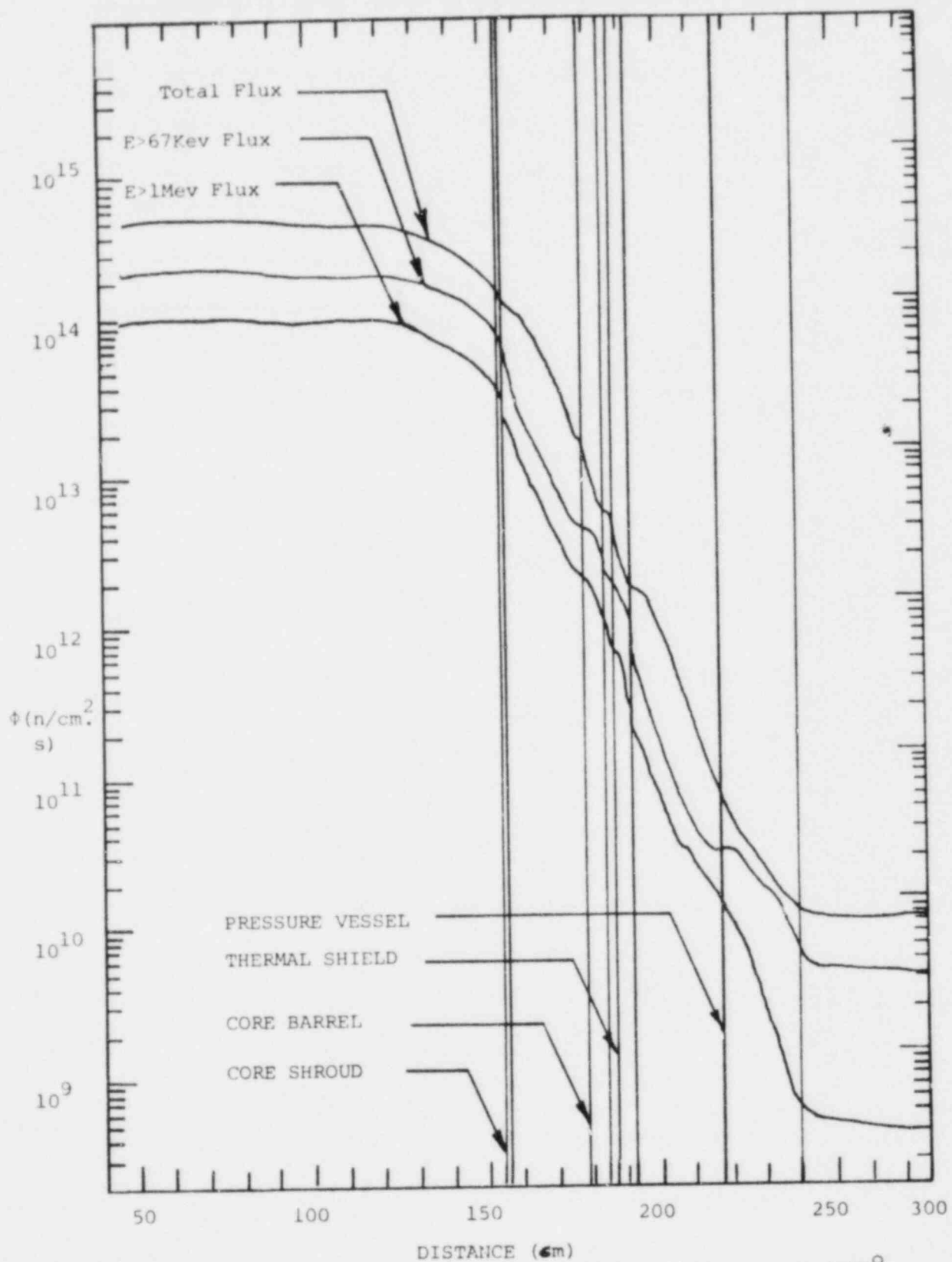
Fig. 6. Integral fluxes as a function of radial distance, at $\theta=23^{\circ}$.

NEUTRON DOSIMETRY IN THE PRESSURE VESSEL CAVITY
OF TWO PRESSURIZED WATER REACTORS

W. E. Brandon, C. O. Cogburn, R. R. Culp,
J. L. Meason*, W. W. Sallee, J. G. Williams+
University of Arkansas
Fayetteville, AR 72701

ABSTRACT

Measurements of the neutron field in the pressure vessel cavity of
two PWR's have been made in order to validate calculations of damage dose
to the vessel and to provide knowledge of the source of radiation stream-
ing. The two reactors are Arkansas Unit One, a Babcock and Wilcox design,
and Unit Two, a Combustion Engineering design.

Foil packages and stainless steel chains, employing a total of 12
dosimetry reactions, have been exposed in detector wells in the cavity of
each reactor. More than twelve separate experiments have been carried
out at various stages of four fuel cycles. Detectors were placed at the
core center-line elevation in all experiments, and at additional positions
from the water-nozzle level down to the bottom of the active fuel, in some
experiments. Detector wells at different azimuthal positions have been
used for the irradiations.

Reaction rates normalized to full power in each reactor are presented.
Spectra unfolded from the data using SAND-II and STAY'SL are also pre-
sented, and compared with calculated spectra from transport calculations
on the Arkansas reactors, described in a companion paper by the University
of Missouri (Rolla) research group.

INTRODUCTION

A study of the radiation field just outside the pressure vessel of
Unit-I at the Arkansas nuclear plant was begun in 1977. This was a joint
study between the University of Arkansas (funded by the Arkansas Power &
Light Co.), the National Bureau of Standards, and Hanford Engineering
Development Laboratory (both funded by the Nuclear Regulatory Commission).
Starting in November 1979, the research became a joint project between

*Present address: White Sands Missile Range, N. M.
+Present address: Imperial College, University of London

the Electric Power Research Institute, AP&L, the U of A, and the University of Missouri-Rolla (UMR).

Measurements began in Unit-II in December 1979, during initial physics tests. These measurements involve the use of activation and fission foils to determine the neutron spectra in the pressure vessel cavity of each of the two AP&L reactors. Unit-I is a Babcock & Wilcox pressurized water reactor; Unit-II is a Combustion Engineering PWR.

Fifteen separate "experiments" are complete or are being irradiated as indicated in Table 1. Detailed measurements have been made at levels of the horizontal centerline, the water nozzle, top of fuel, bottom of fuel, and just below the centerline. Axial flux profiles have been run for both units. Some measurements have been made at different azimuthal positions. These experiments cover most of three fuel cycles in Unit-I and two cycles in Unit-II. Neutron spectra and flux values have been extracted from the foil data in an effort to allow improved predictions for operating nuclear power plants.

EXPERIMENTAL METHOD

In Unit I, two diametrically opposite spare detector wells have been available for the experiments. These are 6-inch, schedule-40 stainless steel pipes running from the top to near the bottom of the pressure vessel cavity. A fixture was designed for supporting the foil capsules in the center of the pipe and for 'facing' the foils toward the core, at the chosen experimental elevation. The fixture holds four sets of foils; one covered with Al, two covered with Cd, and one covered with B-10. The B-10 spherical holder for fission foils gives a different threshold and also reduces the uncertainty of U-235 fission in the depleted (U-238) foils. Measured lengths of stainless steel chain were used for vertical positioning of the foil fixtures. Beads from the stainless steel chain were clipped and counted, providing both fast and thermal flux profile measurements.

Foils of U-235, U-238, Np-237, Cu, Fe, Co, Ni, Ag, Ti, Sc, and Ta, plus pellets of sulfur (loaded on "ladder-rungs" along the chains) have been used.

The same materials have also been irradiated in Unit II. Although Unit II has no spare detector wells, there is sufficient space in the wells, beside the installed instruments, for a foil holder of a somewhat different design. Due to space restrictions, a B-10 sphere cannot be used.

All experiments have been placed and removed during operational outages of the Arkansas plants. On removal of the foils from the reactor building, the entire assembly is decontaminated, checked by health physics staff at the plant, and packed for transportation by auto to the U of A labs. Approximately $2\frac{1}{2}$ hours are required for travel and preparation

for counting. High-resolution germanium-gamma-detector spectroscopy systems are used to count the foils, with computer analysis of the gamma spectra.

DATA REDUCTION AND ANALYSIS

Each relevant gamma energy peak is counted to a statistical accuracy of 1% or better and the net count, along with reactor power history data are input to a computer program. The program takes into account power variations (or brief outages), allows for radioactive buildup and decay, and gives the net reaction rate for each isotope in terms of equivalent full-power operation. Typical reaction rates, in disintegrations per second per atom (dps/atom), are listed in Table 2.

The reaction rates, together with a trial spectrum, serve as input to the computer code SAND-II[1], which provides an iterated 621-group neutron energy spectrum. Initially, for experiments I-1 through I-5, a simulated PWR cavity spectrum from a Monte-Carlo calculation was used as the trial input spectrum. More recently, the calculated spectrum provided by the UMR[2] group has been used for trial input to SAND-II. The ENDF/B-IV dosimetry cross-sections have been used to date, but a change to ENDF/B-V is in progress. The unfolding code STAY'SL[3] has been used as a check on SAND-II results.

SPECTRAL RESULTS

Corrected reaction rates (as in Table 2), along with a trial spectrum or best estimate, are put into the unfolding code. SAND-II has been used for most of the unfolding calculations. Figure 1 shows the SAND-II results for experiment I-5 of Unit-I at the horizontal midplane location. In addition to the SAND-II code, the STAY'SL unfolding code has been run for one of the capsule positions of experiment I-5. The spectra calculated by the two codes agree well.

Also shown in Figure 1 is the SAND-II results for experiment II-2 of Unit-II. The overall intensity is greater and the average energy is somewhat higher for the Unit-II spectrum. The variation in spectra of the units is mainly due to the difference in reactor design. Unit-II has a high-power-density core with no thermal shield and the foil positions are also slightly closer to the core than those of Unit-I.

Tabulation of SAND-II results for both Unit-I and Unit-II at selected energy ranges are given in Table 3. The column labeled "$\phi > 1.0$ MeV" gives an indication of the potential damage to the vessel by fast neutron bombardment. Since 90% of the embrittlement of steel is thought to be caused by neutrons in the energy range from 0.05 to 5.0 MeV, this column

in the table may give an indication of total damage. The total flux
($\phi > 10^{-10}$ MeV) and the log "mid-point" of this energy range, 0.5 MeV, are
listed for comparison purposes. The flux above 0.01 MeV (probably the
threshold for damage) and the average spectrum energy in keV above the
0.01 MeV threshold are also included in the table.

At distances above or below the horizontal mid-plane of the core,
the SAND-II results indicate some softening of the neutron spectrum as
well as a reduction in intensity. A series of flux profiles run for each
reactor also bear out this variation. Figure 2 indicates this variation
in the axial fast flux profile above core mid-plane, measured by the Ni-58
(n,p)Co-58 reaction. Sulfur pellets and iron foils have given similar
results.

A comparison between the UMR[2] calculated 26-energy-group neutron
spectrum for experiment I-7 and the U of A measured spectrum is shown
in Figure 3. The calculated values are higher than the measured values
for the low energy part of the spectrum, up to about 300 keV. Above this
point, the measured values are higher. These differences between measured
and calculated values are now under investigation. The measured spectrum
of Figure 3 was obtained by compaction of a 621-group SAND-II spectrum to
26 groups using integral flux values. Experiment 7 from Unit I data was
selected for comparison because it was a midplane horizontal-center-line
measurement during a time period of fairly steady power.

SUMMARY

The neutron field in the pressure vessel cavity of two PWRs has been
measured by activation and fission foil techniques. Spectra have been
extracted, by use of the SAND-II unfolding code, for several vertical
levels along both units. The neutron flux in the pressure vessel cavity
of Unit-II (built by Combustion Engineering) is somewhat higher than that
for Unit-I (by Babcock & Wilcox). Vertical flux profiles indicate a
softening of the neutron spectrum above and below the horizontal centerline
of both units. Independent calculational investigations by the University
of Missouri are consistent in general with the measurements; however there
are discernable differences in the two results.

Analysis of core burn-up effects have yet to be examined. As more
data for Unit-II is accumulated, the details of the differences between
the spectra of the two PWRs should be better understood. The discrepancies
between measured and calculated neutron spectra have lead to the suspicion
that the published cross-sections and fission yields for irradiation of
fission foils may not be correct for the neutron spectra of the Arkansas
plants.

Planned investigations will focus on correlating the current pressure
vessel dosimetry study with in-vessel dosimetry and metallurgical surveil-
lance specimen analysis at the time of the next refueling of Unit-II.

537

REFERENCES

1. Radiation Shielding Information Center (Oak Ridge National Laboratory), Code Package CCC - 112/SAND, "Neutron Flux Spectra Determination by Multiple Foil Irradiation - - - Iterative Method", Contributed by Atomics International, Air Force Weapons Laboratory, TRW, and Battelle Memorial Institute.

2. N. Tsoulfanidis, et al, companion paper this conference, "Calculation of Neutron Fluxes at the Pressure Vessel and Cavity of a PWR", Fourth ASTM-EURATOM Symposium on Reactor Dosimetry, Washington, D. C. (March, 1982).

3. Radiation Shielding Information Center (Oak Ridge National Laboratory), Code Package PSR - 113/STAY'SL, "Least-Squares Few-Channel Neutron Spectrum Unfolding Code", Contributed by Oak Ridge National Laboratory.

TABLE 1

P.V. CAVITY DOSIMETRY EXPERIMENTS - A P & L PLANT

EXP. NO.	LOCATION	START	END	EFPD	REMARKS
ANO I - 1	Horiz. C/L	12-8-77	1-31-78	41.82	Trial-foils, etc.
ANO I - 2	Horiz. C/L	4-23-78	12-31-78	238.86	Several ramps in PWR
ANO I - 3	Top of fuel	2-5-79	3-30-79	51.63	'Steady' PWR
ANO I - 4	Nozzle level Horiz. C/L	6-24-79	10-20-79	121 da	'Steady' PWR for last 33 da
ANO I - 5	Nozzle level, top of fuel, & horiz. C/L	11-19-79	12-31-79	40.33	One of best irradiations
ANO I - 6	Nozzle level, 31" below C/L, & bottom of fuel	1-3-80	7-17-80	99.11	Erratic PWR
ANO I - 7	Horiz. C/L & flux profile	8-4-80	9-5-80	30.03	Fairly steady PWR
ANO I - 8	Horiz. C/L & flux profile	9-28-80	1-31-81	81.69	Reduced PWR last 30 days
ANO I - 9	Horiz. C/L & flux profile	3-24-81	?		
ANO II - 1	Horiz. C/L	12-1-79	1-29-80	40 da	Physics tests (erratic)
ANO II - 2	Horiz. C/L & flux profile	2-2-80	9-3-80	120.65	Many ramps & trips
ANO II - 3	Horiz. C/L & flux profile	9-7-80	3-27-81	204 da	Several ramps in PWR
ANO II - 4	Horiz. C/L & flux profiles @ 4 radial pos.	7-3-81	9-27-81	62.6	Early ramps & trips
ANO II - 5	" 2 positions	10-11-82	1-7-82	64.7	Many ramps & trips
ANO II - 6	2 positions	1-11-82	?		

TABLE 2

Saturated Reaction Rates
at the Horizontal Midplane

Reaction	ANO - UNIT I				UNIT - II	
	Exp. 4	Exp. 5	Exp. 6	Exp. 7	Exp. 2	Exp. 3
Ti-46(n,p)	2.46E-18	2.35E-18	2.27E-18	2.50E-18	1.18E-17	4.58E-18
Ni-58(n,p)	1.67E-17	1.73E-17	1.70E-17	1.76E-17	8.77E-17	3.56E-17
Fe-54(n,p)	1.13E-17	1.26E-17	1.26E-17	1.27E-17	6.41E-17	2.31E-17
Fe-58(n,γ)	1.21E-16	1.26E-16	1.33E-16	1.33E-16	5.66E-16	3.60E-16
Co-59(n,γ)	8.48E-15	5.57E-15	5.46E-15	5.62E-15	2.20E-14	1.62E-14
Sc-45(n,γ)	1.19E-15	1.02E-15	9.71E-16	1.04E-15	4.47E-15	3.14E-15
Ag-109(n,γ)	5.68E-15	4.33E-15	4.39E-15	4.32E-15	1.92E-14	1.41E-14
Cu-63(n,α)	- - - - -	1.90E-19	1.72E-19	1.70E-19	7.43E-19	2.93E-19
U-235(n,F)	3.37E-14	3.46E-14 4.45E-15*	3.80E-14	3.71E-14	1.55E-13	1.10E-13
U-238(n,F)	6.62E-17	1.23E-16 7.42E-17*	1.19E-16	9.17E-17	not counted	
Np-237(n,F)	1.03E-15	1.07E-15 1.01E-15*	1.34E-15	1.23E-15	5.85E-15	2.91E-15

Note: All rates are dps/atom.

* Reaction rates from Boron-10 covered foils.

TABLE 3

Experimental Spectral Comparison - ANO

Flux at Horizontal Midplane of <u>Unit-I</u> (n/cm^2-sec) x 10^{-9}

Experiment	$\phi > 1 \times 10^{-10}$ MeV	$\phi > 0.01$ MeV	$\phi > 0.05$ MeV	$\phi > 0.5$ MeV	$\phi > 1.0$ MeV	$0.05 < \phi < 5.0$ MeV	$\bar{E} > 0.01$ MeV (keV)
Trial Input Spectrum	4.483	2.264	1.774	0.5556	0.1832	1.761	411.6
4	4.038	2.441	2.019	0.7582	0.2209	2.006	458.9
5	4.543	2.984	2.405	0.8197	0.2470	2.392	420.3
6	4.756	3.196	2.710	1.046	0.2755	2.698	457.6
7	4.565	3.010	2.523	0.9523	0.2617	2.458	454.0
Experimental Average	4.660	3.043	2.471	0.8712	0.2546	2.458	427.1

Flux at Horizontal Midplane of <u>Unit-II</u> (n/cm^2-sec) x 10^{-9}

Trial Input Spectrum	30.32	14.51	11.31	3.615	1.250	11.32	417.5
2	19.73	13.00	11.06	4.530	1.306	11.00	489.2
3	12.35	7.515	6.171	2.237	0.5958	6.147	421.0
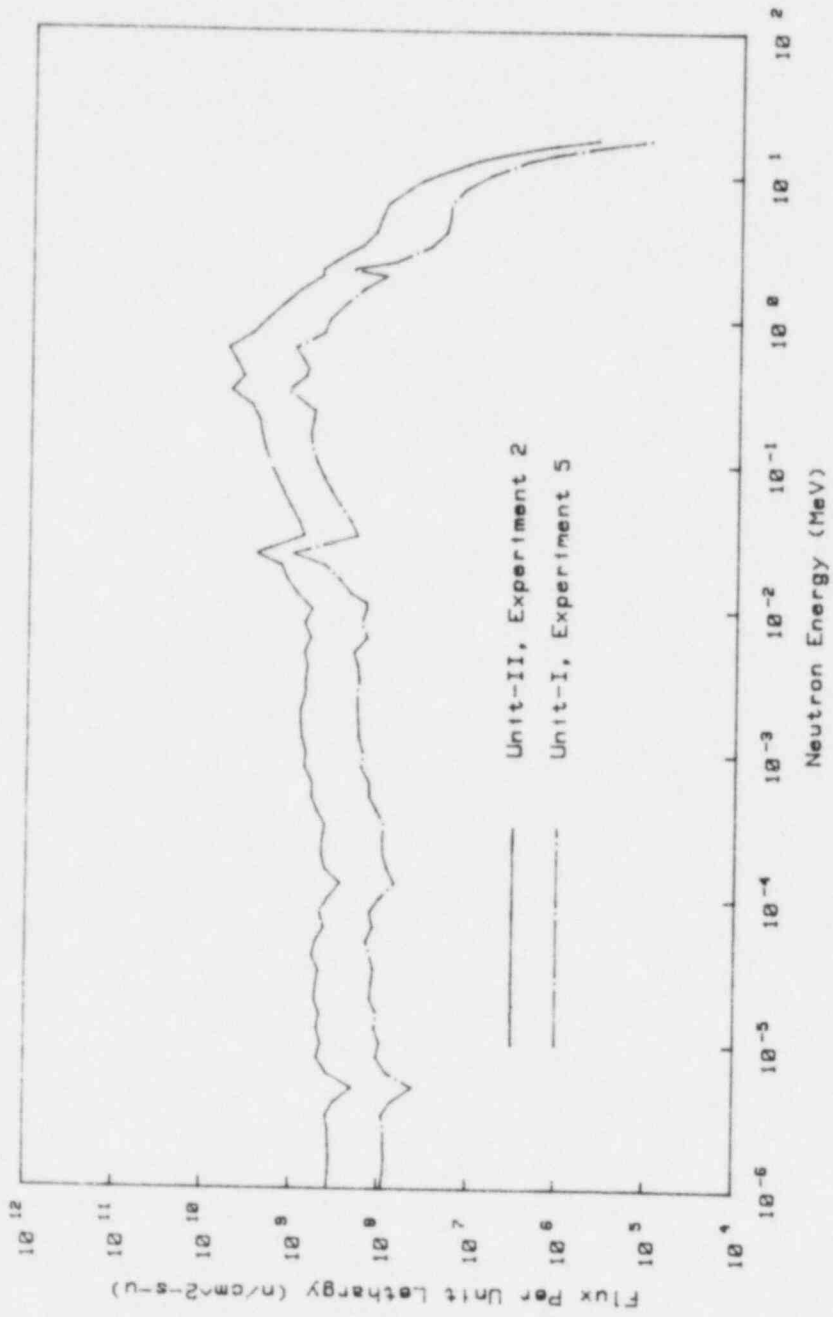
Figure 1 Neutron Spectra at the Horizontal Midplane
for Unit-I and Unit-II, ANO

FIGURE 2
ARKANSAS NUCLEAR ONE, UNIT I, EXP. #7
Axial Flux >2.9 MeV In RPV Cavity

Normalized Flux >2.9 MeV (Arbitrary Units)
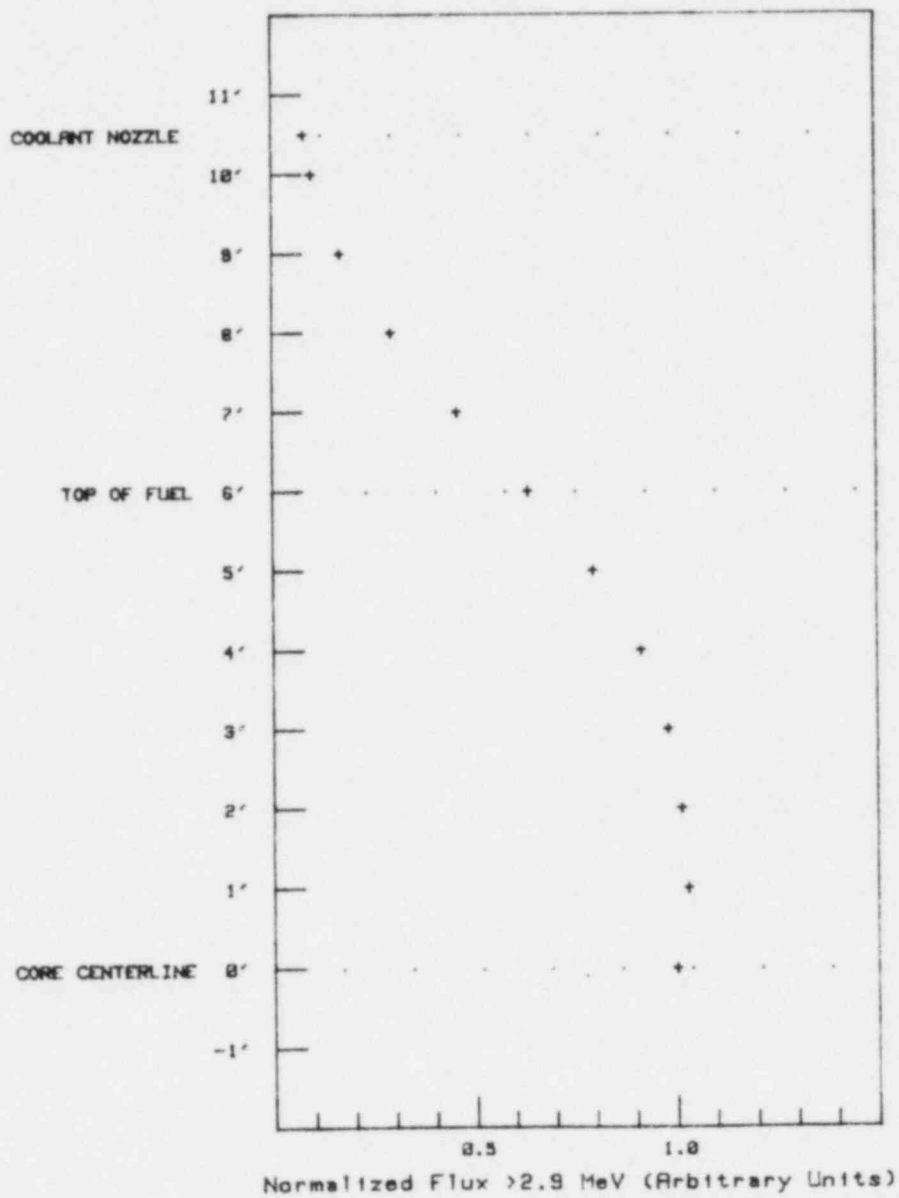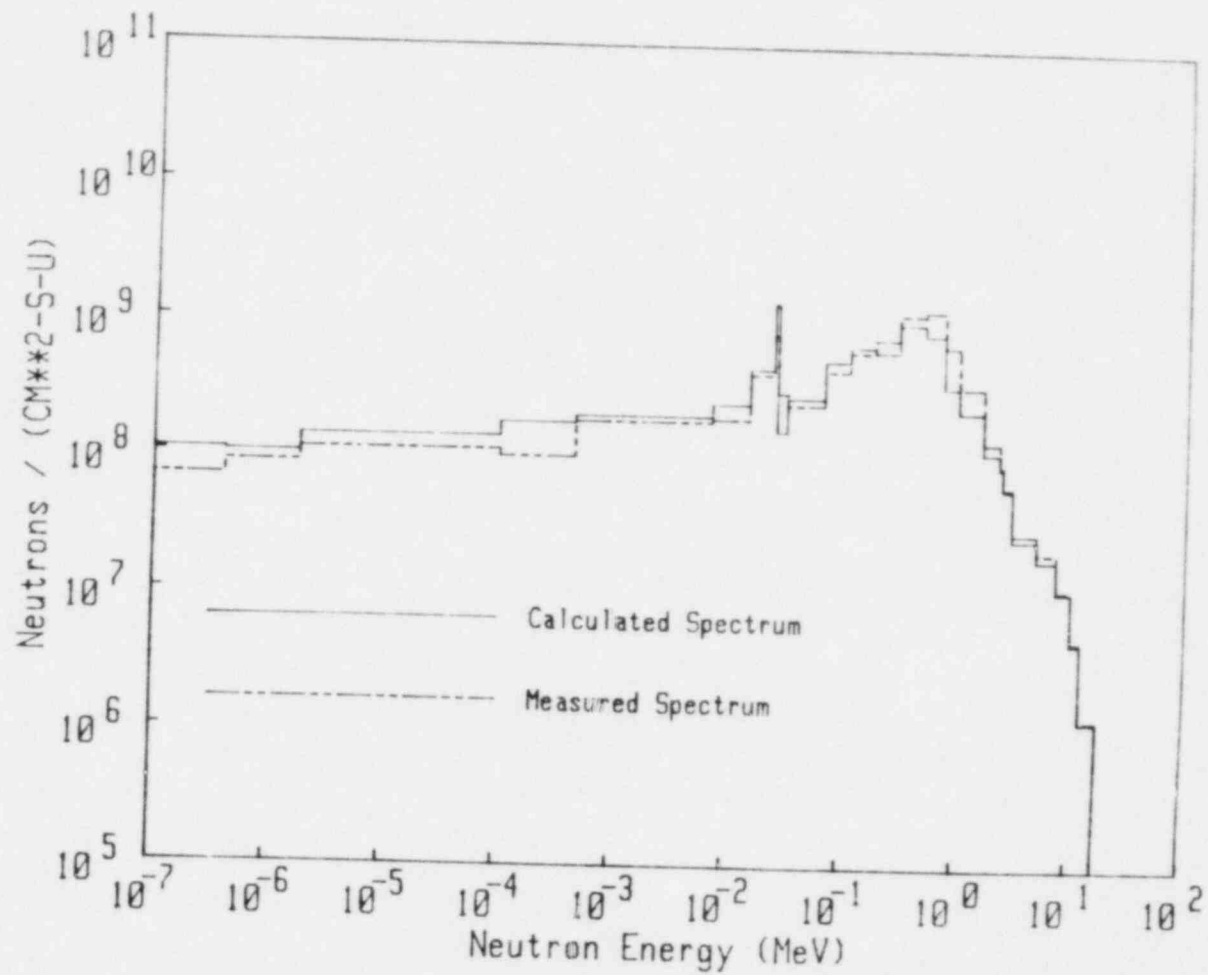
Figure 3 Measured and Calculated 26-Group Spectra for
the Horizontal Midplane of Unit-I, ANO

A NEW ANALYSIS OF THE EXPERIMENT FOR MEASUREMENT OF $\Phi > 1$ MeV IN PRESSURE VESSEL CAVITY OF U.S. LIGHT WATER POWER REACTOR ARKANSAS

Maria Petilli
C.N.E.N., C.S.N. Casaccia
Roma, Italy

ABSTRACT

The new method of multiple unfolding has been applied to the analysis of a complex experiment having as object the evaluation of absolute value of $\Phi > 1$ MeV in the pressure vessel cavity of Arkansas P&L reactor. This approach is different with respect to that used by NBS team in a precedent evaluation. The results show a gain in the accuracy if the multiple unfolding is used and, at the same time, the importance of use of covariances for a good propagation of errors.

I. INTRODUCTION

The NBS organized and performed, with HELD collaboration, a very elaborate experiment in order to evaluate the full power intensity of flux $\Phi > 1$ MeV in Arkansas P&L U.S. reactor pressure vessel cavity.

The result of this experiment has been already calculated by C. M. Eisenhauer et al.,[1] with an accurate evaluatio of uncertainties, by following the traditional proceeding.

The importance of this experiment is either for the result itself or for the adopted method of benchmark referencing and flux transfer, here applied twice, utilizing a lot of informations very useful to reduce the uncertainties. For this reason it seemed very interesting to apply at this experiment the new analysis method, appeared in dosimetry problems in the last few years, which includes the covariances in the error treatment.

The multiple unfolding code, which is an extension of method used by unfolding codes DANTE[2,3] and STAY'SL,[4] derived from this application.

II. THE FLUX TRANSFER METHOD

In the flux transfer method, the flux Φ_s in a studied field is expressed in therms of flux Φ_b of a benchmark field and some ratios between measured and calculated parameters in both spectra. In this way one can take advantage on the knowledge available for characteristics of reference field to have a better accuracy in the evaluation of flux in the other spectrum.[5]

The expression transferring the flux intensity above a fixed energy E_o, from Φ_b to Φ_s, is:[1]

$$\phi_s(>E_o) = \frac{A_s}{A_b} \times \frac{\overline{\sigma}_b(>E_p)}{\overline{\sigma}_s(>E_p)} \times \frac{\psi_b(>E_p)}{\psi_b(>E_o)} : \frac{\psi_s(>E_p)}{\psi_s(>E_o)} \times \phi_b(>E_o) \tag{1}$$

where:

A_s and A_b = measured value of reaction rates, respectively in studied and benchmark field, at the end of irradiation, corrected for the decay.

$\overline{\sigma}(>E_p)$ = average value of cross section in the range of energy with lower limit E_p, giving the percentage "p" of the answer for the reaction observed in the considered spectrum.

$\psi(>E_p)/\psi(>E_o)$ = spectrum coverage factor, equal to the fraction of flux above E_o giving the percentage "p" of the answer.

III. DESCRIPTION OF THE EXPERIMENT

In the considered experiment there are two flux transfers (see: Figure 1).[1]

First there is a flux transfer from the benchmark BIGTEN, having a well known spectrum,[6] to the Arkansas P&L pressure vessel cavity, by mean of activation measurements.[7]   For this purpose four threshold detectors (U^{238}, Ni^{58}, Fe^{54}, Ti^{46}) were used (see: Table 1).[7,8]

Figure 1

NBS-I
Ra-BE
Standard

Cf^{252} Fission
Neutron
Standard

BIGTEN
U metallicum
benchmark

Arkansas
RPV Cavity

Comparison
in
Mn SO$_4$ bath

Flux Transfer
Fission yield in
U^{238} measurement

Flux Transfer
Activation measurements
U^{238}, Ni^{58}, Fe^{54}, Ti^{46}
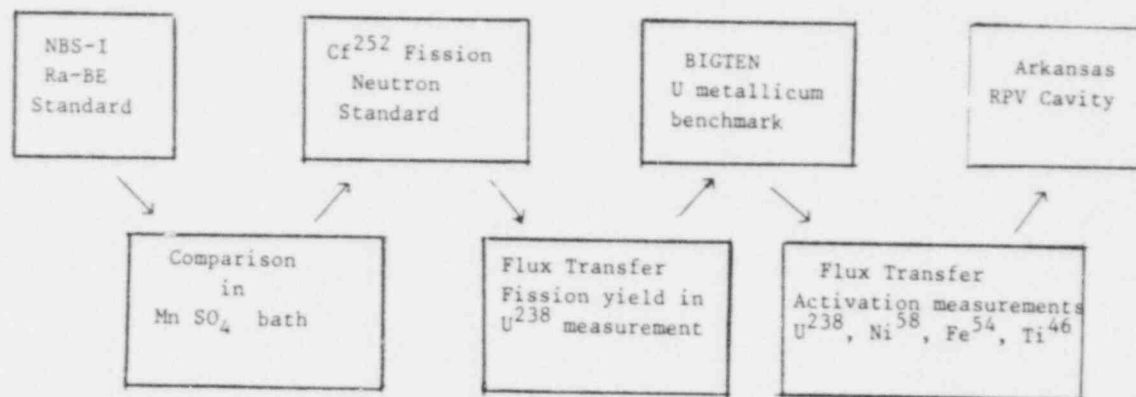
Table 1. Reaction Rates ratio values

		Experimental	Calc. initial (a)	Calc. after M.U. (b)	Correlation matrix of Calculated Values (%) (a)	(b)
A_{Ark}/A_{BT}	U^{238}(n,f)Ba^{140}	.0251 ± 4.0%	.0238 ± 12.2%	.0246 ± 3.6%	100	100
	Ni^{58}(n,p)	.0231 ± 4.0%	.0283 ± 23.0%	.0230 ± 4.0%	67 100	0 100
	Fe^{54}(n,p)	.0221 ± 4.0%	.0227 ± 25.7%	.0221 ± 3.8%	62 68 100	-1 0 100
	Ti^{46}(n,p)	.0294 ± 4.0%	.0324 ± 32.6%	.0293 ± 3.8%	46 46 56 100	-1 0 1 100
$A_{BT}/A_{Cf^{252}}$	U^{238}(n,f)	1012 ± 2.8%	891 ± 6.3%	987 ± 2.8%	-35 -22 -21 -18 100	-7 -1 -1 1 100

Than there was a flux transfer from Cf^{252} source [9,10] to BIGTEN using a fission chamber with fissionable deposits and measuring the fission yield of U^{238} (see: Table 1).[11]

Finally, the Cf^{252} source was calibrated, by a comparison in a manganous sulphate bath, with NBS-I Ra-Be standard source having a measured intensity:[12]

$$\Phi_{Cf^{252}}(>1 \text{ MeV}) = 9.12 \pm 1.2\% \quad n/cm^2 \text{ s}$$

IV. THE MULTIPLE UNFOLDING METHOD

The multiple unfolding consists in a contemporary adjustment of different spectra $\phi^i \equiv \{\phi_j^i\}$ and different cross sections $\Sigma^i \equiv \{\sigma_j^i\}$ from integral measurements. The index "i" identifies the flux or the cross section, and the index "j" is the current index for the energy group.

The theory applied for the calculation of adjusted fluxes and cross sections, is that of least squares already used either in unfolding codes DANTE[2,3] and STAY'SL[4] or in code AMARA[15] for the adjustement of cross sections.

Using a formalism close to that of F. G. Perey,[4] all the fluxes and the cross sections are given in form of vector $\Phi \equiv \{\phi^i\}$ and $\Sigma \equiv \{\Sigma^i\}$ with their variance-covariance matrix N_ϕ and N_Σ respectively.

The measured integral parameters have to be regarding one of the fluxes ϕ^i and one of reactions having cross section Σ^i. They are indicated by a vector A° with its associated variance-covariance matrix N_{A°.

In the multiple unfolding code EOLO,[16] expressly written for this analysis, the integral data can be given as absolute values or as ratios between two measurements. For this reason the multiple unfolding is particulary interesting, from the point of view of calculation, when ratio measurements are given, as in this experiment.

After introduced the vector $P \equiv \begin{vmatrix} \Phi \\ \Sigma \end{vmatrix}$ and its variance-covariance matrix $N_P = \begin{vmatrix} N_\phi & 0 \\ 0 & N_\Sigma \end{vmatrix}$, one calculates the value P' corresponding to the maximum of probability distribution function, supposed than P and A° are given. This corresponds to minimize the function:

$$\chi^2 = \begin{vmatrix} P - \overline{P} \\ A^\circ - \overline{A} \end{vmatrix}^{+} \cdot \begin{vmatrix} N_P & 0 \\ 0 & N_A\circ \end{vmatrix}^{-1} \cdot \begin{vmatrix} P - \overline{P} \\ A^\circ - \overline{A} \end{vmatrix} \tag{2}$$

where $\overline{A}$ is calculated by $\overline{P}$.

The value of P' corresponding to the minimum of χ^2 function is given by:

$$P' - P = N_P \cdot S^{+} \cdot (N_A + N_A\circ)^{-1} \cdot (A^\circ - A) \tag{3}$$

In Eq.2 and Eq.3, N_A represents the variance-covariance matrix of vector A calculated by P, and $S \equiv \{\partial A/\partial P\}$ is the sensitivity matrix of transformation from vector P to vector A.

For the adjusted variance-covariance matrix $N_{P'}$ see: Eq. 4, p. 8 .

Using the Eq.3 and Eq.4, one can calculate the output values Φ' and Σ' of fluxes and cross sections, together with their uncertainties.

V. ANALYSIS OF THE EXPERIMENT

The analysis of the experiment can be divided in four steps:

1. Calculation of adjusted fluxes and cross sections
2. Calculation of parameters for the flux transfer
3. Calculation of $\Phi > 1$ MeV from different detectors
4. Calculation of mean value of $\Phi > 1$ MeV

In Step 1 the fluxes were calculated by EOLO[16] starting by the values of fluxes and cross sections, in five groups, used by C. M. Eisenhauer et al. in their analysis.[17] The results are summarized in Table 2. The values of measured parameters calculated using adjusted fluxes and cross sections are given in Table 1.

In Step 2 the factors appearing in Eq.1 were calculated either for the flux transfer from BIGTEN to Arkansas P&L or for the flux transfer from Cf^{252} to BIGTEN, by mean of fluxes and cross sections obtained in Step 1. For this analysis is: $E_o = 1$ MeV and $p = 95\%$.

The expression giving the variance-covariance matrix of flux transfer parameters in function of $N_{P'}$, is:

$$N_{FT} = S_{FT} \cdot N_{P'} \cdot S_{FT}^{+} \tag{5}$$

Table 2. Group Flux and Cross Section results from
Multiple Unfolding

	Energy MeV	Φ·ΔL (a)	(b)	(c)	$U^{238}(n,f)$ (a)	(b)	(c)	$Ni^{58}(n,p)$ (a)	(b)	(c)	$Fe^{54}(n,p)$ (a)	(b)	(c)	$Ti^{46}(n,p)$ (a)	(b)	(c)
Ark P&L	1.0 – 1.5	33.0	26.8	13.6	20.0	18.5	4.9	20.0	20.0	0.1	–	–	–	–	–	–
	1.5 – 2.3	5.0	4.9	1.0	4.0	3.9	7.0	10.0	10.0	0.1	20.0	20.0	-0.3	–	–	–
	2.3 – 3.7	30.0	19.2	21.6	3.0	3.0	0.2	10.0	9.9	0.2	15.0	14.9	-0.8	40.0	40.3	-2.5
	3.7 – 8.0	27.0	15.6	7.5	5.0	4.9	0.6	15.0	12.3	1.3	15.0	12.9	-2.4	20.0	17.3	-3.7
	8.0 – 12.	15.0	14.9	0.1	6.0	6.0	0.1	20.0	19.9	0.3	30.0	30.1	-1.1	30.0	30.0	-1.8
BIGTEN	1.0 – 1.5	10.0	9.8	1.4	20.0	18.4	5.8	20.0	20.0	-0.1	–	–	–	–	–	–
	1.5 – 2.3	5.0	4.7	1.8	4.0	3.8	1.2	10.0	10.0	-0.1	20.0	19.9	0.2	40.0	39.6	0.8
	2.3 – 3.7	8.0	7.0	4.6	3.0	2.9	0.6	10.0	9.8	-0.3	15.0	14.3	1.1	20.0	15.1	4.1
	3.7 – 8.0	14.0	10.4	12.1	5.0	4.9	1.2	15.0	13.0	-1.2	15.0	12.7	2.2	30.0	29.0	1.8
	8.0 – 12.	15.0	14.7	1.5	6.0	6.0	0.2	20.0	20.0	-0.2	30.0	29.7	0.7			
Cf^{252}	1.0 – 1.5	5.0	5.0	-0.3	20.0	20.9	-5.0									
	1.5 – 2.3	5.0	5.0	-2.3	4.0	4.0	-1.5									
	2.3 – 3.7	5.0	5.0	-2.7	3.0	3.0	-1.0									
	3.7 – 8.0	5.0	5.0	-2.3	5.0	5.0	-2.3									
	8.0 – 12.	10.0	10.1	-0.9	6.0	6.0	-0.3									

(a) errors in input values (%)

(b) errors in output values (%)

(c) corrections of values from M.U. calculation (%)

where: S_{FT} is the sensitivity matrix of transformation, from group fluxes and cross sections, to truncated cross sections and spectrum coverage factors relative to the two flux transfers of this experiment.

The Step 3 gives, as result, the multiple values of $\Phi_{Ark} > 1$ MeV from different detectors, with teir variance-covariance matrix calculated by an expression similar to Eq.5. Now these values have to be combined to obtain the mean value of $\Phi_{Ark} > 1$ MeV (see: Table 3).

Table 3. $\Phi_{Ark} > 1$ Mev from different detectors
$(n/cm^2\ s)$

Detector	with M.U. (a)	without M.U. (b)	Correlation matrix (%) (a)	(b)
U^{238}	$3.56 \times 10^8 \pm 15.2\%$	$3.60 \times 10^8 \pm 17.5\%$	100	100
Ni^{58}	$3.50 \times 10^8 \pm 15.9\%$	$3.53 \times 10^8 \pm 27.4\%$	86 100	72 100
Fe^{54}	$3.48 \times 10^8 \pm 15.1\%$	$3.32 \times 10^8 \pm 29.7\%$	85 86 100	67 72 100
Ti^{46}	$3.46 \times 10^8 \pm 15.1\%$	$3.10 \times 10^8 \pm 36.3\%$	84 85 85 100	53 61 61 100

The evaluation of mean value of $\Phi_{Ark} > 1$ MeV has been done, in Step 4, by code BOLIK,[18] using again the least squares method. That is, it was calculated the best expected value of $\Phi_{Ark} > 1$ MeV, once had available the results from different detectors, and under the hypotesis the $\Phi_{Ark} > 1$ MeV was unknown before this experiment was performed. This hypotesis has been expressed numerically by assuming, for the calculation, an input value with 100% of error. As expected, the result is pratically indipendent on the guess value (see: Table 4).

Table 4. Mean value of $\Phi_{Ark} > 1$ MeV
$(n/cm^2\ s)$

Guess value	Result with M.U.	Result without M.U.
$3.5 \times 10^8 \pm 100\%$	$3.49 \times 10^8 \pm 14.2\%$	$3.58 \times 10^8 \pm 17.2\%$
$5.0 \times 10^9 \pm 100\%$	$3.49 \times 10^8 \pm 14.3\%$	$3.59 \times 10^8 \pm 17.4\%$
$3.5 \times 10^8 \pm 100\%$ [a]	$3.50 \times 10^8 \pm 7.6\%$	$3.46 \times 10^8 \pm 12.3\%$
C.M. Eisenhauer et al.	-	$3.45 \times 10^8 \pm 15.0\%$

[a] without correlation between $\Phi_{Ark} > 1$ MeV from different detectors

To see the influence of multiple unfolding on the result, a calculation has been done with the omission of Step 1. In this way not adjusted fluxes and cross sections have been used in the evaluation of truncated cross sections and spectrum coverage factors (see: Table 4).

VI. CONCLUSIONS

The results (see: Table 3-4) are clearly better in case of calculation with multiple unfolding which gives a 3% of gain in the accuracy. However has to be noted that in the evaluation of mean value of $\Phi_{Ark} > 1$ MeV the reduction of error, with respect to the multiple values from different detectors, is lower for the calculation with multiple unfolding than in the calculation without multiple unfolding. This seems to be depending on the fact that the correlation between the different values of $\Phi_{Ark} > 1$ MeV is higher in the first case. This is confirmed by a calculation done under the assumption the multiple values of $\Phi_{Ark} > 1$ MeV were not correlated (see: Table 4).

The result obtained by C. M. Eisenhauer et al.,[1] calculated by weighting the multiple results on the spectrum coverage factor, indicates that in the traditional proceeding, without the use of variance-covariance matrices, the informations coming from the correlations are not kept in the due account and are lost with an effect on the result (see: Table 4).

Finally, one can conclude that the multiple unfolding and the use of covariances give more accuracy in evaluation and a proper propagation of errors which cannot be completly followed by a traditional proceeding when the experiment is complex as in this case.

ACKNOWLEDGMENTS

To be added at Chapter IV, p. 5 :

$$N_{P'} - N_P = -N_P \cdot S^{\dagger} \cdot (N_A + N_{A^{\circ}})^{-1} \cdot S \cdot N_P^{\dagger} \tag{4}$$

REFERENCES

1. C.M. Eisenhauer, J.A. Grundl, D.M. Gilliam, E.D. McGarry, V. Spiegel, "Benchmark Referencing of Neutron Dosimetry Measurements", Proceedings Third ASTM-Euratom Symposium on Reactor Dosimetry, Ispra(1979), EUR 6813/EN-FR, Vol. II,919(1980)

2. M. Petilli, "The unfolding code DANTE and its applications", ORNL/RSRC-40,79(1976)

3. M. Petilli, "DANTE - Unfolding Code for Energy Spectra Evaluation", Part I : Mathematical Method, CNEN-RT/FI(79)7

4. F.G. Perey, "Least Squares Dosimetry Unfolding: The Program STAY'SL", ORNL/TM-6062, ENDF-254(1977)

5. Compendium of Benchmark and Test Region Neutron Fields for Pressure Vessel Irradiation Surveillance, LWR Pressure Vessel Irradiation Surveillance Dosimetry Quarterly Report, NUREG/CR-0551, July-Sept. 1978, Hanford Engineering Development Laboratory (Dec.1978)

6. E.G. Dowdy, E.J. Lozito, E.A. Plassman, "The Central Neutron Spectrum of the Fast Critical Assembly Big-Ten", Nucear Thecnology 25,381,1975

7. L. Kellog - Private communication

8. L.S. Kellog, W.N. McElroy, "Reaction Rate Measurements", LMFBR Reaction Rate and Dosimetry 10th Progress Report, HELD-TME-75-130 (1976)

9. J.A. Grundl, V. Spiegel, C.M. Eisenhauer, H.T. Heaton II, D.M. Gilliam, Nuclear Technology 32, 315 (1977)

10. J.A. Grundl, C.M. Eisenhauer, "Fission Spectrum Neutrons for Cross Section Validation and Neutron Flux Transfer", NBS Special Publication 425,250,(1975)

11. W.N. McElroy, "Data Development and Testing for Fast Reactor Dosimetry", Nuclear Technology 25,2,p. 177(1975)

12. J.R. Smith, "Manganese Bath Systematic Effects in Measurements of $\bar{\nu}$ and η ", NBS special Publication 425,262(1975)

13. D.M. Gilliam, et al., "Reference and Standard Benchmark Field Con-
    sensus Fission Yields for U.S. Dosimetry Programs", Proceedings 2nd
    ASTM-Euratom Symposium on Reactor Dosimetry, NUREG/CP-0004 (10-77),
    Vol. III

14. H.T. Heaton II, D.M. Gilliam, V. Spiegel, C.M. Eisenhauer, J.A.
    Grundl, "Fission Cross Sections of U^{235}, U^{238}, and Pu^{239} Averaged
    on the Cf^{252} Spectrum", Proc. NEANDC/NEACRP Specialist Meeting,
    ANL-76-90(1976)

15. A. Gandini, M. Petilli, "AMARA. A code using Lagrange Multipliers
    method for nuclear data adjustment", CNEN-RT/FI(73)39

16. Code EOLO, to be published

17. C.M. Eisenhauer, private communication

18. Code BOLIK, to be published

BROWNS FERRY UNIT 3 CAVITY NEUTRON SPECTRAL ANALYSIS

G. C. Martin
General Electric Company, Vallecitos Nuclear Center
Pleasanton, California 94566

H. A. Till
Electric Power Research Institute
Palo Alto, California 94303

ABSTRACT

The General Electric Company at the Vallecitos Nuclear Center (GE-VNC)
has performed neutron dosimetry measurements in the Browns Ferry Unit 3
reactor (BF3) cavity using multiple dosimeter and spectrum unfolding
techniques. These measurements are the first in a BWR cavity and comprise
an important part in a general program related to verification of pressure
vessel integrity and to validation of calculations.

Determinations of BF3 cavity neutron flux densities at five key loca-
tions at full power (1098 MWe) during core cycle 2 (November 1978 to
August 1979) are as follows:

Neutron Energy Region	Neutron Energy (MeV)	Flux Density $(n \cdot cm^{-2} \cdot s^{-1})$ at 1098 MWe			
		$30°, 330°$ Core Midplane	$270°$ Core Midplane	$30°$ 5-ft Below C.M.	$30°$ 6-ft Above C.M.
Thermal	$1x10^{-9}-5x10^{-7}$	$1.8x10^{7}$	--	--	--
Inter-mediate	$5x10^{-7}-0.1$	$1.8x10^{8}$	$1.7x10^{8}$	$1.5x10^{8}$	$1.6x10^{8}$
Fast	$1-15$	$7.0x10^{7}$	$3.1x10^{7}$	$2.9x10^{7}$	$3.5x10^{7}$
Total	$1x10^{-9}-15$	$5.6x10^{8}$	--	--	--

Based on 17 generated neutron spectra, the >0.1/>1 MeV flux density
ratio in the BF3 cavity was determined to be 3.6 ± 0.2 (1σ) and the
determined >1 MeV fast cross section for the $^{54}Fe(n,p)^{54}Mn$ reaction
was 0.083 ± 0.005 (1σ) barns.

Verification of the reaction rate measurements for dosimeters located
at $30°$ core midplane was made by the SCK/CEN (Belgium) laboratory.

INTRODUCTION

The Electric Power Research Institute (EPRI) Advisory Group on Radiation Transport has identified the area of making radiation measurements on operating reactors in the cavity area between the pressure vessel and primary shield wall as being a high priority item. The goal of the program is to obtain accurate neutron and gamma ray data on Boiling Water Reactor (BWR) and Pressurized Water Reactor (PWR) plants.

A knowledge of the neutron flux and spectrum in the reactor cavity is highly desirable for a number of safety and operational reasons. These include assessing the radiation embrittlement of the pressure vessel and support structures and estimating the activation of components.

The effort in this area is directed toward the continued assurance of the safety of new and existing plants and to meet licensing and technical specification requirements set forth in 10CFR50 and USNRC Regulatory Guide 1.99. The neutron dosimetry data would help verify the long term integrity and service life of a light water reactor pressure vessel and help forestall restrictive operating envelops due to neutron damage and reduction in transition temperature considerations.

Under an EPRI contract to the General Electric Company (GE) the major task objective was to determine the fast neutron energy spectra and flux levels in a BWR cavity region. The test was to be performed at selected locations, axially and azimuthally, during high power operating conditions. Complete energy spectra were also to be determined at one or more selected locations. Data on gamma ray flux levels were also to be obtained.

Browns Ferry Unit 3 (BF3) was the reactor of choice since flux-spectrum capsules were already located inside the pressure vessel, the method of capsule insertion and removal in the cavity appeared to be an uncomplicated one (as a result of a visit to BF3), as the cavity annulus is approximately 20 cm wide, and BF3 management had expressed a willingness to cooperate. These measurements, therefore, would complement already-installed in-vessel dosimeters to give a flux mapping from the shroud to the reactor cavity.

The intent of the EPRI-GE program was to provide experimental data to establish a data base for cavity radiation levels in such a form for use in the verification of neutron damage calculations to the beltline and nozzle regions of the pressure vessel and radiation streaming in the reactor cavity. Thus, these experimental data are to be used to benchmark calculations.

The measurement method utilized radioactivity counting data from activation and fission dosimeters in combination with ENDF/B-V differential cross sections and a GE spectrum unfolding computer program.

A series of radiation measurement tests have been performed at the Browns Ferry Unit 3 nuclear power plant which provide a comprehensive study of the neutron and/or gamma radiation levels from the reactor shroud to the exterior drywell wall. BF3 is a 1098-MWe BWR with 8x8 fuel assemblies and is located near Decatur, Alabama, USA, and is operated by the Tennessee Valley Authority (TVA).

The first of the tests consisted of a TVA-GE funded program to determine the neutron flux densities, fluences, and energy spectra between the shroud and inside wall of the pressure vessel.[1] Four special neutron capsule holders were installed in BF3 prior to the initial reactor startup August 1976 and were removed and shipped October 1978 to GE-VNC for analysis.

The second study was an EPRI funded program for GE to perform neutron spectra and gamma radiation measurements in the reactor cavity between the reactor pressure vessel and shield wall.[2] Four strings of neutron capsules and two strings of gamma capsules were suspended in the BF3 cavity. This study took place during the second BF3 fuel cycle (November 1978-August 1979).

The third study was a GE-funded program which extended the reactor cavity neutron and gamma measurements into the drywell proper. This study also was made during the second BF3 fuel cycle.[3]

The locations of the in-vessel, cavity, and two of the drywell capsules are shown in Fig. 1.

The locations of all neutron capsules in the cavity are shown schematically in Fig. 2. The bare and shielded capsules are drawn light and dark, respectively.

This paper describes the experimental studies relating to the neutron fields in the BF3 cavity. Passive activation detectors (dosimeters) at 30 locations were used for determining the neutron spectra. These types of dosimeters are small and are stable over a large temperature gradient (the BF3 cavity temperature was measured to be approximately $54°C$). A relatively small capsule can contain several dosimeters to provide neutron flux density, fluence, and spectral information over a broad range of neutron energies and as a function of location in a reactor.

EXPERIMENTAL

The method of capsule insertion in the BF3 cavity was the suspension at each of four azimuthal locations (30°, 90°, 270°, 330°- see Fig. 1) of a chain of dosimeters from the feedwater nozzle insulation to the
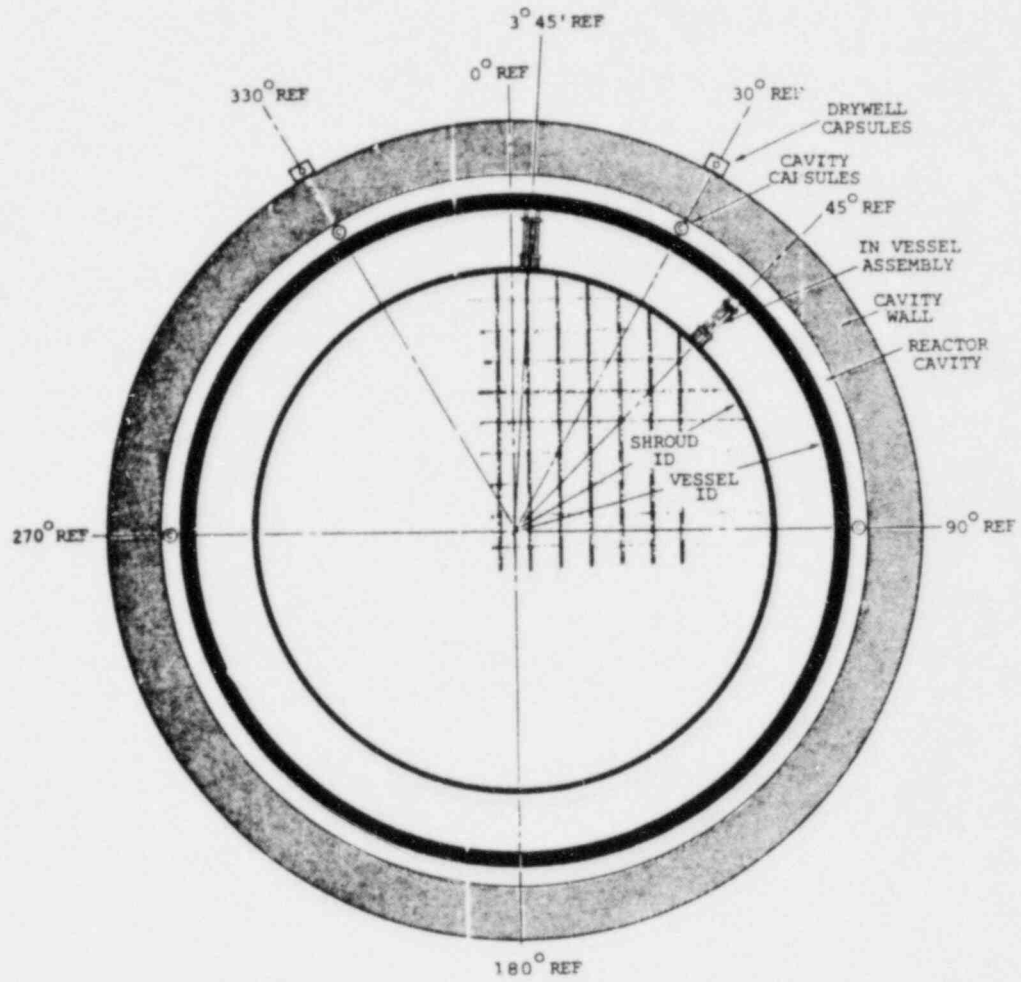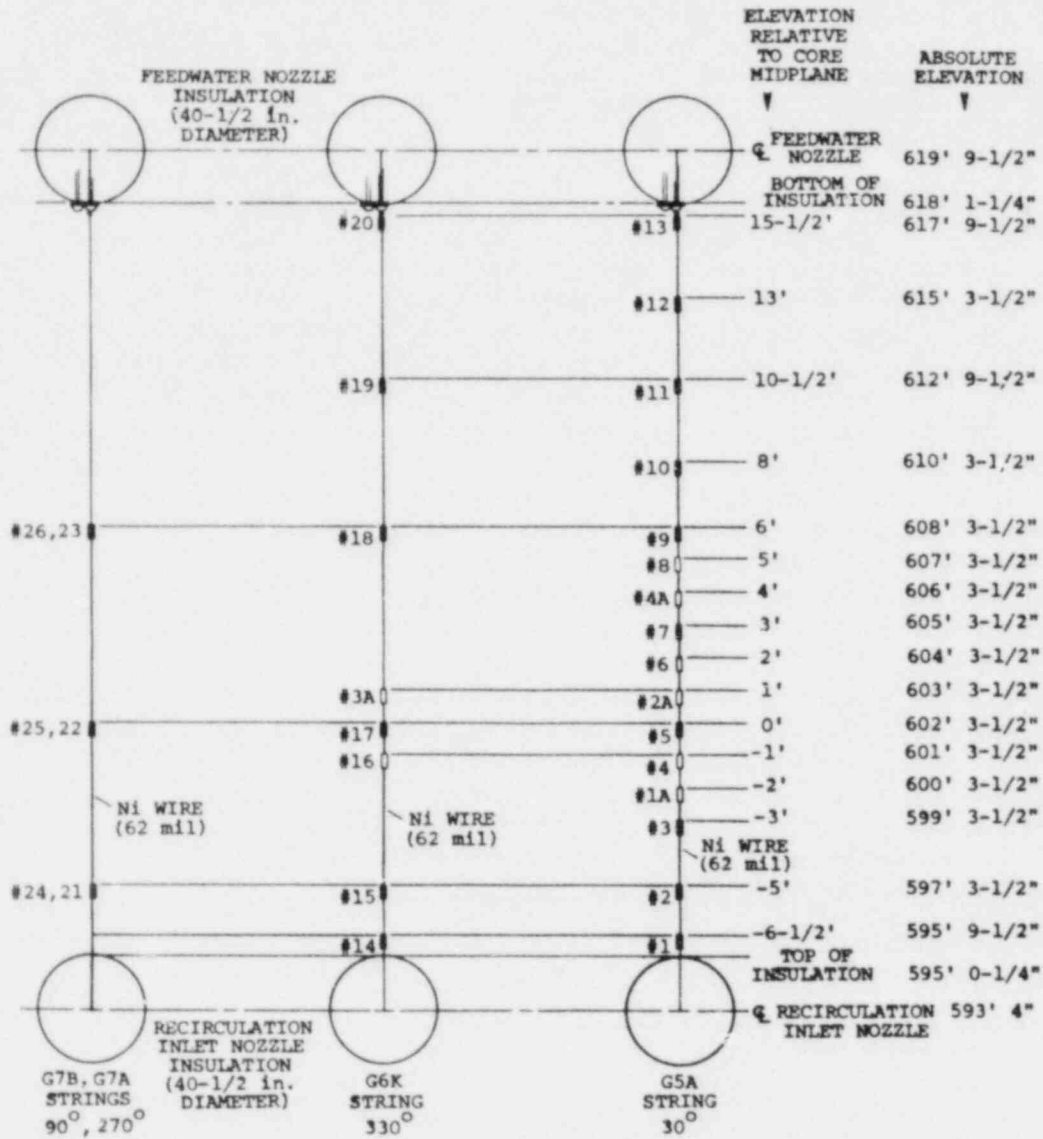
FIGURE 1. Browns Ferry Neutron Capsule Locations

FIGURE 2. Capsule Locations in Cavity

recirculation inlet nozzle insulation, a distance of 23 feet (7 meters). The chain consisted of precut prelabeled sections of 62-mil (1.57 mm) nickel (Ni) wire, itself a fast flux monitor, connecting aluminum capsules which contained the neutron dosimeters.

Thirty aluminum capsules were prepared, 22 contained shielded (cadmium oxide-copper)(45 mils Cd) tubes and eight were unshielded. The neutron dosimeters selected included: oxides of ^{235}U, ^{238}U, ^{237}Np, and ^{232}Th; salts of Ag, Sc, and ^{235}U; and Fe, Ni, Ti, Cu, and AlCo wires.

After irradiation, the dosimeters were non-destructively analyzed for radioactivity activation and fission product content by gamma spectrometry and/or by gross gamma counting. The nickel gradient wires which were located between the cavity capsules were cut into 1-in (2.54 cm) segments before analysis for ^{58}Co activity. Approximately 1300 dosimeters and flux gradient samples were prepared. All counting systems were calibrated with standards procured from the National Bureau of Standards and Amersham Corporation.

Reaction rates were subsequently calculated from the activity data and reactor power history. These reaction rates were then extrapolated to the capsule reference points using flux gradient data. The extrapolated values were inserted into a GE unfolding computer program for neutron spectral analysis.

RESULTS

The measured disintegration rates and measured and extrapolated reaction rates of the neutron dosimeters located within the 30 flux capsules are presented elsewhere.[2]

Many of the ^{235}U, ^{238}U, ^{237}Np, and ^{232}Th dosimeters irradiated within the 30 flux capsules in the cavity required long count times because of low fission product activity. Generally, the ^{137}Cs and ^{103}Ru gamma peaks required relatively high background/Compton corrections. The $^{140}BaLa$ half-life (12.8 d) is too short to be used accurately for a BWR 9-month irradiation. ^{95}Zr, itself, can suffer from natural-background ^{232}Th daughters. For this experiment, ^{95}Nb gave the most consistent measurement of any fission product radionuclide. Based on theoretical calculations of the buildup and decay of ^{95}Zr and ^{95}Nb during and following the BF3 irradiation, and verified by the counting of selected higher-radioactive fission dosimeters, the ^{95}Nb peak has been used to obtain ^{95}Zr activities for ^{235}U, ^{238}U, and ^{237}Np. The photofission (γ,f) factors used for ^{238}U, ^{237}Np, and ^{232}Th are the latest data available.[4] These correction factors are approximately 10% for ^{238}U, 3% for ^{237}Np, and 20% for ^{232}Th.

TABLE 1. Thermal, Intermediate, Fast, and Total Flux Densities – BF3 Cavity

Flux Density at 1098 MWe
$(n \cdot cm^{-2} \cdot s^{-1})$

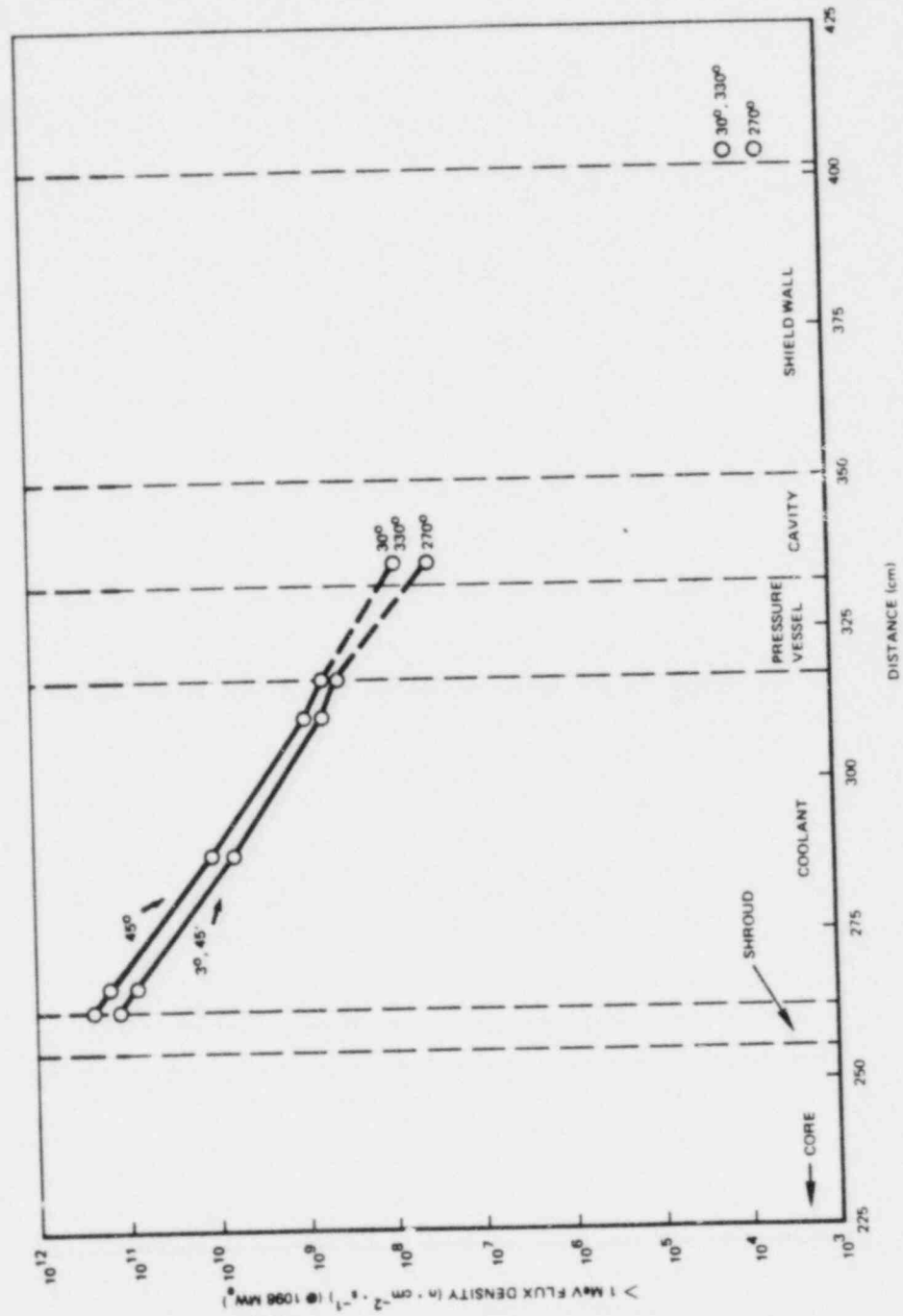| Capsule Number	Elev. Rel. to Core Midplane (ft)	Thermal $1 \times 10^{-9} - 5 \times 10^{-7}$	Intermediate $5 \times 10^{-7} - 0.1$	Fast 1-15	Total $1 \times 10^{-9} - 15$ MeV	Azimuth
1	- 6½	--	8.7×10^7	1.1×10^7	--	30°
2	- 5	--	1.5×10^8	2.9×10^7	--	
3	- 3	--	2.3×10^8	5.2×10^7	--	
1A	- 2	2.1×10^7	2.7×10^8	6.4×10^7	5.5×10^8	
4	- 1	2.9×10^7	2.8×10^8	7.3×10^7	5.6×10^8	
5	0	$.8 \times 10^7$	2.7×10^8	6.9×10^7	5.7×10^8	
2A	+ 1	2.9×10^7	3.1×10^8	7.8×10^7	6.3×10^8	
6	+ 2	3.0×10^7	3.1×10^8	8.0×10^7	6.3×10^8	
7	+ 3	--	3.2×10^8	7.0×10^7	--	
4A	+ 4	2.9×10^7	2.3×10^8	5.9×10^7	4.6×10^8	
8	+ 5	2.6×10^7	--	4.8×10^7	--	
9	+ 6	--	1.6×10^8	3.5×10^7	--	
10	+ 8	--	6.4×10^7	6.0×10^6	--	
11	+10½	--	2.5×10^7	1.2×10^6	--	
12	+13	--	1.0×10^7	--	--	
13	+15½	--	4.6×10^6	--	--	
14	- 6½	--	9.9×10^7	1.3×10^7	--	330°
15	- 5	--	1.6×10^8	3.1×10^7	--	
16	- 1	2.7×10^7	2.6×10^8	6.5×10^7	5.1×10^8	
17	0	2.9×10^7	2.9×10^8	7.1×10^7	5.5×10^8	
3A	+ 1	2.8×10^7	2.3×10^8	7.4×10^7	4.8×10^8	
18	+ 6	--	1.7×10^8	3.6×10^7	--	
19	+10½	--	2.5×10^7	1.3×10^6	--	
20	+15½	--	4.0×10^6	--	--	
21	- 5	--	9.0×10^7	1.5×10^7	--	270°
22	0	--	1.7×10^8	3.1×10^7	--	
23	+ 6	--	8.8×10^7	1.8×10^7	--	

562

FIGURE 3. BF3 >1 MeV Flux Density at Core Midplane vs. Distance from Core Centerline

The extrapolation of measured reaction rates to the capsule reference points (top-center) was based on the radioanalysis of the small (3.2-mm diameter) flux gradient nickel disks or 12.7-mm diameter iron disks which were located at different and measured elevations within the capsules. The horizontal gradient factors ranged from 0.968 to 1.025. The vertical gradient factors per 1/4-inch (6.35 mm) to the tops of the capsules were measured to be approximately 1.01 at core bottom, 1.003 at core midplane, and 0.99 at core top.

Table 1 gives a breakdown of flux densities and fluences into three groups: thermal (1×10^{-9}-5×10^{-7} MeV), intermediate (5×10^{-7}-0.1 MeV), and fast (>1 MeV).

The highest fast flux density determined was at $30°$ at 2-ft above core midplane (capsule No. 6); the >1 Mev value was 8.0×10^7 $n/cm^2 \cdot s$. The $330°$ to $270°$ >1 MeV flux density ratio (edge of core/flat portion of core) was approximately 2.3. The >0.1/>1 MeV flux density ratio in the BF3 cavity was determined to be 3.6 ± 0.2 (1σ).

Based on the radioanalysis of the Ni gradient wires, the >1 MeV fast flux densities at the bottom of the $30°$, $330°$, $270°$ feedwater nozzle insulations were all approximately 2×10^5 $n/cm^2 \cdot s$, and the corresponding >1 MeV values at the top of the recirculation nozzle insulations were approximately 6×10^6 $n/cm^2 \cdot s$ and 3×10^6 $n/cm^2 \cdot s$ at $30°/330°$, and at $270°$, respectively. The peak ^{58}Co activities are located 1 to 2 feet above core midplane.

Calculated >1 MeV fast cross sections determined by the spectrum unfolding method for the $^{54}Fe(n,p)$, $^{58}Ni(n,p)$, $^{63}Cu(n,\alpha)$, $^{137}Np(n,f)$, and $^{238}U(n,f)$ reactions for 17 capsules were 0.083 ± 0.005 (1σ), 0.114 ± 0.005 (1σ), 0.0016 ± 0.0001 (1σ), 2.9 ± 0.1 (1σ), and 0.36 ± 0.02 (1σ) barns, respectively.

Fig. 3 gives determined fast flux densities at core midplane as a function of distance from core centerline for the three BF3 programs.

DISCUSSION AND CONCLUSIONS

The first determination of the neutron spectral shape and integral flux density levels in a BWR cavity has been successful and is an important step in indicating the feasibility of performing pressure vessel dosimetry experiments which can obviate the placement of dosimeter specimens within the pressure vessel.

The advantages of cavity rather than in-vessel dosimetry are 1) the relative ease of handling dosimeter capsules, 2) insertion and removal

of cavity capsules can be made during scheduled or unscheduled plant
outages following the de-inertion of the drywell, 3) no contamination
within the vessel is possible, 4) photofission corrections for fission
dosimeters are smaller (10% for ^{238}U in the cavity versus 35% within
the vessel), 5) laborous calculations of localized power histories were
not necessary for this cavity experiment as opposed to the previous
in-vessel experiment, 6) thermal-to-fast flux density ratios are very
much lower in the cavity (1:10) than at the pressure vessel (3:1) and
therefore reduce the effects of impurities in fast flux dosimeters
during radioanalysis, and 7) lower-level dose rates of cavity capsules
reduce shipping problems.

The disadvantages of cavity experiments are 1) the larger extrapolation
of data from the cavity to the 1/4 T pressure vessel position, and 2)
the lower activities (and therefore longer count times) produced in the
cavity compared to those at the ID of the pressure vessel (a factor of
11 for ^{238}U, a factor of 16 for Fe, Ni, Cu).

An interlaboratory comparison of activity and reaction rate
measurements for all dosimeters from capsule No. 5, located at 30° core
midplane, was made by the SCK/CEN laboratory at Mol, Belgium and
GE-VNC. The agreement between the two laboratories was excellent. For
non-fission dosimeters (i.e., Ag, Co, Cu, Fe, Ni, Sc, Ti) the reaction
rate measurement agreement was better than 2%, except for Ag which was
8%. For the reaction rates of the fission dosimeters (i.e., ^{235}U,
^{238}U, ^{237}Np, ^{232}Th) the agreement was 2-3% for ^{103}Ru, 1-6% for
^{95}ZrNb, and 6-10% for (the low count rate) ^{137}Cs.

REFERENCES

1. G. C. Martin, "Browns Ferry Unit 3 In-Vessel Neutron Spectral
    Analysis," NEDO-24793, August 1980.

2. G. C. Martin, "Browns Ferry Unit 3 Cavity Neutron Spectral
    Analysis," EPRI NP-1997, August 1981.

3. G. C. Martin, "Browns Ferry Unit 3 Drywell Neutron Measurements,"
    NEDO-24946, June 1981.

4. G. L. Simmons and W. K. P an, Science Applications, Inc., Private
    Communication (October 1).

CONTROL OF THE ORR-PSF PRESSURE VESSEL SURVEILLANCE

IRRADIATION EXPERIMENT TEMPERATURE

L. F. Miller
University of Tennessee   Oak Ridge National Laboratory
Knoxville, Tennessee, USA   Oak Ridge, Tennessee, USA

ABSTRACT

Control of the Oak Ridge Research Reactor Pool Side
Facility (ORR-PSF) pressure vessel surveillance irra-
diation experiment temperature is implemented by digital
computer control of electrical heaters under fixed cooling
conditions. Cooling is accomplished with continuous flows
of water in pipes between specimen sets and of helium-neon
gas in the specimen set housings.

Control laws are obtained from solutions of the
discrete-time Riccati equation and are implemented with
direct digital control of solid state relays in the
electrical heater circuit. Power dissipated by the heaters
is determined by variac settings and the percent of time
that the solid state relays allow power to be supplied to
the heaters. Control demands are updated every forty
seconds.

Temperature and power data are recorded on-line at one
hour intervals, except during transient conditions, and are
processed off-line to obtain characterization data for each
thermocouple. Results obtained for each thermocouple
include: average temperature, standard deviation, and a
time histogram of temperatures. Time of irradiation and
megawatt hours of irradiation are also determined. These
results are useful for correlating metallurgical property
data with the irradiation environment and for evaluating
the control algorithm performance. Nearly all of the ther-
mocouple temperatures are maintained within 5°C of 288°C
and have standard deviations of less than 2°C.

1. INTRODUCTION

The United States Nuclear Regulatory Commission is conducting an extensive research program into characterizations of irradiation effects on various steels. This work is funded through the LWR Pressure Vessel Surveillance Dosimetry Improvement Program.[1] Motivation for this program stems primarily from the fact that approximately twenty of the first built Light Water Reactors (LWRs) do not have in-place test specimens made of pressure vessel steels. Thus, several irradiations of appropriate steels are being conducted in research reactors at an accelerated rate relative to power reactors. It is desired that the irradiations relative to this report be performed at essentially the same temperature as the pressure vessel of a typical light water reactor. In particular, the temperature of each irradiation capsule is to be maintained at 288°C ± 10°C. This is accomplished by control of electrical heaters on the front and back faces of each set of irradiation specimens. Cooling conditions are fixed.

Schematics of the Oak Ridge Reactor Pool Side Facility (ORR-PSF) irradiation experiment are shown in Figs. 1 and 2 of reference 6. Note that two irradiation capsules are employed. One simulates the surveillance capsule placed behind the thermal shield in some LWRs and the other simulates the pressure vessel. A single set of specimens is placed in the simulated surveillance capsule (SSC) and three sets of specimens (see Fig. 2 of reference 6) are placed in the pressure vessel capsule. These correspond to pressure vessel positions of: 1) zero thickness (OT) or surface, 2) one-fourth thickness (1/4T), and 3) one-half thickness (1/2T). A schematic of a capsule control system is shown in Fig. 1.

Reactor power and specimen temperature data are recorded every hour during normal operating conditions and more frequently during transients. These data are processed in order to characterize the temperature and neutron fluence environment associated with physical property data obtained from the irradiated metallurgical test specimens. Data selected to characterize the irradiation environment are:

1) time that the experiment is in-place and reactor power is greater than 5 MW (the ORR is not operated for extended periods below 6 MW),
2) accumulated megawatt-hours of irradiation,
3) time histrogram based on five temperature intervals,
4) average temperature of each thermocouple after an average specimen set temperature of 285°C is achieved and the specific thermocouple temperature is greater than 270°C, and
5) standard deviation associated with each thermocouple temperature.

Calculations for items 2-5 are performed consistently with the determination of accumulation of irradiation time as defined by item 1.

2. THEORY

2.1 General Considerations

It is expected that the reactor power will nearly always be constant at 30 MW. Exceptions occur during inadvertent reactor setbacks and planned shutdowns. Thus, the transient response of the control algorithm must have acceptable performance with respect to overshoot and settling time, but the dynamic response with respect to tracking is not very important. Steady-state control of the spatial temperature distribution is the objective of primary concern.

There is a variety of options with regard to methods for implementing a control algorithm. Several state variable approaches include: 1) eigenvalue placement, 2) output feedback stabilization, and 3) optimal control. Each of these methods could be implemented as a discrete-or continuous-time algorithm.

2.2 Development of the Continuous-Time Model

The partial differential equation, with minor assumptions, which describes the temperature distribution with the experiment capsule is given by

$$\dot{T}(\underline{r},t) = \alpha \nabla^2 T(\underline{r},t) + \frac{\dot{q}'''(\underline{r},t)}{\rho C_p} \quad , \tag{2.1}$$

where

$$\alpha = k/\rho C_p$$
$$q''' = \text{internal heat generation rate}$$
$$\rho = \text{material density}$$
$$C_p = \text{heat capacity}$$
$$k = \text{thermal conductivity}$$
$$T = \text{temperature.}$$

Equation 2.1 can be discretized to form a set of ordinary differential equations of the form

$$\underline{\dot{T}}(t) = \underline{A} \, \underline{T}(t) + \underline{\dot{W}}(t) \tag{2.2}$$

where

$$\underline{\dot{W}} = \text{vector which represents the internal heating associated with each temperature node,}$$
$$\underline{T} = \text{vector of temperatures corresponding to selected spatial locations,}$$
$$\underline{A} = \text{coefficient matrix which represents the coupling between temperature nodes.}$$

The internal heating rate, $\dot{\underline{W}}(t)$, may be broken into components which represent the gamma heating, $\dot{\underline{W}}_\gamma(t)$, and electrical heating, $\dot{\underline{W}}_e(t)$, so that

$$\dot{\underline{W}}(t) = \dot{\underline{W}}_\gamma(t) + \dot{\underline{W}}_e(t). \tag{2.3}$$

Note that the internal heating rate vectors, $\dot{\underline{W}}_\gamma$ and $\dot{\underline{W}}_e$, may be represented in terms of measurable parameters which gives,

$$\dot{\underline{W}}_\gamma(t) = \underline{K} \, P_R(t) \tag{2.4}$$

$$\dot{\underline{W}}_e(t) = \underline{B} \, \underline{P}_e(t) \tag{2.5}$$

where

$P_R(t)$ = reactor power,
$\underline{P}_e(t)$ = vector of electrical heater powers,
$\underline{K}$ = vector which converts reactor power to gamma heating,
$\underline{B}$ = matrix which converts electrical heater power to internal heating.

If equations 2.3 through 2.5 are substituted into equation 2.2, one obtains

$$\dot{\underline{T}}(t) = \underline{A} \, \underline{T}(t) + \underline{K} \, P_R(t) + \underline{B} \, \underline{P}_e(t). \tag{2.6}$$

Equation 2.6 is linear and could be employed directly in a set point tracking control algorithm.[2] However, the regulator problem is implemented based on the expansion of equation 2.6 about a reference operating point. This yields,

$$\dot{\underline{\delta T}}(t) = \underline{A} \, \underline{\delta T}(t) + \underline{B} \, \underline{\delta P}_e(t) + \underline{K} \, \delta P_R(t) \tag{2.7}$$

where

$$\underline{\delta T}(t) = \underline{T}(t) - \underline{T}_o,$$

$$\delta P_R(t) = P_R(t) - P_{Ro},$$

$$\underline{\delta P}_e(t) = \underline{P}_e(t) - \underline{P}_{eo}.$$

A first order Taylor series expansion of the temperature vector gives,

$$\underline{\delta T}_{ss} = \frac{\partial \, \underline{\delta T}}{\partial \, \delta P_R} \, \delta P_R + \frac{\partial \, \underline{\delta T}}{\partial \, \underline{\delta P}_e} \, \underline{\delta P}_e. \tag{2.8}$$

Note that at steady state, all $\delta T(t)$ are zero. Thus, if equation 2.8 is substituted into equation 2.7, restricted to steady state, one identifies directly that

$$\underline{B} = - \underline{A} \; \frac{\partial \; \overline{\delta T}}{\partial \; \underline{P}_e} \tag{2.9}$$

and

$$\underline{K} = - \underline{A} \; \frac{\partial \; \overline{\delta T}}{\partial \; P_R} \; . \tag{2.10}$$

The partial derivatives of interest are obtained by perturbations of electrical heaters and reactor power. The system matrix, A, is obtained by analysis of time response data. If variations in reactor power are neglected and the usual text book nomenclature is substituted into equation 2.7, one obtains the following for the continuous-time model:

$$\dot{\underline{X}}(t) = \underline{A} \; \underline{X}(t) + \underline{B} \; \underline{U}(t) + \underline{K} \; V(t). \tag{2.11}$$

If reactor power variations are not included, the continuous-time model becomes,

$$\dot{\underline{X}}(t) = \underline{A} \; \underline{X}(t) + \underline{B} \; \underline{U}(t). \tag{2.12}$$

In order to employ a discrete-time algorithm, the continuous-time model must be transformed to a discrete-time system.[3]

2.3 Transformation from a Continuous- to a Discrete-Time Model

The solution to equation 2.12 is given by

$$\underline{X}(t) = e^{\underline{A}t} \; \underline{X}(0) + \int_o^t e^{\underline{A}(t-\tau)} \; \underline{B} \; \underline{U}(\tau) \; d\tau. \tag{2.13}$$

If we consider a discretized system sampled at intervals of time T, one obtains,[3]

$$\underline{X}(n+1) = e^{\underline{A}T} \; \underline{X}(n) + \int_o^T e^{\underline{A}\tau} d\tau \; \underline{B} \; \underline{U}(\tau), \tag{2.14}$$

which may be written as

$$\underline{X}(n + 1) = \underline{\tilde{A}} \, \underline{X}(n) + \underline{\tilde{B}} \, \underline{U}(n) \tag{2.15}$$

where $\tilde{A}$ and $\tilde{B}$ are defined implicitly with A assumed to be time independent and U assumed to be constant over each time interval. These matrices are computed by expanding the matrix exponential in an infinite series until convergence is obtained.

2.4 Determination of Closed-Loop-State-Variable Control Laws

Implementation of a discrete-time control algorithm with a continuous-time system could be accomplished in a variety of ways. First, one has the choice of calculating the control law with either eigenvalue placement or optimal methods. In neither case can performance parameters such as settling time and overshoot be specified a priori. Input parameters must be adjusted for both methods to obtain acceptable transient response characteristics. Steady-state conditions should be the same regardless of the method for determining the control law. An optimal method is used for this work, and the optimal control law is obtained by solving the discrete-time Riccati equation. The procedure employed is one given by Kirk.[4]

The system in question, an irradiation capsule, is assumed to be time-invariant and completely controllable. In addition, it is assumed that the system states and controls are not constrained. In this case the optimal control law is time-invariant for an infinite-stage process, and the feedback law can be implemented with constant gain factors. The numerical evaluation of the feedback matrix is relatively straightforward, but care must be employed in determining convergence since the convergence rate may be nonuniform. The computer program for this calculation, RCTEQ,[5,6] solves either the continuous- or discrete-time Riccati equation. Implementation software is discussed in references 6 and 7. Results are presented in reference 6.

2.5 Characterization of Capsule Temperature Environment

Most of the five items, listed in the Introduction, which are selected to characterize the capsule irradiation environment require no mathematical explanations. Some mathematical descriptions are presented, however, to illustrate the calculation of average temperature and the standard deviation of the temperature for each thermocouple. Implementation of these algorithms becomes complicated because arbitrary times for insertions and retractions of the capsules, along with temperature and power software switches, must be integrated into a general calendar routine. Details are given in reference 8.

In mathematical terms, the average temperature is defined by

$$\overline{T}(\theta) = \frac{1}{\Gamma} \int_{0}^{\theta} \chi(\tau) \, T(\tau) d\tau, \tag{2.16}$$

$$\Gamma = \int_{0}^{\theta} \chi(\tau) d\tau \tag{2.17}$$

where

θ = time interval over which data are processed,
$\chi(\tau)$ = zero or unity as defined by irradiation and capsule conditions,
Γ = effective irradiation time,
$T(\tau)$ = thermocouple temperature,
$\overline{T}(\theta)$ = average thermocouple temperature defined over θ.

The variance as defined over the irradiation time, θ, is

$$\sigma_{\theta}^{2} = \frac{1}{\Gamma} \int_{0}^{\theta} \chi(\tau) [T(\tau) - \overline{T}(\theta)]^{2} \, d\tau \ . \tag{2.18}$$

Determination of the variance by utilizing equation 2.18 requires that the average temperature be available from equation 2.16 and that the data be processed twice. In order to obtain both the average temperature and the variance of the temperature in a single pass through the data, the average temperature at time $\theta + \Delta$ may be written as

$$\overline{T}(\theta + \Delta) = \frac{\Gamma}{\Gamma + \Delta} \ \overline{T}(\theta) + \frac{1}{\Gamma + \Delta} \int_{\theta}^{\theta + \Delta} \chi(\tau) \, T(\tau) \, d\tau \ . \tag{2.19}$$

If the integral is approximated by using the trapezoidal rule,

$$\overline{T}(\theta + \Delta) = \frac{\Gamma}{\Gamma + \Delta} \overline{T}(\theta) + \frac{\Delta}{\Gamma + \Delta} \ \frac{T(\theta) + T(\theta + \Delta)}{2} \ . \tag{2.20}$$

The same approach may be employed to obtain the variance in a single pass through the data to obtain

$$\sigma_{\theta + \Delta}^{2} = \frac{\Gamma}{\Gamma + \Delta} (\sigma_{\theta}^{2} + C) + \frac{\Delta}{\Gamma + \Delta} [T_{\theta + \Delta/2} - \overline{T}(\theta + \Delta)]^{2} \tag{2.21}$$

where

$$C = \Gamma [\overline{T}(\theta + \Delta) - \overline{T}(\theta)]^{2}$$

$$T_{\theta + \Delta/2} = [T(\theta) + T(\theta + \Delta)]/2 \ .$$

Additional details relative to this development are given in reference 8.

3. EXPERIMENTS AND RESULTS

3.1 Experimental Determination of the System and System Input Matrices

The schematic shown in Fig. 1 is essentially the same for the surveillance position and the three pressure vessel positions. Five heaters are on the front side facing the reactor and five are on the back side of each specimen assembly. Of the thermocouples input to the computer, ten are on the front face and ten are on the back face of each set of irradiation specimens. Several others are input to recorders for protecting the experiment in case of computer failure.

A partial derivative matrix of changes in temperature of all thermocouples due to a power change of each heater is needed for determining the system and system input matrices defined by equation 2.6. Detailed procedures and results are described in reference 6.

Transient heatup and cooldown data for the surveillance capsule are given in Fig. 2. A second order response is indicated by the heatup response but is not indicated by the cooldown response. In each case, however, the effective first order time constant is approximately 12 minutes. This is the case for the response of several individual thermocouples as well as the average of several thermocouples. The system matrix is represented as a diagonal matrix with each entry defined by the reciprocal of the effective first order time constant. The response of a selected thermocouple resulting from heating the pressure vessel capsule is given in Fig. 3. This response indicates that the dynamical model is essentially first order with an effective time constant of 20 minutes.

3.2 Performance Evaluations

Evaluations of the control algorithm are either computer simulations with the system model or real-time test runs. Computer simulation calculations are based on an optimal control law obtained from a solution of a Riccati equation with 500 on the diagonal of the system mode weighting matrix. Results from the computer simulation indicate satisfactory performance; however, several real-time test runs indicate oscillatory control. This is an indication that the feedback gains are too large. Disagreement between the simulation runs and the real-time test runs is probably due to a relatively crude model of the system matrix. Significant effort would be required to obtain an accurate identification of this matrix. In order to eliminate the problem with oscillations, the feedback law is recalculated with a system mode weighting matrix (SMWM) with ten on the diagonal. Results from low temperature real-time test runs demonstrate that the feedback law based on a SMWM with ten on the diagonal performs well. Examples of three tests are given in Fig. 6 of reference 6. The test case methods evaluated

are: 1) proportional only, 2) integral only, and 3) average temperature.

Because the reference setpoint for heater power cannot be easily established with manual operation of the variacs and because this set point changes during the fuel cycle, an integrating component is needed in the algorithm. The relative values of proportional and integral gains are established from several real-time test runs on the surveillance capsule. Difficulties with all integral control compared with a combination of proportional plus integral control are: 1) the response to perturbations is slower, and 2) overshoot is more pronounced. Complete proportional control is unacceptable since the setpoint changes during the fuel cycle and the required heater power for a flat capsule temperature cannot be easily determined.

The algorithm implemented integrates the reference heater power setpoint only during steady-state conditions. Thirty percent of the demanded duty cycle change is added to the reference duty cycle every 80 seconds when steady-state conditions prevail. The criterion for steady state is that the average capsule temperature changes less than 1°C in 80 seconds. Another feature of the algorithm is that a transfer between automatic and on/off control is made within a hysteresis band. Transfer to automatic control is made when the average temperature is within 2°C, and transfer out is made when the average temperature exceeds 5°C.

Characterization data for the first simulated surveillance capsule (SSC-1) are given in Table 1, and for the simulated pressure vessel capsule (PVC) they are given in Table 2 of reference 8. The data for SSC-1 represent final conditions and those for the PVC are cumulative through Dec. 31, 1980. Note that deleted thermocouples have failed and that their output is set to the reference control temperature of 288°C. Standard deviations for these thermocouples should be zero and their average temperature should be 288°C. Relatively large standard deviations are due to erratic thermocouples. Most standard deviations are less than 2°C, and most average temperatures are within 5°C of 288°C.

4. CONCLUSIONS AND RECOMMENDATIONS

A state variable control algorithm is implemented for maintaining temperature control of the ORR-PSF irradiation capsules. The automatic algorithm maintains temperatures within a band about 25% smaller than can be readily accomplished with manual control and makes adjustments for power distribution changes during the fuel cycle. Improved performance could probably be obtained if the system matrix contained coupling terms rather than only first order dynamics. Even though water channels exist between the specimen sets, it is apparent when a particular heater is energized that they are not decoupled. Another performance-limiting factor is that all of the temperatures included in the model (i.e., 20

per specimen set) cannot be driven to a specified temperature simulta-
neously by manual adjustment of the variacs. Refinements in the control
model and capsule design would be worthwhile from the standpoint of
methodology development and from the expected improvement in
performance.

REFERENCES

1. W. N. McElroy, et al, LWR Pressure Vessel Surveillance Dosimetry
   Improvement Program, 1979 Annual Report, NUREG/CR-1291, Hanford
   Engineering Development Laboratory (1979).

2. H. Kwakernaak and R. Sivan, Linear Optimal Control Systems, Wiley-
   Interscience, pp. 237-243 (1972).

3. C. T. Chen, Introduction to Linear System Theory, pp. 404, Holt
   Rinehart and Winston, Inc., New York (1970).

4. Donald E. Kirk, Optimal Control Theory: An Introduction, pp. 83-84,
   Prentice-Hall, Inc., Englewood Cliffs, New Jersey (1970).

5. Laurence F. Miller, Nuclear Reactor Control System Design with
   Sensor Failure, Texas A&M University, College Station, Texas (August
   1976).

6. L. F. Miller, A Computerized Process Control System for the ORR-PSF
   Irradiation Experiment. Part 2: Mathematical Basis and Computer
   Implementation of the Temperature Control Algorithm, NUREG/CR-1710
   Vol. 2 (August 1980).

7. S. H. Merriman, A Computerized Process Control System for the ORR-PSF
   Irradiation Experiment. Part 1: Overall View of the Control System,
   ORNL/NUREG/ TM-405/P1, (to be published in 1982).

8. L. F. Miller, Analysis of Temperature Data from the ORR-PSF Irradia-
   tion Experiment: Methodology and Computer Software, NUREG/CR-2273,
   ORNL/TM-7766 (November 1981).

ORNL-DWG 81-21426R
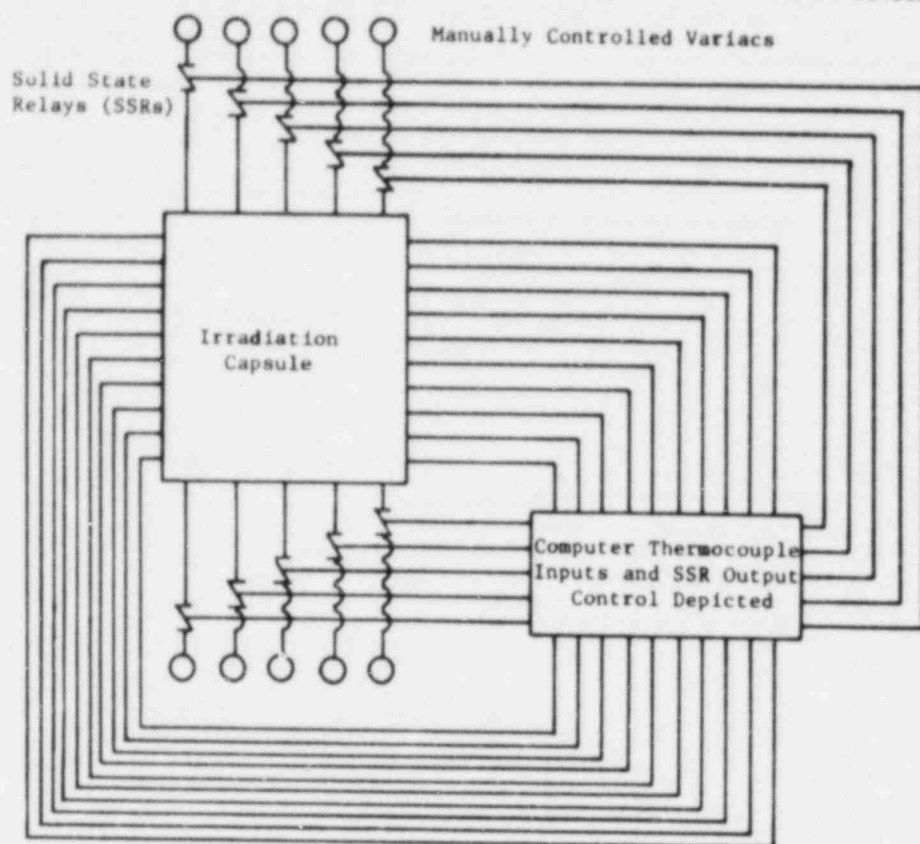
Fig. 1. Schematic Diagram of an Irradiation Capsule with Thermocouple Outputs and Heater Control Depicted. Note that the computer controls the firing of solid-state relays between variacs and electrical heaters.
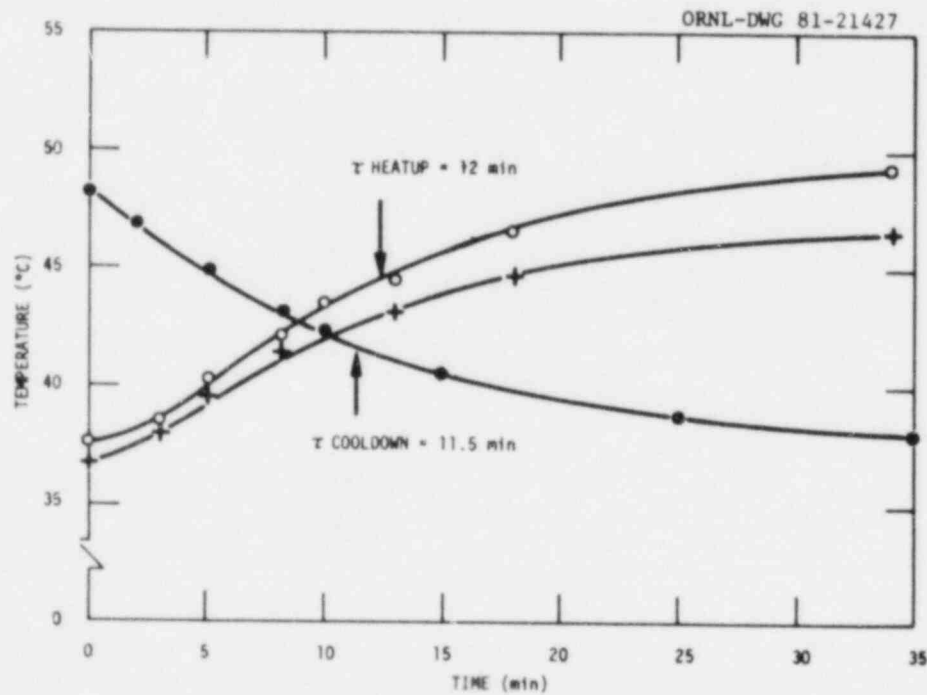
ORNL-DWG 81-21427

Fig 2. Temperature Rise of Thermocouples on the ORR-PSF Surveillance Capsule Due to a Step Input from all Ten Heaters.
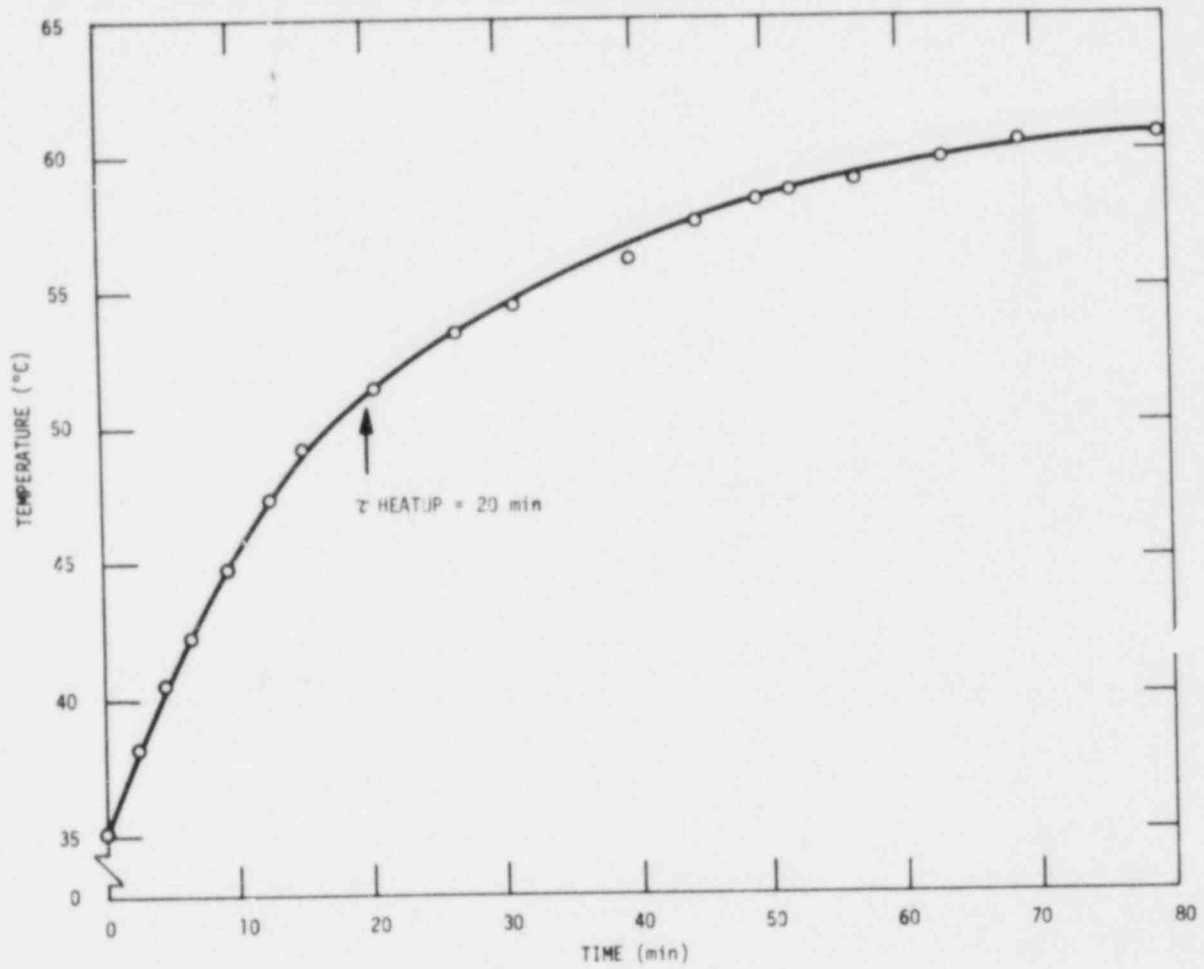
Fig. 3. Temperature Rise of a Pressure Vessel Capsule
Thermocouple Versus Time Due to Heatup with all Heaters.

Table 1. Cumulative Characterization Data for the Simulated Surveillance Capsule Through June 23, 1980.

Hours of Irradiation Time = 1075.29
Megawatt Hours of Irradiation = 32017.57

| Thermocouple | Hours of Irradiation | | | | | Average Temperature | Standard Deviation |
	***<T<270	270<T<280	280<T<296	296<T<306	306<T		
TE 1	20.84	283.91	770.55	0.00	0.00	281.25	2.43
TE 2	15.77	4.70	1045.66	9.17	0.00	291.15	1.64
TE 3	17.82	3.12	1054.34	0.00	0.00	288.49	1.74
TE 4	7.11	9.33	364.74	694.12	0.00	295.39	3.03
TE 5	16.15	3.29	1049.00	6.83	0.00	289.70	1.87
TE 6	8.25	10.78	977.42	78.84	0.00	292.32	1.99
TE 7							
TE 8	19.50	7.78	1047.84	0.17	0.00	286.18	1.82
TE 9	10.81	8.75	702.94	352.80	0.00	295.18	1.87
TE 10							
TE 11	20.05	131.04	924.21	0.00	0.00	281.90	1.40
TE 12	19.23	106.34	949.71	0.00	0.00	283.51	2.84
TE 13	18.63	5.61	1010.84	40.21	0.00	289.42	2.70
TE 14	19.20	2.80	698.51	354.77	0.00	294.82	2.58
TE 15	19.21	5.31	1050.77	0.00	0.00	287.64	1.62
TE 16	23.64	11.49	1040.16	0.00	0.00	285.61	1.69
TE 17	19.20	9.98	1046.09	0.00	0.00	287.05	1.43
TE 18	20.65	11.53	1043.11	0.00	0.00	288.24	2.41
TE 19	19.82	15.85	1039.61	0.00	0.00	284.07	1.43
TE 20	27.85	46.31	1001.14	0.00	0.00	283.61	2.37

NEUTRON DOSIMETRY IN IRRADIATION CAPSULES FOR LARGE REACTOR PRESSURE VESSEL STEEL SPECIMENS

D. Bellmann, J. Ahlf, P. Wille, G. Prillinger[*]
GKSS-Forschungszentrum Geesthacht GmbH
D-2054 Geesthacht, FRG
[*]Universität Stuttgart, IKE
D-7000 Stuttgart 80, FRG

ABSTRACT

RPV steel specimens up to 50 mm in thickness have been irradiated in rigs behind gamma shields of stainless steel in reflector positions of FRG-2, a swimming pool type research reactor operating at 15 MW. To reduce fluence gradients in the specimens the rigs have been rotated several times during the irradiation period. For fast neutron dosimetry the reactions $Fe54(n,p)Mn54$ and $Ni58(n,p)Co58$ have been used. The evaluation of the monitor activation measurements has been based on 1- and 2-dimensional neutron transport calculations. Discrepancies between "Fe- and Ni-fluences" have been reduced by 2-dimensional neutron transport calculations. Fluence and temperature deviations from mean value $\leq 10\%$ respectively $\leq 5K$ can be distinguished, but they lie within the scatter band of the charpy impact test curves of unirradiated material.

INTRODUCTION

Embrittlement of pressure vessels induced by neutrons is a major problem concerning the lifetime of light water reactors. Accurate and appropriate determination of the neutron exposure in the pressure vessel as well as in irradiation rigs is necessary to correlate irradiation damage in different neutron environments. Neutron embrittlement is also very sensitive to irradiation temperature.

Within the reactor safety program of the Federal Republic of Germany irradiation experiments of pressure vessel steel are in progress in order to study the embrittlement due to fast neutrons. Two types of reactor pressure vessel steel ASTM A508 and ASTM A533B in three different conditions, base and welded material and material of heat affected zones are tested with charpy V-notch, tensile, drop weight and fracture mechanics specimens.
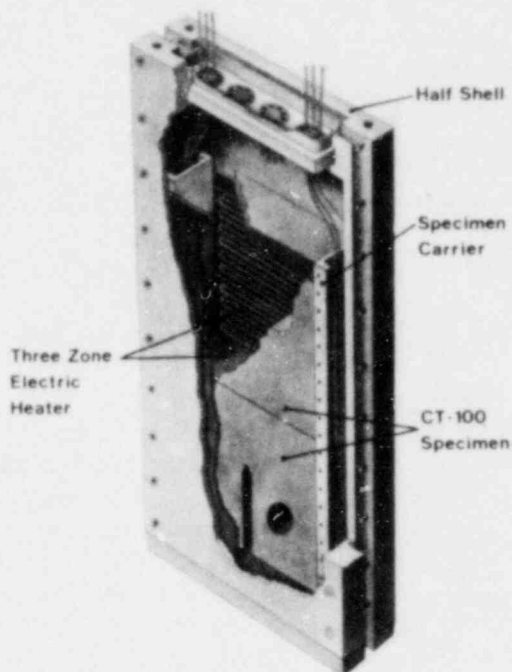
Two protype rigs have already been successfully irradiated in FRG-2 at Geesthacht, a swimming pool type research reactor operating at 15 MW.
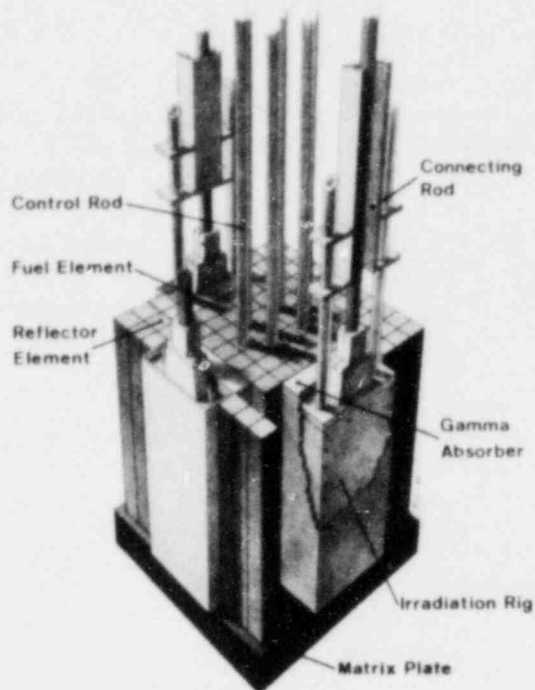
Position of Irradiation Rig in FRG-2

Fig. 1   **GKSS** — FORSCHUNGSZENTRUM GEESTHACHT GMBH

Design of Irradiation Rig

Fig. 2   **GKSS** — FORSCHUNGSZENTRUM GEESTHACHT GMBH

One rig was irradiated up to $2.5 \times 10^{19} n/cm^2$, the other one up to $7.5 \times 10^{19} n/cm^2$, E >1MeV. It is possible to irradiate three rigs of this type at the same time, as shown in fig. 1. The rig, fig. 2, was already described alsewhere[1]. The post irradiation examination of the specimens is in progress now.
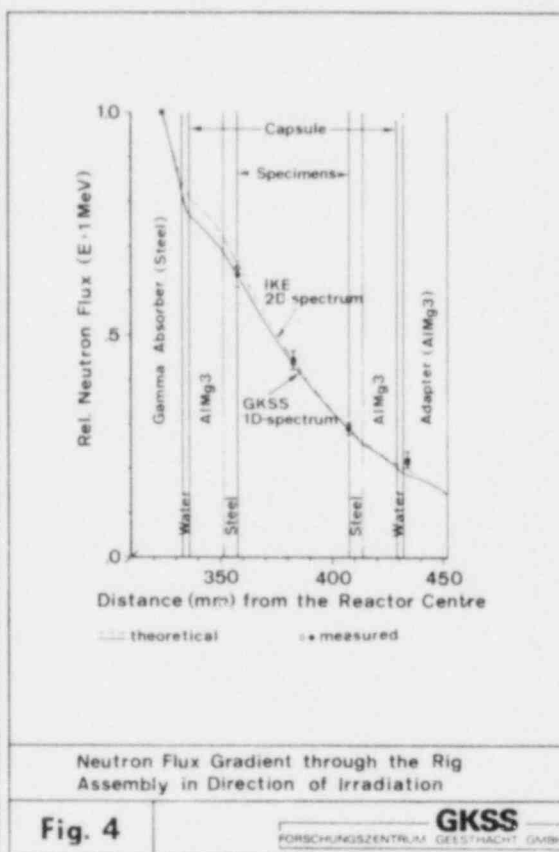
FLUENCE DETERMINATION

The fluence distribution inside the rig was determined by evaluation of activation wires. They consisted of stainless steel (X10CrNiNb 18 9), 0.8 mm in diameter. The Mn54 and Co58 activity was measured by scanning the wire along a Ge(Li)-detector. In order to reduce fluence gradients in irradiation direction the rig was revolved several times along its longitudinal axis during the irradiation period. This had to be taken into account for the evaluation, because each point of a horizontal plane in the rig had seen two different neutron spectra, except the vertical (u-w) middle plane.

First 1-dimensional multigroup neutron transport calculations were carried out with the program NEUTRA[2], based on DTF-IV. The EURLIB-library, condensed to 34 energy groups (10 groups > 1 MeV), was used. The dosimetry cross sections were taken from ENDF/B IV.

It was presumed that neutron spectral effects at the sides could not be neglected because of the large size of the rig compared with the reactor core. Therefore, the calculations were performed with DOT-IV[3] code, using the 100 group EURLIB-library with 31 groups > 1MeV. In this 2-dimensional case the dosimetry cross sections were taken from ENDF/B V.
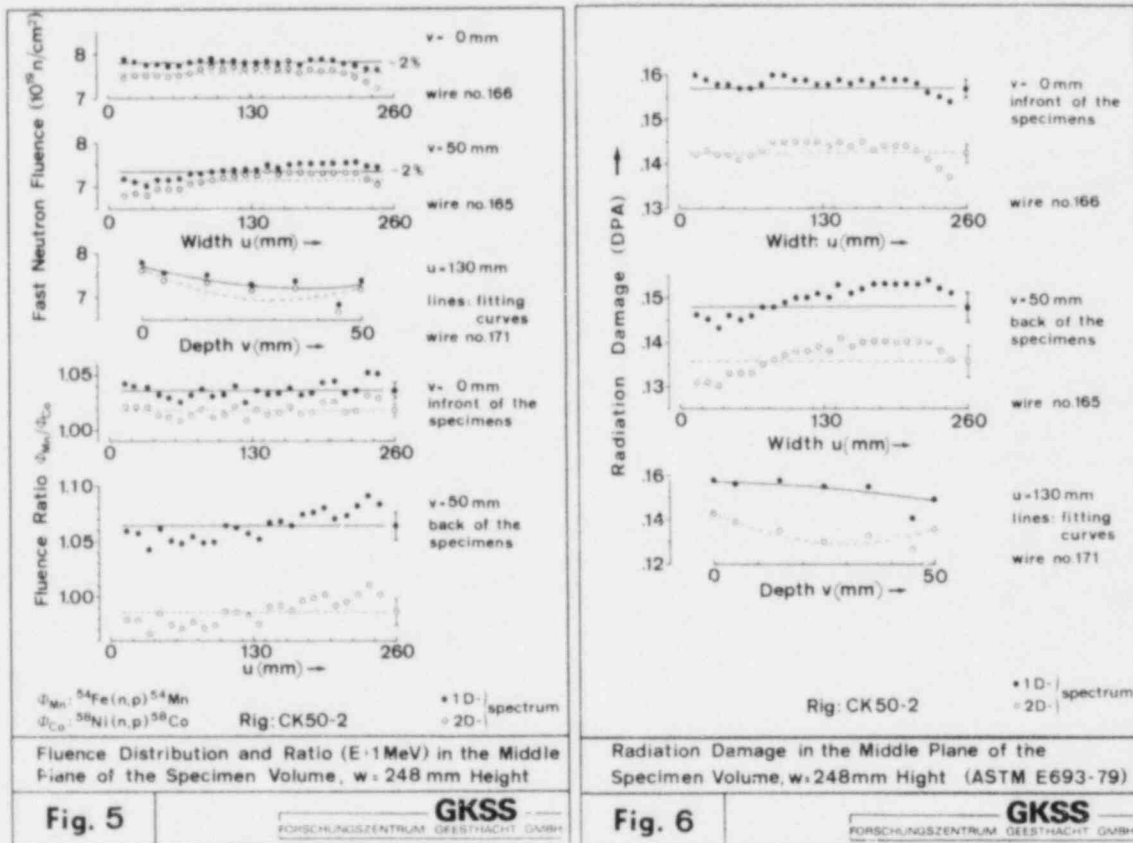
The fast neutron fluence E > 1MeV, obtained from the DOT-calculations are shown in fig. 3. On the left hand the positions of the wires are marked. The fluence distribution was approximated by a modified cosine function. The fluence in u-direction was nearly constant, in v-direction described by a square function. The standard deviation of the approximation was small compared with the errors in the fluence determination. The calculation of the fluence in the fracture plane for each specimen in the rig was made possible by this distribution formula.

The relative neutron flux gradient through the middle of the rig assembly, normalized to a wire position before the rig in the gamma absorber, is shown in fig. 4. Along this center line there are only small differences between 1- and 2-dimensional spectrum calculations. Measured values obtained by evaluation of the activation wires inside the rig agree well with the calculated ones.

Fast Neutron Fluence Distribution, E · 1 MeV
Rig: CK 50-2, v - w - Plane

Fig. 3 — GKSS — FORSCHUNGSZENTRUM GEESTHACHT GMBH

Neutron Flux Gradient through the Rig
Assembly in Direction of Irradiation

Fig. 4 — GKSS — FORSCHUNGSZENTRUM GEESTHACHT GMBH
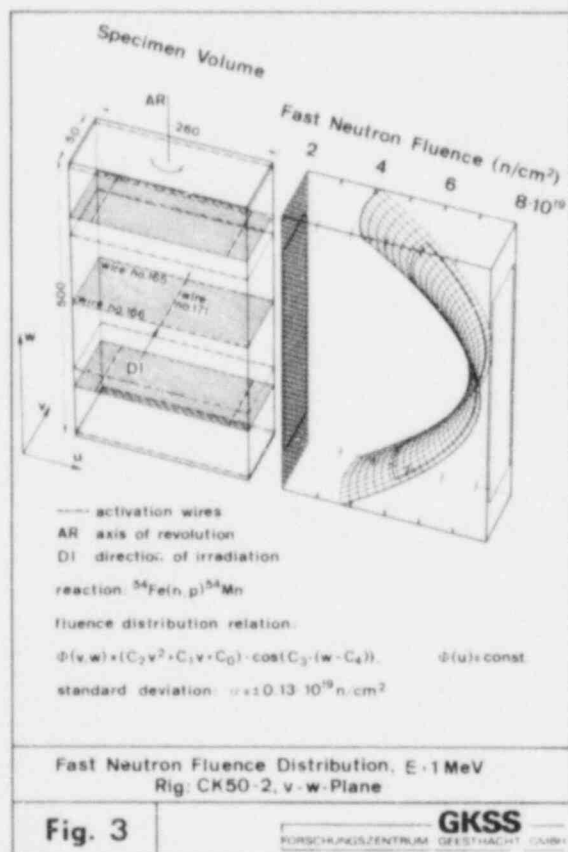
Fast neutron fluence, irradiation damage dpa and averaged neutron cross sections along three activation wires, also marked in fig. 3, are shown in detail in the figures 5, 6, 7 and 8. The results of the other wires show the same tendency. 2-dimensional calculations contrary to 1-dimensional yield a small ascent of the averaged neutron cross sections at the sides of the rig and a slightly steeper slope for the corresponding fast neutron fluence.

In addition the fluence ratio obtained from the Fe(n,p)- and Ni(n,p)-reaction is plotted in fig. 5. It can be seen that the discrepancy between Fe and Ni has been reduced by the 2-dimensional neutron transport calculation.

Fluence Distribution and Ratio (E·1MeV) in the Middle Plane of the Specimen Volume, w·248 mm Height

Fig. 5   GKSS
FORSCHUNGSZENTRUM GEESTHACHT GMBH

Radiation Damage in the Middle Plane of the Specimen Volume, w·248mm Hight (ASTM E693-79)

Fig. 6   GKSS
FORSCHUNGSZENTRUM GEESTHACHT GMBH

583

Neutron Cross Section in the Middle Plane of
the Specimen Volume for $^{54}Fe(n,p)^{54}Mn$, E·1MeV

Fig. 7   **GKSS**
FORSCHUNGSZENTRUM GEESTHACHT GMBH

Neutron Cross Section in the Middle Plane of the
Specimen Volume for $^{58}Ni(n,p)^{58}Co$, E·1MeV

Fig. 8   **GKSS**
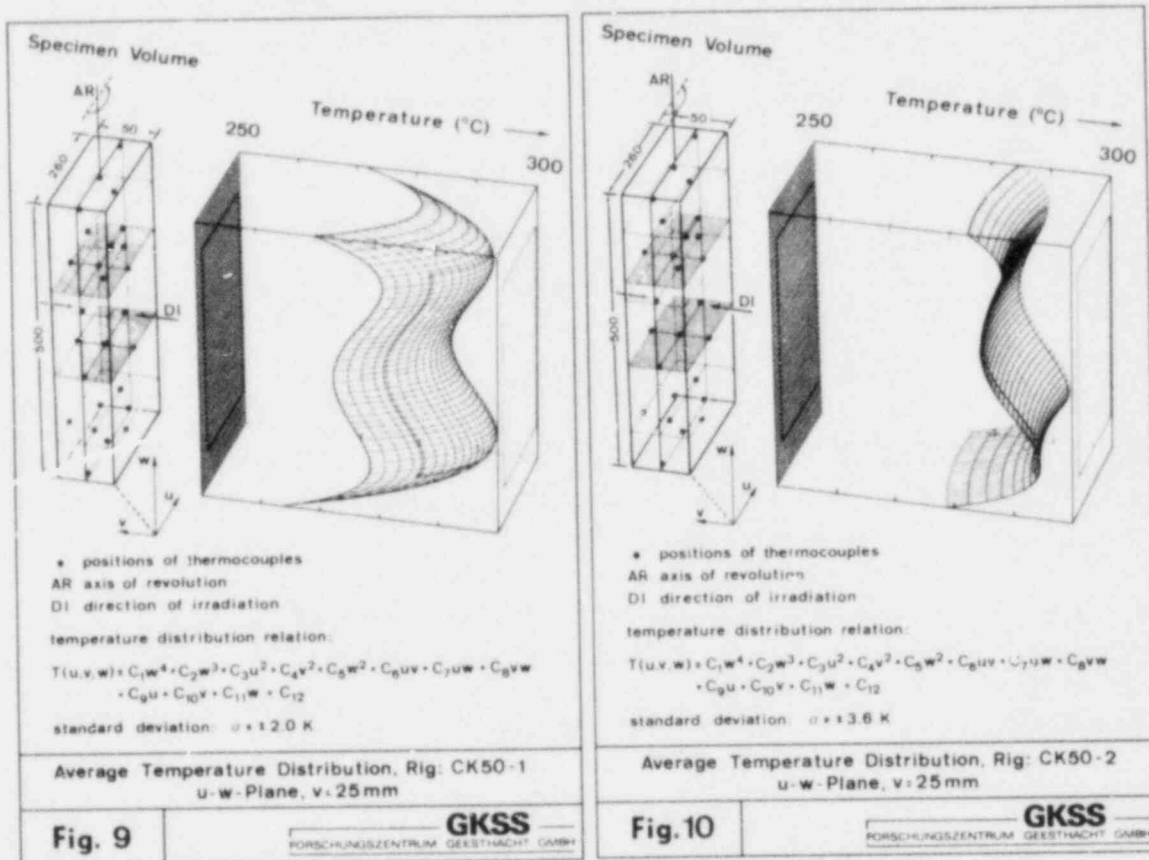FORSCHUNGSZENTRUM GEESTHACHT GMBH

TEMPERATURE DISTRIBUTION

As mentioned before embrittlement is very sensitive to irradiation temperature. Therefore the temperature inside the rig must be measured very exactly and must be constant over the whole irradiation period. Large gradients must be avoided.
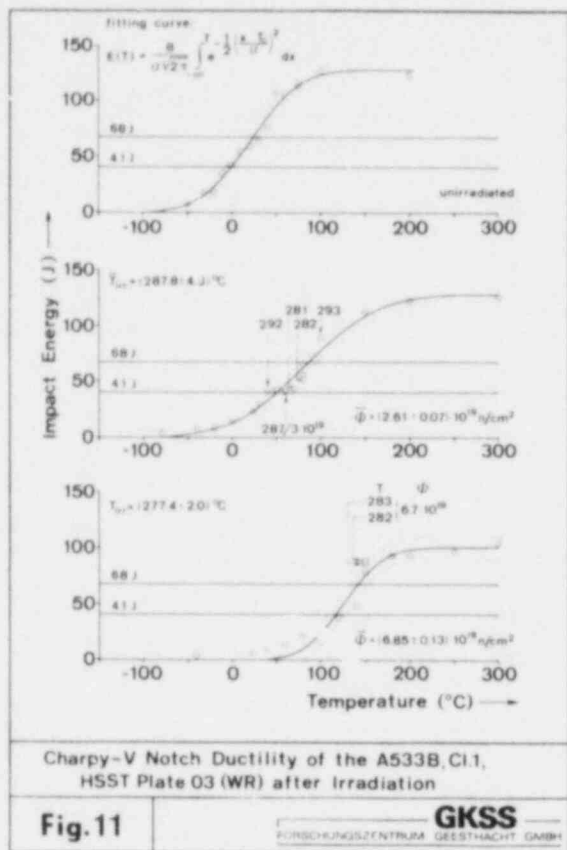
The temperatures inside the rig were traced by 27 thermocouples marked in fig. 9 and 10. The signals were transmitted in a three minute cycle to a processing computer and each signal was averaged over the whole irradiation time.

Fig. 9 — Average Temperature Distribution, Rig: CK50-1, u-w-Plane, v-25mm

Fig. 10 — Average Temperature Distribution, Rig: CK50-2, u-w-Plane, v-25mm

positions of thermocouples
AR axis of revolution
DI direction of irradiation

temperature distribution relation:

$$T(u,v,w) = C_1 w^4 + C_2 w^3 + C_3 u^2 + C_4 v^2 + C_5 w^2 + C_6 uv + C_7 uw + C_8 vw + C_9 u + C_{10} v + C_{11} w + C_{12}$$

standard deviation: $\sigma = \pm 2.0$ K (Fig. 9), $\sigma = \pm 3.6$ K (Fig. 10)

The temperature distribution in the specimen volume was approximated by a polynom of higher order in u-, v-, w-direction. The swing in w-direction originates from the three zone heaters before and behind the specimen volume.

The temperature gradient in u-direction could be avoided in the following rig by auxiliary heaters at both sides, as shown in fig. 10. The temperatures of all specimens lay within 286 ± 9 degrees centigrade.

EFFECTS OF UNCERTAINTIES IN FLUENCE AND TEMPERATURE

Charpy-V Notch Ductility of the A533B, Cl.1,
HSST Plate 03 (WR) after Irradiation

Fig. 11   **GKSS**
FORSCHUNGSZENTRUM GEESTHACHT GMBH

The influence of irradiation temperature and fluence can be seen from charpy impact test plots, fig. 11, for unirradiated and irradiated base material of ASTM A533B, cl. 1, HSST plate 03 in WR orientation. The measured points were fitted to the Gaussian integral. Two charpy V-notch specimen sets were selected for these impact tests. The average irradiation temperature $\overline{T}_{irr}$ and fluence $\overline{\Phi}$, E > 1MeV, of each specimen set with their standard deviations are stated in fig. 11.

Fluence and temperature deviations from mean value $\leq 10\%$, respectively $\leq 5K$ can be distinguished, but they lie within the scatter band of unirradiated material.

REFERENCES

1. J. Ahlf, D. Bellmann, "Irradiation Techniques for large Reactor Pressure Vessel Steel Specimens", p. 483 in Aspects of Nuclear Reactor Safety, P. von der Hardt, H. Röttger, Editor, EUR 6612, 1980

2. A. Krüger, A. Müller, Das Multigruppen-Neutronentransport-Abbrand-programm NEUTRA, GKSS 72/E/15

3. W.A. Rhoades, D.B. Simpson, R.L. Childa, W.W. Engle jr., "The DOT-IV Two-Dimensional Discrete Ordinates Transport Code with Space-Dependent Mesh and Quadrature", ORNL/TM-6529

NEUTRON SPECTRA MEASUREMENTS IN WWR-S REACTOR

B. Ošmera, P. Pittermann, S. Pošta,
Č. Svoboda, F. Tomášek, Z. Turzík,
J. Ulrich, J. Kopecký
Nuclear Research Institute
Řež, Czechoslovakia

ABSTRACT

The neutron energy spectrum for analysis of
the irradiation experiments in WWR-S-10 reactor
has been measured by activation method. For spec-
trum unfolding the SAND-II code has been utilized,
with the cross section data for the detector foils
taken from ENDF/B-IV. The results of measurements
in three channels are presented in multigroup ABBN
format.

EXPERIMENTAL ARRANGEMENTS

The core of the multi-purpose WWR-S-10 irradiation reac-
tor (Nuclear Research Institute Řež) is composed of IRTM ty-
pe fuel elements, Be reflector elements and structural compo-
nents made from normalized aluminum or aluminium based alloy
AD-I and SAV-I+). The lattice pitch is 71.5 mm, the active
fuel lenght 580 mm.

The operational core configuration with marked measuring
points is in Fig. 1. The IRTM fuel elements consists of three
or four concentric tubes of quadratic form. The thickness of
the fuel tube wall is two milimetres, the thickness of the
intrinsic fuel (U - Al metalic dispersion, 80 % U 235 enrich-
ment) is 0.4 mm.

The cladding of the fuel, 0.8 mm thick, is made from
SAV-I alloy. The cross-section of the IRTM fuel element is
presented on the Fig. 2. In the centre of four tube composed

+) The composition of the materials:
   AD-I: Al; impurities (%): Fe 0.3, Si 0.35, Cu 0.05
                             Mg 0.05, others less then 0.1
   SAV-I: 0.7 - 1.2 Si, 0.45 - 0.9 Mg, Al;
      impurities (%): Cu 0.1, Fe 0.2, Zn 0.03, Ti 0.01,
                      Mn 0.01, Ni 0.03, B 0.0001, Cd 0.001

elements is instaled irradiation channel of 16 mm diameter
from SAV-I. The three tube elements are placed at the posi-
tions of the control and safety rods; the fourth tube is re-
placed by rod channel from AD-I alloy. The control rods are
23 mm outer diameter, 1 mm wall thickness, 21 mm boral absor-
ber diameter.

Fuel element
3 tubes

Fuel element
4 tubes

Be reflector

Measuring point
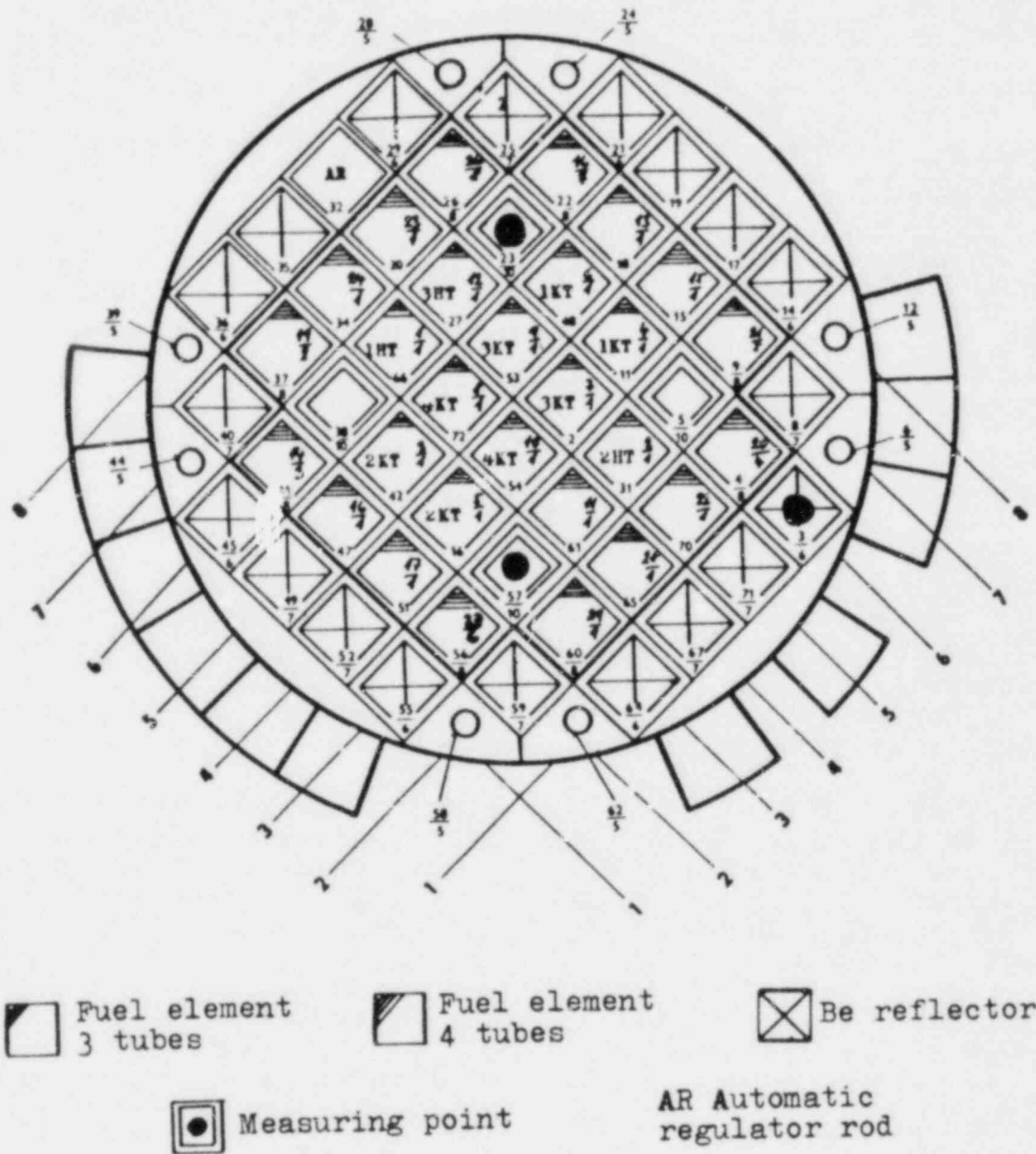
AR Automatic
regulator rod

Fig. 1. The Operational Core Configuration of WWR-S-10
Reactor.

The active lenght of control and safety rods is 600 mm, the bottom part of the rods is joined with aluminium tube of 513 mm lenght and 23 mm diameter. This aluminium part compensates the local increasing of thermal neutron flux density.
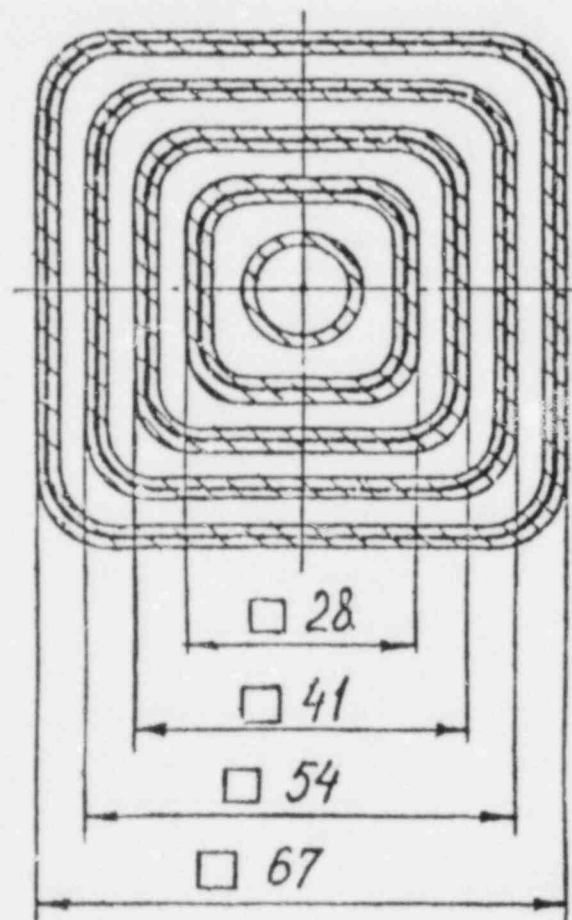
The measuring points location is indicated in Fig. 1; the 57/10 and 3/6 (equiped with pneumatic rabbit) are dry channels, the 23/10 channel is filled with the demineralised water. The inner diameter of 57/10 and 23/10 is 58 mm and 38 mm in channel 3/6.

In this three locations the activation detectors were inserted in aluminium, resp. polyethylene (pneumatic rabbit) capsules with total air volume 94, resp. 50 cubic cm. The weight and composition of the detectors were chosen to follow properly the irradiation scheme (irradiation about 20 minutes at 1 MW power).

The foils were so selected that their combined sensitivities covered the entire energy spectrum from the thermal to the fast neutron region. A set of diluted resonance indicators were prepared by pipetting of the diluted solution of metals (Au, W, U, Mn, Co) on the chromatographic paper foils sealed between two thin (0.1 mm) polyethylene foils (likewise the standard technique in neutron activation analysis). The Au, W and Mn (n,) detectors were also prepared from multicomponent Ni based alloy /3/. All other detectors were prepared from metalic materials, most of them formed disc, 12.7 mm diameter.

Fig. 2. Schematic Cross-
-Section of the IRT-M Fuel
Element.

□ 28

□ 41

□ 54

□ 67

The induced activity was measured by means of gamma -
- spectrometry system Plurimat 20 (Intertechnique), Ge(Li)
detector (NRI) and linear electronics ORTEC. The pulser met-

hod has being used for the pile-up and dead time counting loses correction. The detector efficiency was determined in standardized geometry for 10 cm distance between the foils and detector using the following calibration sources: Am 241, Co 57, Ba 133, Mn 54, Zn 65, Ce 144, Co 60, Cs 134, Eu 152, Ta 182, Ra 226. The decay data of the reactions products from the foil nuclei were taken from the reference /1/. In order to eliminate systematic errors, the reaction rates were also determined by other group with different measuring system (IN-90, Intertechnique, Ge(Li)-NRI, linear electronics ORTEC), the calibrating sources and decay data were the same.

RESULTS

The results of reaction rate measurements at 1 MW power level are presented in Table 1. The SAND-II program /7/ was utilized for spectrum unfolding. The final spectra are presented for two measuring positions in Fig. 3, the normalized group spectra for three channel are presented in Table 2. The group structure from 1 to 25 corespond to ABBN format /2/, the group number 0 contents neutrons above 10.5 MeV, the group 26 is extended down to the 10-10 MeV. The iterative process was performed until satisfaction of the prescribed criterion, which was 5 % total deviation of the measur./calcul. ratio.

The input spectrum was taken from the proton-recoil measurements in ŠR-0 low power reactor loaded with the same type of fuel elements /4,5/. The low energy part was completed with Fermi and Maxwell spectra, the fission spectrum was used in fast region.

The main goal of this work was to improve the neutron monitoring system of the WWR-S-10 irradiation reactor. Practical utility of the listed and other detectors was studied with particular interest in detectors with dominant response in detectors with dominant response in low energy part of neutron spectrum. As well as the previous works /4,5/ the results of recent experiments play an important role in neutron fluence monitoring and analysis of test specimens which are being irradiated in the reactor for the purpose of radiation damage investigation. The pressure vessel lifetime prediction of WWER is also based on the evaluated irradiation experiments in this reactor /6/; the uncertainties in neutron spectra and fluence determination shall be studied furthermore.

REFERENCES

1. W. L. Zijp, J. H. Baard, Nuclear data guide for reactor neutron metrology, report EUR 7164 (1981)

2. L. P. Abagjan et al., Grupovyje konstanty dlja rasčota jaděrnych reaktorov, 1964

3. H. C. Mehner, private communication

4. B. Ošmera et al., Neutron Spectra Measurements and Neutron Flux Monitoring for Radiation Damage Purposes, Procedings of the Third ASTM-EURATOM Symp. on Reactor Dosimetry, p. 1229, Ispra, October 1979

5. B. Ošmera et al., Neutron Spectra Measurements and Neutron Flux Monitoring for Radiation Damage Purposes, report ÚJV 5081-R (Rež, 1979)

6. M. Brumovský, B. Ošmera, V. Valenta, Effect of Uncertainties in Neutron Spectra and Fluences Determination on the WWER Pressure Vessel Lifetime Prediction, IAEA Advisory Group Meeting on Nuclear Data for Radiation Damage Assessment and Related Safety Aspects, Vienna, 12-16 October, 1981

7. W. N. McElroy et al., SAND-II, Neutron Flux Spectra Determinations by Multiple Foil Activation Iterative Method, CCC-112 (1969
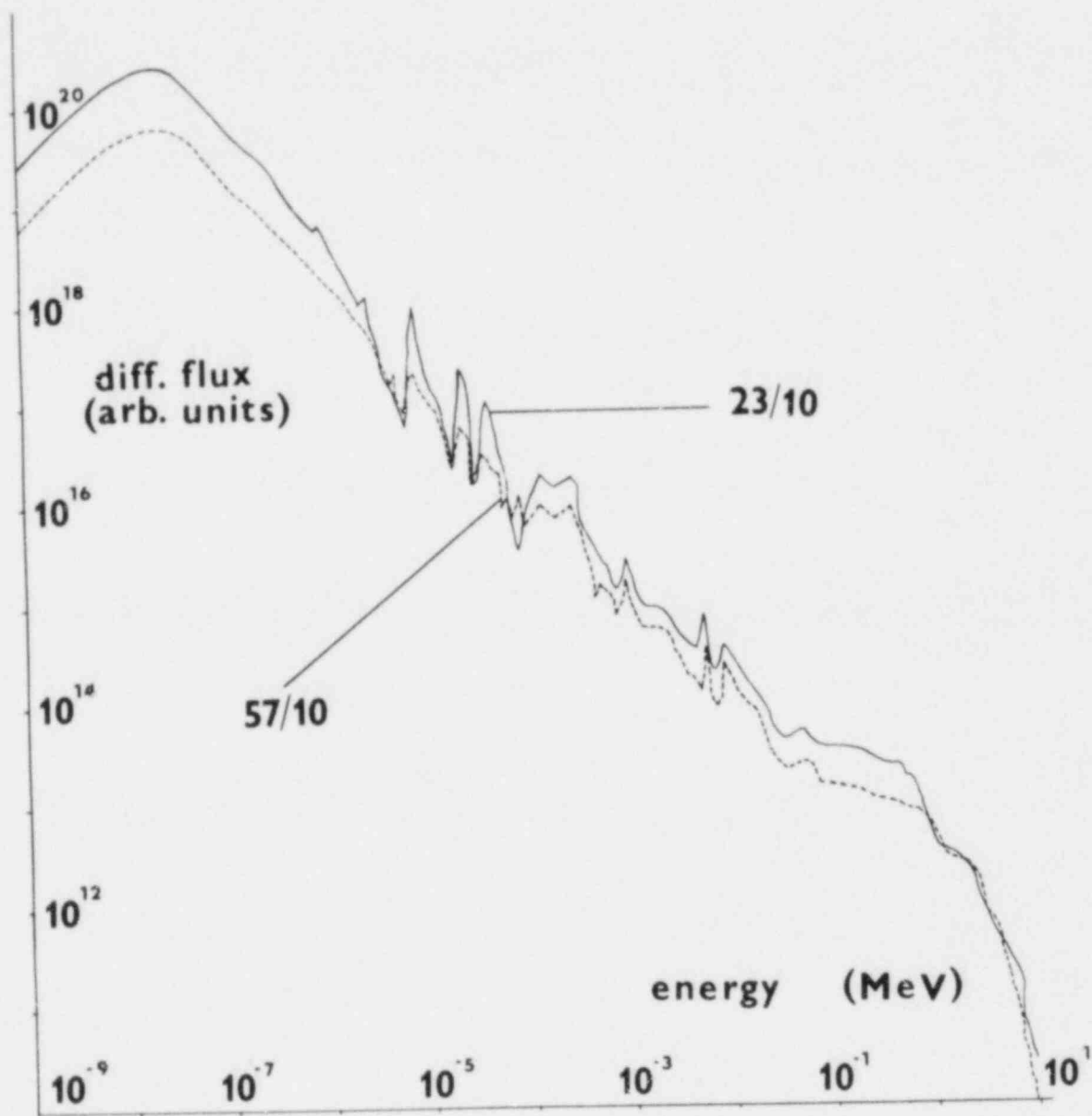
Fig. 3. The Neutron Energy Spectrum in 23/10 and 57/10 Irradiation Channels.

Table 1. Reaction Rates

Reaction	dps/atom		
	23/10	57/10	3/6
^{186}W (n,γ)^{187}W	1.43×10^{-9}	7.16×10^{-10}	5.54×10^{-9}
^{58}Fe(n,γ) ^{59}Fe	2.99×10^{-11}	9.30×10^{-12}	9.12×10^{-12}
^{238}U (n,γ)^{239}U	3.41×10^{-10}	2.68×10^{-10}	1.79×10^{-10}
^{197}Au(n,γ)^{198}Au	3.81×10^{-9}	2.01×10^{-9}	1.50×10^{-10}
^{55}Mn(n,γ) ^{56}Mn	3.27×10^{-10}	1.05×10^{-10}	1.04×10^{-10}
^{59}Co(n,γ) ^{60}Co	9.39×10^{-10}	2.78×10^{-10}	3.28×10^{-10}
^{54}Fe(n,p) ^{54}Mn	7.42×10^{-13}	7.28×10^{-13}	3.00×10^{-13}
^{24}Mg(n,p) ^{24}Na	1.51×10^{-14}	1.56×10^{-14}	6.05×10^{-15}
^{46}Ti(n,p) ^{46}Sc	9.31×10^{-14}	1.03×10^{-13}	
^{47}Ti(n,p) ^{47}Sc	1.74×10^{-13}	1.83×10^{-13}	6.79×10^{-14}
^{48}Ti(n,p) ^{48}Sc	2.77×10^{-15}	2.88×10^{-15}	1.29×10^{-15}
^{56}Fe(n,p) ^{56}Mn	1.05×10^{-14}	1.00×10^{-14}	4.23×10^{-15}
^{238}U (n,f)^{140}Ba	3.13×10^{-12}		
^{235}U (n,f)^{140}Ba	1.28×10^{-8}	4.01×10^{-9}	
^{27}Al(n,α) ^{24}Na	7.66×10^{-15}	7.61×10^{-15}	2.62×10^{-15}
^{27}Al(n,p) ^{27}Mg			1.77×10^{-14}
^{58}Ni(n,p) ^{58}Co	6.74×10^{-13}	7.34×10^{-13}	4.18×10^{-13}
absolute integral neutron flux above 1×10^{-10} MeV (m^{-2} s^{-1})	9.481×10^{17}	4.587×10^{17}	3.475×10^{17}

Table 2. Normalized Group Fluxes

Group	23/10	57/10	3/6
0	1.274-4	2.537-4	1.069-4
1	1.744-3	3.705-3	1.970-3
2	7.245-3	1.756-2	1.106-2
3	2.169-2	4.347-2	2.005-2
4	3.491-2	6.623-2	2.877-2
5	4.381-2	9.003-2	4.638-2
6	8.689-2	8.629-2	8.680-2
7	6.183-2	5.704-2	5.364-2
8	3.861-2	3.689-2	3.649-2
9	2.607-2	2.770-2	2.943-2
10	1.608-2	1.919-2	2.336-2
11	2.393-2	2.967-2	3.769-2
12	1.823-2	2.242-2	2.643-2
13	1.942-2	2.379-2	2.190-2
14	1.649-2	2.224-2	2.411-2
15	1.270-2	1.860-2	1.739-2
16	3.360-2	3.227-2	4.645-2
17	1.863-2	2.314-2	3.389-2
18	1.997-2	2.245-2	3.705-2
19	3.140-2	2.816-2	3.607-2
20	2.367-2	2.447-2	2.570-2
21	3.123-2	2.252-2	2.376-2
22	2.041-2	2.407-2	2.969-2
23	4.017-2	3.439-2	4.554-2
24	4.460-2	3.542-2	4.644-2
25	6.649-2	4.246-2	4.912-2
26	2.401-1	1.456-1	1.603-1

Discarded foils	$^{58}Ni(n,p)$	$^{58}Ni(n,p)$	$^{47}Ti(n,p)$ $^{48}Ti(n,p)$